50 Jahre

RUB

International Conference on
Stone and Concrete Machining

3rd ICSCM

02.-03.11.2015

Ruhr-Universität Bochum
Conference proceedings

3$^{\text{rd}}$ International Conference on Stone and Concrete Machining (ICSCM) –Conference Proceedings–

Bochum, 02.-03.11.2015

Editors: Werner Theisen, Berend Denkena, Wolfgang Tillmann

3rd International Conference on Stone and Concrete Machining – Proceedings

Preamble

The machining and manufacturing of natural stone and of stone-like construction materials are expanding businesses. Concrete drilling and sawing companies as well as granite and marble machining businesses are facing increasing demands for their products and services.

Additionally, there is a need for basic scientific research concerning tool materials, manufacturing process and the interaction between the tool and the work piece material. Therefore, the cooperation and interaction between stone processing and tool producing companies is of great importance. This conference addresses experts from industry and research to present and discuss current developments around the machining and the processing of stone and concrete in industrial applications, as well as the progress in the development of tool materials and surface engineering. Beside this there is a special focus on mechanisms of abrasion and the development of abrasion resistant materials.

The conference is organized by the Institute of Materials Technology (LWT) of the Ruhr-Universität Bochum, The Institute of Materials Engineering (LWT) of the TU-Dortmund and the Institute of Production Engineering and Machine Tools (IFW) of the Leibniz Universität Hannover.

Bochum, November 2015

Prof. Dr.-Ing. Werner Theisen
Head of the Institute of Materials Technology
Ruhr-Universität Bochum
Bochum, Germany

Contents

Contents

Session 1

Numerical simulation of fatigue crack propagation in WC-Co hardmetal

Utku Ahmet Özden, Keng Jiang, Alexander Bezold, Christoph Broeckmann
Institute for Materials Applications in Mechanical Engineering (IWM) RWTH Aachen University,
Augustinerbach 4, 52062, Aachen, Germany
Tel: +492418099537, u.oezden@iwm.rwth-aachen.de

Jose María Tarragó, Alvaro Mestra, Luis Llanes
Departament de Ciència dels Materials i Enginyeria Metallúrgica (CIEFMA), ETSEIB, Universitat
Politècnica de Catalunya, Avda. Diagonal 647, 08028, Barcelona, Spain

ABSTRACT

WC-Co cemented carbides (hardmetals) are a group of composite materials exhibiting outstanding combinations of hardness and toughness. As a consequence, they are extensively used for highly demanding applications, such as cutting and drilling tools, where cyclic loading is one of the most critical service conditions.

A numerical study of the mesoscale fatigue crack growth in WC-Co is here conducted. Within this context, a model based on a continuum damage mechanics approach was implemented in commercial solver Abaqus/Explicit for simulating the crack propagation in the material. Separate damage laws, based on brittle failure and fatigue, were used for describing the mechanical response of WC and Co phases, respectively. Material parameters for the carbide phase were taken from literature, whereas those for the metallic phase were experimentally determined in a model binder-like Co-base alloy, i.e. one with a composition representative of the binder phase within a commercial hardmetal grade.

In order to validate the approach used, a numerical model based on a real damaged microstructure was generated. It is found that proposed model is capable of capturing damage evolution with cyclic loading in WC-Co, as numerical results reflect satisfactory agreement with real crack pattern resulting from experiments.

KEYWORDS

WC-Co; Hardmetals; Finite Element Method (FEM); Continuum Damage Mechanics (CDM); Fatigue; Crack propagation; Microstructure.

INTRODUCTION

WC-Co cemented carbides, also referred to as hardmetals, are one of the most widely used composite materials because of their exceptional combination of hardness, strength and wear resistance. Main reason behind it is the quite different, but complementary, mechanical properties exhibited by their two interpenetrating phases: a hard, brittle (elastic) ceramic phase (WC) and a soft, ductile (elasto-plastic) metallic one (Co). Strength degradation of cemented carbides under cyclic loads is a phenomenon known since the early 1940s [1]. Since then, extensive and systematic research conducted by different groups worldwide has allowed to establish that hardmetals are fatigue-sensitive [2]. In general, a tradeoff between monotonic (fracture strength

and toughness) and cyclic (fatigue strength and crack growth resistance) properties is discerned with increasing binder content and carbide grain size, pointing out the compromising role of the ductile binder as the toughening- and fatigue-susceptible agent in these materials. However, to the best knowledge of the authors, most of the work published regarding fatigue of these materials has mainly concentrated in experimental approaches (e.g. Refs. [3-6]). On the other hand, although some numerical studies dealing with microcrack initiation and propagation in WC-Co materials are found in open literature, they are completely limited to mechanical response under monotonic loading [7,8].

Following the above ideas, it is the main focus of the present study to simulate the mesoscale crack propagation in WC-Co under cyclic loads, using finite element (FE) method. In this study, a model based on a continuum damage mechanics (CDM) approach, together with an element elimination based simulation technique, was used to describe the crack propagation in the material. In this regard, brittle and ductile damage laws were implemented for WC and Co phases respectively. The material parameters for WC are taken from literature. Meanwhile, the material parameters for the metallic phase are experimentally determined from the mechanical response exhibited by a model binder-like alloy. It permits to identify parameters for defining accurate plasticity and damage models in the metallic phase. Details of these works are provided elsewhere [9]. Finally, aiming to validate the developed approach, a numerical model based on a real damaged microstructure is generated, and the results of the two studies are compared.

1. EXPERIMENTAL WORK

In order to conduct fatigue crack growth (FCG) experiments, hardmetal samples specific for the current study were produced. A material containing a relatively high carbide content was preferred for industrial relevance. Accordingly, an experimental grade, referred to as "E10", was produced by Ceratizit S.A. Basic microstructural, physical and mechanical characteristics for the material studied are listed in Table 1.

Table 1. Basic microstructural, physical and mechanical characteristics of the E10 grade.

	WC wt. %	WC vol. %	Vickers Hardness (HV)	WC grain size μm	Elastic Modulus - E (GPa)	Poisson's ratio - ν	Density (g/cm^3)
E10	89.9	83.5	1190	2.09	582.3	0.224	14.5

FCG samples were produced such that chemical composition of the binder within the composite was as close as possible to that exhibited by the referred model binder-like alloy [9]. They were then machined and ground into prismatic specimens having dimensions of 45x10x5 mm. Longitudinal surfaces were polished up to mirror-like finish, in order to avoid residual stresses induced by previous grinding stages. Samples were then single-edge notched (SENB) by electrical discharge machining. It was followed by notch tip sharpening using a razor blade impregnated with diamond paste. The resulting notches had dimension of ~2 mm length with a tip curvature of ~8 μm (Fig.1).

In order to nucleate a sharp crack out of the notch tip, cyclic compressive loads were first applied on the specimens by means of a standard four point bending setup. Stable crack growth was observed during cyclic compression, with nucleated cracks being arrested after an extension of ~30 μm. However, it is already known from literature that, after cyclic compressive loading, residual tensile stresses might occur in the vicinity of the notch due to the cyclic plasticity during unloading

from the maximum compression [10]. This was overcome by further propagation of the microcracks, under cyclic tensile loading, such that they could be extended far from the region close to notch tip [11]. This was done by imposing a stress intensity range just above to the expected threshold one, about 7.2 MPa.m$^{1/2}$ for a hardmetal microstructure similar to the one exhibited by E10 specimen [11], to avoid unstable crack extension. FCG rate measurements were divided into certain number of steps with respect to number of cycles. After each step, crack length was measured and the max/min applied loads were recalculated in order to maintain a constant ΔK. Microcracks were propagated during 50,000 cycles. Image sequence of the above-mentioned process: notching, crack nucleation and stable crack growth in the near threshold regime is shown in Fig.2. A series of samples were successfully cracked, and growth behavior of these microcracks was used for implementing the numerical simulation procedure.
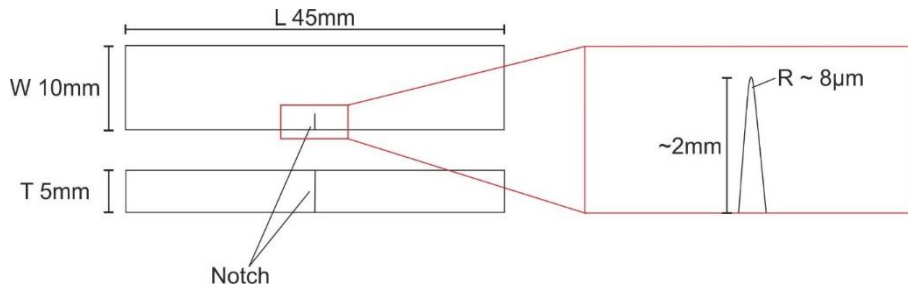
Fig.1. Schematic representation of the E10 test specimen.

Since specimens were through-thickness notched, microcrack formation was observed on both sides of the specimen. Based on detailed SEM imagery, microcrack profile of the sample on both sides was obtained. Microcracks of 226 and 433 μm, running on front and back surfaces of the sample, were recorded. Crack paths in the SEM mosaics are highlighted Fig.3.

As observed from the images, microcracks follow almost a linear pattern, without any branching. However, a detailed inspection indicates that there exist several breaks in the cracks paths. There are a couple of possible explanations for such finding. First, samples were placed in the SEM chamber right after the experiment, without any further surface treatment. Therefore, it is quite a challenge to track the crack path within the binder phase, since the crack pattern mainly diminishes in the background. Second, there is a strong possibility that in-between breaks, crack path is still continuous, but below the surface. Furthermore, since the intensity of the breaks increases mainly at the end of the path, it is possible that crack paths at those regions were not fully developed, resulting then in partial crack patterns. Nevertheless, for each case it was possible to track uninterrupted microcrack patterns, feasible enough for direct comparison with findings from the numerical studies.

Although the microcracks were observed on both surfaces, only the microcracks running on one side of the specimens were selected for the simulation. Cleanness of the notch region and the microcrack profile for the numerical modelling was the major criteria for the selection. In this regard, the back surface of the sample was selected for the simulations.
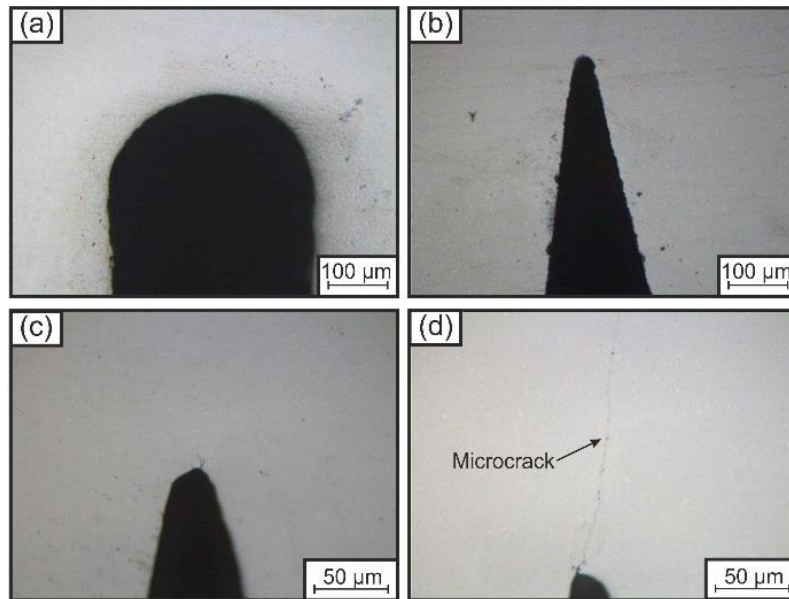
Fig.2 Fatigue precracking of E10 notched specimen, (a) notch generation by EDM (~200 µm), (b) sharpening of the notch by the razor blade (~8 µm), (c) nucleation of the microcracks under cyclic compression (reverse bending), and (d) propagation of the microcrack under cyclic tension (tensile bending).
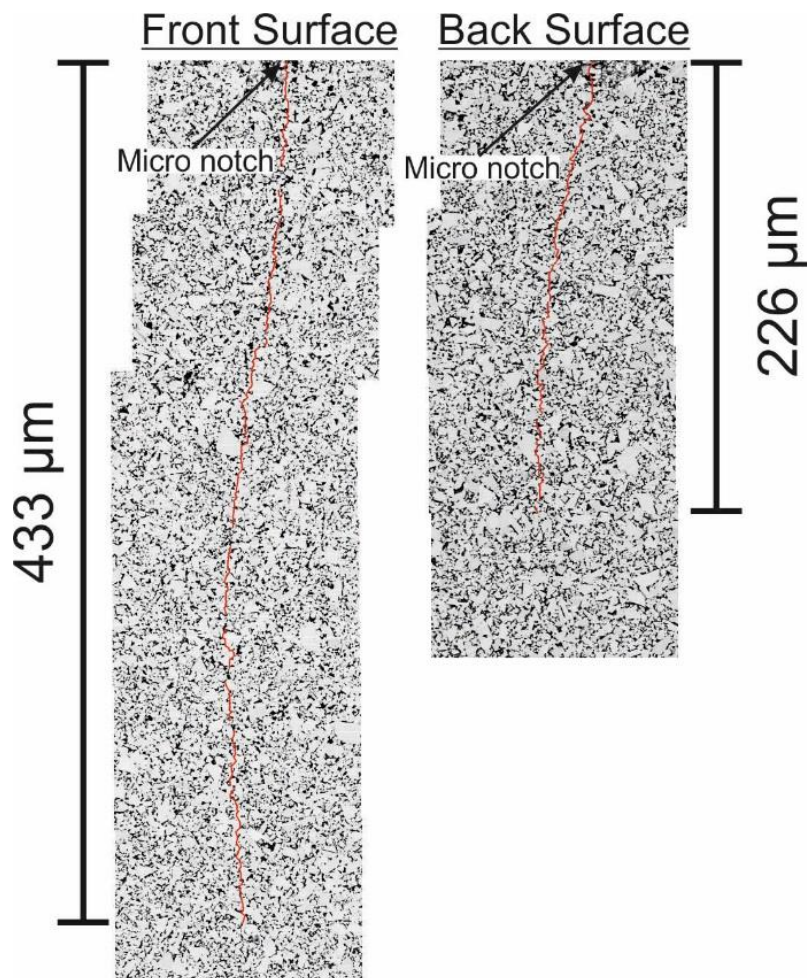
Fig.3 Microcracks observed on the front and back surfaces near the notch region for the experimental specimen ($\Delta K = 7.2$ MPa.m$^{1/2}$, N = 50,000).

2. NUMERICAL METHODOLOGY

Both phases of the material were modeled based on a CDM approach with quite distinct damage laws. Based on this approach, elements are either degraded or removed from the model as soon as certain damage criteria are met, and both lead to a degradation of global stiffness. Similar techniques have also been applied by other researchers [12]. Implementation of this technique required material models for both phases to be developed as user defined material subroutine (VUMAT) in the commercial software Abaqus 6.12 [13]. Solutions were then calculated in the FEM solver Abaqus using an explicit scheme, in order to overcome numerical divergence problems.

A relatively simple damage law based on the maximum principal stress (σ_I) was recalled for the brittle carbide phase. The corresponding linear elastic constitutive equation is defined by generalized Hooke's law:

$$\boldsymbol{\sigma} = \boldsymbol{C}^{el} : \boldsymbol{\varepsilon} \tag{1}$$

where $\boldsymbol{\sigma}$, $\boldsymbol{\varepsilon}$ and $\boldsymbol{C}^{el}$ are the second order stress tensor, strain tensor and fourth order elasticity tensor respectively, and σ_1 is defined in 2D plane stress as:

$$\sigma_1 = \frac{(\sigma_{xx}+\sigma_{yy})}{2} + \sqrt{(\frac{\sigma_{xx}-\sigma_{yy}}{2})^2 + \sigma_{xy}{}^2} \tag{2}$$

where σ_{xx}, σ_{yy}, σ_{xy} are the normal and shear components of the stress tensor. Based on the above law, within the subroutine damage for the WC grain is triggered as soon as the critical failure stress value is achieved ($\sigma_1 \geq \sigma_{1c}$). Thus, the element is eliminated from the global stiffness matrix in the next sequential step.

Material properties such as the elastic modulus (E) and poison's ratio (ν) for the WC were derived from literature. However, to the best knowledge of authors, an exact value of the maximum critical strength for a single carbide grain is not available in open literature. Moreover, it is known that tungsten carbide crystals are highly anisotropic [14]. WC-Co composites with very high carbide content (90-95 wt. % WC) may reach transverse rupture strength values up to 4000 MPa [15]. Therefore, being the most relevant, this value was adopted as an averaged single value for the maximum critical principal stress (σ_{1c}) for the WC phase. Material parameters for this ceramic phase, to be later used for the simulation, are given in Table 2.

Regarding the metallic binder, a non-linear damage law based on accumulated plastic strain was defined. In CDM, formulation of the constitutive equations for strain and damage characterizes the plain material itself, without any volume or surface discontinuity. Hence, the damage parameter D can be defined as the surface density of microcracks and microvoids when only isotropic damage is considered:

$$D = \frac{\delta S_D}{\delta S} \tag{3}$$

where δS_D and δS are the damaged and total surface areas respectively. Thus, considering a homogenized response within a single element, the "effective stress" is defined as the stress acting on the resisting area, i.e. $\delta \bar{S} = \delta S - \delta S_D$.

In the case of isotropic damage under uniaxial loading, without the closure effect of microcracks in compression, the mean value of the microstresses is simply given by the force equilibrium as [16]:

$$\widetilde{\sigma} = \frac{\sigma}{(1-D)} \tag{4}$$

where D is the scalar damage parameter, and σ and $\tilde{\sigma}$ are the actual and effective stresses respectively. The effective yield function based on a non-linear combined hardening law is defined as:

$$\tilde{f} = (\tilde{\boldsymbol{\sigma}} - \boldsymbol{\alpha})_{eq} - R - \sigma_y \tag{5}$$

where α, σ_y, R are the back stress, the yield strength and the isotropic hardening stress respectively. Evolution of α with plastic strain (ε_p) may be described by a function including the hardening modulus c, the dynamic rate of backstress γ and the plastic strain itself, according to [17]:

$$\boldsymbol{\alpha} = \frac{c}{\gamma}(1 - e^{-\gamma \varepsilon_p}) \tag{6}$$

Considering a material subjected to J_2 flow theory, thus (5) can be explicitly written as:

$$F(\tilde{\boldsymbol{\sigma}} - \boldsymbol{\alpha}) = \sqrt{\frac{3}{2}(\tilde{\sigma}_{ij}^D - \alpha_{ij}^D)(\tilde{\sigma}_{ij}^D - \alpha_{ij}^D)} - R - \sigma_y \tag{7}$$

In this equation, $\tilde{\sigma}_{ij}^D$ and α_{ij}^D are the deviatoric part of the effective and backstress tensors, and the associated plastic flow is given by:

$$\dot{\boldsymbol{\varepsilon}} = \dot{\boldsymbol{\varepsilon}}_e + \dot{\boldsymbol{\varepsilon}}_p \tag{8}$$

$$\dot{\boldsymbol{\varepsilon}}_p = \frac{\partial F}{\partial \boldsymbol{\sigma}} \dot{\varepsilon}_{eq}^{pl} \tag{9}$$

$$\dot{\varepsilon}_{eq}^{pl} = \sqrt{\frac{2}{3} \dot{\boldsymbol{\varepsilon}}_p : \dot{\boldsymbol{\varepsilon}}_p} \tag{10}$$

where $\dot{\varepsilon}$, $\dot{\varepsilon}_e$, $\dot{\varepsilon}_p$ are the total, elastic and accumulated plastic strain rates, and $\dot{\varepsilon}_{eq}^{pl}$ is the equivalent (accumulated) plastic stain rate, respectively. The full damage constitutive equation for the Co phase is derived from [18], and defined in the user subroutine as follows:

$$\dot{D} = \begin{cases} \left(\frac{\Gamma}{H}\right)^h \dot{\varepsilon}_{eq}^{pl}, & if \ \varepsilon_{eq}^{pl} > 0 \\ 0, & if \ not \end{cases} \tag{11}$$

where

$$\begin{cases} \Gamma = \frac{\tilde{\sigma}_{eq}^2 R_v}{2E} \\ R_v = \frac{2}{3}(1 + v) + 3(1 - 2v)\left(\frac{\sigma_H}{\sigma_{eq}}\right)^2 \end{cases} \tag{12}$$

being Γ the energy density release rate, R_v the triaxiality function, E the elastic modulus, v the Poisson's ratio, σ_H the hydrostatic stress and σ_{eq} the equivalent stress. Here the variables h and H are two material parameters which depend on temperature. Since temperature has no effect on the current study, both parameters were set to unit values. Similar to the case for the carbide phase, damage for the metallic one is triggered as soon as the critical damage parameter is achieved ($D \geq D_c$), resulting in the elimination of the element from the global stiffness matrix in the next sequential step.

Material properties for the Co phase, required for the simulation, were mainly derived from the experiments conducted with the referred representative binder alloy [9]. Various test specimens were produced from the alloy and material parameters such as the elastic modulus (E), yield stress

(σ_y), hardening modulus (C), and the dynamic rate of the backstress (γ) were determined from standard tensile and cyclic load experiments. The value for the Poison's ratio (v) and the critical damage parameter (D_c) were taken from literature (Table 2).

Table 2. Material properties for the WC and Co phases.

Material	E (GPa)	v (-)	σ_y (MPa)	C (GPa)	γ (-)	D_c	σ_{1c} (MPa)
WC	700[19]	0.24[19]	-	-	-	-	4000
Co	227.28	0.3[19]	683.07	52.38	151.64	0.3[18]	-

3. MULTISCALE SIMULATION

For the numerical simulation, a multiscale approach was preferred. In this regard, initially the FCG specimen (macroscale) was simulated analogue to the experimental setup. In order to simulate fatigue crack evolution, a certain section of the specimen's microstructure (mesoscale) was modelled. Dimensions of this section were chosen based on the computational capacity and robustness of the model. The link between the two scales was conducted by a simplified sub-modelling approach. Since the original orientation of the microcrack surface is already known, the global stresses derived from a single critical element were mapped over the later generated microstructure model. By doing so, a direct link between macro- and meso-scales was generated. The implementation of the selected approach is described below.

A macroscopic numerical model was initially generated. It was done on the basis of the experimental E10 specimen (see Fig.1) and testing conditions. In high cycle fatigue experiments, samples are submitted to very low external loads and the stress caused by these loads do not exceed the macroscopic yield limit at any material point. Therefore, plasticity was neglected for the model, and the linear elastic material parameters (E and v) for the WC-Co were used (Table 1). The model was simplified based on the symmetric nature of the sample and the test setup. The resulting model was composed of 286,225 first order linear elastic hexahedral elements (Fig.4)
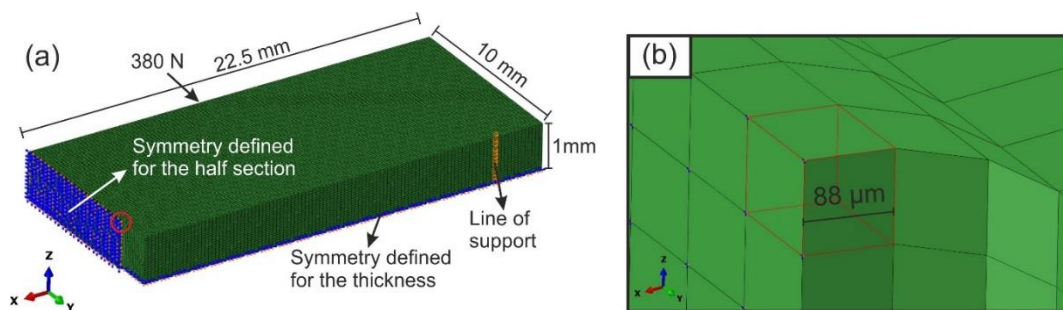
Fig.4 FE model based on the SENB specimen, (a) standard four-point bending configuration, (b) critical hexahedral element for calculating the global stresses.

A single static solution was conducted for the maximum and minimum loads applied on the specimen. Since the applied load over the specimen was cycled with a constant load ratio of 0.1, only the maximum applied load of 1520 N (380 N due to quarter model) was applied on the macroscopic model. As expected, the stress state from the hexahedral element located on the edge of the micronotch was observed to be critical (Fig.4b). Therefore, assuming a stress state unified over the single element, the stress tensor components for this single element were extracted. However, in order to decrease the excessive computational demand, a 2D plane stress simplification was used for the microstructural model. It is known that plane stress elements are suitable for simulating surface cracks [20]; thus, only the surface microstructure of the sample was modeled. Based on the orientation of the 2D surface over the hexahedral element, only the global stress components acting over the surface ($\Sigma_{xx}, \Sigma_{xy}, \Sigma_{yy}$) were mapped to the microstructural model. From the single integration point of the critical element, values of 437.3 MPa, 114.4 MPa and 97.9 MPa were calculated for the $\Sigma_{xx}, \Sigma_{xy}, \Sigma_{yy}$ respectively.

For the modelling of the microstructural model, sections of the SEM images were used. Considering numerical efficiency and complications in model generation, the model was limited to a size of 65x65 µm. The average element size used was calculated to be 0.3 µm for optimum performance; hence, microscopic details below this threshold value were omitted. However, in some critical regions (especially where crack propagation was observed) such details were kept by local enrichment in the mesh. The existing microcrack was deleted from the model, and the microscopic forces derived from the global stress components were applied over the two edges of the model. In order to initiate the microcrack in the correct position, a few elements were deleted to create an initial crack of ~2.5 µm. For the conversion of the global stress components to the microscopic forces, a unit thickness for the model was assumed. For the other edges of the model, simple symmetric boundary conditions were defined (Fig.5). Similar to the experimental testing conditions, cyclic loading was defined as following a constant sinusoidal frequency and under a load ratio of R = 0.1. The predefined material properties were applied for the WC and Co phases (Table 2).
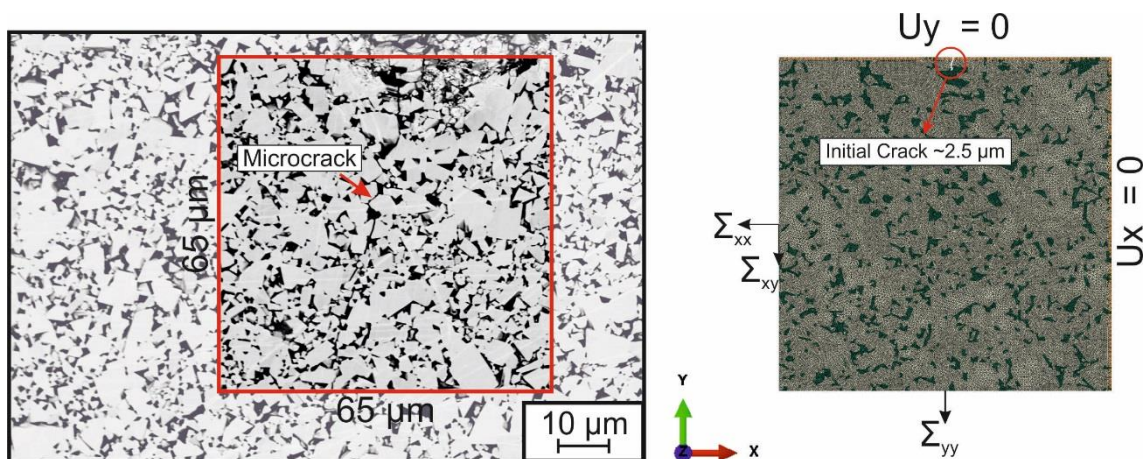
Fig.5 Microstructural FE model and the corresponding boundary conditions, based on the SEM images near the notch region.

4. RESULTS AND DISCUSSION

Based on the simulation results, cyclic evolution of the microcrack was successfully observed within the microstructural model. It is shown in Fig. 6 as a series of sequential images. The microcrack propagates in a stable manner, from the initially defined crack position, up to 330 cycles. As the crack reaches a carbide boundary, the stress level ahead of the crack tip is required to be higher than the defined damage criterion (σ_{1c}) to observed rapid crack propagation through

the WC phase. This extension generally occurs in a single cycle, as expected from the perfectly brittle material definition implemented for the WC phase. On the other hand, as the crack reaches the Co phase, its propagation is controlled by the cyclic accumulation of plastic strain. Further stable crack propagation combined with sudden jumps as the crack meets and overcomes a carbide boundary finally lead to unstable crack growth (Fig. 7). As highlighted before, recent observations in literature indicate degradation (or even inhibition) of toughening mechanism for the Co phase as the driving force for subcritical FCG in hardmetals [6], and this is also captured by the model.
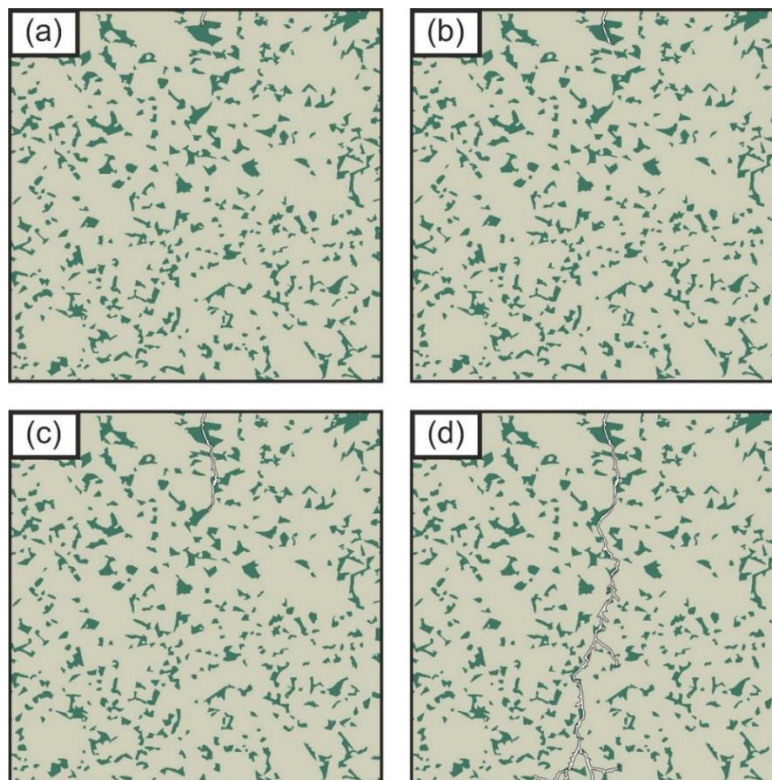
Fig.6 Evolution of damage in the microstructural model at (a) 0 cycles, (b) 300 cycles, (c) 330 cycles, (d) 332 cycles.

The range of the stable crack growth in the model is relatively shorter than the one experimentally discerned. Although it was initially attributed to the overall dimensions of the mode, later studies indicated that size of the model has minimum influence within the stable crack propagation regime. Hence, the observed discrepancy could be rationalized on the basis that assumption done on the brittle response for the WC phase may not correctly reflect the physical nature of this material. In this regard, it is known that certain amount of plastic deformation is also evidenced within the WC particles [21]. This might delay the propagation of the crack during fatigue. Furthermore, it should be recalled that load control was applied during the experiment in order to guarantee stable growth of the crack up to a certain length. However, such a control over the load was not conducted for the numerical simulation, since the model is relatively small in dimensions. Implementation of load control conditions within larger models, in order to increase the range of stable crack growth, is considered as further research actions.

A comparison between the real and the simulated crack patterns is provided in Fig. 8. For the sake of clarity, both crack paths are highlighted on the real microstructure. The results of the simulation reflect excellent agreement with the experimental findings in the short/stable crack growth region. A relatively fair agreement is observed for the unstable crack growth part. However, it has to be indicated that the number of cycles to failure should not be considered in a quantitative manner, since those values are strongly affected by the element size and the overall size of the model.

Nevertheless, it may be pointed out that model does qualitatively capture a fracture pattern similar to that observed in a real cyclic loading experiment.
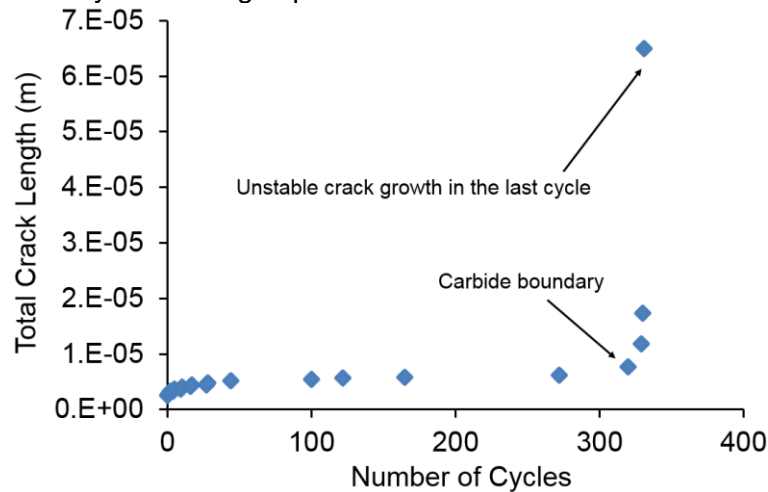
Fig.7 Evolution of the total crack length with respect to number of cycles.
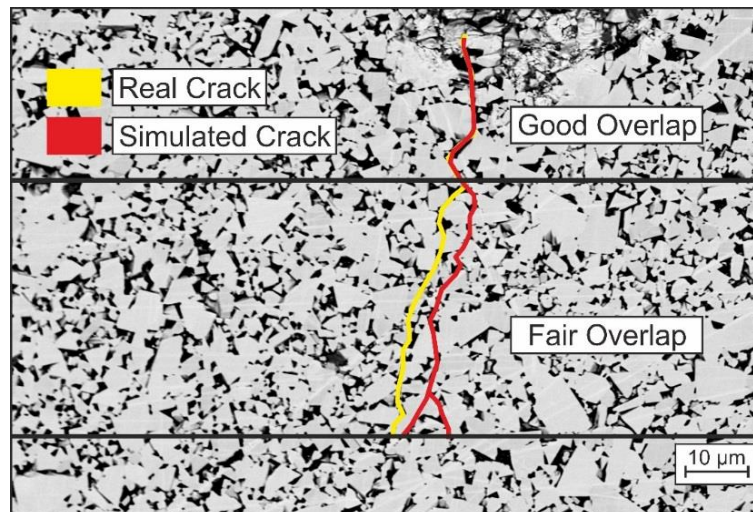
Fig.8 Comparison between the real and simulated crack patterns and various zones of crack propagation.

5. CONCLUSION

In this study, a numerical model based on results obtained from real experimental tests was generated. Main goal behind it was to simulate the microstructural evolution of a fatigue crack in a WC-Co hardmetal. In this regard, a finite element model based on a continuum damage mechanics approach was implemented in commercial solver Abaqus/Explicit for simulating crack extension in the material. Separate damage laws, based on brittle failure and fatigue, are implemented for the WC and the Co phases respectively.

Although a small section of the experimental model was considered, the model is found to be capable of capturing the cyclic evolution of the simulated crack pattern. Moreover, satisfactory agreement between the real and the simulated crack paths were observed.
For the sake of simplicity and computational efficiency, the model excludes many other physical aspects of the fatigue phenomena within WC-Co materials. However, even it is somehow simplified the model was able to capture a realistic fatigue crack propagation behavior for the material studied. In this regard, the model is considered to be valid for conducting comparative studies

based on artificial microstructures. This will be quite useful for evaluating the influence of different microstructural parameters on the FCG performance of hardmetals.

ACKNOWLEDGEMENTS

REFERENCES

[1] Dawihl, W, 1941, Die wissenschaftlichen und technischen grundlagen der pulvermetallurgie, stahl und Eisen, 61, 909-919.

[2] Llanes, L, Anglada, M, Torres, Y, 2014, Fatigue of cemented carbides, Comprehensive Hard Materials, Elsevier, Vol. 1, 345-362.

[3] Schleinkofer, U, Sockel, HG, Görting, K, Heinrich, W, 1997, Fatigue of hard metals and cermets - new results and a better understanding, Int J Refract Met H, 15, 103-112.

[4] Sailer, T, Herr, M, Sockel, HG, Schulte, R, Feld, H, Prakash, LJ, 2001, Microstructure and mechanical properties of ultrafine-grained hardmetals, Int J Refract Met H, 19, 553-559.

[5] Kursawe, S, Pott, Ph Sockel, HG, Heinrich, W, Wolf, M, 2001, On the influence of binder content and binder composition on the mechanical properties of hardmetals, Int J Refract Met H, 19, 335-340.

[6] Tarrago, JM, Jimenez-Pique, E, Turon, M, Rivero, L, Schneider, L, Llanes, L, 2013, Toughening and fatigue micromechanisms in hardmetals: FESEM/FIB tomography characterization, 18th Plansee Seminar, Reutte, paper #HM54.

[7] Fischmeister, HF, Schmauder, S, Sigl LS, 1988, Finite element modelling of crack propagation in WC-Co hard metals, Mater Sci Eng A, 105-106, 305-311.

[8] McHugh, PE, Connolly, PJ, 2003, Micromechanical modelling of ductile crack growth in the binder phase of WC–Co, Comput Mater Sci, 27, 423-436.

[9] Özden, UA, Mingard, KP, Zivcec, M, Bezold, A, Broeckmann, C, 2015, Mesoscopical finite element simulation of fatigue crack propagation in WC/Co-hardmetal, Int J Refract Met H, 49, 261-267.

[10] Godse, R, Gurland, J, Suresh, S, 1988, Effects of residual stresses in fracture toughness testing of hard metals. Mater Sci Eng A, 106, 383-387.

[11] Llanes, L, Torres, Y, Anglada, M, 2002, On the fatigue crack growth behavior of WC-Co cemented carbides: kinetics description, microstructural effects and fatigue sensitivity, Acta Mater., 50, 2381-2393.

[12] Mishnaevsky Jr., L, Dong, M, Hönle, S, Schmauder, S, 1999, Computational mesomechanics of particle-reinforced composites, Comput Mater Sci, 16, 133-143.

[13] Abaqus 6.12, 2013, Abaqus user subroutines reference manual.

[14] Exner, HE, Gurland, J, 1970, A Review of parameters influencing some mechanical properties of tungsten carbide-cobalt alloys. Powder Metall, 13, 13-31.

[15] General Carbide, 2009, The Designer's Guide to Tungsten Carbide, Greensburg.

[16] Rabotnov, YN, 1968, Creep rupture, 12th International Congress of Applied Mechanics, Stanford, California, 342-349.

[17] Dunne, F, Petrinic, N, 2005, Introduction to computational plasticity, Oxford University Press.

[18] Lemaitre, J, Desmorat, R, 2005, Engineering damage mechanics, Springer-Verlag.

[19] Sadowski, T, Nowicki, T, 2008, Numerical investigation of local mechanical properties of WC/Co composite, Comput Mater Sci, 43, 235-241.

[20] Schmauder, S, 2001, Crack growth in multiphase materials, Encyclopedia of Materials: Science and Technology, Pergamon.

[21] Exner, HE, 1979, Physical and chemical nature of cemented carbides, Int Mater Rev, 24, 149-173.

INFLUENCE OF CHROMIUM AS CARBIDE FORMING DOPING ELEMENT ON THE DIAMOND RETENTION IN DIAMOND TOOLS

W. Tillmann[1,a], M. Tolan[2,b], N.F. Lopes-Dias[1], M. Zimpel[1], M. Ferreira[1c], M. Paulus[2]

[1]Institute of Materials Engineering, University of Dortmund,

[2]Fakultät Physik/DELTA, TU Dortmund,

[a]wolfgang.tillmann@udo.edu, [b]Tolan@physik.uni-dortmund.de,

[c]manuel.ferreira@udo.edu

ABSTRACT

Diamond tools are widely used in drill tools, wire saws or circular saws to machine very hard materials such as concrete or natural stone in the construction as well as extractive industries. The mechanical and physical properties, such of these materials call for high requirements concerning the diamond tools. In particular, the bonding between the diamond particles and the metallic binder is an essential criterion for the tool quality. It is known that the type and strength of bonding is influenced by the diamond-metal interaction that occurs during the sintering process. Depending on the element used as a metallic binder, different thermally induced chemical reactions between the diamond and the metallic matrix take place. These reactions are (1) carbide formation, (2) graphite formation, and (3) inert behavior. However, there is still a high demand concerning the research of the diamond-metal interaction influenced by a carbide forming element.

In this work, chromium as a carbide-forming element was used as a doping agent in order to increase the diamond retention in diamond tools. The elements iron, cobalt and nickel were selected as single metallic components due to their catalytic influence on the graphitization of diamonds; whereas three metallic matrix systems were additionally doped with 15% chromium. The samples were sintered by hot pressing. Furthermore, half of the samples were thermally treated in order to ensure a stronger thermal induction of the interfacial reactions. In order to analyze the bonding behavior of the diamonds in the metal matrix, the samples were broken and the interfacial area was analyzed by means scanning of electron microscopy. These experimental studies show an influence of the carbide-forming doping agent on the diamond-metal interaction.

KEYWORDS

Diamond tools, interface reactions, diamond retention, diamond-metal composites, metal diamond interface, SEM - analyses

1. INTRODUCTION

The unique combination of properties makes diamonds attractive for numerous applications. Besides their extreme hardness, diamonds are also characterized by their high thermal conductivity and low thermal expansion as well as by their chemical resistance to most materials. Due to these properties, diamonds are a popular cutting material and widely used for materials processing in the industry [1]. The machining of concrete or natural stone places high demands on the cutting tool. These demands are fulfilled by diamond impregnated cutting tools on the basis of metal matrix composites such as drill bits, wire saws or circular saws [2] [3]. Thus, diamonds provide an abrasive effect on the workpiece, while the metal matrix ensures an optimal diamond

bonding and assures an ideal grain protrusion [4]. Furthermore, diamond impregnated tools provide a self-sharpening behavior as new diamonds are gradually exposed to the surface of the segment simultaneously to the metal matrix wear [5].

Generally, powder metallurgical production techniques are used and well established to fabricate diamond grinding segments. Vacuum sintering and hot pressing processes belong to these procedures and are mainly used for the batch production of diamond impregnated cutting tools. The vacuum sintering process consists of two successive steps: cold pressing and sintering, while the hot pressing process combines compaction and sintering in one step at lower temperatures. Furthermore, hot pressing requires a shorter process time and achieves higher density values and is therefore the widely used technique to manufacture diamond segments in the diamond tool industry [3].

However, tool performance strongly depends on the bonding between the diamond particles and the metallic binder, which in turn is influenced by the sintering parameters as well as by the alloying system of the metal matrix. On the one hand, the sintering parameters, in particular the temperature and time influence the bonding between the diamond particles and the metal matrix component negatively as the degradation of the diamonds into the graphite is thermally induced. However, the degradation can be inhibited by hot pressing due to the lower temperature and shorter process time required. On the other hand, the metallic binder has an influence on the diamond-metal interaction because of the carbon reactivity of its components. Furthermore, the chemical composition of the metallic binder has an influence on the interface between the diamond and the metal matrix. It is known that the carbon reactivity of transition metals in the 4th period of the periodic table increases with its number of electron vacancies in d-orbitals. Elements with fully assigned d-orbitals (e.g. Cu, Zn) are inert to carbon, while elements with minor occupied d-orbitals (e.g. Cr, Ti) are carbide formers. However, elements with medium occupied d-orbitals (e.g. Co, Fe) show a catalytic effect on carbon [7] [8]. In addition, carbon reactivity of binder metals in diamond-metal composites has been verified by means of scanning electron microscopy and X-ray diffraction in a recent work [9]. It was observed that diamond degradation is linked with the formation of graphite and can be reduced by using elements with minor occupied d-orbitals. Furthermore, the formation of a carbide layer on the diamond surface was only induced by chromium.

As a consequence of the chemical reactivity of the metal matrix composites, three different bonding behaviors between diamond and metal were observed in previous investigations: (1) carbide formers induce a carbide formation and cause a strong bonding between carbon and metal; (2) elements with a catalytic effect on carbon lead to graphitization and diamond degradation occurs. The diamond retention is debilitated due to the graphite layer on the diamond surface; (3) an inert behavior takes place when no chemical reaction occurs, leading to a mechanical bonding of the diamond within the metallic binder.

It is therefore expected that the tool performance improves and the diamond retention is strengthened when doping the metal matrix with carbide forming metals. It was already observed that a reduction of the graphitization and an intensification of the carbide formation take place when metallic binders such as Fe, Co or Ni were doped with the carbide-forming element Cr [10]. This behavior is influenced by the formation of the chromium carbide structures Cr_3C_2 and Cr_7C_3 [9, 10]. In Fe or Co metallic binders, the amount of graphite decreases with an increasing Cr content, while a reduction of the graphitization in Ni matrix systems only occurs with a 15 % Cr content [10]. However, a correlation between the diamond-metal-interaction and the diamond

bonding has not been investigated yet, although the diamond retention is an important criterion for the tool performance. For this reason, it was the aim of this work to analyze the influence of the metal matrix components on the bonding behavior of diamonds.

2. EXPERIMENTAL PART

2.1 Hot pressing of diamond impregnated segments

In order to investigate the influence of the metal matrix composition on the diamond bonding behavior, four diamond-metal powder mixtures were used. The elements Fe, Co, as well as Ni were selected as single metallic components due to their catalytic influence on the graphitization of diamonds. Furthermore, the three metallic components were additionally doped with 15 mass% of Cr as carbide forming element. The metal matrix compositions were pre-mixed with 10 vol-% synthetic diamonds (SDB1055: 40-50 mesh). An overview of all diamond-metal-composites used in this work is listed in Table 1.

Table 1: Composition of diamond-metal-composites used

Matrix system	Metallic element [mass%] (grain size)				Diamond content [vol.%]
	Fe (2,5 µm)	Co (0,9 µm)	Ni (5 µm)	Cr (45 µm)	
Fe	100	-	-	-	10
FeCr	85	-	-	15	10
Co	-	100	-	-	10
CoCr	-	85	-	15	10
Ni	-	-	100	-	10
NiCr	-	-	85	15	10

The diamond-powder-mixtures were sintered by the use of a hot press (Dr. Fritsch CSP 100, Germany). All diamond segments were sintered at a pressure of 136 bar for 180 s at a maximum temperature of 1100 °C in an atmosphere consisting of nitrogen. The two component metal matrices were sintered at the same temperature in order to analyze the effect of the carbide forming element on the diamond retention with the same conditions as the single component metal matrices.

2.2 Thermal post-treatment

A thermally induced graphitization as well as a correlated degradation of diamonds might not occur due to the short processing time during hot pressing according to the Arrhenius equation which describes the temperature dependencies of chemical reactions. In order to ensure a thermally induced chemical reaction between the diamond-metal-interface, half of the hot pressed diamond segments were subsequently thermally post-treated. For this purpose, all diamond segments were heated in a vacuum furnace (Leybold Torvac, Germany) at 1100 °C for 120 min. The heating process with its heating rates and holding periods are visualized in Fig. 1.
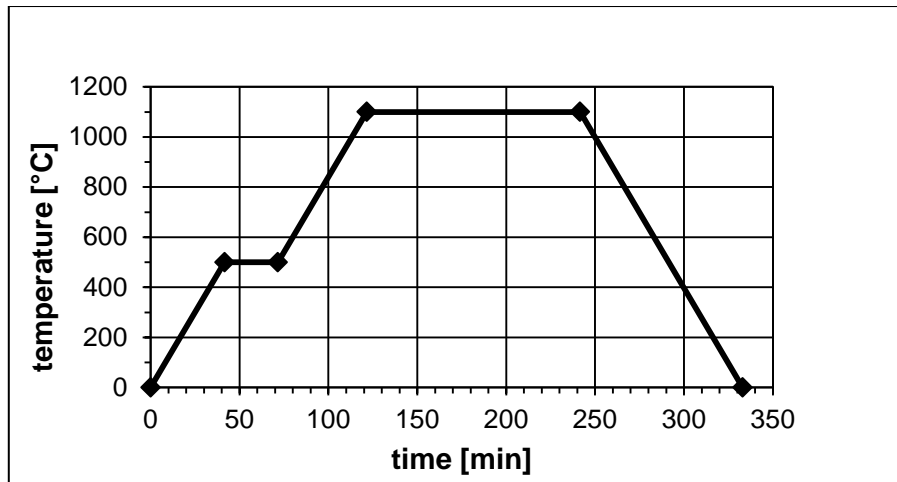
Fig. 1: Heating process of the post-treatment

2.3 SEM investigations

In order to analyze the diamond retention, the diamond segments were mechanically broken and SEM investigations of the both fractured surfaces were performed. All samples were coated with a thin layer of gold to ensure a good image quality of the electrically nonconductive diamonds. Scanning electron micrographs were realized by means of a field emission SEM (Jeol JSM-7001F, Japan). Fig. 2 shows exemplary both fractured surfaces of a Fe diamond segment after being mechanically broken.
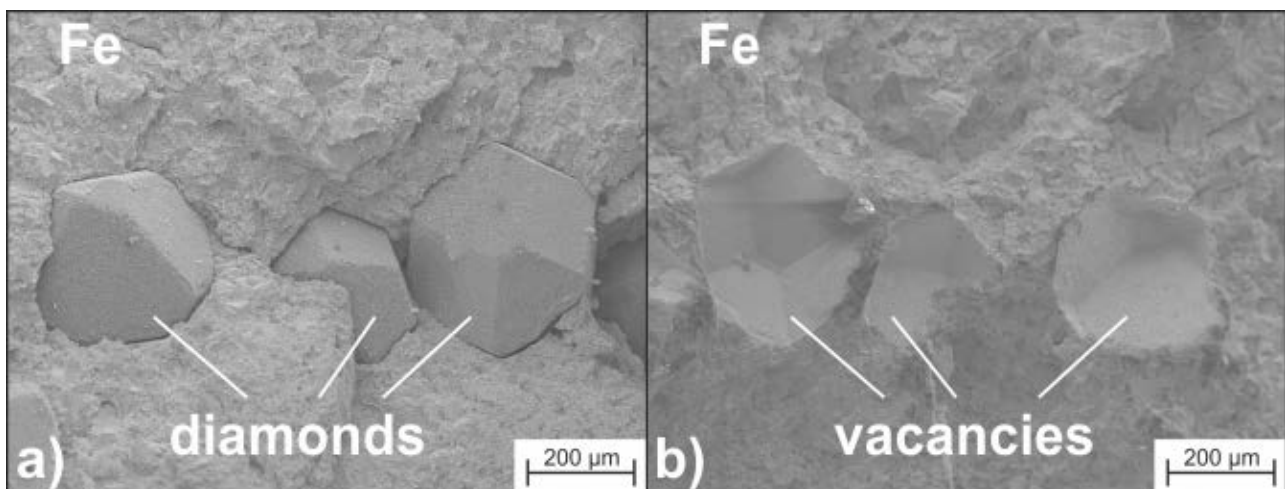
Fig. 2: Fractured surfaces of hot-pressed Fe-based diamond segments

3. RESULTS AND DISCUSSION

3.1 Hot pressed diamond segments

Fig. 2 and Fig. 3 show the fractured surfaces of Fe- and Co-based diamond segments. The diamonds are completely pulled out of the matrix and remain bonded on one site of the fragment. The counterpart shows the vacancies where the diamonds were bonded before. Furthermore, the diamond particles are not fully embedded as they are partially unattached due to a small gap between the diamond and the matrix. The reason for this behavior can be explained by a slight diamond degradation, which is clearly visible on the close up of the diamond surface as presented

in Fig. 4 (a) and (b) for both metallic matrices. The damage to the diamond structure is mainly observed at the corners and edges of the diamonds.
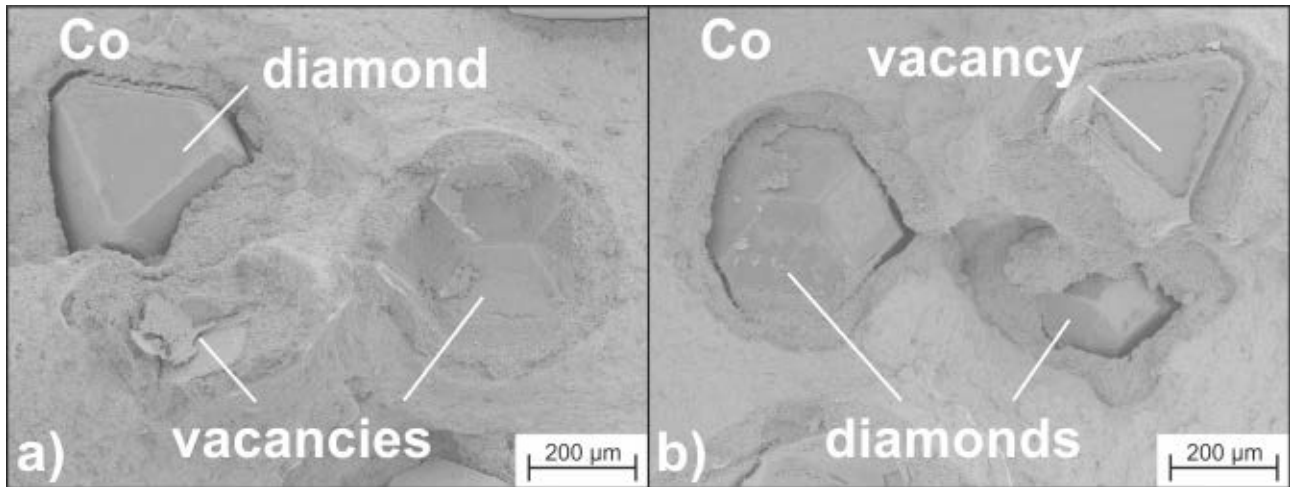
Fig. 3: Fractured surfaces of hot pressed Co-based diamond segments

The hot pressed Ni diamond segments expose a similar bonding behavior as the Fe- and Co-based samples. After being mechanically broken, the diamonds remain entirely embedded on one side of the fragment while the vacancies are visible in the counterpart. A slight formation of graphite on the diamond surface can also be observed in Fig. 4 (c). As a consequence, diamond grains are not completely mechanically bonded due to the graphite layer and a small gap between the diamond-metal-interface.

Even if the short process time of the hot pressing process should inhibit a diamond degradation, a slight diamond degradation occurred by using Fe-, Co- and Ni-based metal matrices due to their catalytic effect on carbon. Besides a minor degradation on the diamond surface, mainly the corners and edges were damaged. Therefore, the diamond particles are not fully embedded into the metallic binder, but rather detached to a certain degree as a result of the graphite layer.
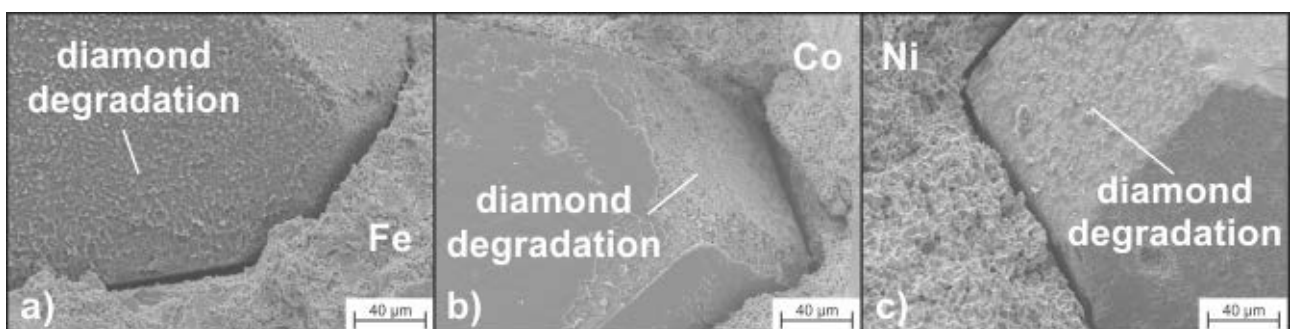
Fig. 4: Close-up of the diamond-metal-interface of hot pressed (a) Fe-based diamond segments, (b) Co-based diamond segments, and (c) Ni-based diamond segments

However, the diamond retention is strengthened by the addition of Cr to the Fe- and Co-based matrix as shown in Fig. 5 and Fig. 6, respectively. Although the diamond segments were broken, the diamonds remain embedded in their position and fractured across the fracture area. The remaining diamond fragment is also fixed tightly in the counterpart of the segment. Still, a few diamond particles of the Fe samples are not fractured but rather surrounded with a layer and bonded to the metallic matrix of the fractured surface, as visible in Fig. 5. A close-up of the diamond-metal-interface of FeCr- and CoCr-based samples reveals that the diamonds are

completely surrounded by the binder, as shown in Fig. 7 (a) and (b). This bonding behavior indicates an improved embedding. This is due to the reduction of graphitization and an intensification of the carbide formation induced by the addition of Cr [9].
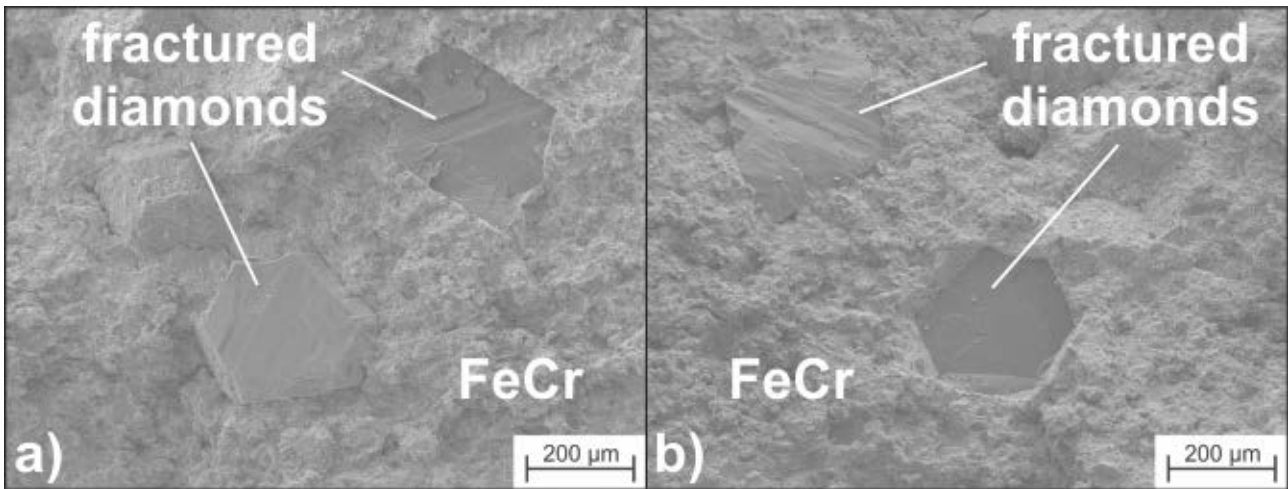
Fig. 5: Fractured surfaces of hot pressed FeCr-based diamond segments
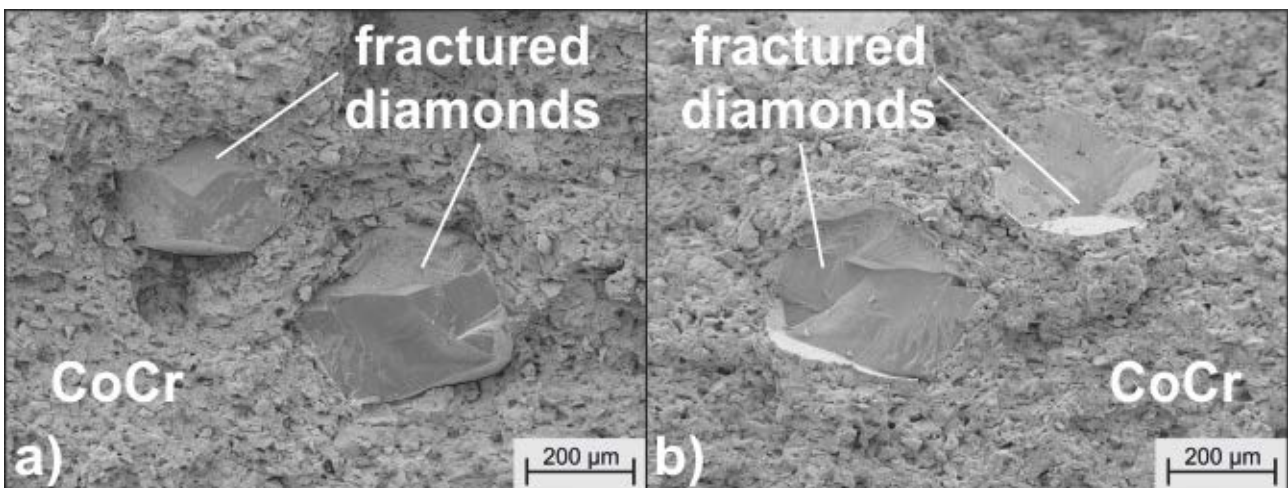
Fig. 6: Fractured surfaces of hot pressed CoCr-based diamond segments
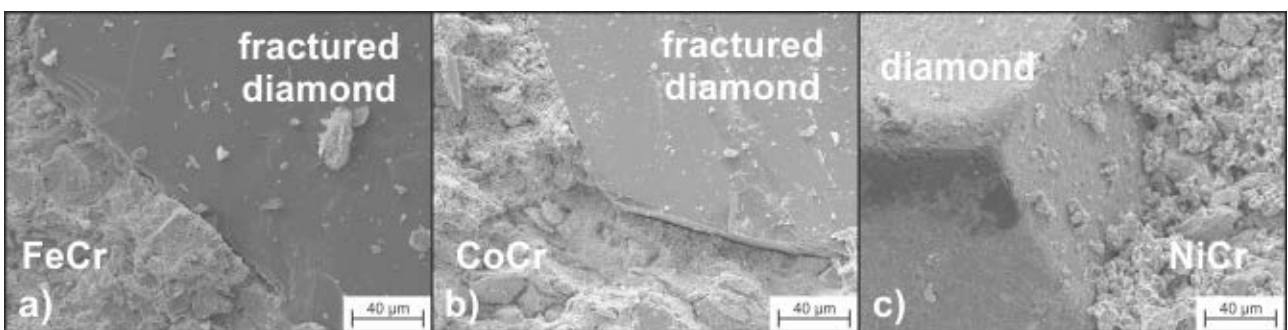
Fig. 7: Close-up of the diamond-metal-interface of hot pressed (a) FeCr-based diamond segments, (b) CoCr-based diamond segments, and (c) NiCr-based diamond segments

Such a strong bonding as presented with FeCr- and CoCr-based matrices is not observed with NiCr samples. After the mechanical fracture, the diamonds remain unbroken on one side of the fragment while its vacancies are marked on the counterpart, similar to the single metallic components, yet with the difference that the diamond particles are fully bonded to the metallic

binder without any gap. Fig. 7 (c) shows the diamond-metal-interface of NiCr-based diamond segments. In comparison to the FeCr- and CoCr-based diamond segments, the diamond retention was weaker. This behavior can be explained with a previous work, which observed a reduction of graphitization by adding 15% Cr to Ni-based matrices although a formation of a carbide structure was not observed [10]. Therefore, no carbide formation occurred but rather a mechanical bonding of the diamonds.

3.2 Thermally post-treated diamond segments

The fractured surfaces of post-treated Fe- and Co-based samples are shown in Fig. 8 and Fig. 9. The diamond particles remain in one part of the fractured surface, while the vacancy of the diamond particles are marked on the counterpart of the diamond segment. The surface of the diamond shows a strong diamond degradation, whereas a reaction product, most probably graphite [9], remains in the vacancies after breaking the segment, as visible in Fig. 9. Furthermore, the gaps between the diamond and metallic binder are larger compared to the hot pressed Fe- as well as Co-based samples. These features indicate a stronger graphitization during the thermal post-treatment which can be explained due to the high temperatures as well as the strong catalytic effect of Fe and Co. The catalytic effect causes an allotropic transformation of the diamond into graphite and is observed as black dots on the diamond surface as seen in Fig. 9.
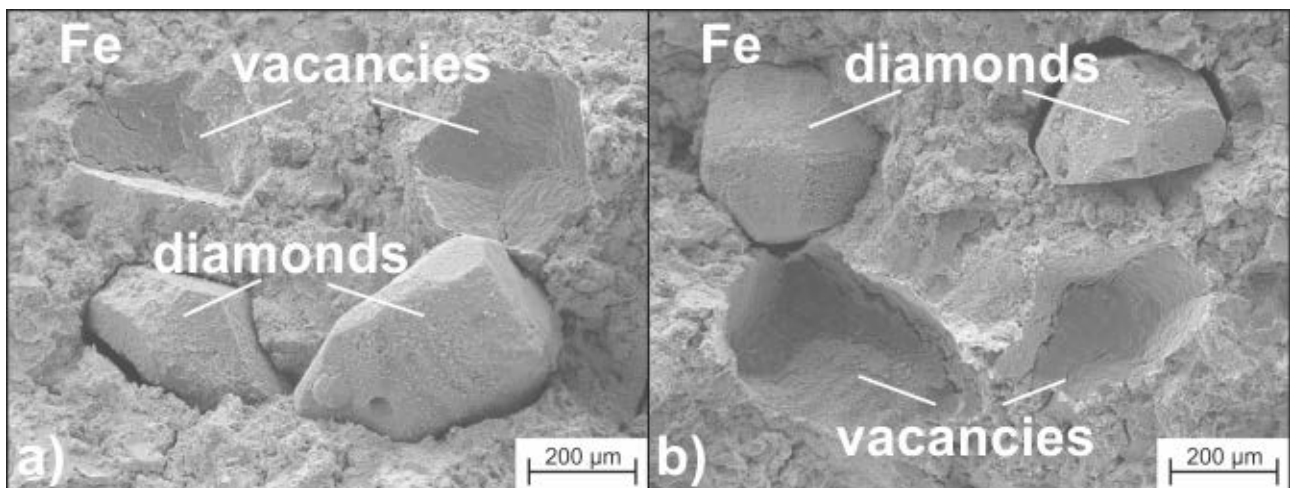
Fig. 8: Fractured surfaces of thermally post-treated Fe-based diamond segments
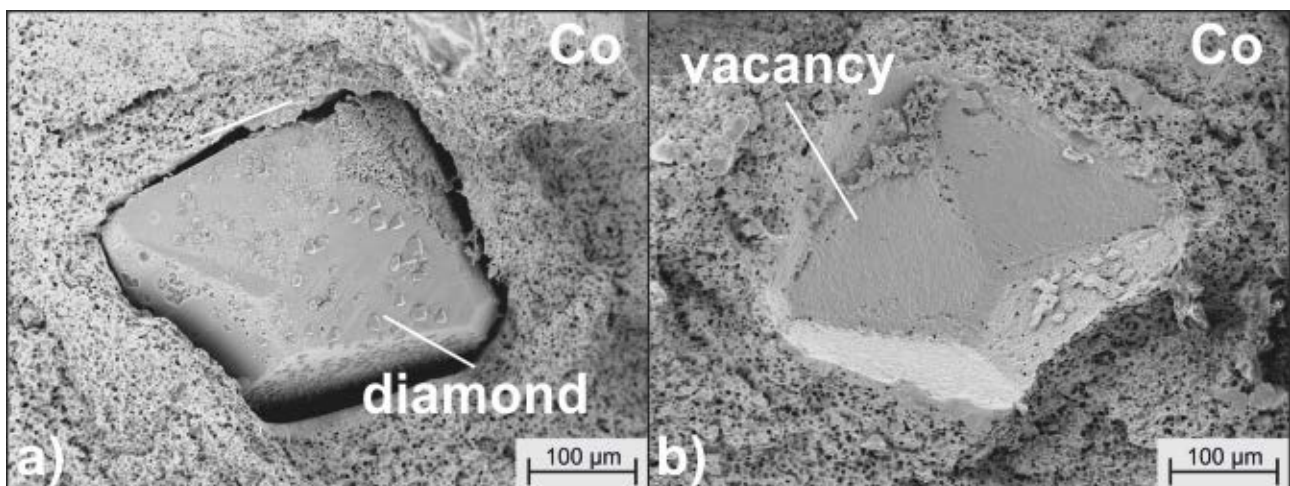
Fig. 9: Fractured surfaces of thermally post-treated Co-based diamond segments

The post-treated Ni-based samples do not show such a strong graphitization of diamond grains as Fe and Co. However, the diamonds are slightly degraded as they present a rough surface which indicates a graphitization. In addition, a large gap between the diamond and matrix is also visible, as shown in Fig. 10. The diamonds of Ni-based samples are not as strongly degraded as the diamonds of Fe- and Co-based samples, which can be explained due to the stronger catalytic effect of Fe and Co.
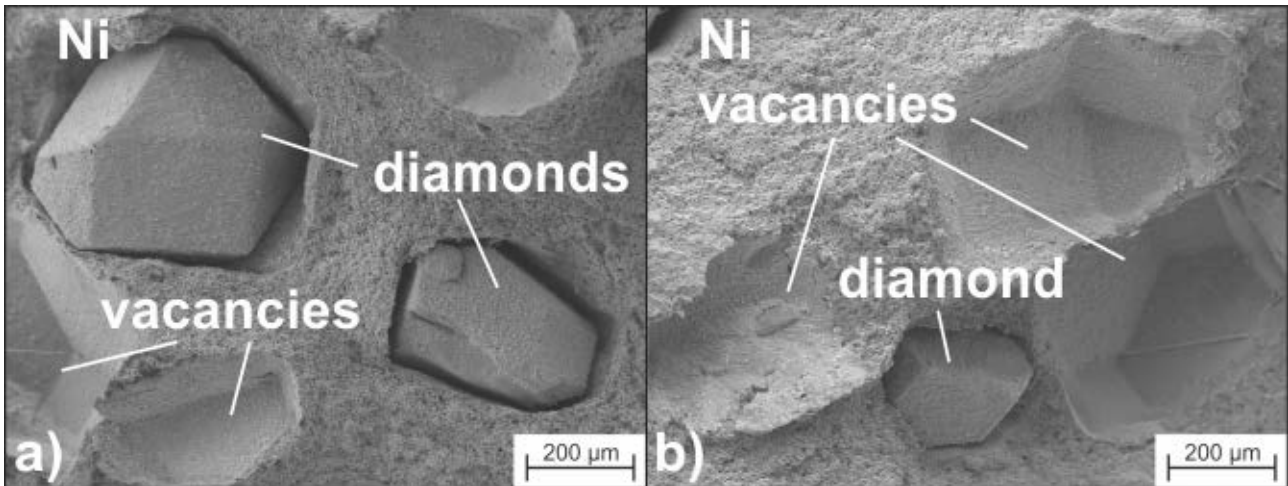
Fig. 10: Fractured surfaces of thermally post-treated Ni-based diamond segments

Fig. 11 and Fig. 12 show the fractured surfaces of thermally post-treated FeCr- and CoCr-based samples. The diamond particles are surrounded by a shell-like structure which is cracked and partially torn off. This shell-like structure indicates the carbide formation that occurred during hot pressing and remained after the thermal post-treatment. However, the diamond retention of post-treated FeCr- and CoCr-based samples is not as strong as after hot-pressing. The post-treatment might have caused the diamond degradation due to the high temperatures, releasing the strong diamond-carbide-bonding. However, the shell-like carbide layer protects the diamond from a stronger degradation as there is no graphitization visible.
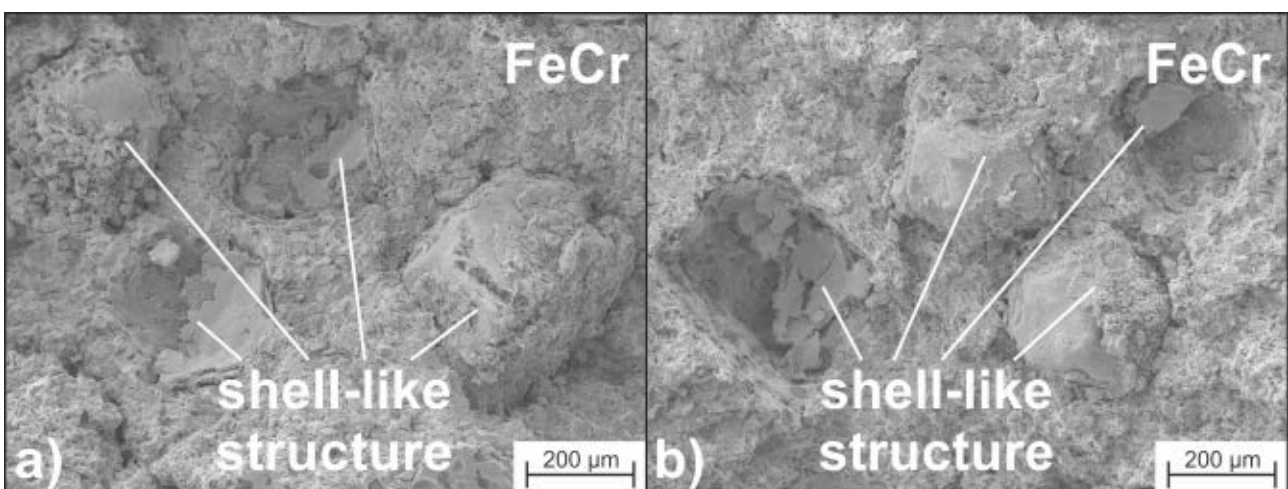
Fig. 11: Fractured surfaces of thermally post-treated FeCr-based diamond segments
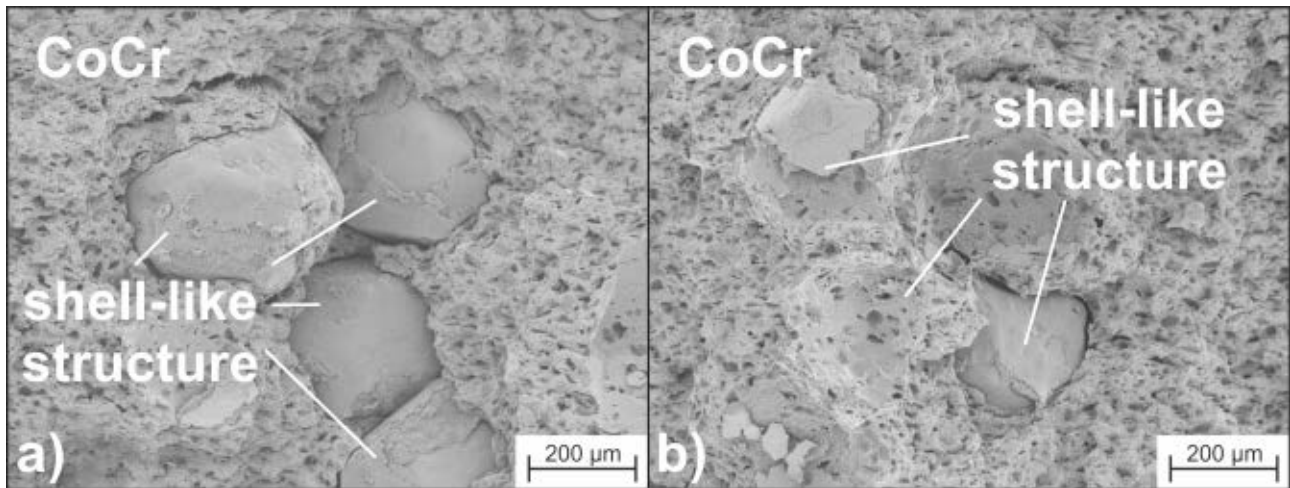
Fig. 12: Fractured surfaces of thermally post-treated CoCr-based diamond segments

A shell-like carbide formation surrounding the diamond particles is not observed with NiCr-based diamond segments. This confirms the results on hot-pressing as there was no indication for the formation of carbide structure as well. However, the diamond bonding is stronger than with single Ni-based diamond segments as the diamonds are tightly embedded into the matrix. Apparently, 15% of Cr content inhibits also the graphitization process and maintains the mechanical bonding of the diamond particles during the thermal post-treatment.
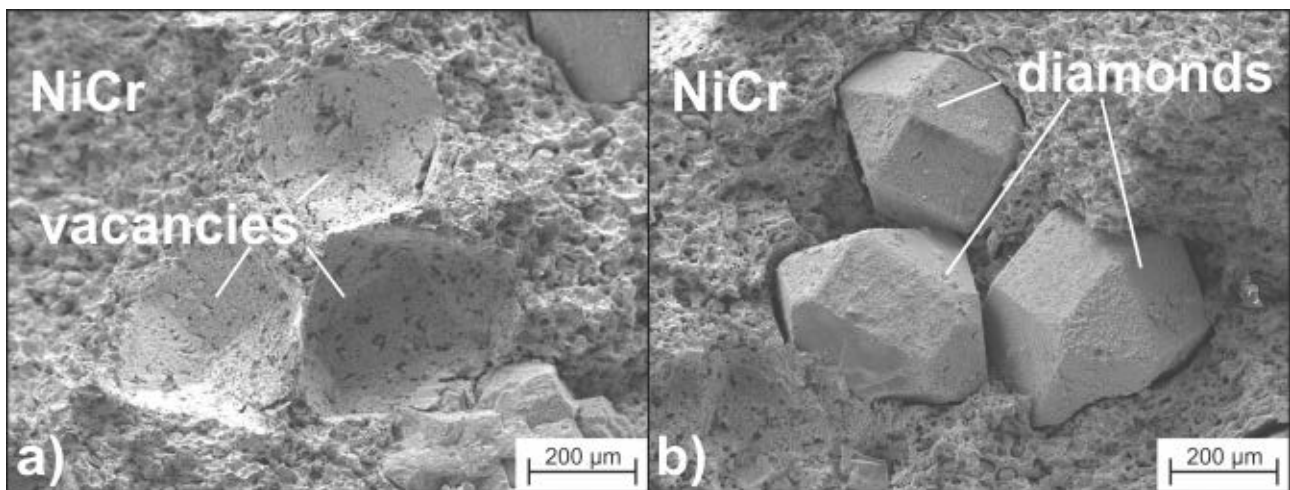
Fig. 13: Fractured surfaces of thermally post-treated NiCr-based diamond segments

4. CONCLUSION

Even though the process time of hot pressing is short, single component matrices with elements with a catalytic influence slightly degrade the diamond particles. By additionally doping 15% Cr to the metallic matrix, the diamond degradation is inhibited. Furthermore, an indication for the formation of a carbide structure is seen with FeCr- and CoCr-based diamond segments due to the strong diamond bonding.

A thermally post-treatment causes a strong degradation of the diamonds impregnated with Fe- and Co-based matrices. The matrices doped with the carbide former do not show any indication for a strong degradation. Furthermore, a shell-like carbide structure is visible in the case of the FeCr-

and CoCr-based diamond segments. However, the diamond retention is not as strong as after hot pressing due to the thermal post-treatment.

REFERENCES

[1] Weinert, K, 2005, Spanende Fertigung: Prozesse, Innovationen, Werkstoffe, Band 10, Vulkan Verlag GmbH

[2] Tillmann, W, 2000, Trends and market perspectives for diamond tools in the construction industry, Refractory Metals & Hard Materials 18, 301-306

[3] Konstanty, J, 2005, Powder Metallurgy Diamond Tools, Elsevier Science & Technology

[4] Kieback, B, Sauer, C, Tillmann, W, 1999, Optimisation of Metallic Binders used in Diamond Tool Production, EuroPM 99, Int. Workshop on Diamond Tool Production, Turin, Italy

[5] Denkena, B, Tönshoff, H.K, Friemuth, T, Gierse, A, Glatzel, Hillmann-Apmann, H, 2002, Innovative Trennschleifprozesse in der Natursteinbearbeitung, Werstatttechnik online, 290-296

[6] Schatt, W, Wieters, K.P, Kieback, B, 2007, Pulvermetallurgie – Technologien und Werkstoffe, Springer Verlag

[7] Sung, C.M, Tai, M.F, 1997, Reactivities of Transition Metals with Carbon: Implications to the Mechanism of Diamond Synthesis Under High Pressure, Journal of Refractory Metals & Hard Materials 15, 237-256

[8] Artini, C, Muolo, M.L, Passerone, A, 2012, Diamond-metal interfaces in cutting tools: a review, Materials Science 47, 3252-3264

[9] Tillmann, W, Ferreira, M, Steffen, A, Rüster, K, Möller, J, Bieder, S, Paulus, M, Tolan, M, 2013, Carbon reactivity of binder metals in diamond–metal composites – characterization by scanning electron microscopy and X-ray diffraction, Diamond & Related Materials 38, 118-123

[10] Steffen, A, 2013, Untersuchung der Diamant-Metall-Grenzfläche in Diamantverbundwerkstoffen – Röntgendiffraktionsstudien mit Synchronstrahlung, PhD thesis, TU Dortmund

SCRATCH TESTS WITH SINGLE DIAMOND TOOLS ON REINFORCED CONCRETE AND ITS COMPONENTS FOR THE ANALYSIS OF THE MATERIAL SEPARATION

Monika Kipp[1, a], Michael Kansteiner[1, b], Dirk Biermann[1, c]

[1)]Institute of Machining Technology, TU Dortmund University, Baroper Straße 303, 44227 Dortmund

[a)]kipp@isf.de, [b)] kansteiner@isf.de, [c)] biermann@isf.de

ABSTRACT

Core drilling with diamond impregnated segments is a common process for the machining of concrete or reinforced concrete. These materials are characterised by their structure consisting of various components. This inhomogeneity influences the cutting process due to changing process forces or varying chip formation. Therefore an analysis regarding the material separation of the single components (cement stone, aggregates like basalt, steel as reinforcement) as well as of the compound materials is necessary. As a basis to analyse the core drilling process and in order to gain detailed knowledge concerning the material separation process of reinforced concrete and its components, scratch tests with single diamonds and varying process strategies were conducted. In analogy with the core drilling process, circular grooves were produced. For the scratch tests steel, cement stone, basalt, high performance concrete and reinforced concrete were used as sample materials. One test series was conducted on a machining centre with the focus on process forces under varying process parameters such as cutting velocity or feed speed. Further experiments focused on the analysis of the development of the scratches due to repeated scratching. For this microscopic investigation a tribometer in combination with a large-chamber scanning electron microscope was used.

KEYWORDS

scratch test, diamond tool, single grain diamond, material removal, reinforced concrete, concrete, process forces, large-chamber scanning electron microscope

INTRODUCTION

Reinforced concrete is a construction material consisting of concrete as a mineral component and steel as a reinforcement. Regarding the machining of this composite material the diverse characteristics of material separation of each constituent have to be investigated in order to analyse grinding processes as e.g. core drilling. The material removal process in grinding metallic materials is characterised by elastic and plastic deformation and chip formation [1]. In contrast scratch tests revealed that chip formation in stone is a consequence of cracking, while also plastic deformation occurs [2]. Regarding concrete differences between the cement and the included aggregates are relevant additionally [3, 4].

Conducting scratch tests with single grain diamonds in order to simplify complex grinding processes is an often used method to examine the characteristics of material separation. Concerning the scratch tests conducted in this research the core drilling process using drill bits with several diamond impregnated segments is the underlying machining process. Therefore tests on a machining centre were performed with a specific kinematic derived from the core drilling process. Moreover, with the aim of obtaining detailed and comprehensive knowledge concerning the material separation of the examined high-strength concrete and reinforced concrete tests were carried out on the composites in addition to the separate components. Material separation of the single constituents was also analysed by force-controlled, iterative scratch tests performed in a large-chamber scanning electron microscope.

1. MATERIALS AND SET-UPS FOR EXPERIMENTAL TESTS

As the basic material for the experimental investigations a concrete categorised as C100/115 in DIN EN 206 due to its compressive strength was used [5]. Hence, it belongs to high-strength concretes [6]. As the cement component CEM I 52,5 R HS/NA was used, whereas the concrete included sand and basalt in different particle sizes as concrete aggregates. Also reinforced concrete was analysed. These samples contained a part out of steel (1.0577) in analogy to a reinforcement. In addition to the concrete samples the material separation of the single materials is considered as well. Therefore samples out of steel (1.0577), basalt and cement stone were utilised separately. In this paper, the analysed cement stone consisted of cement and sand grains. In contrast to the analysed high performance concrete C100, basalt was no component. For both kinds of scratch tests round samples with a ground surface were used.

Scratch tests in a large-chamber scanning electron microscope

One kind of scratch tests was carried out using a tribometer in a large-chamber scanning electron microscope (MIRA XI). The tribometer is used for pin-on-disk tests [7] and was modified for the conducted scratch tests. On the basis of an iterative process strategy the tests enable to analyse the development and changes of the scratches as a result of repeated scratching qualitatively by SEM pictures. An overview of the test set-up and the process principle illustrated by a schematic drawing are shown in figure 1.

Test set-up in the large-chamber SEM **Principle of tests with tribometer**
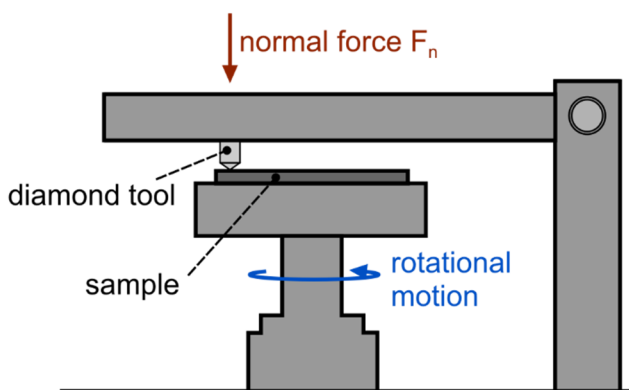
Fig. 1: Set-up with tribometer in a large-chamber SEM

For these scratch tests synthetic diamond grains (Element Six, SDB 1055) with a varying particle shape were used. The rotational and therefore cutting motion was realised by a rotating sample holder driven by a stepper motor as illustrated in figure 1. The normal force F_n for scratching was $F_n = 1.7$ N and the cutting speed was about $v_c \approx 0.2$ m/s. The scratch tests were interrupted every second turn till $n_{max} = 20$ rotations were passed in order to investigate the changes in the trace generated by scratching. A secondary electron detector was employed to take SEM pictures at a defined area of the sample each time. The resulting image sequence allows the qualitative, microscopic analysis of the scratches.

Scratch tests conducted on a machining centre

Additional scratch tests with another process strategy were conducted on a machining centre (IXION TLF 1004) in order to analyse the resulting process forces (normal force F_n and tangential force F_t) depending on the feed speed v_f, the cutting speed v_c and the workpiece material. Information concerning kinematics, tools and varied process parameters for the tests are shown in figure 2. In contrast to the above mentioned scratch tests, dressing diamonds (CVD-diamond, Dr. Kaiser Diamantwerkzeuge) with a regular geometry were used. These diamonds have a pyramidal shape with a point angle of $\sigma = 110°$. Conducting the scratch tests the tools were aligned in the way it is shown in figure 2.

Process kinematics
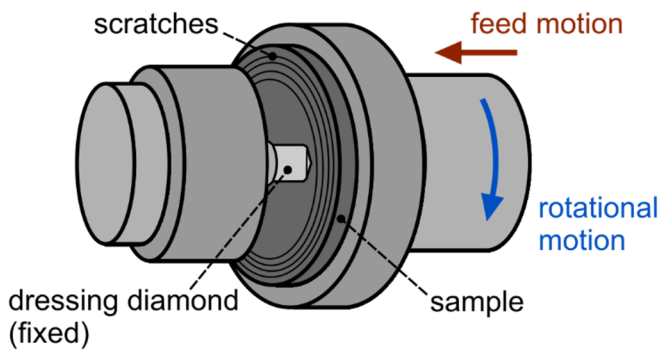
SEM pictures - Single diamond tools
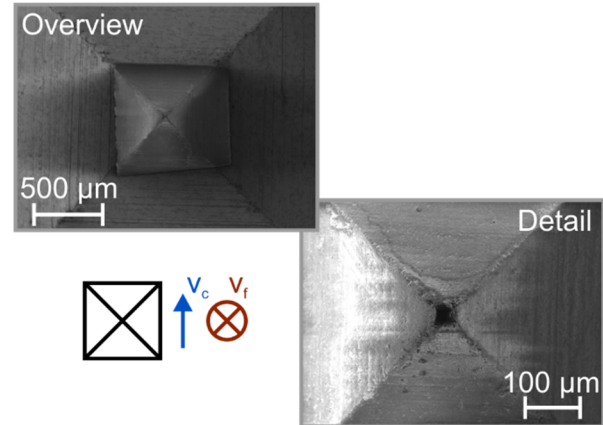
Process parameters

tool	cutting speed v_c	feed speed v_f	total depth a_{tot}
CVD-diamond pyramide point angle σ = 110°	$v_{c,1}$ = 40.5 m/min $v_{c,2}$ = 117 m/min $v_{c,3}$ = 193.5 m/min $v_{c,4}$ = 270 m/min	$v_{f,1}$ = 2.0 mm/min $v_{f,2}$ = 9.5 mm/min	a_{tot} = 0.080 mm

Fig. 2: Kinematics, tools and parameters for scratch tests on the machining centre

Through an eccentric position of the fixed diamond tool relative to the centre of the sample annular scratches were realised. On each sample up to twelve scratch tests with different diameters (d = 32…54 mm) were carried out. The varying diameter is not taken into account as an input value for the analysis of the measured process forces. Due to the rotation of the sample and the feed motion a helical path results which is comparable to the kinematics of the core drilling process with diamond impregnated tools. Whereas tests were performed with varying cutting speed v_c and feed speed v_f, the total depth for the scratch tests a_{tot} = 0.080 mm was invariable. Because of the inhomogeneity of the materials and the short process time of each scratch test, the sampling rate for the measurement of forces was set to f = 200 kHz. Moreover, a light barrier was implemented. Its signal was recorded simultaneously to the process forces during scratching. Hence, it is possible to identify the dependence of the position of the sample and the process forces. This is especially relevant for the detection of the effects resulting from the steel reinforcement in reinforced concrete.

2. RESULTS OF EXPERIMENTAL TESTS

Qualitative analysis of scratches due to scratching in a large-chamber scanning electron microscope

In order to point out qualitative differences in material separation between the components of the analysed high-strength concrete C100 and reinforced concrete respectively, results of the iterative scratch tests conducted in the large-chamber SEM for steel (1.0577), basalt and cement stone are represented in figure 3. SEM pictures of the scratches after n = 10 turns and n = 20 turns in different magnifications (overview, detail) are shown to demonstrate the development of the scratches after different process steps. Additionally, there are microscopic pictures of the resulting scratches after n_{max} = 20 turns and SEM pictures of the particular diamonds used because of their differences in particle shape. In the SEM pictures the cutting direction is given with respect to the relative motion of the diamond to the rotating sample. Furthermore, in figure 4 some exemplary details of scratches in cement stone and basalt after n = 10 turns are shown.

Tool:	Synthetic diamond SDB 1055	Material:	varied
		Normal force F_n:	$F_n = 1.7$ N
Grit size:	40/50 US mesh	Cutting speed v_c:	$v_c \approx 0.2$ m/s
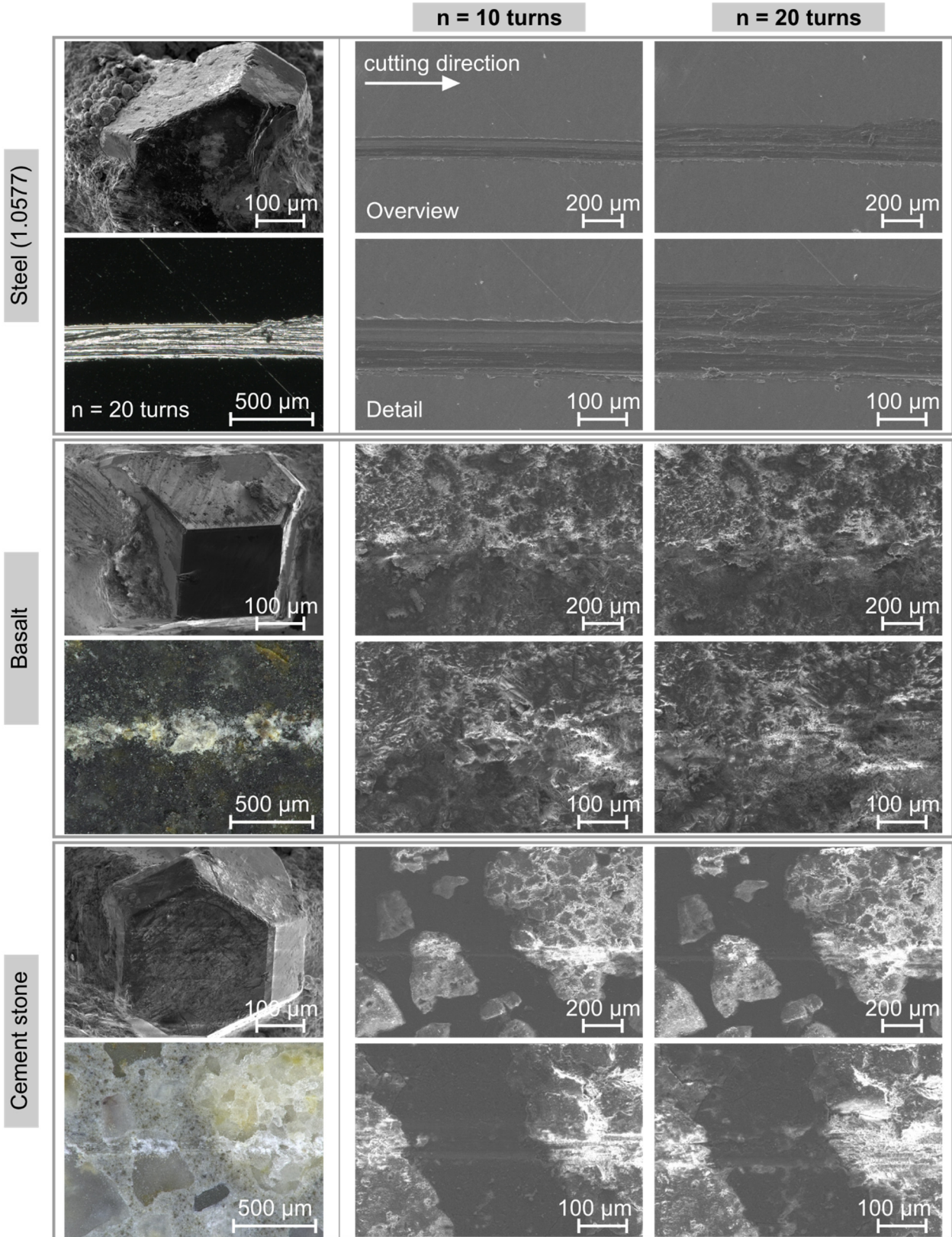
Fig. 3: Scratches in steel, basalt and cement stone after repeated scratching

The scratch in the analysed steel shows a kind of burr at the edges of the scratch (cf. fig. 3, n = 10 turns, detail) due to plastic deformation. After n = 20 turns some traces exist within the scratch which indicate that material was pushed to the outer edge of the scratch. These traces are also observable in the microscopic picture and they point out the ductile characteristics of the examined steel. The irregular surface conditions of the scratch after n = 20 turns are influenced by the repeated scratching. In basalt the resulting scratch is not visible as good in the SEM pictures as the scratch in steel owing to the appearance of the surface of the basalt sample in the SEM. The edges of the scratch cannot be defined exactly. Nevertheless, the processes of material separation can be discussed based on the pictures. There are parts of the scratch appearing comparatively smooth with compacted material (cf. fig. 4). This is a consequence of deformation processes [2]. Such areas are observable after n = 10 turns as well as after n = 20 turns, but in different forms whereby the change of the scratch as a result of further scratching is shown. Areas with fractured material occur as well, what is underlined by the microscopic picture of the scratch and demonstrates brittle material behaviour of the basalt. In the SEM pictures concerning cement stone the structure consisting of sand grains and cement becomes evident. The scratch in pure cement is more uniform compared to the above shown basalt. These resulting differences between cement and aggregates – basalt in this case – based on the force-controlled, iterative tests correspond to results of scratch tests conducted on different kind of concrete [3, 4]. The detailed SEM pictures of cement stone after n = 10 rotations in figure 4 additionally show separated material next to the scratch. Moreover, after n = 20 rotations there are detachments of material recognisable in cement. In sand grains the scratch is less distinct compared to cement and the material seems to fracture. Furthermore, material chips occur in the analysed transition area after multiple scratching as a result of cracking.

Tool:	Synthetic diamond SDB 1055	Material:	varied
		Normal force F_n:	F_n = 1.7 N
Grit size:	40/50 US mesh	Cutting speed v_c:	$v_c \approx 0.2$ m/s
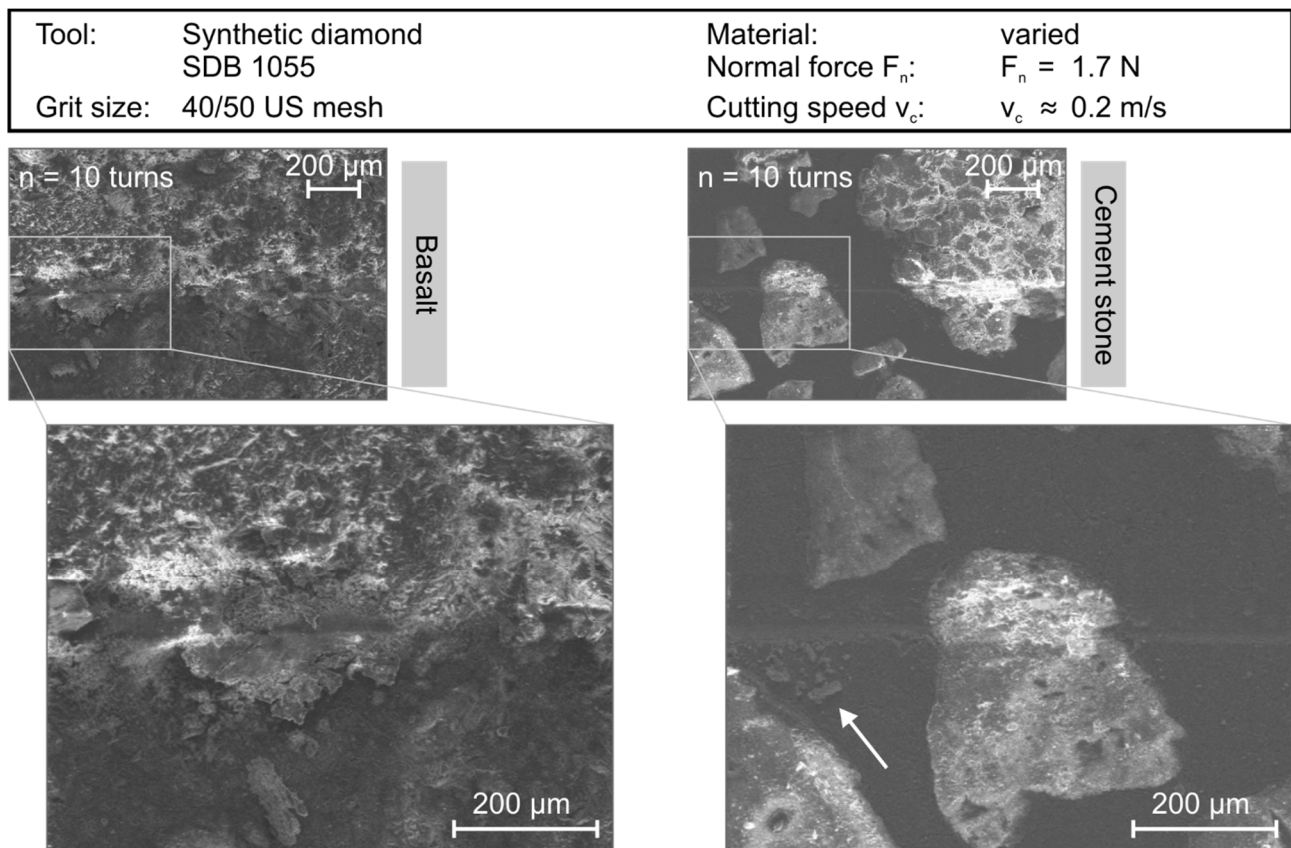
Fig. 4: Details of scratches on basalt and cement stone

The results of the scratch tests conducted in a large-chamber scanning electron microscope point out the qualitative differences of scratching the single components. The influences of the single constituents and the composites on the measured process forces are discussed in the following paragraphs based on the second test series.

Process forces depending on cutting speed and feed speed

On the basis of scratch tests carried out on a machining centre with pyramidal CVD-diamonds the process forces for five investigated materials were analysed. In figure 5 force data for the materials steel, basalt, cement stone and the composite concrete C100 are shown. Due to the fact that the influence of the steel part requires a particular analysis the process forces resulting by scratching the reinforced concrete are discussed separately. The tangential force F_t and the normal force F_n are analysed depending on varying cutting speeds v_c and feed speeds v_f, whereas the influences of different diameters for the tests and different dressing diamonds were not taken into account. The normal force F_n has the same direction as the feed motion and the force F_t is tangential to the rotational motion of the sample in the contact area. For the analysis and the comparison of the forces, the average force in the time period of a process time between $t = 0.35$ s und $t = 0.36$ s was calculated based on smoothed force data for each test. This leads to different covered scratch distances which were analysed for varying cutting speed. In figure 5 the mean value of four scratch tests for each combination of cutting speed v_c and feed speed v_f is shown. Moreover, the minimum and maximum average forces out of the four considered tests are marked. Regarding the results presented in figure 5 concerning steel, it has to be mentioned that because of irregular force signals for low cutting speeds, the force data is only shown for $v_{c,3} = 193.5$ m/min and $v_{c,4} = 270$ m/min.

The data presented in figure 5 reveals higher normal forces F_n than tangential forces F_t for all parameter combinations and analysed materials which is underlined by an adapted scaling in the diagrams for the particular force components. For all cutting speeds, there is a distinctive influence of the feed speed v_f on normal and tangential forces which does not depend on the different materials. Both, the normal forces and the tangential forces are higher for $v_{f,2} = 9.5$ mm/min than for $v_{f,1} = 2$ mm/min. This is generated by an increased feed rate f and therefore a larger area of the pyramidal diamond that is in contact with the material. This results in a higher chip cross-section. Scratch tests by *Apmann* on different types of concrete and steel showed that this has a strong impact on the resulting process forces [4].

Concerning the variation of the cutting speed v_c there is a trend of decreasing forces with increasing cutting speed, especially for $v_f = 9.5$ mm/min. As an exception the normal forces scratching cement stone have to be mentioned (cf. fig. 5, $v_f = 9.5$ mm/min). Lower forces for higher cutting speeds are influenced by the decreasing feed rate f with increased cutting speeds due to the helical process strategy of the conducted scratch tests. Regarding this, it has to be mentioned that the radius influences the feed rate as well wherefore the effect of cutting speed is superimposed. Comparing the different materials there are no distinctive differences between the mineral materials. Just for cement stone the process forces are marginal higher than those measured for basalt and concrete C100 for the majority of parameter combinations. Nevertheless, the absolute difference is low. On the other hand, scratching the steel leads to higher process forces than scratching the mineral materials in the analysed parameter range. In this case the different scale has to be emphasized. An exception are the tangential forces for the lower feed speed $v_{f,1} = 2$ mm/min. They are on comparable level with the tangential forces for the mineral materials.

Fig. 5: Normal and tangential forces in dependency of feed speed and cutting speed

To illustrate why the mean values for the forces in scratching the analysed steel were merely calculated for the higher cutting speeds v_c in the considered range, two exemplary developments of the force components F_n and F_t during scratch processes for two different cuttings speeds ($v_{c,1}$ = 40.5 m/min, $v_{c,4}$ = 270 m/min) are contrasted in figure 6. Due to the set feed speed of $v_{f,2}$ = 9.5 mm/min and the total depth a_e = 0.080 mm the calculated process time for both cuttings speeds is t = 0.51 s.

Tool:	CVD-diamond pyramidal, σ = 110°	Cutting speed v_c: v_c= varied	■ original force data
		Feed speed v_f: v_f= 9.5 mm/min	■ smoothed force data
Material: Steel (1.0577)		Process cooling: without	
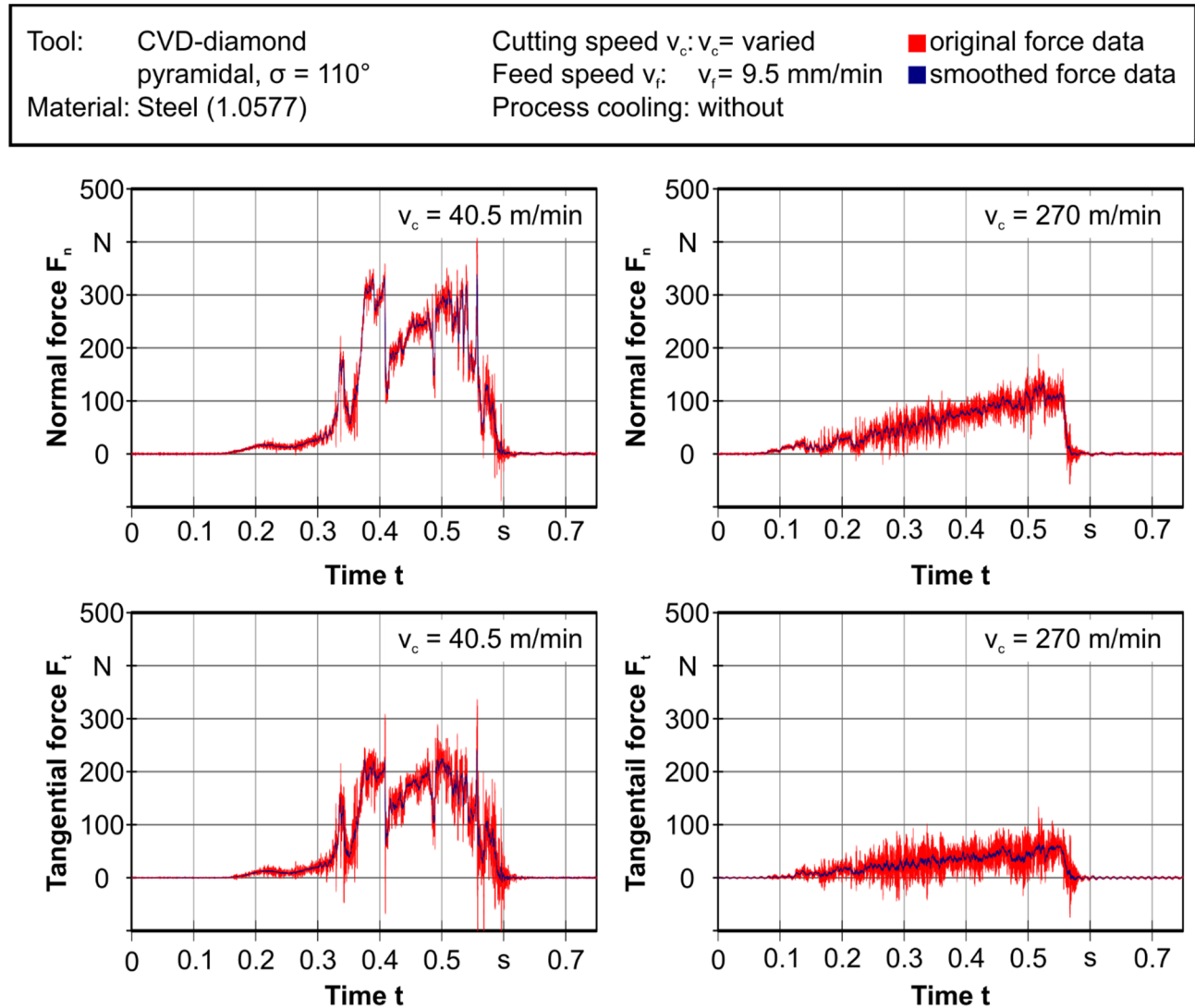
Fig. 6: Process forces for steel depending on cutting speed v_c

There are clear differences in the force signals comparing forces for the varying cutting speeds. For $v_{c,1}$ = 40.5 m/min an irregular force signal with several peaks and discontinuities results. In contrast, for $v_{c,4}$ = 270 m/min the rise of the force components is nearly linear with increasing process time and scratch depth respectively. This increase is generated owing to the increasing area of the diamond tool that is in contact due to the helical process strategy. Such a steady increase of forces does not exist for the shown force signals for $v_{c,1}$ = 40.5 m/min. The irregular development of process forces during the scratch process at low cutting speeds might result as a consequence of irregular chip formation processes or friction. Furthermore, the possibility of some kind of build-up edge has to be taken into account. Nonetheless, comparing the development of the two analysed force components, they are similar, whereas the normal force F_n is higher than the tangential force F_t, as also mentioned discussing figure 5. Despite of irregular force signals for a low cutting speed, the absolute force data can be compared. The absolute values of the two force components are higher for the low cutting speed than for v_c = 270 m/min. This again might be affected by the larger feed rate at lower cutting speeds due to the defined helical path of the diamond tool, but also the above mentioned effects may have an influence.

The steel part in reinforced concrete has a special impact on the process forces. In order to discuss this influence qualitatively, in figure 7 two exemplary force developments for scratch tests on reinforced concrete for different cutting speeds v_c and in this case constant feed speed v_f are shown analogous to figure 6.
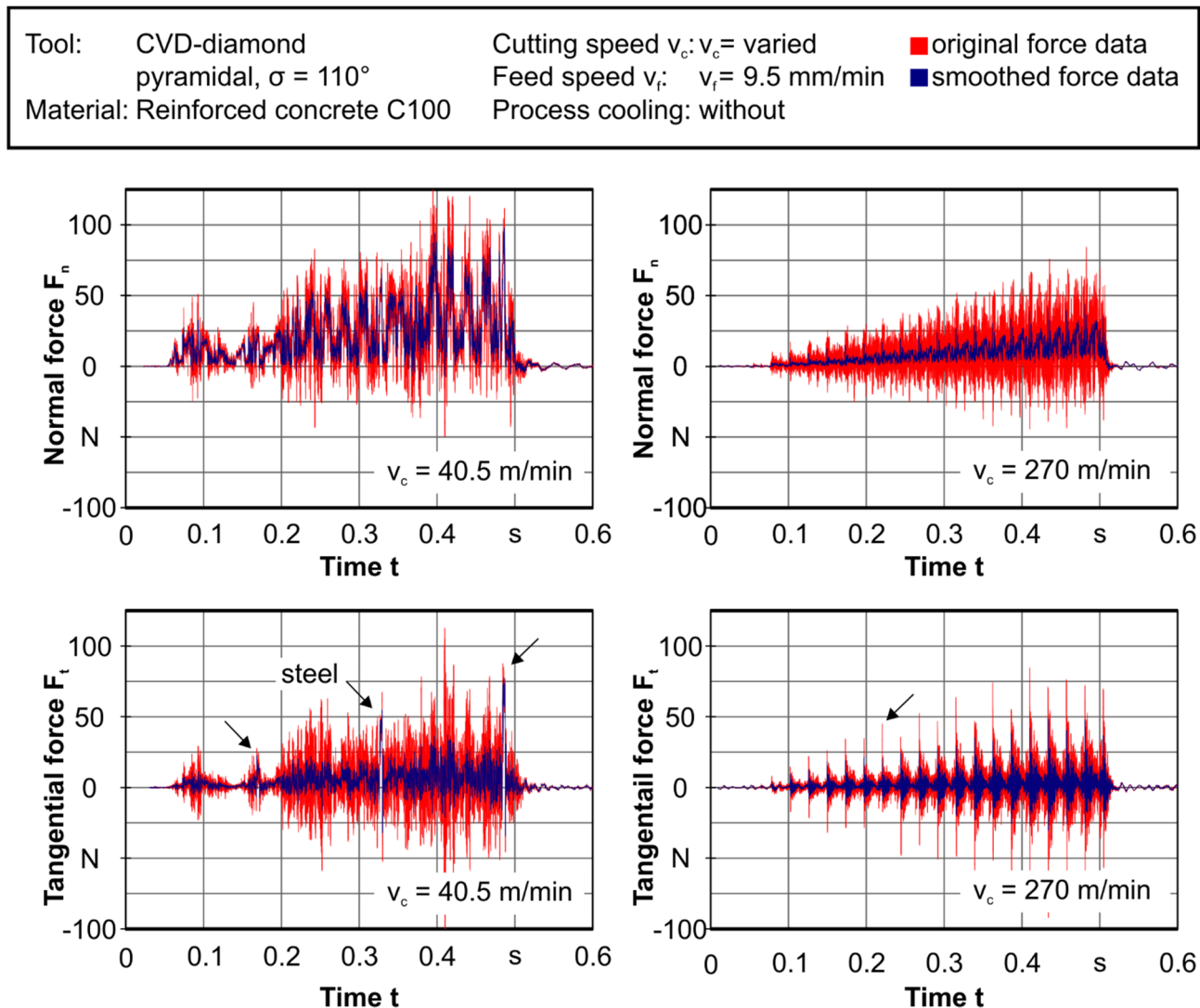
Fig. 7: Process forces for scratching reinforced concrete

The influence of the transition from the mineral material component to the metallic component is directly evident in tangential force signals for both presented cutting speeds. For $v_{c,4}$ = 270 m/min the transition results in high force peaks or kind of pulse as exemplary marked in figure 7. For the lower cutting speed $v_{c,1}$ = 40.5 m/min scratching the steel part causes longer periods with positive, increased tangential forces. In consequence of the chosen helical process strategy and the constant feed speed v_f the number of passing the steel part is reduced for lower cutting speeds. In the shown scratch test for a cutting speed v_c = 40.5 m/min the steel part is scratched three times as marked in the tangential force signal. Comparing those three periods, there is an increase of tangential force amplitudes with longer process time owing to a rise of the active cross section of the pyramidal diamond tool by the increased depth. The transition from mineral to metallic is less significant and not immediately obvious in the signals of the normal forces F_n. Nevertheless, using the additional information generated due to the use of a light barrier reveals the influence of the steel part even in normal forces. In the area of scratching steel there exists a period with comparatively high normal forces and less fluctuation of the force signal than mostly recognised in the signal of mineral material components. Unlike to former test results comparing process forces for concrete and reinforced concrete [8], in this case the influence is observable in the smoothed force data in the form of small peaks (cf. fig. 7, v_c = 270 m/min) as a consequence of an adjusted evaluation method.

3. CONCLUSION

In order to analyse the material separation of reinforced concrete with different approaches the results of two series of scratch tests with single grain diamonds and different objects of investigation were presented. The scratch tests conducted in a large-chamber scanning electron microscope allowed to analyse the qualitative differences concerning the characteristics of the scratches on steel, basalt and cement stone after multiple and iterative scratching on the basis of microscopic SEM pictures. Those scratch tests were carried out with a constant normal force and cutting speed using a tribometer.

Another kind of scratch tests was used to investigate the process forces. Regarding this the influences of varying feed speeds and cutting speeds were considered. The results showed that the feed speed has a strong effect on the force components for each investigated material. Whereas a higher feed speed leads to increased process forces, the increase of the cutting speed mostly causes decreasing forces. Comparing different force signals scratching steel exclusively reveals strong differences in the force development depending on cutting speed. Whereas high cutting speeds result in nearly linear increasing forces, low cutting speeds lead to irregular force signals. Concerning reinforced concrete the impact of the integrated reinforcement is obvious in the tangential force signal. But also in the normal force an impact of the steel is recognisable. Varying cutting speeds influence the signals as well. Aiming to analyse the influence of the steel in reinforced concrete on the process forces in more detail, further scratch tests on reinforced concrete with a higher amount of steel must be conducted.

The conducted scratch tests regarding the analysis of the material separation of the high-strength concrete and the reinforced concrete showed different loads and scratching conditions of the diamonds depending on the material. In contrast to the mineral constituents, for which forces are comparable, scratching or grinding the steel is challenging what is recognisable in core drilling as well. Therefore it is a need to adjust diamond tools and parameters to meet the particular requirements. Further tests could be conducted with varying diamonds (e.g. geometry, rake angle) with the aim of identifying possibilities to reduce process forces and to enhance the performance of core drilling tools.

ACKNOWLEDGEMENT

REFERENCES

[1]   Klocke, F., König, W., 2005, Fertigungsverfahren 2 – Schleifen, Honen, Läppen, Springer-Verlag

[2]   Meding, M., 1993, Beschreibung des Prozeßgeschehens bei der Zerspanung von Gestein und von dessen bruchmechanischem Verhalten unter besonderer Berücksichtigung der Schallemissionsanalyse

[3]   Denkena, B., Tönshoff, H.K., Becker, J.C., Bockhorst, J., Hillmann-Apmann, H., 2003, The mechanisms of material separation at steel and concrete material, in: Euro PM 2003, European Powder Metallurgy Conference on Meeting the Challenges of a Changing Market Place, European Powder Metallurgy Association (EPMA), pp. 87-95

[4]   Apmann, H., 2004, Seilschleifen von metallischen und mineralischen Werkstoffen, PZH Verlag

[5]   DIN EN 206, 2014, Beton – Festlegung, Eigenschaften, Herstellung und Konformität, Beuth Verlag

[6]   Neroth, G., 2011, Beton, in: Wendehorst Baustoffkunde, Vieweg+Teubner Verlag, pp. 247-381

[7]   Luo, W., Tillmann, W., Selvadurai, U., In Situ Wear Test on Thermal Spray Coatings in a Large Chamber Scanning Electron Microscope, Journal of Thermal Spray Technology, 24 (2015) 1-2, pp. 263-270

[8]   Kansteiner, M., Kipp, M., Herbrandt, S., Ferreira, M., Biermann, D., Process Forces and Groove Development in Single Grain Scratch Tests of Concrete and Reinforced Concrete, Applied Mechanics and Materials, 794 (2015), pp. 207-214

Session 2

A new method for the local removal of the surface area of reinforced concrete

Prof. Dr.-Ing. B. Denkena, Dr.-Ing. T. Grove, Dipl.-Ing. U. Hess
Leibniz University Hannover,
Institute of Production Engineering and Machine Tools (IFW),
An der Universität 2, 30823 Garbsen, Germany
+49 (0) 511 – 762 18093, hess@ifw.uni-hannover.de

ABSTRACT

The combined removal of steel and concrete during the removal of building structures is still a challenge due to the different material properties and the resulting requirements on the cutting tool. In this paper the authors will present a methodology, and its results, for enabling a milling process for the machining of reinforced concrete. To identify the different mechanisms taking place during cutting of the two materials concrete and steel, the machining of these materials were studied separately. The aim of this investigation is to identify the dominant wear mechanism and the process factors influencing the resulting cutting forces. Afterwards the observations and conclusions will be assigned to the cutting of the material compound. As influencing variables the size and form of the cross-section and the cutting speed were investigated. Furthermore the benefit of a tool coating in milling concrete and reinforced concrete was investigated.

KEYWORDS

REINFORCED CONCRETE; MILLING; PROCESS FORCES; TUNGSTEN CARBIDE TOOLS; TOOL WEAR

INTRODUCTION

In Germany the nuclear phaseout was resolved and hence, the dismantling of reactors for power generation already started and will continue for the next decades. A big advantage in the direct dismantling is a selective dismantling procedure in which the contamination can be removed by eliminating only a small part of the surface structure. In the next step the predominant part of the building can be recycled. This procedure offers the potential to reduce the amount of nuclear waste and thus the costs of dismantling. For example, in the nuclear plant Obrigheim only 600 t of the total amount of 143,000 t reinforced concrete have to be disposed as nuclear waste [1]. A central element of this strategy is the identification of contaminated areas and thus the local removal of reinforced concrete. In principle the processes and tools for the removal of concrete as well as for cutting pure steel are available. The combined removal in contrast is still a challenge due to the different material properties and the resulting requirements regarding the cutting tool. Furthermore, in areas with cracks or outbreaks in the building structure a removal has to take place. Techniques are available for the removal of concrete as well as for cutting pure steel. The combined removal is still a challenge due to the different material properties and the resulting requirements on the cutting tool.

A promising approach is the application of a dry milling process [2]. Because of its low price and its performance in machining steel, tungsten carbide is chosen as cutting tool material. However, findings of the processing of steel cannot be transferred to the processing of concrete. Concerning the material properties of steel and concrete the load spectrum on the

tools differs. Hence, these materials have different demands on process specifications and cutting tool properties, a process and tool development has to take place.

1. OBJECTIVES

With regard to this aim a classification of existing removal situations was carried out and corresponding concepts were provided. Hence, the situations were classified by the amount of steel in the present working area and their position to the free surface. This classification delivers information about the most important removal situation, affecting the requirements regarding the tool and process specifications. The cutting tool and process design concerns different cutting tool materials to improve tool performance, avoid spontaneous tool fracture and increase tool life time.

In the presented application cutting forces are of special interest because a mobile system is planned to be used and thus the process forces have to be handled. The system should empower the operator to realize removal of reinforced concrete in areas, which are difficult to reach. The process forces are a consequence of the contact conditions of tool and workpiece. Hence feed per tooth f_z, depth of cut a_p and cutting speed v_c were varied and their effect on the specific process forces will be analysed. These investigations were executed regarding the initial tool wear. Here the wear mechanisms are important to get information about the demands to the tool-material specifications. Referring to this tool features the effect of a coating on the used tungsten carbide was included in the investigations.

2. EXPERIMENTAL SETUP

The experiments are carried out on a vertical 3-axis milling machine type Heller PFV 1. The milling forces are measured with a Kistler 3-component dynamometer type 9255C. In order to analyse the resulting cutting forces and tool wear during cutting reinforced concrete, the different components of the material compound will be cut individually. The investigations in this study are conducted with a single tooth face mill with a diameter d = 40 mm. The concrete is composed of cemented stone and aggregates with a maximum size of 8 mm, respectively 32 mm. For the experiments on pure steel S355 J2+N is used as work piece material. The concrete percentage in the reinforced concrete work pieces is made with the same specifications. The reinforcement rods are out of BSt 500S with a diameter of 32 mm.

In this study the depth of cut a_p and the feed per tooth f_z are varied. With these parameters the cross-section of undeformed chip and the direction of the applied forces will be varied. The cutting speed is varied in a range from v_c = 80 - 300 m/min. All investigations are conducted with full immersion.

To identify the influence of a coating of the milling tools on the wear behaviour, the experiments were carried out with one tungsten carbide grade, with and without coating. A TiCN + Al_2O_3 multilayer coating was applied. All used indexable inserts have the geometry specification RDMT 2006 MO. They have a round geometry, with a diameter of 20 mm. All experiments are conducted with two repetitions. The wear of the cutting inserts is analysed with a Keyence VHX 600 video microscope and a scanning electron microscope (SEM).

3. MECHANICAL LOAD IN MILLING STEEL AND CONCRETE

PROCESS FORCES

In Fig.1 the process forces for one spindle revolution during machining steel and concrete is presented. For both materials the same process parameters were used. As depicted in Fig. 1 the process forces during milling steel in feed and feed-normal direction are 300 % higher in

contrast to concrete. Further, the process forces in steel exhibit a distinctive progression over the complete revolution. The maximal feed force occurs for the highest uncut chip thickness h_{max} at a feed motion angle of 90°. During cutting of steel the forces in feed and feed-normal direction are higher than the passive force component. Due to the ductile separation mechanism less friction occurs.

In contrast to steel the process forces in cutting concrete oscillate with the tool-revolution. Considering all experiments the force during cutting concrete in passive direction has a maximum at an arbitrary point during the revolution. This fact can be explained by the stochastic allocation of aggregates in the material. The feed and feed normal force are half the amount of the passive force. This can be explained by the theory about the separating mechanism in brittle materials. This mechanism proceeds in two steps. During the first step the material is pushed out of the kerf. In this step the mechanical load on the tool is low, because concrete withstands tensile strain to a minor degree [3, 4, 5]. Afterwards the material separation takes place under the cutting edge. At first the material is charged under compressive stress, this leads to high process forces in passive direction. If this material is released under the cutting edge, critical tensile strength occurs in the material and leads to brittle material failure behind the cutting tool [6].

Process parameters:

Cutting speed v_C	= 80 m/min
Width of cut a_e	= 40 mm
Depth of cut a_p	= 2 mm
Feed per tooth f_z	= 0.5 mm

Cutting tool:

Tool diameter D	= 40 mm
Insert Diameter d	= 20 mm
Carbide	= K15

Hes/79730 © IFW
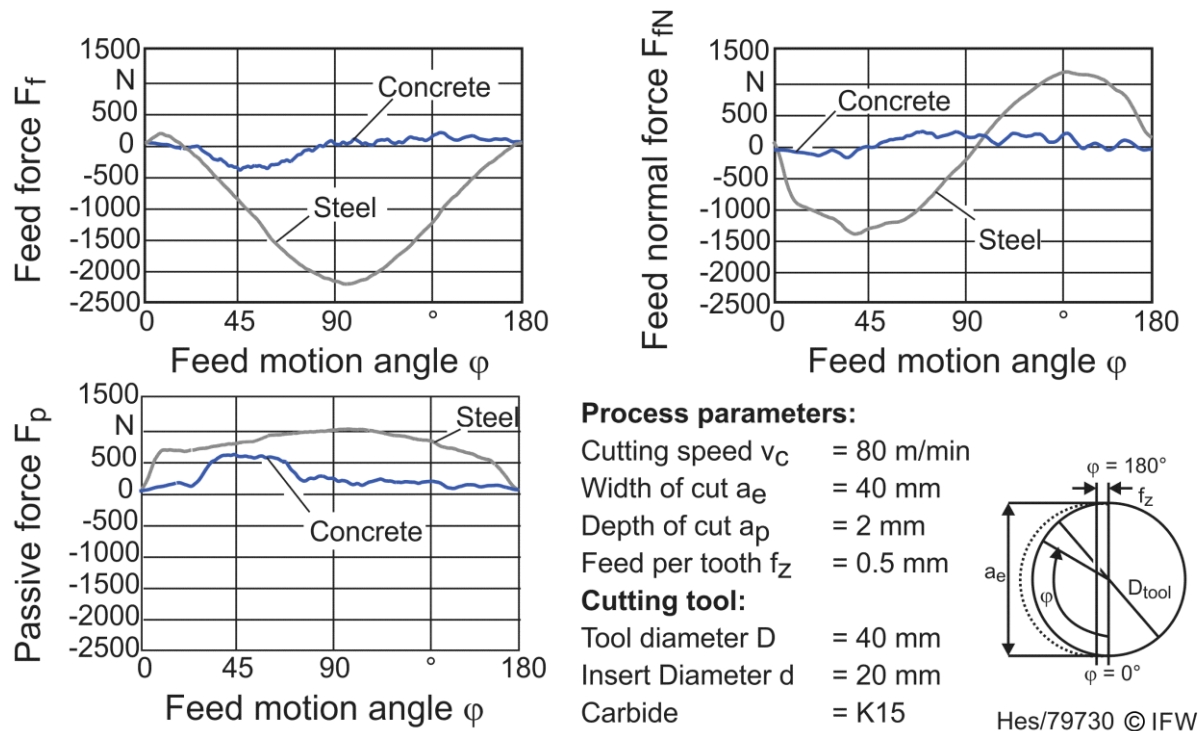
Fig. 1. Process forces during one tool-revolution

INFLUENCE OF CROSS-SECTION

Process forces are limited due to the stiffness of the used machine structure. Therefore the specific forces needed to machine one increment of the cross-section are of special interest. Based on the process forces the material removal can be increased. From this follows an increase of the productivity of the process.

In cutting processes of ductile materials inserts with a rectangular cross-section of undeformed chip are often used. For the cutting of mineral materials, cutting inserts with a round

geometry are advisable because they do not possess corner radius r_ε. On the corner radius the contact area between tool and workpiece can be very small and hence, increased stresses occur. This leads to rapid tool fracture [7]. Following the application of round cutting inserts, the uncut chip thickness varies along the cutting edge (Fig. 2). Based on the cutting insert radius r_ε, the working cutting edge angle κ changes along the cutting edge radius. The working cutting edge angle increases from 0° from the tool centre point to maximum value at the depth of cut. The uncut chip thickness rises similar from $h_o = 0$ mm over the effective uncut chip thickness h_{eff} to a maximum value h_1. Thus the cross-section of undeformed chip depends on the feed direction angle φ, the cutting edge angle κ and the feed per tooth f_z and is calculated by equation (2). Referring to Köhler [8] the effective width of undeformed chip b_{eff} (3) and the effective uncut chip thickness h_{eff} (4) can be calculated from the geometric relations in the cross-section of undeformed chip. The effective cutting edge angle κ_{eff} within this point can be achieved in the same way by equation (5) [9].
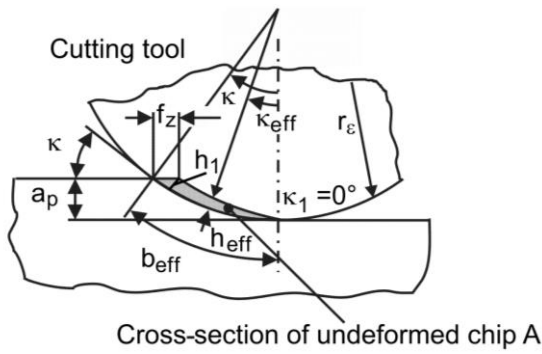
Fig. 2 Overview of the face milling process with round cutting inserts

$$A = a_p * f_c - \frac{1}{3} * f_c * \left(r_\varepsilon - \frac{\sqrt{4 * r_\varepsilon - f_c^2}}{2} \right) \qquad (1)$$

$$b_{eff} = r_\varepsilon * \left[\frac{\pi}{180} \left(k + \sin^{-1} \left(\frac{f_c}{2 * r_\varepsilon} \right) \right) \right] + \frac{[a_p - r_\varepsilon * (1 - \cos k)]}{\sin k} \qquad (2)$$

$$h_{eff} = \frac{A}{b_{eff}} \qquad (3)$$

$$k_{eff} = 90° - \cos^{-1} \frac{(r_\varepsilon^2 - (r_\varepsilon + h_{eff})^2 - f_c^2)}{(-2 * (r_\varepsilon + h_{eff}) * f_c)} \qquad (4)$$

In the following section the influence of the previously described parameters h_{eff} und b_{eff} on the process forces will be discussed for the two materials steel and concrete. For evaluation the maximum forces per revolution are calculated und averaged over all recorded revolutions at full immersion. Fig. 3 shows the dependence of specific cutting forces and cross-section dimensions for milling experiments. This data was recorded in experiments carried out with coated carbide tools on concrete with aggregates up to a size of 32 mm. The higher the effective uncut chip thickness is, the lower are the specific forces in each direction. The effective width of cut has no influence on the specific forces. The effective uncut chip thickness h_{eff} is mainly influenced by the set feed per tooth f_z. The effective chip width b_{eff} can be varied by different values for the depth of cut a_p.
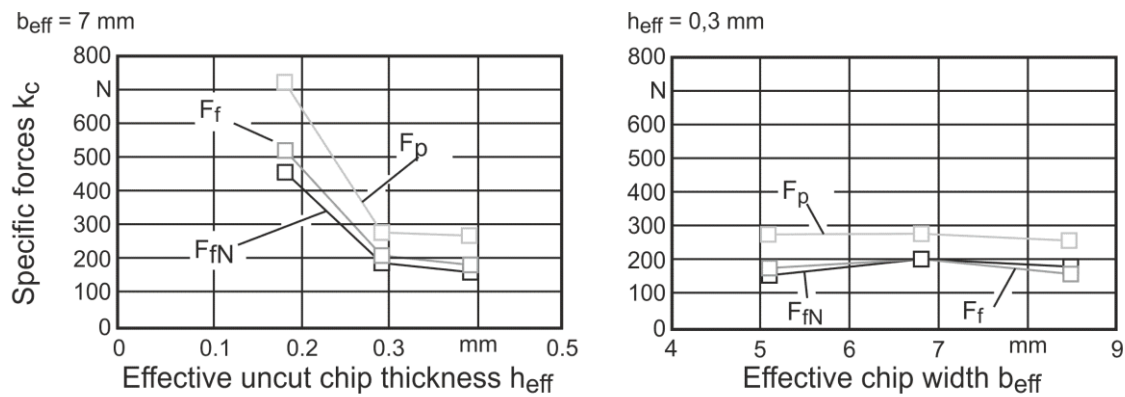
Fig. 3 Influence of cross-section geometry in milling concrete

Milling experiments were conducted with the same tool specification on steel (Fig. 4). For the parameter h_{eff} the same declining correlation could be found. The forces, in contrast to the milling of concrete, are rising linearly with increasing b_{eff} due to negligible influences on the chip formation.

Fig. 4 Influence of cross-section geometry in milling steel

However, concerning the overall forces for the concrete machining process (Fig.5), minor influences by varying the feed can be observed. This can be explained by the chip formation. Additionally, the cross-section of undeformed chip A leads to negligible influences on the process forces due to the secondary separation process. This material separation process is only related to the effective chip width b_{eff}, because this process takes place under the cutting edge. The forces F_i have a linear relationship to b_{eff}. The cross-section is proportional to the

effective chip width, too. For this reason the effective chip width has no influence on the specific forces in Fig. 3.

Furthermore the process stability can be increased for higher values of the feed per tooth. This can be seen by the reduced deviation in process forces between the repetitions represented by the error bars in Fig. 5. An increase of the feed per tooth enlarges the uncut chip thickness and the mechanical load is spread over a larger area. As a consequence the risk of tool fracture is reduced and thus the increase in process forces is prohibited. This statement is valid for the machining of pure concrete.

Process parameters:
Cutting speed v_c = 80 m/min
Width of cut a_e = 40 mm
Depth of cut a_p = 1 mm
Feed per tooth f_z = var.

Cutting tool:
Tool diameter = 40 mm
Insert diameter = 20 mm
Carbide = K15

Workpiece:
Material = var.

Hes/79733 © IFW
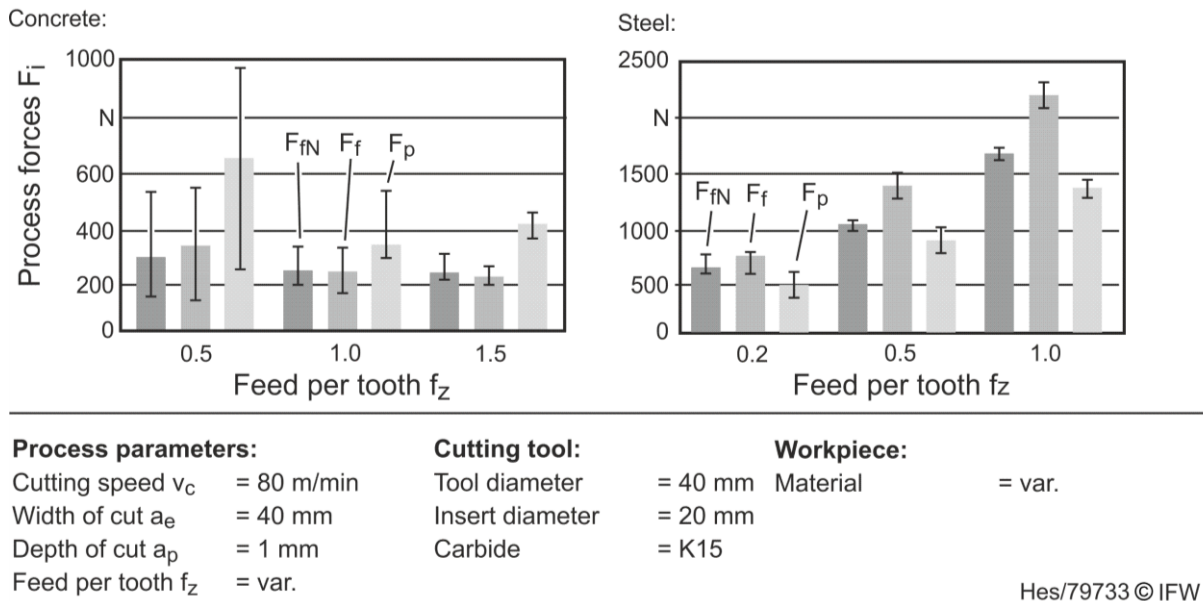
Fig. 5 Process forces in steel and concrete for different size of cross-section

INFLUENCE OF CUTTING SPEED

Besides the cross-section, the cutting speed is a significant factor for machining ductile materials. With increasing cutting speed the cutting forces can be reduced, furthermore the productivity of the process increases. The resulting process forces are shown in Fig. 6 with respect to the cutting speed. In steel the process forces show the known trend due to the variation in cutting speed. The process forces decrease with increasing cutting speed [10]. The dependency of the process forces in steel regard to the thermal softening of metals during the cutting process since the temperature increases with the cutting speed. During milling concrete this trend can't be observed. The measured forces deviate with the set cutting speed. For brittle materials like concrete the thermal softening is negligible. Therefore no relationship between the cutting speed and the process forces was expected. This was shown by Apmann for grinding of concrete, too [11]. However, with increasing cutting speed v_c, the impact on the tools is increasing. Consequently the risk of tool failure rises. This tool failure provides an explanation for varying process forces over the range of investigated cutting speeds.

The conducted investigations regarding the process parameters during machining steel and concrete show that for the right choice of cutting parameters, there is a conflict of objectives. High cross-section is beneficial regarding milling of concrete. In contrast for the machining of steel this is limited by the resulting overall forces. Because of increasing tool wear, when higher cutting forces are applied, cutting speed should be set lower than 100 m/min in con-

crete. While machining steel the process forces can be reduced with cutting speeds larger than 100 m/min.
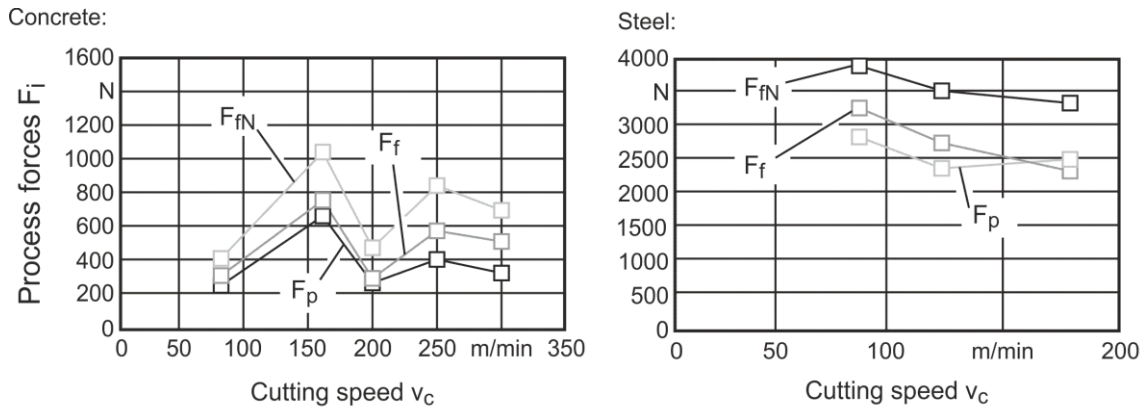
Process parameters:

		Cutting tool:		**Workpiece:**	
Cutting speed v_c	= var.	Tool diameter	= 40 mm	Material	= var.
Width of cut a_e	= 40 mm	Insert diameter	= 20 mm		
Depth of cut a_p	= 2 mm	Carbide	= K15		
Feed per tooth f_z	= 0,5 mm				

Hes/79734 © IFW

Fig. 6 Process forces in steel and concrete for different cutting speeds

4. WEAR MECHANISM

The SEM-micrographs in Fig. 7 present the resulting wear in concrete, after a feed travel l_f of 50 mm, and in steel, after 250 mm. It can be seen that the wear mechanism in steel and concrete differs.

Concrete: l_f = 50 mm
Uncoated tool:

Steel: l_f = 250 mm
Coated tool:

Process parameters:

Cutting speed
v_c = 80 m/min
Width of cut
a_e = 40 mm
Depth of cut
a_p = 1 mm
Feed per tooth
f_z = 0,5 mm

microcracks

chipping

100 µm

100 µm

Uncoated tool:

Uncoated tool:

Cutting tool:

Tool diameter
D = 40 mm
Insert Diameter
d = 20 mm
Carbide= K15

crater wear

flank wear

100 µm

100 µm

Hes/79735 © IFW
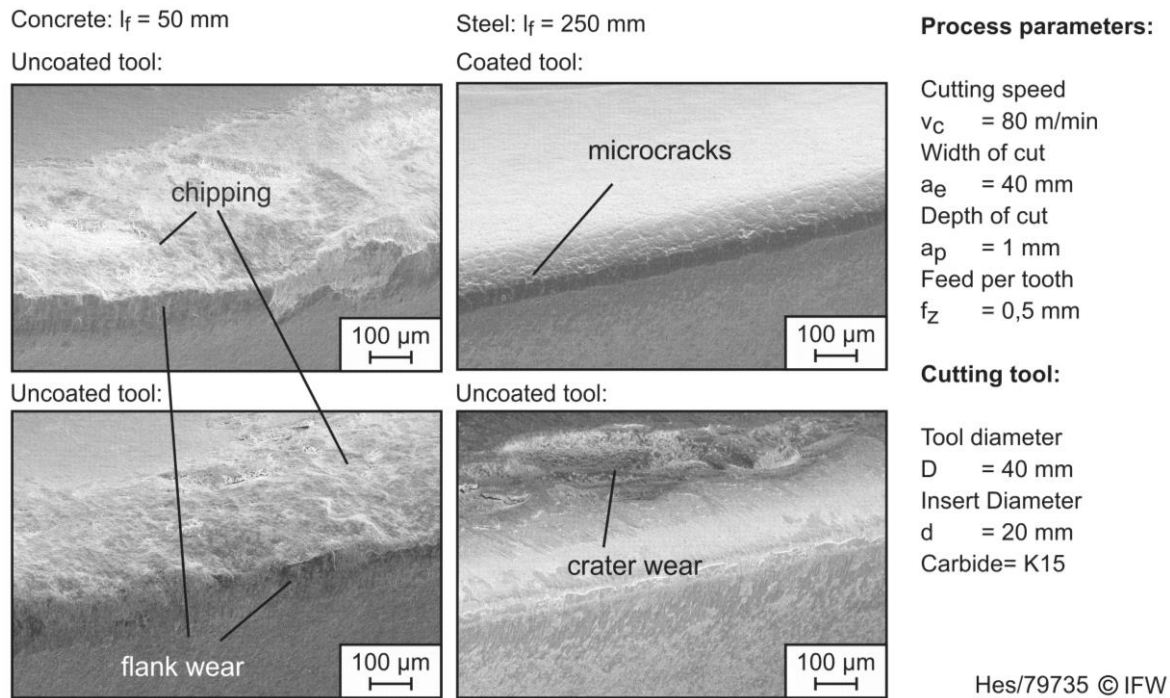
Fig. 7 Wear mechanism of the used tools in concrete and steel

In concrete the wear is a result of the mechanical load which follows in chipping on the cutting face. The flank wear follows from abrasion due to the cement dust in this area [7]. The initial wear of the coated tool increases after first coating failure due to the increased friction between tool and work piece. The observed tool wear mechanism in steel belongs to thermal damage. Here a larger difference between the coated and uncoated tool can be determined. The coated tool exhibits only micro cracks along the cutting edge. However, the uncoated tool shows crater wear with a width of about 200 µm.

5. TRANSFER OF THE FINDINGS TO THE MILLING OF REINFORCED CONCRETE

The experiments in reinforced concrete were conducted in cuts parallel to the reinforcement rods. Parameters in steel are the same used in concrete before.

Each parameter set was carried out with cutting direction from steel into concrete and once from concrete into steel. First of all it can be ascertained that the measured during the cutting of the compound Fig. 8 are higher than in the basic materials Fig. 1.

In concrete it can be shown that it is beneficial to increase the cross-section A-, because the process forces stay nearly constant and the risk of tool failure is decreased. This circumstance can't be used in the same way for the machining of the material compound. As presented in Fig. 8, the overall forces raise about 100% if the feed per tooth is increased from 0.5 mm to 1 mm per revolution due to the part of machined steel. An increase in process forces can also be assigned to the contact sequence concrete-steel because of cement particles getting into the kerf. Due to this, especially the passive force for the steel part is increased by about 300 % caused by the increased friction and the consequential tool-wear on this part of the cutting tool.

Concrete-steel:

Steel-concrete:

Process parameters:

Cutting speed v_c = 80 m/min
Width of cut a_e = 40 mm
Depth of cut a_p = 1 mm
Feed per tooth f_z = var.
Cutting tool:
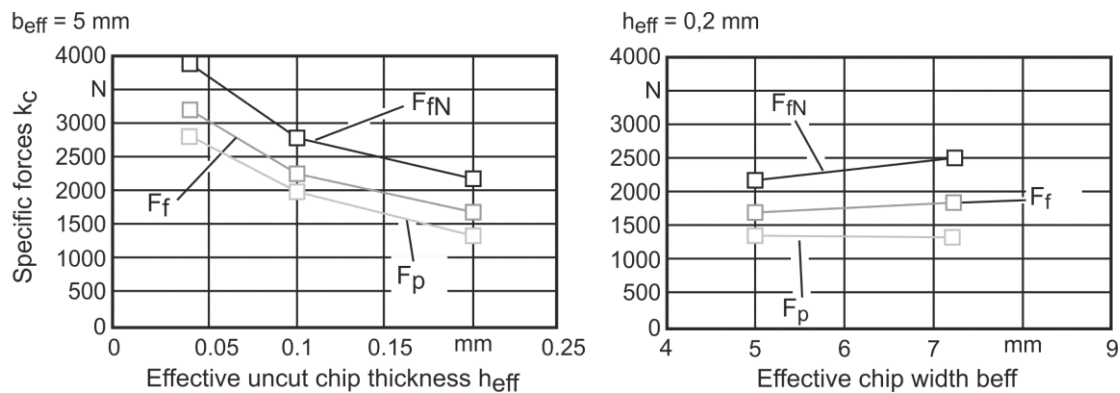Tool diameter D = 40 mm
Insert Diameter d = 20 mm
Carbide = K15 coated
Material: reinforced concrete

Hes/79736 © IFW
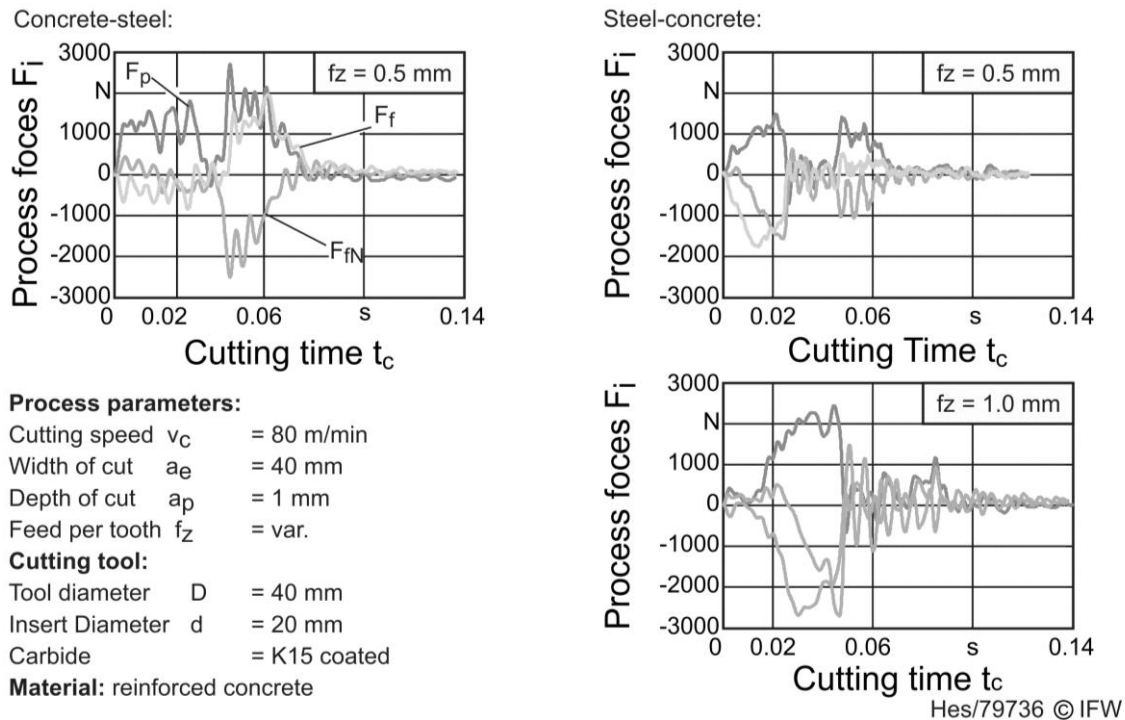
Fig. 8 Process forces in milling reinforced concrete

An increase in cutting speed is, as shown in Fig. 6, a possibility to reduce the process forces in machining ductile materials due to a significant reduction in strength with increasing process temperature. This effect can't be used for the machining of reinforced concrete, as the tools underlie rapid wear. The rapid tool wear leads to high process forces. Fig. 9 shows the tool wear for different cutting speeds and the coated and uncoated tool exemplarily. By applying a cutting speed of v_c = 180 m/min sudden tool fracture occurs. The coating is already removed in the contact area after 200 mm feed travel. However, the uncoated tool shows a higher maximum flank wear width. This can be explained by the hardness of the coating and thus increasing resistance against abrasive wear. The contact area is six times larger due to the flank wear and steel is adhered to the tool surface. At this point the passive forces reach a level of about 12-14 kN. Tools with this kind of wear condition often failed immediately when applied after this point. The reason for this wear is, that the cutting edge first becomes mechanically damaged through chipping when it gets in contact with the concrete. Then, as known from literature, processing ductile material with blunt tools causes high process forces and in consequence of the large contact area a lot of heat is generated on the flank face. These conditions lead to steel adhesions on the flank face, like it can be seen on the right part of Fig. 9. This material is torn away from the flank face and the wear increases further.

Coated tool:

v_c = 80 m/min — Flank wear width — chipping — 250 µm

v_c = 180 m/min — Flank wear width — adhesion — 250 µm

Uncoated tool:

v_c = 80 m/min — Flank wear width — chipping — 250 µm

v_c = 120 m/min — adhesion — 250 µm

Process parameters:

Cutting speed
v_c = var,
Width of cut
a_e = 40 mm
Depth of cut
a_p = 2 mm
Feed per tooth
f_z = 0,5 mm

Cutting tool:

Tool diameter
D = 40 mm
Insert Diameter
d = 20 mm
Carbide= K15

Hes/79737 © IFW
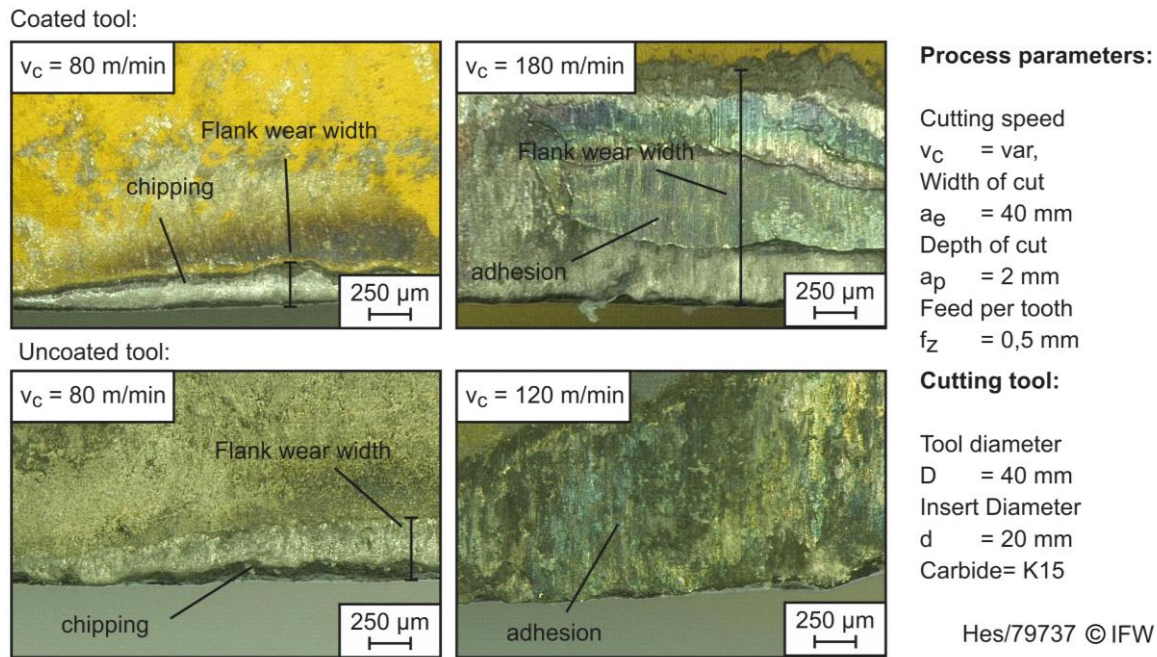
Fig. 9 Tool wear mechanism in machining reinforced concrete

6. CONCLUSION AND OUTLOOK

This study deals with the fundamentals regarding milling of reinforced concrete with tungsten carbide tools. The usage of tungsten carbide tools exhibit benefits with respect to the tool costs in comparison to cBN or PCD tools. In addition tungsten carbide tools have a lot of applications in the machining of ductile materials. For the machining of brittle materials, such as concrete, the capabilities are not known. For this purpose cutting experiments were carried out on concrete, steel and finally reinforced concrete. According to the mechanical load the following conclusions can be drawn:
Increasing the cross-section leads to constant process forces and constant resulting initial tool wear for the machining of concrete. For the machining of steel the process forces decrease with an increase in cutting speed. These two effects offer the opportunity to reduce the tool load if only one material will be machined. The experiments in reinforced concrete show, that larger cross-section results in higher process forces due to the steel. Higher cutting speeds lead to rapid tool failure due to the concrete. From there the smallest investigated cross-section and the lowest cutting speed are advisable for the machining of reinforced concrete.

Nevertheless the used tools underlie fast tool wear. This wear results in sudden tool failure even after short processing time. For this reason the tools have to be further developed for this application. To reduce the abrasive wear the usage of other tool coatings could be advisable. The major factor is the chipping of the cutting edge, this can likely be reduced by higher fracture toughness of the tungsten carbide and a stronger adherence of the coating to the base material.

For the ongoing investigations an approach with different process parameters for the different materials in the compound will be pursued. For this purpose an online and an in advance process monitoring has to be applied. Furthermore the amount of the part of machined concrete should be reduced to increase the tool life time. For this reason a second machining

process will be installed. This process should operate in advance and expose the steel installations.

7. ACKNOWLEDGEMENTS

REFERENCES

[1] N.N., 2013, Kernkraftwerk Obrigheim in Stilllegung, Deutsches Atomforum e.V.

[2] Weidemann, R, et.al., 2013, Confined precise removal of reinforced concrete, KONTEC

[3] Kun, L.; Liao, T.W., 1997, Modelling of ceramic grinding processes, Part I. Number of cutting points and grinding forces per grit, Journal of Materials Processing Technology, Issue 65, pp. 1-10.

[4] Egger, R., 2001, Planschleifen von Keramik mit zykloidischer Wirkbewegung, Dr. Ing. Dissertation, Universität Hannover

[5] Ertingshausen, W., 1984, Zerspanung von Granit mit Diamanttrennschleifscheiben, Dr.-Ing. Thesis, Universität Hannover

[6] Busch, D. M., 1968, Ritz- und Verschleißuntersuchungen an spröden Werkstoffen mit einzelkornbestückten Hartstoffwerkzeugen, Dr.-Ing. Dissertation, Universität Hannover

[7] Reichenbächer, H., 2010, Trennen mineralischer Werkstoffe mit geometrisch bestimmter Schneide, Dr.-Ing. Dissertation, Universität Kassel

[8] Köhler, J., 2010, Berechnung der Zerspankräfte bei variierenden Spanungsquerschnittsformen, Dr.-Ing. Dissertation, Leibniz Universität Hannover

[9] Denkena, B., et. al., 2015, Development of cutting edge geometries for hard milling operations. CIRP Journal of Manufacturing Science and Technology, Vol. 8, S. 43-52

[10] Ben Amor, R., 2003, Thermomechanische Wirkmechanismen und Spanbildung bei der Hochgeschwindigkeitszerspanung. Dr.-Ing. Dissertation, Universität Hannover

[11] Apmann, H., 2004, Seilschleifen von metallischen und mineralischen Bauwerkstoffen. Dr.-Ing. Dissertation, Universität Hannover

ANALYSIS OF THE CUTTING PROCESS FOR MILLING OF MARBLE AND SANDSTONE WITH AN END MILL CUTTER

Prof. Dr. h. c. Dr.-Ing. Eckart Uhlmann, Marcel Manthei

Fraunhofer Institute for Production Systems and Design Technology (IPK), Berlin,

marcel.manthei@ipk.fraunhofer.de

ABSTRACT

Research has shown that it is possible to machine natural stone materials using end mill cutters with geometrically defined cutting edges as they are used in metal cutting processes. The milling process can be used as an energy efficient alternative to the well-known grinding processes. A study of Fraunhofer IPK investigates the cutting process for Postaer Sandstone and Carrara Marble using an end mill cutter. A high speed video camera was used in order to analyze the cutting process. The produced stone particles ("chips") were sorted according to their size distribution and the resulting surface roughness was measured in order to identify possible influences of different cutting parameters. For the study, the depth of cut a_p, the feed per tooth f_z and the cutting speed v_c were varied. For the influence on the surface roughness, results show that all three parameters have a significant influence when machining marble. For the machining of sandstone, no significant influence has been identified. The distribution of sandstone particles after the milling process is independent from the cutting parameters as well, only the depth of cut shows an influence for marble. The high speed videography of the cutting process shows obvious differences between the two investigated natural stone materials. The chip formation for Carrara Marble is a rather continuous process whereas for sandstone the cutting process is rather random and can hardly be influenced by altering the process parameters.

KEYWORDS

Stone Milling, influence of cutting parameters, end mill cutter, high speed video analysis, particle distribution analysis, Postaer Sandstone, Carrara Marble

INTRODUCTION

In recent years many researchers have investigated the cutting process for natural stone machining. Most of the work is based on the use of abrasive diamond tools as they are mainly applied for the cutting of natural stone. The most well-known and referenced work in this area is the work of Wagner [1] who divides the chip formation process into two different steps, stating that the cutting process leads to crushed material on the one hand and discontinuous chips on the other hand. Clausen and Meding [2] use single grain diamonds and perform scratch tests to investigate the cutting process which they divide into three different process steps. The primary chip formation occurs in front of the cutting edge where micro and macro-cracks occur due to the compressive stresses induced by the diamond grain. They state that the cutting process depends on the grain size and the mineral distribution of the workpiece material. For fine grained materials a plastification of the surface occurs under the diamond. The plastified zone is then separated from the surface. This step

is called secondary chip formation. For coarse materials, the secondary chip formation is characterized mostly by transcrystalline cracks. The cutting process model of Tönshoff and Asche [3] is almost the same as Clausen's and Meding's. The main difference is the use of a diamond cutting wheel and a coolant instead of a single diamond grain. Reichenbächer [4] also states that the cutting process of natural stone materials is characterized by a primary and secondary chip formation process. Except Tönshoff and Asche, who use a rotating tool, all of the authors use single diamond grains or tools to perform linear scratch tests. This paper aims to contribute to a better understanding of the cutting process and the influence of the cutting parameters when using a rotating end mill cutter for the machining of natural stone.

1. EXPERIMENTAL SET UP

Two different natural stone materials were selected for the tests: Postaer Sandstone and Carrara Marble. Postaer Sandstone is a sedimentary rock and is mainly used for façade elements of buildings [5]. Carrara Marble, a metamorphic rock, is one of the most well-known natural stone materials in the world. Besides its use for sculptor work and monuments, it is often used as decorative flooring or tiles [6].

A 3-axis milling machine was used in all test presented in this paper. A single bladed end-mill cutter with a diameter of 16 mm was used to investigate the influence of the cutting parameters on the particle size distribution of the chips. After each test run, the particles remaining in the working area of the machine were collected and separated according to their size by using a sieve shaker. Six different sieves with grit sizes of 600 µm, 150 µm, 125 µm, 100 µm, 75 µm and 50 µm were used. Remaining, smaller particles were collected in a pan. For the tests, the cutting speed v_c, the feed per tooth f_z and depth of cut a_p were varied according to table 1. An orthogonal design was used to define the values of the parameters and a regression analysis allowed identifying significant and insignificant influences of the parameters. The value $\alpha = 1.28$ was calculated based on the criterion for an orthogonal design according to Kleppmann [7]. The design of experiments leads to a total of 48 different factor combinations. Each of the factor combinations was tested three times. In order to analyze the results, a factor was introduced which allows to compare the size distribution of the stone particles. The factor is called particle size factor (PSF) and is calculated based on the percentage of mass distribution multiplied by the grit size for each sieve. The lower the factor is, the higher the percentage of small particles is and vice versa. For the video analysis, a high speed video camera using a frame rate of 1000 frames per second. Besides the single blade end mill cutter, other tools have been tested in order to find out if the tool geometry and cutting material have a noticeable influence on the cutting process. All tests are performed without coolant in order to be able to separate the particles and to record the cutting process clearly.

Table 1: Parameters and parameter values

Parameter		Parameter value				
		- α = -1.28	-1	0	1	α = 1.28
A: cutting speed v_c	m/min	53.78	62.8	94.2	125.6	134.62
B: feed per tooth f_z	mm	0.13	0.15	0.225	0.3	0.32
C: depth of cut a_p	mm	0.86	1	1.5	2	2.14

2. PARAMETER INFLUENCE ON THE SURFACE ROUGHNESS

After each test, the roughness of the machined surface was analyzed with a tactile surface measuring device. The roughness average Ra is used to rate the influence of the parameters. The Ra value is the arithmetic average of the profile heights of the surface and hence is hardly influenced by peaks within the measurement distance. This allows investigating the influence of the parameters rather than the influence of the material structure.

In order to identify parameters with a significant influence on the roughness of the natural stone surfaces, regression coefficients and confidence levels were calculated. The results for both Postaer Sandstone and Carrara Marble are shown in figure 1.
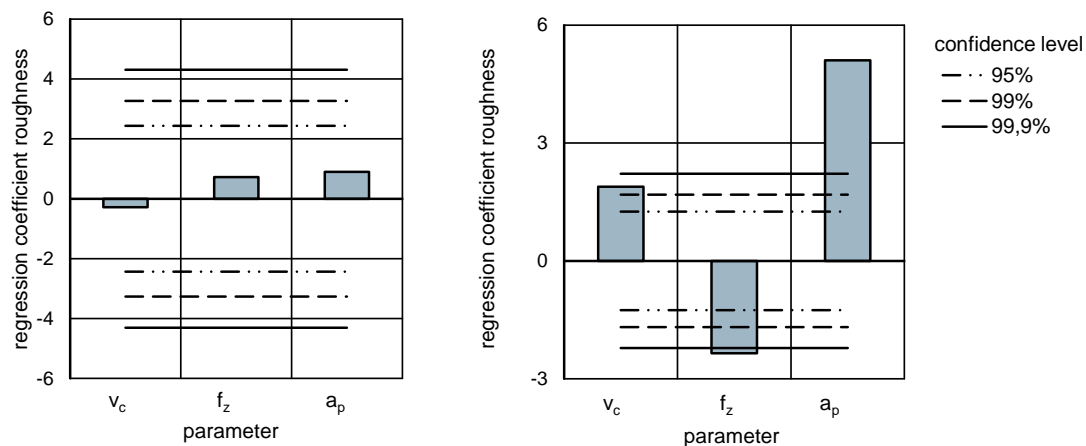
Fig. 1: Regression coefficients for the surface roughness for Postaer Sandstone (left) and Carrara Marble (right)

According to the results of the regression analysis, no significant influence of the cutting parameters on the surface roughness value Ra can be identified for milling Postaer Sandstone. That means a specific manipulation of the resulting surface roughness by altering the milling parameters is not possible. When looking at the results for each parameter combination, the surface roughness seems to be completely independent from the parameters within the investigated range. It is more likely the material influences the results. In several cases, large holes on the surface can be observed. These holes occur when single quartz particles break out of the surface as a result of the milling process.

For Carrara Marble, all three parameters have a significant influence on the surface roughness. The regression analysis shows that the value of the roughness average can be minimized by using low cutting speed v_c, high feed per tooth f_z and a low depth of cut a_p. The influence of all three parameters is linear within the investigated range.

3. PARTICLE DISTRIBUTION ANALYSIS

The stone particles are collected from the working space of the machine after each test run. Figure 2 shows the particles of a test run with Postaer Sandstone for the different sieve sizes. Particles mostly look the same for each sieve. For the large sieve > 600 µm most particles show a footprint area of about 1 mm², but individual, significantly larger particles with a footprint of up to 1 cm x 1.3 cm have been found. A representative image for the particle distribution of marble is given in figure 3.
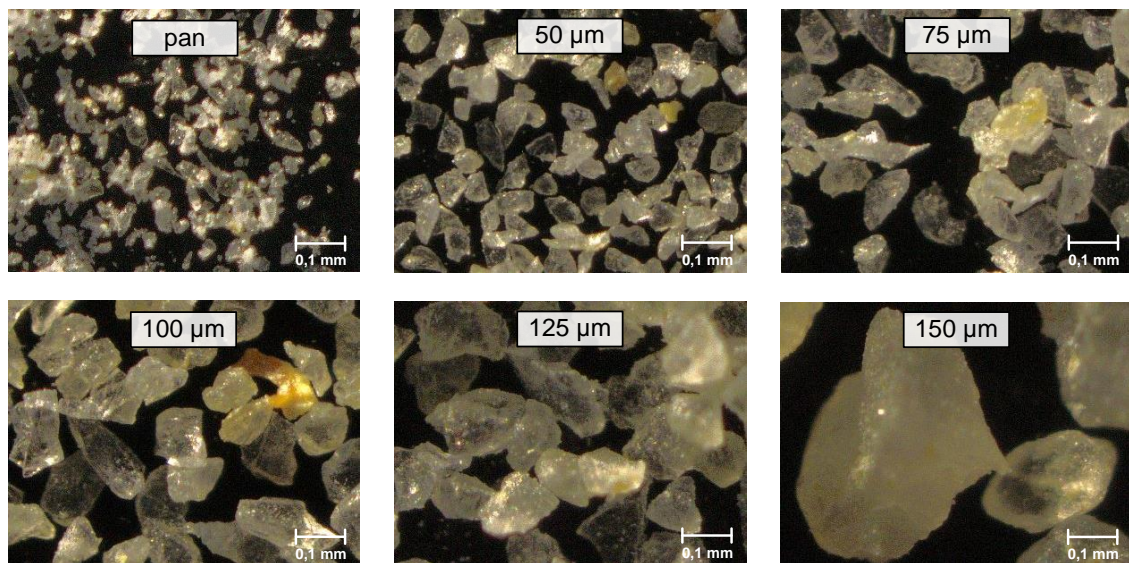
Fig. 2:   Particle distribution for Postaer Sandstone
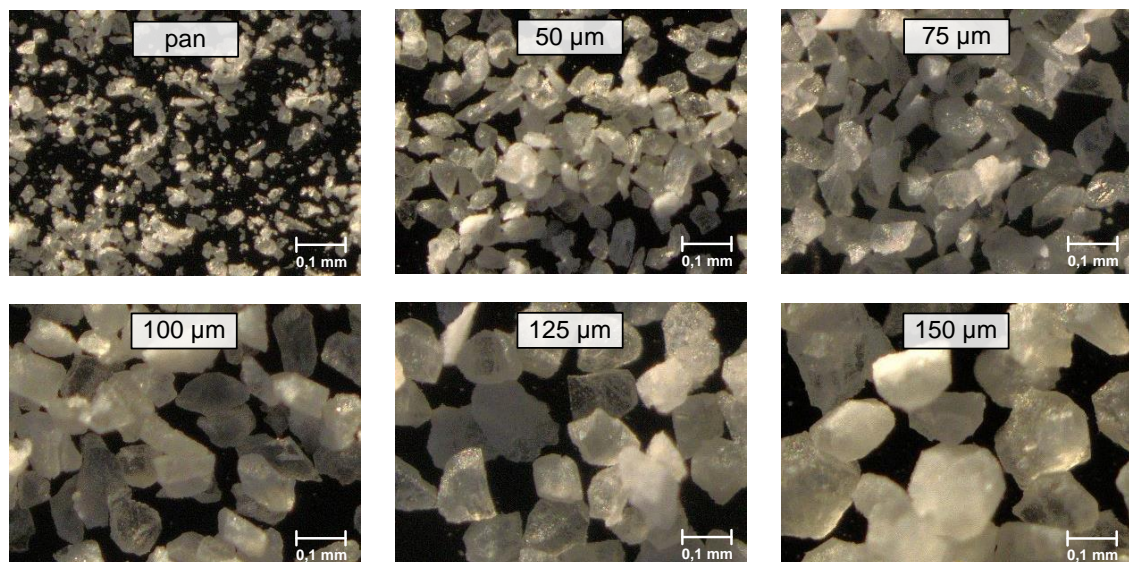
Fig. 3:   Particle distribution for Carrara Marble

When comparing the particles in the figures, they look similar besides the fact that two materials with different properties have been used. The macroscopic analysis of the particles with sizes > 600 µm shows some differences. When milling sandstone, whole material grains are removed from the workpiece. The particles are literally pulled out of the surface. For marble, most of the large resulting particles have a rather two-dimensional shape, the process seems to work more like a chipping process.

The results of the regression analysis for the cutting parameter influence on the particle size factor PSF are shown in figure 4. For Postaer Sandstone, no significant influence has been found, though the feed per tooth shows a tendency to influence the PSF when further increasing it beyond the value that has been used as maximum within this study. When machining marble, parameter C, the depth of cut, has a significant influence on the PSF. Moreover the surface roughness and the

PSF seem not to be linked to each other, as the roughness is influenced by all three parameters and the PSF just by one. The influence of the depth of cut on the PSF is linear, that means a low value for a_p leads to smaller particles and a high value to larger particles.
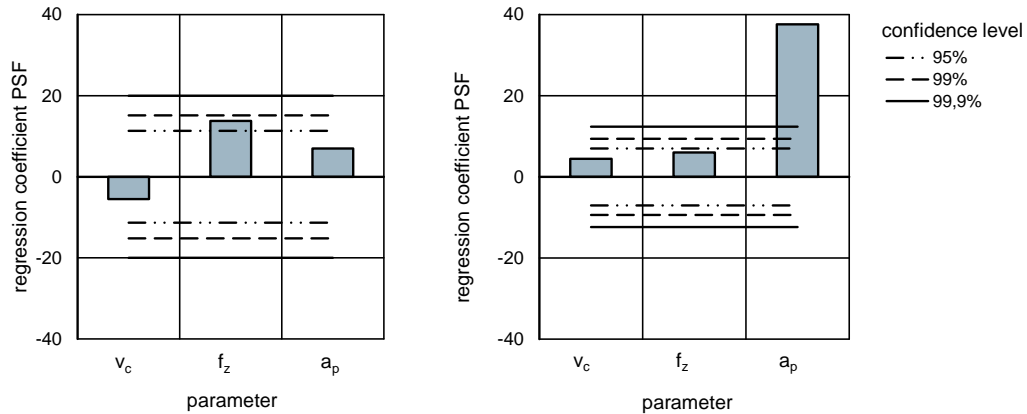
Fig. 4:   Regression coefficients for the particle size factor for Postaer Sandstone (left) and Carrara Marble (right)

4. HIGH SPEED VIDEOGRAPHY

The following figures are snapshots from the high speed videos that were recorded during the test runs. For each parameter combination, small and larger particles are removed from the workpiece. The occurrence of larger particles seems to be random, no correlation with the cutting parameters can be identified. This verifies the previous results regarding the surface roughness and the particle size distribution: The cutting process for milling Postaer Sandstone depends on the material properties and its grains rather than on the cutting parameters. Figure 5 shows an example of the cutting process for Postaer Sandstone. Snapshots were taken at the beginning and after 10 ms and 20 ms. Most of the resulting particles are small-sized, but after 10 ms a pull-out of a significantly larger particle can be seen. The large particle has a footprint area of roughly 4 x 2 mm².

a) 0 ms   b) 10 ms   c) 20 ms

Fig. 5:   Snapshots of the machining of Postaer Sandstone

Figure 6 shows exemplary snapshots from the cutting process of Carrara Marble. The images support the results of the particle distribution analysis. On the one hand,

small, "dusty" particles occur during the whole process and on the other hand rather two-dimensional chips can be found. The chips usually do not occur directly at the cutting edge but mostly just in front of it and in some cases behind the cutting edge. The reason for that might be that the cutting forces lead to compression stress within the workpiece material. If the stresses are too high, material failure occurs and the chips are removed from the workpiece material in front of the cutting edge. In case of the chip formation right behind the cutting edge, a resilient material behavior seems to be a possible reason for the chip formation.

a) 0 ms   b) 5 ms   c) 10 ms

Fig. 6:   Snapshots of the machining of Carrara Marble

5. SUMMARY AND CONCLUSIONS

The results show that the cutting and hence the chip formation process for the milling of natural stone materials mainly depends on the workpiece material. For Postaer Sandstone, which can be characterized as a coarse grain material, the cutting process is rather random. The tested parameters, cutting speed v_c, feed per tooth f_z and depth of cut a_p show no significant influence on the chip formation. The material removal depends on the grain composition which leads to a pull out effect of whole grains due to compressive stresses induced by the tool. A repeatable machining of Postaer Sandstone is not possible for the tested parameters. Even when a test with a defined parameter set up is repeated, the results concerning the surface roughness and the PSF may differ strongly. The high speed videography shows that the process leads to two different kinds of particles and hence confirms the cutting process models by the authors mentioned in the introduction of this paper.

When machining the fine graining Carrara Marble, test results are repeatable and the cutting parameters show an influence on the roughness and the particle size factor. To reach a low surface roughness, a low cutting speed and depth of cut should be used in combination with high feed per tooth. A low depth of cut a_p also helps to produce rather small chips. The formation of large chips occurs mainly at the edges of the workpiece and can be reduced by slot cutting. Stone materials are natural materials, hence their properties differ from material to material or even within the same material. The results show that using end mill cutters for machining and especially shaping of natural stone materials is an effective way for a fast near net shaping of workpieces. Suitable cutting parameters and machining strategies have to be investigated beforehand for each workpiece material.

REFERENCES

[1] Wagner, H, 1971, Der Mechanismus der Spanentstehung beim Zerspanen von Gesteinen, Rock Mechanics, Heft 3, 159-174

[2] Clausen, R, Meding, M, 1994, Untersuchung zum Spanbildungsprozess bei Gestein, Industrie Diamanten Rundschau 4 (1994), S. 224-227

[3] Tönshoff, H.K, Denkena, B, Apmann, H.H, Asche, J, 2013, Diamond Tools in Stone and Civil Engineering Industry – Cutting Principles, Wear and Application. Machining of Natural Stone Materials, Uetikon-Zürich

[4] Reichenbächer, 2010, Trennen mineralischer Werkstoffe mit geometrisch bestimmten Schneiden, Universität Kassel

[5] Börner, K.; Hill, D., Die große Enzyklopädie der Steine. URL: http://www.abraxas-stone-experts.com

[6] Müller, F, 2001, Gesteinskunde, Ebner

[7] Kleppmann, W, 2011, Taschenbuch Versuchsplanung, Hanser

Analysis of the material removing mechanism for an automated chiselling approach

Dipl.-Ing. G. Steinhagen
TU Dortmund, Institut für Produktionssysteme (IPS), Leonhard-Euler-Str. 2, 44227 Dortmund
gregor.steinhagen@ips.tu-dortmund.de

Univ.-Prof. Dr.-Ing. Bernd Kuhlenkötter
2Ruhr-Universität Bochum, Lehrstuhl für Produktionssysteme (LPS), Universitätsstr. 150,
Gebäude IC 02/739, 44801 Bochum
Kuhlenkoetter@lps.rub.de

ABSTRACT:
The European stone industry was exposed to great competition during the last years. However the European market is still the most important one for natural stone products. Especially traditional artistic processing techniques are very expensive due to the high personnel requirement. Thus automation becomes interesting for economic reasons. To process individually designed stone products it is planned to use a robot mounted tool.

One of the issues to achieve this goal is the analysis of the material removal to get repeatable results. We analysed different manual techniques used for sandstone surfaces in a first step and measured the movement of the chisel with a high speed camera system. We chose two techniques for further analysis and designed a first mechanical testbed to achieve repeatable kinetic energies. The material removal was analysed with the camera. Thus we are able to see the movement of the chisel and the flow of the removed material.

With this knowledge the analysis of relevant material and process properties will be shown as well. Furthermore, this paper discusses the relevant result parameters which define the optical quality of the surface. Combining these data it is possible to analyse the working parameters of an automated system which is able to process various sandstones with individual surface geometries.

KEYWORDS

Artistic Stone Production; Traditional Stone Processing Techniques; Analysis of Handcraft; Material Removal with chisel

INTRODUCTION

The European Stone market has the highest per capita consumption of stone products. However the European industry has seen bigger competition over the last years. High personnel costs drive companies to apply more automation to their processes. Especially the application of industrial robots with their flexibility and large workspace are promising for the stone industry. Yet surface finishing with traditional techniques is still mainly manually applied. They are physically demanding, require training and skills and the process is slow. Thus the personnel costs make large surfaces expensive. Other technologies are used to finish stone products or imitate traditional techniques such as milling [1] and waterjet-cutting [2], [3].

The approach to imitate traditional techniques with other tools has not the same optical quality then the original techniques. Therefore, an application to tasks such as restauration is not yet done. The approach of the research presented in this paper is to analyse traditional processing techniques and design a robot mounted tool based on these to produce surface qualities that are similar to original techniques. However, many parameters have to be estimated. There is a high amount of different techniques which developed in centuries. They differ in applied tools, tool handling, required skill of the mason and the applicability to different stones.

Different stones show different material behaviour for the techniques. Stone manufacturers usually use many different stones. Thus, the combination of techniques and stones changes often. The masons adapts to different stones both by experience and controlling his results visually. Sometimes masons make even trial hits to adjust to a stone. This is not possible in automated process. Therefore, it is necessary to analyse the material removal behaviour of traditional techniques to apply the right amount of hitting energy for each stone.

There are analyses of scratching tests for estimating the compressive strength [4], analysis of the brittleness of stones [5] or the application of Schmidt hammers which do not have a sharp tip [6]. But the combination of an energy impulse to a chisel tool and its material removal in a stone has not been analysed to our knowledge. In the literature only anthropological analysis of manual techniques can be found [7]. [4] shows furthermore that there is a ductile and a brittle mode of material removal in stones. Both modes can be seen in our results and will be further described.

In this paper we describe a first selection of analysed techniques (section 1), the description of the quality aspects of traditional stone surfaces (section 2), the design of a preliminary testbed and the analysis of the material removal mechanism (section 3) and the analysis of process parameters which are relevant for the process (section 4).

1. TRADITIONAL STONE PROCESSING TECHNIQUES

Traditional artistic stone processing techniques evolved over a long period of time. Thus many different techniques and patterns of techniques can be found especially on historic buildings but also in new applications. Masons use traditional elements to finish surfaces and create individual stone products. Furthermore, there are local deviations in some techniques and the combination with different natural stones results in a high amount of different techniques and variations for different materials.

Therefore, we did a preliminary selection of techniques, which were both promising to automation and economic usage. We chose four techniques which are tooling, aligned tooling, punching and bush hammering. All these techniques are typically applied to sandstone. Because of this all presented analysis are only made with sandstones. We will give a short description of the techniques, and explain how the tool interacts with the stone. A detailed analysis of the automation of these techniques can be found in [8].

We first analysed the manual techniques using a high speed camera system GOM Pontos HS Figure 1. With this System, we were able to analyse the movement of the tools and the velocity of the hammer right before the impact and thus estimate the kinetic energy applied to the tool for the different techniques.
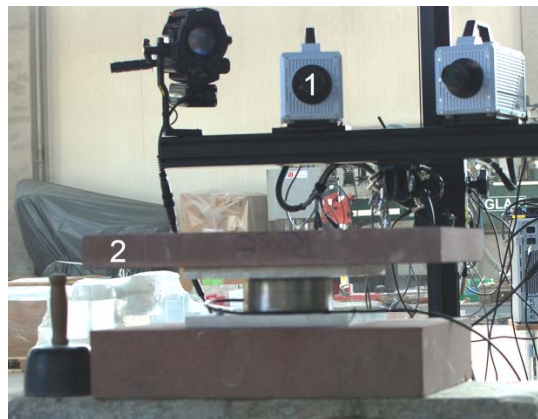

Figure 1: High speed camera system GOM Pontos HS (1) and stone specimen (2)

Tooling:

Tooling is a common technique for traditional surface processing. A drove chisel and a mallet are used for making a groove pattern. The breadth of the drove chisel can be up to 200 mm. The mason positions the chisel on the surface at an angle of about 45° and hits it with the mallet but gives the chisel a rotation that the chisel edge leaves the material after the hit. This results in rounded grooves which are characteristic for this technique (Figure 2). The automation of the movement is challenging but manageable. The material removal for the manual technique is in the ductile mode since only fine grain is removed from the stone. The estimated energy from the manual experiments was 19.46 J for a 76.2 mm chisel on *Röttbacher Sandstein.*
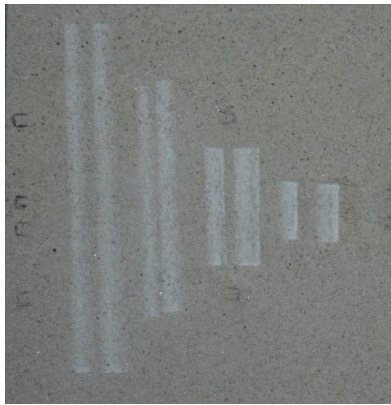

Figure 2: Examples of tooling (left four hits) and aligned tooling (right four hits)

Aligned tooling:

This technique is a variation of the normal tooling. The main difference is that the chisel does not leave the material after the hit. It moves down in a straight line with only little rotation of the chisel and results in triangular formed grooves (Figure 2). This variation is applied when there is not much space and the chisel cannot leave the stone. The material is removed in the ductile mode for small grooves. When the grooves are deeper it is also possible that chips start to break out of the edge of the groove. The removal of this technique will be shown in detail in section 3. The energy level is similar to normal tooling.

Punching:

The punching we analysed was performed with a hammer and a punch. There are different possibilities to apply this technique. One characteristic is if there is only one singular hit or if there are consecutive hits (Figure 3). The first is called point punching and the second is called line punching. Furthermore, regarding to the force applied to the punch one can distinguish between fine punching and rough punching. The energy was estimated with 23.99 J for rough punching.

When performing line punching the first chisel hit drives the punch in the material with a steep angle and the consecutive hits use a flatter angle and drive the punch sideways. Thus a line pattern is achieved. The material breaks out in rough chips in the brittle mode. Therefore, the predictability of the material removal is very low. Thus, consecutive hits are not possible to automate since the positioning of the chisel for the single hits is not manageable without scanning the results each time. This is not reasonable for economic reasons. Only point punching with one hit can be an option for automation since the chisel has to be positioned on the surface once and individual formed surfaces making use of the unpredictable material behaviour are acceptable in artistic stone processing.

Figure 3: Line punching on a sandstone surface

Bush hammering:

The Bush hammering tool has a head with a pattern of tips. The number and size of these tips can vary. A number of 9 to 36 tips in a square pattern are normal sizes. The tool head can be mounted at a normal hand held hammer or to a pneumatic hammering tool. The movement is perpendicular to the stone surface. Since the kinetic energy is low compared to the other techniques (1.14 J) and there are a number of tips, the penetration of the stone is only shallow. The energy was estimated for a pneumatic tool. The surface is processed by moving over the surface and roughing it (Figure 4).

Figure 4: Bush hammered surface on sandstone

For the further automation we chose tooling since the results achieved on this way can be adapted to automate other techniques. However, for getting a general idea of the process of material removal, the simple movement of aligned tooling was analysed first to apply the results to regular tooling. In this paper the results regarding aligned tooling will be shown.

2. QUALITY ASPECTS OF TRADITIONAL STONE TECHNIQUES

The techniques described above are all used to produce decorative surfaces. They do not achieve any further technical function. Therefore, the optical appearance is the main criteria a surface is assessed with. As described above we first analysed tooling and aligned tooling in the project. The main characteristics of a aligned tooling groove are the width, the breadth and the depth. The breadth of the groove is the same as the chisel breadth. The depth and the width are both defined by the material behaviour, the applied energy, the angle of the chisel edge and the angle the tool is set on the surface.

However, the visual appearance is most defined by the width and the breadth since the depth is not so easy to estimate for the human eye. Only large differences can be directly be seen in the depth, where changes in the width are much more visible. Furthermore, the changes can be easier estimated than the absolute value of the width. Thus, the repeatability of results is more interesting than absolute precision.

As described above in aligned tooling at distinct depth there is a transition from ductile to brittle mode in the material removal. When the brittle mode appears larger chips break out of the edge of a tooled groove. This behaviour is a problem when surfaces with a close groove patter should be processed. For other surfaces the mason or designer has to decide whether this is desired optical effect or not.

Another possible defect in surface processing appearing in automated processing is an oblique groove (Figure 5). In the manual process the mason adjusts the chisel edge with the feeling of his hand to the stone surface. An imitation of this behaviour with a force torque sensor would be very expensive. Furthermore, the stones used in this process are previously milled. But there can be variations from the planned part and the resulting product. Therefore the robot path planning is programmed on scanned mesh files of the stone. Furthermore, a previously developed approach for measuring the position of the stone product is applied in the project [9].

Figure 5: Oblique chisel grooves resulting from misalignment of chisel and stone surface

3. DESIGN OF PERLIMINARY TESTBED AND VIDEO ANALYSIS OF MATERIAL REMOVAL

When performing the manual experiments, we realised that the different hits of the masons had different energy levels and also the starting angle of the chisel may vary. But for an efficient design of experiments a higher repeatability and a precise adjustable angle of the tool is required. Since the robot mounted tool was designed parallel to the first experiments we designed a simple mechanical mechanism (Figure 6). Two springs can be compressed to a distinct level and a sledge with a hammer plate can be released with a pneumatic cylinder. The mechanism is robot mounted and can thus be positioned and oriented on the surface for different experiments. By knowing the mass of the sledge and its velocity we know the kinetic energy applied to the chisel. The velocity in respect to the spring compression was calibrated with the GOM camera system. Thus, effects like friction of the bearings are accounted for.

To get an idea of the material behaviour in the stone we positioned the chisel on the edge of the stone and filmed the process of hitting the chisel with the high speed camera. We measured aligned tooling with an angle of 45°. In the left part of Figure 6 is a picture of the chisel in the material. One can see that the materiel is removed in a stream of grain in the ductile mode. When

the chisel reaches a certain depth the edge of the groove start to break out and the removal or the material changes to the brittle mode.
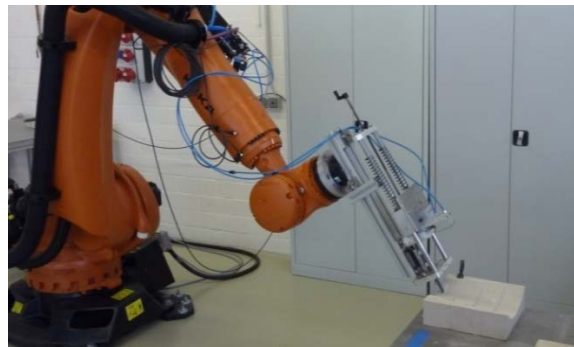
Figure 6: Test mechanism for repeatable hitting energy mounted on a robot for positioning
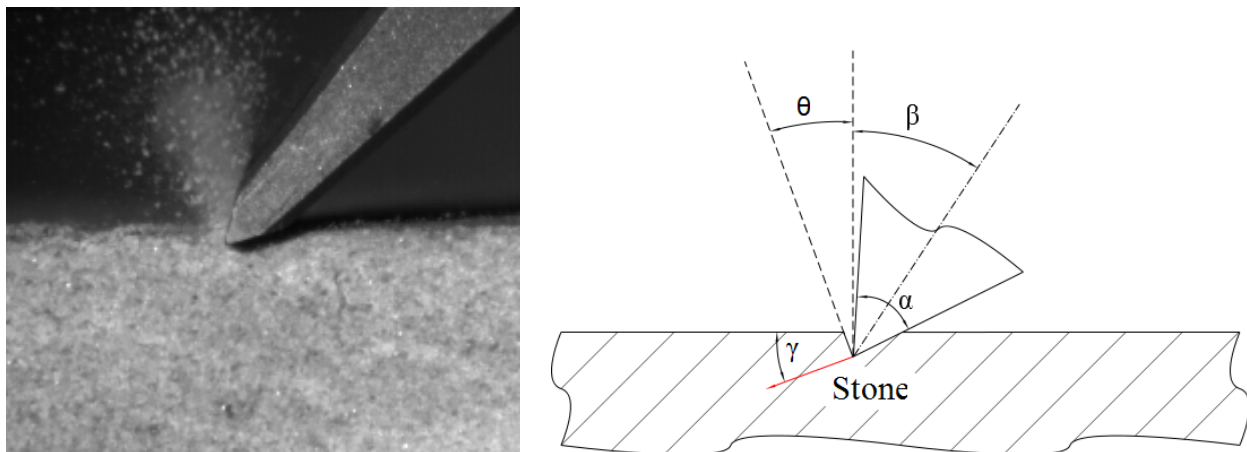
Figure 7: Highspeed camera picture of the chisel in stone (left) and relevant angles of tooling (right)

The geometric parameters that can be altered are the angle of the chisel edge α and the angle of the tool in respect to the surface β. This results in the angle

$$\gamma = 180° - \beta - \frac{\alpha}{2} \tag{1}$$

of the groove in the material. The material is removed through a channel in front of the chisel. This channel results in the angle *θ*. This seems to be a material specific value, but has not yet been analysed in detail. The first analysed values are the depth *d* and the width *b* of the groove which are shown in Figure 7. Resulting from this is also the Volume *V* of the removed material with

$$V = l\frac{bd}{2} \tag{2}$$

with *l* the breadth of the chisel. These values were further analysed and the results are shown in the next section.

Figure 8: Depth *d* and width *b* of a chisel groove

4. RELEVANT PROCESS PARAMETERS OF THE TECHNIQUES

To analyse the relevant parameters of the process in respect to their results we performed two different experiment series. The tools which were 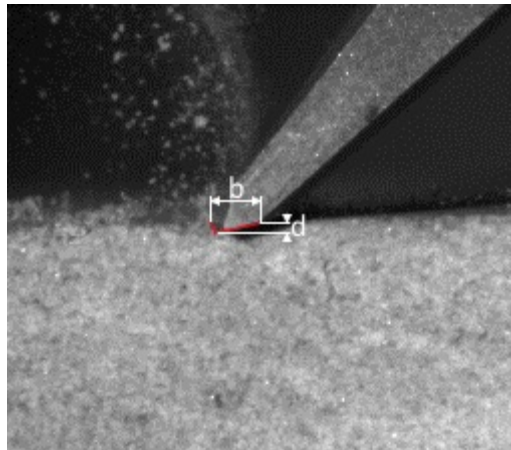used had a breadth of l = 25.4 mm and an angle of α = 62.5°. The other chisel had a breadth l = 50.8 mm and an angle of α = 64°. The angle β was chosen with 45° according to the manual technique. For each tool a test series with ten different kinetic energy levels was done. For each level three punches were performed.

For the tests a set of different sandstones were used. The data of the different sandstones we used for the experiments presented in this publications are given in Table 1. The compressive strengths reach from 49.5 MPa to 100.4 MPa so the experiment behaviour in respect to the compressive strength can be analysed. All experiment series were performed on each stone.

Table 1: Material data for the analysed stone types

Stone Type	Compressive Strength [MPa]	Porosity [%]	Mean grain size [mm]
Leistädter Sandstein	49,5	19,8	0,1 − 0,3
Steigerwald Quarzit	96,8	12,2	0,2 − 0,3
Neckartäler Hartsandstein	100,4	14,6	< 0,3
Udelfanger Schilfsandstein	55	Not available	Not available
Sander Schilfsandstein	57.3	18.1	0.18 − 0.3
Mainsandstein weiß grau	78.3	15.5	0.2 − 0.6

In Figure 8 the results of the chisel with l = 25.4 mm and α = 62.5° can be seen on *Mainsandstein weiß grau*. One can see that beginning at the third series of hits the breakout of bigger chips starts to emerge. The grooves of the single experiments were measured with a coordinate measurement machine (Wenzel LH 54). We measured each groove with 3 different measurement lanes. Figure 9 shows an example of a measured groove. There are differences in the single lanes. Thus, a mean value was reckoned for all single hits.
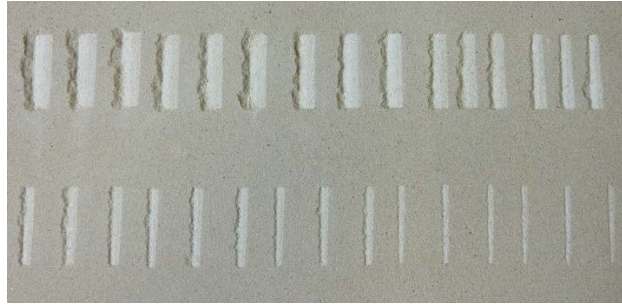
Figure 9: Resulting grooves Mainsandstein weiß grau with *l* = 25.4 mm, *α* = 62.5° and *β* = 45°
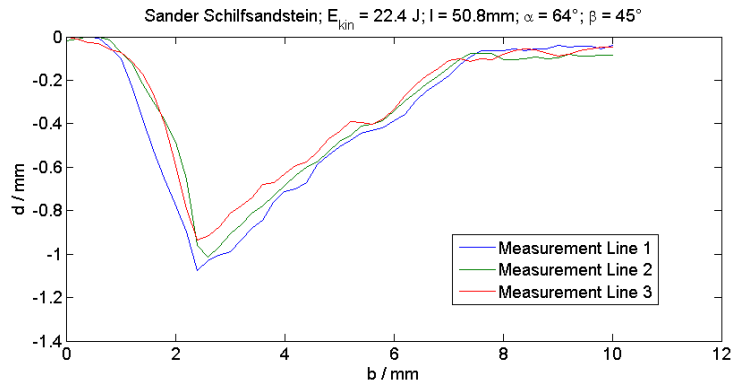
Figure 10: Three measuring curves of a groove

One can see that the relevant process data cannot be directly extracted from these measurements. Therefore, the curves were flattened. First the values of the surface were corrected to a mean value. When the depth value falls under a certain value the edge of the groove is detected. The threshold value depends on the stone since the pore size is different for the stones. However, the error of this flattening is small compared to the overall depth.
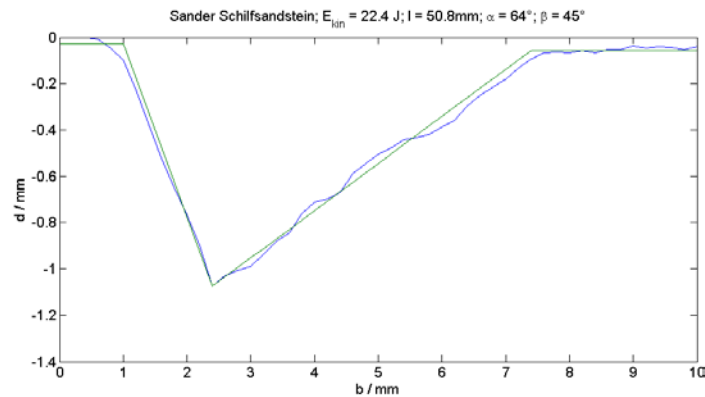
Figure 11: Comparison of original measured curve and flattened curve
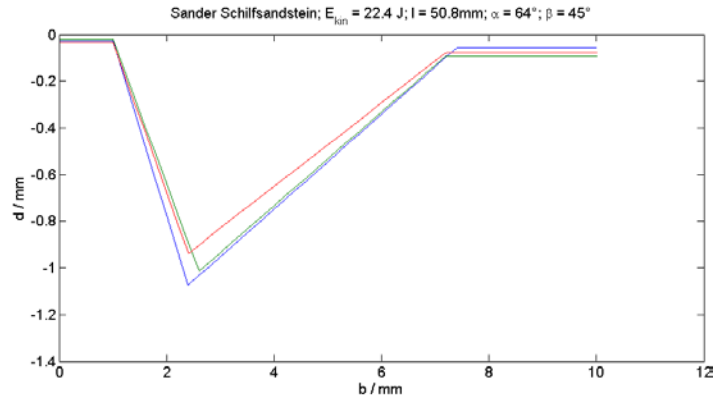
Figure 12: Flattened curves of Figure 9

From these curves the values of *d* and *b* were extracted. The depth *d* was reckoned from the deepest value to the mean value of both surface ends. Each single stroke was combined to mean value. It has to be noted that not all the values could be extracted since in the brittle mode in some experiments too much of the edge broke out and the original size of the groove could not be measured. When it was possible the size of the groove was also estimated in the brittle mode. Figure 12 to Figure 14 show the values of *d, b* and *V* in respect to E_{kin} of the chisel hit.
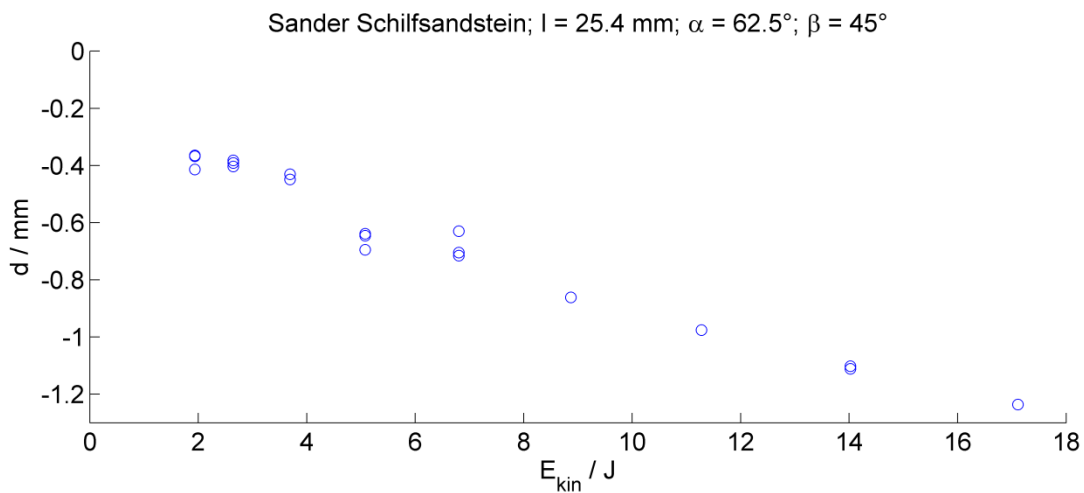
Figure 13: Values of *d* over the E_{kin}
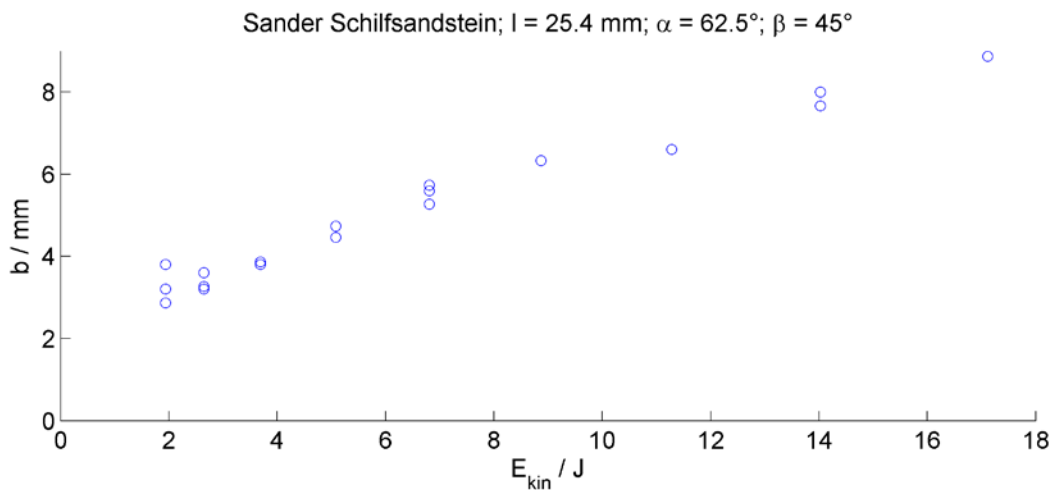
Figure 14: Values of *b* over the E_{kin}
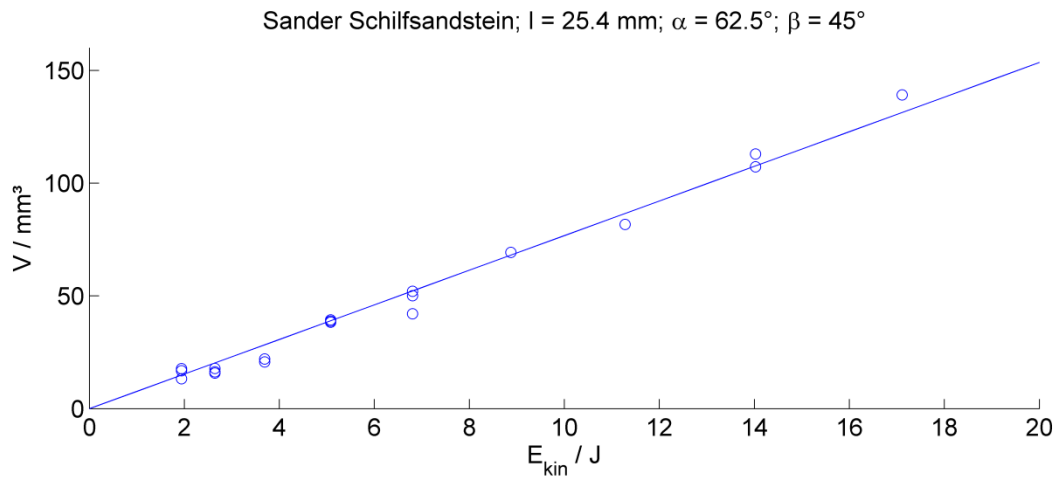
Figure 15: Values of *V* over the *E$_{kin}$*

Figure 14 shows that there is a linear correlation between the Volume of removed stone *V* and the kinetic energy *E$_{kin}$* applied to the chisel. The inverse gradient can be given as the specific kinetic energy necessary for removing material. Table 2 shows this value for each experiment series. One can see that the values differ from the compressive strength of the stone and are higher than that value. This is because the friction of the chisel in the stone could not be measured directly and some of the kinetic energy dissipates during the hit. Also one can notice that the values for the large chisel are all higher than the values for the small chisel. The reason for this is not yet estimated. The values for *Neckartäler Sandstein* are much higher compared to the other values. For chiselling of stones also the ductility of stones has an effect. Thus, not only the compressive strength is a relevant parameter. The relevant stone properties have further to be investigated.

Table 2: Analysed Material Values for different stones and chisel experiments

| Stone Type	Compressive Strength [MPa]	Intrinsic energy measured with *α* =45° *β*= 62.5° and *l*=25.4 mm [MPA]	Intrinsic energy measured with *α* =45° *β*= 64° and *l*=50.8 mm [MPA]
Leistädter Sandstein	49.5	157.9	192.2
Steigerwald Quarzit	96.8	258.1	375.5
Neckartäler Hartsandstein	100.4	696.4	722.3
Udelfanger Schilfsandstein	55	145.0	199.3
Sander Schilfsandstein	57.3	129.6	170.5
Mainsandstein weiß grau	78.3	261.7	385.1

5. CONCLUSION

We presented different traditional stone processing techniques. We build a preliminary testbed to apply repeatable energy levels to a chisel and analysed the material removal for a selected technique with a highspeed camera. Furthermore, the correlation of applied kinetic energy and the Volume of the removed material was analysed and a material parameter for the different kind of stones and chisels estimated. However, it differs for the different chisel sizes and the values are not directly comparable to the compressive strength.

There is yet no analysis of energy dissipation during the hit and friction of the chisel in the material. All these parameters are still part in the material value. Therefore, the transferability of the results

to other mechanisms has to be analysed. Also the material properties besides the compressive strength like the ductility of stones can be further investigated. Furthermore, the influence of the angle β should be analysed. The angle θ can also be further detailed but is at the moment not considered relevant to the process.

The next step will be the analysis of a mechanism which allows the imitation or the regular tooling. The implementation of an automated tool will furthermore allow performing more experiments in a shorter time.

6. ACKNOWLEDGEMENT

LITERATURE

[1] Hayes, J, Fai, S, While, P, 2014, Digitally-Assisted Stone Carving on Canada's Parliament Hill. In Proceedings of the 32nd eCAADe Conference, Newcastle upon Tyne.

[2] Bortolussi, A, Foldyna, J, Ciccu, R, Scucka, J.; Martinec, P, Sitek, L, 2009, Ornamental stone surface treatment by pulsating water jets. In Proceedings of the 9th Pacific Rim International Conference on Water Jetting technology, Koriyama-city.

[3] Ciccu, R, Bortolussi, A, 2010, Stone Surface Finishing by Pulsed Waterjets. In Proceedings of the Global Stone Congress 2010, Alicanta.

[4] Richard, T, Dagrain, F, Poyol, E, Detourrnay, E, 2012, Rock strength determination from scratch tests, Engineering Geology, 147-148

[5] Wilfing, L, Käsling, H, Thuro, K, 2013, Ansätze für eine einheitliche Definition der Zähigkeit zur verbesserten Penetrationsprognose bei TBM-Vortrieben, In 19. Tagung Ingenieurgeologie

[6] Aydin, A, Basu, A, 2005, The Schmidt hammer in rock material characterization, Engineering Geology, 81

[7] Williams, E.M, Gordon, A.D, Richmond, B.G, 2010, Upper Limb Kinematics and the Role of the Wrist During Stone Tool Production, In American Journal of Physical Anthropology, 143

[8] Steinhagen, G, Brüninghaus, J, Kuhlenkötter, B, 2015, Robotergestützte künstlerische Steinbearbeitung, In Tagungsband Mechatronik 2015

[9] Müller, M, Brüninghaus, J, Kuhlenkötter, B, 2014, Konzept zur vollautomatischen Bauteillagebestimmung von Freiformbauteilen zur Korrektur für die Roboterbearbeitung, In Konferenzband Automation 2014

Session 3

Development of Cuttability Chart for a Marble Cutting with Monowire Cutting Machine

Dr. Emre Yilmazkaya, Prof. Dr. Yilmaz Ozcelik

Department of Mining Engineering, Hacettepe University, 06800, Beytepe Ankara, Turkey
Phone: +90 312 297 76 00
Fax: +90 312 299 21 55
emreyil@hacettepe.edu.tr

ABSTRACT

Monowire block cutting machines can be used for natural stone block squaring operations and slab cutting operations from natural stone blocks. The efficient use of these machines reduces operating costs by ensuring less diamond wire wear and longer wire life at high speeds. The purpose of this study is to develop cuttability chart for real marble sample based on unit wear and unit energy in monowire cutting system and also perform cutting optimization. For this purpose, the full automatically servo controlled monowire cutting system which can cut blocks in three dimensions were developed in Hacettepe University Mining Engineering Department. Cutting experiments were performed at different wire rotation speed (peripheral speed) and wire downward movement speed (cutting speed) on the real marble block which was transported to the laboratory. A cuttability abacus in monowire cutting system taking into consideration the unit energy consumption during cutting operation and unit wear on diamond beads was developed with Design Expert 7.1 software for real marble sample by using the results obtained.

KEYWORDS

Monowire cutting; diamond wire; marble; wear; energy; optimization.

INTRODUCTION

Diamond wire cutting machines are indispensible machines used in several stages ranging from marble block production in natural stone quarries to the final product in processing plants. Today these machines are widely used in natural stone quarries and have evolved continuously in line with the consumers' demands so far and have opened a new era in natural stone mining [1, 2]. Generally, the diamond wire cutting method is used in natural stone quarries and decorative cutting tests, cutting and lifting basic construction structures, railway bridges, old concrete chimneys and dams [3].

The process of reducing large or irregularly shaped blocks produced in natural stone quarries to commercial size or arranging randomly sized blocks into cube or rectangular parallelepiped shapes is called 'block sizing' or 'squaring'. Various machines are used in the squaring process on blocks taken from quarries where marble and limestone production is performed [4]. One such machine is the mono-wire block cutting machine, which is important for sizing natural stone blocks and of slab-sawing from the blocks.

In plants where cutting processes are performed, the aim is to manufacture products of the desired quality at the lowest possible cost. The most important performance parameters affecting the economy of mono-wire block cutting are the energy consumed and the wear of diamond beads during cutting. Wear is important as it decreases cutting efficiency and reduces wire life [3].

Until today, many researchers have studied the machine parameters used in cutting and the properties of the material to be cut. Some researchers investigated wire structure and the number of beads on the wire [2-3], the dimensions of the marble block to be cut [5-6], cutting geometry [2, 7], bead structure [2, 6-10] and diamond wire cutting [11-13].

Although there are several studies about diamond wires in the literature, the number of studies about mono-wire cutting machines is limited. Researchers investigated effective parameters on cutting; [4, 14-16]; cutting hard materials [14, 17-18]; bead shape, structure and type [15-16, 19-20] and bead wear [4, 19, 21].

When the studies on mono-wire cutting systems are assessed, it is understood that there are no computer-controlled precision machines and that no cutting optimization has been performed on the basis of unit wear and unit energy values. Therefore, the cutting performance in mono-wire cutting machines should be analyzed in detail depending on operating parameters. This type of work is only possible with a computer-controlled precision machine. This study aims to investigate the effect of wire rotational speed (peripheral speed) and wire descending speed (cutting speed) on cutting performance parameters (i.e. unit wear and unit energy) in real marble cutting. Furthermore, using the obtained results, it is also intended to create cuttability charts and perform cutting optimizations for real marble sample on the basis of unit energy and unit wear values.

To achieve these goals, a computer-controlled, fully automatic cutting machine was initially developed in the Mining Engineering Department of Hacettepe University. Some experiments were then performed with a fully automatic, computer-controlled mono-wire block cutting machine on real marble sample selected from natural stone quarry located in Turkey. Subsequently, the effects of wire peripheral speed (PS) and cutting speed (CS) variations on cutting performance parameters were investigated. On the basis of a statistical analysis of the obtained data, cutting charts were created and optimum cutting points were determined by considering the unit wear and unit energy for real marble sample. A lack of this type of optimization work in the natural stone industry means that rocks in these facilities are not cut using the proper parameters. With this study, it was intended that the appropriate cutting parameters would be determined for the rock to be cut.

1. EXPERIMENTAL STUDY

1.1. Mono-wire Block Cutting Machine

Mono-wire block cutting machines can be used for squaring natural stone blocks and slab-cutting processes on the blocks. In facilities where these cutting processes are performed, the aim is to manufacture products of the desired quality for the lowest possible cost. With these machines, cutting is performed using diamond wire. The use of diamond wire in the mono-wire cutting process ensures a low degree of diamond wire wear and a longer wire life while helping to perform cuts at high cutting speeds, thus reducing the cutting costs. Therefore, when this machine was designed, it was equipped with various sensors and measuring devices.

The designed and manufactured mono-wire block cutting machine (Figure 1) was composed of four main units:

- Mechanical unit
- Hydraulic unit
- Electrical and electronic unit
- Automation unit

The mechanical unit comprised eight motors and a gearbox that provided movement to the wire. A wagon and bridge system and screw shafts provided the up-down motion system for the pulleys. The hydraulic unit consisted of a hydraulic motor providing power and a cutting deck to move around the wire axis. A tensioning system applied tension on the wire. The electrical and electronic units included load cells, vibration gauges, a flow metre, bridge termination switches (to terminate the movements of the wagon and bridge) and a control panel. The automation unit comprised a computer that provided automatic control of the mono-wire cutting machine [4].

Fig. 1 General view of the mono-wire block cutting machine.

1.2. Methodology

The purpose of this study was to develop cuttability charts on the basis of unit wear and unit energy observed during the cutting of Mugla Lilac real marble block with a computer-controlled mono-wire cutting system and optimize the cutting process. Therefore, the cutting of real marble sample brought from Mugla was performed with the mono-wire cutting machine operated at different peripheral speed (PS) and cutting speeds (CS). Cutting angle values of the wire-driving pulleys were constant. Cutting charts were formed on the basis of the energy consumed during cutting and the wear that occurred on the diamond beads in the cut and at optimum cut points that were determined according to unit wear and unit energy. Some physical and mechanical properties of the sample used in the study determined according to ISRM [22] are given in Table 1.

Table 1. Physical and mechanical properties of Mugla Lilac

UWV (g/cm^3)	AP (%)	UCS (MPa)	TS (MPa)	IS (MPa)	BAR (cm^3/50cm^2)
2.73	0.23	89.1	8.5	3.0	13.26

UWV: Unit Volume Weight; AP: Apparent Porosity; UCS: Uniaxial Compressive Strength; TS: Tensile Strength; IS: Impact Strength; BAR: Bohme Abrasion Resistance

At the beginning of the study, the parameters to be set during the cutting operations were determined. In this context, the peripheral speed and cutting speed values used in previous studies (from the literature), the speed values of machines used in industry and the limits of the machine developed for this study were considered. As a result of these investigations, a 25–35 m/s interval was chosen as the wire rotation speed and a 10–20 mm/min interval was chosen as the cutting speed. In the tests performed in this study, the operating parameters used were applied according to the layout shown in Figure 2.
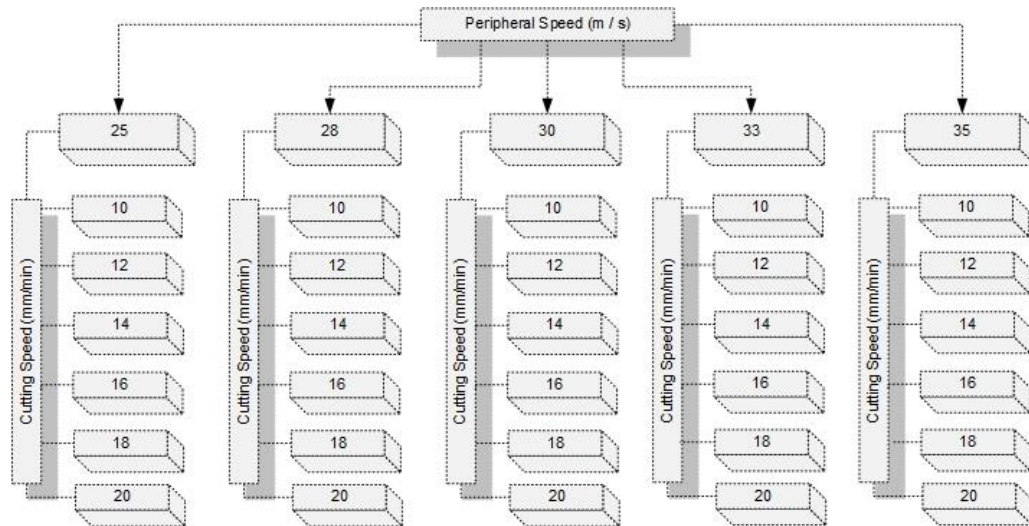
Fig. 2 Peripheral and cutting speed values at which the cuts were performed.

The cutting parameters given in Fig. 2 were used in mono-wire cutting experiments. In the cuts, a CC250/4 coded spring manufactured by the HRK firm and a 12 m long, plastic-coated diamond wire were used (Figure 3).

Fig. 3 Image of the diamond wire used in the experiments.

Machine parameters measured during all cutting processes:

- Reaction cutting force in the x-direction in both pulley guides (N)
- Reaction cutting force in the y-direction in both pulley guides (N)
- Tension in wire (MPa)
- Electrical Power (W)
- Vibration of wire (Hz) (in x- and y-directions)
- Water consumption (l/min)

Reactional cutting forces during cutting were measured using load cells. An energy analyser was used for instantaneous energy measurement during cutting, vibration metres were used to measure vibrations on the diamond wire and a flow metre was used to measure the amount of water used. The average amount of water used in cuttings was kept constant between 6 and 8 l/min during the cutting tests. The tensioning piston of the tensioning pulley was stressed up to 1 MPa, and this value was kept constant for all cuts. The width of the rocks cut was 1 metre. Cuts were made for 45 min.

2. STATISTICAL ANALYSIS

Within the scope of this study, Design Expert 7.1 was used for data analysis and for determining the optimum points of peripheral and cutting speed values for Mugla Lilac real marble sample. Design Expert 7.1 [23] is a widely used program which was developed for the experimental optimization process and which can effectively design the experiments in the most suitable way according to different methods. After making the experiments based on the design selected and entering the results obtained in the program, it derives the most suitable equations for dependent variables (response) and can realize the determination process of the optimum points by means of the derived equations. Identifying the optimum working points and the estimated results obtained as a result of the experiments made on these points is possible with this program. For building the models, interpolation method was used [24].

2.1 Design Summary

Before initializing the statistical analysis, information that reflects the properties of each variable regarding the factors and response was analyzed. This information is composed of the data such as mean and standard deviation for describing the frequencies about the variables and also definitions of the methods and models to be used in modeling studies. The design properties used in this study are demonstrated in Table 2 and the descriptive statistical data regarding factors and response are shown in Table 3 and 4, respectively.

Table 2. Statistical design properties of study.

Study Type	Initial Design	Design Model	Runs
Factorial	D-optimal, Point Exchange	2FI (two-factor interactions)	30

Table 3. Descriptive statistical analysis of the factors.

Factor Name	Unit	Type	Low Actual	High Actual	Mean	Std. Dev.
Peripheral Speed (PS)	m/s	Numeric	25.00	35.00	30.13	3.57
Cutting Speed (CS)	mm/min	Numeric	10.00	20.00	15.00	3.42

Table 4. Descriptive statistical analysis of the responses.

Response Name	Units	Obs	Analysis	Min.	Max.	Mean	Std. Dev.	Model
Unit Energy (UE)	kWh/m^2	30	Polynomial	1.14	2.24	1.70	0.32	Cubic
Unit Wear (UW)	μm/m^2	30	Polynomial	14.00	29.7	20.69	3.88	Quadratic

A micrometer instrument was used to perform wear measurements. Before the cuts, 20 beads were selected on the diamond wire and these beads were painted with a spray paint. At the end of the cut, the paint on the beads was erased but the paint on the plastic was not. Marked beads could be easily identified by the paint marks on the plastic. The diameters of 20 selected beads were measured two times. Measurements were made using the micrometre device in five different directions before starting the cuts, and the average of two measurements was used. Thus, the measured diameter was constant along the bead axis. At the end of each cut, the diameters of the marked beads were measured two times. The average of the differences between the diameter values before and after the cutting process gave the average wear amount on the diamond beads.

Depending on the area being cut and the cutting time, wear amounts could be found to be either very high or very low using different cutting parameters. To compare the wear values observed in different cuts, they were divided into area values for each cut and the wear occurring on the beads while cutting the unit area (i.e. unit wear values).

The unit energy term used in the study represents the amount of energy per unit area (kWh/m^2) required to cut the stone. It is calculated by multiplying the test time by the average of net power values and dividing by the surface area of the cut. Power values used in the calculations were recorded during cutting with the aid of a power analyser located on the machine. In the unit energy calculations, the average power values before the diamond wire entered the cut were determined and subtracted from the average power values during the cut. Thus, unit energy changes were determined through net energy values.

2.2 Statistical assessment related to unit wear

Statistical analysis were made for the purpose of estimating unit wear by using peripheral speed and cutting speed and the unit wear model equation was obtained. The quadratic model for Mugla Lilac, which was found to be statistically the most significant in the analysis, was chosen as the most suitable model for estimating the unit wear (Table 5). The validity of the models (quadratic) was tested with variance analysis. The results were presented in Table 6 and 7, respectively. The model based on the regression coefficients given in Table 6 is statistically significant at 99% (α=0.01) confidence level. The estimation graph of the developed model is given in Figure 4. The relationship between the observed values of the unit wear from experimental studies and the predicted values from the unit wear model was also investigated and the result is given in Figure 5.
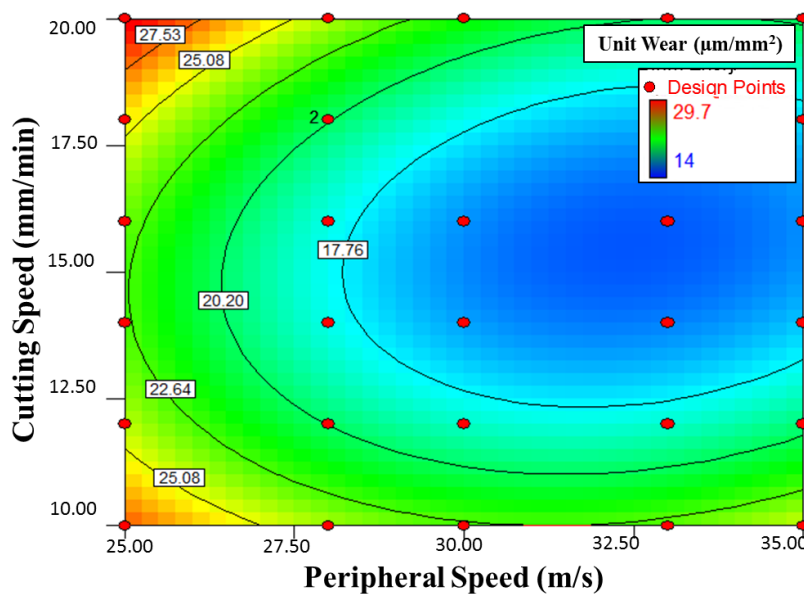

Fig. 4. The estimation graph of the unit wear model for Mugla Lilac

The equation of the quadratic model for Mugla Lilac was obtained according to Table 8 is as follows.

$$\text{Unit Wear} = 16.15 - 3.24 * (PS) - 0.53 * (CS) - 1.53 * (PS) * (CS) + 3.39 * (PS)^2 + 6.19 * (CS)^2 \quad (1)$$

Table 5. Results of the statistical analysis for selecting of suitable model for unit wear

Source	Std. Dev.	R-Squared	Adjusted R-Squared	Predicted R-Squared	
Linear	3.32	0.34	0.29	0.14	
2FI	3.29	0.37	0.30	-0.01	
Quad.	1.30	0.91	0.89	0.84	Suggested
Cubic	1.20	0.94	0.91	0.82	

Table 6. The results of the multiple regression analysis for unit wear

Factor	Coefficient Estimate	df	Standard Error
Intercept	16.15	1	0.47
(PS)	-3.24	1	0.33
(CS)	-0.53	1	0.35
(PS) (CS)	-1.53	1	0.49
$(PS)^2$	3.39	1	0.57
$(CS)^2$	6.19	1	0.59

Table 7. The ANOVA of the regression model for unit wear

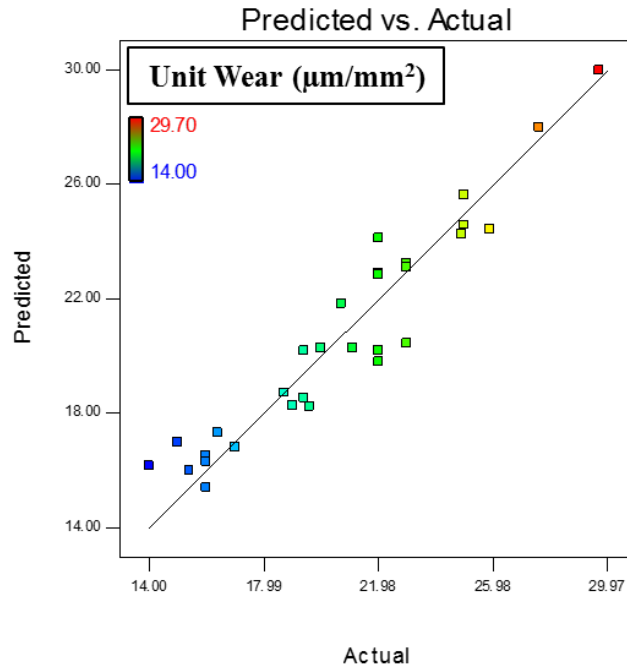| Source	Sum of Squares	df	Mean Square	F Value	p-value Prob > F	
Model	410.27	5	82.05	48.78	< 0.0001	sig.
(PS)	159.51	1	159.51	94.83	< 0.0001	
(CS)	3.97	1	3.97	2.36	0.1374	
(PS)(CS)	16.65	1	16.65	9.90	0.0044	
(PS)2	59.47	1	59.47	35.35	< 0.0001	
(CS)2	182.95	1	182.95	108.77	< 0.0001	
Residual	40.37	24	1.68			
Lack of Fit	39.76	23	1.73	2.86	0.4401	not sig.
Pure Error	0.61	1	0.61			
Cor Total	450.64	29				

Fig. 5. The relationships between observed values from experimental studies and predicted values obtained from the unit wear model for Mugla Lilac

2.3 Statistical assessment related to unit energy

Statistical analysis were performed with different kind of models given in Table 8 for estimating the unit energy by using peripheral speed and cutting speed. The cubic model for Mugla Lilac was found to be the best models for estimating the cutting rate (Table 8). The validity of the model (cubic) was tested with variance analysis. Results of the multiple regression analysis are given in Table 9 and the results of the variance analysis are given in Table 10. The model based on the regression coefficients given in Table 9 is statistically significant at 99% (α=0,01) confidence level. The estimation graph of the developed model is given in Figure 6.
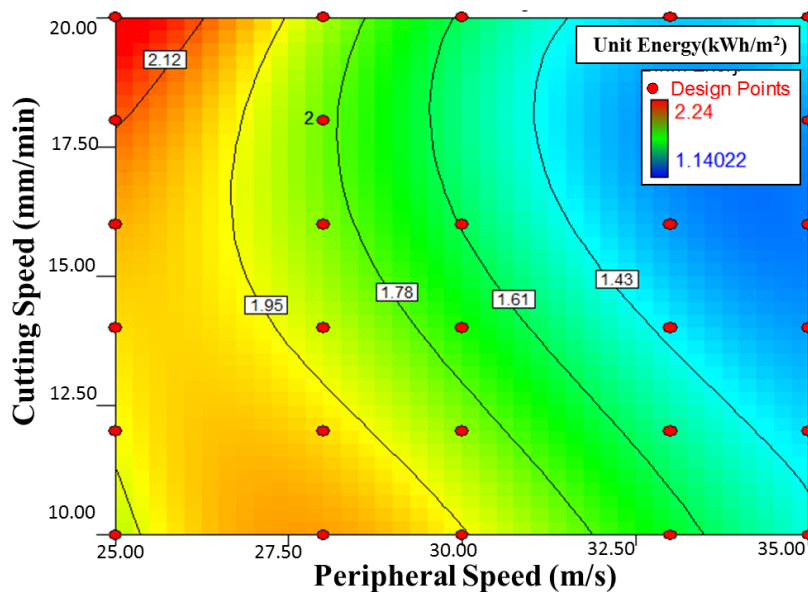

Fig. 6. The estimation graph of the unit energy model for Mugla Lilac

The equation of the cubic model for Mugla Lilac was obtained according to Table 9 is as follows.

Unit Energy = 1.65 − 0.55 * (PS) - 0.28 * (CS) - 0.10 * (PS) * (CS) + 0.01 * (PS)^2 + 0.12 * (CS)^2 + 0.28 * (PS)^2 * (CS) + 0.04 * (PS) * (CS)^2 + 0.18 * (PS)^3 + 0.09 *(CS)^3 (2)

Table 8. Results of the statistical for selecting of suitable model for unit energy

Source	Std. Dev.	R-Squared	Adjusted R-Squared	Predicted R-Squared	
Linear	0,17	0,73	0,71	0,67	
2FI	0,17	0,76	0,73	0,68	
Quad.	0,16	0,78	0,74	0,65	
Cubic	0,14	0,86	0,80	0,71	Suggested

Table 9. The results of multiple regression analysis for unit energy

Factor	Coefficient Estimate	df	Standard Error
Intercept	1.65	1	0.05
(PS)	-0.55	1	0.12
(CS)	-0.28	1	0.12
(PS) (CS)	-0.10	1	0.05
(PS)^2	0.01	1	0.06
(CS)^2	0.12	1	0.07
(PS)^2 (CS)	0.28	1	0.09
(PS) (CS)^2	0.04	1	0.09
(PS)^3	0.18	1	0.13
(CS)^3	0.09	1	0.13

Table 10. The ANOVA of the regression model for unit energy

Source	Sum of Squares	df	Mean Square	F Value	p-value Prob > F	
Model	2.56	9	0.28	13.65	< 0.0001	Sig.
(PS)	0.43	1	0.43	20.42	0.0002	
(CS)	0.11	1	0.11	5.35	0.0315	
(PS)(CS)	0.08	1	0.08	3.65	0.0704	
(PS)^2	0.00	1	0.00	0.00	0.9735	
(CS)^2	0.07	1	0.07	3.50	0.0761	
(PS)^2(CS)	0.18	1	0.18	8.87	0.0074	
(PS)(CS)^2	0.00	1	0.00	0.22	0.6427	
(PS)^3	0.04	1	0.04	2.09	0.1637	
(CS)^3	0.01	1	0.01	0.52	0.4797	
Residual	0.42	20	0.02			
Lack of Fit	0.39	19	0.02	0.85	0.7075	
Pure Error	0.02	1	0.02			
Cor Total	2.97	29				

The relationship between the observed values of the unit energy from experimental studies and the predicted values from the unit energy model was also investigated and the result is given in Figure 7. Figure 7 indicates that the results obtained from the model well reflect the real condition.
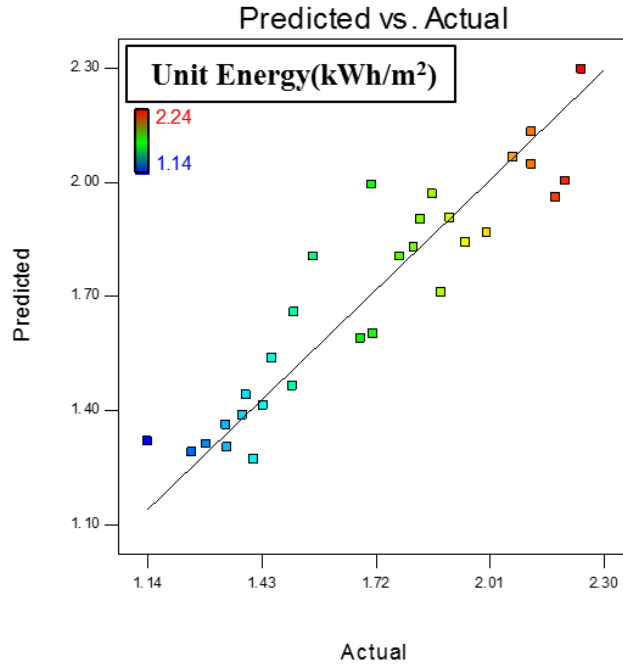
Fig. 7. Relationships between observed values from experimental studies and predicted values obtained from the unit energy model for Mugla Lilac

The results obtained from the statistical analysis show that developed unit wear and unit energy models are statistically significant and unit wear and unit energy can be modeled by these ways. By using the model equations and also estimation graphs, it is possible to estimate the unit wear and unit energy before starting the cutting with diamond wire.

2.4 Optimization

The main purpose of this study is to determine the optimum peripheral speed and cutting speed values that would minimize the unit wear and unit energy values in cutting Mugla Lilac real marble sample with monowire cutting system and also to develop cuttability charts for monowire cutting. For this purpose, the aforesaid Design Expert 7.1 program was used, and firstly the constraints were defined (Table 11). Later, the constraints were used to determine the optimum points for Mugla Lilac real marble sample.

Table 11. Design constraints for optimization

Name	Goal	Lower Limit	Upper Limit	Importance
PS (m/s)	Min.	25	35	3
CS (mm/min)	Max.	10	20	5
UW ($\mu m/m^2$)	Min.	14	29.7	5
UE (kWh/m^2)	Min.	1.14	2.24	5

The optimum point was determined by using Design Expert 7.1 program for Mugla Lilac real marble sample considering the design constraints. Numerical optimization was done by setting goals for each response to generate optimal conditions. The optimization module in Design-Expert searches for a combination of factor levels that simultaneously satisfy the requirements placed on each of the responses and factors. The results are given in Table 12.

Table 12. The optimum working conditions for sample

PS (m/s)	CS (mm/min)	UE (kWh/m^2)	UW (μm/m^2)
31.22	18.27	1.41	17.62

By using the model equations obtained from the statistical analyses, cuttability charts for Mugla Lilac real marble sample was developed with respect to unit wear and unit energy separately. The results are given in Figure 8 and 9 for unit wear and unit energy, respectively. The cuttability charts show the optimum working conditions and estimated unit wear and unit energy values that will be occurred under these conditions.

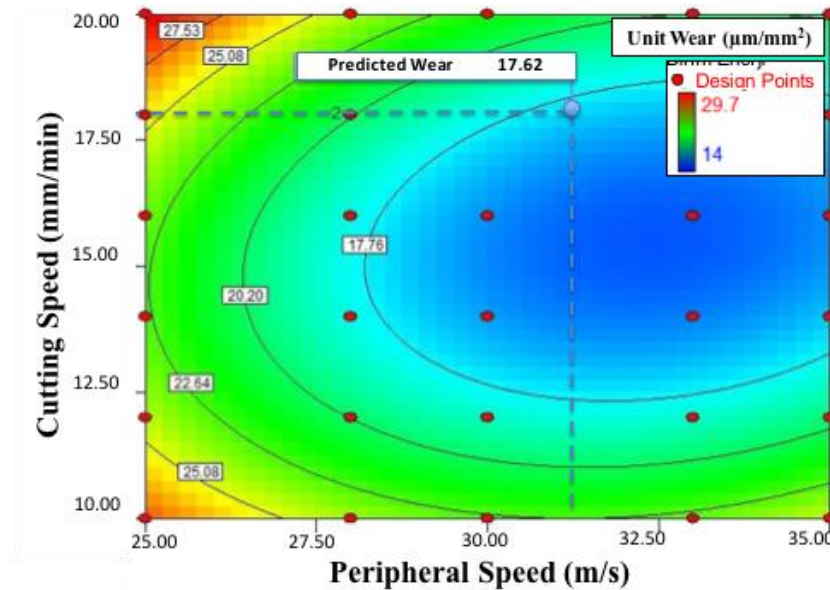Fig. 8. The cuttability chart including the optimum conditions with respect to unit wear
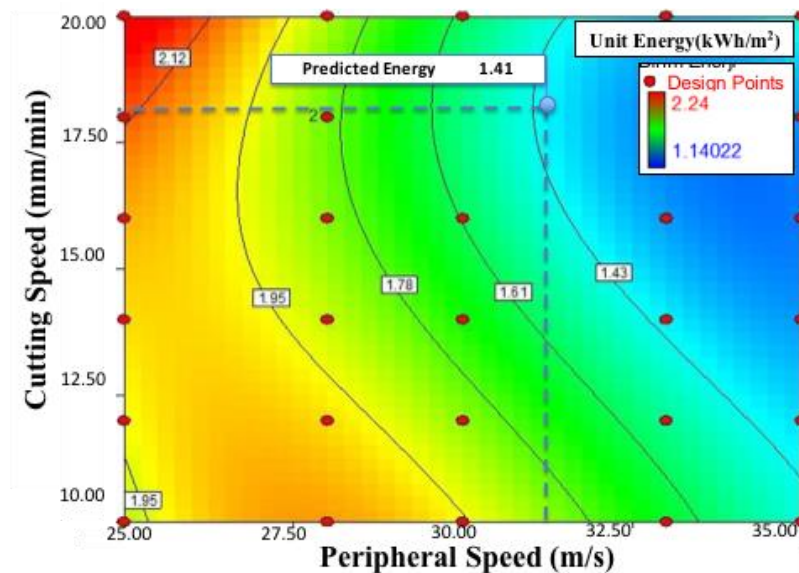

Fig. 9. The cuttability chart including the optimum conditions with respect to unit energy

By using these charts, it is easy to determine the values of the unit wear and the unit energy in different working condition before starting the cutting operation with monowire cutting machine for Mugla Lilac real marble sample.

3. CONCLUSION

In this study, determination of the optimum working conditions for Mugla Lilac real marble sample in terms of cutting performance parameters including unit wear and cutting rate and the development of cuttability charts with respect to cutting performance parameters were aimed. As a result of this study, the optimum working parameters for Mugla Lilac real marble of 31.22 m/s peripheral speed and 18.27 mm/min cutting speed were found in mono-wire cutting machine. Cuttability charts for Mugla Lilac was developed depending on the performance parameters namely unit wear and unit energy. These charts would contribute to natural stone industry for more efficient usage of mono-wire cutting machine. By using these charts, it is easy to determine the values of the unit wear and the unit energy in different working condition before starting the cutting operation with diamond wire for Mugla Lilac real marble.

REFERENCES

[1] Yilmazkaya, E, Ozcelik, Y, 2015, The Effects of Operational Parameters on a Mono-wire Cutting System: Efficiency in Marble Processing, Rock Mechanics and Rock Engineering, DOI 10.1007/s00603-015-0743-9 (in press).

[2] Ozcelik, Y, 1999, Investigation of the working conditions of diamond wire cutting machines in marble industry, PhD Thesis, Hacettepe University, Ankara (in Turkish).

[3] Yılmazkaya, E, 2007, Investigation of some factors affecting block production with diamond wire cutting method, MSc Thesis, Hacettepe University, Turkey (in Turkish).

[4] Yılmazkaya, E, 2013, Investigation of effective parameters on computer controlled monowire block cutting system, PhD Thesis, Hacettepe University, Turkey (in Turkish).

[5] Berry, P, 1989, Optimum use of diamond wire equipment in stone quarrying, In: Proceedings of the 21st APCOM symposium, Colorado Society of Mining Engineers, Littleton, Las Vegas, Nevada, pp 351-365.

[6] Ozcelik, Y, Bayram, F, 2004, Investigation of the effects of block size to cutting performance of diamond wire cutting, Marble 40:46-54 (in Turkish)

[7] Ozcelik, Y, Kulaksız, S, Çetin, MC, 2002, Assessment of the wearing on diamond beads in the cutting of different rock types by the ridge regression, J Mater Process Tech 127(3):392-400.

[8] Capuzzi, Q, 1989, Diamond wire cutting technology in granite quarry, ACIMM for Marble, November-December.

[9] Biasco, G, 1993, Diamond wire for quarrying hard rocks, Ind Diamond Rev 5:252-255.

[10] Cook, M, Smith, BA, 1993, A study of diamond wire bead rotation, Ind Diamond Rev 2:79-81.

[11] Ozcelik, Y, 2005, Optimum working conditions of diamond wire cutting machines in marble industry, Ind Diamond Rev 65:58-64.

[12] Bortolussi, A, Ciccu, R, Manca, PP, Massacci, G, 1990, Simulation and optimization of rock cutting with diamond wire, In: Proceedings of the XXII. International Symposium APCOM (17-21 September 1990), Berlin, pp 163-176.

[13] Bortolussi, A, Ciccu, R, Manca, PP, Massacci, G, 1994, Computer simulation of diamond-wire cutting of hard rock and abrasive rock, T I Min Metall A 103:55-128.

[14] Butler-Smith, PW, Gryzagoridis, J, Davis, PR, 1999, A single bead test for assessing diamond wire performance, Ind Diamond Rev 2(99):93-101.

[15] Huang, G, Xu, X, 2013 Sawing performance comparison of brazed and sintered diamond wires, Chin J Mech Eng 26: 1.

[16] Huang, G, Huang, H, Xu, X, 2009, Analysis on the fracture failure of brazed diamonds in wire sawing, Key Eng Mat 389-390:436-441.

[17] Denkena, B, Köhler, J, Ermisch, A, 2011, Wire cutting tool concepts for steel machining, Adv Mat Res 325:238-243.

[18] Denkena, B, Seiffert, LLF, 2010, Process influences in the wire cutting of concrete, Adv Mat Res 126-128:70-76.

[19] Risso, L, Vicenzi, B, Bernieri, S, 2007, Improved cutting performance of diamond beads by means of innovative shape, In: Proceedings of the 2nd International Industrial Diamond Conference 2007, Rome, Italy (18-19 April 2007), B.1.1.

[20] Huang, GQ, Xu, XP, 2006, Analysis of the breakage of diamond wire saws in sawing of stone, Key Eng Mat 304-305:123-126.

[21] Zhang, JS, Wang, Z, 2004, Technical parameters and wear resistibility of diamond wire-saw in granite cutting, Key Eng Mat 259-260:122-126.

[22] ISRM, 1981, Rock characterization testing and monitoring; suggested methods, Oxford.

[23] Stat-Ease Inc, 2014, Design Expert, Version 7.1.

[24] Kanbir, ES, Ozcelik, Y, 2012, Development of Cuttability Charts for a Marble Cutting with Diamond Wire in Quarry, Proceedings of 22nd MERSEM - 8. International Marble and Natural Stone Congress Afyonkarahisar, Turkey, pp. 345-353.

Influence of diamond wire pretension on process behaviour

B. Denkena, T. Grove, L. Tatzig
Leibniz Universität Hannover, Institute of Production Engineering and Machine Tools (IFW)
An der Universität 2, 30823 Garbsen
tatzig@ifw.uni-hannover.de

ABSTRACT

Wire sawing with diamond tools is a highly flexible cut-off grinding process with regard to machinable component structure and composition. Therefore, it is nowadays not only used in the processing of natural stone, but also increasingly deployed on dismantling of nuclear or industrial plants. In this field of application, concrete, reinforced concrete and steel have to be cut. In particular, the processing of reinforcements and steel structures results in higher process forces compared to the machining of natural stone or concrete. Consequently, the diamond wire is deflected leading to decreased cutting performance in terms of the material removal rate. To overcome these challenges, the diamond wire can be pretensioned which directly affects the stiffness of the tool. Thereby, the deflection of the diamond wire can be reduced and the material removal rate can be increased.

This paper presents initial results concerning the influence of the wire pretension on the process behaviour of a diamond wire when cutting steel S355JR. For these investigations, the wire pretension was varied in a range of 300 N up to 2000 N. For the evaluation of the process behaviour, resulting process forces, cutting power, wire deflection and surface removal rate were analysed.

KEYWORDS

cut-off grinding, wire sawing, wire pretension, diamond tools, dismantling

INTRODUCTION

Initially, wire sawing was introduced in the processing of natural stone [1]. Due to its unlimited cutting depth, wire sawing allows the exploitation of blocks of huge dimensions. Based on the high flexibility concerning the machinable component structure and composition, wire sawing is frequently used in the construction industry to cut-off concrete, reinforced concrete or steel [2,3,4]. Compared to competitive cut-off processes, the machines used for wire sawing are small, easy to set up and inexpensive (Fig. 1).

Because of the mentioned advantages, wire sawing is nowadays used in the dismantling of nuclear or industrial plants [5,6]. The number of dismantling activities for nuclear power plants is going to grow significantly in the future. Many plants have reached their designated operating time or are going to be decommissioned due to political decisions. In Germany alone, 9 nuclear facilities for commercial power generation have to be decommissioned until 2022. Together with 23 already decommissioned plants they have to be dismantled afterwards [7]. In the dismantling of nuclear power plants, specific challenges have to be taken into account. Large components consisting of different materials have to be cut-off. Depending on the size of the reactor, 200,000 to 400,000 t of concrete have to be removed. In addition, several 10,000 t of reinforcement steel and steel structures have to be disassembled [6,8].

The cutting of steel results in higher process forces that lead to a deflection of the diamond wire. As a consequence, the material removal rate is reduced. In this paper the influence of the wire pretension on the process behaviour is investigated. Therefore, steel S355JR was cut and the process forces, power consumptions, wire deflections and surface removal rates were measured.
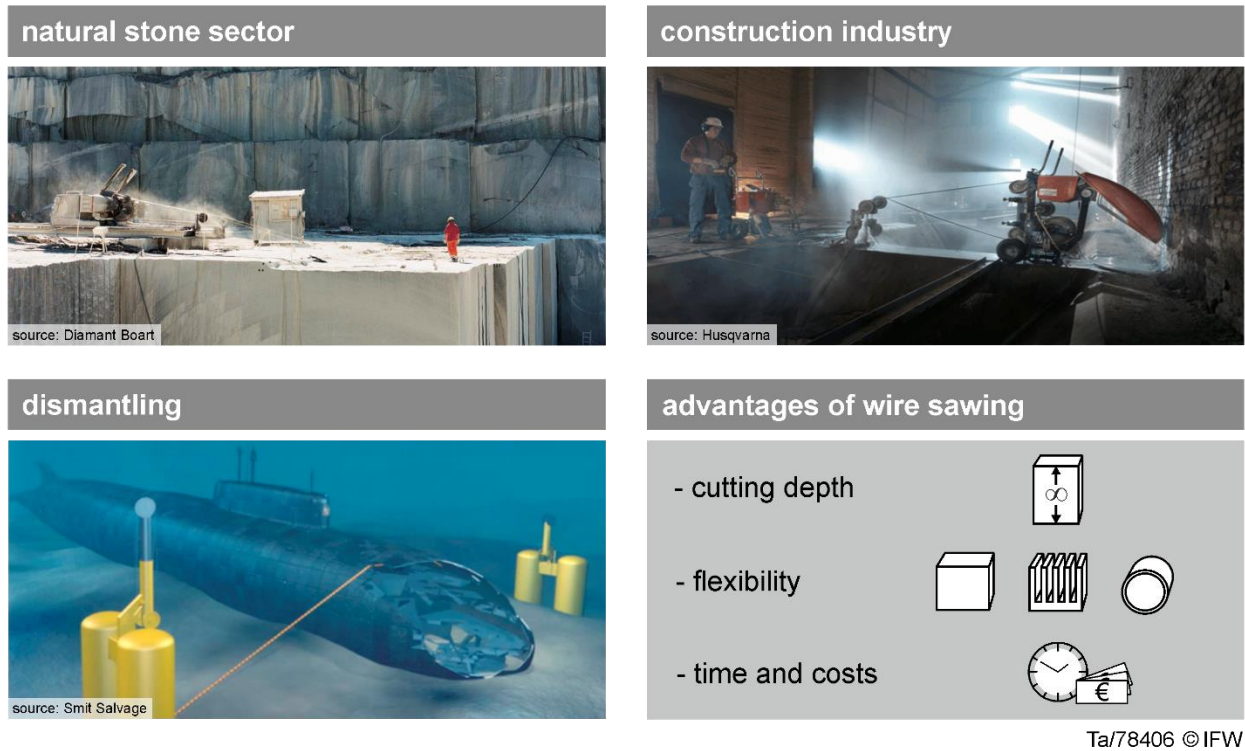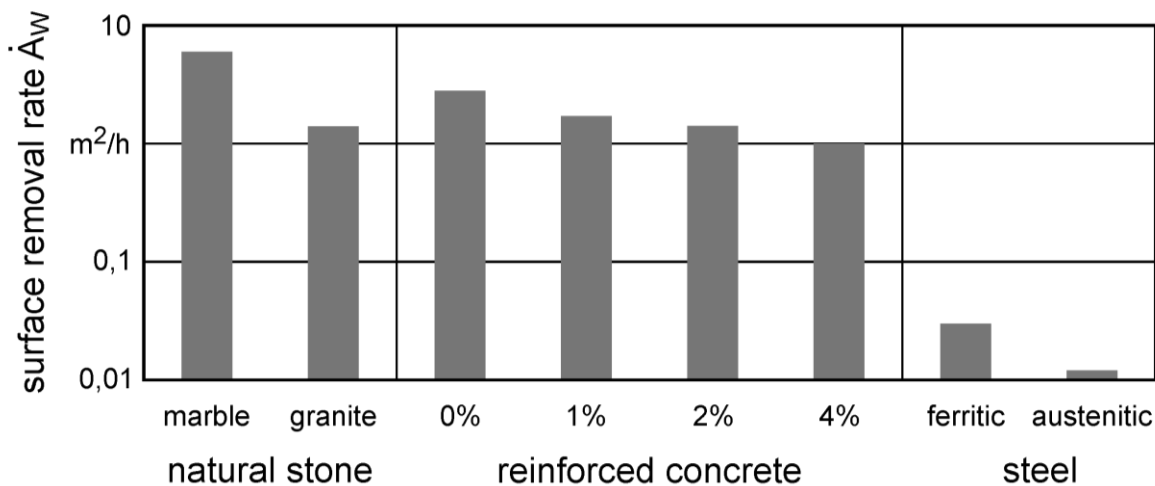
Fig. 1: Fields of application and advantages of wire sawing

1. WIRE SAWING OF STEEL

Wire sawing of steel is generally applicable [2,4,9]. Nevertheless, the achievable surface removal rate is significantly lower compared to the processing of natural stone or concrete (Fig. 2).

[source of natural stone data: DIABÜ 20123 [10], source of reinforced concrete and steel data: Apmann 2004 [2]] Ta/78419 © IFW

Fig. 2: Surface removal rates for natural stone, reinforced concrete with % reinforcement and steel

The reason for the lower surface removal rates is seen in the ductile cutting mechanism of steel. Furthermore, this leads to higher resulting process forces. In addition, the tool life in terms of the cut surface per metre tool is significantly lower when cutting-off metal [2]. Cut-off experiments showed that the surface removal rate can be increased by higher infeeds while the cutting speed has no

significant effect on the surface removal rate [2,11]. The influence of the diamond wire pretension pressure on the material removal rate of steel with path-driven infeed has not been investigated thus far.

2. EXPERIMENTAL SETUP

In order to investigate the influence of the wire pretension on the process behaviour, cutting experiments were conducted. The experiments were performed on a wire saw with high stiffness and a high-performance electrical drive (P_N = 30 kW) (Fig. 3).
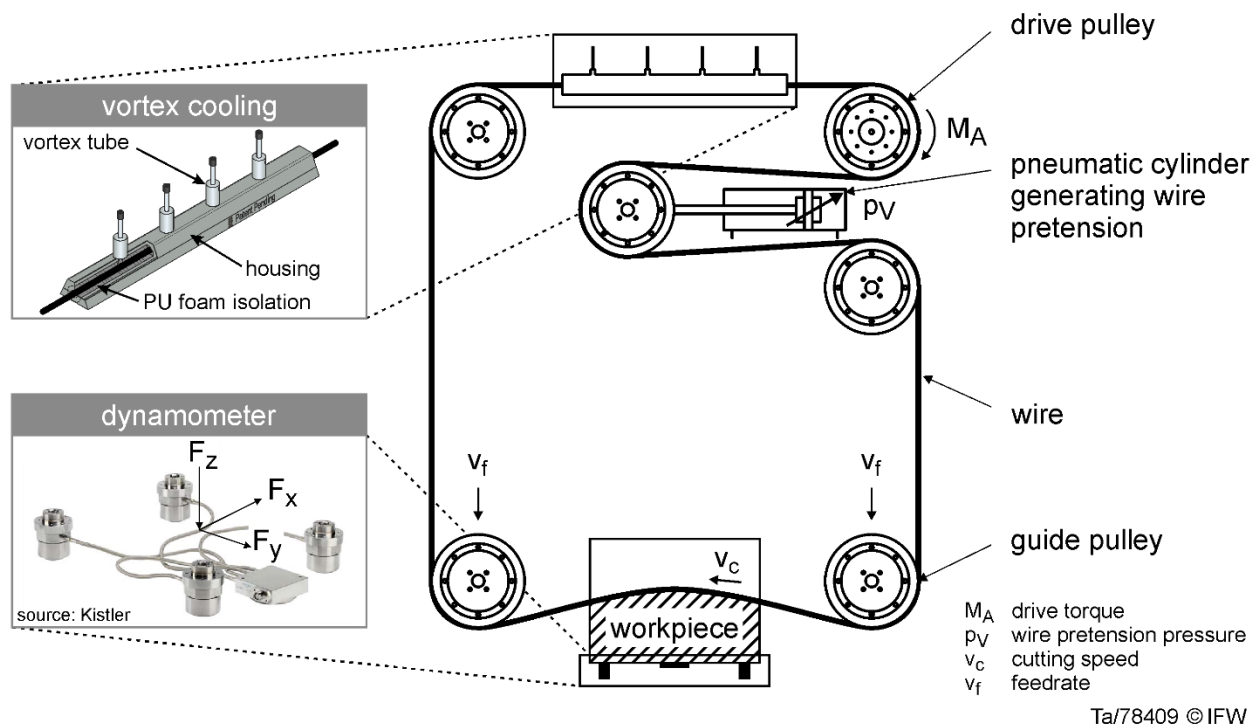

Fig. 3: Experimental setup

When dismantling a nuclear power plant cross-contamination by secondary cutting products has to be avoided. As a result, a wire sawing process without cooling lubricant is required. Therefore, during these experiments a non-liquid compressed air cooling with vortex tubes by Husqvarna was deployed matching this requirement. Four vortex tubes are positioned equidistantly on a cooling channel and generate a temperature of -14 °C inside the cooling channel. The wire saw operates in a plunging mode. The infeed is realized path-driven. A pneumatic cylinder generates the wire pretension resulting in pretension forces F_V and wire pretensions σ_V. The pretension forces were measured as a function of the wire pretension pressure with hanging scale Kern HCB 200K500. The results are depicted in Fig. 4. Process forces were measured beneath the workpiece with a 3-component dynamometer of type 9366CC by Kistler. The resulting effective power was tapped at the inverter of the drive engine. After the experiments, the height of the machined surface was measured with a digital calliper at three characteristic positions. Based on these measurements, the machined surface A_W was approximated by means of a circular segment. The surface removal rate was calculated as quotient of the machined surface A_W and the cutting time t_c.
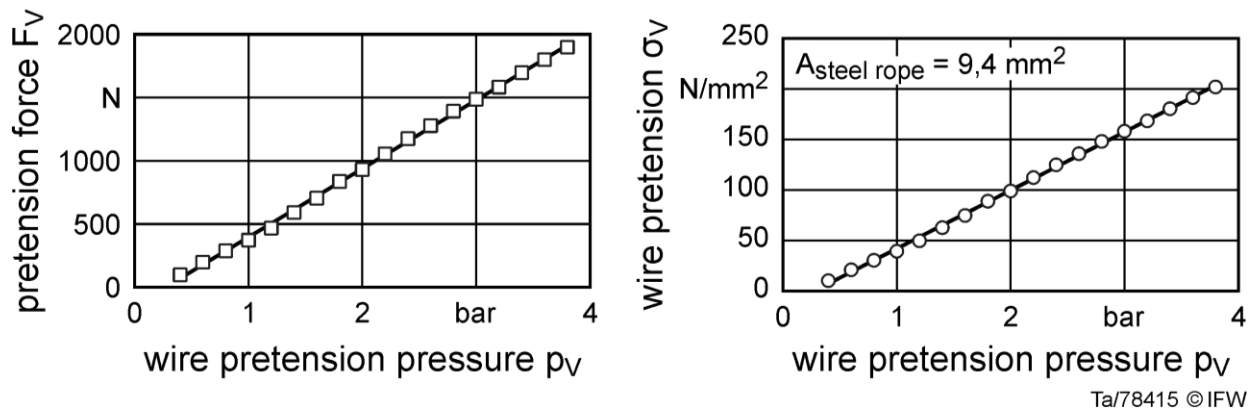
Fig. 4: Resulting pretension force and wire pretension

A solid workpiece with a cutting length of l_W = 250 mm of construction steel S355JR was cut with a diamond wire of type C1000 by Husqvarna (Fig. 5). As stated by the manufacturer, this tool is qualified for cutting steel. Diamonds are brazed in a single layer on grinding segments that are mounted on a steel rope of type 7 x 19. The diameter of the grinding segments is 10.3 mm. The spaces between the 44 grinding segments per metre are reinforced with springs and injected with synthetic rubber. The ends of the wire are linked by a connector.
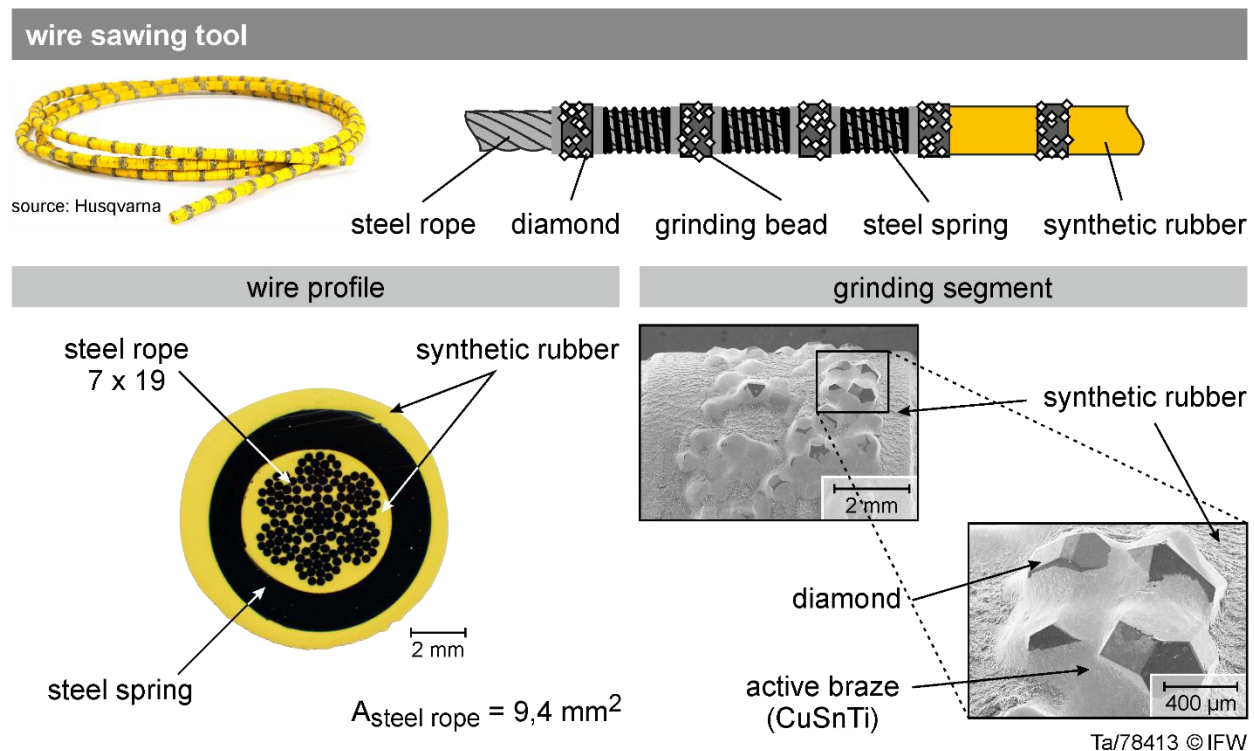
Fig. 5: Tool specifications

3. Process behaviour as a function of wire pretension

In order to evaluate the process behaviour of wire sawing tools as a function of the wire pretension pressure when cutting steel, grinding experiments were conducted. During experiments, the cutting speed v_c = 23.7 m/s, the feedrate of the guide pulleys v_f = 10 mm/min, the tool and the workpiece were kept constant. The wire pretension pressure p_V was varied in a range of 1 to 4 bar. A lower

pretension pressure results in an insufficient grinding process because the idling power used to generate the cutting speed exceeds the cutting power. In preliminary tests, the connector was torn out repeatedly at pretension pressures higher than 4 bar. Therefore, this value marks the upper limit of the wire pretension pressure range. In order to reduce the influence of external variables the experiments were performed in random order.

The influence of the wire pretension pressure p_V on the surface removal rate $\dot{A}_W$ is illustrated in Fig. 6. The surface removal rate increases degressively with higher wire pretension pressures p_V. This relation can be approximated by a quadratic polynomial in a sufficient way (coefficient of determination $R^2 = 95.43$ %). Compared to a wire pretension pressure of $p_V = 1$ bar the surface removal rate $\dot{A}_W$ is increased by 120 % at $p_V = 4$ bar. When the applied wire pretension pressure is higher, the bending stiffness of the wire is increased. Ceteris paribus, this effect leads to a reduction of the wire deflection height h_W as seen in Fig. 6 in the right diagram. Alternatively, the deflection can be expressed in terms of the deflection radius r_W (Fig. 6). A higher deflection radius r_W is equivalent to a lower deflection h_W. Both values depend on the wire pretension pressure in a linear manner (both $R^2 = 94$ %).
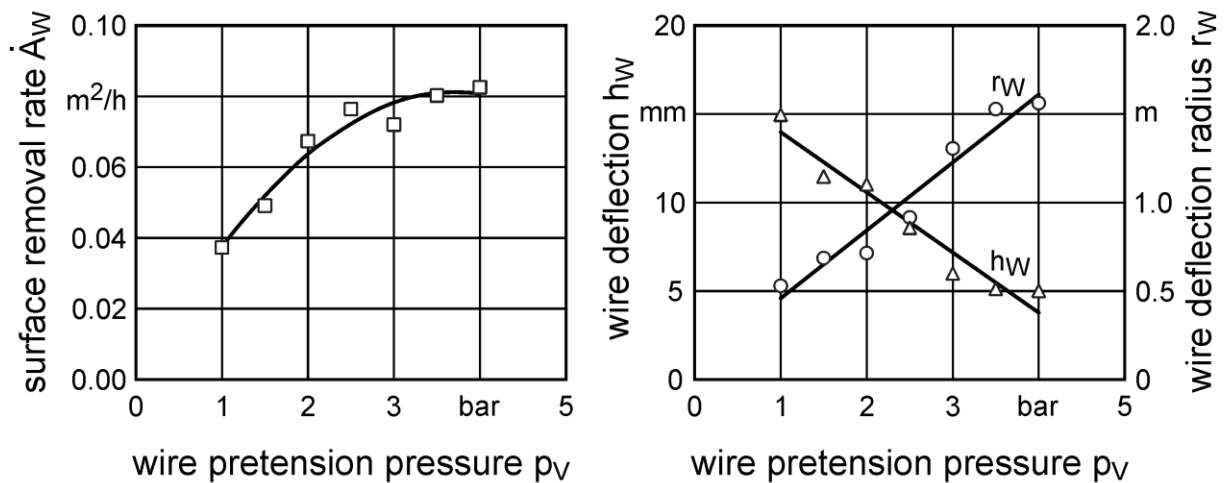
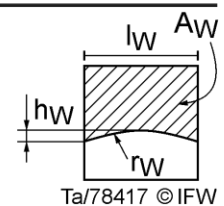| process	tool	workpiece	
$v_c = 23.7$ m/s	vacuum brazed diamond	S 355 JR (non-alloy)	
$v_f = 10$ mm/min	44 beads/m	solid	
$p_V =$ var.	$d_P = 10.3$ mm	$l_W = 250$ mm	

Ta/78417 © IFW

Fig. 6: Surface removal rate, wire deflection and deflection radius as a function of the wire pretension pressure

The higher bending stiffness due to the increased wire pretension pressures should result in a higher contact pressure on the workpiece as well. This assumption can be approved considering the resulting normal forces F_n. In addition, process forces are used to determine the in-process mechanical load during grinding. In Fig. 7, normal forces F_n and tangential forces F_t are depicted versus the wire pretension pressure p_V. In cutting times t_c between 800 s and 1000 s the average process forces were evaluated. Like the surface removal rate, the normal as well as the tangential forces increase with the wire pretension pressure degressively. The grinding force ratio $\mu = F_t/F_n$ is independent of the wire pretension pressure. Values of $\mu \approx 0.6$ generated in these experiments represent an effective cutting process [12].

The effective power consumption P required for a specific cutting operation is important for the machine design and the effectiveness of the process. Particularly in the context of mobile machines,

this factor cannot be ignored. The effective power is the sum of the cutting power P_c, the infeed power P_f and the idling Power P_l [12]:

$$P = P_c + P_f + P_l \tag{1}$$

In comparison to the cutting speed v_c the feedrate v_f is negligibly small (here: $v_f/v_c = 7 \cdot 10^{-6}$) permitting the following simplification for the cutting power P_c:

$$v_f \ll v_c \rightarrow P_c \approx P - P_l \tag{2}$$

During grinding experiments, the effective power P and the idling power P_l were measured. In Fig. 7, both values are depicted in combination with the calculated cutting power P_c according to Equation (2). The idling power P_l slightly increases with higher wire pretension pressures due to increased friction at the pulleys. The progression of the effective power P and cutting power P_c equal the dependency of normal and tangential forces qualitatively. Furthermore, the cutting power can be calculated as product of cutting speed and the force component in the same direction [12]:

$$P_c = F_t \cdot v_c \tag{3}$$

The values calculated as difference between effective power and idling power (Eq. (2)) correlate with the cutting power calculated according to Eq. (3) in a nearly perfect positive way (Pearson product-moment correlation coefficient of r = 99,96 %).
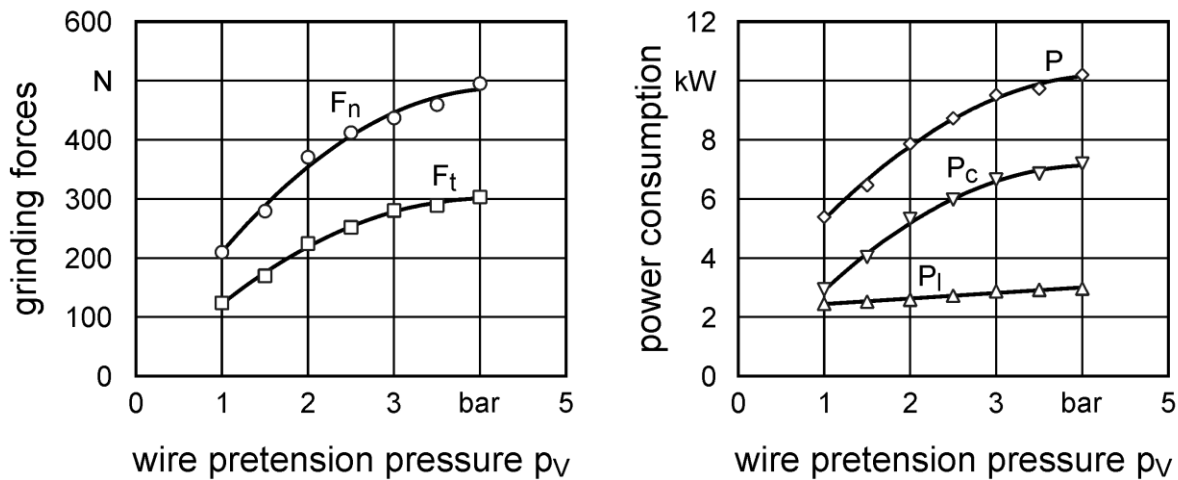
process	tool	workpiece	
v_C = 23.7 m/s	vacuum brazed diamond	S 355 JR (non-alloy)	
v_f = 10 mm/min	44 beads/m	solid	
p_V= var.	d_P= 10.3 mm	l_W= 250 mm	

Ta/78416 © IFW
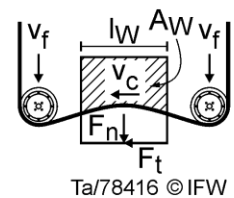
Fig. 7: Process forces and power consumptions as a function of the wire pretension pressure

The degressive behaviour of the surface removal rate $\dot{A}_W$ and the process forces F_n and F_t as a function of the wire pretension pressure p_V suggests that some kind of saturation occurs retaining all other parameters constant. The explanation is assumed as follows: At higher pretension pressures, the contact pressure is increased as well due to the higher bending stiffness. As a result, the plunge of the single grains is enhanced. By this, every grain cuts-off more workpiece material. Therefore, the surface removal rate $\dot{A}_W$ is increased. This inclination should have a theoretical maximum. After

the contact pressure exceeds a specific value, the flexible wire is forced back and the surface removal cannot be increased any further.

CONCLUSION AND OUTLOOK

In this paper, the influence of the wire pretension pressure on the surface removal rate, the process forces and power was presented. Grinding experiments show that the variation of the wire pretension pressure has the potential to increase the cut-off performance of steel significantly. With a higher pretension pressure, the bending stiffness of the flexible wire is increased. As a result, a deeper penetration of the grains is achieved leading to higher single grain chip thicknesses. An increase of up to 120 % of the surface removal is measured. Nevertheless, the mechanical load on the tool and the required power are increased as well in the range of 135 % and 90 %, respectively. The relation between the wire pretension pressure and the surface removal rate, process forces as well as cutting power can be described by a degressive polynomial function in each case.

In further experiments, the tool wear will be investigated as a function of the wire pretension pressure. Furthermore, the interactions between the wire pretension pressure, cutting velocity and feed rate will be analysed. In addition, the process behaviour of wire sawing tools when cutting non-solid steel structures will be evaluated.

REFERENCES

[1]   Panhorst, H-J, 1970, Seilsägen von Granit mit Diamantwerkzeugen - systematische Entwicklung eines Trennwerkzeugs, Dr.-Ing. thesis, Universität Hannover
[2]   Apmann, H, 2004, Seilschleifen von metallischen und mineralischen Strukturen, Dr.-Ing. thesis, Universität Hannover
[3]   Denkena, B, Glatzel, T, Bockhorst, J, Lünemann, M, 2005, Machining of construction materials with wire saws, Industrial Diamond Review 2/05
[4]   Tönshoff, H K, Hillmann-Apmann, H, 2002, Diamond tools for wire sawing metal components, Diamond and Related Materials 11, 742-748
[5]   E.ON Kernkraft GmbH, 2008, Vom Kernkraftwerk zur „Grünen Wiese" – Stilllegung und Rückbau des Kernkraftwerks Würgassen
[6]   International Atomic Energy Agency (IAEA), 2008, Managing low radioactivity material from the decommissioning of nuclear facilities, Technical reports series No. 462
[7]   Thierfeldt, S, Schartmann, F, 2012, Stillegung und Rückbau kerntechnischer Anlagen, 4. Auflage, Brenk Systemplanung, Aachen
[8]   Thierfeldt, S, 2010, Decommissioning and Waste Management, Proceedings of 3 rd European IRPA Congress 2010, 14-16 June 2010, Helsinki, Finnland
[9]   Knecht, D, 2015, Untersuchungen zum Seilsägeprozess an Stählen ausgewählter Geometrien im umschlingenden Verfahren, Dr.-Ing. thesis, Karslruhe Institute of Technology
[10]   DIABÜ®, 2013, Diamond wires of DIABÜ®, product catalog, http://www.diabue.com/download/diabue_catalogue_2013_en_k1.pdf
[11]   Denkena, B, Köhler, J, Seiffert, F, 2012, Prozessentwicklung zur trockenen Bearbeitung metallischer und mineralischer Strukturen beim Rückbau kerntechnischer Anlagen, dihw - Diamant Hochleistungswerkstoffe 04/2012, 16-22
[12]   Klocke, F, König, W, 2005, Fertigungsverfahren 2 - Schleifen, Honen, Läppen, Springer

An experimental investigation of vibration characteristics in the diamond wire sawing of granite

Hui Huang*, Guoqin Huang, Hua Guo, Xipeng Xu
Institute of Manufacturing Engineering, Huaqiao University, Xiamen, 361021, Fujian, P. R. China
huangh@hqu.edu.cn

ABSTRACT

Compared with circular and gang sawing, diamond wire sawing is a flexible machining mode due to its special structure characteristic. The diamond wire with the elastic steel core bends and vibrates in sawing process. In this paper, the vibration characteristics are analyzed in the granite sawing with the diamond wire. The vibration signals in the sawing process are simultaneously measured at six different measurement points along the cutting zone. The influences of sawing parameters on the vibration characteristics are explored. The results show that the vibration amplitude is a U-shaped distribution in the sawing arc. The vibration amplitude decreases with the increase of wire speeds, feed rates and the tension forces. The vibration fundamental frequency is certainly proportional to the number of wheel speed times the number of beads per meter, which has no related to the feed rates and tension forces in the saw process. The wire vibration indicates the impact of bead acted on the workpiece.

INTRODUCTION

Diamond wire sawing technology has been introduced to the stone processing industry since 1970s. It has been regarded as one key technology lighting up the future of diamond tools in the stone processing due to their environmental benefits, higher extraction rates, greater yield and ultimately cost competitiveness [1]. Nowadays, diamond wire sawing has been developed for many applications in the field of natural stone [2], construction materials [3] and metal materials [4], especially for very thick materials or components that are difficult to access.

The diamond wire is made up of a steel wire where small beads bonded with diamond grits are mounted at a regular distance with spacing material placed between the beads, as shown in Fig. 1. The steel wire acts as a spine to join all the beads. The beads provide the actual cutting action in machining process. The spacing materials acted to fix and insulate the beads are steel spring, molded plastic, rubber or the combination of the mentioned spacing materials, e.g. springs and rubber. The diamond wire bends and vibrates in cutting process due to the elasticity of twist steel, as shown in Fig. 1. The vibration of wire sawing is more obviously than in the case of the circular and gang sawing. Understanding the vibration behavior of the system is very pivotal in the prediction of dynamic behaviors and machining mechanism of the wire cutting process.

Linear and nonlinear vibration behaviors of a translating media, such as string, sheet, beam, have been studied. The vibration of moving media which is directly related to the wire saw process is shown in the references, especially in the wafer slicing with thin wire [5-7]. The vibration of wire is modeled as the transverse vibration of an axially moving string under tension. Some papers are presented the eigenfunctions and natural modes of transverse vibration.
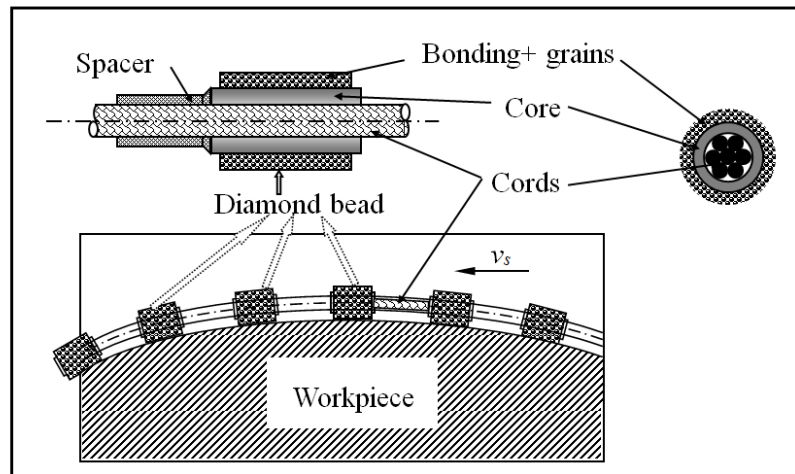
Fig. 1: Illustration of the diamond wire sawing

The structure of the wire used in the wafer slicing and the stone sawing is very different, as shown in Fig. 2. The wire used in the wafer slicing is homogeneous structure. However, the wire in the stone sawing is heterogeneous structure, as shown in Fig. 2(a). In this paper, the vibration characteristics of granite sawing with diamond wire were experimentally studied with a special device. The effect of machining parameter on the wire vibration was discussed.
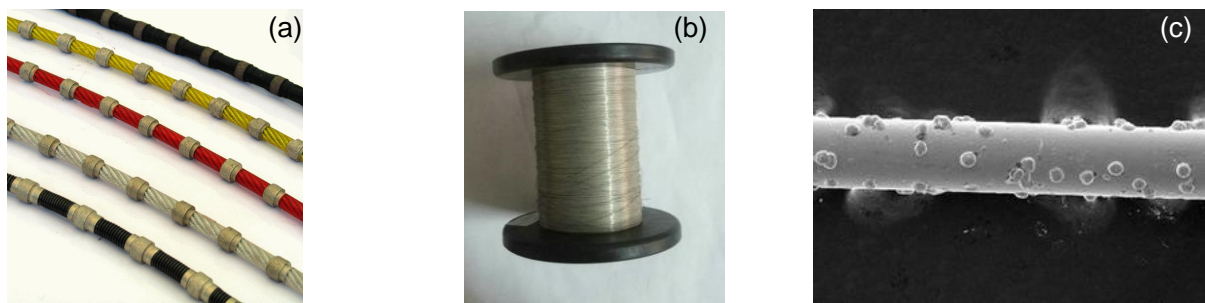
(a) Wire for the stone sawing   (b) Wire for the wafer slicing   (c) Enlarged photo of (b)
Fig. 2: Wire used in the stone sawing and the wafer slicing

1 EXPERIMENTAL DETAIL

1.1 Sawing procedure

Wire sawing experiments were carried out on a developed CNC diamond wire machine which was smaller than commercial machines as illustrated in Fig. 3. The power of the spindle drive motor was 5.5 kW. The diamond wire was 5.5 m long, with a maximum wire speed of 45 m/s. The wire had 38 abrasive beads per meter length. The cylindrical sintered diamond beads were 7 mm in diameter and 6.5 mm in length, which contained diamond abrasives of mesh size of 40/50 (in US standard) and had a diamond concentration of 10 volume percentage. The gap between two adjacent beads was approximately 20 mm, giving a diamond bead ratio (λ, is the bead length over one meter of wire length) of 0.247. Prior to sawing, diamond beads were dressed by gently rubbing a refractory brick installed on the machine for 20 minutes until the diamond grits were fully exposed. The infeed of the diamond wire were carried out through two bevels gears driven by an electrical feed drive.

The workpiece material is typical natural granite (G603) which is the medium hard granite. The

composition and mechanical properties of the workpiece are listed in Table 1. The rectangular specimens for testing were 600 mm long, 300 mm wide and 300 mm thick. A traditional grinding coolant nozzle was used to provide coolant and city water was used as the cutting fluids with the flow rate 0.25 l/s. The flow rate and the position of nozzle were kept constant.

Table 1: Compositions and mechanical properties of the workpiece

Workpiece name	Shore's hardness	Compression strength [MPa]	Percentage of main minerals [%]			Texture
			Quartz	Feldspar	Others	
G603	106	104.4	69.66	19.29	11.01	Fine and Compact

1.2 Sawing vibration measurement

The vibration of wire was measured with a high-precision laser displacement sensor (LK-G150), as shown in Fig. 3. Six different measurement points along the cutting zone were simultaneously measured to obtain the vibration signals in the cutting process due to the long cutting arc of wire sawing. The distances for the six measurement points were 50mm, 150mm, 250mm, 350mm, 450mm, 550mm, from the wire entrance into workpiece (as shown in Fig. 3). In order to avoid the effect of the vibration of sawing machine, the sensors were locked in special fixtures which are fixed in a bracket. The bracket was mounted on the ground and insulated from sawing machine. The vibration signals from sensors were fed to a Model View signal acquisition system at a sampling frequency of 10 kHz and recorded by a PC. The machining parameters used in the vibration test are listed in Table 2.
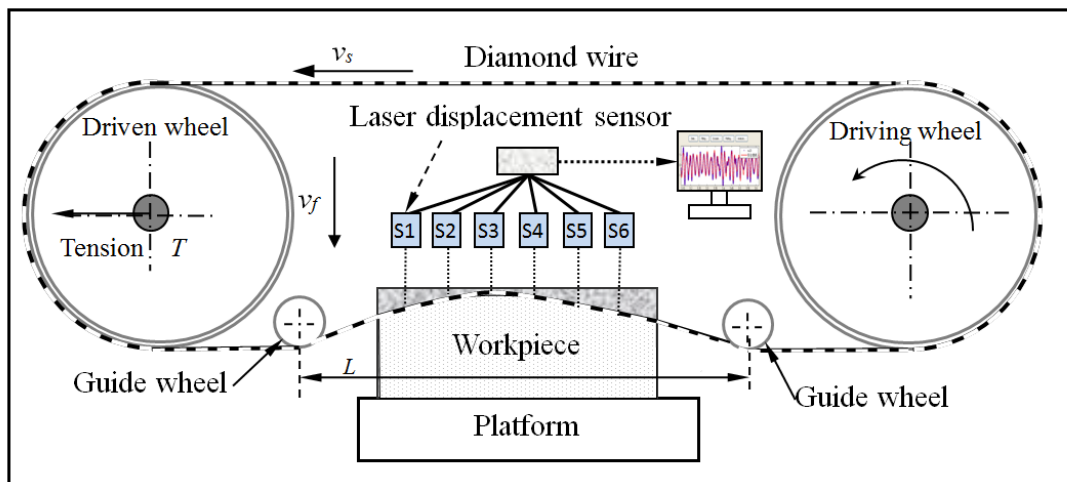

Fig. 3 Illustration of the wire vibration measurement

Table 2: The machining parameter used in vibration test

Wheel speed v_s [m/s]	18.32, 21.85, 25.38
Feed rate v_f [mm/min]	5, 8, 12
Tensile force T [N]	1380, 1500, 1650
Distance of the guide wheels L [mm]	650, 700, 750

2. RESULTS AND DISCUSSION

2.1 General aspects

Typical curves of sawing vibration obtained at different measurement displacements are shown in Fig. 4a. In general, the vibration signal is characterized by the vibration frequency and vibration amplitude. Fast Fourier Transform (FFT) is widely used in the frequency analysis of the vibration signal. The FFT curves of the vibration at different measurement displacements are shown in Fig. 4b. Although there are some differences in the vibration signal at each measurement displacement, the FFT curves are more similar. It is shown that the vibration fundamental frequency in this machining parameter is about 972 Hz. The values of the other dominant frequencies are similar equal to the multiplication of the fundamental frequency. Only fundamental frequency is recorded in the subsequent analysis. RMS (root mean square) is a statistical measure of the magnitude of a varying quantity. The vibration amplitude of wire sawing is described with RMS value defined as the square root of the arithmetic mean of the squares of the original amplitude values.
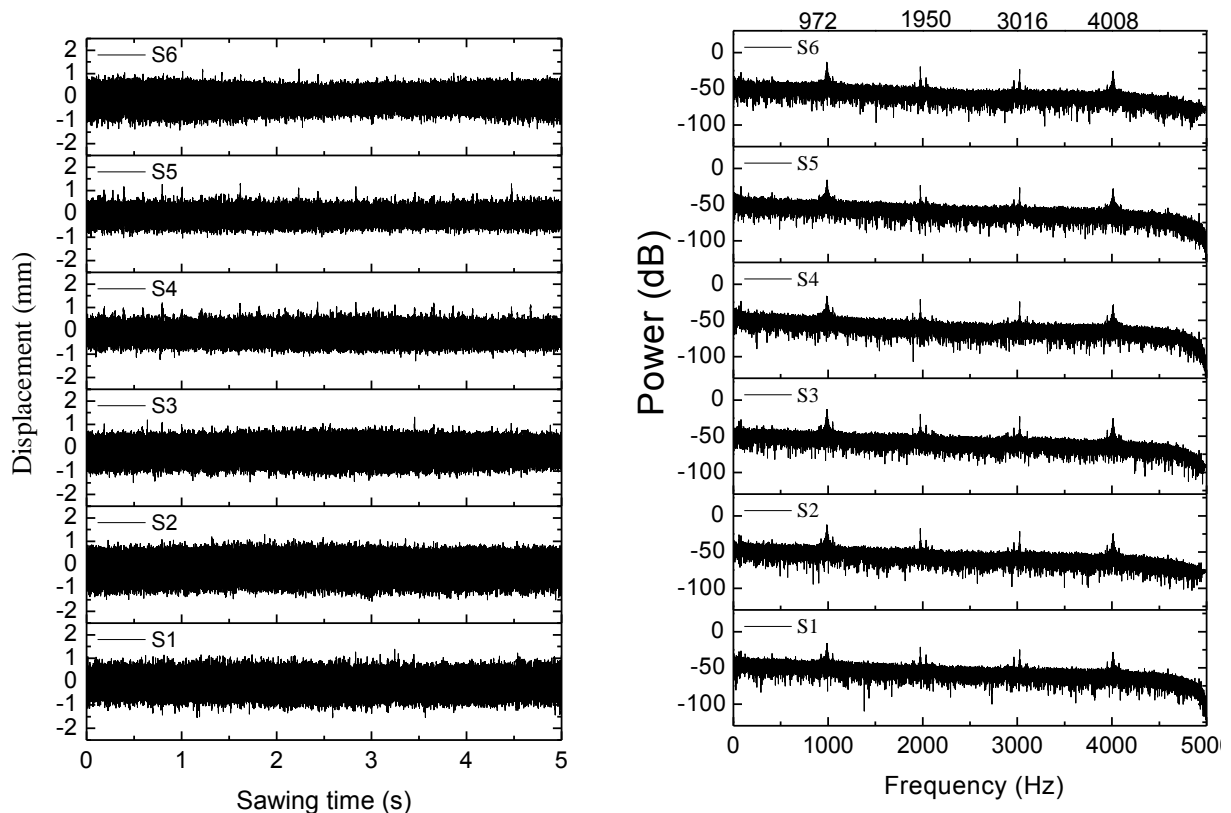
(a)Typical vibrations at different measurement points   (b)FFT curves of vibration signal
Fig.4 Typical vibration signals and FFT curves obtained at different measurement points, where a wire speed of 25 m/s, a feed rate of 12 mm/min, a tension force of 1500N and a distance of 700 mm were used.

2.2 Effect of the parameters on the vibration amplitude

Figure 5-8 show plots of vibration amplitude versus machining parameters. It is found that the RMS values of the wire vibration amplitudes are about 0.4-1.6 mm. The vibration amplitudes on the different measurement displacements are obviously different. The vibration amplitude values at both ends of cutting region are bigger than that in the middle. There is U-shaped distribution of the vibration amplitude in the sawing arc. It is interesting that the RMS values are not symmetrical in the sawing arc. The position of the lowest RMS values is about 350 mm. This case may due to the cutting force distribution in the sawing region, which will be investigated in the future. The amplitude values are decreasing with the increasing wire speed, feed rate and

tension force. The decreasing distance of the guide wheels could effectively decrease the vibration amplitude.

The vibration amplitude describes the impact degree of bead acted on the workpiece, which is relate to the contact condition of bead and workpiece. With the increasing feed rate and the tension force, the wire bending degree is decrease; therefore the vibration amplitude is correspondingly decreased. The increasing wheel speed increases the bead number into the cutting arc in per unit time. The material removal rate of each bead decreases and subsequently results in the decrease of impact of each bead. The vibration amplitude is also decreased.

In the other hand, the higher wire speed and shorter guide wheels distance improve the dynamic stiffness of wire, which also decrease the vibration amplitude.
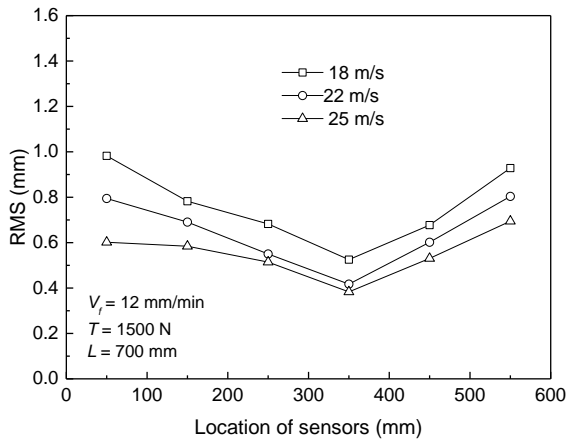
Fig. 5 Effect of the wire speed on wire amplitude
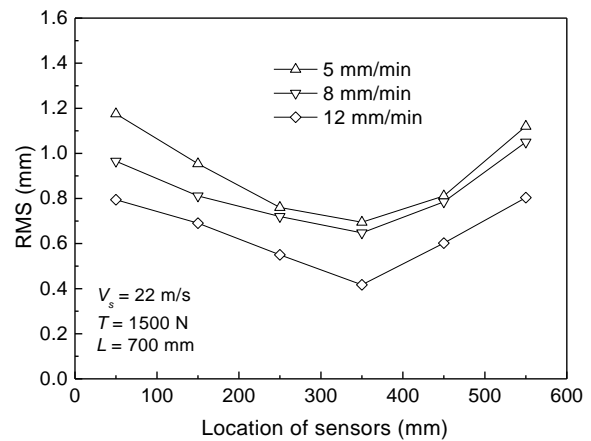
Fig. 6 Effect of the feed rate on wire amplitude
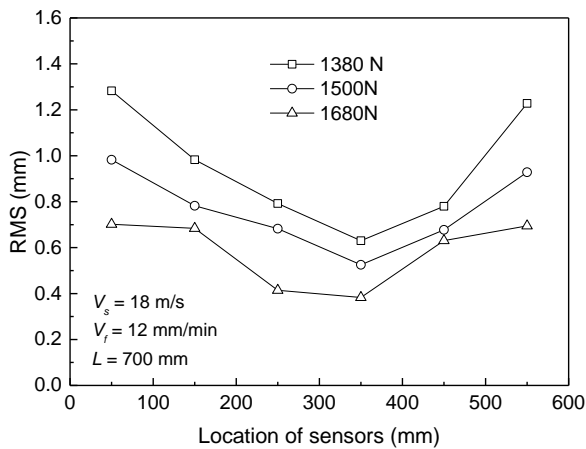
Fig. 7 Effect of the tension force
on wire amplitude
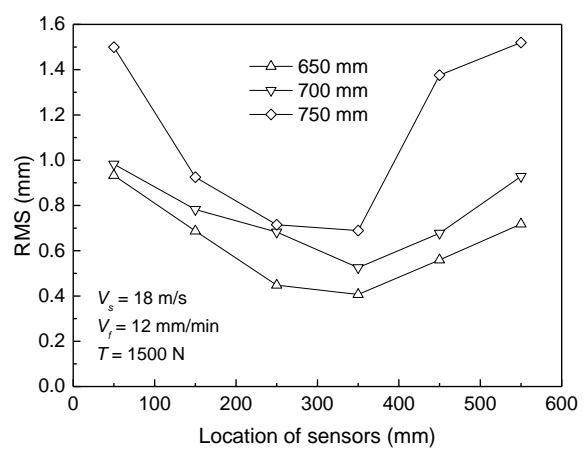
Fig. 8 Effect of the guide wheels distance
on wire amplitude

2.3 Effect of the parameters on the vibration frequencies

Figure 9-11 show plots of vibration fundamental frequencies versus machining parameters. It is seen that the fundamental frequencies increase with the increasing wire speed as shown in Fig.9. Feed rate, tension force and the distance of guide wheels have no influence on the fundamental frequencies as shown in Fig.9-11. Therefore, the relationship between the wire speed and the fundamental vibration frequencies was reploted in Fig. 12. There exists a good linear correlation (R^2=0.997) between the vibration frequency and wheel speed, as shown in Fig. 12. The indicated slopes of N = 42.8 which is similar to the number of beads per meter.

From the experimental results, it is found that the fundamental frequency in wire sawing has no relevance to the feed rate, tension force and guide wheels distance. It is certainly proportional to

the number of wire speed times the number of beads per meter. For understanding the implication of the wire vibration, it is useful to consider the structure of wire and the cutting kinematics at the interface between the abrasive tool and the workpiece in Fig.1. The product of the number of wheel speed and the number of beads per meter can be indicated the number of beads entering the cutting interface per time. From the diamond wire structure as shown in Fig. 1, it is found that there is the gap between the diamond bead and spacer. The gap causes the wire bounce up and down when the beads enter the cutting interface. Therefore, the wire vibration is the results of diamond beads entering the cutting region which is very different from the vibration of thin wire used in the photoelectric material cutting [7].
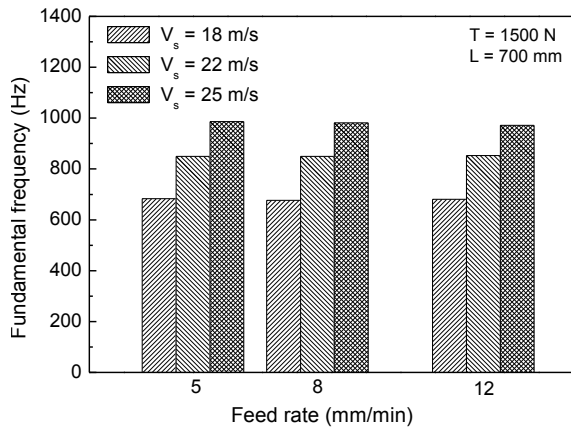
Fig.9 Effect of feed rate and wire speed
on the vibration frquences
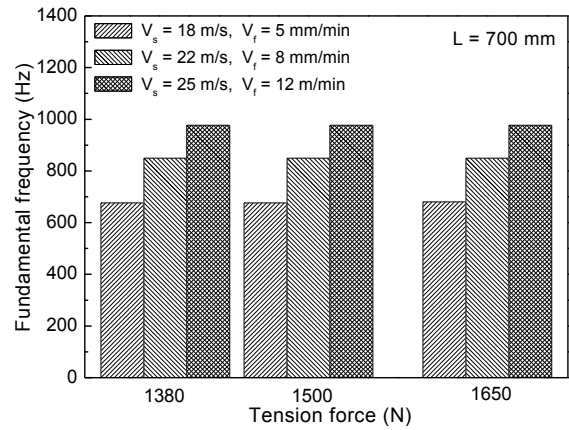
Fig. 10 Effect of tension forec
on the vibration frequencies
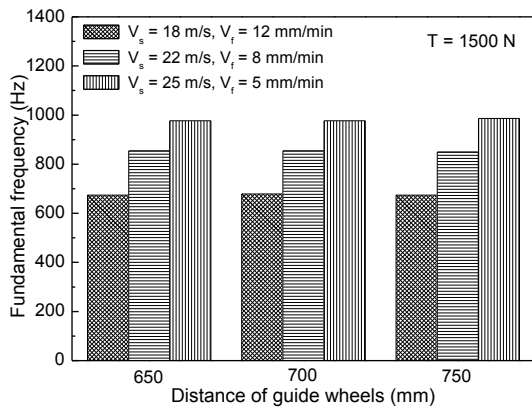
Fig. 11 Effect of guide wheels distance
on the vibration frequencies
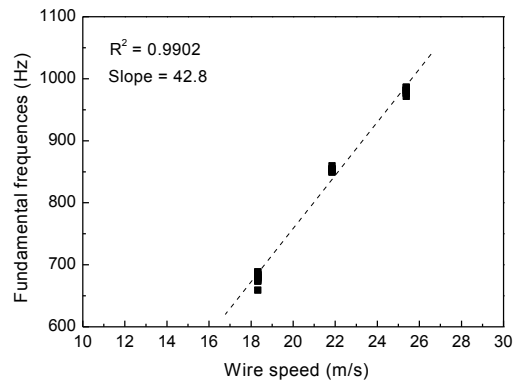
Fig. 12 Ralationship between the wire speed
and the fundamental vibration frequencies

3. CONCLUSIONS

The vibration in the sawing arc for the granite sawing with a diamond wire was successfully measured at six difference points of the sawing arc with laser displacement sensors. The RMS values of the wire vibration amplitudes are about 0.4-1.6 mm. The vibration amplitude decreases with the increase of wire speeds, feed rates and the tension forces. The fundamental frequencies of the wire sawing is similar to the product of wire speed and number of beads per meter. However, fundamental frequency has little been influenced by the feed rate, tension force and the distance of the guide wheels.

ACKNOWLEDGMENT

REFERENCE

[1] P.R. Davis, 2002, The future of diamond abrasives in stone processing, An International Technical Conference on Diamond, Cubic Boron Nitride and their Applications (INTERTECH 2000), Vancouver, Canada: 1 -14

[2] D.N. Wright, J.A. Engels, 2003, The environmental and cost benefits of using diamond wire for quarrying and processing of natural stone, Industry Diamond Review, 63 (4): 16-24

[3] B. Denkena, T. Glatzel, J. Bockhorst, M. Lünemann, 2005, Machining of construction materials with wire saws, Industry Diamond Review, 65 (2): 58-64

[4] H.K. Tonshoff, H. Hillmann-Apmann, 2002, Diamond tools for wire sawing metal components, Diamond and Related Materials, (11): 742-748.

[5] L.Q. Zhu, I. Kao, 2005, Galerkin-based modal analysis on the vibration of wire-slurry system in wafer slicing using a wiresaw, Journal of Sound and Vibration 283: 589-620

[6] Z. H. Cheng, C.K. Xu, R.Q. Pei, 2007, The vibration and control of multi-wire saw, Proceeding of the Sixth International Conference on Machine Learning and Cybernetics, Hoang Kong, 19-22, Aug.: 735-738

[7] S.B. Wei I. Kao, 2000, Vibration analysis of wire and frequency response in the modern wiresaw manufacturing process. Journal of Sound and Vibration 231 (5): 1383-1395

Session 4

SINGLE SEGMENT TESTS FOR THE ANALYSIS OF THE CORE DRILLING PROCESS OF CONCRETE MATERIALS

Michael Kansteiner[1, a)], Dirk Biermann[1, b)]

[1)]Institute of Machining Technology, TU Dortmund University, Baroper Straße 303, 44227 Dortmund

[a)] kansteiner@isf.de, [b)] biermann@isf.de

ABSTRACT

Diamond impregnated tools, like drill bits or circular saws, are used for the machining of mineral materials like stones or the compound material concrete. Drill bits comprise several single diamond impregnated segments which are attached to the top of the tool body by brazing or laser welding processes. Fields of application of these tools can be found at the construction industry, the stone processing and the mining industry. The segments consist of a sintered powder-metal matrix and randomly distributed diamond grains. Hence, the number of exposed grains on the tool surface varies even for tools of the same specification. To simplify the analysis of the core drilling process with several segments and therefore diamonds in contact, tests with single segments were carried out. Thus, the number of exposed grains is reduced to a manageable number. To analyse the influence of grit size and concentration in diamond impregnated tools on the process behaviour when machining concrete materials, path-controlled tests on a machining centre were conducted. High performance concrete (C100) and reinforced concrete were machined and process forces were measured to quantify the influence of the tool specification. Additional information were gained by analysing the generated tool tracks.

KEYWORDS

grinding, core drilling, diamond, diamond impregnated tool, concrete, reinforced concrete

INTRODUCTION

The core drilling process is a flexible, simple and widely used method in construction industry to generate openings/holes in different types of materials like (reinforced) concrete, brickwork, asphalt or rock material. Core drilling tools comprise several diamond impregnated segments. Therefore a core drilling tool is also called "bit" or "crown". The segments consist of a sintered metal matrix and randomly distributed diamond grains throughout the metal binder volume. Hence, tools with diamond impregnated segments can be classified as grinding tools, because the segments comprise several cutting grains with undefined cutting edges. In dependency of the field of application, e. g. construction industry or geological exploration, different configurations of segments exist. This article focuses on diamond impregnated segments which are used for the machining of concrete materials in the construction industry.

1.   STATE OF THE ART

A core drilling tool is composed of three main parts: the connection part, the main body (barrel, pipe) and the diamond impregnated segments. In construction industry an electronical drilling motor usually generates the necessary rotational motion while at the same time the drill bit is pressed into the material. The required force is applied by the operator either hand-guided or using a drill stand with a lever. Hence, core drilling in the construction industry is a force-controlled process. A specific value describing the drilling process is the weight-on-bit (WOB) value (also load or pressure on bit) which is the result of the division of the necessary force in feed direction by the surface area of the segments in contact [1, 2].

Diamond impregnated segments are manufactured by sintering procedures, like hot pressing [1]. Within this procedure a metallic powder and synthetic diamonds are mixed and sintered. The metallic matrix acts as the bonding and has two main functions. First of all, it has to hold the diamonds in place during cutting as long as they are sharp. Secondly, the metal matrix also needs to release diamonds before they become dull. Hence, matrix wear has to be adjusted to the diamond wear state for an efficient grinding process. This change of the segment due to wear is generated by the machining process itself and therefore called self-sharpening. Commonly, cobalt-based metallic powders are used as the metal matrix, because of its advantageous properties concerning diamond retention and wear. Due to different reasons, mainly economical but also environmental, developments lead to a replacement of cobalt-based matrices by iron-based ones having low cobalt content [3, 4]. The majority of today's diamond tools is manufactured with synthetic diamonds. The right choice and composition of diamond size, quality and concentration together with the metallic matrix material influences the efficiency of the grinding process. Hence, for different types of materials or concrete compositions, different types of segment configurations have to be chosen.

Concrete is a composite material which is manufactured by mixing cement, aggregates, water and if required further additives. Chemical reactions between cement and water lead to hardening processes. Within this composition the hardened cement acts like a binder which holds different types of aggregates like silicates, sand grains and stones together. Further additives e.g. superplasticizer are used to improve the mechanical properties of the manufactured concrete. Despite the hardened concrete is able to bear high compressive loads, its possibility to withstand tensile loads is very low. Hence, in construction elements steel bars are embedded as reinforcement. These steel bars, also called rebars, are carrying the tensile loads. Regarding the machining of reinforced concrete, the steel elements cause a reduction of the tool performance and increase the wear rate [5].

Despite the wide usage of diamond impregnated tools, the grinding process itself, e.g. the material separation and removal and the wear behaviour of diamonds and bonding, is not fully understood. Due to a large number of influencing factors, measurement results gained from drilling tests provide only global information, because interdependencies cannot be distinguished clearly [2]. Hence, the first logical step is to reduce the influencing factors by reducing the number of segments which are used for a drilling operation. This approach leads also to a reduction of exposed and active grains to a manageable number. As a consequence, the analysis of the process is simplified.

As mentioned before, core drilling processes are generally force-controlled. Nevertheless, path-controlled tests can be an appropriate method for analysing the process behaviour of diamond impregnated segments. *Franca*, *Mostofi* and *Richard* are motivating path-controlled test with single segments for different reasons [2]. The major advantage mentioned there is the shorter duration of drilling tests. Further advantages are the increased accuracy of measurement results and the higher stiffness of the set-up which reduces vibrations.

2. MATERIALS AND METHODS

Single segment tests were conducted on a machining centre FZ 12 S (Chiron-Werke) which consists of a travelling column with a vertical spindle and a fixed machine table. It is designed for drilling and milling operations of metal materials. Like it is common for these kinds of processes, the machining centre allows path-controlled motions. The experimental set-up (without coolant supply) and the kinematics of the test procedure are shown in figure 1. For testing single segments, a tool holder was attached to the spindle of the machining centre. During the tests, a constant infeed velocity and number of revolutions were set, so that annular tool tracks were generated. Because the infeed velocity is of major interest concerning tool performance in core drilling processes, tests with different infeed velocities v_f were conducted and varied in a range of $v_f = 0.25$ to 2 mm/min. This parameter field was deduced from force-controlled drilling tests with
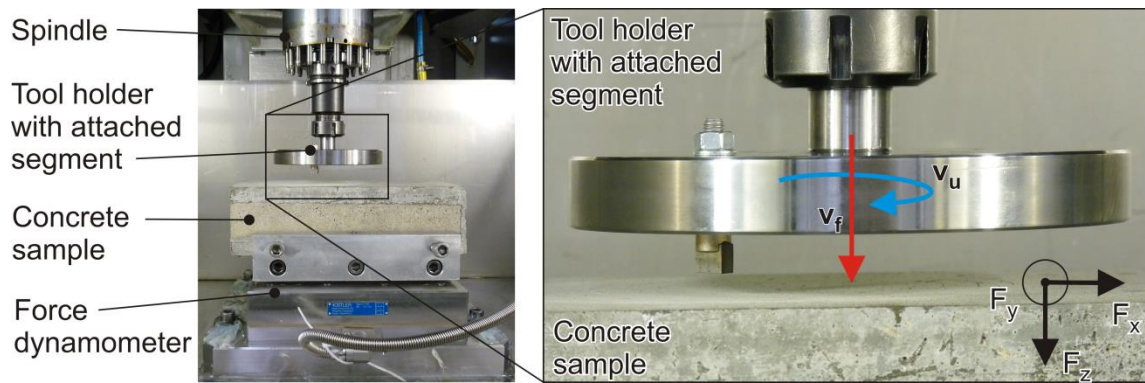
Fig. 1: Experimental set-up

core drilling bits comprising eight segments which are not subject of this article. The circumferential speed was kept at a constant value of v_u = 2.35 m/s for all tests which corresponds with typical circumferential speeds in core drilling processes of concrete with diamond impregnated segments. For testing a segment, a drilling depth of at least l = 0.5 mm was set. Several tests were conducted on the same position. Hence, the total depth of the generated tool track was increased gradually to a limit of l_{tot} = 4 mm.

For measuring the process forces while drilling, a force dynamometer of Kistler Instruments, type 9255C, was used and attached on the machine's table. With this dynamometer the forces in the three axes F_x, F_y and F_z can be measured. A frequency of f = 10.000 Hz was set to measure the process forces. Qualitative data was gained by microscopical pictures of the segments which were taken showing side and plane view.

To remove debris and slurry from the contact zone while drilling water without further additives is usually used but in order to avoid corrosion within the machining centre it was necessary to use a water miscible lubricant (Bechem Avantin 361, concentration p = 7 %) as additive. During the tests a sufficient amount of water was supplied to remove the slurry from the tool track.

The tested segments had got a rectangular shape with an initial segment height of h_{seg} = 10 mm, a width of w_{seg} = 5 mm and a length of l_{seg} = 10 mm. Before testing, a preparation routine (run-in) was carried out to expose the first diamond layer within the segment. Diamond impregnated segments made of the metal bonding Diabase-V21 (Dr. Fritsch) and synthesized diamond grains type Syngrit SDB1055 (Element Six) were tested. According to Dr. Fritsch, this type of metal bonding is designed for drilling and sawing operations of concrete and granite [6]. Its main components are iron, copper, cobalt and tin. The used synthesized diamonds are uncoated and have got impurities and an irregular shape. The segments were manufactured comprising three different mesh sizes (d_k = 20/30 mesh, d_k = 40/50 mesh and d_k = 70/80 mesh) and three different diamond grain concentrations (c = C8, c = C20 and c =C40). For testing, a segment was attached to a tool holder at a diameter of d = 100 mm which corresponds to commonly used core drilling tools.

The tests were conducted on samples made of concrete and reinforced concrete. On the basis of its compressive strength the concrete utilised for both types of samples is assigned to category C100/115 according to DIN EN 206 [7]. A further classification ranks the tested concrete as high-strength concrete [8]. The concrete samples were made of Portland cement 52,5 (Holcim AG), basalt in two different grain sizes (2/8, 8/16), sand (0/2), microsilica type 971-U (Elkem) and super-plasticiser type Glenium 51 (BASF). Two rebars made of steel (B 500 B) with a diameter of d = 12 mm were embedded in the concrete as a reinforcement. Because of a distance of s = 110 mm between the rebars, both rebars were cut during a drilling test.

Franca, Mostofi, and Richard describe two types of possible single segment tests [2]. These were called tests with "invariant topography" and tests with "variant topography". This classification is

based on the effect of self-sharpening. Hence, "invariant topography" tests mean no or minor changes of the segment while testing. According to this classification the majority of the conducted tests can be described as "invariant".

3. FORCE SIGNALS

The forces which can be measured during tests carried out on concrete or reinforced concrete are significant different owing to the rebars in reinforced concrete. These cause different material separation processes resulting in different process forces. In figure 2 and figure 3 the measured force signals F_x, F_y, F_z and the corresponding process force signals F_n and F_t are illustrated. All force data shown was smoothed by a moving arithmetic mean having a width of 151 data points. The graph on the left hand side (a) in figure 2 demonstrates the general progress of force signal F_n while conducting a segment test. The force signal comprises a nearly stationary period after the process start. During the whole process fluctuations of the force signal with a high frequency exist. Minor changes of the bonding and the inhomogeneous material to be machined may cause fluctuations over a longer period of time (low frequency) in the force signal.

As expected a sinus wave in the force signals F_x and F_y occurs (cf. fig. 2 (b)), because of the rotational motion of the tool and the stationary force dynamometer. Whereas the measured force signal F_z corresponds with the normal force F_n, the tangential force F_t has to be calculated by a trigonometric function (1) using the force signals F_x, F_y and the period time of one revolution T. Here, it has to be considered that the starting point of the calculation must be a maximum in the F_x signal. For the comparison of the tests on concrete, the average of the force signals of F_t and F_n within a time period of t = 2 s in the stationary phase of the tests was calculated.

$$F_t(t) = F_x(t) * \cos\left(\frac{2*\pi}{T} * t\right) + F_y(t) * \sin\left(\frac{2*\pi}{T} * t\right) \qquad (1)$$

On reinforced concrete the measured force signal is highly influenced by the reinforcement (cf. fig. 3). As mentioned before, two rebars are embedded in the concrete. Figure 3 illustrates that the general progress of the force signal for F_n is comparable to the signal on concrete. But the reinforcement leads to two main differences. The force is marked higher on reinforced concrete
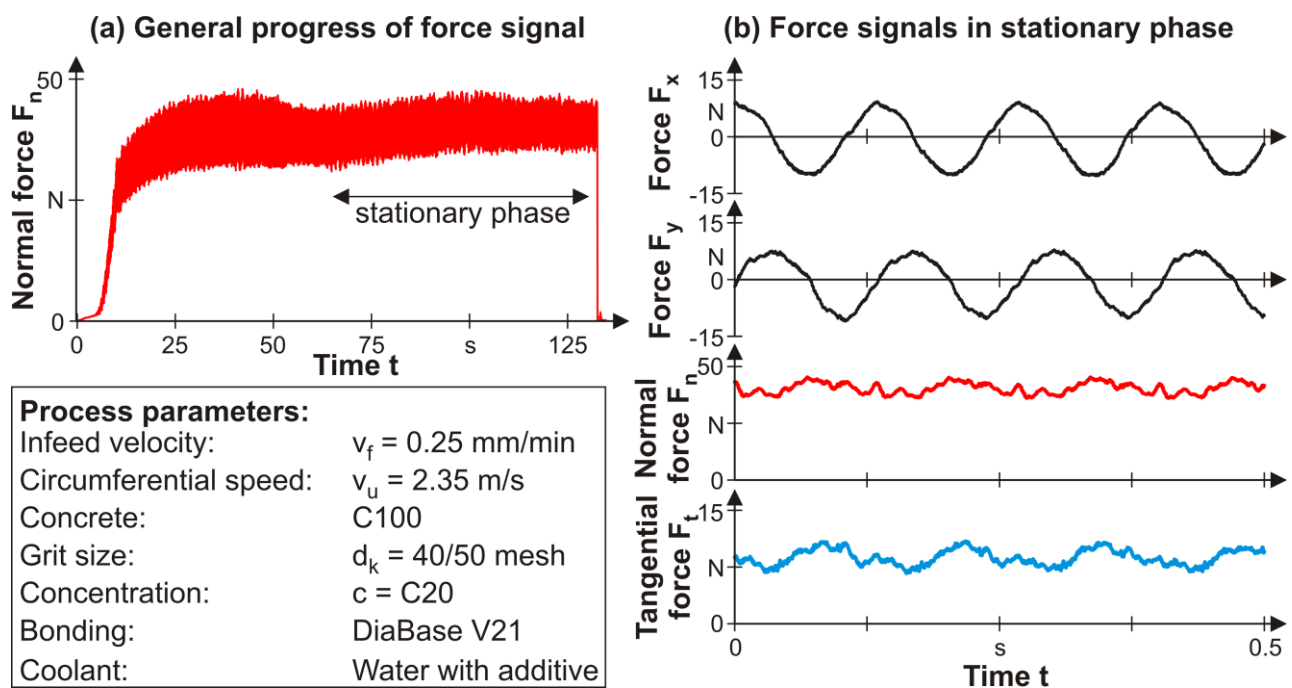

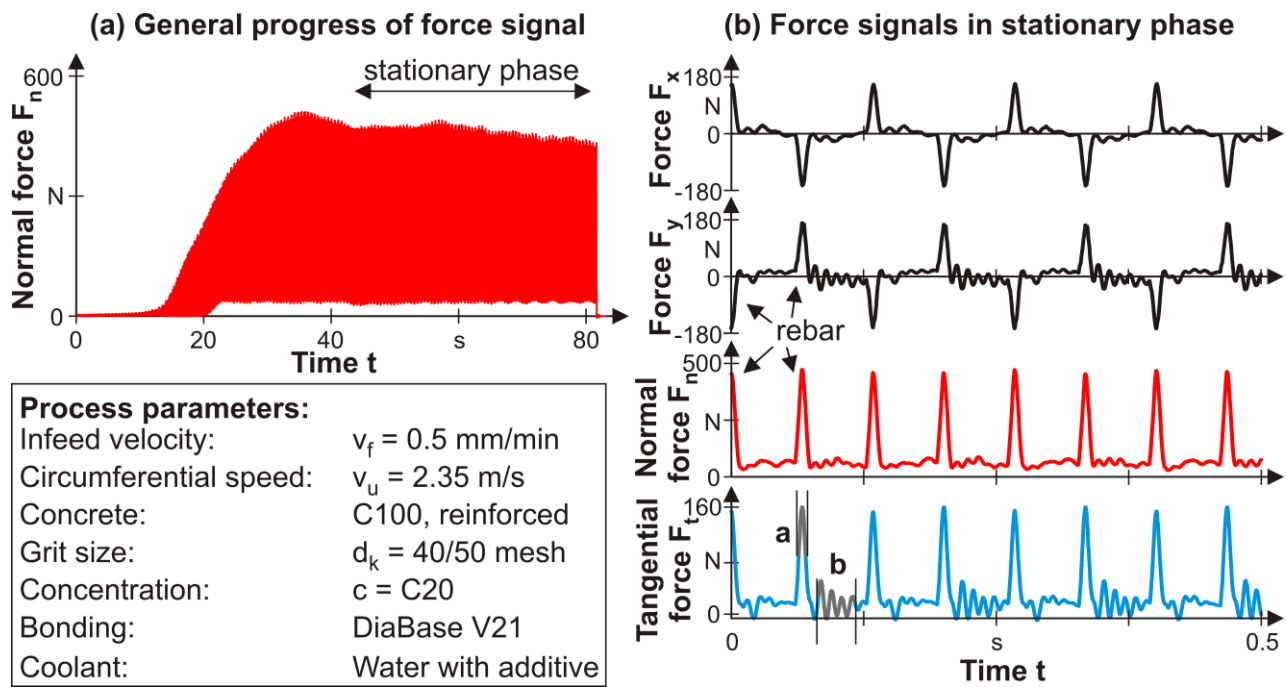Fig. 2: Force signals when cutting concrete

Process parameters:

Infeed velocity:	$v_f = 0.5$ mm/min
Circumferential speed:	$v_u = 2.35$ m/s
Concrete:	C100, reinforced
Grit size:	$d_k = 40/50$ mesh
Concentration:	$c = C20$
Bonding:	DiaBase V21
Coolant:	Water with additive

Fig. 3: Force signals when cutting reinforced concrete

and therefore the fluctuation deduced from the general progress of the force signal seems to be very high. However, these fluctuations are caused by cutting the rebars as it can be seen in figure 3 (b). Cutting the rebars has got a great impact on the force signals causing rapid rises (peaks). Because of the stationary coordinate system and the rotational moving force peaks in F_x and F_y the direction changes from positive to negative and vice versa within one rotation. Whereas the alternation of the force F_x is comprehensible, the alternation in F_y signal depends of the position of the rebar and the way the rebar is cut. Because the segment cuts only through one half of the round rebar, the segment is pushed aside directed to the centre of the rotational motion.

For the comparison of the tests on reinforced concrete, a special analysis has to be conducted considering the two different phases in reinforced concrete. It was chosen to consider $m = 100$ sections in steel, as shown in figure 4 (b), detail a, and to calculate the average of these sections quantifying the influence of the rebar on the process forces. In concrete a similar method was chosen. Here also $m = 100$ sections were considered and the average was calculated (cf. fig. 3, detail b). Hence, force signals occurring during $n = 50$ rotations were considered for the analysis. The calculated averages are used for the comparison of the segment tests shown in the following chapters.

4. INFLUENCE OF DIAMOND SIZE AND CONCENTRATION ON PROCESS FORCES

The first test series was conducted on samples of high-strength concrete without reinforcement. Within this test series all of the nine segment specifications mentioned before were used. Two segments of each specification were tested for a general understanding of the deviation caused by the tool. Hereby, deviations could be expected due to a diverse number of exposed diamonds. In table 1 the number of exposed diamonds is given for all tested segments.

The influence of the infeed velocity on the resulting process forces is of major interest, because the achievable infeed velocity is decisive for the performance of actual force-controlled drilling processes. Therefore, each segment was tested at three different infeed velocities, $v_f = 0.5$, 1.25 and 2.0 mm/min. Tests with the infeed velocity of $v_f = 1.25$ mm/min were conducted two-times with each segment, whereas tests with the infeed velocity of $v_f = 0.5$ and 2.0 mm/min

Tab. 1: Number of exposed diamonds for tested segments

	First test series on concrete						Second test series on reinforced concrete
	d_k = 20/30 mesh		d_k = 40/50 mesh		d_k = 70/80 mesh		d_k = 40/50 mesh
	Segment 1	Segment 2	Segment 1	Segment 2	Segment 1	Segment 2	Segment 1
c = C8	5	10	12	15	28	31	21
c = C20	11	9	22	22	37	59	30
c = C40	15	13	43	39	101	96	46

were carried out only once with each segment. Resulting process forces are arranged in a matrix form shown in figure 4. In the rows this matrix comprises test results with the same diamond concentration and in the columns test results with the same grain size are shown. Within the conducted tests, significant changes, like diamond break-out, which could influence the process forces only seldom occurred. Hence, the vast majority of the tests can be described as tests with "invariant topography". An exception are the tests with diamond concentration c = C8 and grain size d_k = 20/30 mesh. This segment composition leads to comparatively high wear. Thus, fewer tests can be described as "invariant" and be considered for the graph shown in figure 4.

In figure 4 the results for the normal force F_n and the tangential force F_t in dependency of the infeed velocity are shown. For all tests an increasing infeed velocity causes a gradual rise of the process forces F_n and F_t. Within the tested range, the results indicate a linear correlation with steady growth between infeed velocity and process forces. Increasing infeed velocities correspond

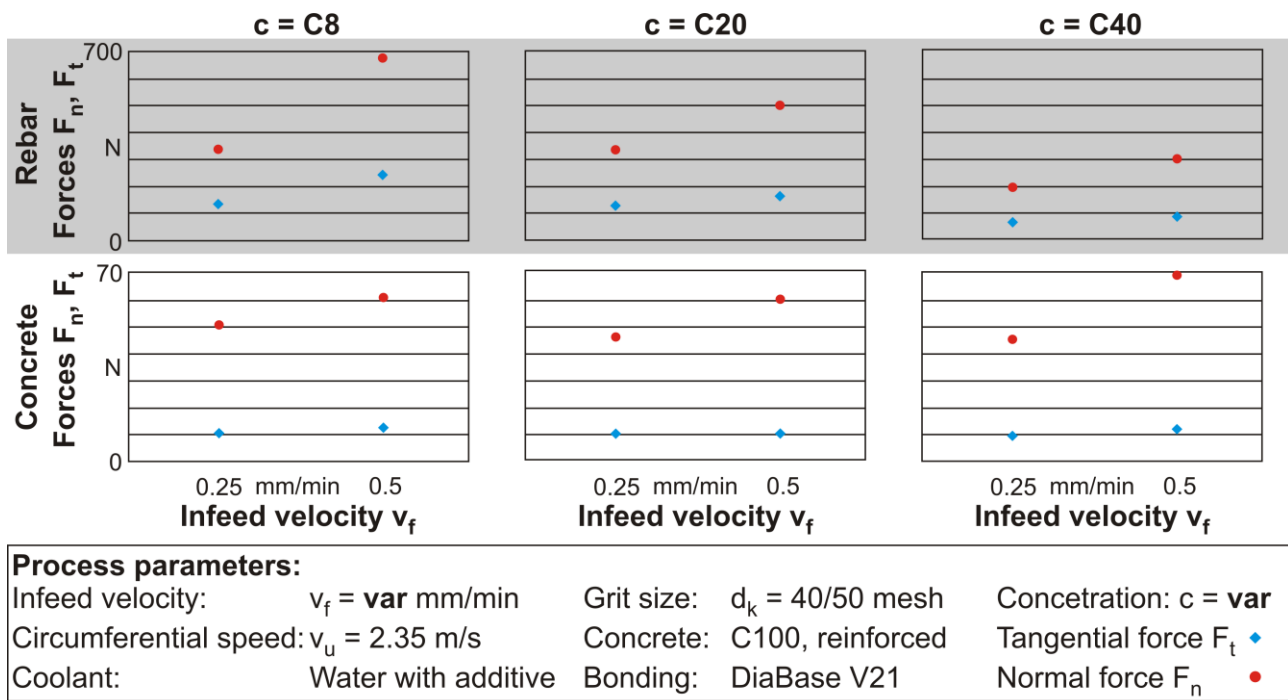**Fig. 4: Process forces for segment tests on concrete**

Fig. 5: Process forces for segment tests on reinforced concrete

with a higher infeed per revolution therefore also larger values of chip thickness are generated which are resulting in higher process forces. The greatest forces exist for an infeed velocity of $v_f = 2$ mm/min and diamond concentration of c = C40 independent of the diamond size. For these tests forces of about $F_n = 95$ N and $F_t = 20$ N were measured which results in maximum weight-on-bit values of about WOB = 190 N/cm². Minimum normal forces occur for small infeed velocities (about $F_n = 25$ N). In contrast, the tangential force F_t is always lower than $F_t = 25$ N, but not less than $F_t = 5$ N. For a diamond concentration of c = C8, comparing force results for an infeed velocity of $v_f = 1.25$ mm/min, the results represent a slight decrease of process forces with increasing diamond sizes. Due to smaller diamond size but a constant diamond concentration the number of exposed diamonds increases (cf. tab. 1). Hence, it can be assumed that a larger contact area between diamonds and concrete exists which causes higher process forces. Nevertheless, considering also the tangential force, the results reveal a higher cutting efficiency for segments with a diamond size of $d_k = 40/50$ mesh. A higher cutting efficiency in grinding is achieved when the relation between the tangential and the normal force increases ($\mu = F_t/F_n$). For a diamond concentration of c = C20 significant differences between the measured normal forces do not exist for different grain sizes. However, the tangential force is maximal for a diamond size of $d_k = 20/30$ mesh. Here, the results also indicate that the material separation with a diamond size of $d_k = 20/30$ mesh is more efficient. Bigger diamonds lead to a higher protrusion of the diamonds which could cause a larger chip thickness and therefore an increasing cutting efficiency. For a diamond concentration of c = C40 no remarkable differences between process forces for infeed velocities $v_f > 1.25$ mm/min exist. This could be influenced by the large number of exposed diamonds for the entire tested segments.

The second test series was carried out on reinforced concrete samples with two rebars. Because of a significant rise of process forces due to cutting the rebars, it was necessary to readjust the infeed velocity to smaller values. Consequently, tests with two different infeed velocities and three different segments were conducted (cf. fig. 5). The process forces when cutting the ductile metal rebar material is remarkable higher than in cutting concrete. Hence, the scale for graphs which illustrate the process forces in rebar is ten-times magnified than the scale for process forces in concrete. The results for normal forces when cutting the rebar are at least five-times higher within the conducted tests. For all tested segment specifications an increase in infeed velocities causes higher process forces. The maximal normal force measured is at about $F_n = 680$ N

(WOB = 1360 N/cm²) for rebar and at about $F_n = 61$ N (WOB = 122 N/cm²) for concrete. The test results for rebar show a marked drop of the process forces F_n and F_t for an increased diamond concentration. However, this drop is not visible in the process forces when cutting concrete. Comparing the test results for concrete (cf. fig. 5) with the test results of the first series conducted (cf. fig. 4) no significant difference can be observed. The marked differences regarding process forces in rebar and concrete indicate significant differences for material separation as expected.

5. INLFUENCE OF DIAMOND CONCENTRATION ON TOOL TRACKS

For an efficient cutting process it is of interest to minimize friction and to increase material removal. This will be achieved, if every exposed diamond creates an individual cutting track. Therefore a certain distance should exist between two diamonds and each exposed diamond should not be located in direct line with another diamond. In this case, its capability of generating material removal is limited. Instead, primarily frictional processes have to be expected which cause wear flat of the diamond [9]. When cutting ductile metal materials, a minimum depth of cut has to be reached before a material removal with chip formation can be generated [10]. Otherwise, only frictional processes, elastic and plastic deformations occur. For detailed analysis of the material separation in the cutting zone three-dimensional scans for gaining profile information were carried out. Scans of the tool tracks in the rebar and the concrete were made with a confocal white-light microscope (µsurf, Nanofocus).

In figure 6, profiles and microscopical pictures of the used segments are shown. The profiles and pictures indicate that with an increase of diamond concentration which corresponds to a rise of the number of exposed diamonds, a more levelled and smoothed tool track is produced. This can be observed for the rebar as well as for the concrete profiles. Due to the increased number of exposed diamonds several cutting tracks by several different diamonds occur. These are spread uniformly across the tool track width causing a levelled tool track surface (cf. fig. 6, c = C40). In contrast, the tool track generated by the segment with the lowest diamond concentration of c = C8 reveals individual cutting tracks. Comparing the profiles generated in rebar and in concrete the difference of material properties become apparent. The ductile material behaviour of the rebar

Process parameters:

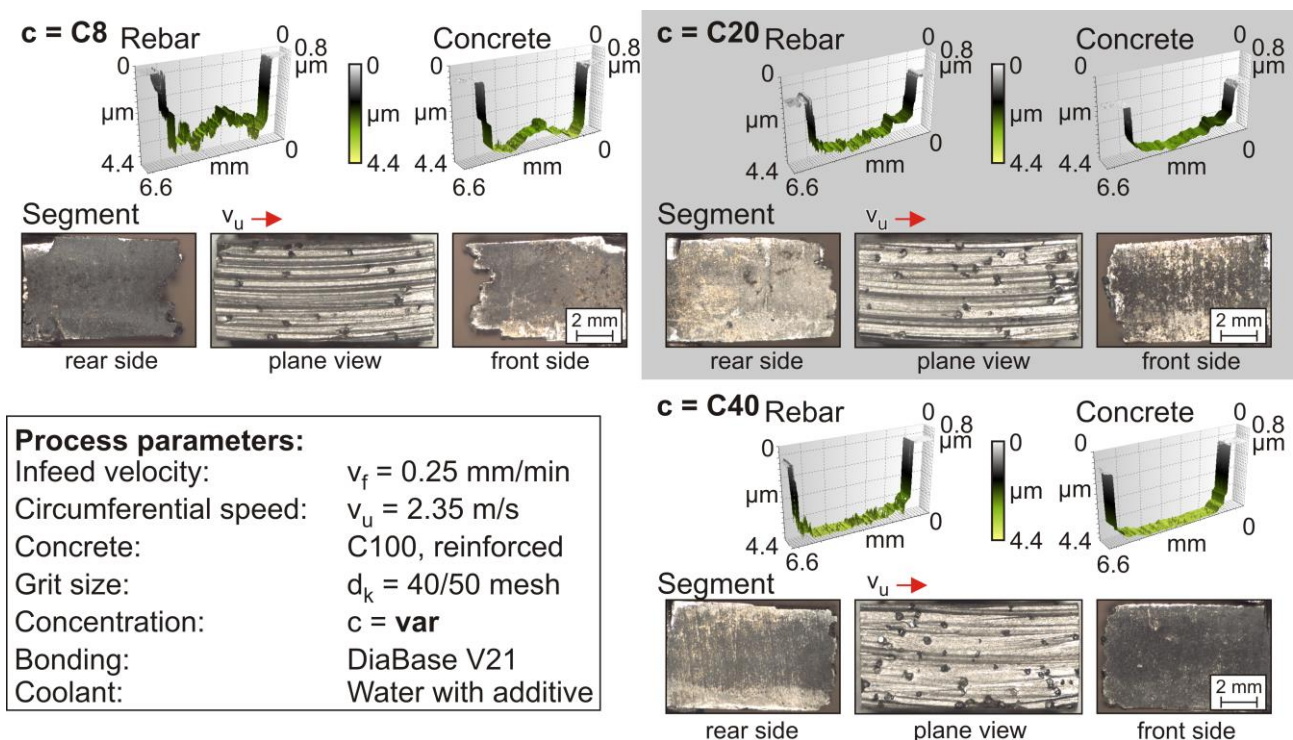|	
Infeed velocity:	$v_f = 0.25$ mm/min
Circumferential speed:	$v_u = 2.35$ m/s
Concrete:	C100, reinforced
Grit size:	$d_k = 40/50$ mesh
Concentration:	c = **var**
Bonding:	DiaBase V21
Coolant:	Water with additive

Fig. 6: Profiles of tool tracks and microscopical pictures of used segments

enables elastic and plastic deformation during cutting. Hence, different grooves and peaks in the profile of rebar exist. Due to the fact that the position of the grooves and the position of the single diamonds correspond it is possible to assign grooves to single diamonds on the segment. The profiles in concrete show less peaks in comparison to the profiles in rebar. Concrete has got brittle material properties; hence, the material separation is predominately generated by cracking and fracturing of material. The profiles of concrete do not reveal distinctive grooves or peaks which are comparable to the grooves in the rebar. Instead, the profile of concrete show wider grooves. For the diamond concentration of c = C40 in the profile of concrete no single cutting tracks can be observed because there are presumable superimposed. In contrast such single cutting tracks are visible in the profile for concrete generated by the segment with a diamond concentration of c = C8.

The tests with the segment having a diamond concentration of c = C8 reveal an influence of the diamond distribution on the cutting behaviour. Due to a non-uniform distribution of exposed diamonds on the segment surface, cutting tracks are not generated across the whole tool track width. Hence, an increased bonding wear appears in line where no diamond is set. Thus, distinctive deep grooves are generated by wear of the bonding. Furthermore, a specific material peak in the concrete and in the rebar profile arises. The depth of the groove in the segment, i.e. material peak increases with the depth of drilling. This type of wear is not representative for actual drilling tests, because in core drilling several diamond impregnated segments in row create several cutting tracks which are superimposed.

6.   SUMMARY AND CONCLUSION

Within this research, tests with single diamond impregnated segments of drill bits were conducted. The testing procedure was derived from the force-controlled core drilling process. However, the tests were driven path-controlled using a machining centre to analyse the occurring process forces and the generated tool tracks in concrete and in reinforced concrete respectively. The test procedure proved to be an appropriate method for the detailed analysis of the drilling process with diamond impregnated segments.

Two series of segment tests on concrete and reinforced concrete were carried out. The vast majority of these tests showed minor wear so that an invariant segment topography existed throughout the tests. As expected, tests on concrete as well as on reinforced concrete revealed higher process forces due to higher infeed velocities. On concrete nine different segment specifications (diamond size, diamond concentration) were tested. The results on concrete showed similar process forces for segments with high diamond concentrations (c = C20 and C40). For the lowest diamond concentration c = C8 tested and a constant infeed velocity the results indicate a decrease of this process forces with an increasing diamond size. Regarding cutting efficiency based on µ, the biggest diamond size revealed the highest values. Bigger diamonds result in higher protrusion heights which might contribute to a more efficient cutting process. Furthermore, higher protrusion heights increase the necessary free volume in the cutting zone for slurry whereby frictional processes between removed material and segment could be minimized. In contrast, high diamond concentrations in combination with smaller diamonds could not leave enough free volume for debris and slurry so that similar process forces are generated.

The measurement of the profile of the generated tool tracks in reinforced concrete provided further information for a detailed analysis of the material removal process. A high diamond concentration creates several superimposed cutting tracks whereas a low diamond concentration leads to cutting tracks which can be assigned to single diamonds on the segment. In the case of a high diamond concentration, it has to be assumed that single diamonds cannot cut efficiently. Possible reasons are low cutting depths, either due to imposed cutting tracks or due to their position in a line of another diamond. These circumstances can result in undesired wear of diamonds like wear flat in drilling tests. On the other hand, the interactions between two actual cutting diamonds could cause an increased material removal by interactive material fracturing [11].

Measured force signals during tests on reinforced concrete showed distinctive peaks when cutting the metal rebars. Within the conducted tests, the average values of these peaks were at least five-times higher than the process forces for concrete. Three different segments comprising the same diamond size but different diamond concentration were tested. In concrete for both test series no significant differences regarding process forces in dependency of the diamond concentration existed. In contrast differences in rebar occurred. The results showed lower forces in rebar for higher diamond concentrations. The analysis of the tool tracks in the rebar and in the concrete shows that the cutting tracks in the concrete are wider and deeper than the corresponding cutting tracks in the rebar owing to the different material removal processes [12]. For the rebar, in tests with a low diamond concentration, the profile has got a high roughness (sharp peaks) in contrast to a smooth profile for the tests with a high diamond concentration. A small number of active grains may cause high plastic deformations and material bulging which might lead to extensive frictional processes and therefore process forces and rough tool track profiles. Instead, with a higher number of active grains smaller chips by microcutting and microfatigue, defined by *Zum Gahr* [13], could be generated and plastic deformations are limited to a smaller range.

In further test series the parameter field will be extended to cover a wider range of applications. Due to significant differing test results concerning process forces and cutting tracks, a detailed analysis has to be carried out on the material separation and the material clearance of the cutting zone while drilling reinforced concrete. Furthermore, the still current topic of arranged diamond settings has to be considered for future tests. Hereby a more stable and uniform process behaviour with respect to material removal and wear is to be expected which will improve the output of tests.

ACKNOWLEDGEMENT

REFERENCES

[1]   Konstanty, J., 2005, Powder metallurgy diamond tools, Elsevier

[2]   Franca, L.F.P., Mostofi, M., Richard, T., Interface laws for impregnated diamond tools for a given state of wear, International Journal of Rock Mechanics and Mining Sciences, 73 (2015), pp. 184-193

[3]   Tillmann, W., Gathen, M., Vogli, E., Kronholz, C., New materials and methods beckon for diamond tools, Metal Powder Report, 62 (2007) 7, pp. 43-48

[4]   Konstanty, J., New Nanocrystalline Matrix Materials for Sintered Diamond Tools, Materials Sciences and Applications, 03 (2012) 11, pp. 779-783

[5]   Köhler, A., Jakob, H., Hassel, T., Bach, F.W., 2011, MMC based materials as an alternative cutting material for cutting densely filled and heavily reinforced concrete structures, in: ICSCM, 1st International Conference on Stone and Concrete Machining, PZH Produktionstechnisches Zentrum, pp. 25-31

[6]   DR. FRITSCH GmbH & Co. KG, 2015, Sintering data sheet Diabase-V21, www.dr-fritsch.de

[7]   DIN EN 206, 2014, Beton – Festlegung, Eigenschaften, Herstellung und Konformität, Beuth Verlag

[8]   Neroth, G., 2011, Beton, in: Wendehorst Baustoffkunde, Vieweg+Teubner Verlag, pp. 247-381

[9]   Miller, D., Ball, A., The wear of diamonds in impregnated diamond bit drilling, Wear, 141 (1991) 2, pp. 311-320

[10]   Klocke, F., König, W., 2005, Fertigungsverfahren 2 – Schleifen, Honen, Läppen, Springer-Verlag

[11]   Denkena, B., Bockhorst, J., Seiffert, F., 2009, Auslegung von Schneidkörpern für das Seilschleifen - Mehrkornritzuntersuchungen als Basis für die Trennmechanismen-basierte Auslegung von Schneidperlen, ZWF Zeitschrift für wirtschaftlichen Fabrikbetrieb, 104 (2009) 5, pp. 340-347

[12]   Denkena, B., Tönshoff, H.K., Becker, J.C., Bockhorst, J., Hillmann-Apmann, H., 2003, The mechanisms of material separation at steel and concrete material, in: Euro PM 2003, European Powder Metallurgy Conference on Meeting the Challenges of a Changing Market Place, European Powder Metallurgy Association (EPMA), pp. 87-95

[13]   Zum Gahr, K.-H., 1987, Microstructure and wear of materials, Elsevier

DIAMOND WIRE – STONE INTERACTION DURING THE CUTTING PROCESS: MECHANICAL, PHYSICAL AND CHEMICAL INVESTIGATIONS

S. Spriano[1], S. Ferraris[1], R. Bellopede[2], P. Marini[2], L. Zichella[2], A. Tori[3]

[1]Department of Applied Science and Technology, Politecnico di Torino, Turin, Italy.
[2]Department of Environment, Land and Infrastructure, Politecnico di Torino, Turin, Italy.
[3] CO.FI.PLAST SRL, Lessolo, Italy

ABSTRACT

Stone cutting with diamond wires results in the progressive and concurrent wear of the natural stone and the cutting tool (diamond wires - diamond beads). This phenomenon has been investigated since the beginning of stone machining, but there are still several open questions concerning the parameters controlling it. The aim of this study is to establish correlations between the natural stone mineralogical composition and the diamond wires cut performance in terms of efficiency, productivity and diamond beads consumption. This investigation requires a multidisciplinary approach. Microscopic analysis have been done in order to investigate the wear processes of the diamond beads in terms of super-abrasive grains (diamond grits) damage and pull out. Petrographic analysis and mineralogical investigation have been considered in order to correlate the removal rate during the cutting action with the characteristics of the stones. Muds derived from cutting have been characterized for the complete comprehension of the cutting process. The erosion analysis concerned both stone debris and diamond beads, characterizing both the metal powder and super-abrasive grains (diamond) in the cut waste (mud). Moreover, the metal matrix is the core of the diamond wire technology and it drives cutting performance and efficiency.

KEYWORDS

stone workability, diamond wires, corrosion, diamond beads characterization, diamond wires-stone interaction, granite, sienite, diorite.

INTRODUCTION

Diamond wires are cutting tools for stones (marble, granite, etc.) and concrete. They are composed of a stainless steel cable on which diamond sintered beads, containing diamond grains, are assembled with a regular space between them. A sintered bead is a composite material containing super-abrasive grains (diamond) hold in a metallic matrix, usually cobalt. The main functions of the metal matrix consist in holding the diamond grains (the diamond crystal has to protrude from the matrix during the whole cutting action) and in preventing premature detachment of the diamonds from the matrix (the mechanical and chemical bonding between the diamond crystal and metal matrix must guarantee a stable bond, until the worn diamonds come off, in order to re-establish the best cutting condition). The steel cable is protected from erosion and corrosion by a polymeric coating of polyurethane (TPU), through a plasticization process. The selection of the diamond wire depends on two parameters: (1) the smallest possible diameter, for minimal scrap generation during the cut; (2) the correct diameter because the tool will be shock-proof. [1-2-3] The aim of this study is to establish interactions between the natural stone mineralogical composition and the cut performance of diamond wires, in term of efficiency, productivity and diamond beads consumption.

MATERIALS AND METHODS

A multidisciplinary approach has been adopted during this study in order to combine several investigations and tests for a global correlation of cutting parameters: stone, cutting tool, cutting machine. [4-5]

Sintered and plasticized diamond wires, diameter 7 mm, have been assumed as reference standards for the stone slabbing (granite stone, multiwires machine). Moreover, the metal matrix is the core of the diamond wire technology and it drives cutting performance and efficiency.

Microscopic analysis has been done in order to investigate the wear processes of the diamond beads in terms of super-abrasive grains (diamond) pull out and damage. Worn diamond beads coming from diamond wires used in cutting of Fe containing stones were observed by means of a Scanning Electron Microscope (SEM, SEM-FEI, Quanta Inspect 200, FEI), equipped with the back scattering mode (BS-SEM) and with an EDS that was used to verify the elemental composition of the specimens in different areas.

The chemical affinity between iron-based minerals and super-abrasive grains (diamond) gives an answer to early wear of the diamond wire in some case studies.

Petrographic analysis and mineralogical investigation have been performed on the stones and on the muds derived from their cutting. Both have been analyzed by means of the optical microscope Leitz Wetzlar. Image analyzer software IMAGE J (an open source image processing program designed for scientific multidimensional image), in order to define size, dimension and ratio between quartz and feldspar. *In*

Figure 1 the thin sections of two different kind of Sardinian granite (RG and GP) are reported.
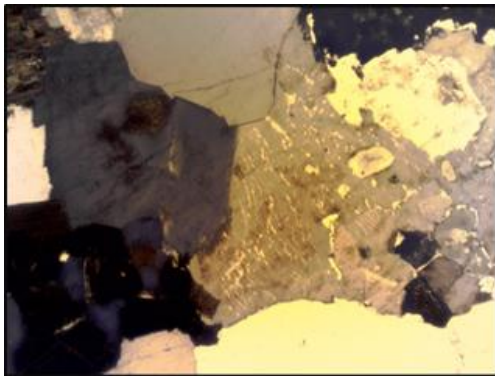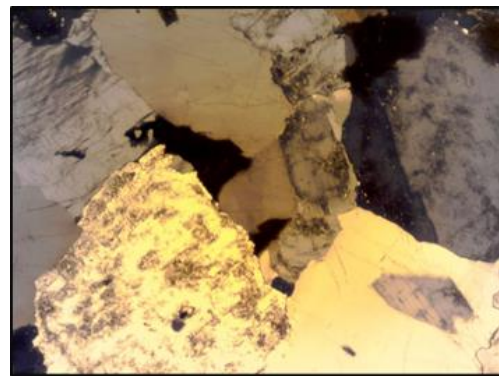
A. RG granite   B. GP granite

Figure 1: Thin sections of RG and GP granite (long side 4.3mm): microscopy crossed nicols, in black the ferrous components (biotite).

The granulometric curve of multiwire muds is shown in Figure 2; it is characterized by an high percentage (40.2%) of particles minor than 0,038mm.

>0,212 mm

0,212--0,106 mm

0,106 -0,063 mm

0,063-0,038 mm and in the tank <0,038 mm

Figure 2: size distribution process and characterization of multiwire muds

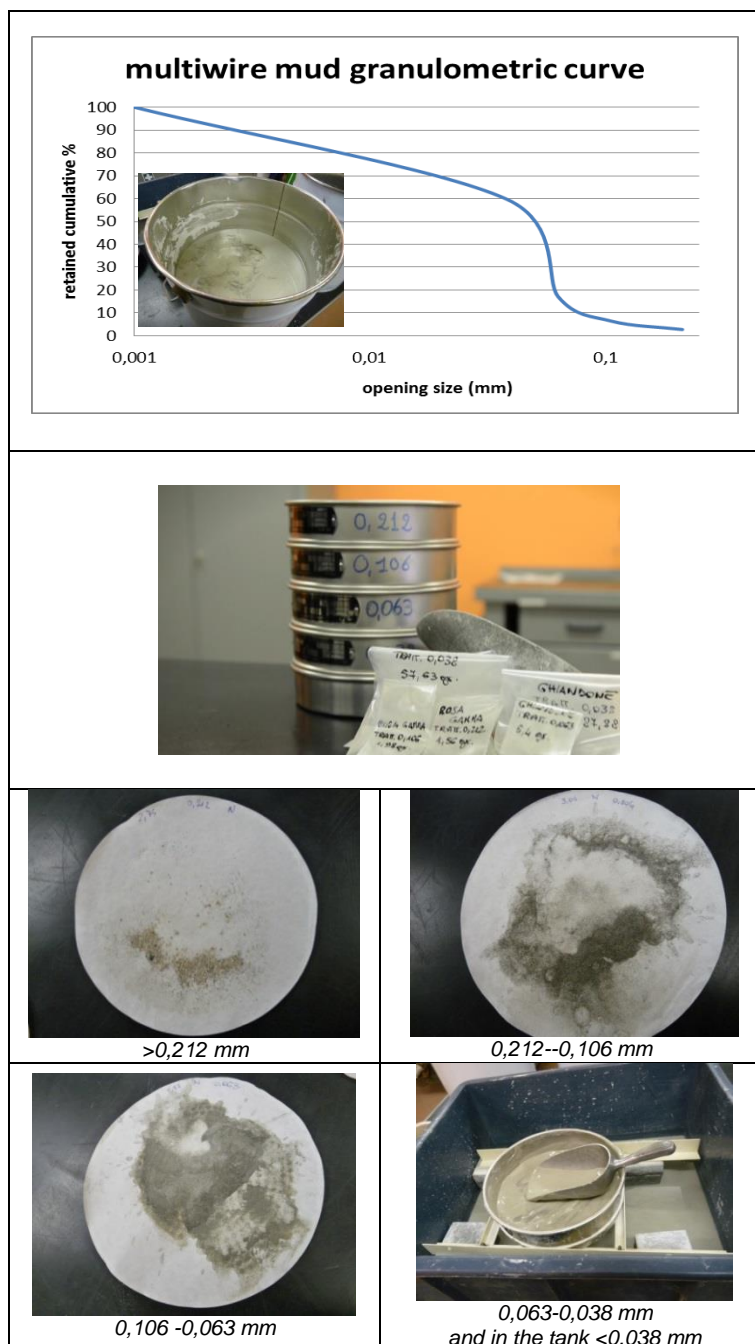Each one of the classes obtained through the granulometric separation has been processed with a wet magnetic separation (Co-Al – Ni magnet). On the size classes minor than 0,063mm a further analysis by means of X – Ray Diffraction (XRD) have been performed.

RESULTS AND DISCUSSION

There are significant differences in the interaction between stone and diamond beads when considering different stones. The major variability consists in the mud particles dimension and in the type of wear and damage of the diamond beads, but also the shape and conformation of the mud particles are important parameters to be considered. A double examination (beads and stones) represents a whole and complete approach to the issue under investigation, characterizing both the metal powder and super-abrasive grains.

In the case of diamond wires used in cutting of Fe containing stones, we observed by SEM that the junction between the diamond beads and the steel cable is good and no wear was observed in this area (Figure 3). The steel cable is well covered by a thin or thick polymeric coating (polyurethane) at the junction between the cable and the diamond bead, without any erosion, detachment or wear of the coating (Figure 4).
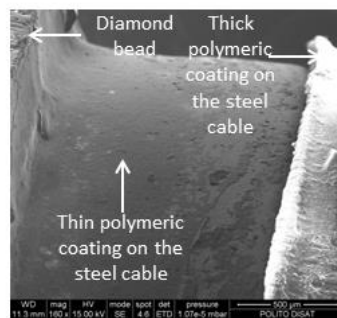

Figure 3: SEM image at low magnification of the junction between the diamond beads and the steel cable

On the other side, erosion of the metal matrix and damage of the diamonds can be clearly observed on the beads after stone cutting: this is the main issue in the wear of diamond wires and it will be one of the main focus of the present work. [6]

As first, we observed at low magnification that the beads almost maintain their shape after stone cutting and they are almost uniformly worn (see Figure 4) on all their length. The direction of cutting and rotation of the diamond wire can be derived by observing the presence of "comet tails" behind the diamond grits and the slight lower diameter of the bead on the left of the image: the first impact of the bead with the stone during cutting was on the left side, in this case.
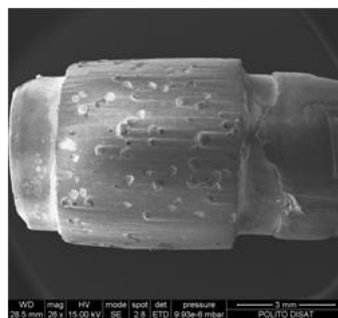
Figure 4: SEM image at low magnification of a worn diamond bead

Diamonds are well dispersed on the surface of the bead without evidence of clusters and polycrystalline agglomerates. The diamond beads wear rate can be classified according to diamond grits pull out, damage or breakage, and to the diamond retention ability of the metal matrix, through a morphological analysis of the beads surface.

The diamond grains observable on the surface of a worn diamond bead used in stone cutting can be classified in the following way: diamonds arising from the surface without any damage, diamonds protrusive from the surface, diamonds polished, micro-fractured, macro-fractured, pulled out and etched. [7]

In this case, we observed diamonds arising from the surface without any damage, macro fractured, pulled out and etched (Figure 5).
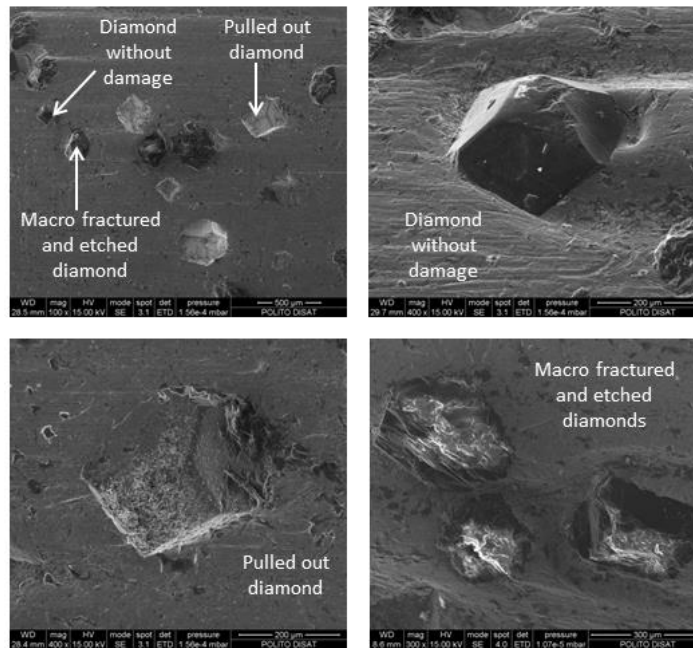
Figure 5: Image of the surface of a worn diamond bead with diamond bits differently damaged

Diamonds without any damage are diamonds still able to cut stones and a "comet tail" is clearly visible behind them, because their presence prevent erosion of the metal matrix behind them by stone debris, during cutting. [8] The interface between the un-damaged diamond bits and the metal matrix is continuous and without any cracks, showing a high retention ability of the metal matrix and good sintering of the beads. [9] EDS analysis performed on the smooth surface of the un-damaged diamonds only shows the presence of carbon.

Some diamonds were pulled out during cutting and some voids are observable on the surface; the voids are often quite deep, showing that in these cases diamonds were pulled out before they were highly worn. The EDS analysis performed inside the voids deriving from pulled out diamonds shows the presence of Co and WC, which are the main components of the matrix. No porosity can be seen inside the voids of the pulled out diamonds, confirming a good sintering of the metal matrix.

The most interesting diamonds grits are the macro fractured and etched ones. These diamonds are no longer able to cut stones and they do not show any "comet tail" behind them. Macro fractured diamonds do not highly protrude from the surface level and they still show a good interface with the metal matrix, showing that in some cases the retention ability of the metal matrix is too high: un-efficient diamonds without cutting ability are still maintained on the surface by the strong interface with the metal matrix. [10] The surface of the macro fractured diamonds shows both some smooth cleavage planes, deriving from a brittle fracture mechanism, and some rough areas probably deriving from etching (Figure 6). On the rough areas of the etched diamonds, EDS analysis shows the presence of an adherent layer of stone containing Fe, Ca Na, K, Mg and Si, suggesting that Fe containing stones are able to react with the diamonds causing a high degree of damage and macro fractures follow this etching.
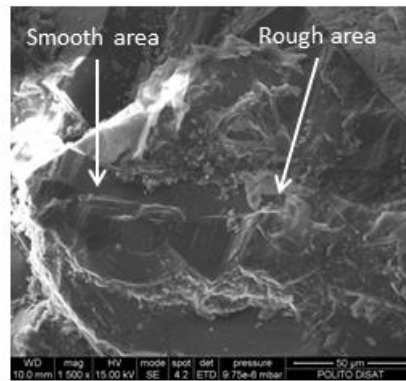
Figure 6: Macro fractured and etched diamond

On one diamond grain, arising from the surface with an almost un-damaged and smooth surface, it was interesting to see the damage, probably due to etching and reaction with iron, in a first stage (Figure 7Figure 7), limited to small areas: in this case macro fractures did not occur because of the limited etching.
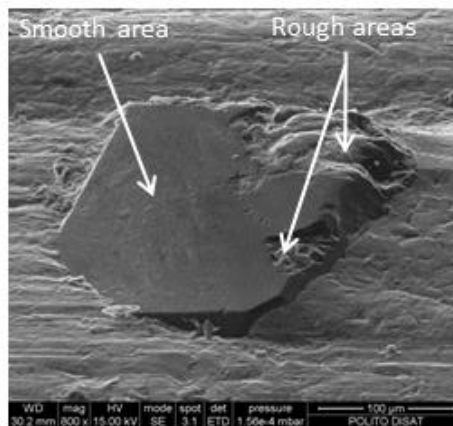
Figure 7: An almost un-damaged diamond bit showing etching in a first stage

Muds generated by stone cutting are mainly composed by stones debris and fraction of heavy metals (e.g. Co, Ni, Cu, Zn, Cr, W and their alloys) deriving from metal matrix. In particular, the magnetic separation shows, in the 0,038mm-0,063mm class, a higher amount of ferromagnetic particles coming from the metal matrix erosion, while, in the fine class (<0,038mm) the rock minerals (quartz in particular) are predominant: this is confirmed from the diffractometric analysis too (Figure 8). The sawmill mud contains heavy metals coming from the sawing tools: an example of 4 different muds sample (M1-M2-M3-M4) is in
Table 1 and
Table 2.
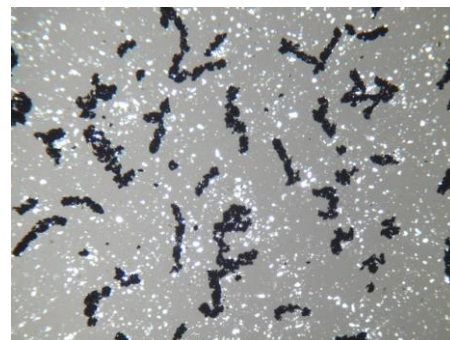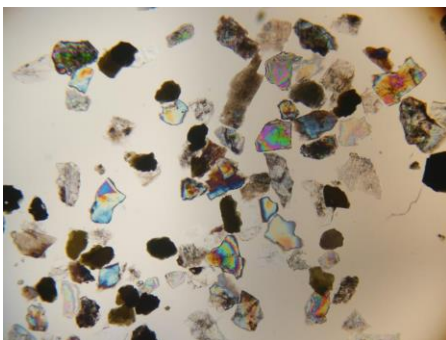
Figure 8: On the left micro-photo (6.9x5,19mm) with crossed nicols of mud particles >0.212mm and on the right micro photo (10.6 x 8mm)with parallel nicols of mud particles between 0.038-0.063mm.
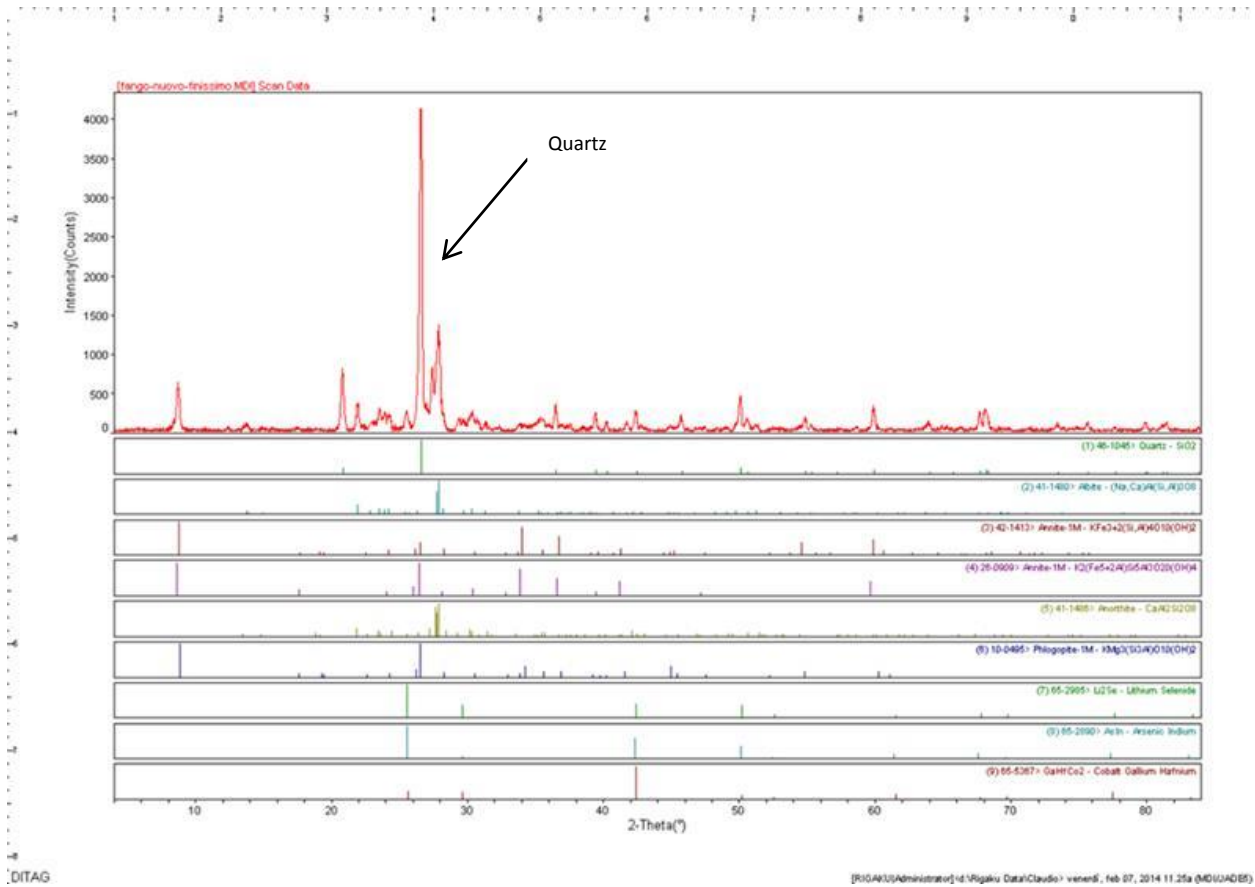
Figure 9: X- Ray Diffration of muds <0,038 mm

Content in weight (%)	M 1	M 2	M 3	M 4
SiO2	77.1			
TiO2	0.1			
Al2O3	12.0			
Fe2O3	1.2	1.1	1.4	1.1
MgO	0.8	0.6	0.4	0.4
CaO	0.7	0.8	0.6	0.6
Na2O	5.7	5.5	5.9	4.2
K2O	5.1	5.0	5.3	5.2

Table 1: Oxydes in % in muds coming from gneiss and granites cutting

Content in ppm	M1	M2	M3	M4
Cd	<1.0	1.0	<1.0	<1.0
Co	140.0	76.0	78.0	180.0
Cr	5.0	36.0	20.0	26.0
Cu	162.0	230.0	162.0	110.0
Mn	114.0	100.0	82.0	90.0
Ni	2.0	3.0	3.4	3.0
Pb	82.0	78.0	72.0	72.0
Zn	100.0	98.0	92.0	106.0

Table 2: Metals in ppm in multiwire diamond machine muds

CONCLUSIONS

The obtained results confirm that deep knowledge of interaction between the diamond beads and stones turns into a whole comprehension of the cutting process. This will allow to optimize cutting action: a double examination (stones and beads) represents a whole and complete approach to the comprehension of the wear processes during stone cutting.

Petrographic analysis and mineralogical investigation gave us the opportunity to understand the interactions between stone and diamond beads. The major variability consists in the muds particles dimension, but also the shape and conformation of stone debris are important parameters to be considered.

Erosion analysis concerned both the stone debris and diamond beads, characterizing both the metal powder and super-abrasive grains (diamond beads) in the cut waste.

Chemical composition of the metal matrix of the diamond beads directly impact on the efficiency of the diamond wire cutting action, because of the great influence in the diamond grains retention. Diamonds must be firmly retained till they show cutting ability, but the must be pulled out when they have no cutting efficiency. In the considered case study, this equilibrium was obtained, even if some highly damaged diamonds are still present on the worn surface of diamond beads.

Chemical interaction between the diamonds and Fe-based stones would accelerate the wear processes through etching phenomena, drastically reducing the long-life of the diamond wire.

REFERENCES

[1] Bellopede, R, Marini, P, Tori, A, Zichella, L, 2014, Proposal of a new methodology for stone classification in diamond wire cutting technology (EASE R3), Diamante A & T, edizione 79, anno XX, dicembre 2014, pp. 19-26

[2] Amaral, P, Cruz Fernandes, J, Frisa, A, Guerra Rosa, J, Manfredotti, L, Marini, P, 2000, Evaluation of the workability by means of diamond tools of a series of portuguese commercial granites, pp.323-329.

[3] Ersoy, A, Buyuksagic, S, Atici, U, 2005, Wear characteristics of circular diamond saws in the cutting of different hard abrasive rocks, Wear, 258 (9), 1422-1436, DOI:10.1016/j.wear.2004.09.060.

[4] Gokhan, A, Izzet, K, Kerim, A, 2013, Wear Performance of Saw Blades in Processing of Granitic Rocks and Development of Models for Wear Estimation, Rock Mech Rock Eng, 46:1559–1575. DOI 10.1007/s00603-013-0382-y.

[5] Ribeiro, R P, Paraguassú, A B, Rodrigues, J E, 2007, Sawing of blocks of siliceous dimension stone: influence of texture and mineralogy, Bull Eng Geol Env 66:101:107

[6] A. Romanski, factors affecting diamond retention in powder metallurgy diamond tools, archives of metallurgy and materials, Volume 55 2010 Issue 4

[7] Tesi di dottorato, tecnologie di lavorazione delle pietre naturali, università degli studi di cassino, ing. Sandro Turchetta, a.a. 2002-2003

[8] Brian E. MacMillin, Christopher D. Roll, Paul Funkenbusch, Erosion and surface structure development of metal–diamond
particulate composites, Wear, Wear 269 (2010) 875–883

[9] W. Polini∗, S. Turchetta, Test protocol for micro-geometric wear of sintered diamond tools, Wear, Wear 257 (2004) 246–256

[10] A. Ersoya,∗, S. Buyuksagicb, U. Aticia, Wear characteristics of circular diamond saws in the cutting of different hard abrasive rocks, Wear, Wear 258 (2005) 1422–1436

DIAMOND WIRE CUTTING TECHNOLOGY AND WORKABILITY OF NATURAL STONES: VALIDATION OF A NEW CLASSIFICATION METHOD (EASE R3)

R. Bellopede[1], P. Marini[1], L. Zichella[1], A. Tori[2]
DIATI - Department of Environment, Land and Infrastructure Engineering, Politecnico di Torino, Turin, Italy.
[2] CO.FI.PLAST S.r.l., Lessolo, Italy

ABSTRACT

In the diamond wire stone cutting process the objective is to remove a chip of material or a layer of uniform thickness from the entire length of the cut. The aim of this study is to correlate the cutting performance to the characteristics of the natural stone and subsequently to propose a method of classification strictly connected to stone workability.
Hardness and micro-hardness tests are currently considered important methods for acquiring useful information about the workability of natural stones, but such gathered data alone do not give enough information to establish a satisfying classification. The concept of workability and stone machining has been, for the past thirty years, one of the main area of investigation in national and international researches. This study endorses a method for the prediction of stone-cutting tools interaction (mainly diamond wires) combining the micro-hardness and the UPV measurements, that better represent the mechanical, physical and petrographical stone properties.
This paper studies eight different stones classified according to an "easy-to-cut" scale based on the historical company know-how (HIC - Historical Industrial Classification). This classification is based upon experience and not on explicit or really scientifically quantified parameters, nonetheless, it describes the stones workability completely.
In previous works, however, criteria based on quantifiable parameters (SSC - Scientific Stone Classification) have been pursued and this led to a scientific correlation with the industrial classification. For each stone the following investigation techniques were performed: petrographic analysis, micro-hardness, Schmidt rebound, Ultrasound Pulse Velocity (UPV). Moreover UPV measures in indirect and direct method have been executed on stone blocks in the cutting plant and compared with those performed on slabs. The results of all the performed tests were analyzed and good correlations with the industrial classification were found.

Introduction

The prediction of stone - diamond wire interaction is crucial for the extractive sector, both to improve the productivity and efficiency of quarry work and to avoid dangerous and expensive endeavors of cutting when an unknown stone has to be introduced in the plant.
The diamond wire users themselves determined an empirical classification of the stone (Industrial Workability Classification) mainly taking into account the greater or lesser ease of cutting. However the new classification suggested by Bellopede et al . (2014) [1] has been obtained by means of a scientific approach with easy and expeditious test methods. In particular, while the IWC is characterized by 9 classes, with the new technical classification the classes decrease to 7, thus reducing the case of overlapping and uncertainty due to the intrinsic variability of the materials.
Diamond-wire cutting operations are affected essentially by two different kinds of parameters: partially controlled and non-controlled. The partially controlled ones refer to the properties of the cutting tools and equipment, such as the cutting speed (peripheral speed of the diamond-wire – m/s), the feed rate (cm/h), and the machine absorption (ampere/m). Instead, the non-controlled parameters refer to the stone properties, such as the petrographic and mineralogical composition, grain size, water content, weathering, discontinuities/anisotropy and hardness.
Previous studies demonstrated that the uncontrolled parameters can be measured indirectly by different techniques but the Knoop microhardness and the Ultrasonic Pulse Velocity (UPV) measures best correlate with workability and are therefore more significant [1,2,3,4]. From 1982 Mancini and Morandini [5] and more recently in 2003 Beste and Jacobson [6] have underlined the

importance of the microhardness measurement to study the tool wear. However, very little is reported in the literature on the relationship between the petrographic characteristics and the industrial process involved in the stone cutting and finishing, as pointed out by Riberiro et al (2007) [7]. UPV measures can be considered an expedite and reliable testing of the mechanical properties of a rock (quarry face or block), and gives also available information on the stone slab quality [8,9,10]

This research is part of the EASE-R3 (FoF.NMP.2013-8-608771 -Integrated framework for a cost-effective and ease of Repair, Renovation and Re-use of machine tools within a modern factory – ESS project). It's aimed at developing a novel integrated framework for a cost-effective and easy Repair, Renovation and Re-use of machine tools in modern factories , oriented towards both SME and OEM/end-users, and covering the entire life cycle of the system, from the design stage through the operative life.

The aim of the present work is to validate this scientific classification with new stone categories by means of measurement performed directly on stone blocks and therefore to evaluate the applicability of this methodology to the stone plant.

Materials and Methods

Eight different kinds of stone have been studied. Their names, identification codes and petrographic description are shown in table 1, where the IWC classes and their determining cutting parameters are reported. In fact, as for the granite GRP and RBE, sienite SIE and diorite DIOS, feed rate (cm/h) and machine absorption (A/wire) were recorded in plant in order to compare them with the physical-petrographic properties of the examined stone.

Table1 Mineralogical composition , textural characteristics of the stone tested , IWC and main cutting parameters.

Stone	Rock type	Acronym	Mineralogical composition	Industrial Workability Classification	Feed rate (cm/h)	Machine absorption (A/wire)
SERIZZO	Gneiss	SER	K- Feldspar plagioclase 70% Quartz 20% Biotite + access 10%	1-2	n.a.	n.a.
MONTORFANO	Granite	MON	K-feldspar and plagioclase 55%; quartzs 40% ; biotite 5%	3	n.a.	n.a.
DIORITE SCURA	Diorite	DIOs	Plagioclase 65% Hornblende + Biotite 30% Opaque min 5%	3	16,52	1,43
DIORITE CHIARA (TRAVERSELLA)	Diorite	DIOc	Plagioclase 55% Quartz 10% Hornblende + Biotite 30% Opaque min 5%	3	n.a.	n.a.
SIENITE	Sienite	SIE	Feldspar 50% Biotite + Hornblenda 25% Quartz 15%	3	24,36	1,65
LUSERNA	Gneiss	LUS	K- Feldspar plagioclase 40% Quartz 50% White mica5% opaque 5%	3	n.a.	n.a.
ROSA BETA	Granite	RBE	Plagioclase 25% Feldspar 30% Quartz 35%	3-4	25,00	2,78
GRIGIO PERLA	Granite	GRP	K- Feldspar + Plagioclase 65% Quartz 30% biotie + pyroxene 5%	4	23,8	2,83

In situ measurements of UPV in indirect method and in direct method (figure 1) and Schmidt rebound tests have been performed. In laboratory, Knoop hardness have been measured on the same slabs tested in situ.

Fig 1 – ultrasonic measurements by direct method on DIOs block

In the Figure 2 a general scheme of the measurements carried out on the blocks is reported.
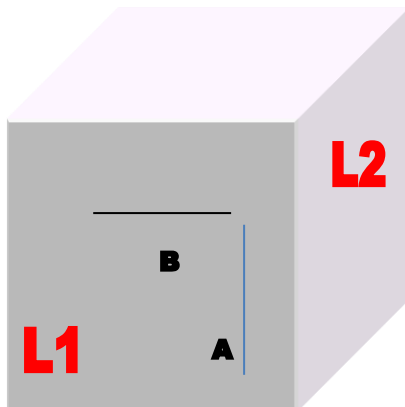
Legend:

L1: Face parallel to the drill holes

L2: Face perpendicular to the drill holes

A and B: Lines followed for UPV

Fig 2 - General scheme of the measurements carried out on the blocks

The indirect method with ultrasonic measurements were performed on two contiguous faces L1 (parallel to drill holes) and L2 (perpendicular to drill holes) along the directions A and B shown in

the figure 2. In the indirect method, according to the EN 14579 (2004) [11], measurements were made using conic 33 kHz frequency transducers and by placing the transmitter transducer on a fixed point and the receiver at progressive distances – 25mm far one from another, up to 175 mm distance – on the same surface. A reference slab of the same kind of stone, provided by the plant's owner, has been tested by indirect method. A specimen for Knoop determinations has been cut from that slab.

The direct method measurements have been carried out by taking the transducers with frequency of 54kHz on two opposite faces of the block up to 3m distance, the maximum dimension of the tested blocks.

Schmidt rebound index has been measured on all the stone blocks except RBE and GRP. The test has been performed by making three rebounds on the same eight points of the UPV alignment, and recording the third one.

The Knoop measurements have been performed according to ASTM E384-11 [12] by a pyramidal diamond point pressed into the polished surface of the test material with a specific load a for a specified dwell time (40 s). The resulting indentation has been measured by microscope.

The rock hardness is determined by the cumulative frequency curve of 40 micro-hardness Knoop (HK) measurements detected. The test results are expressed through the characteristic values of the diagram, corresponding to the 25% (HK25), 50% (HK50) and 75% (HK75) cumulative frequencies, respectively. In this work, HK 25 has been used for the correlations.

Results and Discussion

In the table 2 the results of UPV measures, the in situ Schmidt rebound and the values of HK25 on the same slabs tested in situ are reported. As clearly shown in that table, the Schmidt values are the same for all the rock tested except for DIOS. As a result, Schmidt rebound doesn't give useful information about the technical classification of stone workability.

Table 2. In situ UPV measures by direct and indirect method on stone slabs and block and HK25 values obtained in laboratory.

Rock acronym	UPV indirect method on block B direction (m/s)	UPV indirect method on block A direction (m/s)	UPV indirect method on slab B direction (m/s)	UPV indirect method on slab A direction (m/s)	UPV direct method on block (m/s)	Schmidt rebound on block B direction	Schmidt rebound on block A direction	HK25 –MPa-
SER	1801	1801	1927	1737	3931	60	60	2109
MON	1714	1752	1628	1704	3490	60	60	2789
RBE	2387	2310	2754	2430	3530	n.a	n.a.	4049
LUS	2024	2154	2230	1756	3960	61	60	4358
DIOs	2287	2352	2708	2443	5450	53	53	2789
DIOc	2197	2482	2511	2420	5550	61	59	3260
SIE	2482	2172	2449	2299	4730	61	60	3602
GRP	2601	2510	2785	2780	4500	n.a.	n.a.	5234

As shown in table 2, there is a ratio from 2 to 2,2 between the UPV measures by direct method and those performed by indirect method.

In figure 3, the mean values of the UPV data obtained by direct and indirect method on blocks are reported: a linear correlation, with a good regression coefficient, has been computed and drawn.
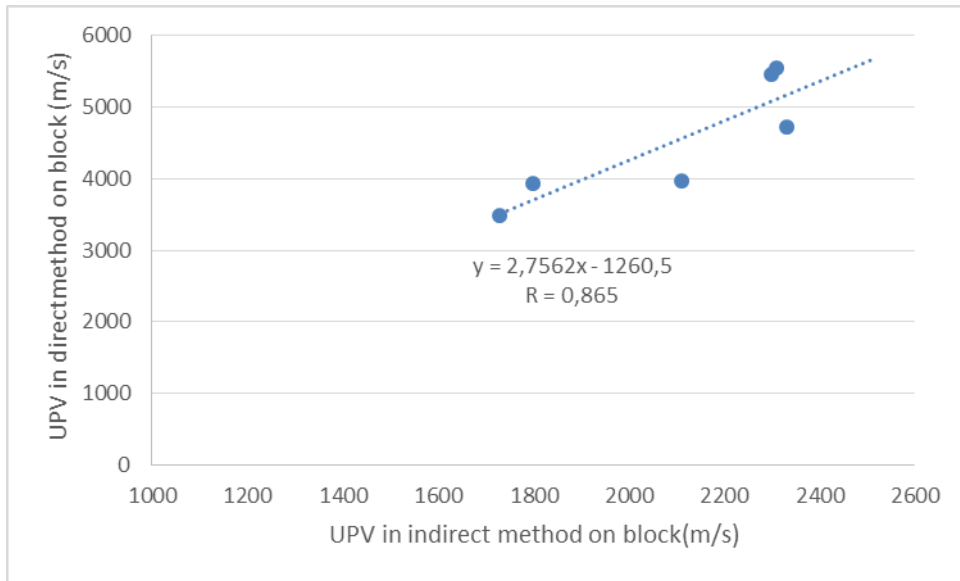
Fig. 3. Correlation between UPV by direct method and UPV by indirect method on block performed in plant

Moreover, taking into account that the of the UPV measurements is about the 3-5%, it is possible to assert that there is no difference between the results obtained on the B direction and those on the A.

Another important result of this investigation is the good correspondence between indirect measurement on blocks and the indirect ones performed on slabs, - in situ on the same day – figure 4.

Fig. 4. Comparison between UPV by indirect method on blocks and on slabs

The petrographic characterization of the tested stone (table 1) show the lack of a direct relation between the workability classification and the mineral composition. For example granite GRP with a 50% of quartz content is in classes n. 4 while gneiss LUS, with the same content in quartz is in class n. 3.

There are, therefore, other factors that affect the workability of natural stone, as previously asserted, and they can be well represented by Knoop hardness and ultrasonic pulse velocity data and by the graph of figure 5 where the new data have been plotted on the graph proposed in previous work.

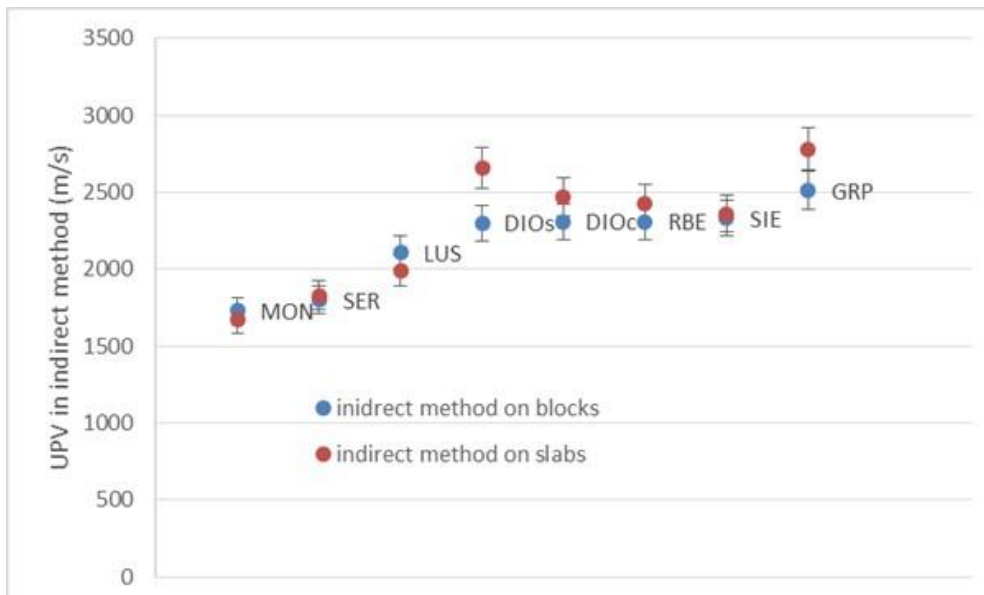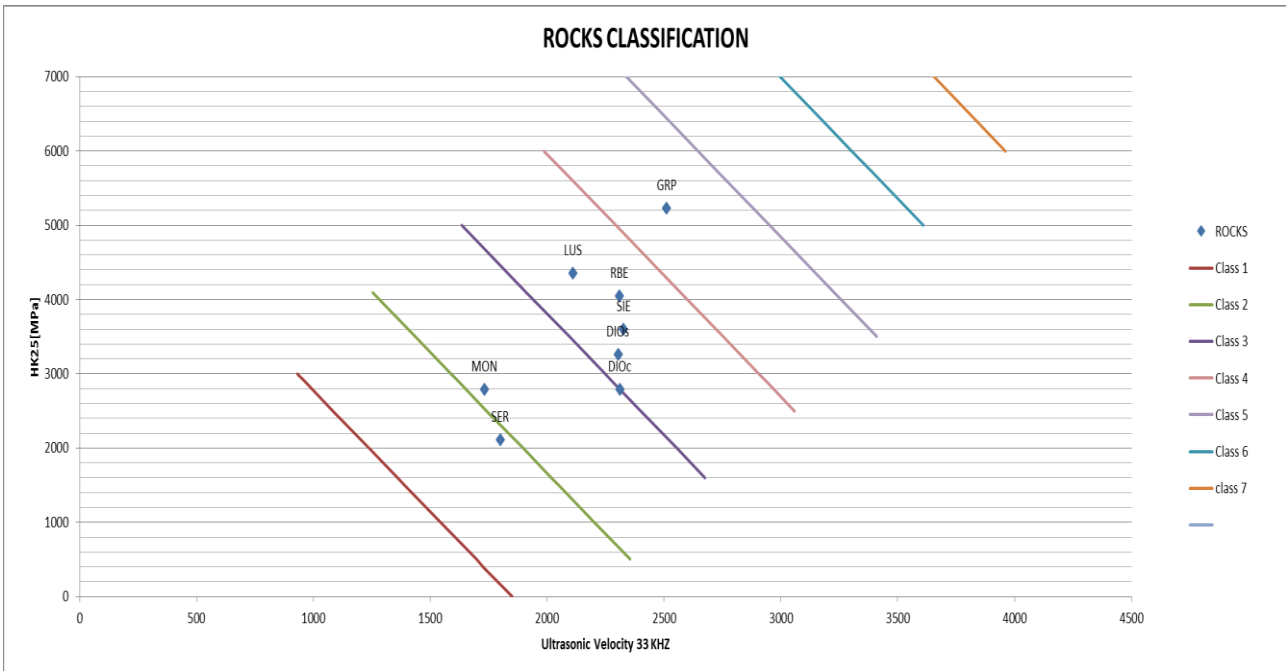*Fig. 5 Scientific classification of the tested stone.*

On the basis of the recently scientific classification [1], the eight tested stone are all classified in class no.3, except the GRP which is placed in class no.4 , MON in class no.2 and SER in class no.1 (see figure 5). The scientific classification corresponds to the industrial classification (IWC) based on the experience. UPV values obtained by indirect method on blocks have been used for the correlation.

Concerning the relation of cutting parameters with quartz content, as described in figure 6, the machine absorption is well correlate with to the quartz content of the tested stone. However, the cutting parameters weren't measured for all the stones, consequently it not possible to demonstrate the full correlation with quartz content. From the table 1, in fact, there wasn't a direct correspondence between IWC and quartz content for all the different kinds of stone. This could be due to the different content of feldspar and their degree of alteration in the analysed stones and it should be further studied in the next researches.

In the figure 7 the correlation among machine absorption and HK25/UPVind (as mean values of UPV performed by indirect method on the block) is reported. The exponential regression has a correlation coefficient of 0,91. The correlation between KH25, UPV and workability class demonstrated in the previous research [1] has been confirmed here.

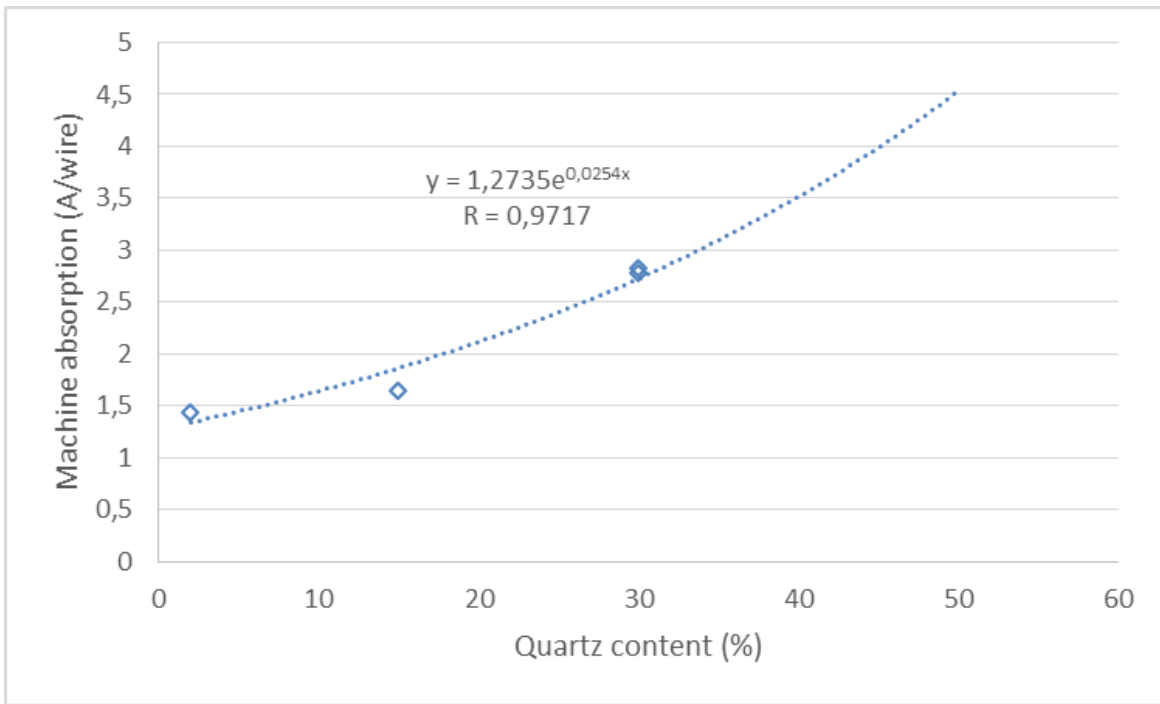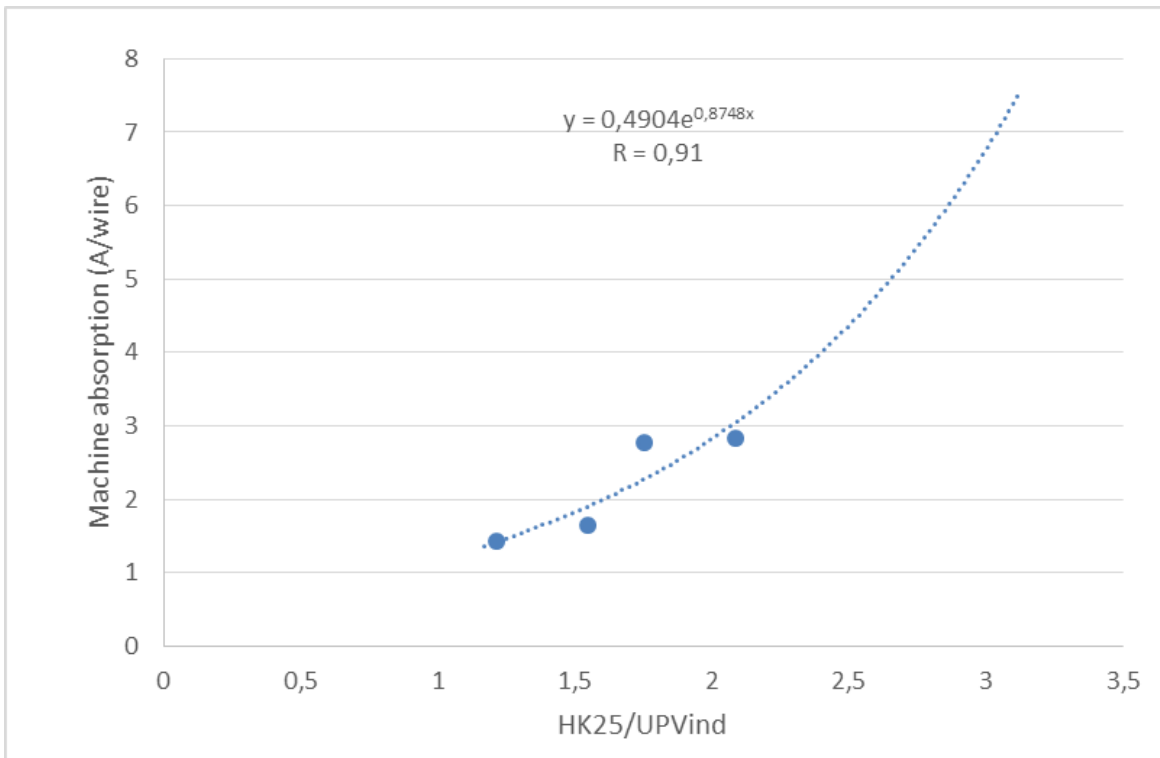*Figure 6. Machine absorption vs quartz content for RBE, SIE, DIOs and GRP.*

Figure 7. Machine absorption vs H25/UPVind for RBE, SIE, DIOs and GRP.

Conclusions

The in situ measurements on blocks on eight different types of stone allowed to verify the reliability of the different measurement techniques used and to validate a new scientific classification for the workability of natural stones.

From the result analysis, itis possible to confirm that the Schmidt test doesn't discriminate the workability of the rock and therefore it isn't a useful method for this technological classification. Instead, the ultrasonic measurements on blocks are well correlate with those performed on the slabs on the same stone. Moreover, the UPV measurements by indirect method can be considered reliable because they match with those by direct method.

The combination of ultrasonic measurements by indirect method with the index HK25 allowed to order the stones in classes of workability that correspond to what the owners of the plant used to give to such stones. The correspondence with the in situ cutting parameters has confirmed the reliability of this scientific methodology.

With the proposed classification, technical and scientific criteria, have been applied, so to help the choice of the diamond wire and of the cutting parameter,

Acknowledgements

References

[1]Bellopede R., Marini P., Tori A., Zichella L. (2014). Proposal of a new methodology for stone classification in diamond wire cutting technology (EASE R3). Diamante A & T, edizione 79, anno XX, dicembre 2014, pp. 19-26

[2] Amaral, P., Cruz Fernandes, J., Frisa, A., Guerra Rosa, J., Manfredotti, L., & Marini, P. (2000). Evaluation of the workability by means of diamond tools of a series of portuguese commercial granites.pp.323-329.

[3] Ersoy, A., Buyuksagic, S., & Atici, U. (2005). Wear characteristics of circular diamond saws in the cutting of different hard abrasive rocks. Wear, 258(9), 1422-1436. DOI:10.1016/j.wear.2004.09.060.

[4] Gokhan Aydin, Izzet Karakurt , Kerim Aydiner (2013). Wear Performance of Saw Blades in Processing of Granitic Rocks and Development of Models for Wear Estimation. Rock Mech Rock Eng (2013) 46:1559–1575. DOI 10.1007/s00603-013-0382-y.

[5] Mancini and Morandini 1982 Mancini R, Frisa Morandini A (1982) Applications of microhardness tests to the technical evaluation of dimension stones. Fourth Congress International Association of Engineering Geology, New Delhi, p 321–331

[6] Beste U., Jacobson S., (2003) Micro scale hardness distribution of rock types related to rock drill wear. WEAR 254: 1147:1154

[7] Ribeiro R. P., Paraguassú A. B., Rodrigues J. E. (2007) Sawing of blocks of siliceous dimension stone: influence of texture and mineralogy. Bull Eng Geol Env 66:101:107

[8]. Bellopede R., De Regibus C., Manfredotti L. & Marini P., 2005 *Natural stone diagnosis with the means of non-destructive tests: case studies* in MPES05, Canada, CD-ROM

[9] Vasconcelos, G., Lourenço, P. B., Alves, C. A. S., & Pamplona, J. (2008). Ultrasonic evaluation of the physical and mechanical properties of granites. Ultrasonics, 48(5), 453-466. DOI:10.1016/j.ultras.2008.03.008.

[10] Khandelwal M., Ranjith P.G. (2010) Correlating index properties of rocks with P-wave measurements. Journal of Applied Geophysics. Volume 71, Issue 1, May 2010, Pages 1–5

[11]EN14579: 2004 Natural stone test methods - Determination of sound speed propagation CEN-European Committee for Standardiza

[12] ASTM E384-11e1, Standard Test Method for Knoop and Vickers Hardness of Materials , ASTM International, West Conshohocken, PA, 2011, www.astm.org

AKNOWLEDGEMENTS

Session 5

DESIGN OF AN ACTIVE FLUID DAMPING SYSTEM FOR VIBRATION CONTROL OF DISK-SHAPED TOOLS

B. Denkena[1], D. Dahlmann[1], C. Teige[1]

[1]Leibniz Universität Hannover, Institute of Production Engineering and Machine Tools (IFW), An der Universität 2, 30823 Garbsen

teige@ifw.uni-hannover.de

ABSTRACT

To meet the requirements of today´s cutting process of natural stones thin disk-shaped tools with large diameter are applied at high cutting velocities. To use these tools, guiding systems for the disks are needed. Therewith, tool vibration magnitudes and deflections can be reduced. The risk of producing scrap parts or tool damage are decreased. However, the guidance being placed close to the cutting zone reduces the cutting depth, so that the process is limited to the production of small slabs and tiles. To use the advantage of a guidance without limiting depth of cut, a new guidance concept is presented. Thereby the guiding areas are placed opposite to the cutting zone. This enables the reduction of tool vibration without decreasing the depth of cut. In this paper the compensation of tool vibration by this guiding concept is investigated. Different types of guidance are compared and the most suitable compensation approach is identified. Further on, the problem of the decreasing compensation effect, due to the increasing distance between the excitation and the guidance is considered. To increase the compensation effect, the guidance is optimized regarding to the number and positon of guiding areas. The capability of the presented concept is verified by a comparison with a conventionally placed guiding system.

KEYWORDS

Cut-off grinding, disk-shaped tools, guidance, fluid actuator, optimization

INTRODUCTION

Cut-off grinding with disk-shaped tools is preferred for machining of natural stones. It enables faster chip removal with a lower cutting width compared to wire or gang saws [2]. Nowadays, the market requires slabs and tiles with increasing lengths and widths but decreasing thicknesses, for instance as facade plates [5]. Simultaneously, the production costs should be reduced by increasing cutting velocity and decreasing tool width. To meet these demands, tools with increased diameters, reduced thicknesses and high cutting velocities are applied. However, an increasing ratio of blade diameter to thickness reduces the lateral tool stiffness. Therefore, the magnitudes of tool vibrations and the deflection are increased. The consequences are higher parallelism errors of cutting kerfs resulting in scrap parts and reduced tool life. Guiding systems are applied to compensate vibrations and deflections.

PRINCIPLES OF GUIDING SYSTEMS

Contact, aerostatic and hydrostatic principles are mainly used for guiding systems [3]. The contact guidance uses the mechanical contact between saw and guiding areas. Large contact forces are reached caused by the high stiffness of solid-state guidance. Therefore, the capability for compensation of tool vibrations and deflections is increased. The friction between guidance and saw generates thermal and mechanical stresses. These stresses are increasing with rising rotation velocities. Thus, unacceptable wear and heating of the tool and the guidance are induced [8]. To overcome this problem Fronius [3] and Szymani [8] recommend the application of an aerostatic or hydrostatic guidance.

The aerostatic guidance is a non-contact principle, generating counteracting forces by compressed air. There is no friction, no wear and negligible tool heating. High tool rotation velocities can be applied. The disadvantage of this principle is a reduced stiffness compared to contact guidance. This results in a reduced compensation of tool vibrations and deflections. Furthermore there is the possibility of pneumatic instability in form of self-excited vibrations. This could lead to an excitation of resonances.

Hydrostatic guidance is applied to overcome these problems. Instead of compressed air a hydraulic fluid is used. In case of cutting natural stones, water is applied. The higher viscosity of the water leads to an increasing compensation capability. Another advantage is the squeeze-film effect. It uses shear forces within fluids to damp vibrations. The vibration between saw and guidance induces time variant displacements of the fluid between the saw and guidance. Due to the inner fluid friction, energy dissipates, leading to a reduction of the vibration magnitudes [6]. More benefits are the process of cooling and the transport of chips out of the cutting zone. High power losses due to shear friction is a disadvantage of this principle. Viswanath [9] shows, that the power loss is directly proportional to the size of guiding areas. To reduce the power losses, the size of hydrostatic guidance has to be decreased, whereby the compensation effect is reduced. Due to the advantages, the hydrostatic guidance is the most suitable system to compensate tool vibrations.

The position of the guidance is also from great importance. Fronius and Schajer [7] have dealt with the influence of position of guiding systems on the compensation of tool vibrations and deflections. They recommend positioning the system as close as possible to the cutting zone, in order to get the highest reduction of parallelism error. The disadvantage of this positioning is the limitation of cutting depth. But to meet the demands of today´s cutting process the guidance must not be placed at this position. Therefore a new guiding system is proposed, being placed counterpart of the cutting zone and using the hydrostatic principle to compensate tool vibrations efficiently. The following investigation deals with the compensation capability of this guiding concept. To increase its compensation effect the guiding areas are optimized regarding to their number and position. A comparison between the optimized concept and a recommended placed guidance illustrates the compensation effect of the proposed concept.

DEFINITION OF TOOL AND GUIDING PARAMETERS

Fig. 1 illustrates the geometry of the tool and guidance. For the optimization, a disk-shaped tool with a diameter of $D = 1000$ mm, a thickness of $w = 5$ mm and a flange diameter of $D_f = 300$ mm is assumed. The guidance is described by the number of guiding areas n, their diameters $D_{d,i}$ and positions being presented by the radial and angular positions $r_{d,i}$ and β_i. The index i describes the parameter of the guiding area i. To simplify the optimization process, the number of variable parameters has to be reduced. Therefore, the parameters $r_{d,i}$ and $D_{d,i}$ are defined as constant. The radial positions of the guiding areas are $r_{d,i} = 400$ mm and the area diameters are $D_{d,i} = 30$ mm. Preliminary tests determined that these values enable a high compensation effect. The number and angular positions of guiding areas are variable parameters. Thereby, the number of guiding areas n is a discrete parameter with a domain from 1 to 3. The angular positions β_i are continuous parameters defined between 90° and 270°. The boundaries ensure that the guidance is positioned counterpart

to the cutting zone. To evaluate the optimized guidance a reference guidance is defined. It is represented by one guiding area being positioned close to the cutting edge ($\beta_1 = 0°$) with a guiding area radius of $r_{d,i} = 400$ mm and a guiding area diameter of $D_{d,i} = 30$ mm. To compensate tool vibrations, the guidance areas are defined as dampers. The damper have a constant damping ratio of 2 Ns/mm. This value is determined by a convergence analysis of the tool vibration magnitude depending on the damping ratio of three dampers. Thereby the tool magnitudes, presented in Table 2 for three dampers, are reached. A further increase of the damping ratio does not lead to an additional increase of the compensation effect. Fig. 1 summarizes the tool and guidance parameter.
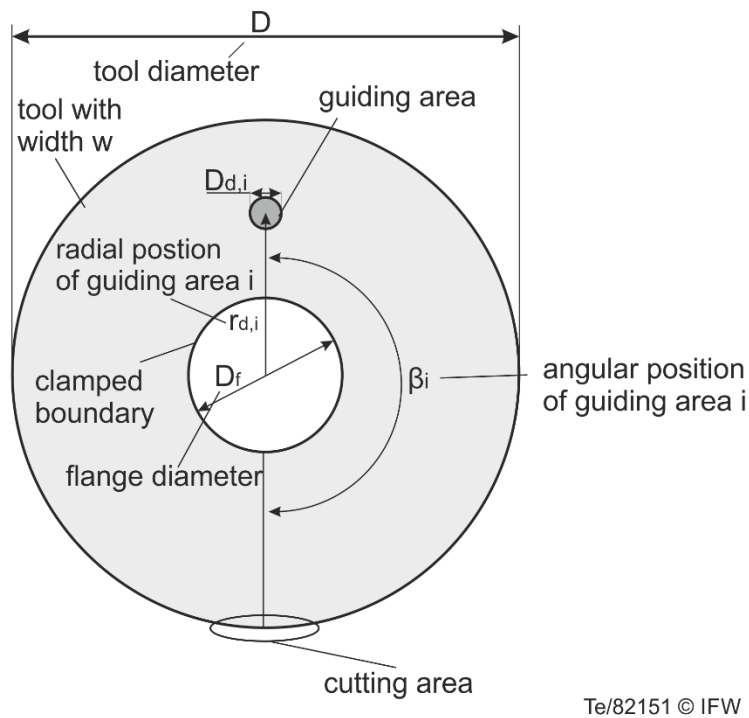
Fig. 1: Definition of tool and guiding parameter

OPTIMIZATION OF GUIDING PARAMETERS

After defining constant and variable parameters the optimal configuration of area, number and their angular positions are determined. Fig. 2 illustrates the optimization process exemplarily for two guiding areas. The compensation effect of the guiding system is maximized. This effect can be quantified by the tool vibration magnitudes within the cutting zone of the first and second eigenfrequency. Asche [1] and Bockhorst [2] mentioned, that dynamic loads induce high parallelism errors. The highest vibration magnitudes occur during the excitation of the first and second eigenfrequency. The reduction of these vibration magnitudes describes the compensation effect of the guidance. Therefore, it is used as optimization criterion. The tool vibration magnitudes are determined by a numerical harmonic analysis. A finite element model is created, that exists of shell elements with a total of 2910 nodes. Shell elements are chosen due to the abstinence of the locking effect by a large element length-to-thickness ratio compared with solid elements. The minimum number of required nodes is determined by a convergence analysis of the eigenfrequencies.
Following conditions are defined for the simulation: the tool is clamped at its center and is excited in the cutting zone by a lateral frequency variant oscillating force with an amplitude of 10 N. A frequency band from 0 to 200 Hz is considered. The resonance excitation of 10 N over 200 Hz of the unguided tool induces tool magnitudes in the cutting zone being less than 0.1 mm (Fig. 3). Due to the small amplitudes, frequencies over 200 Hz are neglected. Initially discrete design points are created with a design of experiments (DOE) to describe the magnitudes of tool vibration in the cutting zone for

certain parameter configurations. The design points are used to create a response surface. The response surface is a multidimensional continuous function representing the magnitudes of vibration depending on the variable guiding parameters. To exactly describe the multidimensional system, a minimum number of design points is required. This number increases exponentially with the number of variable parameters. Therefore, just the number and angular positions of the guiding areas are varied in this investigation. Five optimization processes are executed to analyze the influence of the number of guiding area and angular positions on the compensation effect of guiding systems being placed counterpart to the cutting zone. The defined values of tool and guiding parameter are shown in Table 1.

Table 1: Parameter configuration for the optimization processes:

Optimization process / Parameter	1	2	3	4	5
Tool diameter D [mm]	1000	1000	1000	1000	1000
Flange diameter D_f [mm]	300	300	300	300	300
Tool width w [mm]	5	5	5	5	5
Radial position of guiding areas r_{di} [mm]	400	400	400	400	400
Guiding diameter D_{di} [mm]	30	30	30	30	30
Angular position of guiding areas β_i [°]	**Var.**	**Var.**	**Var.**	**Var.**	**Var.**
Number of guiding areas n [-]	1	2	3	2	3
Number of design Points $n_{p,i}$ [-]	42	200	400	500	1000

The first three optimization processes differ on the number of guiding areas n. The guiding angular positions are the optimization parameter of each optimization process. Initially the first optimization considers one area with the optimization parameter β_1. To analyze the influence of the angular position on the compensation effect exactly the number of design points should be as high as possible. Referring to the diameter $D_{d,i} = 30$ mm and the radii of $r_{d,i} = 400$ mm, a number of positons $n_{p,1} = 42$ are created for one guiding area. This number realizes a small variation of β_i between neighboring design points without an overlapping. The determined design points include information about the magnitudes of the tool in the cutting area depending on the angular position β_1. Subsequent two (β_1, β_2) and three (β_1, β_2, β_3) guiding areas are examined. The increasing number of areas induces an increasing number of design points to create an exact response surface. Based on the number of design points of $n_p = 42$ for a guiding area, the possible number of design points for two areas is $n_{pmax,2} = 903$ and for three areas $n_{pmax,3} = 796446$. These numbers are too high for an efficient optimization. Therefore, a reduced number of design points have to be applied for two and three guiding areas. To reduce the number of design points a Latin hypercube sampling is applied as DOE. It enables the reduction of design points with a simultaneously uniform distribution in the definition ranges of β_i. However, if the number of design points is too low, the response surface will describe the vibration magnitudes inaccurately. For the optimization of two and three areas, the number of design point are $n_{p,2} = 200$ and respectively $n_{p,3} = 400$. These numbers are significantly lower than the possible numbers $n_{pmax,2}$ and $n_{pmax,3}$. Therefore the correctness of the response surface based on these design points have to be evaluated. For the evaluation, the optimization processes four and five are executed. These simulations have the same parameter values like process two and three, but the numbers of design points are increased to $n_{p,2} = 500$ and $n_{p,3} = 1000$ respectively. The comparison between the results of the optimization processes two and four as well as three and five illustrates the influence of the number of design points on the optimization results.

Based on the different number of design points a response surface for each optimization process is created. Thereby, the design points are interpolated by the Kriging method to get continuous functions of the tool vibration magnitude depending on the appropriate variable guiding parameter β_i. Kriging is a statistical method using the number and distribution of the design points for interpolation

to enable a good estimation of interim values [4]. The Kriging result is a multidimensional continuous function of tool vibration in the cutting zone depending on β_i. The created response surfaces are used by the optimization algorithm to calculate the optimal damper positions for each number of damper. A genetic algorithm is used for optimization of damper positions with 20 iteration steps and 1000 individuals per step. An investigation has determined that this combination of steps and number of individuals produces repeatable and plausible optimization results.
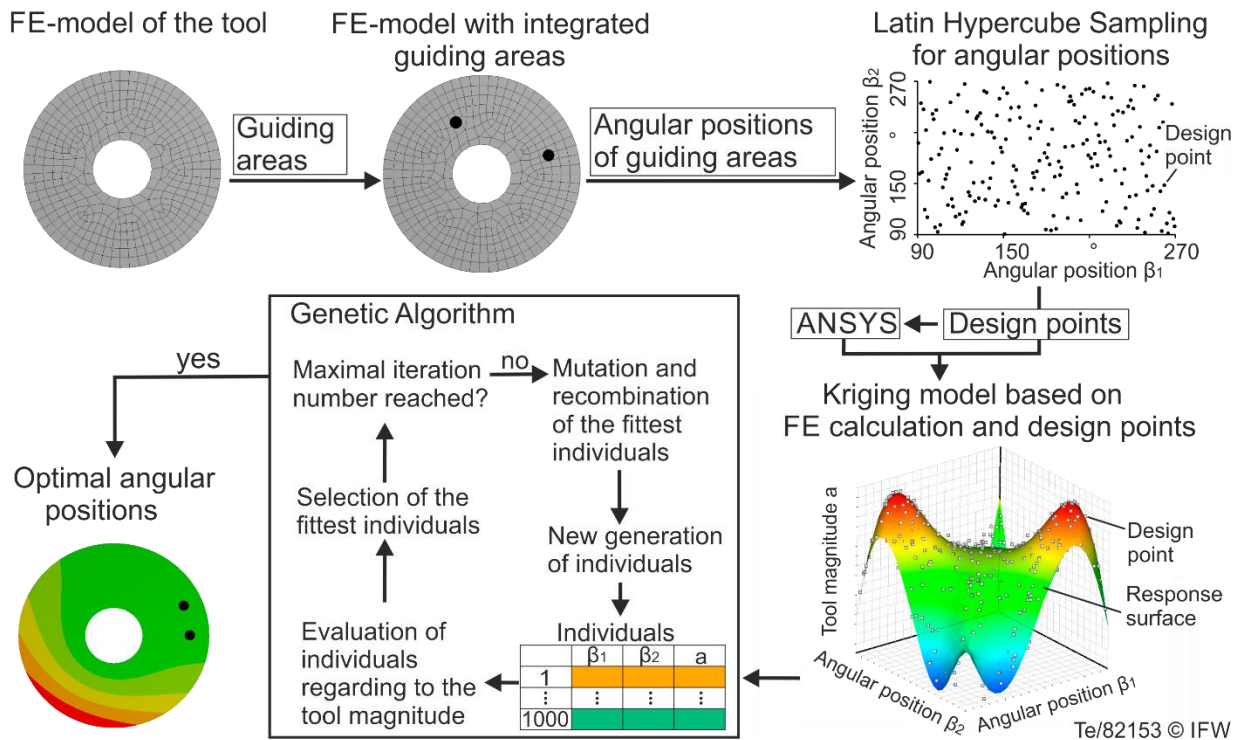

Fig. 2: Schematical process of optimization for two guiding areas

Fig. 3 and Table 2 show, that the compensation effect increases with rising number of guiding areas. An application of three guiding areas reduce the tool magnitude by 36% for the first and 52% for the second eigenfrequency compared with an unguided tool. Two dampers can reduce the magnitude by 31% and 40%, respectively. One guiding area is not able to compensate the resonance effects of the tool. The optimal positions of the guiding areas are not directly counterpart of the cutting zone. The optimization determined nearly rectangular positions between guiding and cutting area. A possible reason is the shorter distance between the cutting zone and guiding areas. Thereby induced tool vibrations are damped earlier and the resonance effect can be reduced. The number of design points has a small influence on the determined angular positions. The differences between the calculated angular positions are small, whereby low differences of the magnitudes with 2.5% for the first eigenfrequency and 2.1% for the second eigenfrequency are induced. Further on Table 2 illustrates that a damper being positioned close to the cutting area can reduce the magnitude more effective than a counterpart positioned guidance. The magnitudes are decreased by 99% and 91% respectively for the first two eigenfrequencies. The high compensation effect is caused by the increase of local tool stiffness. Thereby, the resonance frequencies are changed to higher values. The frequency response spectrum in Fig. 3 illustrates the vibration magnitudes of an unguided and guided tools in a frequency range of 0 to 200 Hz. The results shows, that the guiding systems are able to reduce the vibration magnitude of further eigenfrequencies at 70 Hz, 110 Hz and 165 Hz.
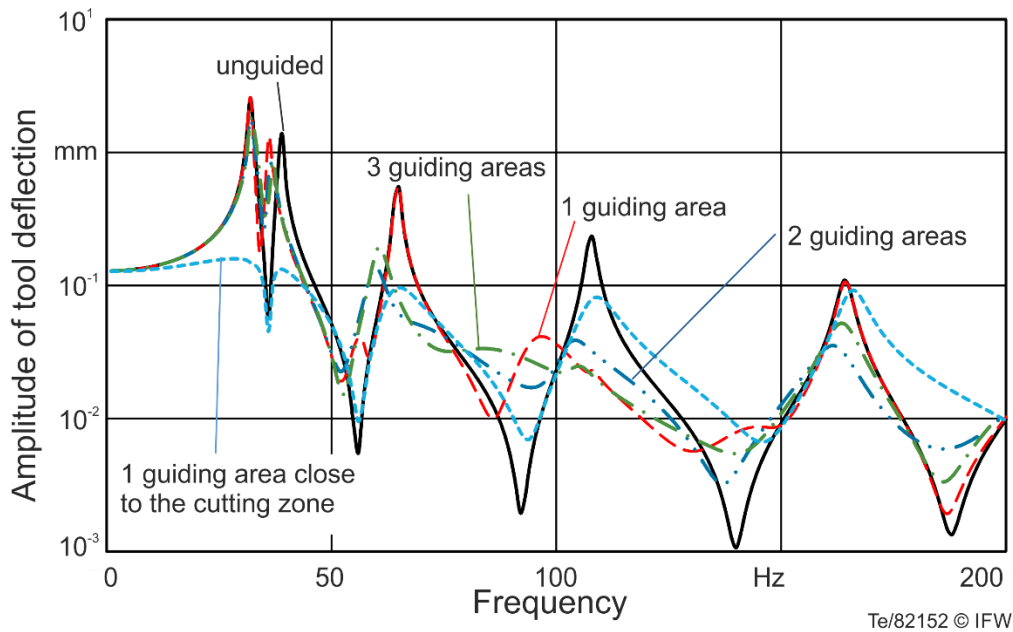
Fig. 3: Frequency response of tool vibrations at the cutting area of guided and unguided tools

Table 2: Results of the optimization process

Number of guiding areas n	Number of design points n_p	angle of damper $\beta_1 / \beta_2 / \beta_3$	Magnitude 1. eigenfrequency a_1	Magnitude 2. eigenfrequency a_2
0	1	-	2.56 mm	1.38 mm
1	1	0°/ - / -	0.15 mm	0.13 mm
1	42	270.0°/ - / -	2.57 mm	1.45 mm
2	200	132.8°/ 90.1° / -	1.85 mm	0.86 mm
2	500	114.0°/ 90.1° / -	1.77 mm	0.84 mm
3	400	115.5°/ 98.4°/ 260.0°	1.67 mm	0.69 mm
3	1000	110.5°/ 91.8°/ 248.4°	1.63 mm	0.67 mm

SUMMARY AND OUTLOOK

The guiding system being placed counterpart to the cutting area can reduce the magnitude of tool vibration significantly. A rising number of guiding areas leads to an increasing compensation effect. But the long distance between excitation and guiding zone induces a decreasing compensation compared with a damper placed close to the cutting area. With respect to a constant damping ratio the guidance being positioned close to the cutting area is more effective but decreases the depth of cut significantly. The presented investigation has dealt with a variable number and angular position of the guiding areas. Following analysis could consider the influence of the diameter of the guiding area D_{di} and their radial position r_{di}. This enables the calculation of an optimum for all guidance parameters. But the effort of time and resources increases due to more parameters. Therefore the DOE has to be adapted. Another approach to raise the compensation effect is the use of a time variant guiding force instead of a constant damping ratio. Thereby, the effects of destructive interferences between the excitation of the cutting process and the guidance are investigated to reduce the tool vibration.

ACKNOWLEDGEMENT

REFERENCES

[1] Asche, J, 2000, Development of advanced tools for ecological and economic sawing of granite (DATEG), European Commission Industrial and Materials Technologies.

[2] Bockhorst, J, 2011, Machining of Granite with High Cutting Speeds, 1st International Conference on Stone and Concrete Machining, S. 17 – 24.

[3] Fronius, J, 2006, Untersuchungen zum Betrieb von Kreissägeblättern mit minimaler Schnittfuge, Dr.-Ing Dissertation, Universität Stuttgart.

[4] Matheron, G, 1963, Principles of geostatistics, Economic Geology, Ausgabe 58, S. 1246 – 1266.

[5] MWK Natursteinhandel, http://www.mwk-natursteinfliesen.de/granitfliesen/granitfliesen-preise, [Stand: 07.07.2015].

[6] Nayfeh, A, et al., 2004, A new approach to the modeling and simulation of flexible microstructures under the effect of squeeze-film damping, Journal of Micromechanics and Microengineering, Ausgabe 14, S. 170 – 181.

[7] Schajer, G S, 1986, Why are guided circular saws more stable than unguided saws, Holz als Roh- und Werkstoff, Ausgabe 44, S. 465 – 469.

[8] Szymani, R, 1977, Principal developments in thin circular saw vibration and control research, Holz als Roh- und Werkstoff, Ausgabe 35, S. 219 – 225.

[9] Viswanath, D S, 2007, Viscosity of liquids, Springer.

INVESTIGATION OF PROCESS FORCES OF ULTRASONICALLY ASSISTED SCRATCH TESTS

T. Stehle[1], R. Eisseler[1], K. Drewle[1], S. Weiland[1], P. Bruns[2], J. Twiefel[2]

[1]Institut für Werkzeugmaschinen, Universität Stuttgart, 70174 Stuttgart Germany
[2]Institut für Dynamik und Schwingungen, Leibniz Universität Hannover, 30167 Hannover Germany

thomas.stehle@ifw.uni-stuttgart.de

KEYWORDS

stone, ultrasonic, diamond grain, scratch test, cutting force

ABSTRACT

Due to their abrasive qualities, machining of hard and brittle materials is predominantly performed using tools with geometrically indefinite cutting edge. However, these processing methods offer only low productivity, which often can be increased by superimposing ultrasonic vibrations to the process. At the same time this hybrid process design involves great uncertainties, as influencing factors and the mechanism of action are not sufficiently described yet. In order to close this knowledge gap, firstly the occurrences on the scale of single abrasive grains shall be observed. This should increase the overall process understanding and reveal fundamental interrelations of machining with geometrically indefinite cutting edge. To achieve this, scratch tests with well-defined boundary conditions will be performed, analyzed and compared. As a result of the experiments the interdependencies of process forces, cutting speed, ultrasonic amplitude and depth of cut will be presented.

INTRODUCTION

Using stone as material is extremely varied and has a long tradition. Applications range from sculpture to horticulture and interior decoration to industrial applications. The widespread applicability of stone is a result of its distinguished properties, which often cannot be attained by competing individual or combined materials. [1]

Whereas the aesthetic aspects of stone are important in art, the outstanding technical properties are to the fore in industrial applications. Granite is often chosen as material to produce measuring components thanks to its temperature stability and wear resistance [2]. It is, however, difficult to machine this natural stone due to its great hardness and abrasive material properties so that it is indispensable to use diamond tools.

In principle, material removal can be divided into cutting and abrasive processes according to DIN 8589. The remarkable features of cutting processes are generally their high productivity, a great accuracy of the manufactured products and an efficient use of the process energy input [3]. These numerous advantages are opposed by an enormous tool wear in stone machining, making the cutting of hard, brittle materials uneconomic despite the advantages mentioned. For this reason, processes with diamond-tipped grinding tools are preferred by industry to manufacture stone products. The tool attains a continual sharpness due to the constant breakaway of worn diamonds and the exposure of new grains [4]. The productivity of abrasive machining processes is, however, low owing to little material removal rates and great frictional heat.

Hybrid machining methods broaden the existing process boundaries of conventional production processes in material removal technology. Especially the superposition of a mechanical vibration in the ultrasonic range has proved to be favourable in the machining of hard, brittle materials and hence is increasingly used in industry [5]. Different effects can arise, depending on the action direction of the ultrasonic vibration. Microhammering is an important work-

ing mechanism in vibration-assisted machining and comes particularly into effect in the case of machining processes with parallel feed and vibration directions [6]. The hard, brittle material properties of stone are used here to achieve the smashing of the material by applying varying loads. Due to a lower tensile strength of hard, brittle stone, the resilience of the loaded material induces great tensile stresses so that the material splinters. In addition, pulsed loads onto the tool cutting edges lead to the microsplintering of diamonds so that new, sharp cutting edges arise and the tool always remains sharp [7]. Apart from microhammering, the cleaning effect is another phenomenon of vibration-assisted machining. It is assumed here that the ultrasonically excited tools show a self-cleaning effect in connection with a coolant. Because the tool is lifted briefly, the coolant directly reaches the machining zone and removes the cut particles better. Hence the cutting edges and the chambers remain empty, which improves the efficiency of the grinding tools. Another effect of ultrasonically assisted machining is supposed to be the reduction in Coulomb friction [8]. The decrease in mean friction here results from the periodic change in direction of the relative speeds between tool and workpiece. Hence the ratio between base speed and directed speed amplitude is crucial for how high the Coulomb friction is. Friction is completely missing in the borderline case of an insignificant speed ratio.

In principle there are several possibilities for how a conventional machining process can be superimposed by vibrations in the ultrasonic range [9]. The most widespread application here is to add vibrations via a tool excitation. Compared with a vibration excitation of the workpiece, the advantages of this excitation form are the discretely distributed antinodes and nodes as well as the independence of the vibrational system characteristics from the machining position and the mass of the workpiece. Compared with an excitation of the whole spindle unit, a tool excitation can be realised more economical and energy-efficient. In this way it is not necessary any more to design the spindle individually for each application, and the accelerated masses can be kept small.

Vibrating systems are usually designed for a no-load operation. It is intended here to reach a resonant-near operation with discretely distributed nodes and antinodes. The important influencing parameters are the material-related properties, defining the stiffness of the system, and the distribution of the inert masses. Systems designed in such a way change their vibration properties if they are affected by process forces [10 - 11]. Especially the forces directed parallel to the vibrations affect the stiffness of the system by distorting or stretching the actuator unit like a spring. Consequently, the nodes and antinodes are shifted, and the system becomes off-resonance [12].

The vibration system thus must be designed individually for each application to realise an optimum operation. It is not sufficient here to examine only the process kinematics by taking all process-relevant parameters into account. The design process of a vibrating system rather requires that the interactions between tool and workpiece are taken into consideration permanently. The iterative feedback of the resultant forces arising is central to the design process here. Concerning tools for cutting processes, it is relatively easy to determine both the amount and the direction of the loads arising. By machining cylindrical specimens with different diameters, it is even possible to identify resultant forces on individual cutting edge segments [13]. Establishing the loads on tools for abrasive processes is fundamentally different. Both the shape and the number of simultaneously engaged cutting edges are unknown here. Hence it is impossible to reliably determine the resultant forces for the entire tool. In addition, it is sensible to restrict the process loads to one grain at first. Thus scratch tests with a single grain were carried out to permit evaluation of process forces and observation of the interaction between workpiece and the vibrating tool as well. This, in turn, can serve as a first step towards process-oriented design of ultrasonic tools.

SET-UP AND PROCEDURE

The scratch tests were carried out with a linear test stand, which is used by the Institute for Machine Tools to examine the true machining characteristics of single teeth. This test stand

consists of an adjustable vertical table, which is fastened to the stationary frame, and a movable slide unit, which can perform a uniaxially directed movement underneath the portal-shaped frame. The portal frame is prestressed in order to achieve a great static and dynamic stiffness. Hence, this test stand is ideally suited to carry out single grain cutting tests. Thanks to a linear direct drive it is possible to achieve cutting speeds of up to $v_c = 200$ m/min, which is within the usual cutting speed range of $v_c = 60 - 180$ m/min in the machining of hard stone [14].

A scratch was produced here by moving a stone specimen that was fastened to the slide unit at a defined cutting speed under the stationary tool. The depth of cut a_p was set at the tool by changing the vertical position of the table (z-axis). In addition, a fine adjusting element was fitted to the workpiece to compensate for tilting errors of the test specimens so that it was possible to attain accuracy within the micrometre range. Figure 1 shows an illustration of the equipment used as well as the entire flow of information.
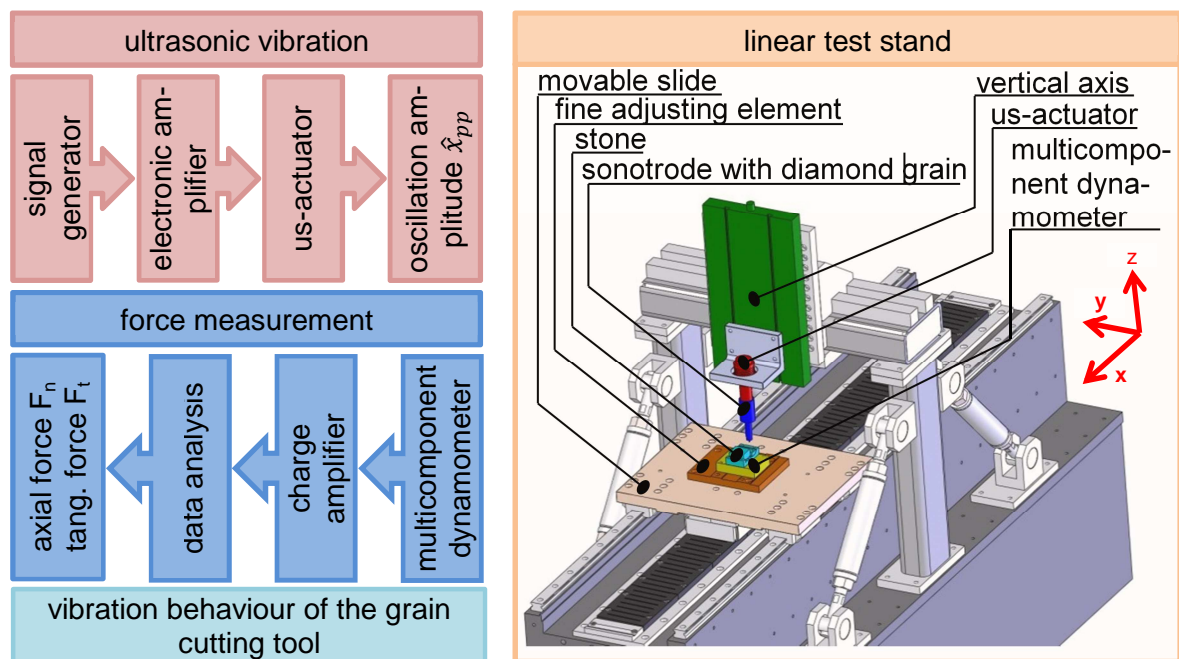

Figure 1: experimental setup and flow of information

Different tools were necessary to establish the measuring data and control the ultrasonic actuator. The process forces were measured with a multicomponent dynamometer by Kistler and an accompanying charge amplifier. The components of the resultant force are measured in a quasi-static way here, since the dynamics of the process at an ultrasonic vibration frequency cannot be established with this measuring technique. A digital phase control unit (dPLL 500/100k) developed by the Institute of Dynamics and Vibration Research was used for driving the ultrasonic actuator. This unit permits a resonant operation of the actuator due to an appropriate phase control. In addition constant amplitude of current and displacement respectively is achieved by an integrated closed-loop amplitude control. Furthermore, the vibration behaviour of the grain cutting tools were monitored with a 3D one point laser vibrometer by Polytec by means of focusing on a measuring point on the grain cutting tool near the shear zone and measuring its spatial shifting. The high dynamic properties of the measuring system make it possible to visualise the technical vibration behaviour of the grain cutting tools in every detail.

EXPERIMENTAL DESIGN

To be able to represent the effects of the three test parameters of cutting speed v_c, depth of cut a_p and the peak-to-peak value of the ultrasonic vibration $\hat{x}_{pp}$ as response surface a procedure was worked out by using design of experiments (DOE). Every single test was repeat-

ed at least three times to compensate for the scattering in the composition and the material properties of the stone specimens. The values of the single parameters here range between the limits listed in Table 1.

Table 1: parameter variation

depth of cut a_p [µm]	cutting speed v_c [m/min]	oscillation amplitude $\hat{x}_{pp}$ [µm]
10 – 50	15 - 180	0 - 40

A three-level experimental design in accordance with Box-Behnken [14] was used in the first test step. In this first experimental design, it was intended to quickly create a preliminary, rough database in only a few single tests, in order to detect nonlinear dependences on the forces of the influencing factors and to decide on the further design of experiments. Assessing this first test stage leeds to the conclusion, that additional support is required for a future utilisation in the complete kinematic model. In addition, it is also necessary to make a finer grading than the three levels per influencing factor as used in the Box-Behnken experimental design.

In the next two steps the experimental design was consequently expanded by two intermediate levels per each influencing factor. A D-optimal design was selected both times, which contains the preceding results and is supplemented with new points. Using this refined experimental design, it is possible to generate response surfaces of sufficient accuracy.

TOOLS

There are no restrictions in the design of tools for carrying out scratch tests in stone regarding conventional grain cutting without ultrasonic superposition. Central requirements here are not only a sufficient static strength but also a fast exchangeability of worn diamond grains and a resource-saving design. In highly dynamic processes, these requirements fade into the background because they do not take account of the dynamic structural properties of tools at varying high-frequency loads. The essential aspects in ultrasonically assisted scratching are to transmit energy to the cutting region with as little loss as possible and to maximise the vibration amplitude at the tool tip.

With respect to an efficiency of resources, it was sensible to carry out the conventional as well as the ultrasonically assisted scratch tests with a modular tool. Consisting of a base and a diamond-tipped grain holder, the modular design enables a fast and easy exchange of grain holders if the diamond grains are worn out or broken off. The two tool parts were connected by an M6 thread, making a good compromise as it presents a slip-free connection with a great tightening torque. The diamond grains were fixed to the grain holders by vacuum soldering with silver solder. This method provides a good connection of the single grains to the grain holder at a moderate temperature below the oxidation temperature of diamond. Alternate methods such as bonding and mounting were ruled out in preliminary tests as the load-carrying capacity of the joint proved to be insufficient.

The above-mentioned requirements on a dynamic vibration system were met by designing the grain cutting tool with the λ/2 method. In this method all members of a vibration chain are tuned to half the length of a sound wave axially propagating in the medium or to a multiple of half its length. In this way a standing wave with constructive interference characteristics is formed, so that a tool which is excited at the base has maximum amplitude at its tip. The vibration amplitude was amplified by tapering the tool geometry. The system has to be operated in or at least close to the resonant frequency of the desired natural mode to guarantee that energy is transmitted as completely as possible. Vibratory systems have the highest values of flexibility in this resonant-near frequency range and hence can absorb higher amounts of energy. Figure 2 shows the geometric and vibrational characteristics of the designed grain cutting tool.
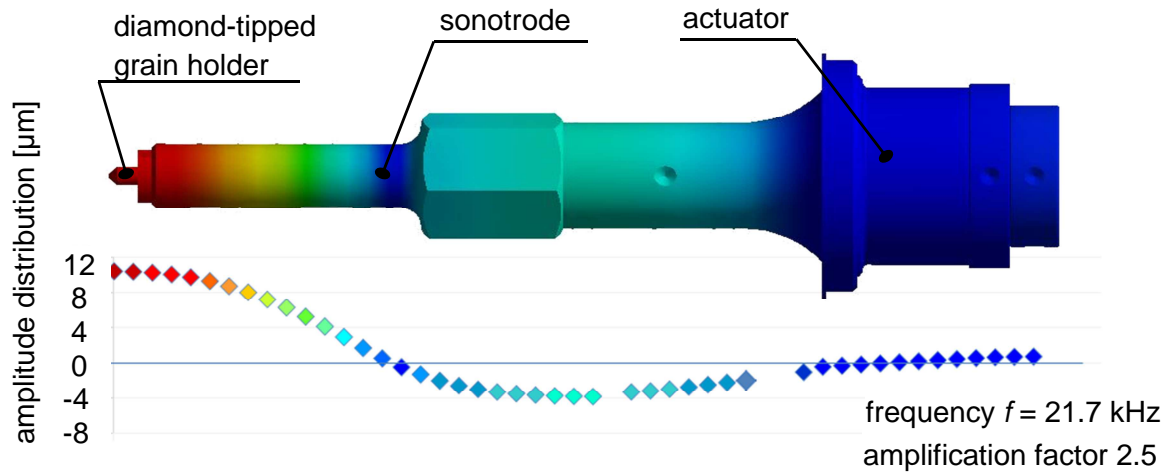
Figure 2: geometric and vibrational characteristics of the ultrasonic system

All diamond grains differ fundamentally from each other in shape and size. As a rule, the shape of a grain growing without being disturbed varies between a cube and an octahedron, but all intermediate forms can occur. Before the scratch tests were conducted, all diamond grains were classified and selected from a representative amount of grains with roughly the same geometric properties, so that these geometric shapes have as little effect as possible. Figure 3 presents the statistical distribution of the measured diamond grains with respect to the shape and the size of a single grain.
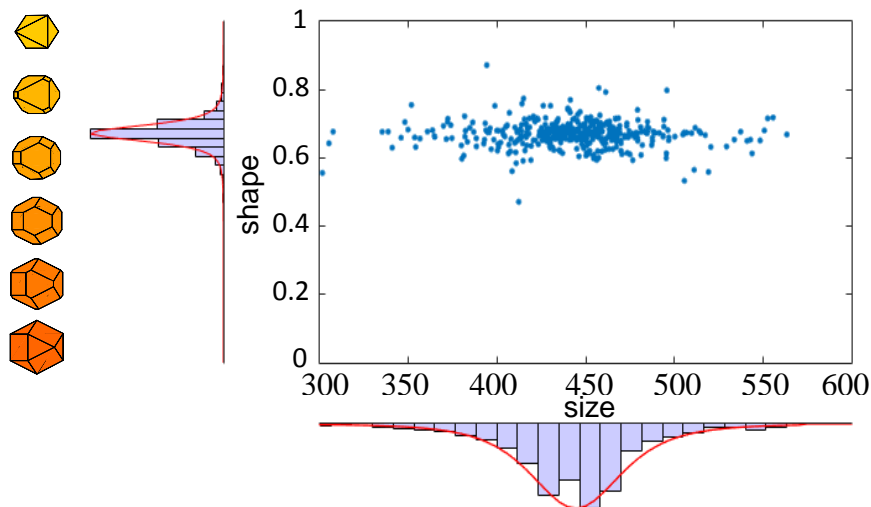

Figure 3: statistical distribution of shapes and sizes of single grains

RESULTS

The resultant force is analysed depending on the depth of cut of the diamond grain a_p, the cutting speed v_c and the peak-to-peak amplitude of the tool $\hat{x}_{pp}$, in order to find out how the boundary conditions affect the arising process forces. These are measured here component by component, in the direction of primary motion F_t and of depth setting F_n as well as orthogonally to both directions and then summed as medians. Since only dependences on two parameter variables can be sensibly represented by a three-dimensional graph, the third parameter has to be constant each time.

The results of the scratch tests without vibration superposition can be seen in Figure 4. As expected, the medians of both process force components F_n and F_t rise as the depth of cut

a_p of the diamond grain as well as the cutting speed are increasing. With growing depth of cut, the chip cross-sectional area and the resistance on the diamond grain penetrating the material are greater. The increase in force components with rising cutting speed is based on a greater material removal rate, which requires more cutting energy.
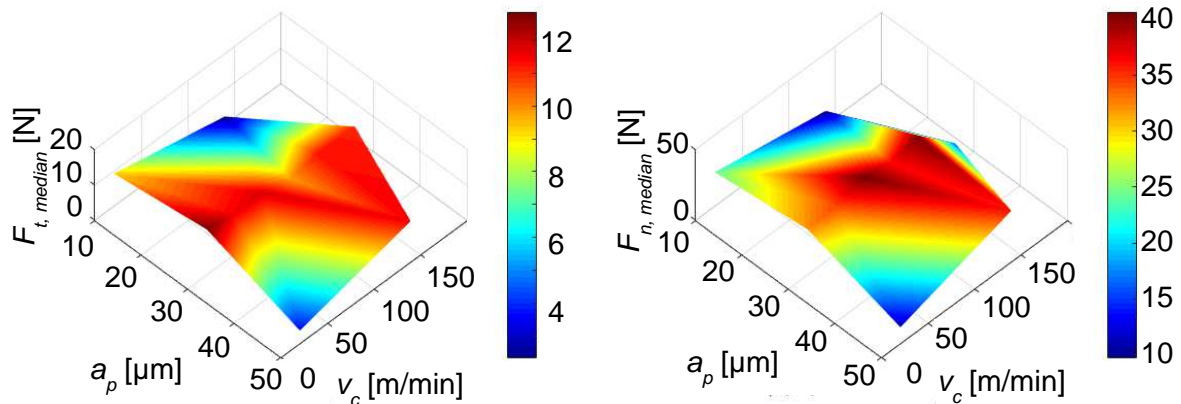

Figure 4: dependency of tangential (left) and normal force (right) on the cutting speed and the depth of cut for x_{pp} = 0 µm

The fact described above can also be detected in vibration-assisted scratch tests with a vibration amplitude of $\hat{x}_{pp}$ = 20 µm (Figure 5). The represented response surfaces show that the two components of resultant force depend on the parameter variables of depth of cut a_p and cutting speed v_c as well. In contrast to conventional scratch tests, the two force components here increase with growing depth of cut if speed is low. If cutting speed is increased, the effect of the depth of cut is getting less until there is none at all in the case of high cutting speeds. The cutting speed affects the amount of the resultant force components much greater. The individual components of the resultant force increase with rising cutting speed, reaching their maximum at the highest examined cutting speed.
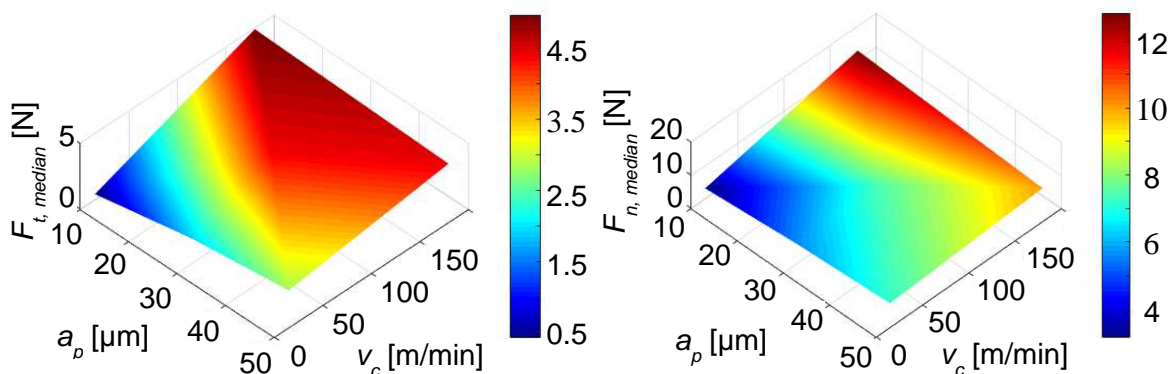

Figure 5: dependency of tangential (left) and normal force (right) on the cutting speed and the depth of cut for x_{pp} = 20 µm

It is obvious that the amplitude of the superimposed vibration affects the amount of the arising process forces as well. As an example, Figure 6 shows this correlation for a constant depth of cut of a_p = 30 µm.
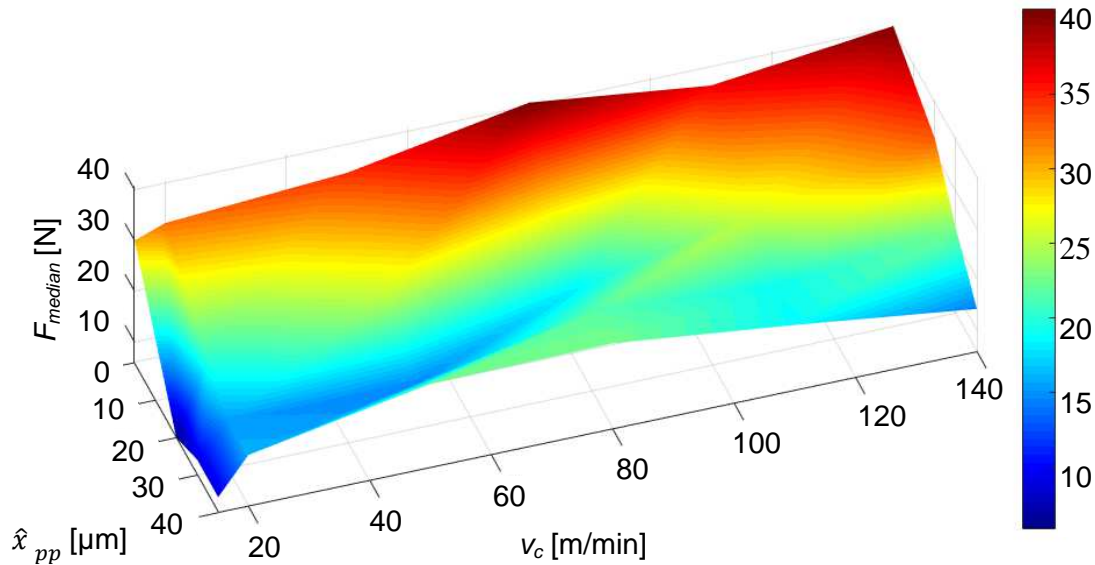
Figure 6: dependency of the cutting force on the cutting speed and the oscillation amplitude for a_p = 30 µm

It follows from this diagram that the mean process force is reduced down to 20 % of the initial value due to the vibration superposition. For example, the maximum reduction in process force is already reached at lower vibration amplitudes in the case of lower speed ranges (v_c = 15 - 80 m/min). If the vibration amplitude is increased further, the process forces rise in the case of low cutting speeds. The maximum reduction in resultant force occurs at high vibration amplitudes regarding the examined upper ranges of cutting speed (v_c = 110 -140 m/min). It is remarkable here that process force gradually decreases with increasing vibration amplitude.

At first, the kinematics of the grain cutting process have to be examined more closely to clarify the correlations described. In the case of scratch tests without ultrasonic assistance, the diamond grain moves parallel to the surface of the stone specimen and exerts continuously increasing compressive stresses on the material in front of and under the cutting edge. If a critical material value is exceeded, these compressive stresses lead to material failure and the forming of primary chips. Due to the continual contact in the shear zone this process is characterised by great friction, which, together with the grain cutting process characteristics, leads to high loads on the diamond grain. The established medians of the resultant forces are comparatively high in scratch tests without ultrasonic superposition. In contrast to this, the continual contact between the diamond grain and the stone specimen is periodically interrupted due to ultrasonic superposition, which reduces the average friction in the shear zone. This is also the reason for the generally lower level of the determined medians of resultant force. Moreover, the contact period becomes shorter with growing vibration amplitude and constant operating frequency. Hence, a further reduction in friction is to be expected at higher amplitudes. But at the same time, the rising vibration amplitudes increase the effective depth of cut of the diamond grain. This is the sum of real depth of cut and vibration amplitude and counteracts the effect of friction reduction, diminishing resultant force. It can be clearly seen how these two contrary effects interact in the lower range of cutting speeds (v_c = 15 - 80 m/min). At first, the effect of friction reduction is predominant in the case of low vibration amplitudes thus the resultant forces decrease with increasing amplitude. If the vibration amplitudes are high, the effectively greater depth of cut becomes noticeable by a renewed increase in process forces. In the examined upper ranges of cutting speed (v_c = 110 -140 m/min), the maximum reduction in resultant force is reached at high vibration amplitudes. It is obvious here that the force-reducing effect of the superimposed ultrasonic vibration predominates the counteractive influence of the increasing chip cross-sectional ar-

ea. Hence, the medians of the process force gradually decrease despite a greater effective depth of cut.

Apart from the medians of the measured resultant force, the examination of the individual force components (normal and tangential force) should provide more insight into correlations prevailing in the process. For that purpose, the ratio of tangential force to normal force has also to be analysed for a constant depth of cut of $a_p = 30$ µm, depending on cutting speed and vibration amplitude (see Figure 7).

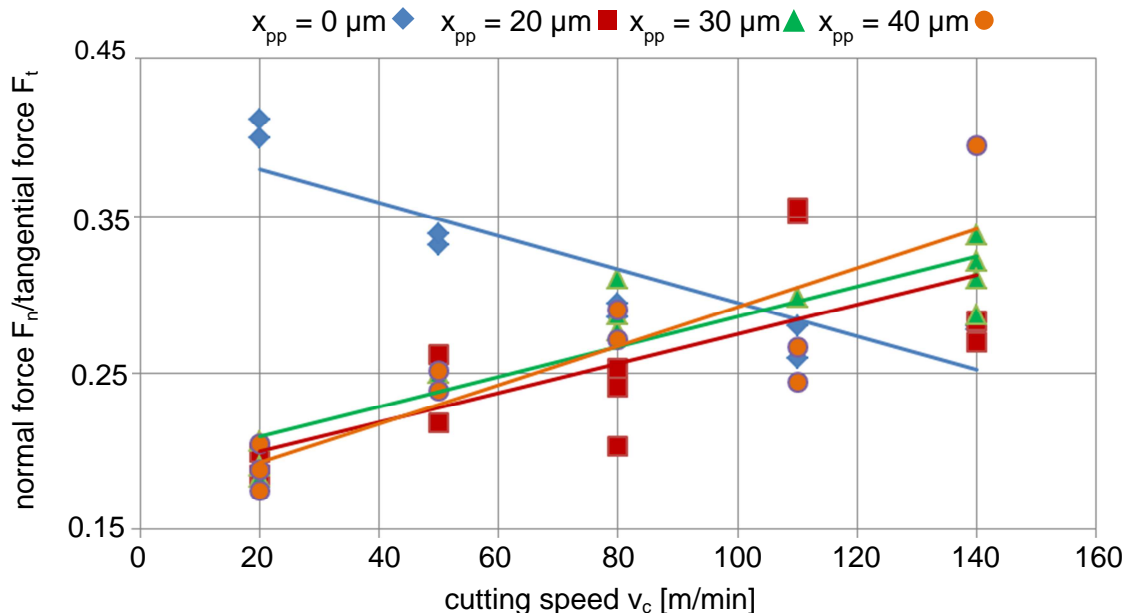Figure 7: ratio of tangential (left) and normal force (right) for $a_p = 30$ µm

The trend lines presented in the diagram above visualise the direction towards which the behaviour of the ratio between the resultant force components tends and are calculated from the minimum sum of error squares. It can be seen from this that the gradient of the trend line shows higher values in the case of greater vibration amplitudes. The trend line of conventional scratch tests have a negative gradient.

The different trend line gradients can be accounted for with diverse material removal mechanisms prevailing in the respective series of tests. In conventional grain cutting, the material is largely cut by a pushing movement due to a linearly increasing load in the contact zone. In ultrasonically assisted grain cutting by contrast, the surface splinters predominantly due to the pulsed hits of the diamond grain. Especially the tangential force here depends on the speed ratios prevailing in the contact zone. If the ratio of vibration speed to cutting speed is sufficiently high, the diamond grain hits the stone surface almost vertically and smashes the material underneath. The two components of resultant force result almost entirely from the geometric boundary conditions in the contact zone so that material removal can be attributed exclusively to microhammering. As the ratio of vibration speed to cutting speed decreases, the material to be machined exerts a force on the diamond grain so that the tangential component of the resultant force rises. Consequently, there is a mixed material removal mechanism. In conventional grain cutting, however, the entire tangential force results from the cutting energy produced.

CONCLUSIONS

This paper presents the results of the conducted scratch experiments, machining stone with single diamond grains. Thereby, the occurring machining forces, with and without ultrasonic superimposition, were determined and analyzed in dependence of the depth of cut, the cutting speed and the vibration amplitude of the tool.

The presented examinations show, that an increase in cutting speed and the depth of cut results in an increase in process forces. These observations originate in the increase in cutting work due to higher material removal rates. The superimposition of ultrasonic vibrations has a categorically positive effect on the process forces. The occurent cutting force was reduced by up to 80% during the scratch tests. An augmentation of the vibration amplitude didn't necessarily entail a reduction of the cutting force, since changing the amplitude also altered the effective cut of depth. Another fundamental influence on the force reduction was the ratio of ultrasonic velocity to cutting speed. With increasing ratios of the two velocities the cutting force did always decrease. This is founded in the different dominant separation mechanism in the machining zone.

The influence of ultrasonic vibrations on machining precision will be one topic of further examinations. For this purpose the relation of removed material and the process forces will be examined under varying parameter settings. This will increase the understanding of the complex interdependencies in ultrasonically assisted machining of stone. The influence of process forces on the vibration characteristics of the ultrasonic system will be another topic.

ACKNOWLEDGMENT

[1] Okrusch, M, Matthes, S, 2014, Eine Einführung in die spezielle Mineralogie, Springer Verlag
[2] Schadek, S, 2014 Granit garantiert Genauigkeit, MM Verzahnungsmesstechnik
[3] Reichenbächer, H, 2010, Trennen mineralischer Werkstoffe mit geometrisch bestimmten Schneiden, kassel university press
[4] Ertingshausen, W, 1985, Zerspanung von Granit mit Diamant – Trennschleifscheiben, Universität Hannover
[5] http://www.dmgmori.com, 2015
[6] Heisel, U, Eber, R, 2010, Ultraschallbohren von Gestein, Werkstattstechnik online
[7] Zabel, A, 1998, Ultraschallunterstütztes Schleifen von Hochleistungskeramik, TU Kaiserslautern
[8] Littmann, W, Storck, H, Wallaschek, J, 2002, Reibung bei Ultraschallschwingungen VDI-Verlag
[9] Neugebauer, R, Stoll, A, 2004, Ultrasonic application in drilling. Journal of Materials Processing Technology
[10] Bruns, P, Twiefel, J, 2015, Influences of Non-axial Process Loads on the Transducer and the Associated Mounting in Ultrasonic Machining
[11] Ille, I., Twiefel, J, 2015, Model-Based Feedback Control of an Ultrasonic Transducer for Ultrasonic Assisted Turning Using a Novel Digital Controller,
[12] Twiefel, J, 2010, Experimentelle und modellbasierte Untersuchung von Stehwellenantrieben, IDS Hannover
[13] Michna, J, 2014, Numerische und experimentelle Untersuchung zerspanungsbedingter Gefügeumwandlungen und Modellierung des thermo-mechanischen Lastkollektivs beim Bohren von 42CrMo4
[14] DIABÜ, 32015, Produktprogramm 2013-2014
[15] Box, G, Behnken, D, 1960, Some new three level designs for the study of quantitative variables

New Simulation based Method for the Design of Cut-Off Grinding Segments for Circular Saws

B. Denkena, T. Grove, A. Ermisch, T. Göttsching
Leibniz Universität Hannover,
Institute of Production Engineering and Machine Tools (IFW),
An der Universität 2, 30823 Garbsen, Germany
tatzig@ifw.uni-hannover.de

ABSTRACT

A new trend in the field of cut-off grinding tools such as circular saws is the application of deterministic grain pattern, e.g. the ARIX-System. Although the improved performance of these tools has been proven in a quarry exemplarily, it is not clear how to configure an optimized grain pattern. It is assumed that the work material, the cutting parameters and the tool dimensions have an influence on these pattern. In this paper a new method is presented for the design of cut-off grinding segments for circular saws with defined grain pattern, which is based on the in-house material removal simulation software CutS. With this simulation, the influence of variable grain pattern on tool performance and tool life can be tested without the need for cutting experiments. It is possible to test different material specifications through the consideration of brittle and ductile material removal mechanisms and adjustable material removal factors. The influence of macroscopic and microscopic tool wear on the optimized positioning of grains by means of material removal rate and wear rate is investigated. With special algorithms, it is also possible to simulate standard tools with stochastically distributed diamond grains. Computed results will be compared to real cutting experiments of granite with cut-off grinding segments designed with CutS.

KEYWORDS

Material Removal Simulation, Deterministic Grain Pattern, Tool Design, Circular Saw, Cut-Off Grinding, Natural Stone, Reinforced Concrete

INTRODUCTION

In natural and artificial stone processing multiple new demands for cutting tools appear. Tools like circular saws have to gain a higher productivity by means of faster cuttings combined with longer tool life to make natural stone products competitive to other construction materials. In the construction industry, the focus of improvement lies upon tool life and process forces due to the usage of transportable machines. To meet transportability demands and weight limits for the operating of these machines, the available power is often reduced which explains the need of cut-off grinding tools with low process forces.

All these demands can be faced by special designs of the cutting segments. Besides the choice of the right binder material, the diamond size, quality and concentration, defined grain pattern realized by systems such as ARIX and DiaSet can be deployed [1, 2]. Those grain pattern can be designed to fit the challenging demands in both natural stone and construction industry. Because the improved performance of such tools has only been exemplary proven in a quarry, it is not clear how to configure an optimized grain pattern. It is assumed that the work material, the cutting parameters and the tool dimensions have an influence on these pattern.

1. STATE OF THE ART

Deterministic grain pattern are a research topic in many fields of application. In surface grinding, grain pattern are used to improve the temperature behaviour of the grinding tool. Therefore, making dry grinding without any coolant fluid possible for normal grinding operations is the main goal of these researches [3]. Here, the pattern are designed to reduce the number of active grains and increase the available chip space. Other studies put the workpiece surface topography in focus. In addition, the influence of grain pattern on the wear behaviour of the grinding tool was investigated in former studies using simulation approaches with regard to the surface topography of the workpiece only [4].

In the field of stone and concrete cutting the main focus of the usage of deterministic grain patterns is the optimization of the material removal rate and the wear behaviour of the cutting tools. Sung had shown that with single layer electroplated deterministic grain pattern both, the relative cutting speed in square meter per hour and the tool life, can be increased [5]. In concrete cutting, grain pattern have the potential to increase tool life compared to stochastically grain pattern due to lower adhesion wear [6, 7]. The focus of this work was the influence of the work material by means of material removal mechanism on the positioning of diamond grains. With single grain scratch tests material removal factors were identified. Therefore, a brittle material removal mechanism allows the reduction of the number of grains on the grinding tool surface by increasing the distance between the single grains. Cutting of ductile materials needs an increase in the number of grains and smaller distances between them to guaranty a complete material removal on the workpiece surface [8].

Since sintered tool with grain pattern are easier to manufacture than brazed or electro-plated tools grain pattern are only available for circular saws [9]. Up to now, only parameters for single layer tools are defined [3, 4], though the technology for manufacturing 3D cut-off-grinding segments is available [1, 2]. New methods are needed to define optimized grain pattern for multi-layer cut-off grinding tools.

2. SIMULATION APPROACH

A material removal simulation is set-up to compute different grain patterns and determine their influence on material removal and wear rate. The simulation is based on the in-house material removal software CutS© which was already used for the determination of optimized grain pattern for wire cutting tools [10]. To reduce computing time simplified grain models are used, like truncated octahedrons or truncated dodecahedrons. These models are statistically orientated with a statistically chosen size within the tolerances given by FEPA and have statistically chosen grain shapes.

For the computing of cut-off-grinding segments, several changes had to be done. First of all a new parametrisation of grain distances in every three room axes including displacement possibilities was necessary to install in order to create multi-layer cut-off-grinding segments. Second, to determine the optimum position of a grain in segment height the wear mechanisms had to be considered. At least the possibility to deactivate grains had to be implemented, in order to simulate the break out of grains. But since the grain shapes are changing in real contact, e.g. getting split or flattened, the microscopic tool wear also has an influence on the positioning of the grains within a cutting segment. Third, the load acting on each single grain has to be detectable. Real cutting experiments with segmented tools have shown that the front of a segment, which is the first to come in contact with the work material, underlies a higher wear than the segment ending. Here, an optimized grain alignment could help to even the tool wear. Therefore, every single grain model inside the cut-off-grinding segment is a single tool within the software. When it comes to contact between the tool and the workpiece model the grains in contact are coloured depending on the amount of the actual material removal. The colour changes on a scale from blue to red. This is an optical

indication of the load level of the single grains. After passing the adjustable maximum load within the simulation (colour red) the grains will break out. In the simulation, the grains will be deactivated and removed from the tool model (Fig. 1).
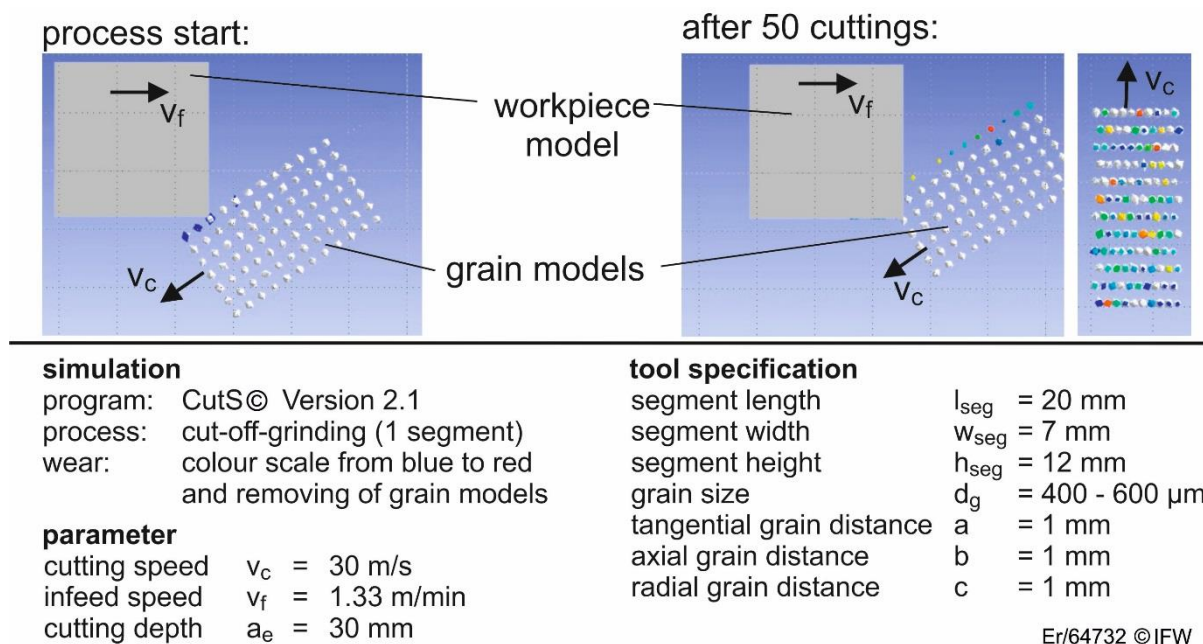

Fig. 1: Simulation approach, visual representation of tool contact and tool wear

Another influence on the grain positioning is the material removal mechanism. The material removal mechanism can be described by the material removal factor k, which is defined as the removed material cross section divided by the tool cross section. For brittle materials, the factor values are k > 1 while for ductile materials like reinforcement steel k ≤ 1. Therefore, algorithms were included to scale the single grain models by means of factor k when the simulation has detected contact between grain and work piece model (Fig. 2).

After the cutting operation is computed the grain will be instantly scaled to its original size and a new detection of contact is made. The same principal is used to calculate a simplified wear mechanism. A real diamond grain can wear in multiple ways, like flattening fracturing, breaking. Simplified, all wear mechanisms lead to a size reduction of the grain. Therefore, the wear of grains is calculated as a size reduction that depends on the individual load acting on a single grain. After the cutting operation is computed the removed material by a single grain is calculated and the grain size will be reduced proportionally to the removed volume for the next simulation step.
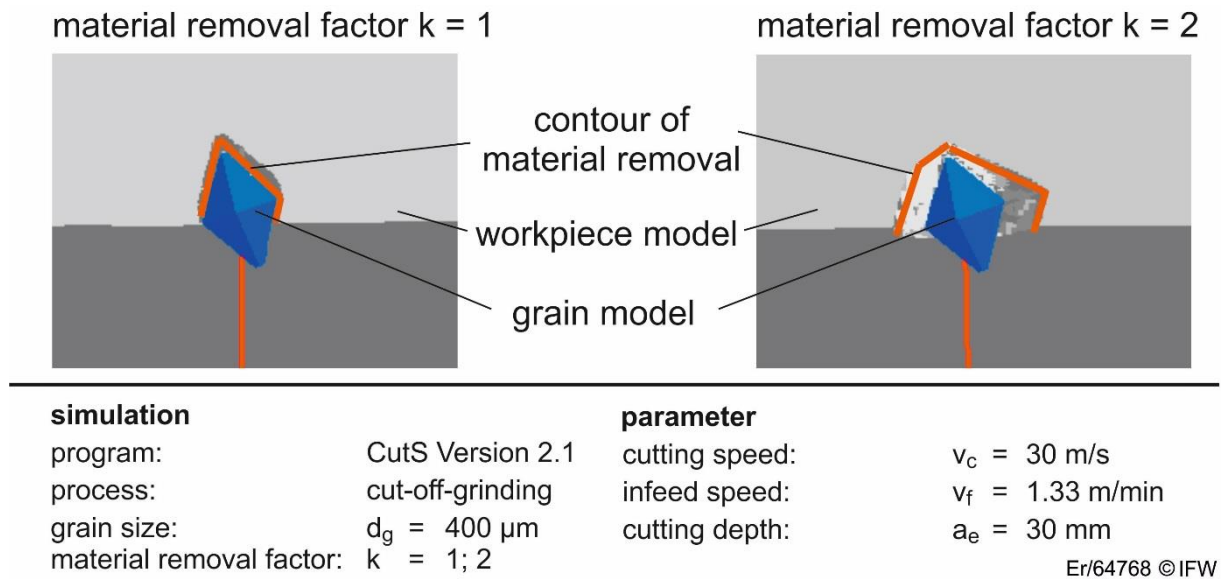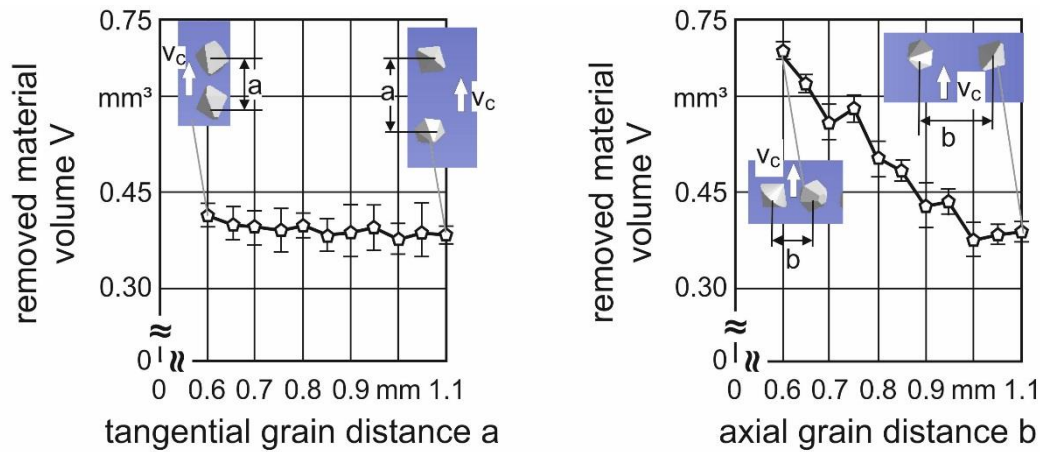
material removal factor k = 1   material removal factor k = 2

contour of
material removal

workpiece model

grain model

simulation		parameter	
program:	CutS Version 2.1	cutting speed:	v_c = 30 m/s
process:	cut-off-grinding	infeed speed:	v_f = 1.33 m/min
grain size:	d_g = 400 µm	cutting depth:	a_e = 30 mm
material removal factor:	k = 1; 2		Er/64768 © IFW

Fig. 2: Single grain simulation with material removal factor k = 1 for ductile material removal and k = 2 for brittle material removal

3. SIMULATION RESULTS

With the help of the described simulation approach the influence of different grain distances on removed material volume was investigated (Fig. 3). Therefore, single segments were computed with varying distances either in tangential, axial or radial direction while the other directions were kept constant. A standard segment size for cutting of natural stone with segment width w_{seg} = 7 mm, segment length l_{seg} = 20 mm and segment height h_{seg} = 12 mm was used. The number of grains in the segment and more important on the surface of the segment changes with varying grain distances. This leads to varying removed material volumes and gives an indication of the most important parameters for an optimized grain alignment. In dependence on real cutting segments the simulated grain models have a diameter of d_g = 400-600 µm.

It was found that the axial distance b between grains along the segment width is directly connected to the removed material volume (Fig. 3, right). Due to the reduction of the number of grains on the segment surface $n_{surface}$ with increasing axial grain distances b by a given segment size less material is removed. When the grains are set next to each other up to eleven grains can be set along the segment width regarding the maximum grain diameter d_g = 600 µm. Is the axial grain distance doubled, a maximum of six grains can be set. To gain a complete material removal in segment width the axial grain distance b has to be minimal. If that is not possible then grain displacements of the following grains can help to improve the removed material volume. The following grains should be set right in the gap of the leading grains to maximise the material removal. Concerning material removal mechanisms of brittle materials the simulation suggests an axial distance b = 0.7 mm with no grain displacement since more material is removed by a single grain compared to ductile removal mechanisms.

Fig. 3: Removed material volume depending on varying grain distances in tangential and axial directions

The tangential distance a, which is the grain distance in circumferential direction or in the direction of the length of a segment, has no significant effect on the removed material volume (Fig. 3, left). Found deviations are due to the randomized choice of grain type, grain size and grain direction, although the number of grains on the segment surface $n_{surface}$ is also reduced for increasing tangential distances a. This means that the following grains set with the distance a are not taking part in the material removal. This can be explained by the given process kinematics. The number of grains on the tool circumference N of one diamond row is influenced by the tangential distance a (1).

$$N = \frac{2\pi r}{a}$$ (1)

With r being the radius of the tool (2).

$$r = \frac{D_{tool}}{2}$$ (2)

As the grains have a deterministic distance to each other the infeed for every grain f_z can be calculated (3).

$$f_z = \frac{v_f}{n \cdot N}$$ (3)

The number of revolutions n is given by the cutting velocity v_c and tool dimensions (4).

$$n = \frac{v_c}{2\pi r}$$ (4)

Therefore, the tangential distance a can be calculated by the equation (5) for given process parameters.

$$a = f_z \cdot \frac{v_c}{v_f} \tag{5}$$

Fig. 4 shows the necessary tangential distances a for certain single grain chip thicknesses of the following grains. It can be seen that for low tangential distances (parameter a) the single grain chip thickness is nearly zero. To gain equal chip thicknesses of $h_{cu} = 10$ µm, which is found to be positive for the wear behaviour by Glatzel [11], the tangential distance should be a = 13.5 mm for ductile material removal (k = 1). With regard to cutting natural stone which occurs to have a brittle material removal mechanism and a material removal factor k = 2 the tangential distance is calculated to a = 27.1 mm which is more than the given segment length. These values are valid for the assumption that the tool is used in full cut and $f_z = h_{cu}$. Since this is not the case, the tool dimensions and the process parameters have an influence on the tangential distance as well. The values of Fig. 4 were calculated with the help of the depth of cut $a_e = 30$ mm, the cutting speed $v_c = 30$ m/s and the infeed speed $v_f = 1.33$ m/min. The tool diameter was assumed to be $D_{tool} = 1$ m. The left side of the picture shows the overall process kinematics. It can be seen that the maximum single grain chip thickness h_{cu} which occurs in the cutting process is smaller than the infeed f_z. Equation (6) describes the relation between these two values. Here, the influence of the tool dimension is given by the cutting angle φ (7).

$$f_z = \frac{h_{cu}}{\sin \varphi} \tag{6}$$

$$\cos \varphi = \frac{(r - a_e)}{r} \tag{7}$$
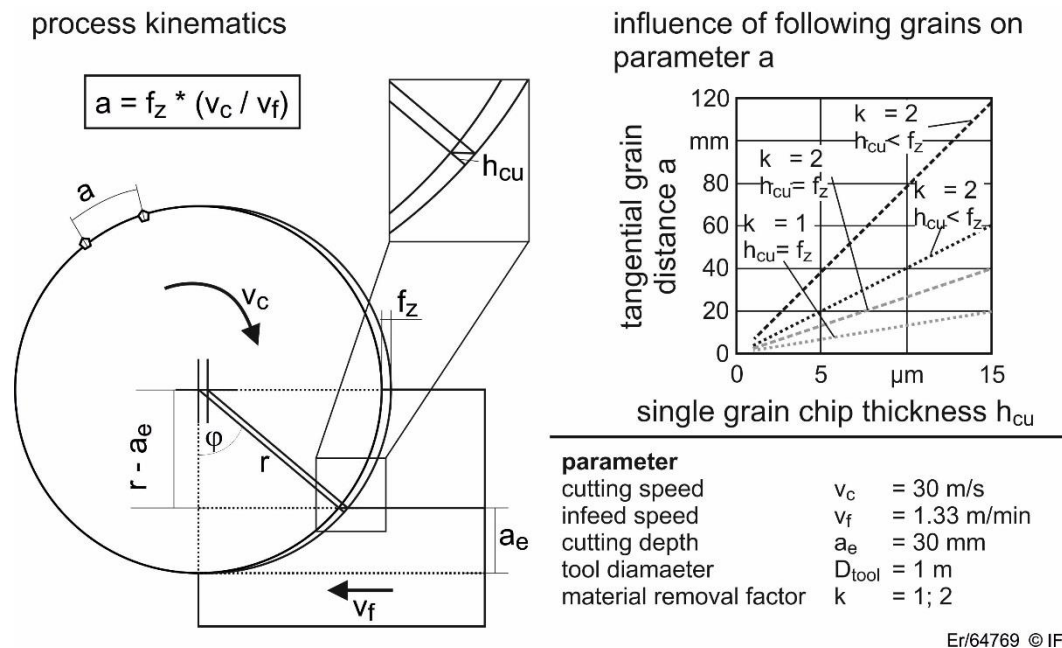
Fig. 4: Tangential distance a in dependence on single grain chip thickness of the following grains

With regard to the given process kinematics and equation (6) the actual necessary tangential distance a for an optimum single grain chip thickness $h_{cu} = 10$ µm is calculated to a (k = 1) = 39.7 mm respectively a (k = 2) = 79.3 mm. This would mean that only every second segment has one single grain in circumferential direction on its surface. Further investigations suggest that grains aligned with small distances a can improve the wear behaviour. Grains directly behind the first grains in contact take over the cutting load only

when the first grains start to wear. This has an influence on the radial wear. When the first grains breakout the following grains in circumferential direction, which have not taken part in the cutting process until now, take over the cutting operation. The loss of the first grain in contact due to wear means for segments with large tangential distances also a reduction of the segment height, at least a reduction equal to the grain size. If the tangential distances are smaller, the segment height stays the same if the first grains are worn out until the last grain of one layer is worn. So the radial wear rate is reduced. The smaller the tangential distance, the higher the wear stock and the lower is the radial wear rate. But, it is known, that for standard tools with stochastically grain distributions used for cutting of hard and brittle materials the grain concentration is lowered or the segment length is shortened, or both. This leads to higher average tangential grain distances with regard to reduce process forces. If a small average tangential grain distance and therefore, a large number of grains on the segment surface means higher process forces, then there is a limit for building up a wear stock through small tangential distances on segments with deterministic grain distributions. The simulation suggests a tangential distance of $a = 3$ mm to not flatten following grains by ploughing effects but also have a wear stock to reduce radial wear.

For the increase of the removed material volume the grain alignment in segment width (axial distance b) is more important since it directly determines how many grains are actually in contact with the workpiece. The tangential distance a has no effect on the removed material volume since the following grains do not take part in the cutting operation until the first grains start to wear. Nevertheless, this effect can be used as a wear stock so the radial wear can be reduced. The influence of the radial grain distance c on the tool behaviour, removed material volume and wear rate was investigated in experimental cutting tests with the goal to set up a wear model of the segment bonding to be implemented within the material removal simulation.

4. CUTTING EXPERIMENTS

To proof the simulation results and get information about the wear mechanisms and the wear rate real cutting experiments were conducted on a natural stone bridge saw type Hensel Gigant 459. The cutting parameters were set as described before. As work material a hard to cut granite type Rosa Sardo was used with the dimension of 1.2 x 1.2 x 0.35 m³. The process forces were measured with a Kistler three-component dynamometer. The dynamometer is directly mounted under the workpiece. The workpiece is cut into joints with a square surface of $A = 0.36$ m² with 10 infeed steps. After three joints with $A = 1.08$ m² the radial wear of the tools was measured. To gain information about the wear behaviour of the tools and the influence of different grain distributions 33 joints were cut with each tool. This enables an evaluation of the self-sharpening mechanisms and an analysis on how grains appear at the segment surface when the bonding is set back.

For the experiments four different sawing blades with a diameter $D_{tool} = 1$ m and a diamond grain size of $d_g = 400 - 600$ μm were used. Two of the tools, tools 1 and 2, have cutting segments with a deterministic grain distribution equal in tangential, axial and radial distance of $a = 3$ mm, $b = 0.7$ mm, $c = 1.15$ mm. Here, c is a result of fitting the total number of grains within one segment for standard tools with a concentration C15 into a segment with given height, length and width also as given parameters a and b. Tool 2 has further a grain displacement in radial direction of $l_c = 0.55$ mm. In addition, two standard tools with stochastically distributed diamond grains, tool 1_{stoch} and tool 2_{stoch} were investigated. The concentration of those tools correlates with the total number of diamond grains in tool 1 and tool 2, respectively. Since tool 2 has additional grains in radial direction the total number of diamonds is 1.5 times higher than for tool 1. Therefore, tool 2_{stoch} has also a 1.5 times higher concentration than tool 1_{stoch}.

5. CUTTING RESULTS

The upper part of Fig. 5 displays the resulting process forces for every tested saw blade. At first there occurs a grinding-in process until a cut surface of A = 2 - 3 m². The normal forces as well as the tangential forces are increasing during that period. After finishing the grind-in process the process forces are decreasing and start to oscillate around a stationary process force level. It can be seen that the tools with a larger number of grains (tool 2 and tool 2_{stoch}) gain higher process force levels. The number of grains on the surface has an influence on the process forces. For stochastically grain distributions the average tangential grain distance depends on the grain concentration. The higher the concentration the more grains are on the segment surface and the smaller is the average tangential grain distance. The results of chapter three have shown that the single grain chip thickness of the grains with small tangential distances a are very low. Hence, these grains do not take part in the cutting process but ploughing effects occur which result in higher friction and therefore in higher process forces. Comparing photographs of tool 1 and 2 depicts that the number of grains on the cutting segment surface is higher for tool 2 although the tangential grain distance a is equal. Due to the wear processes the bonding is set back and underlying diamond grains appear at the segments surface. Since tool 1 lacks additional diamond grains in radial direction there are no underlying grains that come into contact with the workpiece, immediately. For tool 2 these additional radial diamond grains increase the number of grains on the segment surface. There is a state were underlying diamond grains are in contact with the workpiece while there are still diamond grains of the first diamond layer on the surface of the cut-off-grinding segment. This results in a partially higher number of diamond grains on the segment surface. Therefore, the average tangential grain distance is reduced which explains the high increase of normal forces at the first grinding-in period. After reaching a stable self-sharpening effect, the forces of tool 1 and 2 are approaching, due to equal numbers of diamond grains on the surface of the cut-off-grinding segment. Additionally, the overall behaviour of the segments is changing with the number of grains. The segments get a higher stiffness, due to reinforcement effects by additional grains, which leads to less elastic deformations. Therefore, the process forces are increasing as well for tool 2.

Since the number of grains on the segment surface is nearly equal, the radial wear increases similar for all tools in the first period until a cut surface of A = 4 m² (Fig. 5, bottom). After that the radial wear has reached $\Delta r = 0.4$ mm, the same value as the diamond grain size. Therefore, the first layer of diamond grains is worn or broken out. For tool 1, the radial wear increases rapidly from the cut surface A = 4 m² to A = 6 m², due to the lack of grains in radial direction (Fig. 5, right). At this cut surface the radial wear reaches the value of the radial grain distance c in tool 1. Here, finally new diamond grains appear at the surface on the cut-off-grinding segments which immediately leads to a decrease of the wear rate. In the following period the radial wear increases parallel to the first period. It is assumed, that after the second layer of diamonds is worn out, the radial wear rate increases again significantly. The radial wear of tool 1_{stoch} oscillates around a linear best-fit line. Due to the stochastically distribution of grains, there are active grains cutting throughout the complete segment height. Therefore, a sudden increase in radial wear like it is shown by tool 1 is missing. The oscillating behaviour can be explained by the changeable number of diamond grains on the surface of the cut-off-grinding segment due to the stochastically distributed diamond grains within the cutting segments. Hence, the radial wear rate increases for a low number of diamond grains on the surface and decreases for a higher number.

specification:

tool 1	tool 2	tool 1,2$_{stoch}$
a = 3 mm	a = 3 mm	stochastical grain distribution,
b = 0.7 mm	b = 0.7 mm	$n_{grain1stoch} = n_{grain,Tool1}$
c = 1.15 mm	c = 1.15 mm	$n_{grain2stoch} = n_{grain,Tool2}$
	l_{ca} = 0.55 mm	

segment topography at A = 5 m²

tool 1

tool 1$_{stoch}$

tool 2

tool 2$_{stoch}$

parameter:

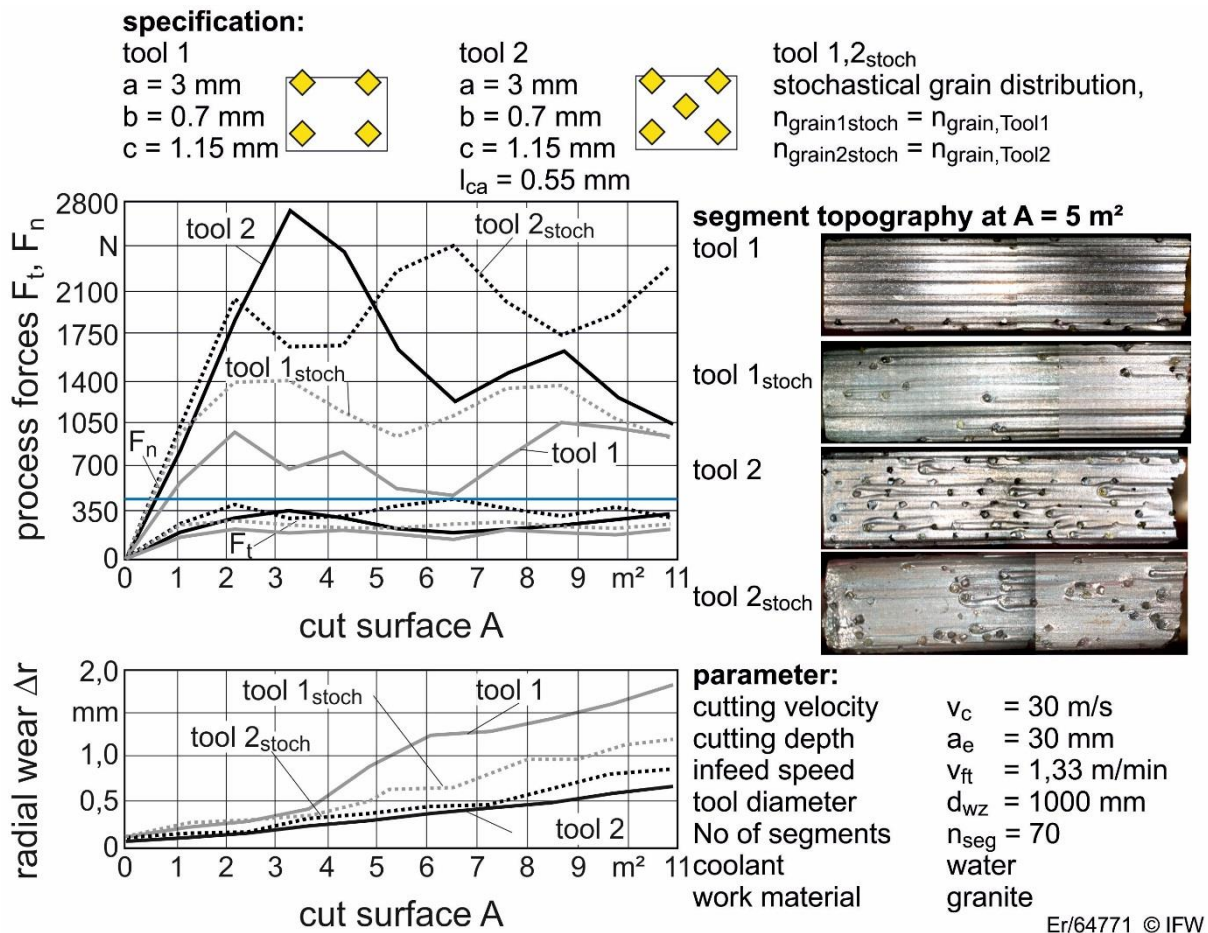|		
cutting velocity	v_c	= 30 m/s
cutting depth	a_e	= 30 mm
infeed speed	v_{ft}	= 1,33 m/min
tool diameter	d_{wz}	= 1000 mm
No of segments	n_{seg}	= 70
coolant	water	
work material	granite	

Er/64771 © IFW

Fig. 5: Process forces and radial wear for tools with different grain distributions

The oscillating of the radial wear curve can also be seen for tool 2$_{stoch}$. Here again, the stochastic distribution of diamond grains within the cutting segments leads to varying numbers of grains on the actual surface of the segments and therefore, to a faster (less diamond grains) or a slower increase of the radial wear. Due to its higher concentration compared to tool 1$_{stoch}$, the radial wear proceeds slower.

The radial wear of tool 2 does not show an oscillating behaviour. Compared to the stochastically distributed tool 2$_{stoch}$ the wear can be lowered although both tools should have the same total number of grains within the cutting segments. Here, in every height of the cutting segment of tool 2 the number of diamond grains is nearly constant. This leads to an even wear rate and to an approximately longer tool life than stochastically distributed cut-off-grinding segments.

The experimental results have shown that with higher number of grains on the segment surface the process forces are increasing. Hence, it is assumed that there is a limit for the number of grains on the segment surface which are set as wear stock to not exceed machine power limits and therefore, the tangential grain distance is limited. With the help of grain pattern the wear behaviour of sawing blades using cut-off-grinding segments can be influenced. It was shown that the radial grain distribution can smoothen the increase in radial wear and reduce the amount of the radial wear which leads to a longer tool life. It is assumed that with further use of additional displacements of diamond grains the radial wear can be lowered further.

5. CONCLUSION AND OUTLOOK

A new simulation approach for the determination of grain pattern was introduced. Compared to existing approaches a new possibility of creating 3D grain pattern and the consideration of material removal mechanisms of ductile and brittle materials was introduced. Therefore, a new parametrisation of possible grain positions was done and additional algorithms were implemented. With a simplified wear model the simulation cannot only be used for maximizing the removed material volume but also gives indications about the expectable wear rate.

With the help of the simulation it was found that the axial grain distance b in a cut-off-grinding segment is the most important parameter to maximize the removed material volume. It was also shown that in tangential direction following grains can be set directly behind the first ones with the parameter a and therefore, a wear stock can be build up. It was also shown that the process parameters, the tool dimension and the work material have an influence on the optimum position of grains within a cutting segment.

Real cutting experiments in natural stone have shown that the parameter tangential grain distance a has an influence on the cutting forces and is therefore limited for the use of setting up a wear stock. It was also found that the radial wear is predicted by the radial grain distance c. Compared to tools with stochastically distributed diamond grains a smoothening of the wear rate is possible due to the same amount of diamond grains in every height of the cut-off-grinding segments.

In future work the dependencies of the parameters among one another will be analysed by changing different grain distances at the same time using a design-of-experiments method (DoE). It is believed that combined with grain displacements in each direction a model can be derived for the calculation of optimized grain pattern for a given application by work material, tool dimension and possible process parameters. With the experimental results shown, only two layers of diamond grains were used. The segments consist of nine to twelve layers, depending on the pattern. Future experiments should focus on the process stability regarding the wear behaviour and the process force development, when more material is cut.

REFERENCES

[1] Park, H, 2005, ARIX – a major advance in diamond segment design, Ind. Diamond Rev. 65, pp. 40-42

[2] Weber, G, Weiss, C, Idler, R, 2011, DiaSet: A giant playground for the engineer or a superior differentiator for the salesman?, Proceedings of the 1st International Conference on Stone and Concrete Machining – ICSCM, pp. 190-196

[3] Aurich, JC, Herzenstiel, P, Sudermann, H, Magg, T, 2008, High performance dry grinding using a grinding wheel with a defined grain pattern, CIRP Annals – Manufacturing Technology 57, pp. 357-362.

[4] Pinto, FW, Vargas, GE, Wegener, K, 2008, Simulation for optimizing grain pattern on Engineered Grinding Tools, CIRP Annals – Manufacturing Technology 57, pp. 353-356

[5] Sung, C-M, 1999, Brazed diamond grid: a revolutionary design for diamond saws, Diamond and Related Materials 8, pp. 1540–1543

[6] Denkena, B, Köhler, J, Seiffert, F, Ermisch, A, 2011, Trennschleifen von Beton und Stahlbeton – Geometrisch bestimmte Schneidstoffanordnung auf Trennschleifscheiben, dihw - Diamant Hochleistungswerkzeuge, 3 (2011), pp. 38-43

[7] Denkena, B, Köhler, J, Seiffert, F, 2011 Deterministic Grain Distribution on Cut-Off Grinding Wheels, Proceedings of the 1st International Conference on Stone and Concrete Machining – ICSCM, pp. 99-104.

[8] Denkena, B, Köhler, J, Seiffert, F, 2011, Stahlbetonbearbeitung mit gesetzten Trennschleifwerkzeugen – Ritzuntersuchungen zu Materialtrennmechanismen, wt Werkstattstechnik online, Issue 6, pp. 398-406

[9] Konstanty, J, 2013, Sintered diamond tools: trends, challenges and prospects, Powder Metallurgy, Vol. 56, Nr. 3, pp. 184-188

[10] Denkena, B, Köhler, J, Ermisch, A, 2013, Material Removal Simulation of Wire Cutting Processes for an adapted Tool Design, Proceedings of the 2nd International Conference on Stone and Concrete Machining – ICSCM, pp. 119-124

[11] Glatzel, T, 2004, Trennschleifen von Granit mit dünnen Werkzeugen, Dr.-Ing. Thesis, Universität Hannover

ACKNOWLEDGEMENT

Session 6

Evaluation of the operational costs for chain saw cutting

Dr Ir Fabrice DAGRAIN
Stone Assistance sprl, 4317 Viemme, Belgium
fabrice.dagrain@stoneassistance.be

ABSTRACT

Chain saw cutting technology has been widely described by the author those last years in several scientific and technical articles. The main problems encountered on chain saw machines have been described. Several experimental approaches have been developed in laboratory to better understand the stone cutting mechanisms and to improve the efficiency of the machines. New cutting designs have been developed increasing the performances of the machines. Monitoring systems have been introduced on the machines to follow their performances while operating in quarries. Even if the technology is well described, very few information can be found on the costs of the technique.

This paper overcomes this lack of information and introduces a rigorous methodology to estimate the real costs of the sawing operations with chain saw machines. The technological parameters introduced and described in the literature have been implemented in a cost evaluation program developed by Stone Assistance, in order to evaluate their influence on the chain saw operational costs. The objective of the paper is to present some interesting results that should be considered by the engineers or operators working with chain saw machines, and that could help them to manage the operations with chain saw machines in quarries.

KEYWORDS

Chain saw, tools, optimization, efficiency, operational cost, profitability

INTRODUCTION

Stone Assistance is working since several years on the improvement of the sawing technique with chain saw machines in quarries. The technology has been revisited thanks to a research program undergone at University of Mons in collaboration with PMDS sa, a manufacturer of diamond tools for chain saw machines, and granted by the Walloon Region.

At the very beginning of the project started a serious discussion with operators regarding the profitability of the chain saw process. Two different points of view were identified on the evaluation of the operational costs of the chain saw technique. From an operational point of view, the purchasing cost of the tools was crucial; from the R&D point of view the cutting speed of the tools was fundamental. Those points of view raised a serious question: do we have to keep using lower price tools, or is it more profitable to use more expensive tools? To answer this question, a complete research program has been performed in order to collect any important information that would help answering the question.

The research program has been focused on the understanding of the cutting mechanisms and improvement of the sawing technique. An experimental approach has been followed in laboratory to better understand the stone cutting mechanisms [1]. Based on the experimental results obtained in laboratory, a new cutting typology has been designed in order to increase the performances of the machines (higher production rate, increase of the tool life span) [2]. The new cutting concept has then been validated in quarry thanks to a monitoring system that has been developed to record cutting parameters while sawing and to evaluate the performances of the machine [3]. An evaluation method of the life span of the chain links and tools has also been developed [4] [5].

Many different types of information have been collected in order to determine the most realistic cost of the sawing operations with chain saw machines. And finally, a simple cost evaluation program has been developed in order to compute the operational costs.

1. THE COST EVALUATION PROGRAM

Advanced cost evaluation methods are rarely used in the stone industry to accurately determine economic gain of using high technology tools. Most of the stone processors evaluate the performances of their tools using a basic formula:

$$\frac{\text{Tool cost}}{\text{m}^2 \text{ of material cut}} \tag{1}$$

Unfortunately, such formula does not take into account several hidden costs related to the efficiency of the tools, or the cutting speed of the machines.

The cost evaluation program developed by Stone Assistance is based on a classical cost evaluation methodology for heavy construction equipments [6]. For instance, the cost computation methodology in use in the Caterpillar® Fleet Production and Cost analysis software [7] has been adapted for chain saw machines.

The program takes into account a large number of characteristics of the chain saw machines (purchase price, estimated residual resale value, depreciation period, electrical power, etc.), and integrates the performance parameters measured while operating (chain speed, cutting speed, working efficiency, staff efficiency, etc.) or other information related to machine maintenance (tools and chain life span, maintenance frequency, etc.). Those data enable to assess both the fixed costs (depreciation, interest on loans, equipment insurance, various taxes...) and the variable costs (chains, tools, other consumables, energy consumption, and labor).

Note that the program currently incorporates the main economic parameters, but the calculation model could be very easily adapted to take into account any other specific parameters. We will not detail the all calculation method in this article. However, anyone interested in more information, or in a practical implementation for his quarry or processing plant should contact the author.

The main objective of such a method of assessment is to get a correct evaluation of the true operational costs which should allow the process engineer to quantify the potential benefits of strategic decisions to optimize the stone processing (modification of the technical parameters, use of high-tech tools, replacement of a machine, etc). On another hand, the method also gives the opportunity to the stone processors to size the fleet of machines to achieve the annual quarry and plant productivity. The use of very similar concepts already allowed significant improvements of sawing techniques for plant processing [8].

2. THEORY OF PRODUCTIVITY

The theory of productivity is not recent in process engineering. Coromant-Sandvik, for example, is one of the main instigators of this theory for metal machining. It is well known in this industry, and in metal turning for example, that the cost of the cutting tools represents only a very small part (on the order of 3%) of total production cost. The major gains in productivity and on the operational cost are obtained by adapting the working methods. <u>Choosing the right tool and applying it correctly</u> allows, in metal turning, to increase significantly the productivity and to bring down the operational cost by 10 to 15% [9].

The theory of productivity should also be applied to stone processing. From the experience in metal turning, it can be expected that the technological parameters of the tools, such as cutting speed and depth of cut, are variables that have the largest impact on the improvement of the productivity and on the reduction of the costs. The paper will try to quantify their influence on the operational cost.

3. INFLUENCE OF SEVERAL VARIABLES ON THE OPERATIONAL COST

The objective of this study is to demonstrate the importance of some variables of the cost evaluation program and to illustrate the range of possible gains that could be reached by modifying them. For each study case, the operational cost will be divided in six costs categories: fixed costs, chain costs, tool costs, consumable costs, energy costs, and man power costs.

In any case, the main variables will be listed in front of the cost diagrams for each study case. The stone considered is the Belgian Blue Limestone which has been studied in the research program.

By reason of discretion, the costs provided by the evaluation program will be normalized by the maximum one of each study case.

3.1 CUTTING SPEED

The cutting speed of the chain saw machine ($v_{machine}$) depends on the chain speed (v_{chain}), the depth of cut (d), the length of the cutting typology (*n.step*, with *n* the number of cutter holders in the configuration and *step* the distance between successive cutter holders), and the inclination of the arm of the machine (α) [1]:

$$v_{machine} = v_{chain} \frac{d}{n \cdot step} \sin \alpha \qquad (2)$$

The increase of the cutting speed of the machine can be obtained by increasing either the depth of cut or the chain speed, or by decreasing the length of the cutting typology. No detailed discussion will be done in this article on the change of the different variables that may affect the cutting speed of the machine. Just remind that the depth of cut results from the thrust applied by the arm of the machine on the stone to be cut and the length of the typology is a characteristic of the cutting design.

The example presented in Fig.1 illustrates the influence, on the operational cost, of a change in cutting speed from 1 to 5 cm/min. At any other settings kept constant, the only variation of the cutting speed enables to significantly reduce the total operational cost. Cutting speed has a direct effect on the fixed costs of the machine, the energy and labor costs. This example shows the interest to increase cutting speed of the machine regardless of the design of tools used. More than 60 % of cost reduction may be expected in the example.

Note that if the rotational speed of the chain has been correctly set up, the cutting speed has no immediate effect on the tools and chain costs. But a bad choice of rotational speed of the chain will have a non-negligible consequence on the tool life span. Several rotational speeds are indeed critical as they generate vibrations that may be responsible for the breakage of tools. However, we do not consider this parameter in this example.
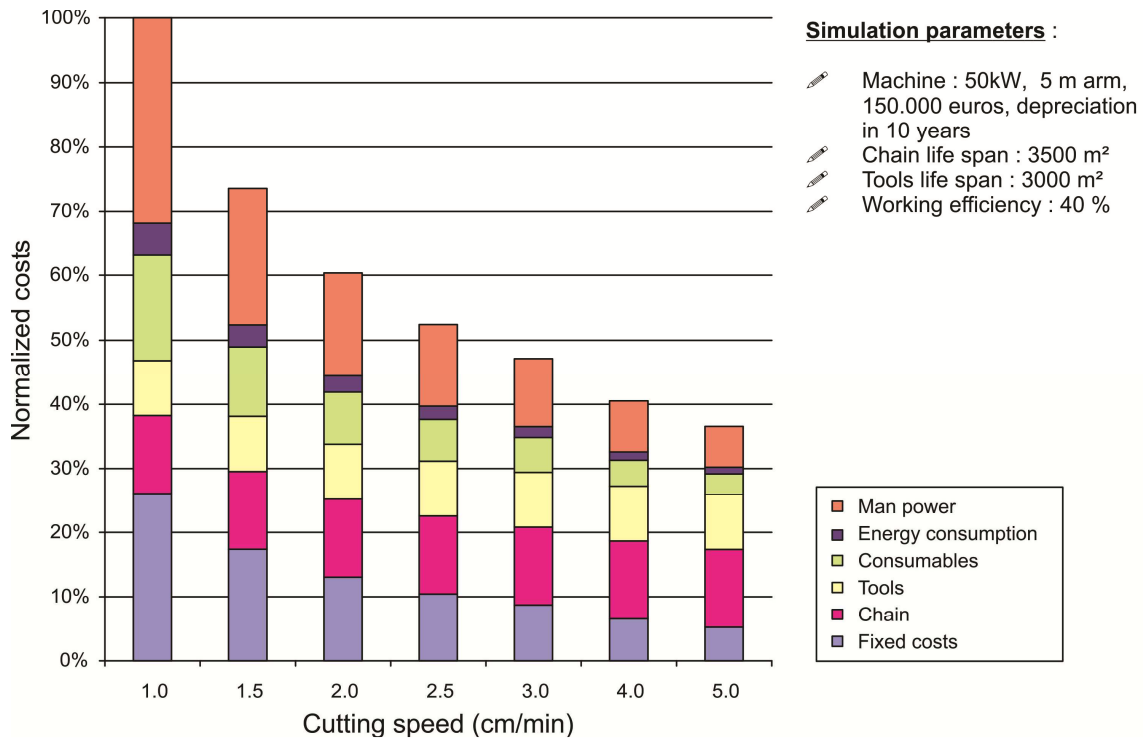
Fig.1 : Example of the influence of the cutting speed of the machine for the same cutting configuration, and any other setting kept constant.

3.2   WORKING EFFICIENCY

The working efficiency (η_w) is a performance parameter which reflects the amount of time lost in machine immobilization due for example to breakdowns and repairs, or to any other organizational reasons. These time-outs are therefore affecting this performance:

$$\eta_w = \frac{\text{effective working time}}{\text{theoretical working time}} = 1 - \frac{\text{time-outs}}{\text{theoretical working time}} \qquad (3)$$

Whatever the industrial sector, it is not uncommon that machines operators spend more than 20% of their time to search or wait for their tools. This is not without consequence on the productivity and the operational cost.

The site-specific organizational aspects (working methods, preventive maintenance or not, etc.) are not the topics of this paper and will not be discussed. Keep in mind that the tool selection will have consequences on the final process organization. A non suitable cutting tool choice can be responsible for breakdowns that require handling and immobilization of the machines.

From the monitoring of the machine [3], the working efficiency of chain saw machines have been estimated in a first approximation to 45%. The example presented in Figure 5 illustrates the influence, on the operational cost, of the increase of the working efficiency of the machine from 30 to 60 %.

The benefits are mainly obtained on the fixed costs. Depending on the initial and final working efficiency, the operational cost may decrease up to nearly 20 %.
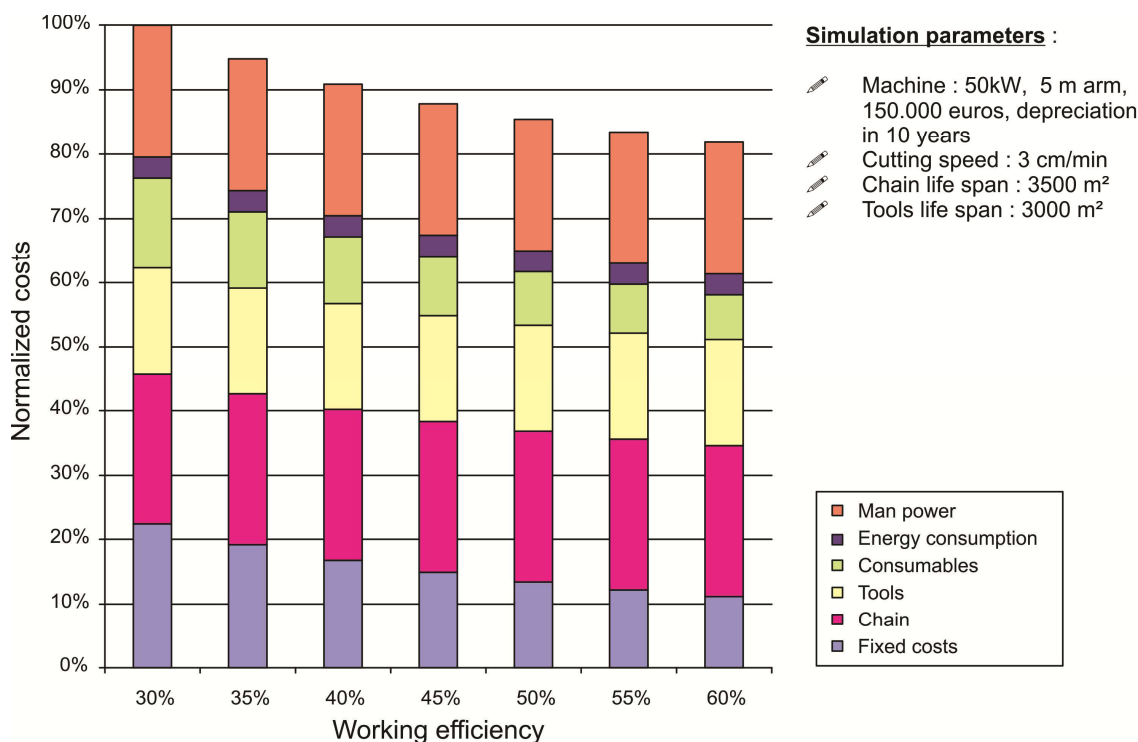
Fig.2 : Example of the influence of the working efficiency for the same cutting configuration, and any other setting kept constant.

3.3   LIFE SPAN OF THE TOOLS AND CHAIN LINKS

The tools and chain links life spans are not intrinsic characteristics. They strongly depend on the conditions of use of the machines. For instance, a non appropriate rotational speed of the chain can cause vibrations of the machine and tool breakage [3]. A bad force distribution on the cutting configuration can generate fatigue phenomena leading to the ruin of the chain links [4].

The example presented in Fig.3 shows the influence, on operational cost, of the increase of the life span of the chain from 3000 to 6000 m². In the example, the increase of chain links life span allows to reduce the operational cost up to 15%.

The example presented in Fig.4 illustrates the influence of the increase of the tools life span from 3000 to 6000 m². In this example, the reduction the operational is around 10%.
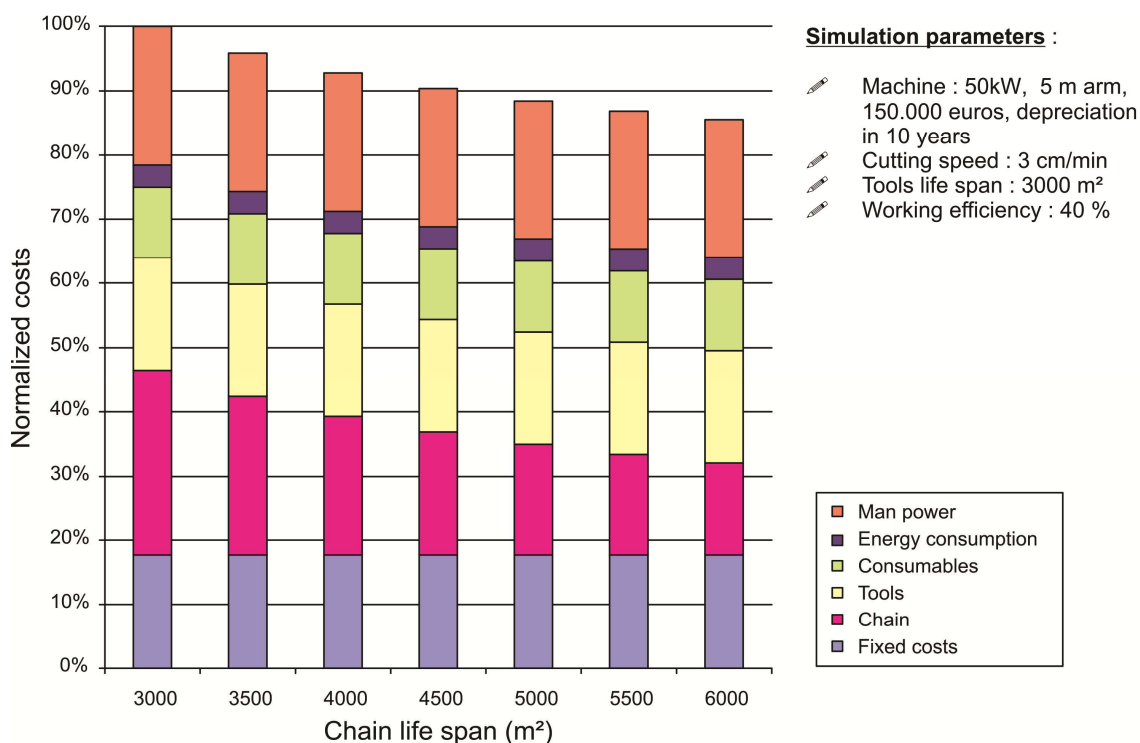
Fig.3 : Example of the influence of the chain links life span for the same cutting configuration, and any other setting kept constant.
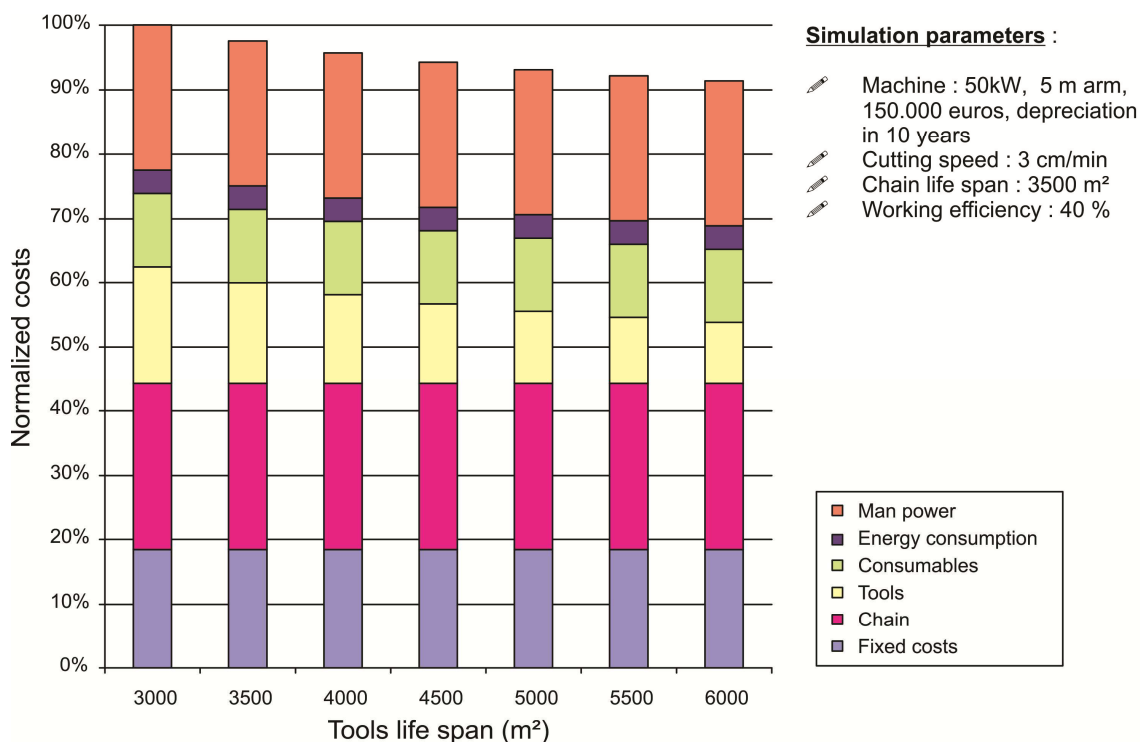

Fig.4 : Example of the influence of the tool life span for the same cutting configuration, and any other settings kept constant.

3.4   TOOL PRICE

The tool price is of course a variable that influences directly the operational cost. And it is generally the variable that will be taken into account when buying the tools.

The example presented in Fig.5 illustrates the influence, on the operational costs, of a price reduction from the full price to 60% reduction. The reduction of the operational cost is less than 10%.
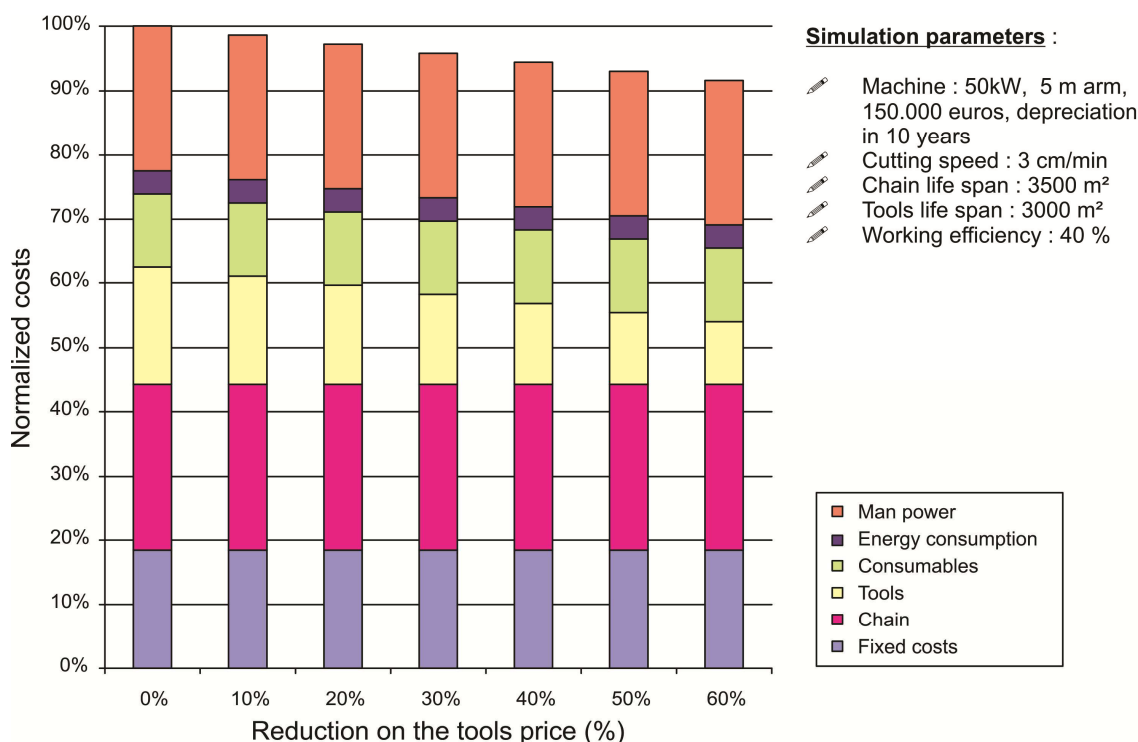

Simulation parameters :

✐ Machine : 50kW, 5 m arm, 150.000 euros, depreciation in 10 years
✐ Cutting speed : 3 cm/min
✐ Chain life span : 3500 m²
✐ Tools life span : 3000 m²
✐ Working efficiency : 40 %

Fig.5 : Example of the influence tool price for the same cutting configuration, and any other setting kept constant.

4.   APPLICATION OF THE COST EVALUATION PROGRAM

Several cutting configurations have been studied in the previous articles (see Fig.6) :

1. a configuration with 9.4 mm width squared cutters,
2. a configuration with 8 mm diameter circular cutters,
3. a configuration with 13 mm diameter circular cutters,
4. the new concave cutting configuration with 10 mm diameter circular cutters.

Most of the technical parameters and economic variables have been measured or determined and introduced in the evaluation program.

Fig.6 presents the different operational costs estimated with the cost evaluation program for the different cutting configurations studied. The last simulation corresponds to the new concave configuration working at the maximum chain speed without generating vibration.

Simulation parameters :

- Machine : 50kW, 5 m arm, 150.000 euros, depreciation in 10 years
- Working efficiency : 40 %
- Chain speed (RPM) : (1) 40 - (2) 40 - (3) 40 - (4) 40 - (5) 70
- Cutting speed (cm/min) : (1) 3.2 - (2) 1.8 - (3) 2.3 - (4) 3.5 - (5) 10
- Chain life span (m²) : (1) 3500 - (2) 5000 - (3) 2800 - (4) 4500 - (5) 4500
- Tools life span (m²) : (1) 3500 - (2) 7000 - (3) 6000 - (4) 4500 - (5) 4500
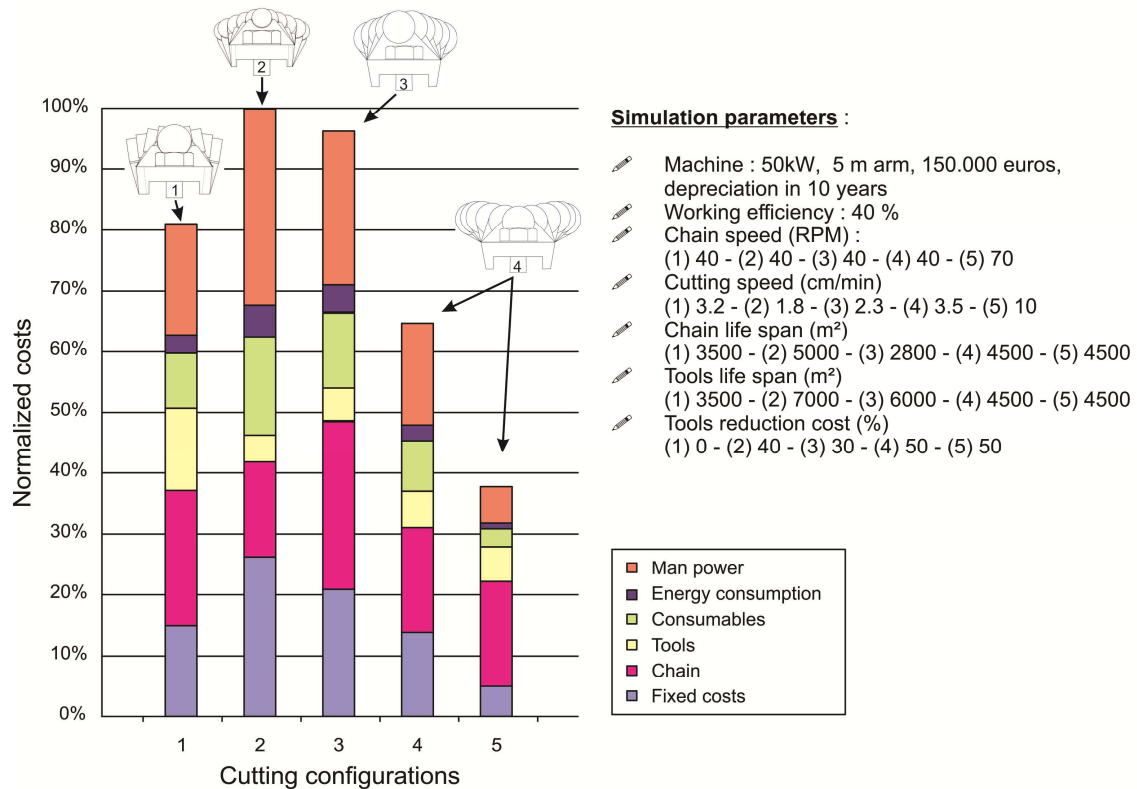- Tools reduction cost (%) : (1) 0 - (2) 40 - (3) 30 - (4) 50 - (5) 50

Fig.6 : Comparison of the three cutting configurations in use in the Belgian Blue Limestone quarries (1,2 and 3), with the new concave configuration developed (4) and the same configuration working with the maximum chain speed of the machine without vibration (5).

Based on the different data, the fleet of machines necessary to reach the productivity of a quarry has been defined. Fig.7 illustrates the number of identical machines that should be needed for an annual quarry productivity of 40.000 m³, actual volume extracted in the Blue Limestone Quarry which has been studied.

It can be clearly observed that the tools choice and its final performances has an effect on the operational cost and the amount of machines necessary to achieve the productivity.

5.   CONCLUSION

The research project on chain saw machine technology has been initiated in order to understand why problems were appearing in hard stone cutting. The experience acquired during the project allows the design of an innovative cutting typology. The use of a cost evaluation program specially developed for chain saw machine in combination with the experimental approach in laboratory and the monitoring of the machines in quarry gives the opportunity to stone processors to evaluate the benefits of using new high-tech tools to optimize chain sawing operations.

From the evaluation of several variables implemented in the program, it has been shown that the cutting speed of the machine is the main variable which allows significant decrease of the operational cost. The development of new efficient cutting configuration based on a scientific approach allows the increase of the working efficiency, and the increase of the tools and links life spans which finally also induces additional decrease of the operational cost. The effect of the tool price reduction on the operational cost stays marginal in comparison to what can be expected from the other variables. Evaluating the performances of tools based only on their direct cost should be disregarded. However, the cutting tool must be correctly chosen based on the expected cutting speed, the life span of tools and machine parts, or the energy consumption.
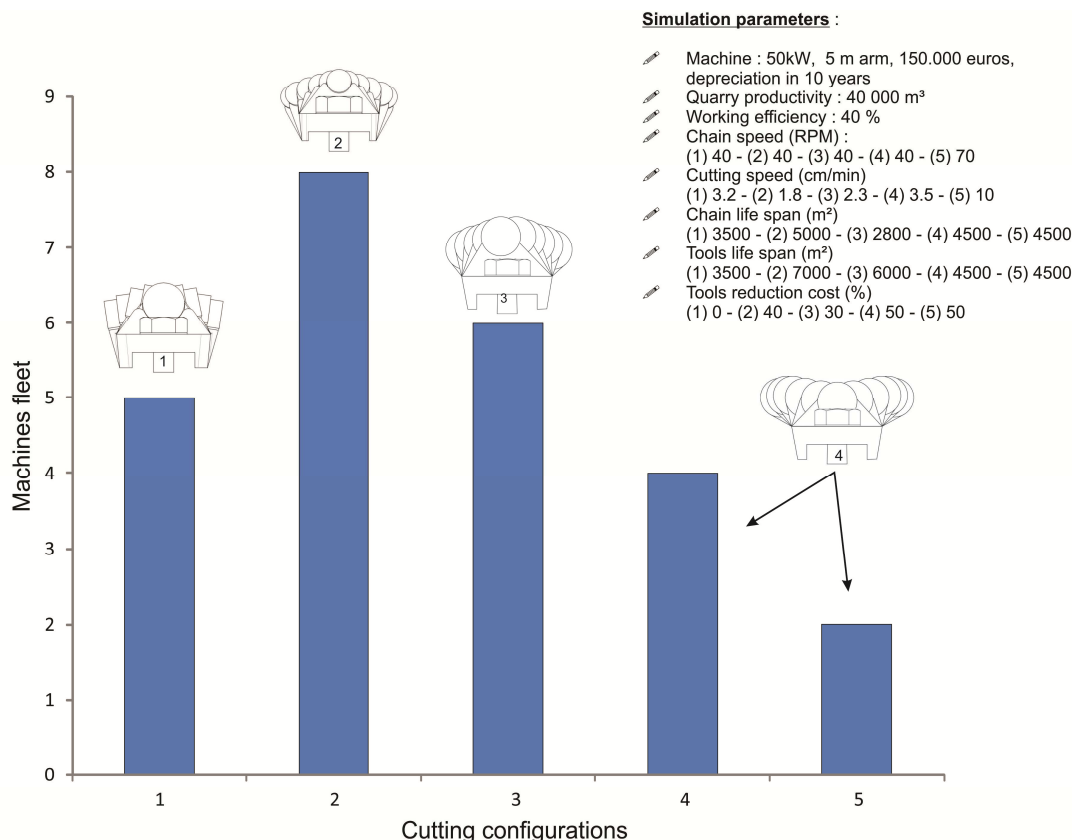
Simulation parameters :

- Machine : 50kW, 5 m arm, 150.000 euros, depreciation in 10 years
- Quarry productivity : 40 000 m³
- Working efficiency : 40 %
- Chain speed (RPM) :
  (1) 40 - (2) 40 - (3) 40 - (4) 40 - (5) 70
- Cutting speed (cm/min)
  (1) 3.2 - (2) 1.8 - (3) 2.3 - (4) 3.5 - (5) 10
- Chain life span (m²)
  (1) 3500 - (2) 5000 - (3) 2800 - (4) 4500 - (5) 4500
- Tools life span (m²)
  (1) 3500 - (2) 7000 - (3) 6000 - (4) 4500 - (5) 4500
- Tools reduction cost (%)
  (1) 0 - (2) 40 - (3) 30 - (4) 50 - (5) 50

Fig.7 : Evaluation of the machine fleet necessary to reach a productivity of 40 000 m³ with identical machines for the different cutting configurations evaluated.

The experimental approach in laboratory and the continuous monitoring of the machine combined with an efficient cost evaluation program is an innovative methodology that helps increasing the productivity and reducing the operational cost in the stone industry. Their use will bring additional innovations. Working methods and tasks organization will also allow additional gains in terms of working efficiency.

REFERENCES

[1] F. Dagrain. Understanding stone cutting mechanisms for the design of new cutting tools sequences and the cutting optimization of chain saw machines in Belgian Blue Stone quarries. *Diamante Applicazioni & Tecnologia*, n°66, Septembre 2011, pp 54-67.

[2] F. Dagrain, P. Marchandise, S. Desmette. Design of a new cutting configuration to optimize the cutting operations of chain saw machines in quarries. *Diamante Applicazioni & Tecnologia*, n°67, December 2011, pp 51-58.

[3] F. Dagrain, P. Marchandise, P. Brux. Monitoring of chain saw machines to follow their performances in quarries. *Diamante Applicazioni & Tecnologia*, n°69, June 2012, pp 43-49.

[4] F. Dagrain, J.Noël. Assessment of the state of stress in the links of chain saw machines. *Diamante Applicazioni & Tecnologia*, Volume 71, January 2013, pp 73-78.

[5] F. Dagrain. The Weartool project : Characterization of the wear resistance of cutting tools for application on chain saw machines. *Diamante Applicazioni & Tecnologia*, Volume 74, Septembre 2013, pp 69-78.

[6] A. Gabay, J. Zemp. *Les engins mécaniques de chantier : excavation, transport, remblayage, damage équipement accessoire, organisation.* 3 éd. - Paris : Bordas, 1971. – 390 p.

[7] Caterpillar Dealer Channel Systems (1996). *Fleet Production & Cost Analysis*. Caterpillar. U.S.A.

[8] Diamond Innovations. Benefits of high grade Diamond. Advanced cost evaluation program for stone processing, 2004.

[9] Sandvik
http://www2.coromant.sandvik.com/coromant/products/steelturning/turn_prod_theory.htm

Study of Influence of Natural Stone Surface Roughness on Wetting Characteristics for the Application of Liquid Coating Systems and on the Adhesive Strength of Thin Epoxy Coatings Over Natural Stone Substrates

Alfonso Cortes Izurdiaga[a], Antonio Jose Fernandez Barbero[b], Benjamin Sierra Martin[b], Ana de la Cruz González[a]

[a] Fundación Centro Tecnologico Andaluz de Piedra, Ctra. Olula – Macael Km 1,7, 04867 Macael (Almería), Spain
acizurdiaga@ctap.es, anacruz@ctap.es
[b] Universidad de Almeria, Ctra. Sacramento, s/n, 04120 La Cañada de San Urbano, Almería, Spain
afernand@ual.es, bsierra@ual.es

ABSTRACT

In this work, the influence of surface roughness of a natural stone material on two important parameters for the performance of the industrial coating process will be studied. The selected parameters are contact liquid drop angle, to assess the best conditions for the application of the liquid coatings, and the adhesion strength, to assess the best coating performance once the coating has been applied and dried. These two parameters are quantitative and may allow the comparison between different case studies. The study of influence will be addressed in this work from a practical point of view, so that results can be applied in a current industrial process for optimization purposes. The obtained conclusions are expected to be used to propose recommendations for the stone industry to guarantee the performances of the coating systems applied.

KEYWORDS

Natural stone, surface engineering, coatings, adhesion strength, wetting contact angle, roughness.

INTRODUCTION

In the current Natural Stone industrial sector, applying polymeric resins over the surface of natural stone slabs has become a very common task. The main objectives of the resin treatment are, on the one hand, the filling and sealing of natural cavities and, on the other hand, the consolidation of the stone surface to improve its cohesion and avoid problems of surface brokerage. To improve the cohesive effect, the resins are often applied on the back side of the slabs along with a mesh of fiberglass. Many stone materials are resin treated on both their sides (face side and reverse side). Out of many existing chemical families that could be used for this purpose, polyester and epoxy resin are the preferred ones in the natural stone industry [1].

However, in some circumstances these resins present adhesive failures and it is difficult to identify if the problem is derived from an incorrect industrial application, a non optimal state of the initial substrate (surface dirt, moisture and roughness), ageing effects due to environmental factors, an insufficient curing process of the resin or even because the chosen resin is not enough physico – chemically compatible with the natural stone substrate and so a limited adhesion should be expected.

Although some experimental works have been performed to study the mechanical improvements obtained by natural stone materials reinforced by different resin systems, reference [2] can be taken as an example, there is a lack of information in literature about stone surface characteristics and their influence in adhesion processes.

It has been experimentally demonstrated that the adhesion strength of a coating, and therefore the substrate – coating system stability, is influenced not only by the mechanical properties of the

system under test, but also by the nature and preparation of the substrate, the method of coating application, the drying conditions of the coating, the temperature, the humidity and other factors as e.g. the type of the test instrument used [3].

In this work, the influence of surface roughness of a natural stone material on two important parameters for the performance of the industrial coating process will be studied. The selected parameters are the contact liquid drop angle and the adhesion strength.

The contact angle is a measurable physical property to assess the wetting process of a liquid on a substrate. For a liquid to be used as a coating system, a high wettability is recommended, implying that both the substrate and the coating are compatible from a Physicochemical point of view. High wettability systems are those in which contact angle is below 90 degrees, being the ideal perfect wetting state at contact angles of 0 degress. The contact angle is, therefore, a quantitative measurement that can be used to compare different case studies. The physical behavior can also be affected by microscopic surface roughness that can have an effect on localized contact angles. The combinations of contact angle measurements, surface roughness and surface chemical analysis can be used to unambiguously assess the affects of manufacturing process modification and formulation changes improving product performance or reliability of in-line processes such as paint coating, laminate or adhesive systems. Comparing different liquids, the contact angle measurement instantly shows if one liquid 'wets' a surface better than another. In the same way, if the liquid is maintained in the tests, the influence of the substrate can also be studied, which will be the chosen procedure in this experimental work. Surface homogeneity can also be demonstrated using this method. If several drops of known liquid are dispensed onto a surface, differences in contact angles will indicate the degree of inhomogeneity of the surface [4], [5].

On the other hand, the adhesion between the coating, once it has been dried and cured, and the substrate can be taken as a quantitative measurement of the system global stability. The adhesion strength of a coating can be determined by a pull-off test which measures the mechanical resistance of the coating to separation from the substrate when a perpendicular tensile force is applied. The obtained adhesive strength along with the identification of the nature of the adhesive fracture (cohesive or adhesive failure) are the main identifiers of the mentioned coated system stability [6].

There are experimental works in which the influence of roughness has been demonstrated on the adhesive strength of a coating system [7]. That influence appears from a minimum value of surface roughness and makes adhesion strength increase with the increase of roughness surface until a maximum obtainable adhesive strength with a practical rough substrate is reached. One of the objectives of this experimental work is to validate if that effect occurs in the selected system (natural stone substrate and epoxy system) with the different surface roughness values practically attainable in an industrial natural stone polishing line with different abrasive sequences.

1. MATERIALS AND EXPERIMENTAL PROCEDURES

The study will be performed over different samples of a single natural stone material. The chosen material is the limestone known as Crema Marfil, extracted in the Spanish region of Novelda, in the province of Alicante. The choice of this material is justified under the fact that it is a very popular natural stone material at international level and that almost all the material that is processed and elaborated for commercial use in the form of tiles and slabs is treated with chemical resins (polyester and / or epoxy) on both material sides (face side and back side) in order to consolidate the material, to reinforce it and to avoid it being split into small fragments in case of breakage. From the petrography point of view, Crema Marfil is a fossiliferous limestone (bioesparite or grainstone), mainly composed by calcite (99%) but also containing opaques and clay minerals. Its structure is homogeneous and there is evidence of the presence of stylolites, which are serrated surfaces within the rock mass at which mineral material has been removed by pressure dissolution, in a process that decreases the total volume of the rock. The texture of the rock is mainly composed by fossils of protozoa foraminifera, on the microscale and the macroscale, presenting also fragments of red algae and echinoderms.

The chosen coating system is a two component epoxy resin from DOW trade house. The system is composed by a very pure Bisphenol A resin and an aminic hardener in a ratio of 2:1. The fresh mixture has a density of 1.12 g/cm3 and a viscosity of 3,000 cP at 25ºC. The potlife of the mixture is approximately 10 min, which was determined in the laboratory.

Stone samples with different grades of roughness surfaces have been obtained by the application of different sequences of abrasives. In this sense, an industrial polishing line for natural stone with sequential calibrating and polishing heads was used. Eight different samples have been considered, in the form of (30 x 30 x 2) cm tiles, which have been extracted at different points of the polishing line, implying an increasing sequence of the abrasive grains applied (following the FEPA Nomenclature). In table 1, the abrasive sequence is shown and also the points of the polishing line from where each tile was extracted. As mentioned before, the complete sequence goes from coarse to fine abrasives, so that the first abrasives are very aggressive and have the function of grinding and leveling the tiles thickness and the last abrasives remove much less surface material and have the function of generating a polished surface by closing surface porosity. These eight samples represent the different surface roughness states for the natural stone material surface. Each sample was extracted at the output of the abrasive head with which it is related in the table and is numbered according to the sequence of abrasives with which it has been treated. For example, sample 1 was extracted at the output of the first polishing head, implying an initial calibration and a posterior treatment with abrasives of grain 60. In the same way, sample 8 was extracted at the end of the line, implying the treatment with a complete sequence of calibration and polishing heads and a very smooth and glossy surface finish. The polishing line feed rate used was of 1.1 m/min.

Table 1: Abrasive sequence and points of extraction of the samples

Head number	Grain size (FEPA Nomenclature)	Extracted sample
3 calibration heads	-	-
1	60	8
2	80	-
3	120	7
4	220	6
5	320	5
6	340	-
7	400	4
8	600	3
9	800	2
10	Hard abrasive for gloss	-
11	Soft abrasive for gloss	-
12	Cleaning head	1

Each selected tile was cut into smaller samples of (7.5 x 7.5 x 2) cm, to generate the laboratory specimens, and a set of 6 random samples out of a total of 16 were selected, meeting the statistical assumptions proposed in the testing procedures. This composes a total of 8 sets, with 6 specimens in each set.

The complete preparation, coating application and test sequence was applied over all the specimens to guarantee a direct correspondence of the results. The used methodological sequence was as follows:

i.   Sample cleaning and surface preparation. The cleaning process was composed by pressured air exposition, a 15 min bath in acetone with ultrasound followed by drying in an oven for 24 h.

ii. Contact angle determination. The chosen liquid for wetting tests was distilled water, instead of the final coating liquid. This decision was made upon the fact that the epoxy coating liquid properties, once the two components are mixed, are highly time dependent and also that the epoxy could leave residues on the surface of the samples. The proposed contact angle test can be considered as an indicator of how surface energy is affected by roughness when a polar liquid drop is applied on the samples surface, but not to determine the real contact angle existing between the samples and the liquid coating resin. The contact angle determination was performed using the standard procedure defined in ASTM D 5725 – 99 [8], determining the contact angle at three times from the drop application: 0.1, 1 and 10s. The test equipment used for conducting angle measurements was an OCA 20LH from Data Physics. One drop was evaluated for each sample and for each set of samples the average values and standard deviations were calculated.
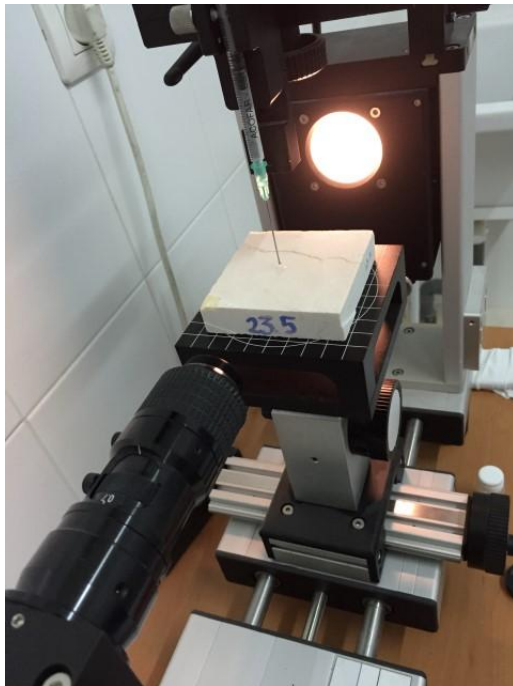
Fig. 1 and 2: Drop Angle measurement equipment (left) and adhesion strength measurement equipment and dolly – sample assembly (right).

iii. Application of coating system and dollies. A total mass of approximately 1g was homogenously manually applied on the surface of the samples using a laboratory rod, implying a coating of 0.15 mm thickness. The samples were previously dried in an oven at 70ºC for a period of 18 h and allowed to achieve an equilibrium temperature in laboratory for 5 h. The coatings were applied at laboratory conditions, complying with the requirements of the standard procedure. Once the coating system was applied, the samples were cured for a minimum period of 24 h before applying the dollies for the adhesive test. According to the adhesive test procedure, 2 cm dollies were glued on the coating surface using the same epoxy resin of the coating system and the minimum possible quantity (around 0.07 g). The obtained assembly was left for resin curing an additional period of 48 hours at laboratory conditions (25ºC and 50% RH).

iv. Determination of the coating adhesion strength by the pull off test. The used procedure for determining the coating adhesion strength over the substrate was the standard procedure defined in ISO 4624-2003 [6] using cylindrical dollies with 2 cm diameter. The used equipment was a portable electronic adhesion tester KN-10 from Neurtek. As the coating thickness was 0.15 mm, the coating was not cut around the dolly diameter. The adhesion strength was determined for each sample and the mean value, the range and standard deviation were

calculated for each set of samples. The nature of the fracture was estimated by means of percentage areas using the following three categories:

- A: cohesive failure of the substrate.
- A/B: adhesive failure between the substrate and the coating system.
- Y/Z: adhesive failure between adhesive and dolly.

No adhesive cohesive failure was identified. Samples with a 100% Y/Z adhesive failure were discarded for statistical analysis, considering that the obtained values were not representative for the coating adhesion strength. For each set of samples the average value of the percentage fracture areas was also calculated. This is not indicated in the standard but was considered as a quantitative way of studying the variation on the type of fracture from one set of samples to the others.

Fig. 3 and 4: Specimens showing a 100% adhesive failure (A/B) on the left and a 100 % substrate cohesive failure (A) on the right.

2. RESULTS

In the following chart the final statistical parameters (mean and standard deviation) of the obtained experimental angles for the distilled water drops at 0.1, 1 and 10 s over each set of samples are shown:

Table 2: Statistical results for contact angle.

SAMPLE 1		
Time [s]	Mean angle [º]	SD Angle [º]
0.1	69.4	6.2
1	63.5	7.2
10	58.8	4.8

SAMPLE 2		
Time [s]	Mean angle [º]	SD Angle [º]
0.1	63.2	7.7
1	55.6	5.0
10	53.4	3.8

SAMPLE 3		
Time [s]	Mean angle [º]	SD Angle [º]
0.1	72.2	15.3
1	68.6	16.1
10	65.7	16.4

SAMPLE 4		
Time [s]	Mean angle [º]	SD Angle [º]
0.1	66.0	14.3
1	59.3	10.2
10	56.3	9.2

SAMPLE 5		
Time [s]	Mean angle [º]	SD Angle [º]
0.1	62.1	17.5
1	55.0	11.0
10	51.2	9.1

SAMPLE 6		
Time [s]	Mean angle [º]	SD Angle [º]
0.1	74.7	12.1
1	62.5	7.0
10	55.5	7.4

SAMPLE 7		
Time [s]	Mean angle [º]	SD Angle [º]
0.1	55.5	8.6
1	48.6	6.2
10	43.5	6.0

SAMPLE 8		
Time [s]	Mean angle [º]	SD Angle [º]
0.1	89.2	29.4
1	77.4	23.0
10	66.5	16.3

The statistical graphs representative of the six specimens for each sample, summarizing all the data collected, can be also shown:
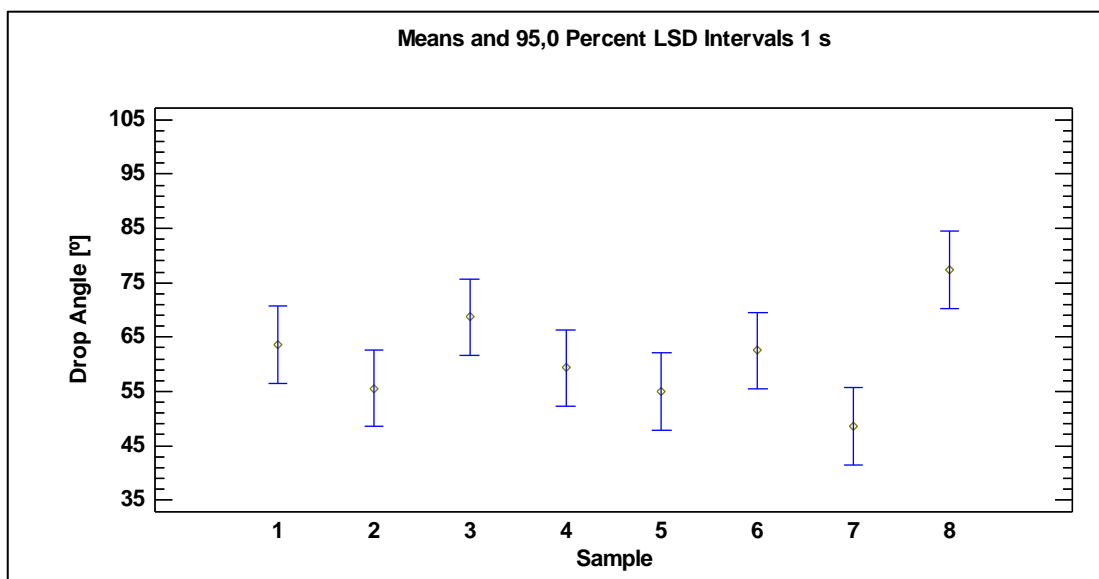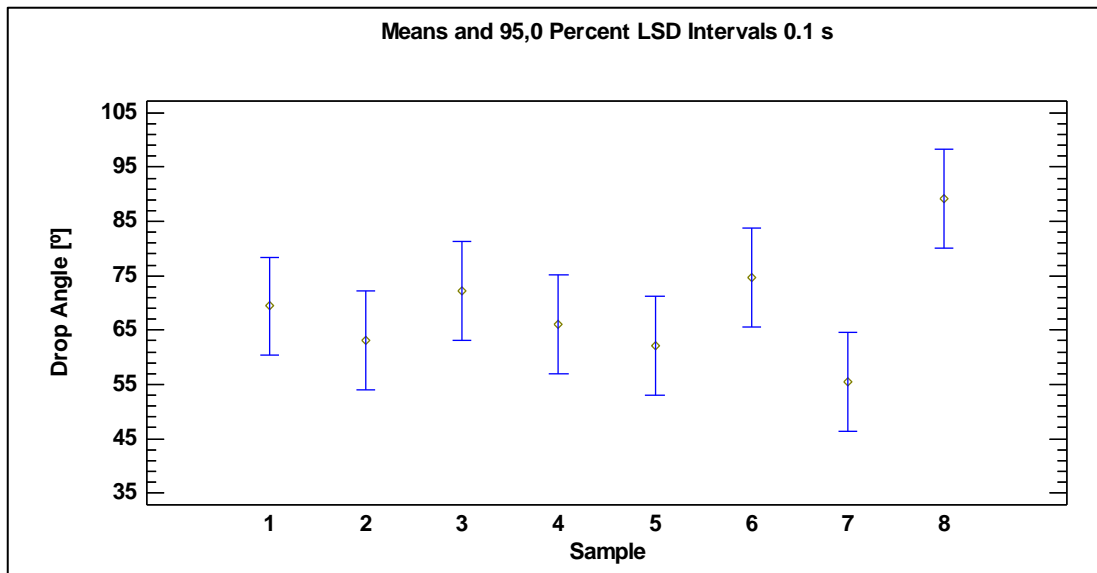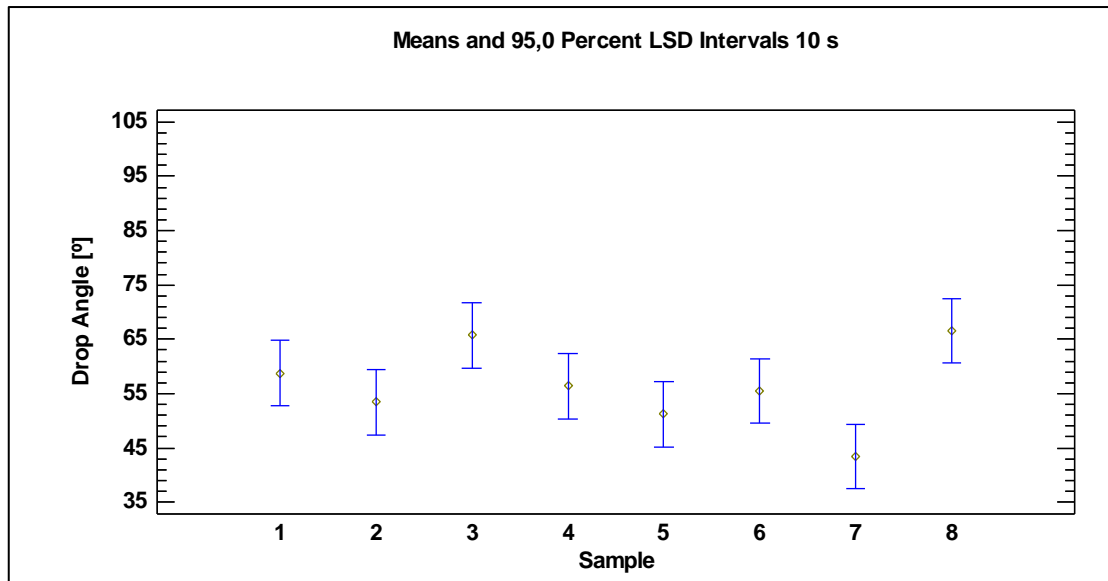
Fig. 5, 6 and 7: statistical graphs for drop contact angle at 0.1, 1 and 10 s from drop application.

In the same way, the obtained statistical data for the adhesion strength are shown below:

Table 3: Statistical results for adhesion strength.

	Adhesion strenght Sample 1 (kgf)	Adhesion strenght Sample 2 (kgf)	Adhesion strenght Sample 3 (kgf)	Adhesion strenght Sample 4 (kgf)	Adhesion strenght Sample 5 (kgf)	Adhesion strenght Sample 6 (kgf)	Adhesion strenght Sample 7 (kgf)	Adhesion strenght Sample 8 (kgf)
Mean:	181	126	165	183	172	202	168	195
Range:	170	70	163	142	176	140	54	170
Standard Deviation:	83	26	61	63	91	70	26	70

The statistical graphs representative of the six specimens for each sample, summarizing all the data collected, can be also shown:
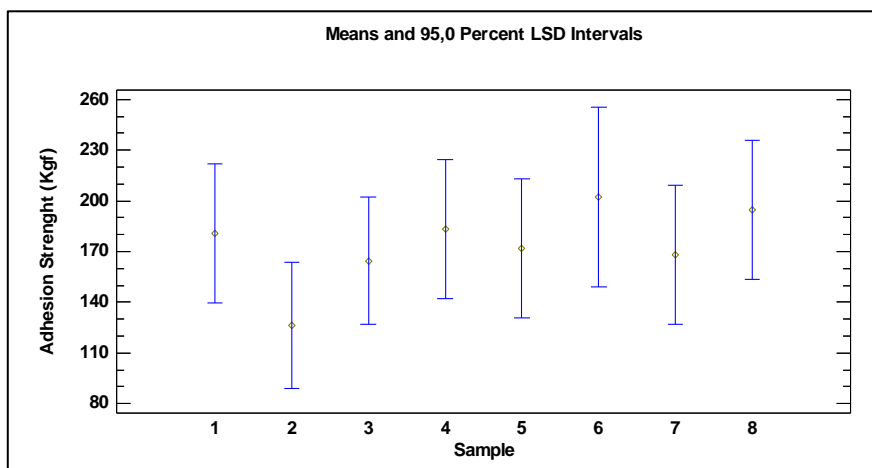
Fig 8: statistical graph for adhesion strength

The results of the average fracture regions are also shown in the following table:

Table 4: Table with the average contributions of the adhesive failure.

Sample	Type of adhesive failure (% of contribution) (nearest 10 %)	
	A (Cohesive)	A / B (Adhesive)
1	0	100
2	5	95
3	8	92
4	16	84
5	22	78
6	20	80
7	76	24
8	28	72

3. RESULTS DISCUSION AND CONCLUSIONS

As it can be seen from Table 2 and Fig. 5, 6 and 7, the obtained statistical results for drop angle show big dispersion, especially at 0.1s and in samples 3, 4, 5 and 8, in which standard deviation value exceeds the 20% of the mean value. Two possible factors can be the reasons of this dispersion: the drop shape is not completely stabilized at early times and the material surface is very heterogeneous (as it can be deduced by the petrography study). The first factor can be reduced by establishing the drop angle comparative study at 10 s (although some samples maintain a high standard deviation at those times). The second factor can't be avoided and it is a general characteristic of any kind of property of natural stone determined in the laboratory.

A multiple sample comparison study can be performed using software for statistics. ANOVA provides a statistical test of whether or not the means of several groups are equal, so ANOVAs are useful for comparing (testing) three or more means (groups or variables) for statistical significance. An ANOVA test between the means of the 8 drop angle variables at the 95.0% confidence level shows that there is a statistical difference between the variables. Repeating the same ANOVA test removing sample 8, the same result comes from the test. If sample 7 is also removed, the ANOVA test shows that the rest of the variables are statistically equivalent at the 95.0% confidence level. Sample 7 and 8 are statistically independent if we perform the ANOVA test for the two variables. Similar conclusions can be extracted from the statistical comparison of angles at 0.1 and 1 s.

These statistical results can lead to the following conclusions, relating to the experimental results obtained in this work:

- The drop angle variable can be considered statistically constant for those samples treated with fine abrasives (from grain 220 to the smaller ones). The mean value of the drop angle at 10 s from drop application considering the six equivalent sets of samples is 56.8º, which means that the surfaces are weattable by water and similar liquids.
- The drop angle variable of samples treated with a coarse abrasive sequence stopping at grain 120 (sample 7) is statistically independent and has a mean value at 10 s of deposition of 43.5º, which means an improvement in the wetting behavior from samples which continue in the polishing line with finer abrasives.
- The drop angle variable of calibrated samples after treated with an abrasive of grain 60 (sample 8) is statistically independent and has a mean value at 10 s of deposition of 66.5º, which means a worse wetting behavior from samples that are further treated with abrasives. If we also show the individual results for each tested specimen, as we do in Fig. 9, we can observe that there are several points in the

sample set in which the drop angle was near to 90º, implying areas with a change in the wetting behavior and an inconvenience for a liquid coating application.
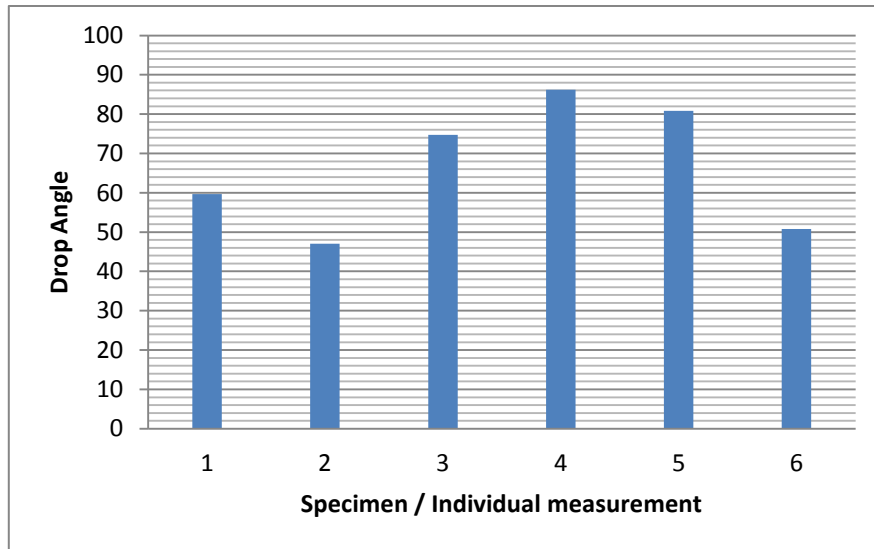

Fig. 9: Individual values for drop angle for Sample 8

Regarding the adhesion strength, again a big dispersion of values is presented, represented by high values of the range and the standard deviation (in samples 1 and 5 the standard deviation value is around the 50% of the mean value). The statistical study of the 8 means obtained via the ANOVA test, shows that there is no significant difference between the means of the experimentally obtained adhesion strengths and that they are statistically equivalent at 95.0% confident level. However, it can be seen an evolution in the behavior of the fracture mechanism from the samples treated with the complete sequences of abrasives including the finest granes to the ones just treated with the coarser granes. Adhesive failure is the complete dominant mechanism in fine grain treated samples, while a mixture of adhesive and cohesive failure occurs on samples at the beginning of the polishing process. Samples treated with coarse abrasives, however, do not continue the trend and this can be due to different surface characteristics, induced by previous calibrating process and that have not been completely removed by the action of just one abrasive. This should have to be studied in the future, as no microscopic characterization of the surfaces has been done in this work.

The main result derived from these facts about adhesion strength and applicable to this case study is that the ideal adhesive state, in which the most predominant adhesive failure is cohesive for the substrate (near to 100%), has not been obtained with the coating systems considered in this experimental work. The best results regarding the type of adhesive failure has been obtained at a point within the polishing sequence, after calibration and the treatment of coarse abrasives (60, 80 and 120).

As a general conclusion, at the view of the partial conclusions showed, it can be said that samples that are calibrated and treated by coarse abrasives (grains 60 and 80) are the most suitable for the coating process with the considered epoxy resin, as they show the lowest contact angles and the highest probability of cohesive failure, implying that the best adhesive conditions are met.

From these results, some activities will be pending for the future to complete the study:

- More detailed study of drop angle and adhesion strength with samples treated with sequences of coarse abrasives (from 60 to 120) and including the study of samples just calibrated.

- Surface topography / profilometry and porosity study of the different surface obtained by the different adhesive sequencies. Reference article [9] can be taken as model for the kind of surface characterization to be performed.
- Study of influence of the liquid characteristics (viscosity and density) of the liquid coating over the final coating adhesive strength. The selected resin for this experimental work was very viscous and it has to be demonstrated if the obtained results can be achievable with other resins.
- Validation of the obtained results with a bigger statistical sample.

REFERENCES

[1] The marble and granite resin process: How and why, June 4, 2003 http://www.stoneworld.com/articles/82382-the-marble-and-granite-resin-process-how-and-why

[2] Verónica Morote-Martínez, Verónica Pascual-Sánchez, José Miguel Martín-Martínez. Improvement in mechanical and structural integrity of natural Stone by applying unsaturated polyester resin-nanosilica hybrid thin coating. European Polymer Journal 44 (2008) 3146–3155.

[3] Rajiv Asthana, Ashok Kumar and Narendra B. Dahotre. Materials processing and manufacturing science. Chapter 5: Coatings and Surface Engineering. Pages 313-395. (2006).

[4] G. Bracco, B. Holst (eds.). Surface Science Techniques, Chapter 1 Contact Angle and Wetting Properties. Springer Series in Surface Sciences 51. 2013.

[5] Jinbo Wu, Mengying Zhang, Xiang Wang, Shunbo Li and Weijia Wen. A Simple Approach for Local Contact Angle Determination on a Heterogeneous Surface. Langmuir 27 (2011) 5705–5708.

[6] ISO 4624-2003. Paints, varnishes and plastics. Pull-off test for adhesion

[7] Y.-Y. Wang, C.-J Li, A. Ohmori. Influence of substrate roughness on the bonding mechanisms of high velocity oxy-fuel sprayed coatings. Thin Solid Films 485 (2005) 141–147.

[8] ASTM D 5725 – 99. Standard Test Method for Surface Wettability and Absorbency of Sheeted Materials Using an Automated Contact Angle Tester.

[9] Jurgen Jopp, Holger Grull, Rachel Yerushalmi-Rozen. Wetting Behavior of Water Droplets on Hydrophobic Microtextures of Comparable Size. Langmuir 2004, 20, 10015-10019.

A contribution for an optimization of the polishing quality of stone slabs: simulation and experimental study using a single-head polishing machine

A.R. Barbosa[1], A. Coelho[2], J.C. Fernandes[1], P.M. Amaral[1], L.G. Rosa[1], J.C. Pereira[3]

[1] Universidade de Lisboa, IDMEC & Dept. of Mech. Engineering, Instituto Superior Técnico, Av. Rovisco Pais, 1049-001 Lisboa, Portugal

[2] FrontWave, Rua do Comércio nº15, 7150-321 Borba, Portugal

[3] Universidade de Lisboa, Dept. of Chemical Engineering, Instituto Superior Técnico, Av. Rovisco Pais, 1049-001 Lisboa, Portugal

luisguerra@tecnico.ulisboa.pt

ABSTRACT

This paper describes recent research regarding: 1) the influence of the water flow and the pressure in order to attain the best polishing in portuguese limestones; 2) the experimental validation of a polishing simulator under development at Instituto Superior Tecnico (Lisbon). The research work was carried out using slabs of calcareous stone Moleanos, from Portugal, and the polishing sequence employed commercial Frankfurt-type abrasive tools applied for the last 3 stages of the process in order to attain maximum surface gloss. The study was conducted with a single-head laboratory-type polishing machine, where all test conditions are adequately monitored and controlled. The polishing head contains 6 Frankfurt abrasives of the same grit size (320#, 400# and 5Extra). The surface quality was assessed, after each polishing stage, by means of a glossmeter. In the end, it was possible to identify the optimum working parameters for each polishing stage. The results obtained also show that indeed a correlation exists between experimental values of gloss and the abrasion data given by the simulator.

KEYWORDS

Polishing, Pressure, Water Flow, Ornamental Stone, Gloss, Frankfurt Abrasives, Modelling

INTRODUCTION

Surface finishing processes alter the surface of a manufactured item to achieve a certain property. Aesthetic characteristics are very important when rocks are used as construction or ornamental materials, and therefore surface finishing processes are considered essential by the stone processing industry. Among the different types of surface finishes (such as: polished, honed, flamed, tumbled, brushed, etc.) the polished finish is perhaps the one which best enhances the rock attractiveness. Roughness (R) and gloss (G), as well as colour (C), are surface properties generally used to assess the rock polishing. The polishing quality depends very much from the type of abrasives used and on the optimal abrasive sequence utilized for a specific type of stone material (marble, limestone, onyx, granite, sandstone, and other natural stones or even engineered artificial stones). Some recent publications appearing in the open literature and dedicated to studies on surface finish evaluation on ornamental stones are listed in the references [1-3].

In industry, polishing is a finishing process, formed by several successive operations aiming to decrease the roughness of the surface and to increase its gloss intensity. This technique uses friction movements of abrasive elements over the material to obtain the required polishing degree. On modern slabs polishing machines, the stone slabs move on a wide belt and are processed by multiple polishing heads installed on the machine's bridge (see Fig. 1).

Fig. 1. Typical multiple head polishing machine used by the ornamental stone industry. [4]

Typically, polishing machines for marble have spindle motors of 10-15 hp and the diameter of the polishing head is 450 mm, installing 6 polishing "Frankfurt" abrasive elements; while for granite, machines are more powerful (spindle motors of 15-20 hp or more) and use 470 mm diameter polishing heads with 6 "Fickert (Tangential)" abrasives. There are machines that allow to process (polish) slabs of both marble and granite. There are also other types of polishing machines which use one single head.

A schematic representation of the polishing process in a polishing line is shown in Fig. 2. The abrasive elements installed at each polishing head, in contact with the stone slab, perform the polishing under well-established operating parameters: conveyor belt speed, V_L; cross-head or transverse velocity, V_T; head rotation speed, ω; water flow, Q; and pressure of polishing head, P. The abrasives have, progressively, a lower grit (between polishing heads), providing a gradual treatment through the belt.
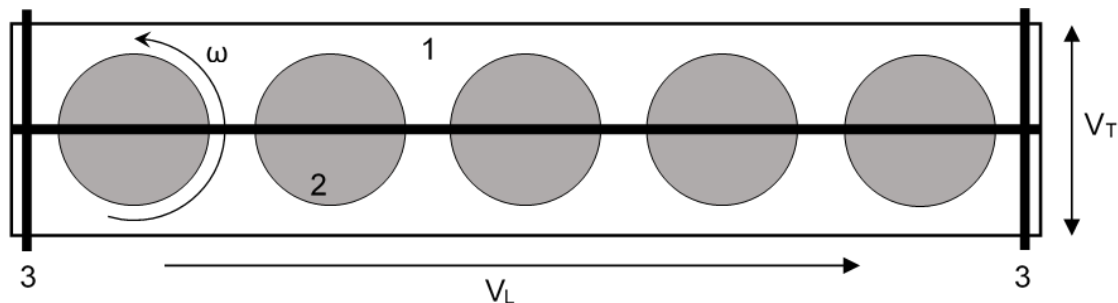
Fig. 2. Schematic representation of the polishing process in a polishing line:
1 - conveyor belt; 2 - polishing head; 3 - crosshead beam.

The water flow, Q, is employed to clean, lubricate and cool the polishing process. The effective pressure P, applied in the polishing head, allows obtaining a permanent and stable contact between the tool and the surface of the stone. As detailed in [5], the vertical movement of the polishing heads is performed by a pair of pneumatic cylinders working in counter pressure. In modern polishing machines, the lifting of polish spindle is controlled according to the stone profile perceived by sensors; and in fact, the control system inspects and optimizes the movement of polish head, crossbeam and belt to expert polishing.

The investigation described in the present paper has two objectives: 1) the optimization of the working conditions, namely pressure and water flow, in order to attain the best polishing in portuguese limestones; 2) to validate a polishing simulator developed at Instituto Superior Tecnico (Lisboa).

For this type of study, the choice of an adequate limestone is relevant and the following stone characteristics may simplify the comparison between simulation and experiment: - minimum mineralogical differences; - absence of tonalities (i.e. great homogeneity); - absence of defects (seen to the naked eye); - easy to be polished (i.e. getting easily high gloss to be measured by the glossmeter).

1. EXPERIMENTAL

1.1 Stone and abrasives used in polishing experiments

The experimental work was carried out using slabs of calcareous stone Moleanos, from Portugal. Figure 3 depicts the typical use in flooring of Moleanos limestone. As it will explained further on, each tile was divided into referenced areas that were used to attain the gloss readings after each stage of polishing.

Fig. 3. An example of typical use of Moleanos limestone in flooring.

Three different Frankfurt abrasives were used throughout this work (see Fig. 4), mounted in groups of six in the polishing head (as schematically shown in Fig. 6). These abrasives, typically applied in the three final polishing stages, were chosen in order to maximize gloss, thus making it simpler to measure and study surface changes after polishment.

320TX is a magnesite abrasive containing silicon carbide particles of grit size 320#; 400T is a resin bonded abrasive containing silicon carbide particles of grit size 400#; and 5Extra is an oxalic acid abrasive containing fine (5 micrometer) silicon carbide particles used on final polishing step to get mirror-like polishing.

| (a) | (b) | (c) |
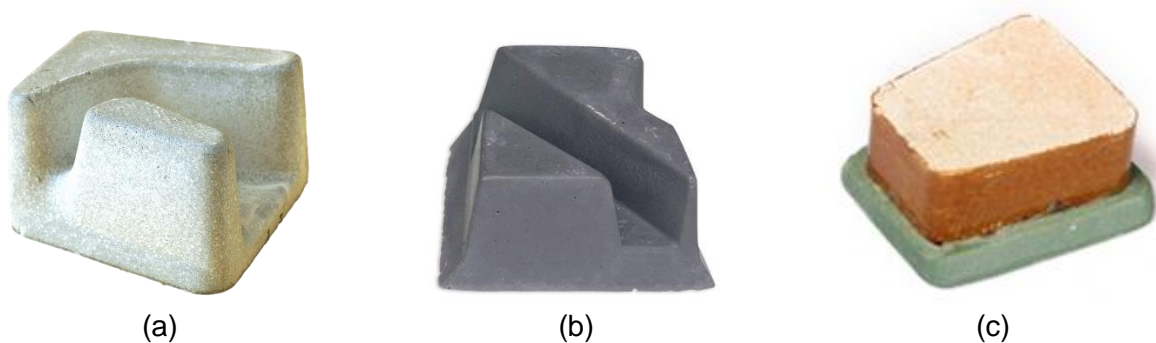
Fig. 4. Frankfurt abrasives used in this work: (a) 320TX; (b) 400T; (c) 5Extra.

1.2 Equipment used for polishing tests and gloss readings

The polishing tests were carried out with a laboratory-type linear polishing machine (see Fig. 5.a) equipped with a single polishing head, so changes in surface characteristics (like, gloss or roughness) can be simply correlated with the local abrasive action applied in each polishing experiment. The machine is instrumented to control and monitor all the most important processing variables: conveyor belt speed, transverse speed, head rotation speed, tool pressures and water flow. The correct knowledge of all these variables is of crucial importance to study and optimize the polishing process [5].

| (a) | (b) |

Fig. 5. Equipment used in this work: (a) laboratory-type polishing machine; (b) glossmeter.

The surface quality of stone tiles was assessed by measuring gloss values after each polishing stage. The gloss readings were made with a glossmeter TQC PolyGloss [6] allowing measurements at angles of 20º/60º/85º. The readings were taken at different locations of the stone tiles, according to a planned grid, and the results were submitted to statistical analysis.

2. SIMULATION OF THE POLISHING

PAM (Polishing Analysis Modelling) is a 2D geometric simulator aiming to reproduce the macroscopic action of a polishing tool, rotating and moving over a stone surface, both considered flat. PAM is unable to simulate the complex Materials Science mechanisms governing the polishing at a microscopic scale, involving the deformation and wear of the asperities in the stone / tool interface. PAM instead divides the stone and tool surfaces in tiny 2D cells, from now on called pixels, and assumes that the accumulated contact between the pixels of both surfaces, from now on called abrasion, can be used to determine the main aspects of a polishing process. As in many other modelling techniques, the processing time is divided in tiny time steps, small enough to properly simulate the fast changing pattern of the tool over the stone.

Different polishing tools can be simulated simply defining the abrasion intensity for each tool pixel, from 0 (no contact) to any positive number. For example, a tool surface might be designed to have a given distribution of diamond and binder pixels. Tools with relatively simple geometric shapes can be created using PAM own functions. More complex tools can be designed using CAD or image software and then imported into PAM as images. Figure 6 shows three different polishing tools, each formed by six Frankfurt abrasives, mentioned earlier: 320TX, 400T and 5Extra.

Fig. 6. Simulated polishing tools, formed by six Frankfurt abrasives: 320TX (left),
400T (center) and 5Extra (right).

Different simulation sections can be created, with different tools, different rotation and translation tool speeds, even different time steps. Figure 7 shows the polishing results produced by the same tools of Fig. 6, after one rotation at 10 rps (no translation), with a time step of 0.001 s, corresponding to an angular step of 3.6 degrees between each impression.
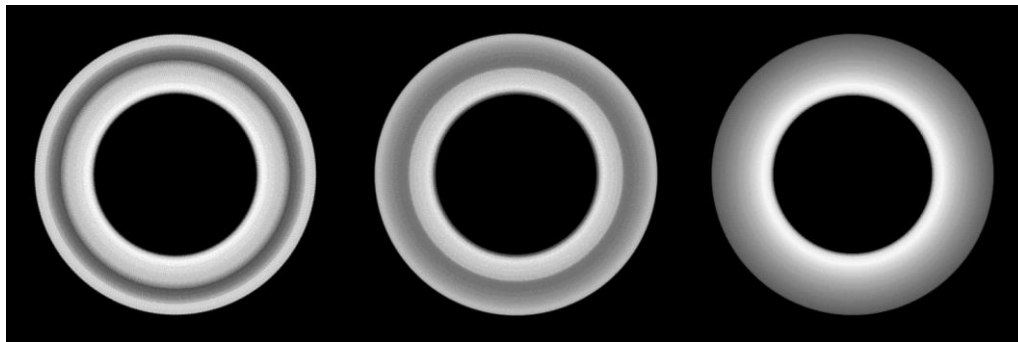

Fig. 7. Simulated polishing by the same tools as in Fig. 6, with abrasives: 320TX (left),
400T (center) and 5Extra (right), after one rotation at 10 rps, with a time step of 0.001 s.

PAM provides a very simple (only five instructions!) but powerful language to define the path followed by the tool over the stone, including multilevel loops and arbitrary sequences of linear segments and circumference arcs, powered by a wide range of parameter options. This functionality allows users to study a virtually unlimited number of trajectories, certainly covering the small subset of interest for the industry. Figure 8 shows the polishing results produced with a simple tool disk for two different polishing trajectories: a mostly linear polishing path and a more complex, mostly circular, path.
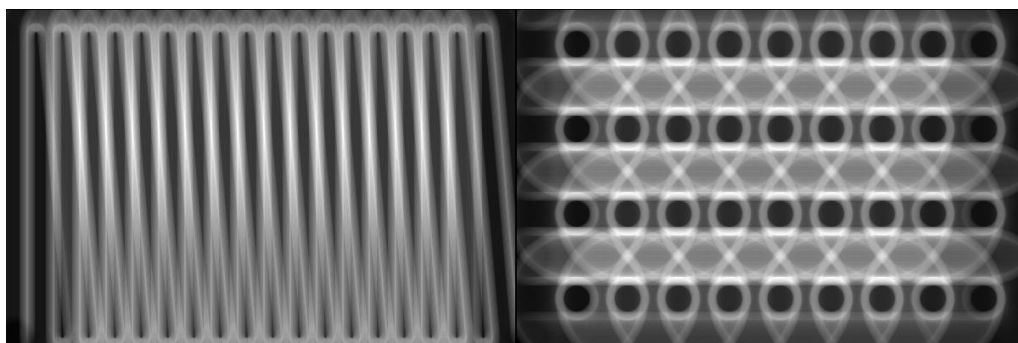
Fig. 8. Simulated polishing by a simple circular disk, for two different tool trajectories. Left: a mostly linear, up-and-down trajectory, circular on the borders. Right: a complex, four-row trajectory, mostly formed by circular movements, simulating multi-level circular hand polishing.

The accumulated simulation results for each stone pixel are stored in files describing the five properties that so far we identified as useful to assert the quality of a polishing process: 1) the total abrasion; 2-3) the shift in pixels (in horizontal and vertical directions) between each polished pixel and the tool central pixel; 4-5) the mean distance and standard deviation between the polished pixel and the tool central pixel. The data thus acquired throughout the entire simulation (or just during a single section) can then be reported in image and statistical formats, including different colour schemes, different statistical treatments, histograms, etc.

To obtain a properly polished stone surface, is not enough to achieve high levels of abrasion throughout the stone surface: abrasion should be as homogeneous and randomly applied as possible to avoid scratches and other visual defects on the surface. For economic reasons, polishing trajectories should be as short and quick to process as possible, and stone surface should not be unnecessarily over-polished.

The main goal we want to achieve with PAM is to create a modelling laboratory that help us optimize: 1) the polishing trajectories automatically generated by algorithm-controlled cutting machines (robot-based and CNC-based) in industrial contexts; 2) the shape and texture of new polishing tools, that can be simulated first to eliminate bad designs, before real tool prototypes are made and experimental tests begin.

3. RESULTS AND DISCUSSION

3.1 Influence of water flow

The assessment of the influence of water flow, Q (litre per minute), was made by varying Q (litre per minute), while keeping the pressure constant (P = 3 bar). Figure 9 summarizes the results obtained after conducting this series of polishing tests.
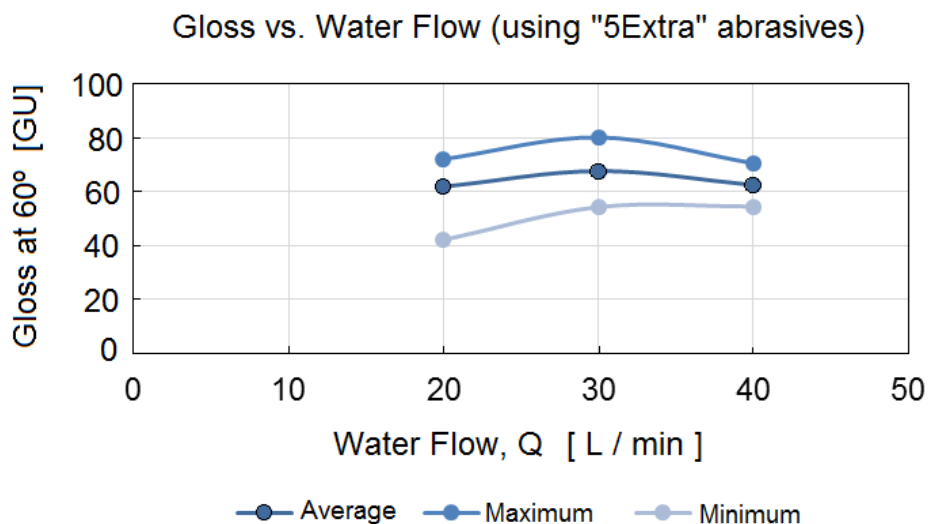
Fig. 9. Results of gloss (average, maximum, and minimum values) after the tests with "5Extra" abrasives at different water flow: 20, 30 and 40 litre per minute.

3.2 Influence of pressure

Polishing tests were conducted at pressure P = 1 bar, 2 bar, 3 bar or 4 bar, but keeping the water flow constant (Q = 30 l/min). Figure 10 shows the average values of final gloss found at different positions (along the stone tile) after tests with "5Extra" abrasives.
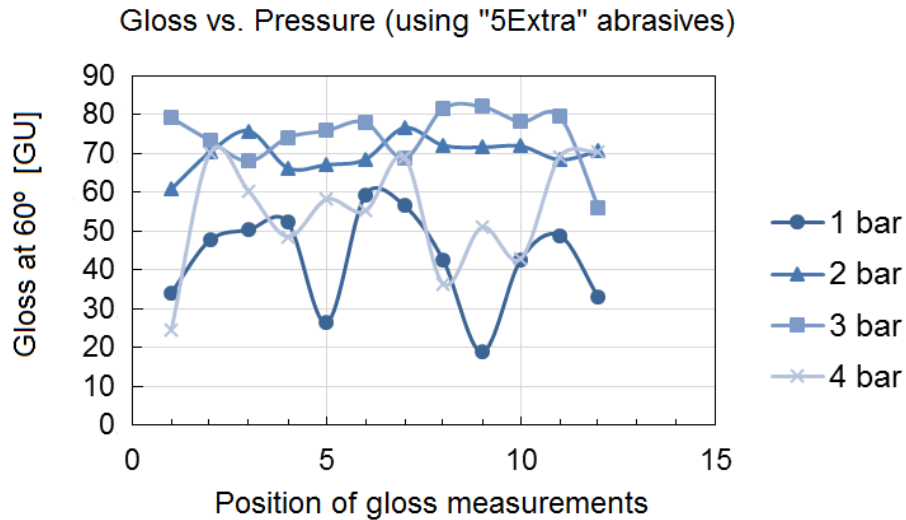
Fig. 10. Results of average gloss after the tests with "5Extra" abrasives at different pressure: 1 bar, 2 bar, 3 bar and 4 bar.

It is noticeable from Fig. 10 that there is a better polish (i.e. higher average-values of gloss) when P = 2 bar or P = 3 bar, compared to the results for P = 1 bar or P = 4 bar. The high variation of gloss across the stone tile found for P = 1 bar is attributed to vibrations occurring at the Frankfurt abrasives installed at the polishing head. The vibrations appear due to the low pressure contact between tool and stone. On the contrary, the variation of gloss for P = 4 bar is attributed to a high pressure contact. In this case, average values of gloss are higher compared to those for P = 1 bar; but the variation between minimum and maximum values for P = 4 bar is of the same order of magnitude as for P = 1 bar. The reason is that for P = 4 bar the contact areas between the Frankfurt abrasives and the stone tile are probably overloaded and this originates a less homogeneous polishment and premature deterioration of the abrasives. Table 1 summarizes the results of the total average value of gloss (for the whole area under study), as well as it presents the values concerning the standard deviation of the gloss measurements.

Table 1. Results of gloss (total average value, standard deviation, and % of standard deviation) after the tests with "5Extra" abrasives at different pressures.

	Pressure in the polishing head			
	1 bar	2 bar	3 bar	4 bar
Gloss at 60º, average [GU]	42.7	70.0	74.6	54.6
Standard deviation [GU]	12.4	4.3	7.4	14.7
% of standard deviation	29%	6%	10%	27%

Based on the results of the experiments described here before, we may consider that pressures in the range of 2–3 bar are suitable for a high gloss polishing. Note that P = 2 bar causes a slightly lower (circa 6%) final value of gloss (70.0 GU) compared to P = 3 bar (74.6 GU) but the deviation in gloss values is lower in P = 2 bar i.e. the gloss is more homogenously distributed along the stone tile. Therefore, we have considered that the best conditions for polishing the stone material under consideration are P = 2 Bar and Q = 30 liter/minute.

3.3 Some results showing the validation of the simulator

Figure 11 shows the PAM simulated abrasion produced by a polishing head equipped with six 400T abrasives that is rotating only, suggesting that abrasion is higher in the inner region, decreases in the middle and increases slightly in the outer region. A comparison between abrasion

measured along the indicated radial region and equivalent gloss experimental values is shown in Fig. 12.
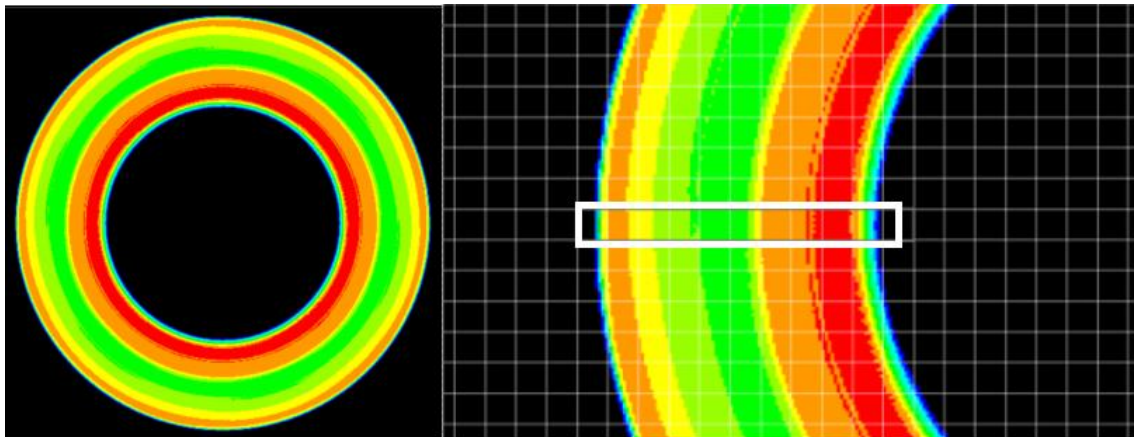

Fig. 11. Abrasion simulated with PAM for a polishing head with six 400T abrasives that is rotating only, showing the radial measuring region. Colour scheme: from blue (low abrasion) to red (high abrasion).
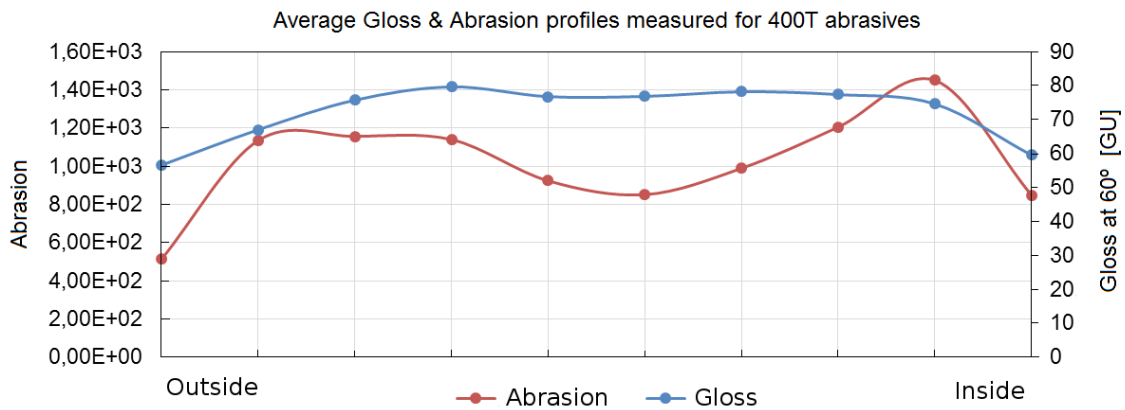

Fig. 12. Comparison between simulated abrasion and experimental gloss for a polishing head with six 400T abrasives that is rotating only.

Although changes in experimental gloss are much smaller than in simulated abrasion (because gloss tends to an asymptote and abrasion increases linearly), the same trend can be observed in both: a decrease in the middle region that is easily explained considering the geometry of the 400T abrasive used in this experiment (see Fig. 13).
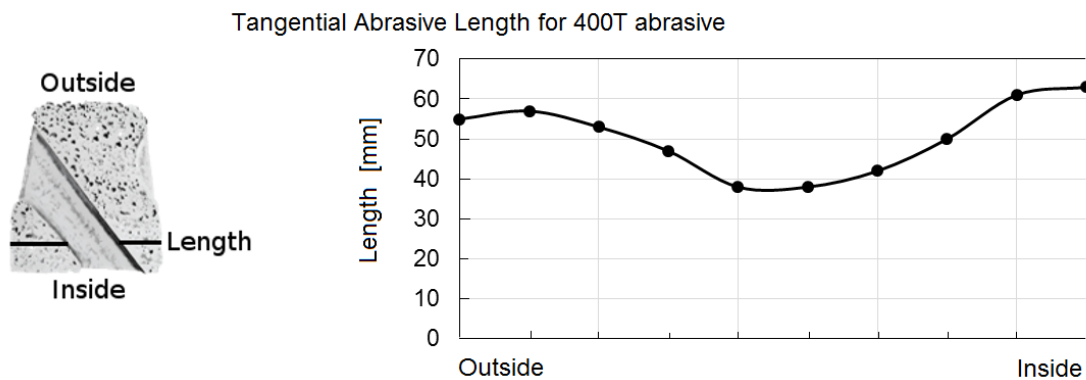
Fig. 13. Abrasive length for 400T abrasive, measured from outside to inside, in the tangential direction, showing a minimum in the central region.

Measuring the effective abrasive length along the radial direction, every 10 mm, from outside to inside, the length increases in the beginning, then decreases until the central region, where it increases again until the end. Although this abrasive tangential length cannot be directly compared with the abrasion simulated from inside to outside (because the perimeter is smaller in the inside than in the outside region, so equal tangential length abrasives are more effective in the inside region), it clearly shows the same trend observed before in experimental and simulated results. So PAM simulations of polishing tools (as shown in Fig. 7) seems to be effective in predicting the polishing behaviour of new tools.

A comparison between abrasion and gloss for a complete polishment sequence, with the three types of abrasives (320TX, 400T and 5Extra) is shown in Fig. 14. Clearly there is a good correlation between experimental gloss and simulated abrasion although, as mentioned before, gloss tends to an asymptote while abrasion just increases linearly. This explains the flat regions observed in experimental measures of gloss while accumulated abrasion always seems to increase or decrease linearly. The whole result for the polished surface, as simulated with abrasion and in agreement with gloss results, is shown in Fig. 15. The colour code uses "blue" for gloss values from 40 up to 50 GU; "green" for values from 50 up to 70 GU; and "red" for values higher than 70 GU.
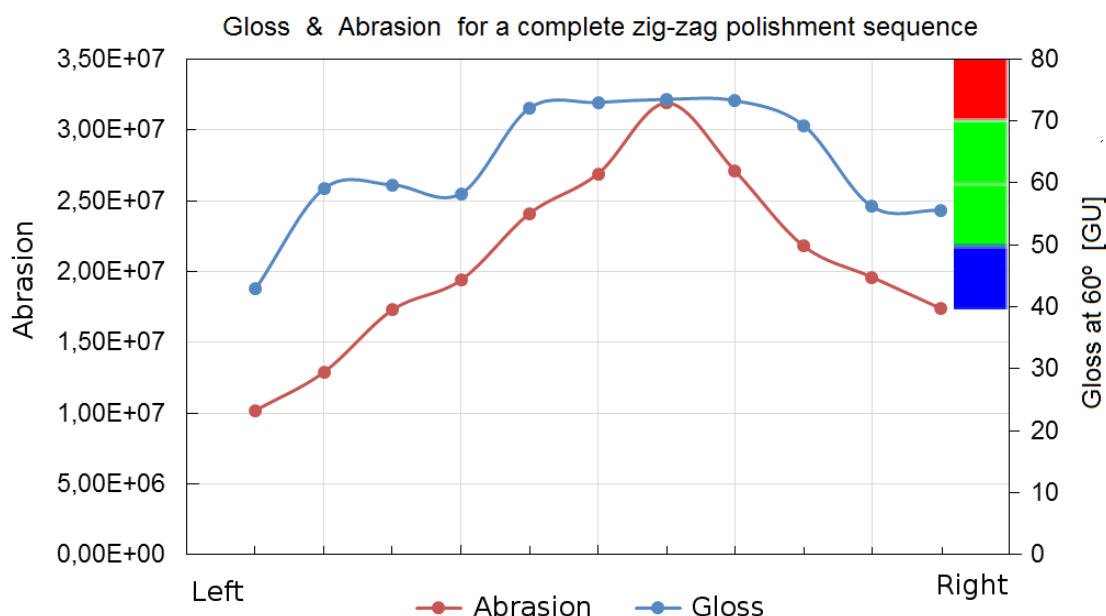
Fig. 14. Gloss and abrasion measured for a complete zig-zag polishment sequence, using the three types of abrasives (320TX, 400T and 5Extra).
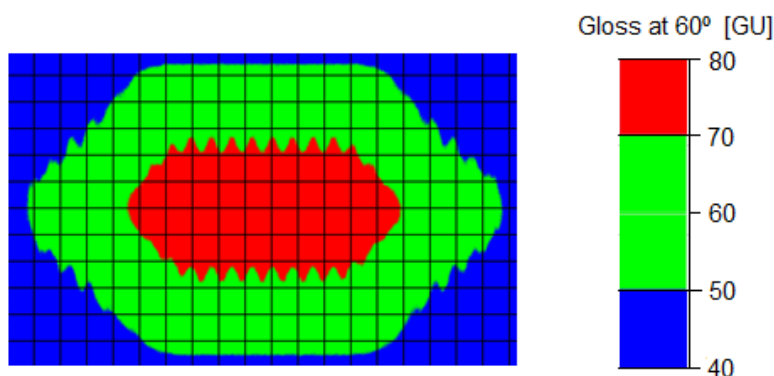
Fig. 15. Prediction of average gloss distribution, given by PAM, for the entire polished surface of a stone tile, considering a complete zig-zag polishment sequence with the three types of abrasives (320TX, 400T and 5Extra) as simulated with abrasion.

4. CONCLUSIONS

This study was conducted with commercial Frankfurt-type abrasive tools applied for the last 3 stages of the process in order to attain a maximum surface gloss in a portuguese limestone (Moleanos). The first part of the work was dedicated to the assessment of the influence of the water flow (Q) and the pressure (P) on the distribution of gloss over the polished area. Concerning to this part, we may conclude that the best conditions for polishing the stone material under consideration are attained with values of P and Q which are close to P = 2 Bar and Q = 30 liter/minute.

The second part of the work was devoted to the experimental validation of the polishing simulator named PAM. Systematic comparison tests between experimental and simulation results have been done so far only in limestones and marbles (tests on marbles were not included in this paper), with Frankfurt-like tools and linear polishing machines. The results show that indeed a correlation exists between experimental values of gloss and the abrasion data given by the simulator.

Despite the fact that the results obtained so far are positive and several correlation effects could be established, it is clear that much more research work and effort is needed to fully assert the validity of the PAM simulations, namely testing different types of stone and more complex polishing trajectories than those provided by simple linear polishing machines.

Although PAM has been specifically designed for the ornamental stone processing industry, the simplicity of the fundamental ideas behind its 2D geometric model should made it equally valid for a wide range of other polishing processes, involving different materials and polishing techniques.

These studies also lead to a better understanding of the influence of the polishing process parameters, namely the polishing time and contact area between tool and polishing surface.

REFERENCES

[1] Sousa, L M O, Goncalves, B M M, 2013, Differences in the quality of polishing between sound and weathered granites, Environmental Earth Sciences, 69/4:1347-1359 (DOI: 10.1007/s12665-012-2035-y)

[2] Yavuz, H, Ozkahraman, T, Demirdag, S, 2011, Polishing experiments on surface quality of building stones tiles, Construction Building Materials, 25/4:1707-1711 (DOI:10.1016/j.conbuildmat.2010.10.016)

[3] Ferreira, T C P, Silveira, L L L, 2011, Análise da influência de variáveis operacionais na qualidade do polimento de rochas ornamentais. In: Anais da XIX Jornada de Iniciação Científica, CETEM/MCT, Brazil.

[4] Carosio, S, Paspaliaris, I (editors), 2003, Machines and Tools for Stone Quarrying and Processing, Volume 1 of OSNET Editions, Laboratory of Metallurgy, National Technical University of Athens, Greece.

[5] Amaral, P M, Rosa, L G, Pinto, S, Pozo, D, 2004, New line of diamond tools raise productivity in polishing stone, Industrial Diamond Review, Issue 3/04:33-37

[6] TQC B.V., 2013, Glossmeter User Guide V1.01 092013, The Netherlands.

Session 7

CHARACTERISATION OF SINGLE-CRYSTAL DIAMOND GRIT FOR CONSTRUCTION APPLICATIONS

Dr S. Nailer, T. Klein, M. Müller, Dr. S. Grasberger
Development Diamond Insert Tools, Hilti Corporation, 9494 Schaan, Liechtenstein
stuart.nailer@hilti.com

ABSTRACT

The last ten years have seen a step-change in the ability to position diamond particles in metal-matrix segments for drilling and sawing applications. Advances in segment assembly technology allow diamonds to be positioned at specific locations within the segment. Performance of the segment can be optimized when the diamond particles are themselves selected to best exploit arranged-diamond segment design and other cutting conditions (such as tool drive parameters).

Diamond 'grit' products for stone and construction applications each comprise particles of various sizes, shapes, strengths and purities. Consequently, effective selection of diamond types is dependent upon measurement using appropriate laboratory 'characterisation' techniques. As many of these techniques yield results on individual particles rather than bulk 'figures-of-merit', effective interpretation of these results is dependent on appropriate statistical analyses.

This paper will introduce the key characteristics of diamond products for construction applications, provide insights into appropriate laboratory characterisation techniques, and describe how their results may be best interpreted to facilitate understanding and consequent diamond selection.

KEYWORDS

Diamond, diamond segment, drilling, sawing, particle characterisation, particle size, particle shape, diamond strength, friability, image analysis

INTRODUCTION

In the conventional method of segment manufacture for stone and construction applications, diamond particles are mixed with metal powders and pressed to form segments. The diamonds are 'randomly distributed' (or 'statistically distributed') and efforts are made to reduce the probability of the 'clustering' of multiple diamonds in a small region. Recent developments in segment assembly technology allow diamond particles to be positioned at specific locations in the segment. As well as eliminating the possibility of diamond clustering, such 'arranged-diamond segment' technologies enable the diamonds to be assigned to a suitable position for the application conditions (such as the expected drilling/sawing performance, drive parameters of the tool motor, and 'base material' to be drilled/sawn). The performance of the diamond 'insert tool' (core bit, saw blade) can be optimized when the diamond particles are themselves selected to best exploit the design of the arranged-diamond segment and the application conditions. That is, the *right particles* come into operation in the right place, at the right time.

Particulate diamond products used in stone and construction sawing and drilling applications (commonly known as 'saw grit') each comprise particles of various sizes, shapes, strengths and purities. It is far from the case that all particles in a saw grit product exhibit similar characteristics. Consequently, the effective selection of diamond types for use in arranged-diamond segments is dependent on the quality of the laboratory measurements used to quantify the particle characteristics. Whilst some of these laboratory techniques provide simple single-value 'figures-of-merit', other techniques yield results from every individual particle. Thus, effective interpretation is dependent on the correct statistical analysis of these 'distributions' of results.

1. DIAMOND SAW GRIT AND ITS CHARACTERISTICS

Synthetic diamond grit products (produced by high-pressure, high-temperature conversion from graphite) are normally graded and selected according to the key characteristics of size and strength. The size band of the product is selected according to whether the priority is surface finish (as in 80µm diamond for polishing) or material removal rate (as in 600µm diamond for drilling) [1]. The strength (or 'grade') of the product is then selected according to the characteristics of the base material to be cut and the drive parameters of the tool to be used. Diamond grit works most effectively by maintaining sharp cutting edges. The optimal diamond strength should therefore be high enough to prevent premature fracture and thus short working life, without being too high that the particles polish to a smooth surface and lose their cutting ability.

The term 'diamond characterisation' may be defined as the laboratory measurement of the properties of diamond believed to play important roles in behaviour in application. Two of the most important behaviours of insert tools for construction applications are speed (typically the depth drilled or area sawn per unit time) and lifetime (the total depth drilled or area sawn before the segments are fully worn). As previously implied, speed may be considered to be mostly dependent on particle size, whereas lifetime may be considered to be mostly dependent on particle strength (and its contributing factors, particle shape and metallic inclusion content).

The following sections describe in greater detail these key diamond characteristics, together with laboratory techniques for their quantification and the mathematical/statistical forms of their results.

2. CHARACTERISATION OF PARTICLE SIZE

There are perhaps three important methods of characterising or expressing the size of diamond particles: sieving, image analysis, and particles per carat. Particles per carat ('PPC') describes the number of particles per unit mass (one carat being 0.2g), and is valuable to the segment manufacturer for expressing how a certain mass of diamond put into a segment translates into the number of available particles. Systems for measuring PPC are not widely commercially available, so particles are commonly counted manually and then weighed. Sieving and image analysis are described in further detail below.

2.1 SIEVING

Sieving uses sieves of sizes defined by international standards [2] to physically separate diamond particles into size fractions. Sieves are traditionally defined by the number of lines per inch (the 'US mesh' system), with a corresponding aperture size specification in microns. Due to its principle of physical separation, sieving is used for the creation of diamond size bands (as well as their measurement). US mesh sizes may take the form of 'half sizes' or 'full sizes'. A half size is defined by a pair of sieves where the coarser ('upper defining') sieve has an aperture size 25-30% larger than that of the finer ('lower defining') sieve. For example, a size 30/35 US mesh half size diamond product is that which sits between a 30 mesh (645µm) sieve and a 35 mesh (505µm) sieve. Adjacent half sizes may be blended together to form a full size.

Whilst the particle size distributions of the graded half sizes are approximately 'normal' (Gaussian) in form, the blended full sizes tend to exhibit 'bimodal' particle size distributions containing the two modes (peaks) of the component half sizes. A graph showing the theoretical particle size distribution of a 30/40 US mesh full size is shown in Fig. 1.
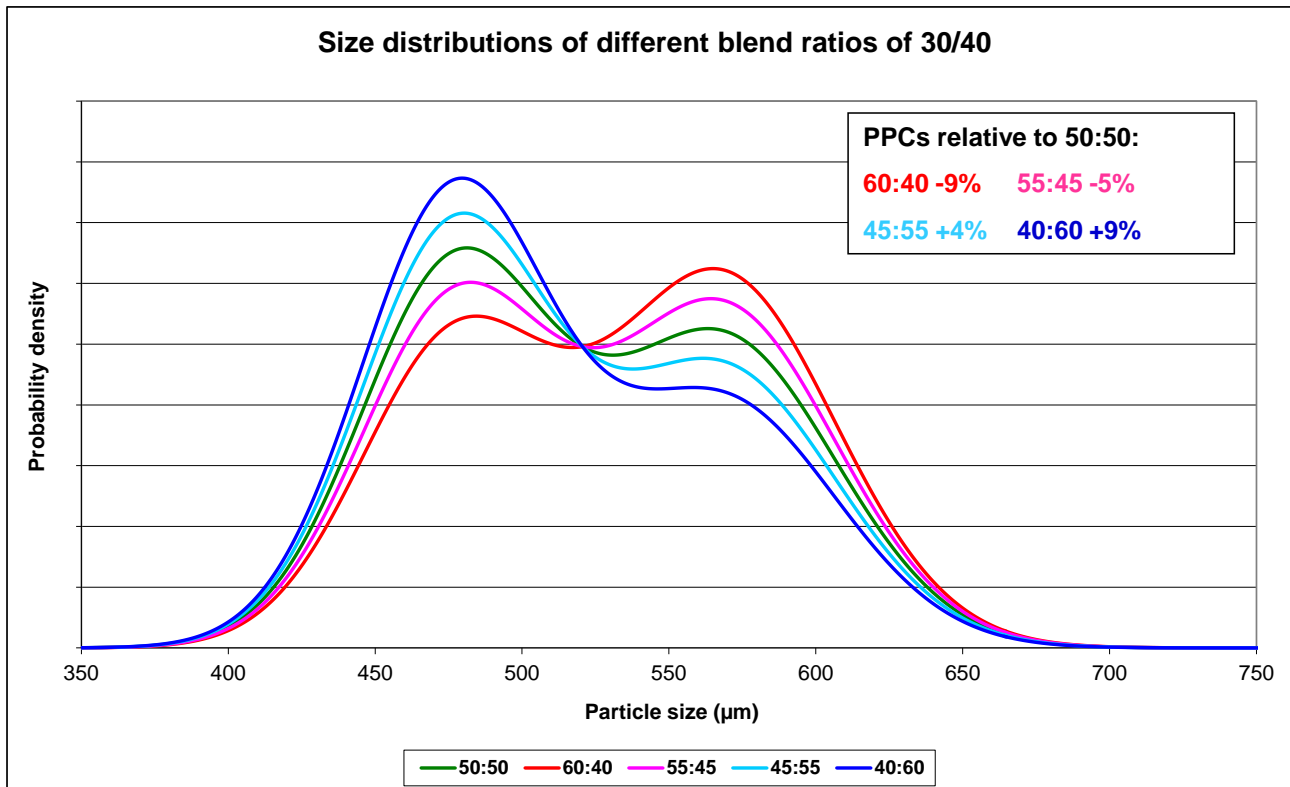
Fig. 1. Particle size distributions of 30/40 mesh diamond with different blend ratios.

The green curve in Fig. 1 represents the particle size distribution from 30/35 and 35/40 blended together in a 50:50 ratio. However, such blend ratios are not specified by international standards. Any blend of the two half sizes is therefore permitted, provided that the 'oversize' and 'undersize' fractions (in this case, coarser than 30 mesh and finer than 40 mesh) do not exceed a few percent.

Five curves representing five different blend ratios are shown in Fig. 1. It can be seen that, even within this fairly narrow range of blend ratios (60:40 to 40:60), the size distributions appear quite different. More significantly, there is a difference of around 18% in the particles per carat (PPC) of the 60:40 and 40:60 blend ratios, which could result in marked differences in application between the two blends even though they would both be correctly classified as '30/40 mesh'. As has been previously demonstrated [3], it is clear that understanding the underlying size distribution (and not just the nominal mesh size) is important for controlling diamond behaviour in application.

2.2 IMAGE ANALYSIS

Image analysis uses a computerised optical microscope to capture digital images of individual particles, which are then measured using various size and shape parameters. Measurement of individual particles enables full particle size distributions to be recorded. However, it should be noted that image analysis generates two-dimensional images, the third dimension not being visible.

A commonly-favoured image analysis size parameter is 'equivalent circle diameter' (illustrated schematically in Fig. 2). The equivalent circle diameter is calculated from the projected area of the particle, and is defined as the diameter of a circle with the same projected area as the particle. Equivalent circle diameter is sensitive to the longer visible dimension of the particle, and so the measured particle size distributions are larger than might be expected from sieving results. However, equivalent circle diameter, being derived from the area, has a good measurement resolution and gives smooth size distributions where small size differences are easily detected.
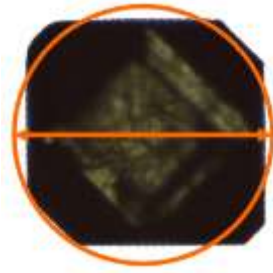
Fig. 2. Schematic illustration of equivalent circle diameter.

Particle size distributions of US mesh half sizes are typically normal (Gaussian), and can be described by the well-known distribution statistics of the 'mean' (average) and 'standard deviation' (spread). However, when a US mesh full size is created by blending two half sizes, the resulting size distribution is 'bimodal' (it has two peaks, as previously shown in Fig. 1). Equivalent circle diameter distributions of typical 30/35 and 35/40 half sizes are shown in Fig. 3, together with the 30/40 full size (blended using a 50:50 ratio of the half sizes). These distributions are shown in cumulative form. The lines entitled 'raw' show the as-measured data, and the lines entitled 'normal fit' show normal distributions with the same means and standard deviations as the 'raw' data.
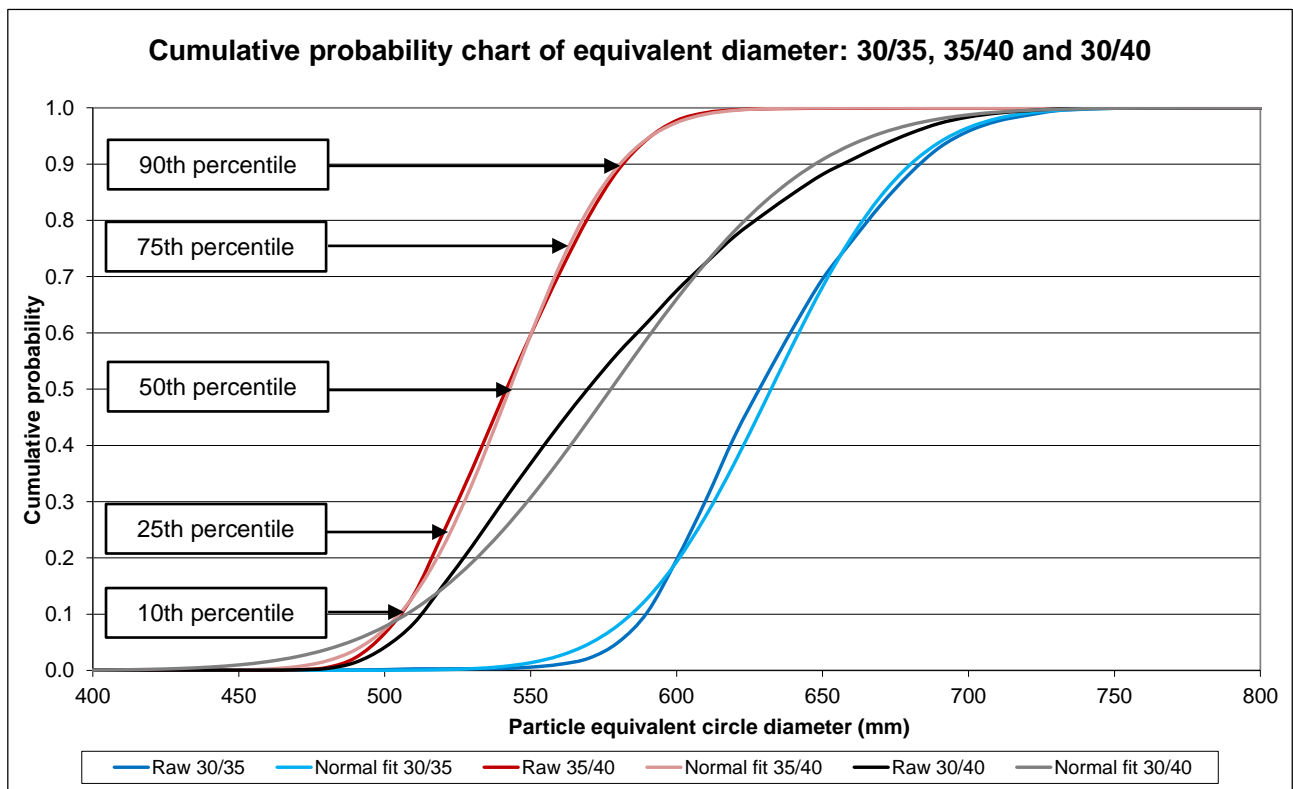
Fig. 3. Cumulative probability chart of equivalent circle diameter for US mesh half and full sizes.

It can be seen in Fig. 3 that the normal fits match the as-measured distributions quite well in the half sizes, but the normal fit for the 30/40 full size deviates substantially from the as-measured data. This is because means and standard deviations always assume a normal (Gaussian) symmetrical distribution shape, and are therefore inappropriate for describing distributions that have multiple peaks or are excessively peaked, flattened or skewed. A more appropriate method of describing distributions of any shapes or number of peak is to use 'percentiles', where the Xth percentile is the value below which X% of the data points lie (when ordered smallest to largest). The most commonly-used percentile is the 50th percentile ('median'), which represents the middle value in the distribution. By using additionally the 10th, 25th, 75th and 90th percentiles, a distribution shape can be conveniently described by five 'non-parametric' statistics.

3. CHARACTERISATION OF PARTICLE SHAPE

The particle images used to measure particle size can also be used to measure particle shape. A useful shape parameter for saw grit diamond is compactness, defined as the ratio of the actual perimeter and the perimeter of a circle of the same area as the particle. A particle that appears circular (such as a highly crystalline cubo-octahedral diamond) will have a compactness near to 1, whereas particles which appear less round (for example, diamonds with elongation or lower crystallinity) will have compactness values higher than 1 (see Fig. 4).
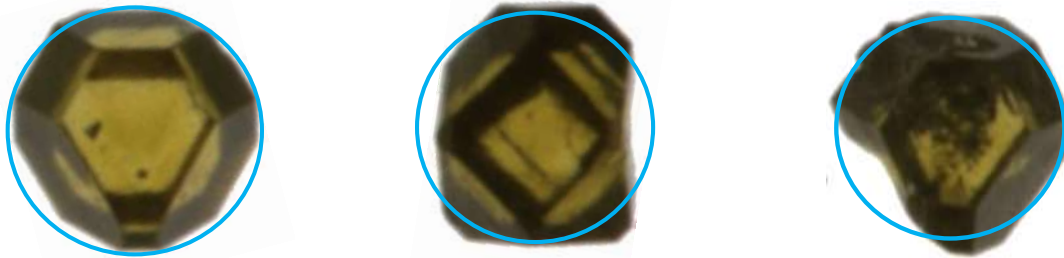
Fig. 4. Schematic illusion of compactness, with highly crystalline (left), elongated (centre) and less crystalline (right) diamond particles.

Compactness measurements on four adjacent saw grit product grades in size 30/35 are now demonstrated. Fig. 5 presents example images of these products, ranging from Grade 1 (a top-grade product) through to Grade 4 (a medium-grade product). It can be seen from the small selections of particle images in Fig. 5 that there are no dramatic differences in particle shape from Grade 1 to Grade 4. More noticeable are the increased populations of darker particles in the images to the right, and the reason for this is discussed later.
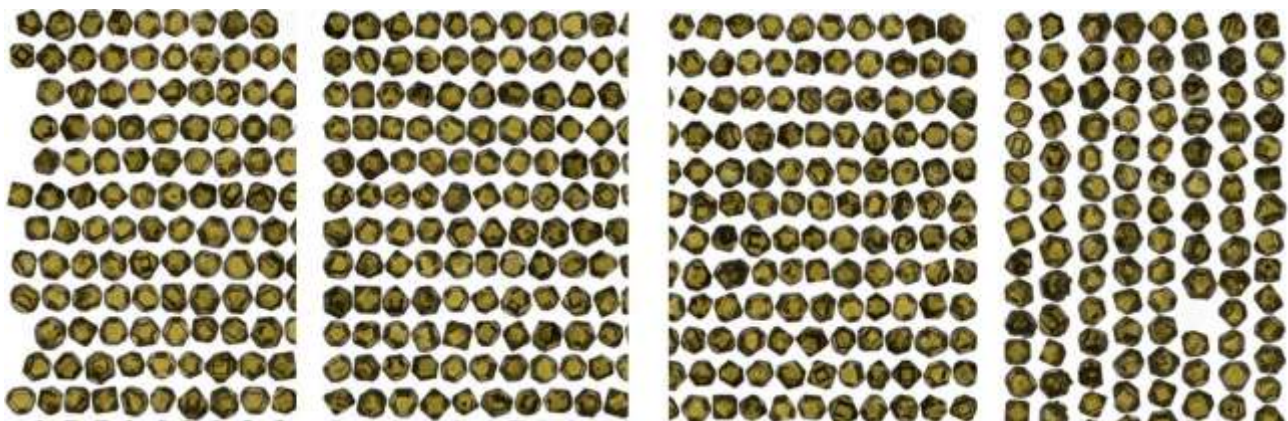
Fig. 5. Images of four 30/35 saw grit products: Grade 1 (left) to Grade 4 (right).

These observations of particle shape are confirmed by the distributions of compactness in Fig. 6. The compactness distributions of the four grades are close to one another, and furthermore, Grade 4 appears to have a better shape than Grade 3 (the Grade 4 compactness distributions being further to the left and therefore closer to the minimum compactness value 1). From this graph it may be concluded that adjacent saw grit products are not substantially different in their particle shapes because they are differentiated only by small differences in the amounts of well-shaped or poorly-shaped particles. Also, particle shape does not always rank correctly with the perceived product grade.
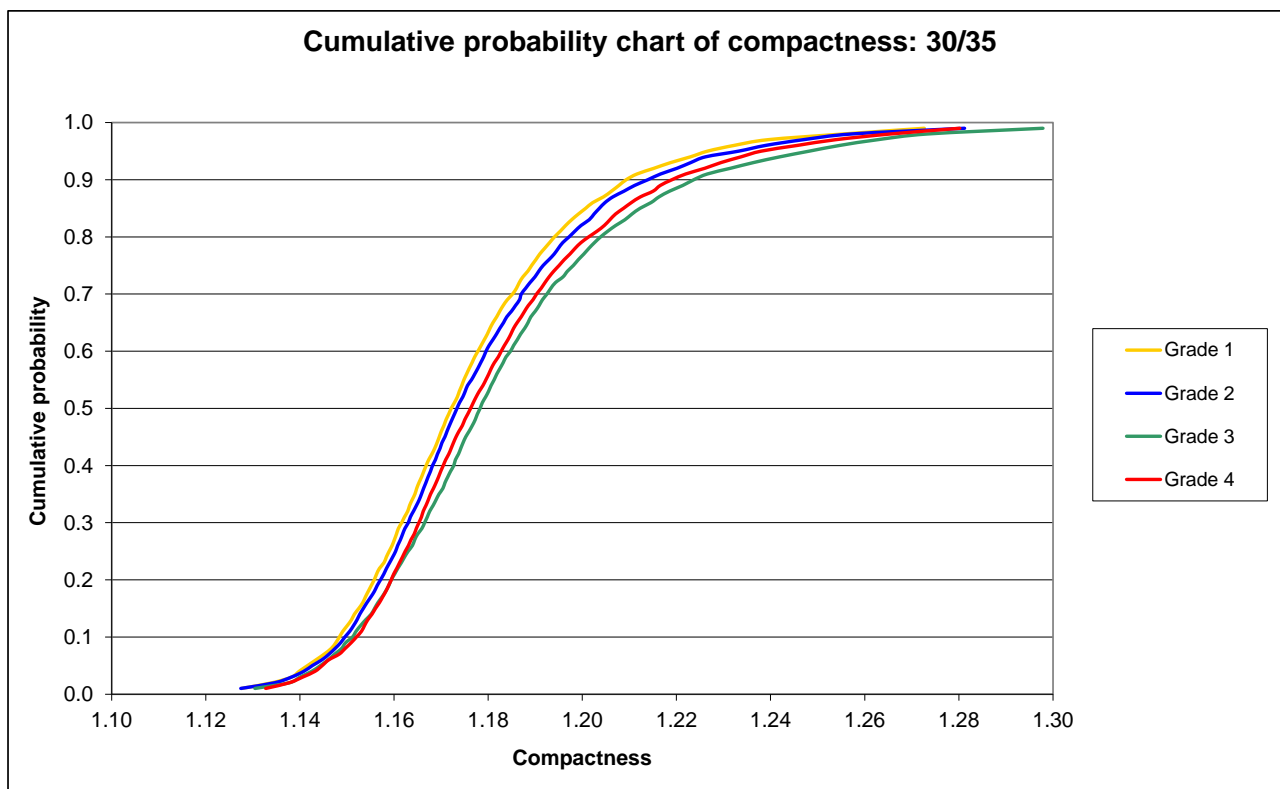
Fig. 6. Cumulative probability distributions of compactness of four saw grit grades in size 30/35.

4. CHARACTERISATION OF PARTICLE STRENGTH

Diamond product strength is typically characterised by two techniques: friability (or 'toughness') testing, and compressive strength testing.

4.1. FRIABILITY (TOUGHNESS) TESTING

Friability testing [4] measures the resistance of a bulk diamond product to cyclical impacts. The product is sieved to remove 'oversize' and 'undersize' particles, and the remaining 'on-size' particles are put into a steel capsule with a steel ball and subjected to a fixed number of oscillations ('cycles'). The product is then removed from the capsule and poured over a slightly finer 'post-impact' sieve. The diamond that has survived sits on this sieve, and is called the 'residue'. A stronger product registers a higher percentage residue (also called 'toughness index').

Friability testing is typically performed at a given number of cycles. For example, size 30/35 saw grit products are commonly tested using 1000 cycles. In this case, the test delivers a single percentage residue (toughness index) value – a figure-of-merit of product strength. However, all diamond products contain a distribution of particle strengths, and this distribution can be explored by testing at a range of different cycles. This provides a friability 'residue-time' curve, such as that in Fig. 7, which shows the friability residue-time curves of the four saw grit grades in size 30/35. At all cycles, the four grades show the 'correct' ranking (Grade 1 being the strongest, Grade 4 the weakest), but their relative strengths vary as a function of the number of cycles. The data points at different cycles may be connected by fitting a negative exponential curve according to the 'Rosin-Rammler equation' [5] (named after two scientists that studied the crushing behaviour of coal). The Rosin-Rammer equation is shown in Fig. 7, the constants k and n being characteristics of the diamond product. As well as allowing the prediction of percentage residue at any number of cycles, this equation enables the prediction of the number of cycles required for 50% residue – the 'half-life'.
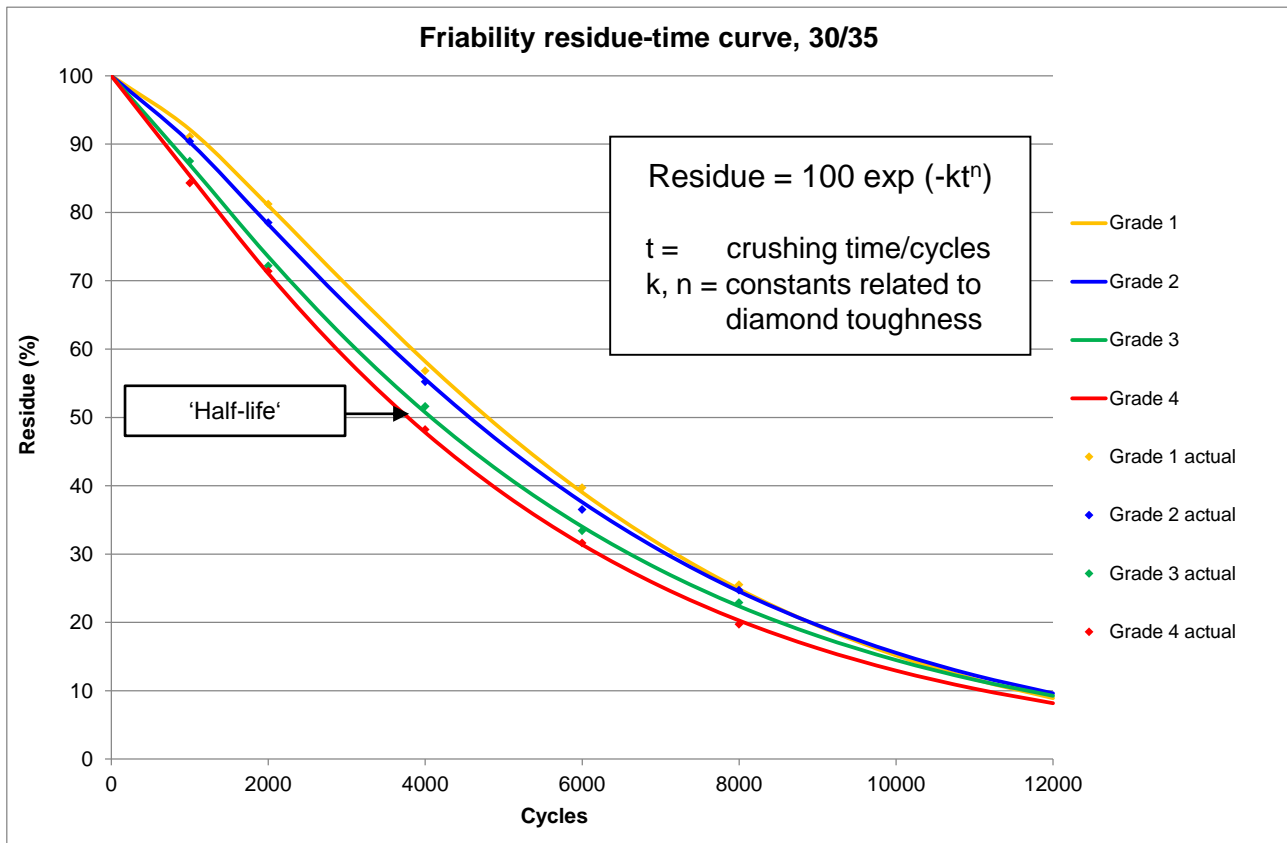
Friability residue-time curve, 30/35

$$\text{Residue} = 100 \exp(-kt^n)$$

$t =$ crushing time/cycles
$k, n =$ constants related to diamond toughness

'Half-life'

Fig. 7. Friability residue-time curves of four saw grit grades in size 30/35.

4.2. COMPRESSIVE STRENGTH TESTING

Compressive strength testing of diamond measures the force required to crush individual particles. Particles are crushed between two polycrystalline diamond 'anvils', and the load cell connected to the lower anvil measures the force required to fracture each diamond particle [6]. This method provides a distribution of particle strengths ('fracture forces') for each product. Fig. 8 shows the strength distributions of the four saw grit grades. For easier comparison with the friability residue-time curves, the vertical axis shows the probability of survival (rather than failure). Furthermore, the as-measured results have been replaced by Weibull distributions, which tend to fit compressive strength distributions well [7]. In this graph, the four grades rank as expected, with Grade 1 having the highest median compressive fracture force and Grade 4 the lowest.
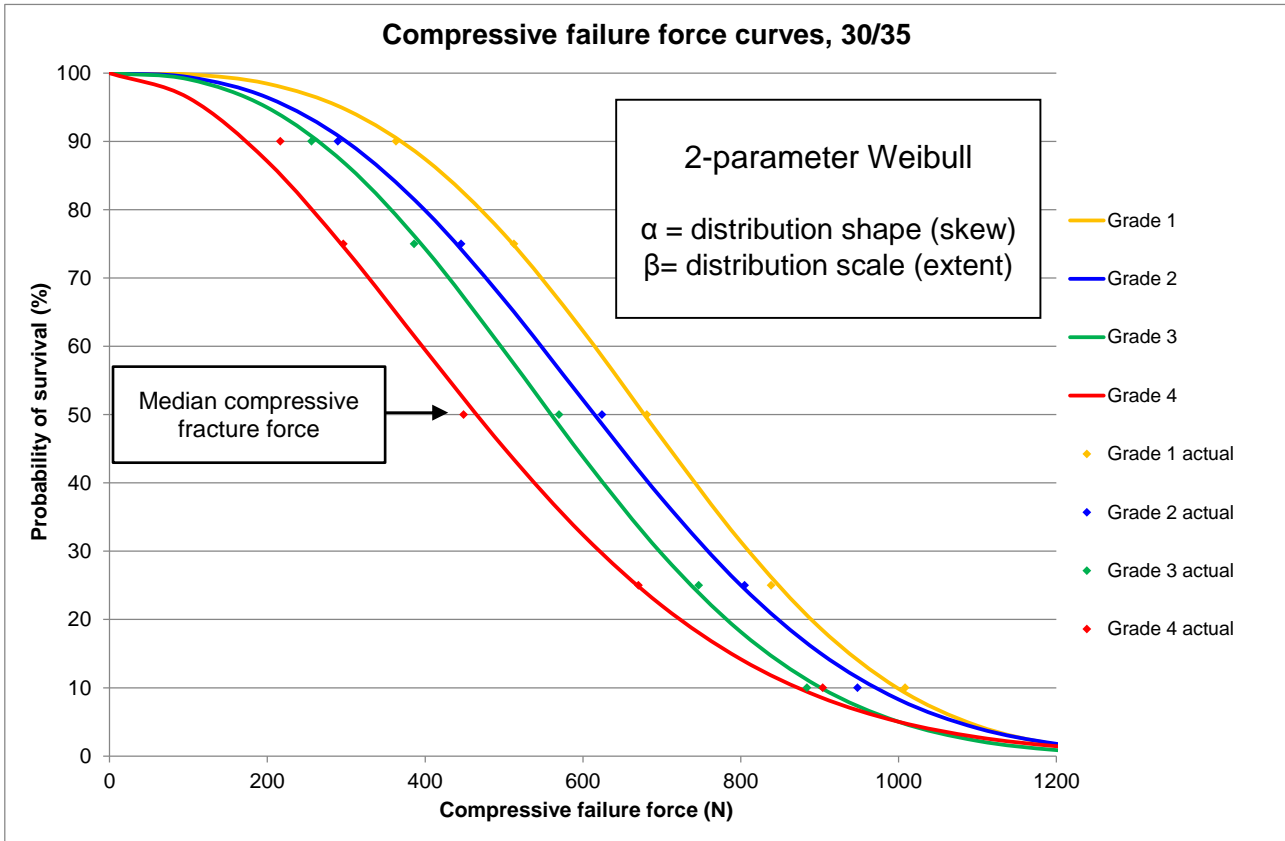
Fig. 8. Compressive strength distributions of four saw grit grades in size 30/35.

Whilst these two methods of strength testing can give complementary results, there are practical reasons for selecting one method or the other. Friability testing at one cycle selection is comparatively quick (around 10 minutes) but will only provide a single value figure-of-merit. The measurements required for a full residue-time curve would require over an hour. However, friability testing does have a good experimental error (around ±1%), and is therefore commonly used for quality control. Compressive strength testing enables a full distribution from 500 particles to be obtained in around 30 minutes, but the experimental error is usually greater due to damage of the polycrystalline diamond anvils influencing the fracture force measurements [8].

5. CHARACTERISATION OF METALLIC INCLUSION CONTENT

Saw grit diamonds are synthesised by the high-pressure, high-temperature conversion of graphite to diamond. Transition-metal alloys (typically iron-nickel) are used to lower the pressures and temperatures required for this conversion, and small traces of these alloys ('inclusions') can be trapped in the diamond crystals during the synthesis process (see Fig. 9 (left)). These inclusions can adversely affect diamond strength during high-temperature segment manufacture (by promoting re-graphitisation), but even at room temperatures the inclusions can act as 'weak points'. As these inclusions are ferromagnetic, their levels can be quantified in terms of 'magnetic susceptibility'. By measuring the magnetic dipole moment of the bulk diamond sample **M** in response to a magnetic field **H**, the (unitless) magnetic susceptibility χ_v can be obtained. Fig. 9 (right) shows the magnetic susceptibility values of the four saw grit grades in size 30/35. These results show that Grades 1 and 2 have similar inclusion levels, whilst Grade 4 (with the highest magnetic susceptibility) has much greater inclusion content than Grade 3. This contributes to the darker appearance of many of the Grade 4 particles in the images shown in Fig. 5.
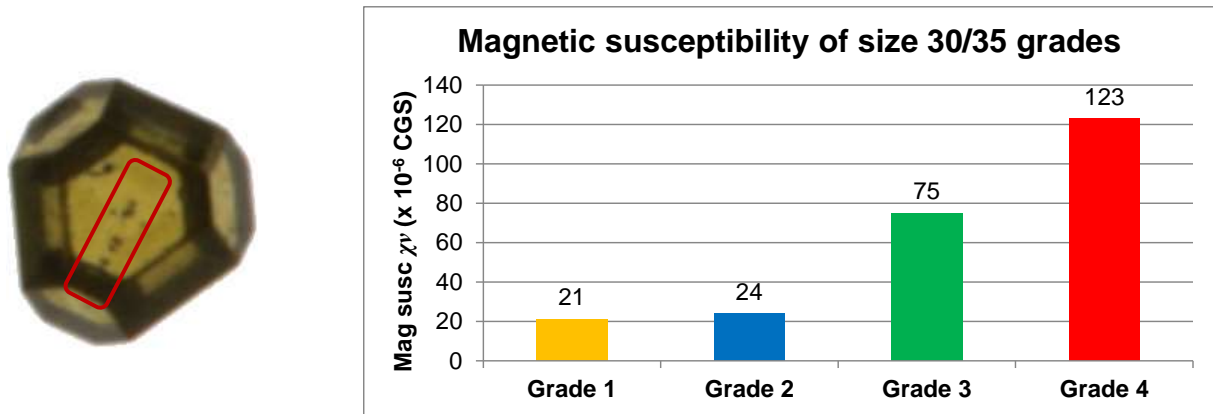
Fig. 9. Metallic inclusions in diamond (left, in red) and magnetic susceptibility results (right).

6. DISCUSSION AND CONCLUSIONS

Comparison of the shape, strength and inclusion measurements from these four grades enables the influences on diamond strength to be understood. These grades were ranked by the diamond manufacturer in the order 1, 2, 3 and 4 (strongest to weakest), and the results of both friability (toughness) and compressive strength confirm this. Whilst image analyses suggested that the particle shapes of Grade 4 were slightly better than those of Grade 3, magnetic susceptibility measurements showed the metal content of Grade 4 to be much higher. Consequently, Grade 4 delivered lower strength values than Grade 3.

The detailed results presented above focused on the mesh size 30/35. Particle shape, magnetic susceptibility and friability (toughness) results have also been obtained from the same grades in sizes 35/40 and 40/45, and compiling all these results leads to the contour plot in Fig. 10.
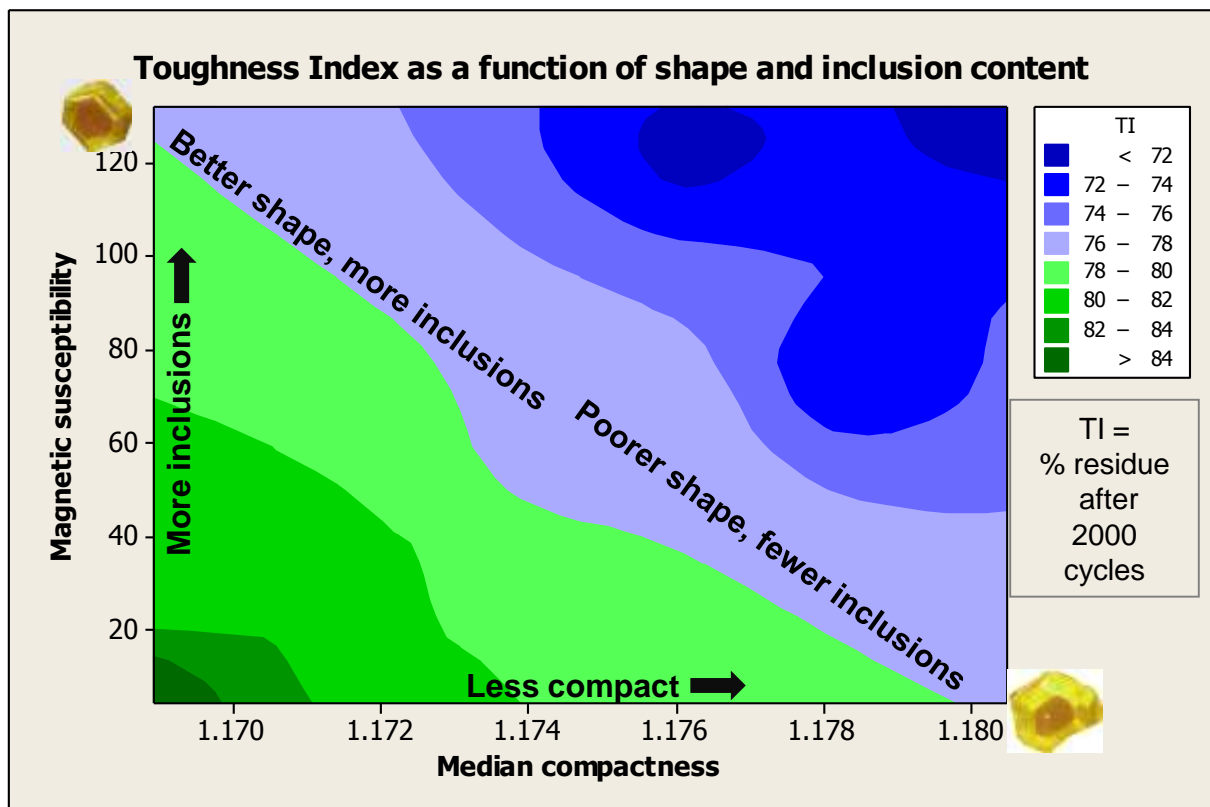
Fig. 10. Toughness index (friability residue) as a function of particle shape and inclusion content.

In Fig. 10 the vertical axis shows magnetic susceptibility and the horizontal axis the median compactness. The colours in the contour plot represent the toughness index (percentage residue), from less than 72 (dark blue) to greater than 84 (dark green). It can be seen that the highest toughness comes from products with the lowest magnetic susceptibility (inclusion content) and the lowest median compactness (most circular particle shape). Furthermore, by following the border between light blue and light green (a toughness index of 78), it can be seen that the same toughness values are obtained by products with low median compactness but high magnetic susceptibility and products with low magnetic susceptibility but high median compactness. From this, it can be concluded that saw grit product strength is primarily influenced by a combination of particle shape and inclusion content.

REFERENCES

[1] Gielisse, P.J., 1998, 'Mechanical properties of diamond films and related materials'. In Gielisse, P.J. (ed.), Diamond and Diamond-Like Film Applications, Technomic, Pennsylvania, pp. 281-296.
[2] 'Abrasive products – Checking the grain size of superabrasives', ISO 6106:2013.
[3] Engels, A., 2003, 'The role of particles per carat in diamond tool behaviour', Industrial Diamond Review, 2/03, pp. 39-45.
[4] Belling, N.G. and Dyer, H.B., 1964, 'Impact strength determination of diamond abrasive grit', Industrial Diamond Information Bureau booklet, London.
[5] Rosin, P. and Rammler, E., 1933, 'The laws governing the fineness of powdered coal', Journal of the Institute of Fuel, pp. 29-36.
[6] Vollstädt, H. and List, E., 2003, 'Controlling the stability of the properties of superabrasive powders', 4th Zhengzhou International Superhard Materials and Related Products Conference.
[7] Gallagher, J., Scanlon, P. and Nailer, S.G., 2006, 'Characterisation techniques for the study of high-strength, coarse diamond', Industrial Diamond Review, 3/06, pp. 58-65.
[8] Nailer, S.G., 2006, 'Synthetic industrial diamond grit products – Single-particle compressive failure strength: "DiaTest-SI" system', ISO Technical Report ISO/TR 24857:2006.

ACKNOWLEDGEMENTS

The background for the use of hartmetals and MMCs based on Niobium Carbide (NbC) as cutting tools and for wear resistant tribosystems

M. Woydt[1]   and H. Mohrbacher[2]

[1] Division 6.3 Tribology and Wear Protection, BAM (Federal Institute for Material Research and Testing), Unter den Eichen 87, Berlin 12205, Germany
mathias.woydt@bam.de, m.woydt@matrilub.de
[2] Niobelcon BVBA, Swaenebeecklaan 5, BE-2970 Schilde, Belgium

ABSTRACT

In this present study, the mechanical properties (strength, hardness, moduli) and the dry sliding properties of stoichiometric and sub-stoichiometric NbC were compared. Micro-hardness and elastic properties of NbC depend from the C/Nb ratio, because the binary phase diagram Nb-C shows a region of homogeneity of NbC_x of $0.72 \leq x \leq 1.0$. At RT, hard metals of stoichiometric NbC have an elastic modulus E of ~440 GPa, those of sub-stochiometric $NbC_{0.88}$ an E of 405 GPa. The hot hardness of sub-stoichiometric NbC is above 600°C higher than of WC. The dry sliding wear resistance (0,1-7/10 m/s) of the present Fe_3Al-$NbC_{0,94}$ with ~61 vol.-% NbC as hard phase was close to those known of NbC-based hard metals. No grain pull-outs or fragmentations of the NbC grains were seen in the wear tracks of the Fe_3Al-NbC composite (MMC), as a metallurgical interphase was formed between matrix and NbC grains. Stoichiometric and sub-stoichiometric niobium carbides have at RT and 400°C under dry sliding a prone intrinsic wear resistance more or less inde-pendent from sliding speed, either as hardmetal or as hard phase in metal matrix composite, associated with an exceptional high load carrying capacity.

Keywords: NbC, niobium carbide, cobalt, Fe_3Al, hardmetal, metal matric composite, wear resistance, cutting, milling

INTRODUCTION

Historically, "wear protection" is dominated by tungsten carbide (WC), either under abrasive conditions or especially for tool materials. Due to the high solubility of WC in alloys and in their melts as well as due to the mismatch in density between melts and WC, hardmetals are mainly produced by sintering or powder metallurgy. Niobium carbide, a refractory metal, like tungsten, has been well known for decades. The tribological properties of niobium carbide are, thus far, unexplored. The supply of niobium is today assured and the reserves of the actual operating niobium mines, including the known deposit and secondary resources, largely exceed those of Tungsten. Niobium carbide offers several benefits:

a. the density of NbC is with 7,71-7,81 gr./cm³ close to Fe, Ni, Co-alloys favorable for casting and dynamic, mechanical applications,
b. the solubility of NbC_x at high temperatures in alloys are few percents (reduced tribo-chemical wear at cutting edges) and enables casting of MMCs,
c. NbC has a thermo-mechanical fit (linear expansion coefficient times elastic modulus) to alloys in comparison to WC.

The recently established tribological profile of NbC bearing materials revealed a strong position under tribological considerations and for closed tribosystems against established ceramics and hard metals [1].

EXPERIMENTAL

-Material

The procedures for plasma-spark sintering (SPS) of the different NbC grades bonded with cobalt or Fe_3Al shown in Table 1 are described elsewhere [1,2]. The cobalt and Fe_3Al bonded NbC hard-metals were SPS sintered using a stoichiometric and commercially available $NbC_{1.0}$ (Treibacher 100, Austria; d_{90}= 3.66 µm, measured powder raw density= 7.60 gr./cm³) denoted in the diagrams by "T. The sub-stoichiometric powder $NbC_{0.87}$ had a granulometry of d_{90}= 7.42 µm) with a measured powder raw density of 7.37 gr./cm³ and is denoted in the diagrams as "H1. Its primary grain size was ~100 nm.

The MMC was directly produced by alumino-carbothermic reduction of powder mixtures of Nb_2O_5, Fe_2O_3, Fe_3O_4, Fluoride, Lime, aluminium and excess of carbon (as coke). This Fe_3Al-NbC MMC had ~61 % of $NbC_{0.94}$ as hard phase. The carbon content was determined by combustion analysis (LEUCO test) NbC grains leached out of the MC. Figure 1 displays the microstructure of the MMC with coarse NbC grains metallurgically bonded in the metallic matrix, where the colours "light-brown" (Fe_3AlC) and "light-blue" (Fe_3Al) distinct the two metallic phases [3]. The hardness of the metallic matrix can be tailored from ~480 HV0,05 by Fe_3Al to ~670 HV0.05 with Fe_3AlC.
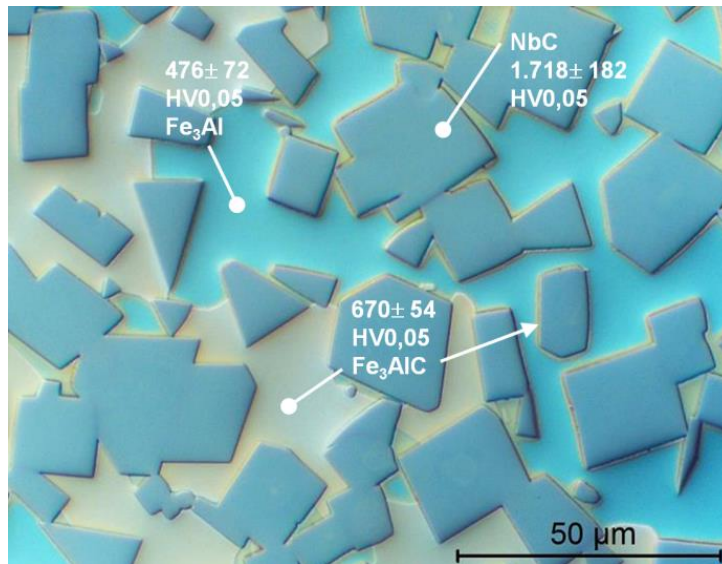
Figure 1: Microstructure of NbC-based MMC (light optical microscope, polished with SiO_2-based suspension "OP-U")

Table 1 Properties of Niobium Carbides (development grades)

Property		T	Method	HP-NbC	NbC-8Co	NbC-12Co	NbC-12Fe₃Al	NbC₀,₈₈-12Co
Powder		—	—	NbC (AO7132)	NbC100	NbC100	NbC100	NbC₀,₈₈ (H1)
Densification		—	—	HP	SPS	SPS	SPS	SPS
Densification temperature [°C]		—	—	2.150 (4 h; 50 MPa)	1.280 (4 min; 30 MPa)	1.280 (4 min; 30 MPa)	1.300 (4 min; 30 MPa)	1.285 (6 min; 30 MPa)
Binder [vol.-%]			—	0	8	12	12	12
Density [gr./cm³]		RT		7,67	7,78	7,76	7,50	7,62
Elastic modulus [GPa]		RT	ASTM E1875	477	443	437	447	406
		1000°C		—	382	368	379	341
Bulk modulus [GPa]		RT		—	181	177,5	183,5	164
Poisson ratio		RT		—	0,22	0,225	0,22	0,235
4-point bending strength [MPa]		RT	DIN EN 843-1	353 ±42	742 ±180	1.215 ±197	822 ±117	1.005 ±158
Microhardness	HV0.2	RT		1.681± 92	1.451±54	1.453±41	1.632±50	1.765±130
	HV0.5	700°C		539±20	—	734±60	553±30	—

HP= hot pressing; SPS= Spark Plasma sintering

Figure 1 illuminates a rim of Fe_3AlC around the NbC grains. In consequence, an interphase is present, because carbon from the NbC dissolved into the Fe_3Al matrix. This clearly indicates a metallurgical bonding of NbC in the Fe_3Al matrix, which is beneficial in order to transduce tribological shear stresses. The present study compares the effect of increasing the binder (or matrix) content to ~40% on wear resistance in comparison to hard metals of NbC densified by spark plasma sintering (SPS) as well as the effect of stoichiometry on friction and wear.

-Properties of niobium carbides
The mechanical properties (strength, hardness, moduli) of different niobium carbide hardmetals are displayed in Table 1.
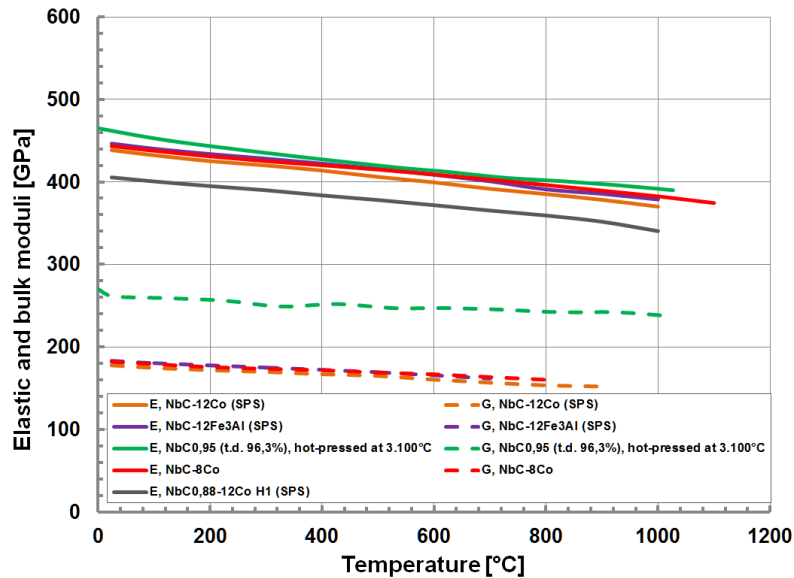
Figure 2 Evolution of moduli with temperature of stoichiometric NbC grades versus WC
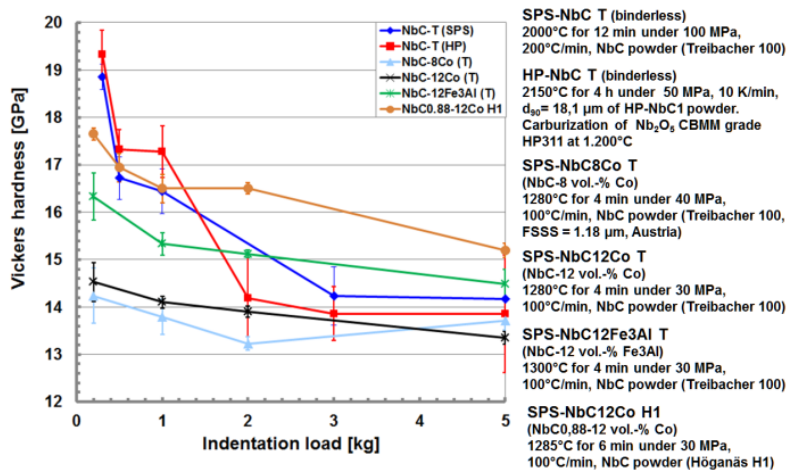
Figure 3 Micro-hardness as function of indentation load for binderless and metal bonded NbC hard metal grades

RESULTS AND DISCUSSIONS

-Properties

The evolution of moduli in Figure 2 is for NbCs less dependent from temperature and can be tailored through stoichiometry. The sub-stoichiometry reduced the elastic modulus of $NbC_{0.88}$-12Co H1 by ~7%.The micro-hardness can be tailored by the stoichiometry and the type on binder. Overall, the NbC bonded by the intermetallic phase Fe_3Al had a significantly higher hardness at any

indentation load than the cobalt-bonded homologues (see Figure **3**). The use of sub-stoichiometric NbC$_x$ and Fe$_3$Al increased the micro-hardness of the NbC based hardmetal. The hot hardness is also of great importance for cutting. The drop in hot hardness is less pronounced for NbC grades than for WC grades. At 700°C, the NbC-12Co T presented the same hardness as the WC grades. The evolution of micro-hardness (See Figure **4**) of the sub-stoichiometric NbC$_{0.88}$-12Co H1 was parallel to the WC grades, whereas above 700°C, NbC$_{0.88}$-12Co H1 had a higher hardness.
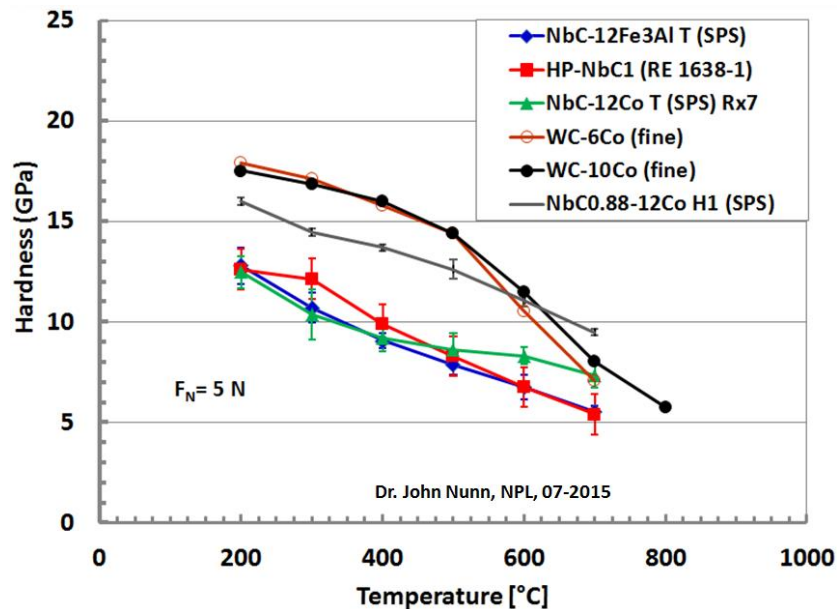
Figure 4 Micro-hardness as function of temperature for metal bonded NbC hard metal grades

-Wear resistance in closed tribosystems
The tribometers for unidirectional sliding are proprietary developments of BAM and the details are disclosed elsewhere [4]. Total wear rate is the sum of both specimen. As shown in Figure 5, the RT wear rates of the MMC Fe$_3$Al-NbC$_{0,94}$ are slightly higher than those of the NbC-bearing hardmetals and for all NbC grades the wear rates decreased with increasing sliding speed, what is beneficial for cutting applications. It is also apparent, that metallurgically synthesized or sintered NbC bearing materials tribologically compete with WC and Cr$_3$C$_2$ bearing hardmetals or cermets. The wear resistance of Co- and Fe$_3$Al-bonded NbC hard metals is highest at RT and high sliding velocities. The low solubility of NbC in alloys in association with the wear resistance enables casted MMCs with a high hard phase content. These casted MMCs give a high freedom in design (size, geometry) of wear resistant components, in comparison to sintered hard metals or ceramics.
At 400°C, the cobalt bonded NbCs presented lower wear rates than the NbCs bonded with Fe$_3$Al or having such a matrix, because of the well-known effect of Co$_3$O$_4$ formed by tribo-oxidation lowering the wear rate [5]. Basically, the wear particles from the wear tracks displayed in Figure 6 were wiped away. The microstructure of the matrix and NbC is still clearly visible and nor grain pull-out or fragmentation of NbC grains became predominant. The metallurgical interphase NbC-matrix withstands shear and NbC didn´t fragment (See Figure **6**).
The wear resistance of niobium carbide is determined by different material properties:
a. First, NbC has a very high melting point of 3,522°C, whereas WC melts at ~2.870°C
b. Tribo-oxidatively formed Nb$_2$O$_5$ melts at 1,512°C, whereas WO$_3$ tends to sublimate above 750-800°C and WC looses its tribo-oxidative wear protection. Nb$_2$O$_5$ is with 500-650 HV0.2 not so soft.
c. The elastic moduli and hardnesses of NbC are quite stable with increasing temperature as well as can be tailored through stoichiometry. The micro-hardness and hot hardness can tailored exceed those from WC.
d. It was recently shown, that reduced Nb$_{12}$O$_{29}$ contributes to the wear resistance of NbC [6], especially at high sliding speeds at RT, where the wear rate of Nb$_{12}$O$_{29}$ at 7 m/s of k$_v$= 4.9 10^{-6}

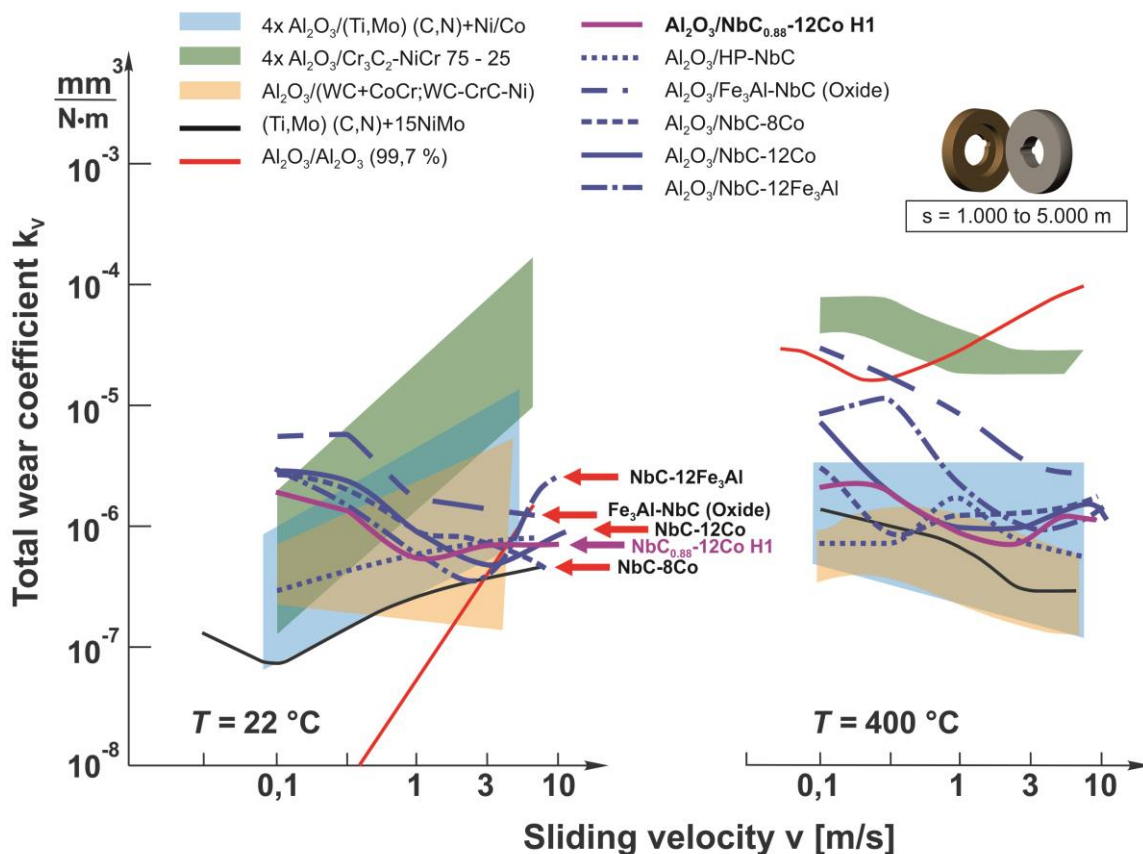mm³/N·m is close to that of NbC-based cermets in Figure 5.

Figure 5 Total wear coefficients of cobalt or Fe_3Al bonded NbCs and Fe_3Al-NbC (MMC) compared to different ceramics and hard metals under dry friction
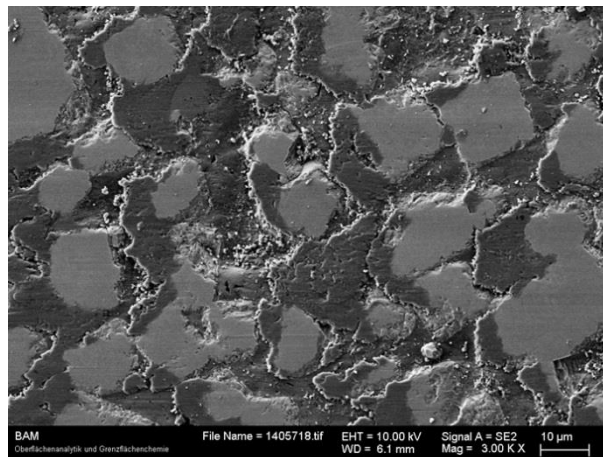

Figure 6 Morphology of wear tracks at 22°C (Fe_3Al-NbC, AD5258, (counter body: 99,7% alumina; v= 1 m/s, s= 5.000 m (or 50.000 cycles), P_{0max}= ~1020 MPa)

Figure **7** displays the load carrying capacity expressed as P·V values (contact pressure times sliding velocity). For all NbC grades P·V increased at room temperature from 1-2 MPa·m/s at 0,1 m/s up to 100 MPa·m/s at 8,0 m/s, because tribo-oxidation of NbC to different polytypes of Nb_2O_5 was enhanced with increasing sliding speed (or generated frictional heat) and a stable, non-volatile Nb_2O_5 was formed. In contrast at 400°C, the P·V values ranged more or less on the same level as at RT. The NbC grades illuminated a high wear resistance under dry sliding associated with exceptional load carrying capacity. Normally, P·V values of dry sliding tribo-couples decrease with increasing

sliding speed [7]. The triboactive materials [8,9] like $Ti_{n-2}Cr_2O_{2n-1}$-phases, (Ti,Mo)(C,N) are coming close to NbC-based materials having slightly lower P·V values or maximum frictional heat flows.
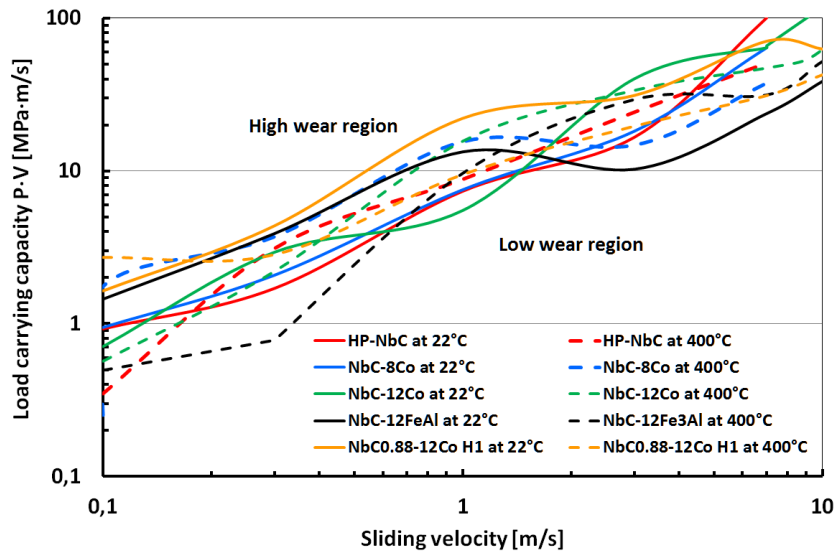
Figure 7 Load carrying capacity (maximum frictional power loss) of NbC-based materials as function of sliding speed under dry sliding conditions at room temperature and 400°C

-Cutting

Cutting tests of inserts in SNMA geometry are presented in Figure 8 and Figure 9 [10]. In semi-finishing with an emulsion under 10 bar, the NbC inserts have a very good strength. The NbC-12Fe$_3$Al (SPS) insert is less sensitive to sticking of machined material [10]. The comparison of the flank wear and the crater wear is shown in Figure 8 for WC-6%Co and NbC-12%Fe$_3$Al. The flank wear is until 50% of the turning distance parallel between both. The advantages in flank wear of the WC-6%Co insert can be explained by its (Ti,Al)N coating applied on the WC-6%Co insert. The crater wear was even 3 times greater for the WC-6%Co than for the NbC-12%Fe$_3$Al after only 1 minute of machining. These results show that uncoated NbC inserts exhibit a higher resistance to abrasive wear than coated WC inserts. The low solubility of NbC in alloys and its stable hot hardness determines the high wear resistance of NbC inserts.
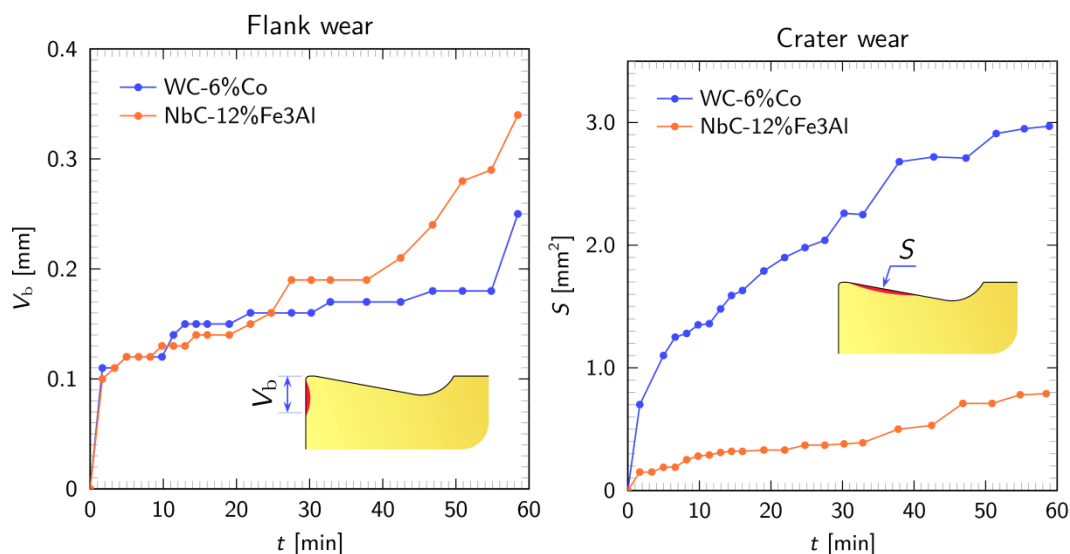
Figure 8 Comparison of the flank wear (left) and the crater wear (right) between the WC-6%Co insert and the NbC-12%Fe$_3$Al insert for the semi-finishing tests (100Cr6 205 HB, Vc =100 m/min, hex.= 0,2 mm, DoC = 1,5 mm, 10 bars emulsion, lead angle at 75°, nose radius 0,8 mm) [10]

In hard turning with an emulsion under 10 bar, the cratering for the WC insert is substantial, while the flank wear remains acceptable as shown in Figure 9. In contrast, for the uncoated NbC insert, the wear on flank wear and cratering (See Figure **9**) remained acceptable. The initial machining striae from the edge preparation are still visible indicating a very low crater wear. On the other hand, after about five minutes of hard turning, a crack appeared from released residual stresses generated during SPS sintering.

Figure 9 Comparison of crater wear in hard turning of NbC-8Co SPS (left) and WC-6Co (right) (100Cr6 (205 HB), machining time= 5 min. 33 s., Vc= 100 m/min, f = 0,415 mm/rev, hex= 0,4, DoC = 3 mm, Kr (lead angle) = 75°, nose radius= 1,5 mm, emulsion 10 bars) [10]
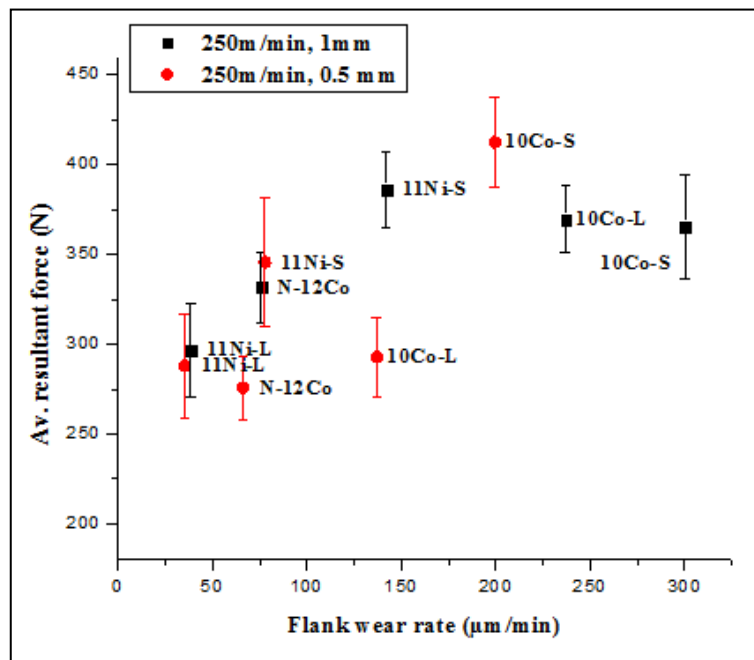
Figure 10 Comparison of insert behaviour during coolant-free interrupted milling of SABS 1431:300WA-SS (98,2 ± 0,66 HRC) at v_c = 250 m/min (a_p = 0,5/1 mm) [11]

Effect of reduction of axial depth of cut a_p from 1 mm to 0.5 mm at a v_c of 250 m/min in coolant-free

interrupted milling of uncoated SNMA inserts is shown in Figure 10. During coolant-free milling at 250 m/min, the NbC-12Co SPS insert performed better than both the SPS and LPS WC-10Co (wt%) [11]. It has to be noted, that the N-12Co (NbC-12Co) presented an attractive profile with low friction and flank wear rates, which compete with nickel bonded WC. The nickel bonded WC grades (7Ni and 11Ni) contained secondary carbides, like TiC and Mo_2C, which improved the resistance to chemical wear, whereas the NbC-12Co were straight grades without secondary carbides.

CONCLUSIONS

Stoichiometric or sub-stoichiometric niobium carbides have under dry sliding at RT and 400°C a pronounced intrinsic wear resistance associated with an exceptional high load carrying capacity, either as hard metal or as metal matrix composite. The wear rates decreased with increasing sliding speed and were associated with high load carrying capacities (P·V-values), in excess of 100 MPa·m/s. Tribological properties, micro-hardness and elastic modulus can be tailored through stoichiometry and/or binder type. The dry sliding wear resistance of the sub-stoichiometric $NbC_{0.88}$-12Co H1 were at the lower end of the stochiometric NbC grades. From the tribological point of view, the cobalt binder in the NbC hardmetals can be substituted by Fe_3Al. At RT, the wear rates of the MMC Fe_3Al-$NbC_{0,94}$ are very close to those of the NbC-bearing hard metals.Cobalt-free niobium carbide inserts have been shown to be very efficient for semi-finishing operations and are very promising under hard turning. Properties, like micro-hardness, hot hardness, sliding wear resistance, elastic modulus and toughness can be tailored by the C/Nb ratio, the addition of secondary carbides and the type of binder.

REFERENCES

[1] M. Woydt and H. Mohrbacher, The tribological and mechanical properties of niobium carbides (NbC) bonded with cobalt or Fe_3Al, WEAR 321 (2014) 1-7 (open access)

[2] S. Huang, K. Vanmeensel, H. Mohrbacher, M. Woydt, J. Vleugels, Microstructure and mechanical properties of NbC-matrix hardmetals with secondary carbide addition and different metal binder, Int. J. of Refractory Metals and Hard Materials 48 (2015) 418-425

[3] M. Scheibe, S. Binkowski, S. Benemann and R. Saliwan-Neumann, Comparison of different preparation techniques for the characterization of niobium carbides, STRUCTURE News #19, Dec. 2014, bilingual (EN/DE), available online as open access http://www.struers.com/resources/elements/12/274090/Structure%20News%2019.pdf

[4] M. Woydt and K.-H. Habig, High temperature tribology of ceramics, Tribology International 22 (1989) 75-88

[5] M. Thoma, High wear resistance at high temperatures by $Co+Cr_2O_3$ electrodeposited composite coating, Berichte der Motoren und Turbinen Union (MTU) GmbH, D-80995 Munich (Germany), Heft 41, 1985 or in WEAR, 162-164 (1993) 1045-1047.

[6] S.G. Huang, J. Vleugels, H. Mohrbacher and M. Woydt, Densification and tribological profile of niobium oxide, submitted to WEAR

[7] M. Woydt, Tribologie des céramiques (Tribology of ceramics), Encyclopédie Techniques de l´Ingénieur, Paris, March 2013, Tri 4 550.

[8] L.-M. Berger, C. C. Stahr, S. Saaro, S. Thiele, M. Woydt and N. Kelling, Dry sliding up to 7.5 m/s and 800°C of thermally sprayed coatings of the TiO_2–Cr_2O_3 system and (Ti,Mo)(C,N)-Ni(Co), WEAR 267 (2009) 954-964

[9] L.-M. Berger, S. Saaro, M. Woydt, WC-(W,Cr),C-Ni – the unknown hardmetal coating, Thermal Spray Bulletin 1/08 (2008) 37-40

[10] G. Le Quilliec, R. Leroy, C. Richard, M. Woydt, A. Morandeau, Comparison of the life-span of NbC-Co and WC-Co inserts during different machining operations on 100Cr6 (SAE 52100) bearing steel, Proc. Int. Symp. on Wear Resistant Alloys for the Mining and Processing Industry, 04.-07. May 2015, Campinas, São Paulo, Brazil

[11] R.M. Genga, L.A. Cornish, M. Woydt, K. Sobiyi and C. Polese
Wear and mechanical properties of SPS and LPS WC and NbC based cemented carbide inserts, Proc. Int. Symp. on Wear Resistant Alloys for the Mining and Processing Industry, 04.-07. May 2015, Campinas, São Paulo, Brazil

Keynote 1

ABRASION RESISTANT MATERIALS ON FE-BASE

W. Theisen[1] (theisen@wtech.rub.de, phone: +49(0)234-32-25964,
fax: + 49(0)234-32-14104),

[1]Lehrstuhl Werkstofftechnik, Ruhr-Universität Bochum, 44801 Bochum, Germany

Introduction

Abrasion is one of the four main wear mechanisms that is determined in components being in contact with mineral goods. Typical examples of use are found in the processing technology during chopping up, classification, transport and storage of mineral goods as well as in contact of tools with hard counterbodies like rock or concrete [1]. Characteristic for this kind of undesirable material loss is a penetration of harder particles that, with movement relative to the surface, generate grooving abrasion. Worn surfaces are characterized through indentation marks of mineral particles and grooves which, in their geometry, are defined through the particle size, their form and through the normal force in the tribological system.

Material engineering countermeasures are firstly based on an increase of the material hardness, as it can be derived in ferrous materials by martensitic transformation. A high hardness causes a large resistance against the indentation of mineral particles into the surface. This leads to less abrasion through reduction of the groove depth. Against deep grooves, hard phases are especially effective, such as carbides that are introduced into a metallic matrix. They further increase the hardness and impede the penetration of the mineral particles into the material surface. Besides, they put themselves against the grooving mineral as an obstacle if they are harder than the attacking minerals (**Figure 1**). Thereby, the abrasion resistance can be increased with increasing hard phase volume fraction. A dispersive distribution of hard phases is favourable, albeit with high hard phase proportion, especially when the mean free matrix path length is reduced so that only a small matrix area is exposed to grooving [2].
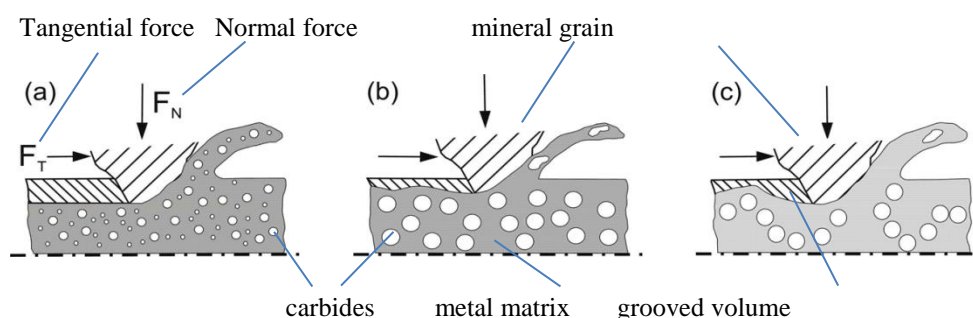

Figure 1: Schematic diagram of abrasion caused by a mineral grain according to [2]

The design of Fe-base alloys against abrasion must take the above implementations into account. However, in technical materials, the influence of the manufacturing on the desired microstructure is also to be considered. Here, powder metallurgical production offers greater design freedom than fuse metallurgy.
Hereinafter, the fundamental material aspects of the metal matrix and the hard phases will be discussed first. Subsequently, wear resistant materials that are nowadays employed will be introduced and described with regard to the effectiveness of the material-technical countermeasures

against abrasion. The materials range from simple wear-resistant structural steels to hardened and tempered steels and tool steels up to wear-resistant white cast iron, weld deposits and powder metallurgy- generated Metal Matrix Composits (MMC).

2. Structural constituents

2.1   Metal matrix

The properties of Fe- base metal matrices are based essentially on the mechanisms that are also exploited for the heat treatment of steel. The solid solution hardening of ferrous matrices is based - as in steel - on the substitutional incorporation of the elements chromium, molybdenum, manganese, nickel, silicon and vanadium as well as the interstitial incorporation of carbon, wherein the hardening through carbon in the martensite is the most effective. Nowadays [4], calculations according to the Calphad method deliver a major gain in knowledge. With commercial software packages and databases, it is possible to calculate the originating phases in nearly any compositions in equilibrium and to issue them as phase diagrams. This may save a lot of experimental work and time in alloy development.

Fe- base alloys are hardened martensitically. A specific tempering treatment - where hardness decreases with the tempering temperature and the toughness increases - follows after a rapid cooling after austenitizing for martensitic transformation. In the presence of the elements chromium, molybdenum, vanadin or niobium, secondary carbides can be solidified which cause a secondary hardness maximum at tempering temperatures around 500 °C and thus confer a certain hot strength of the metal matrix. At high hardness temperature or while cooling down from the casting heat, the martensitic transformation is often incomplete at C- contents above 0.5 wt.-%. In these cases, the martensite finish temperature is below RT, so that residual austenite remains behind in the microstructure. Soft, stable residual austenite in contents above approx. 30 Vol.-% reduces the wear resistance against abrasion, however, offers a certain deformation reserve at the same time. Alloy-technically, the stability of the residual austenite can be reduced, so that this can be transformed into a strain or stress induced martensite during grooving wear. As a positive effect, this leads to a hardness increase in the near-surface edge zone while the bulk material beneath, however, remains tough [3].

2.2   Hard phases

Hard phases are generally designated according to their composition with the chemical structural equation Y_aX_b. They can be divided, with respect to the predominant binding character of their atoms, into covalent, ionic and metallic hard phases, where the latter are suited in a special way for embedding them into metallic matrices. Typical properties are high hardness, a high modulus of elasticity and high melting point as well as a low thermal coefficient of expansion with good chemical and thermal stability [4].

In Fe- base alloys, in particular the carbides of the transition metals have acquired a significant importance. They are designated according to their chemical structure with M_aC_b, where, in M depending on carbide type, more or less metal atoms from the alloy are bound. Thus, Fe_3C - known as cementite in Fe-C- alloys - also dissolves chromium and becomes a little harder thereby. In higher chromium-containing and carbonaceous Fe- alloys, the carbides $M_{23}C_6$ and M_7C_3 are stable, in which iron as well as chromium is dissolved at high proportions in the metal part. This also has effects on the properties of these carbides. While a pure chromium carbide of the type M_7C_3 reveals a micro hardness well above 2000 HV0,05, the hardness decreases with increasing Fe- content in the carbide to about 1350 HV0,05. With regard to a high wear resistance, the three mono carbides of the elements titanium, niobium and vanadium have turned out to be favourable as MC

carbides with the same amount of metal and carbon. They show micro hardness levels above 2000 HV0.05 and therefore cannot be grooved by many minerals (**Table 1**). All three of them are face-centred cubic and due to the fact that they are isomorphic they appear in hybrid forms in which carbon may also be partially replaced by nitrogen so that mono- carbonitrides emerge [4].

The solubility for other metal atoms is very different in the NbC, in the TiC and in the VC. The NbC has proved to be extremely advantageous in stainless Fe- materials because it hardly dissolves Fe, Cr or other alloy elements in the steel. Therefore, the early forming high hardness NbC can be solidified with niobium and carbon from the molten bath, which leave behind chromium in contents above 12 wt.-% in the Fe-Matrix for corrosion resistance.

Table 1. Physical properties of metallic hard phases used in Fe-base alloys [2] and predominantly own measurements

	hard-ness [HV0,05]	density [g/cm^3]	α [10^{-6} K^{-1}]	E-Module [GPa]	T$_S$ [°C]
Fe$_3$C	850	7.67[a]	4.2[b]	177[c]	1152[d]
(FeCr)$_7$C$_3$	1400	6.92	10.3	360	1780
Cr$_3$C$_2$	2150	6.68	10.6	400	1890
WC/W$_2$C	2560	16.53	5.9	680	2800
NbC	2200	7.78	7.2	580	3613
VC	2900	5.41	7.3	430	2800
TiC	2950	493	8.3	470	3070

a: [5]
b: [6]
c: [7]
d: [8]

2.3 Properties of hard phases and metal matrices

Important properties of hard phases and metal matrices can be gained in an easy way from indentation experiments. With micro- and nano-indenters, load-indentation curves can be accommodated in nearly arbitrarily small structural phases from which the indentation hardness and the modulus of elasticity can be determined (**Figure 2**). In addition, the cracks often appearing in hard phases in and around the indentations can be used for the evaluation of the fracture toughness. Very important knowledge of the interaction of mineral particles with the microstructure constituents is being provided by individual scratch tests that can also be carried out on a micro- and nano-scale. Here, a geometrically determined indenter made from diamond or cubic boron nitride (CBN) is exposed to normal force and moved over the surface of a wear material for the generation of single grooves. If here the tangential force measured is related to the cross-sectional area of the grooving, the so-called specific scratch energy e$_s$ can be calculated, which constitutes a measure of the resistance of a phase against grooving. **Figure 3** shows the scratch energies for some hard materials and select metal matrices. The diagram shows that the temperature-related softening in Fe-Matrices is large, in the hard phases smaller and differs according to hard phase type. As the service temperature increases, the hardness of the metal matrix decreases and recovery as well as recrystallisation processes take place. Up to ≈ 500°C the scratch energy of a martensitic metal matrix (X40CrMoV5-1; 1060°C/oil/620°C) is about twice as high as that of a ferritic (X2Cr11) or an austenitic (X2CrNiMo17-13-2) matrix. However, at higher temperatures the scratch energy of a bcc matrix decreases to a greater degree than the fcc matrix, which exhibits the higher scratch resistance above 800°C.

Beside the specific scratch energy, the micromechanisms of abrasion (micro cutting, micro plough-ing and micro cracking) provide information about the behaviour of the respective structural con-stituents during grooving wear. Out of this, another characteristic value follows, which indicates the relative ratio of micro cutting to micro ploughing f_{ab}, in particular for the area of the metal matrix. Here, micro cutting means material loss, while micro ploughing causes plastical deformation and the displacement of the groove volume to the groove edge without material loss. Hence, a low f_{ab}-value means a lower wear amount can be expected.
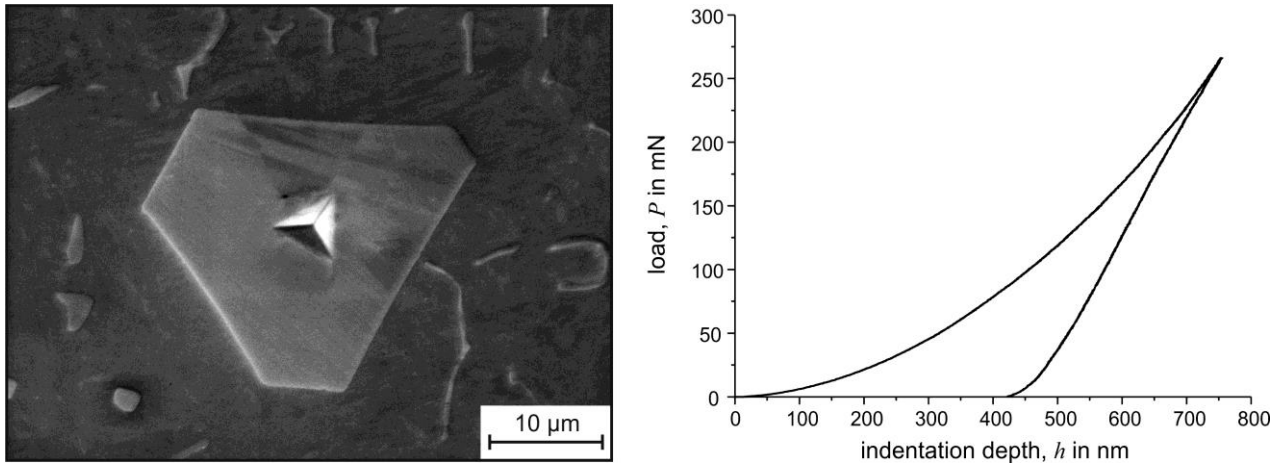
Figure 2: Indentation mark with typical load-penetration curve (h_{max} = 750 nm) in NbC carbide
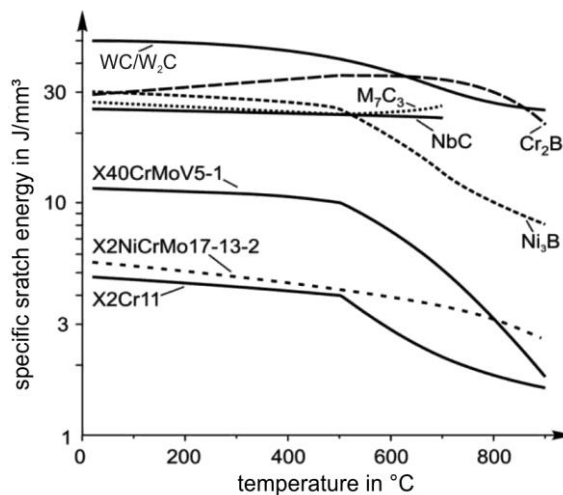
Figure 3: Specific scratch energy as a function of temperature from single scratch tests for select-ed hard phases and metal matrices (CBN-Indenter, angle of attack α=90°C, flank angle 2θ=115°C, F_N=0.3N, scratch velocity v=2 µm/s) [2]

As in other cases of the engineering sciences, the simulation of the material stress is also applied in the course of the design of wear-resistant materials [9]. Though it is not possible to the present day to dependably simulate the material loss occurring through repeated grooving, however, the efforts concerning the individual events of indentation and scratching are partly far advanced. **Fig-ure 4 a)** shows the stress field that can be simulated through indentation with a geometrically de-termined indenter. Nowadays, such calculations can already very well illustrate the behaviour of metal matrices and hard phases in the indentation test. **Figure 4 b)** shows the result of a Fe- simu-lation in a metal matrix with small hard phases (with respect to the indentation size). In this man-ner, it is possible to simulate the contributions of hard phases in the interplay with the metal matrix and to utilize it for the microstructure design. Such simulations are explained in more detail in an-other contribution to this conference.
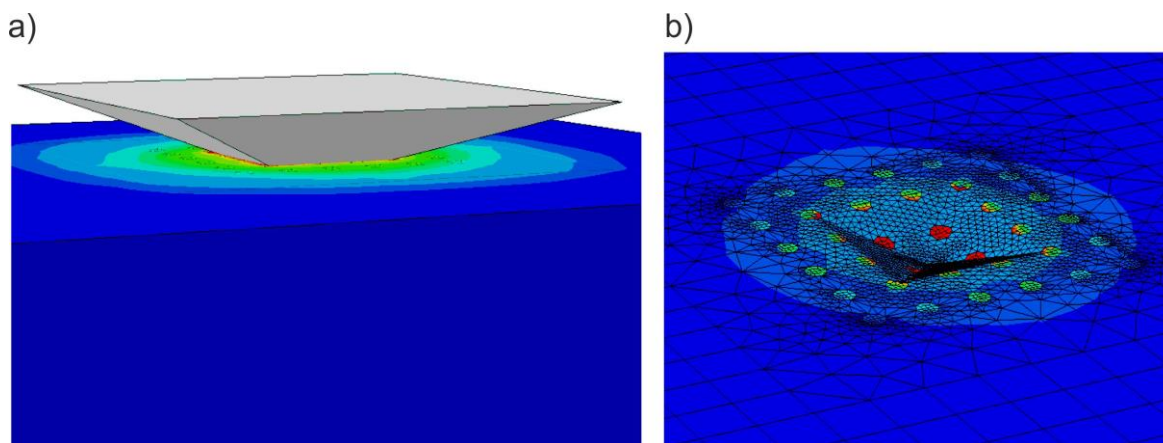
Figure 4: FEM-Simulation of the Indentation in a) a hard phase and b) a hard phase containing material

3. Abrasion resistant materials

3.1 Special wear-resistant structural steels

In many application cases, abrasion-resistant and at the same time economical metal sheets are required that have to be weldable, too. In these cases, wear-resistant special structural steels are being used. With C- contents ranging between 0,2 and 0,3, there are different varieties named after their hardness (e.g. Hardox 500 working hardness 500 HB), containing approx. 1,5 % Mn, 1,2 % Cr and up to 0,5 % Mo as well as to increase the hardenability 0,005 % B. They are water quenched and tempered at the steel manufacturer so that a tempered martensite is present, which due to the low C- content can still be welded crack-free with preheating. Typical application cases include linings of hoppers, chutes and shovels of construction vehicles, where abrasion occurs through mineral sliding wear.

3.2 Quenched and tempered steels

For the crushing of mineral goods and/or under high surface pressures, harder steels with carbon contents between 0.3 – 0.6 % C are being used. There is widespread (e.g. for chain links of caterpillar vehicles) use of the steel 34MnB5 that can be martensitically hardened in small cross sections. Crushing hammers in hammer mills are produced, for example, from tempered steel castings 55NiCrMoV6. Via the tempering temperature, the tempering hardness and/or the notched impact strength is set. In hammers from tempered steel, the impact tip is set to a working hardness above 52 HRC and the hammer eye, because of the higher toughness important there, is heat-treated to less than 40 HRC. Briquetting and compacting rollers for potash, fertilizer, gypsum, dusts and fine ores consist of similar steels, according to operating conditions (56NiCrMoV7). Steel rings for the cutting discs of shields in tunnel boring machines are made from the higher alloyed steel X50CrMoV5-1, because a higher working hardness and a high strength are required. After martensitic hardening and tempering in the secondary hardness range, tensile strengths are achieved of up to 2000 MPa while the working hardness reaches 56 HRC. Surface hardening with flame or induction heating has proved itself beside continuous heat treatment of the bulk [2].

3.3 Hard phase containing steels and white cast iron

With greater abrasion stress, ledeburitic cold work steels are used. They often contain up to 12 % of chromium and 1.6 % C (e.g. X153CrMoV12-1) because through this carbide of the type M_7C_3

can be solidified from the melt. The alloys often designed as casting tools are martensitically hardenable and are suited as crimping tools for ceramic bodies and as crushing tools. If the carbon content is further raised in the direction of 3 % of carbon, the hard phase content increases further and the group the white cast iron is achieved. With Cr- contents < 4 wt.-% carbides solidify, whereby the matrix becomes martensitic as a rule through cooling from the casting heat. Higher alloyed varieties contain between 15 and 30 % Cr, so that the harder M_7C_3 can be embedded in a martensitic matrix. If niobium is added in contents between 5 – 7 %, then the significantly harder niobium monocarbides NbC will form from the molten bath first, which further increase the abrasion resistance [10]. It is advisable, to lower carbon and Cr- content then, however, because the risk of cracking in the necessary hardness treatment increases with the hard phase content.
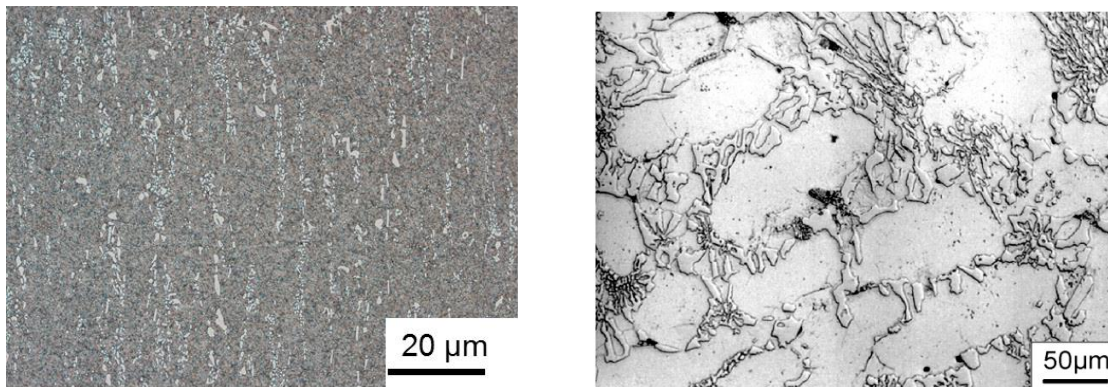
Figure 5: Microstructure of hard phase containing Fe-base alloys
      a.) ledeburitic tool steel X153CrMoV12
      b.) white cast iron GX300CrMo15-3

Austenitic manganese steel castings (e.g. GX140MnCr17-2) pursue another microstructure concept. The alloy system is designed thus that an austenitic microstructure without hard phases originates. Therefore, the alloys are toughs, however, are able to increase the hardness, in particular with impact load in the surface, through cold work hardening, to up to 58 HRC in their hardness, whereby the self-generated surface zone is less than 100 µm thick [2].

3.4 Weld deposites and MMC for HIP Cladding

There is still the possibility to provide economical substrate materials with a high hard material containing layer through flux cored wire deposition welding. The range of coating materials extends from simple martensitic steels with 0.3 - 0.5% C to hypereutectic alloys containing superhard phases and up to 6%C, 2% B, 40% Cr and further metallic elements (Nb, V, W, Mo, Co). In alloys with up to 5 % of carbon and 30 % of chromium, M_7C_3- carbides are eliminated primarily from the molten bath in the maximum 15 mm thick layers in a volume fraction > 50 Vol.-%. Alternatively, during the Plasma-Transfer-Arc (PTA-) welding, hard material powder (e.g. fused tungsten carbide WC/W_2C) can be sprinkled into the molten bath. More recent developments replace the expensive Ni-Matrices commonly used in by hardenable Fe-Basis-Matrices into which, at the same time, alternative oxidic hard materials can be deposited [11].

By hot-isostatic pressing (HIP) hard phases containing Metal Matrix Composites (MMC) can be produced by powder metallurgy and be applied as a several millimetres thick layer on wear parts (HIP-Cladding). This happens on the basis of gas atomisation tool steel powders to which, from case to case, hard materials in contents between 5 and 30 Vol.-% are admixed. Through a compacting process at a temperature of 1150 °C and a pressure of 1000 bar, the powder particles are

compacted up to theoretical density and at the same time bonded with a base metal. MMC have the advantage compared with microstructures produced by melting metallurgy that the hard phases can be freely selected and hence be optimally coordinated to the attacking minerals. In addition, by means of HIP-Cladding coatings, mechanically more stable layers can be produced than is possible by means of deposition welding or through thermal spraying.
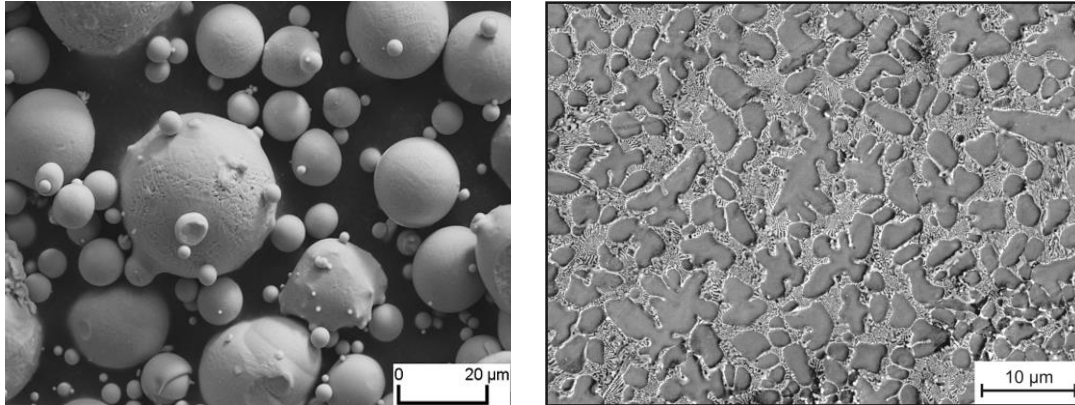

Figure 6: Gas atomized steel powder (a.) and fine hypoeutectic microstructure (b.) in the as sprayed condition

Figure 6 shows a photograph of a steel powder and the typical solidification microstructure of a ledeburitic cold work steel powder of the type X230CrVMo13-4 in the gas atomisation state. These are identified through very fine metal cells are surrounded by a fine eutectic mixture of M_7C_3- carbides and an austenitic/martensitic metal matrix (Fig. 6b). With above-mentioned process conditions and dwell times of four hours, the fine eutectic carbide lamellae will transform to a rounded shape and will grow, through Ostwald ripening, to a size of 3 – 5 µm and finally, are dispersed in the metal matrix. (Figure 7a) A similar microstructure can be achieved with a steel powder of the type X240VCrMo10-5-1, where the dispersion carbides are mono carbides of the type VC in this case because of the high vanadium content.
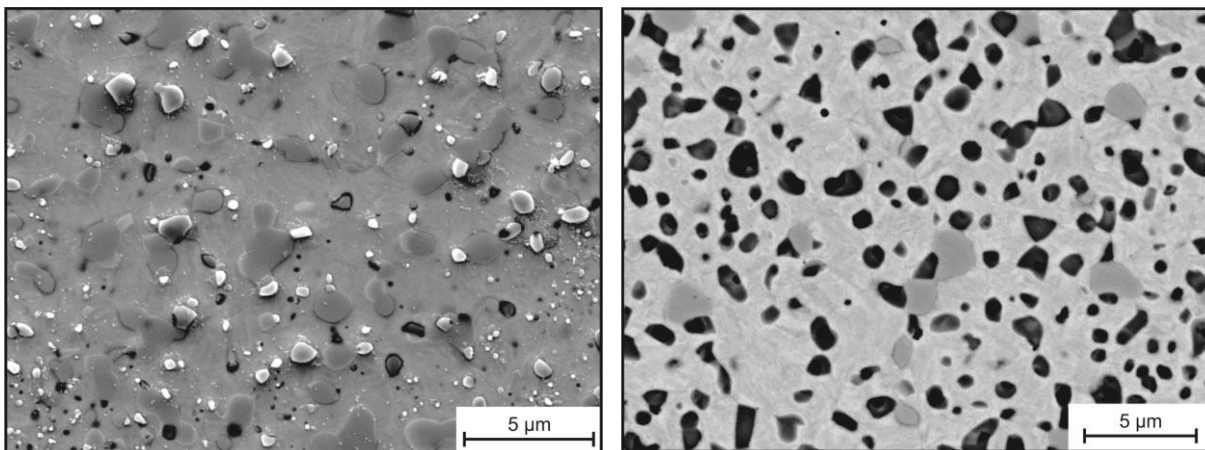
Figure 7: Microstructure of ledeburitic steels in the as hipped condition containing M_7C_3 carbides
(light grey) an VC (black)
   a.) X230 CrVMo13-4
   b.) X240VCrMo10-5-1

The microstructure of the MMC is governed by the processes occurring during hot compaction, significantly interdiffusion of elements, as well as by the grain-size ratio of the powered components (Fig. 8a) [4]. As a consequence of approaching a thermodynamic equilibrium, a diffusive shell develops in the steel matrix around the original hard phases during hot compaction, e.g. for fused tungsten carbide (WC/W2C). This shell consists of W2C as well as M6C towards the outer regions and has a positive effect on embedding the hard phase in the steel matrix because it lessens sudden changes in the properties (E, HV, α) at the hard-phase/matrix interface. The distribution of hard phases can be influenced by the grain-size ratio and by the volume fractions of hard phase and matrix powders. Hard-phase fractions of < 30 volume-% can form brittle networks if the hard-phase powder is significantly finer than the matrix powder (Fig. 8b). In contrast, a respective hard-phase fraction with a narrow range of grain sizes similar to or larger than that of the matrix powder produces a tough material with a dispersed hard phase (Fig. 8a) [12].
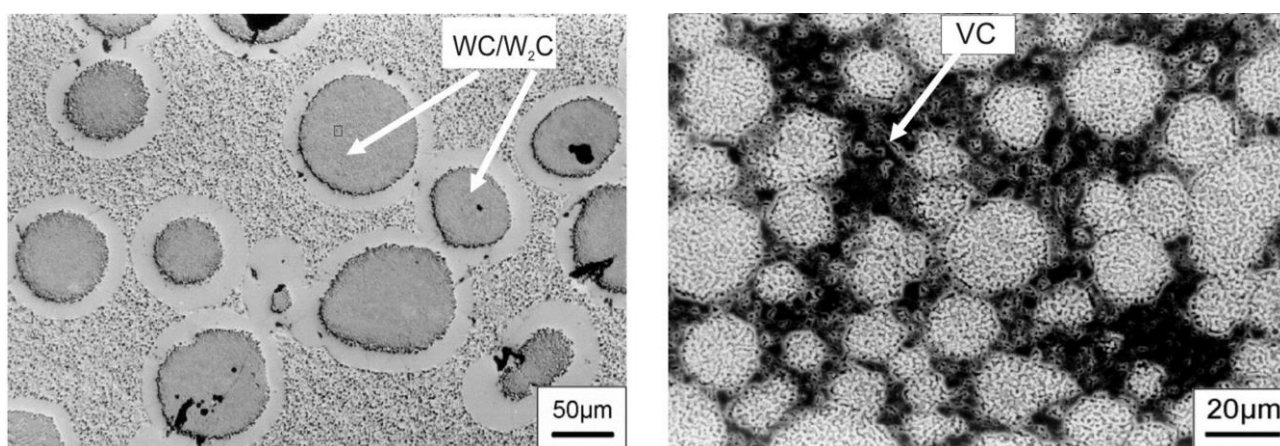
Figure 8: MMC on base of a cold-work steel matrix X225CrVMo13-4 (~150 μm) with
a) Fused Tungsten Carbide WC/W$_2$C (~150 μm)
b) Vanadium Carbide VC (< 40 μm) according to [11]

4. Abrasive wear resistance

In the pin-on-disk test using abrasive paper with flint (80 mesh), which is softer than the hard phases in the microstructure of the materials investigated, the wear resistance W_{ab}^{-1} increases with the proportion of hard phases. Tool steels, martensitic chromium white cast iron and welding alloys generally contain M$_7$C^3 carbide and lie within the same scatter band. Despite their high proportions of hard phases, martensitic nickel white cast iron lie underneath the band because they contain softer M$_3$C. The MMC layers, which can have almost any thickness, exhibit excellent wear resistance.
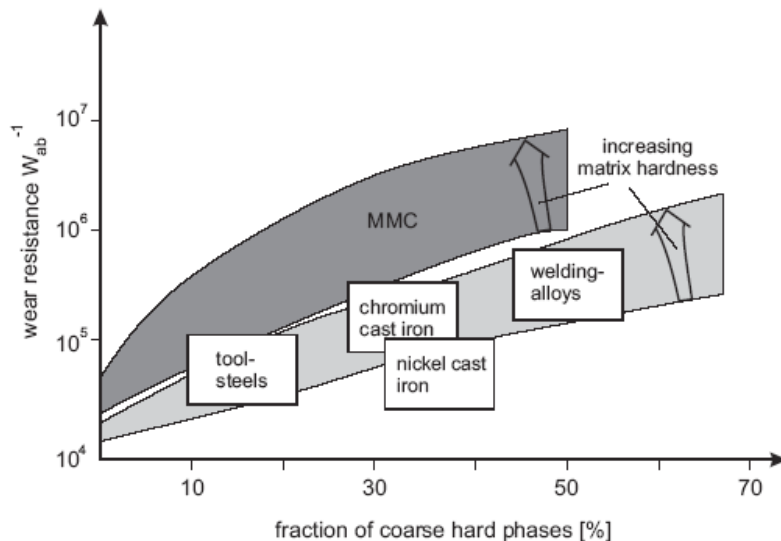
Figure 9: Results from pin-on-disk test against flint (80 mesh) [2]

A MMC made of atomized X225CrVMo13-4 and a hard-phase fraction of 30 volume-% WC/W_2C (150 μm) shows a wear resistance that is greater by a factor of 40 than that of the pure steel matrix and greater by a factor of 6 than the martensitic chromium cast iron GX300CrMo5-3 hardened to 800 HV30. This is due not only to the high hardness of the tungsten carbides but also to their high fracture toughness. They have proven very resistant, even against Al_2O_3, and give the composite a significantly greater wear resistance compared to a weld deposit.

References

[1]   W. Theisen, Mat.-wiss. u. Werkstofftech. 2005, 36, 8, 360 – 364, Herstellung verschleißbe-
         ständiger Metallmatrix-Verbunde auf Fe-Basis

[2]   H. Berns, W. Theisen, Eisenwerkstoffe, 4th edition Springer-Verlag, Berlin, 2008, p. 252

[3]   W. Theisen, Fortschr. Ber. 1997, VDI-Reihe 2, Nr. 428, VDI-Verlag, Düsseldorf, Bearbeiten
         verschleißbeständiger Legierungen aus werkstofftechnischer Sicht

[4]   H. Berns, Ed.: Hartlegierungen und Verbundwerkstoffe, Springer Verlag, Berlin 1998, 33-52

[5]   F.X. Kayser, A. Litwinchuk, G.L. Stowe, Metallurgical Transactions A 1975, 6, 55 – 58, The
         densities of high-purity iron-carbon alloys in the spheroidized condition

[6]   K.D. Litasov, S.V. Rashchenko, A.N. Shmakov, Y.N. Palyanov, Journal of Alloys and
         Compounds 2015, 628, 102 – 106, Thermal expansion of iron carbides, Fe7C3 and Fe3C,
         at 297–911 K determined by in situ X-ray diffraction

[7]   H. Mizubayashi, S.J. Li, H. Yumoto, M. Shimotomai, Scripta Materialia 1999, 40, 7,
         773 – 777, Young's modulus of single phase cementite

[8]   L.S.I. Liyanage, J. Houze, S. Kim, M.A. Tschopp, S.G. Kim, M.I. Baskes, M.F.
         Horstemeyer, Physical Review B, 89, 2014, 1 – 12, Structural, elastic, and thermal proper-
         ties of cementite (Fe3C) calculated using a modified embedded atom method

[9]   F. Pöhl, S. Huth, W. Theisen, Materials Science and Engineering: A 2013, 559, 822 – 828, Finite element method-assisted acquisition of the matrix influence on the indentation results of an embedded hard phase

[10]   W. Theisen, G. Gevelmann, Journal of ASTM International 2011, 8, 9, 1 – 8, New Cast Iron Alloys with High Wear Resistance at Elevated Temperatures

[11]   A. Röttger, S. Weber, W. Theisen, R. Winkelmann, DVS-Congress und DVS-Expo 2011, 272 – 279, Alternative hartstoffhaltige Beschichtungen durch InduClad

[12]   W. Theisen: Design of wear resistant alloys against abrasion, M. Pellizzari, editor Proceeding of ABRASION 2008 in Trento

TOOL STEELS FOR HOT STAMPING OF HIGH STRENGTH AUTOMOTIVE BODY PARTS

Dr.-Ing. Ch. Escher, Dr.-Ing. J. J. Wilzer

Dörrenberg Edelstahl GmbH, Qualitätszentrale, 51766 Engelskirchen, Germany

Christoph.Escher@doerrenberg.de, Jens.Wilzer@doerrenberg.de

ABSTRACT

Hot stamping of high strength automotive body parts is a key technology to fulfill safety requirements and CO_2-emmision limit values which are made by the EU. In the last ten years, high effort was made to improve the hot stamping process. Besides optimizing workflow and heating of the sheet metal blanks, new tools steel grades were developed which show beneficial properties with respect to hot stamping and hard cutting of high strength body parts. Furthermore, engineering of cooling systems results in different cooling strategies which all shall improve the cooling efficiency of hot stamping tools. In combination, these improvements lead to a reduction of cycle time and maintenance work and therefore increases productivity of hot stamping processes. This paper gives a short summary of the latest developments with respect to tool steels for hot stamping and hard cutting tools including concepts for active cooled hot stamping tools.

KEYWORDS

High strength steels, hot stamping, hard cutting, tool steels, cooling concepts

1. INTRODUCTION

The demand of high strength steels for automotive body parts increased continuously in the last 30 years (Fig. 1 a). One reason is the increasing safety standard for passengers. As it can be seen in Fig. 1 b, the passenger cab of the VW Golf VII is made of high strength steels which shall protected the passenger in case of accident.
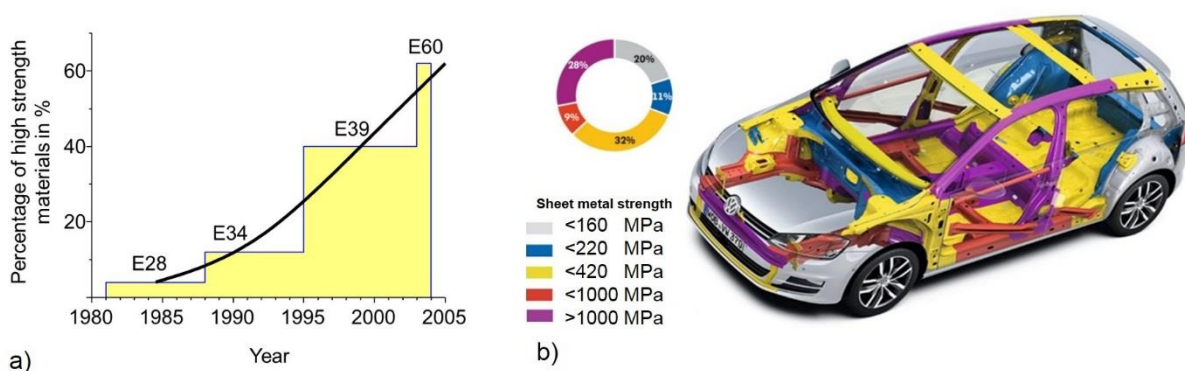
Fig. 1: a) Increasing demand of high strength material for automotive body parts; b) Sheet metals used for automotive body parts for the VW Golf VII [1].

Another driving forces are the CO2-emission limit values for the automobile industry. One strategy to fulfill these requirements is the reduction of weight and therefore the reduction of petrol consumption [2]. As an example, the autobody weight of the new VW Golf VII was reduced by 23 kg just by including a higher amount of high strength steels [1]. Therefore, the use of high strength steels for automotive body parts has two big benefits. However, the production of high strength body parts is not easy. Cold forming of high strength steels has many disadvantages. Besides high

deformations forces and mechanical loads on the cold forming tools, the spring back and the risk of cracking of the deformed parts is very high. Therefore, engineers reused a production method which was developed in the seventies of the last century and was first used to produce high strength body parts in the year 1987 [3, 4]. It is called hot stamping – sometimes also hot forming or press hardening – and it evolved to a key technology with respect to the production of automotive body parts. As it is shown in Fig. 2, the demand on hot stamped body parts has been increasing continuously since the beginning in 1984 and it was suggested that it achieves 350 million parts in 2015.
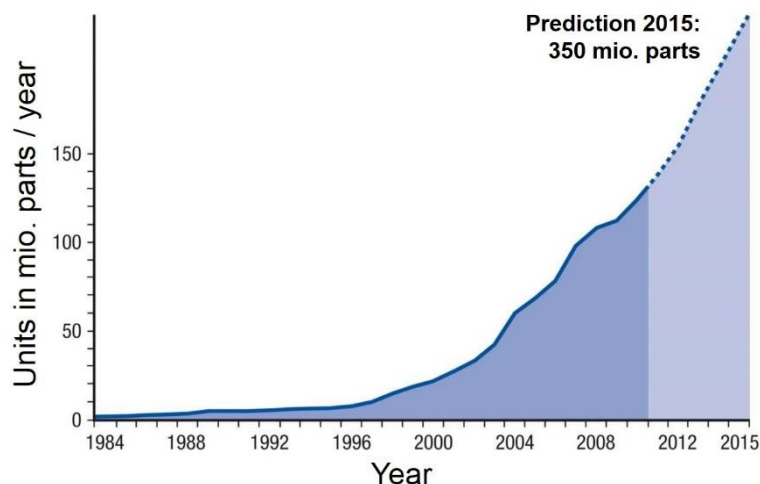
Fig. 2: Demand on hot stamped body parts in the automotive industry [5].

There are two different hot stamping processes which have to be distinguished (Fig. 3). Using the direct hot stamping process, a sheet metal blank is directly formed and quenched in a single hot stamping tool. In comparison, using the indirect process, forming and quenching is done in two separate tools. In the first tool, the blank is preformed. In the second tool, the preformed parts is quenched and calibrated after austenitization [4]. Due to the long process chain of the indirect hot stamping, it is not widely used in the automotive industry. Most assembly lines work according to the direct method.
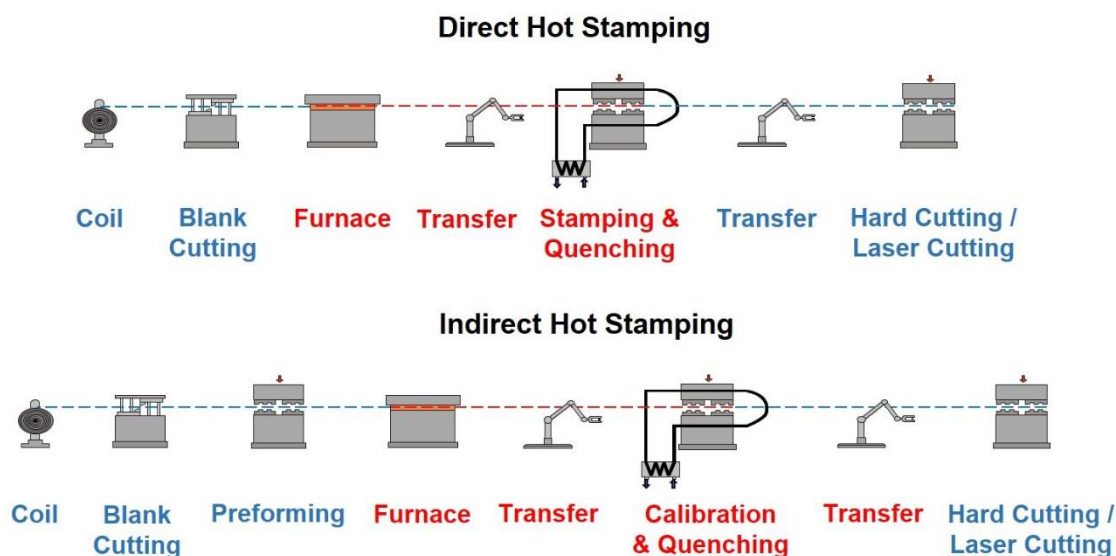
Fig. 3: Process flow of the direct and indirect hot stamping.

However, using the direct hot stamping process, there is a significant higher impact on the hot stamping tool. The major failure is abrasive and adhesive wear which is caused by sliding of the

sheet metal against the tool surface [6]. It is also influenced by sheet metal coating which is usually used to protect the blank against oxidization during austenitizing [7]. Furthermore, during forming of the sheet metal blank, high mechanical loads are induced which might lead to deformation or cracking of the tool. In addition, inserting a hot sheet metal blank into the tool results in additional thermal loads which will add to the mechanical loads [8].

To resist wear, mechanical, and thermal impact, tool steels have to fulfill several requirements when used for hot stamping tools. They should offer a high hardness and tensile strength to withstand thermal and mechanical stresses and to increase wear resistance. However, they also should offer a sufficient toughness to avoid spontaneous cracking. Furthermore, they should exhibit a high thermal conductivity to reduce thermal stresses which are caused by internal thermal gradients. Additionally, a high thermal conductivity also improves product quality and the productivity of the hot stamping process because heat can be transferred much faster from the sheet metal into the tool. Therefore, the risk of bainitic or pearlitic transformation is reduced and the hot formed body part can be removed much faster from the tool which increases the number of hot stamped parts per hour.

However, after hot stamping, the high strength body parts have to be hard cut. In this case, thermal conductivity is less important whereas the demand on hardness, wear resistance, and toughness increases. Therefore, hot stamping and hard cutting of high strength automotive body parts require special tool steel material properties which have to be ensured by using different tool steel grades or by performing special heat treatments for each application.

The present article gives a concise overview of the state of the art with respect to hot stamping and hard cutting tool steels. It is shown that during the last 15 years many different tool steel grades were developed which already established in practice.

2. GENERAL CLASSIFICATION

As it is shown in Fig. 4, tool steels used for hot stamping and hard cutting of automotive body parts can be divided into three groups. Steels in group 1 show a good toughness and resistance against thermal fatigue. Steels in group 2 achieve a higher hardness and therefore offer a higher wear resistance. Steels in group 3 have a high carbide volume fraction. They can be heat treated to a very high hardness and exhibit a very high wear resistance.

Tab. 1: Tool steels used for hot stamping and hard cutting of high strength body parts.

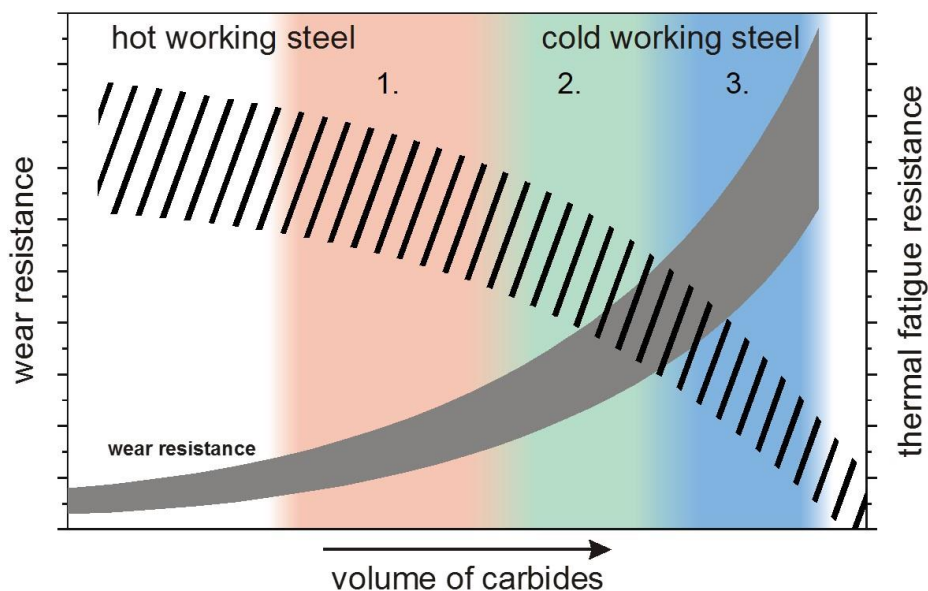| Group	Material	Nominal Chemical Composition in wt.%					
		C	Si	Cr	Mo	V	W
1.	X38CrMoV5-3	0,38	0,40	5,00	3,00	0,50	-
	X40CrMoV5-1	0,40	1,00	5,30	1,40	1,00	-
	WP7V	0,50	0,90	7,80	1,50	1,50	-
2.	AMO / GAMO	0,60	0,35	4,50	0,50	0,20	-
	CP4M® / GP4M®	0,60	1,00	5,00	+	+	-
	CP2M® / GP2M®	0,65	0,20	2,00	+	+	+
3.	CPOH	1,00	1,10	8,00	2,50	0,30	-
	CPR	1,20	0,25	12,00	1,40	1,70	2,50
	X153CrMoV12	1,55	0,35	12,00	0,80	0,90	-

Fig. 4: Classification of tool steels used for hot stamping and hard cutting of high strength body parts.

It is obvious that steels in group 1 show advantages with respect to hot stamping whereas steels in group 3 have benefits in case of hard cutting. Steels in group 2 exhibit advantages for both applications. However, as it was already mentioned, lifetime of tools used for hot stamping and hard cutting is not just a question of wear resistance and resistance to thermal fatigue. There are much more requirements which have to be fulfilled and which change from tool to tool.

3. TOOL STEELS USED FOR HOT STAMPING TOOLS

Tool steels used for hot stamping tools should offer a high hardness and good wear resistance to withstand tribological attack during service time. However, they should also have a sufficient toughness to avoid cracking due to thermal and mechanical overloads. A high thermal conductivity is beneficial to reduce thermal gradients inside tools which produce high thermal loads. Furthermore, using tool steels with high thermal conductivities, there is a faster heat transfer from the hot blank into the tool which reduces closing times and increases productivity of the hot stamping process. Additionally, tool steels should also show a good tempering resistance, especially with respect to tailored tempering applications. However, the materials should also have a good machinability and they should be nitridable and coatable to increase wear resistance.

In the past, many different tool steel grades were developed which show some advantages with respect to hot stamping applications. As it is shown in Fig. 5, the standard grade X38CrMoV5-3 (1.2367) has advantages with respect to toughness and machinability. However, its wear resistance and thermal conductivity is low compared to other tool steels. X38CrMoV5-3 is widely-used for hot stamping tools and it is sometimes taken as a reference material when new tool steel grades are tested.

The special steel WP7V is an 8%-chromium steel which shows a low thermal conductivity. However, it has a good toughness and sufficient wear resistance which can be increased by nitriding of the surface. WP7V is also widely-used for hot stamping tools and it shows very good results with respect to wear and lifetime.
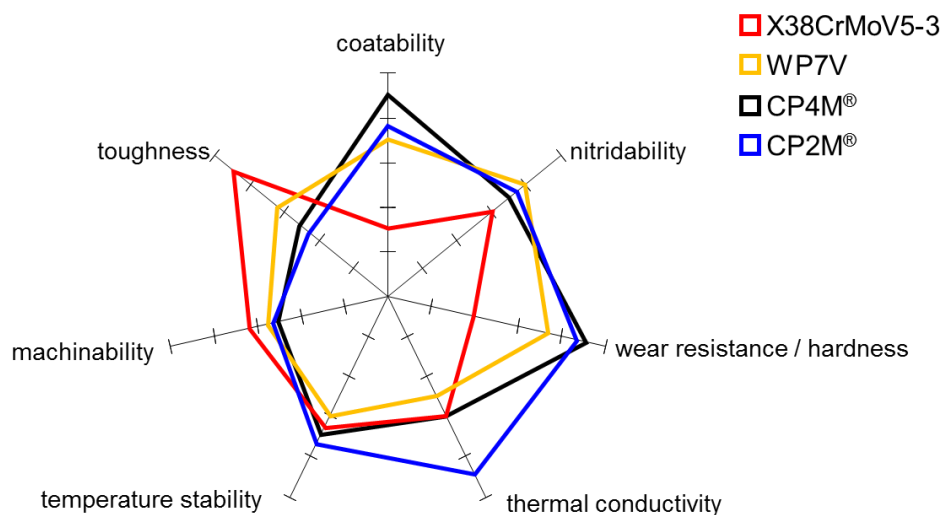
Fig. 5: Comparison of the properties of steels X38CrMoV5-3, WP7V, CP4M®, and CP2M® which are used for hot stamping tools.

CP4M® was developed for high wear impact. Its wear resistance can be enhanced by nitriding and coating. However, its toughness is lower compared to X38CrMoV5-3 and WP7V. In case of hot stamping tools, it is recommended to use CP4M® quenched and tempered to a hardness of 56-58 HRC.

The new special steel CP2M® was particularly developed for hot stamping tools [9]. Besides a high thermal conductivity it also offers a high wear resistance and temperature stability. As it shown in Fig. 6, CP2M® can be quenched and tempered to high hardness which is comparable to CP4M®. However, at lower hardness it achieves significant higher thermal conductivities than CP4M®. In these conditions it is comparable to the high conductive steel 30MoW33-7. In comparison to the standard grade X38CrMoV5-3, CP2M® shows always a better performance with respect to hardness and thermal conductivity. The wear resistance of steel CP2M® was investigated according to ASTM G 65 (rubber wheel). The results are shown in Fig. 7. Here, CP2M® was tested in comparison to the standard grade X38CrMoV5-3 and the high conductive steel 30MoW33-7, all quenched and tempered to a hardness of 50-52 HRC. As one can see, CP2M® shows a significant lower wear loss and therefore a higher wear resistance.
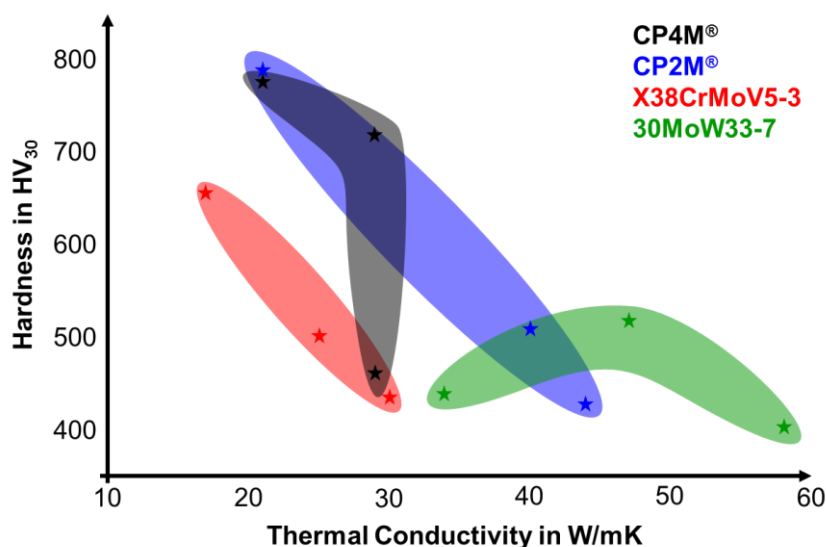
Fig. 6: Thermal conductivities of the special steels CP4M® and CP2M® in comparison to the standard grade X38CrMoV5-3 and the high conductive steel 30MoW33-7 after quenching and tempering to working hardness.
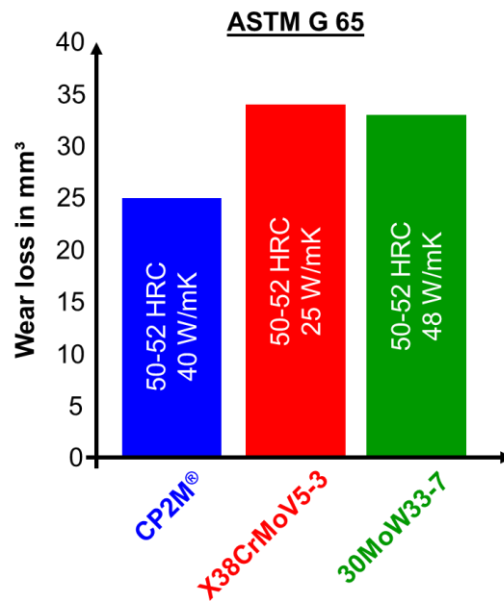
Fig. 7: Results of wear test according to a) ASTM G 65 and b) ASTM G 75 for steels CP2M®, X38CrMoV5-3, and 30MoW33-7.

First practice with CP2M® confirms that it shows a better wear resistance than other steels used for hot stamping tools. Trials were made for segments used in a bumper tool for the Golf VII. The segments were quenched and tempered to 58-60 HRC and plasma-nitrided and the drawing radius was measured continuously during service time. Using the standard steel grade X38CrMoV5-3 (52-54 HRC, plasma-nitrided) the tool have to be changed after 120,000 to 150,000 parts. With CP2M® wear was reduced and lifetime was enhanced up to 200,000 parts which is 25-67% longer service time of the tools.

To improve chilling by the hot stamping tools, most tool segments have internal cooling channels. Up to date there are three constructive ways for active cooled tools (Fig. 8). Most operators use drilled holes which have to be machined in the soft the soft annealed material. Although drilling is a well-known process, this production way shows many disadvantages. There are many machining operations which cost time and money. Furthermore, it is just possible to drill straight holes. Curved cooling channels are not possible although this would enhance cooling effect.
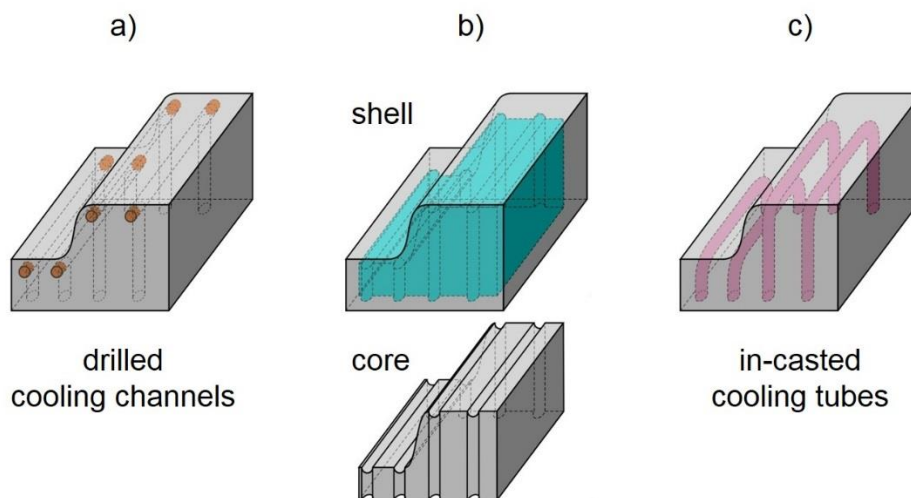
Fig. 8: Cooling strategies for hot stamping tool: a) one-part with drilled cooling channels, b) two-parts with shell and core segment, c) one-part with in-casted cooling tubes.

Another way is to use tools which are divided into an upper (shell) and a lower (core) part. In this case there is a higher degree of flexibility with respect to the cooling channel construction. However,

there are still high machining cost and time consumption and one need a good sealing of the two parts to avoid leakage during service time.

The third way is to use in-casted cooling channels. In the past this was done by inserting tubes which were fixed in the sand mold [10]. However, fixing the tubes is very difficult and there is always a risk of melting when pouring the melt into the sand mold. A new approach is to use sand molds which were 3D-printed (Fig. 9). In this case, fixing the cooling channels is much easier and there is a big flexibility for cooling channel construction. However, casting is still very difficult.
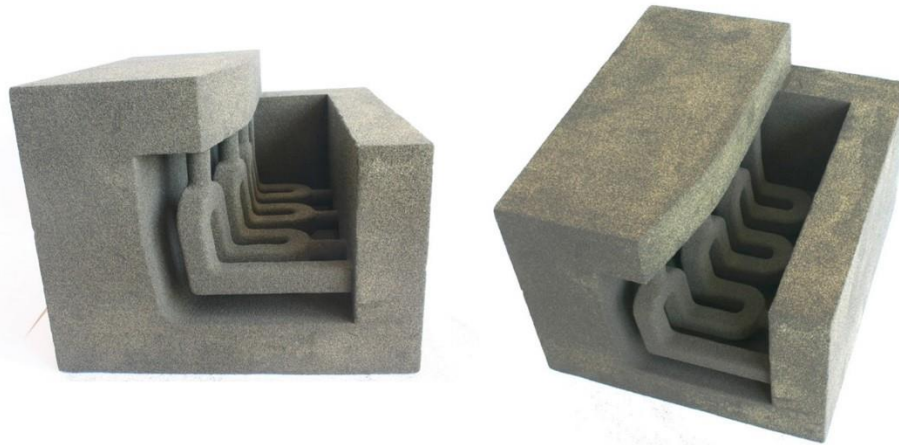
Fig. 9: A printed sand mold with cavity and cores for cooling channels.

Ongoing research projects are dealing with new processing technologies. In case of selective laser melting (SLM), a metal powder is used to build up a bulk material in layers. Every powder layer is melted using a special laser system. By means of SLM it is also possible to produce very complex cooling channels which is beneficial with respect to cooling efficiency. A related technology is called selective laser sintering (SLS) where the metal powder is not melted but sintered. Similar processes can also be done by electron beam which is then called electron beam melting (EBM). Another processes are build-up welding and cold spray deposition which are also used to build up 3D tools by processing metal powders.

4. TOOL STEELS USED FOR HARD CUTTING TOOLS

After hot stamping, automotive body parts have a high tensile strength and are in semifinish condition. They just need to be cut to bring them into final dimension. There are two ways to cut the high strength parts. Laser cutting is a very flexible and non-tool-dependent process. However, laser cutting is an energy and time consuming process [11]. Therefore, hard cutting is a common process to bring hot stamped body parts into final shape.

Hot stamped body parts normally have a tensile strength of about 1500 N/mm² (Fig. 10). Therefore, cutting tools need to have a high compressive strength and toughness. Furthermore, they should also offer a high working hardness and wear resistance. Due to sliding of the sheet metal against the tool surface there is a high friction and adhesive and abrasive wear.
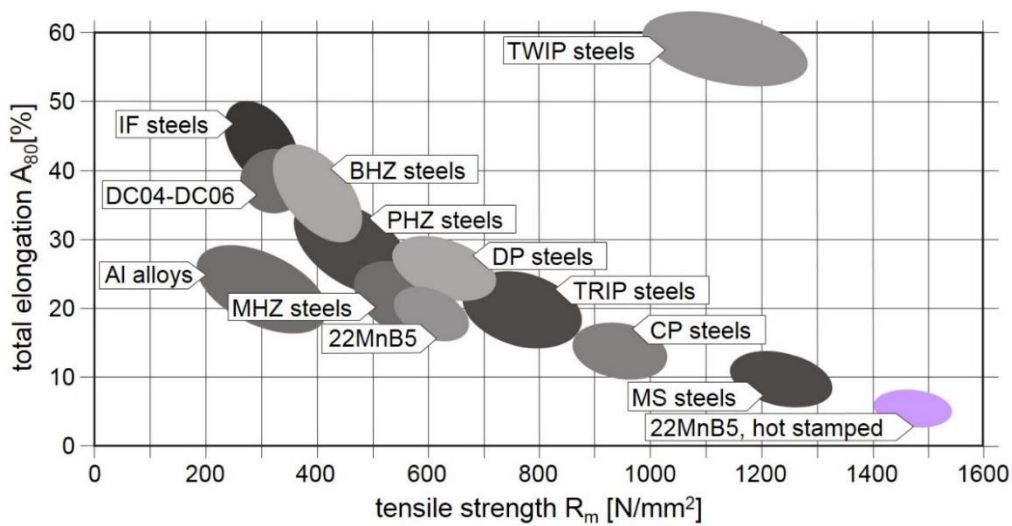
Fig. 10: Total elongation vs. tensile strength of different steels used for automotive body parts.

For hard cutting applications, hard and wear resistant steels show the best results. As it can be seen in Fig. 11, there are three types of steel which fulfill these requirements. For high wear resistance, cold work tool steels with a high carbide volume fraction are used which are quenched and tempered to a working hardness of 60-64 HRC. With increasing demand on toughness steels are used which show lower carbide volume fraction. Those steels are normally quenched and tempered to a working hardness of 58-62 HRC. If wear resistance and toughness are both of high importance it is also possible to use high speed steels like 1.3343 which can be heat treated to 60-64 HRC and still show a sufficient toughness. The third group of cold work tool steels show a low carbide volume fraction and therefore offer a higher toughness. However, they still reach a hardness between 56-60 HRC and provide a sufficient wear resistance.

For high demands on wear resistance and toughness there are two ways to ensure a good tool lifetime. The first way is to use powder metallurgical (PM) steels like CPOH^{PLUS}. According to the PM-processing route, these steels show a very fine microstructure although they exhibit a very high carbide volume fraction. These steels offer a very good wear resistance and toughness and are used for advance cutting applications. A second way is to use hard and tough steels which are nitrided and PVD-coated. In this case the base material still shows a sufficient toughness whereas the surface is covered with a very hard and wear resistant layer.
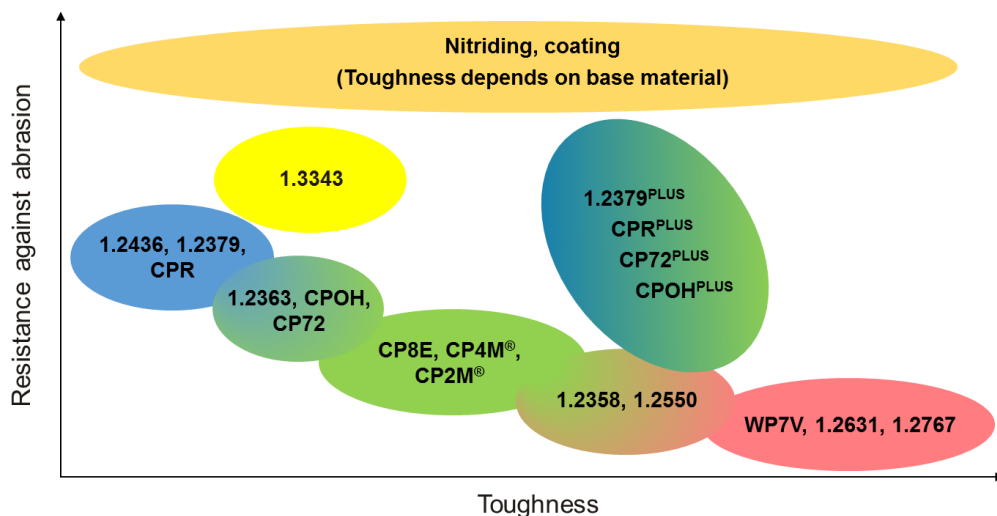

Fig. 11: Wear resistance vs. toughness of tool steels used for cutting tools.

Hot work tools steels and very tough cold work tool steels are normally not used for hard cutting applications. There is a too high risk of deformation and mechanical fatigue during service time. However, if sheet metal thickness increases the demand on toughness will increase in the same way. For these special applications it can be beneficial to use very tough tool steels to avoid cracking according to mechanical overload.

5. SUMMARY

During hot stamping, sheet metal blanks are hot stamped and afterwards hard cut. Both sub-processes require special tooling strategies. In case of hot stamping, a fast heat transfer from the hot blank into the tool is required. Furthermore, wear resistance, tempering resistance and resistance against thermal and mechanical loads are required. Therefore, hot stamping tools are normally made of hot working tool steels which exhibit a good tempering resistance and toughness. For higher wear resistance cold work tool steels are used which can be quenched and tempered to approximately 58-60 HRC and which still exhibit a good toughness. New steel grades were developed which offer higher thermal conductivities. One of these developments is the special steel CP2M® which achieves thermal conductivities between 30 and 45 W/mK in dependence of heat treatment condition. Practice shows that CP2M® additionally shows a high wear resistance which is significant higher than compared to X38CrMoV5-3.

To improve chilling of hot stamping tools, cooling channels are machined into the tools. The standard procedure is to drill bore holes into forged steel products. A second way is to use tools which are divided into a shell and a core segment. In both cases, there is a high machining effort which cost time and money. The third way is to use cast tools with in-casted cooling tubes. A new development is the 3D-printing of sand molds which improves the design of cooling channels. Future technologies are additive manufacturing processes like selective laser melting with which tools can be printed using metal powders.

For hard cutting applications, tools are exposed to high mechanical and tribological loads. They need to be hard, tough, and wear resistant. If wear resistance is of major importance, carbide containing cold work tool steels are normally used for hard cutting tool. With increasing demand on toughness hard cold work tool steel with lower carbide volume fraction are beneficial with respect to tool life time. For advanced cutting application it is favorable to use PM-tool steels or nitrided and coated cold work tool steels.

The aim of current developments is to combine the hot stamping and hard cutting process in one operations. This will affect the requirements of tool steels used for those tools because wear impact, mechanical and thermal loads will increase. Therefore, new advanced tool steels have to be developed with respect to these new requirements.

REFERENCES

[1]   M. Kleimann, T. Schorn, ATZ extra, 17 (2012) 6, pp. 38-47

[2]   Bundesministerium für Umwelt, Naturschutz, Bau und Reaktorsicherheit, 2009, Die EU-Verordnung zur Verminderung der CO2-Emissionen von Personenkraftwagen

[3]   Norrbottens Jaernverk AB, 1977, Manufacturing a hardened steel article, GB1490535

[4]   H. Karbasian, A. E. Tekkaya, J. Mater. Process. Technol., 210 (2010), pp. 2103-2118

[5]   Stahl-Informations-Zentrum, 2011, Automobiler Leichtbau mit Stahl – Heißes Eisen: warmumgeformte Stähle

[6]   C. Boher, S. Le Roux, L. Penazzi, C. Dessain, Wear, 294-295 (2012), pp. 286-295

[7]   J. Hardell, B. Prakash, Tribol. Int., 41 (2008) 7, pp. 663-671

[8]   I. Valls, B. Casas, N. Rodriguez, U. Paar, La Metallu. Ital., 11-12 (2010), pp. 23-28,

[9]   J. J. Wilzer, 2014, Wärmeleitfähigkeit martensitisch härtbarer Stähle – Physikalische Zusammenhänge, Einflussfaktoren und technischer Nutzen, Eigenverlag des Lehrstuhls Werkstofftechnik der Ruhr-Universität Bochum

[10]   T. Henke, C. Escher, F. Baumhof, 2008, Entwicklung von neuen Werkzeugkonzepten für das Presshärten, Dörrenberg Edelstahl GmbH

[11]   U. Götze, S. Zönnchen, J. Schönherr, 2013, Wirtschaftliche Bewertung von Prozesskettenvarianten am Beispiel von Strukturbauteilen, Verlag Wissenschaftliche Scripten

WEAR MECHANISMS OF COATED STEELS DURING PRESS HARDENING

M. Windmann[1] (windmannn@wtech.rub.de, tel. +49(0)234-32-25962, fax: + 49(0)234-32-14104),

A. Röttger[1] (roettger@wtech.rub.de),

W. Theisen[1] (theisen@wtech.rub.de)

[1]Lehrstuhl Werkstofftechnik, Ruhr-Universität Bochum, 44801 Bochum, Germany

Abstract

In this work microstructure of Al-base coated press-hardening steel 22MnB5, austenitized at 920°C, was analyzed with respect to the phase formation at the steel/coating interface. Thereby, iron diffusion into the Al-base coating led to the formation of intermetallic Al_xFe_y phases. The intermetallic phases transformed to more Fe-rich phases with increasing dwell time. The coating was characterized by a layered structure of phases Al_5Fe_2 and AlFe after a dwell time of $t_{Aus} = 6$ min (conventional press-hardening parameters). Cracks were formed in the coating due to the low fracture toughness of the formed intermetallic phases mainly of type Al13Fe4, Al5Fe2 and AlFe. Forming and quenching in the press-hardening tools took place at a temperature range of approx. 800°C to room temperature (RT). We found that the high hardness (520-1130 HV) and low fracture toughness of the intermetallic phases led to strong wear of the press-hardening hot-work tool steel X38CrMoV5-3. The hardness of the intermetallic phases decreased in the direction of a higher temperature, leading to less abrasive wear at higher forming temperatures, thus wear by adhesion is more pronounced. Phase AlFe was found to mainly induce adhesive wear, while phase Al_5Fe_2 led to strong abrasive wear due to the delamination of coating particles.

Keywords: Al-base coating, Intermetallic phases, Hardness, Wear, Press-hardening, Temperature

Introduction

Security relevant structures in automotive bodyworks are conventionally manufactured using high strength steels which possess a high strength to density ratio. Component parts such as longitudinal rear rails, B-pillar reinforcements and inner roof rails are produced using the high strength steel 22MnB5 [1,2]. The steel 22MnB5 is processed by direct press-hardening due to its low formability in hardened condition. During direct press-hardening, steel sheets are austenitized at temperatures of 880-950°C. Subsequently, the steel sheets are transported into the forming tool and then formed and quenched in one step [3]. After cooling, the formed steel sheets have a fully martensitic microstructure and a strength of 1500 MPa [4]. A protective Al-base coating is commonly deposited on the steel surface prior to the press hardening process, thus preventing strong oxidation of the steel sheets during austenitization. Thereby, high austenitization temperatures (880-950°C) lead to diffusion processes at the steel/Al-coating interface and to the formation of intermetallic Al_xFe_y phases in the coating [5,6].
Wear of the press hardening tools strongly depends on the mechanical properties (hardness, fracture toughness) of the Al-base coating during cooling and quenching. The mechanical properties of the Al_xFe_y intermetallics were only fragmentary investigated by Köster et al. and Kobayashi et al. [7,8]. They found that especially Al-rich Al_xFe_y intermetallics of types of $Al_{13}Fe_4$ and Al_5Fe_2 exhibited high hardness and low fracture toughness, simoultaneously. In this context, low fracture toughness promotes crack formation and propagation in the Al-base coating microstructure which may lead to the delamination of coating constituents and thus can cause

wear of the press hardening tools. However, mechanical properties of the intermetallic phase were only measured at room temperature. Mechanical properties at higher temperatures of the forming and quenching process (800°C to RT) were not published.

This work deals with the investigation of the phase formation in the Al-base coating of steel 22MnB5 during press-hardening. The hardness of the formed intermetallic phases was measured at different temperatures according to the forming and quenching process. Furthermore, the wear behavior of the press-hardening hot–work tool steel X38CrMoV5-3 was investigated with respect the formed intermetallic Al_xFe_y phases at different temperatures.

1. Experimental

Materials and heat treatment

Steel sheets of 22MnB5 with a thickness of 1.5 mm were coated with an AlSi10Fe3 layer (17 to 25 µm) by hot dipping and manufactured industrially by Thyssen Krupp Steel in Duisburg (Germany). The chemical composition of steel sheets of 22MnB5 and the AlSi10Fe3 coating is given in **Table 1**.

Table 1: Chemical composition of the materials used [mass%]; measured by spark spectrometry (22MnB5) and EDS (AlSi10Fe3) in hot-dipped condition [5]

	C	Si	Al	Mn	Cr	Ti	B	Fe
22MnB5	0.234	0.289	0.034	1.258	0.119	0.028	0.002	bal.
AlSi10Fe3		10.23	bal.					2.16

Squared specimens (20 x 20 mm) of the Al-base coated 22MnB5 sheets were heat-treated in argon atmosphere at T_{AUS}= 920 for t_{Aus} = 1, 2 and 6 min. The cross-section of each specimen was ground with 18 µm abrasive paper and polished with a 3 µm diamond paste and ¼ µm SiO_2 polishing suspension. Microstructural examinations were performed by means of scanning electron microscopy (SEM) using device Leo-Gemini 1530VP at a working distance of 12 mm and a current of 21 keV. The chemical composition of the structural constituents was analyzed by energy-dispersive X-ray spectrometry (EDS) using an acceleration voltage of 10 keV and a working distance of 8.5 mm.

Wear specimens of the hot work tool steel X38CrMoV5-3 with a spherical testing surface (r = 5 mm) were hardened and tempered in accordance to the manufacturer's instructions (T_{AUS}= 1060°C, T_{temp}= 520°C) in an inert gas furnace to a hardness of 630 HV30. Specimens of the intermetallic phases Al_5Fe_2 and AlFe were produced by powder metallurgical route. Aluminum and iron powder was mixed in accordance to the respective stoichiometry. The powder mixture was then fully melted at 1300°C for 1 h under argon atmosphere in a hot press. The intermetallic phases were formed by solidification during slow cooling down to room temperature. The existence of the formed phases was confirmed by EBSD investigations.

Phase Analyzing

Determination of the formed phases in the AlSi10Fe3 coating was performed by diffraction measurements using synchrotron radiation. The measurements took place at the Delta electron storage ring in Dortmund (Germany) using a wavelength of λ= 0.45919 Å. Debye-Scherrer circle segments (140-155°) were integrated and conditioned with the program Fit2D (ESRF). Integrated diffractograms were analyzed using X-Pert analyzing software and ICDD-JCDPS database PDF-2. The local distribution of phases in the coating microstructure was performed by EBSD measurements with a Leo 1530 VP Gemini SEM equipped with an EBSD camera (TSL-DigiView1612). The EBSD measurements were carried out at a working distance of 13 mm with a tilt of 70°, an acceleration voltage of 20 keV, and an extractor voltage of 6.2 keV. The results were conditioned and evaluated using OIM analysis software (TSL).

Hardness measurements and wear experiments

Hardness and wear measurements were performed with an Optimol SRV4 measuring device at room temperature, 400 and 800°C. Hardness measurements were carried out in accordance to DIN EN ISO 6507-1 with an applied load of 4,903 N (HV0.5). Steel X38CrMoV5-3 specimens were tested against the before polished surface of the Al_5Fe_2 and AlFe specimens with a frequency of 10 Hz over a distance of 4 mm (F = 10 N, t = 30 s) in a sliding wear test. Hardness and wear measurements were performed in forming gas to avoid strong oxidation of the worn surfaces.

2. Results and Discussion

In the first section, the phase formation at the steel/coating interface during press-hardening will be presented. Subsequently, the mechanical properties of the formed intermetallic phases and the wear behavior of the hot-work tool steel X38CrMoV5-3 will be discussed.

2.1 Phase formation at the steel/coating interface during press-hardening

Thin layers of intermetallic phases at the steel/coating interface were already formed during hot dipping of the steel sheets in the Al-base melt. On this account, intermetallic phases Al_8Fe_2Si, Al_5Fe_2, and $Al_2Fe_3Si_3$ could be identified after hot dipping (**Fig. 1**). The formation of these phases can be explained by intensive iron diffusion into the liquid aluminum during hot dipping. With increasing iron content in the aluminum melt, the liquidus temperature increases and phase Al_8Fe_2Si was formed as a result of solidification processes. The phase Al_8Fe_2Si transforms to Al_5Fe_2 with increasing iron diffusion into the coating and thus increasing iron content. In addition, $Al_2Fe_3Si_3$ precipitates were formed at the Al_5Fe_2 boundaries, as a result of the low solubility of the element silicon in the phase Al_5Fe_2. The phase formation during hot dipping and the following press hardening process was analyzed in detail in [5].
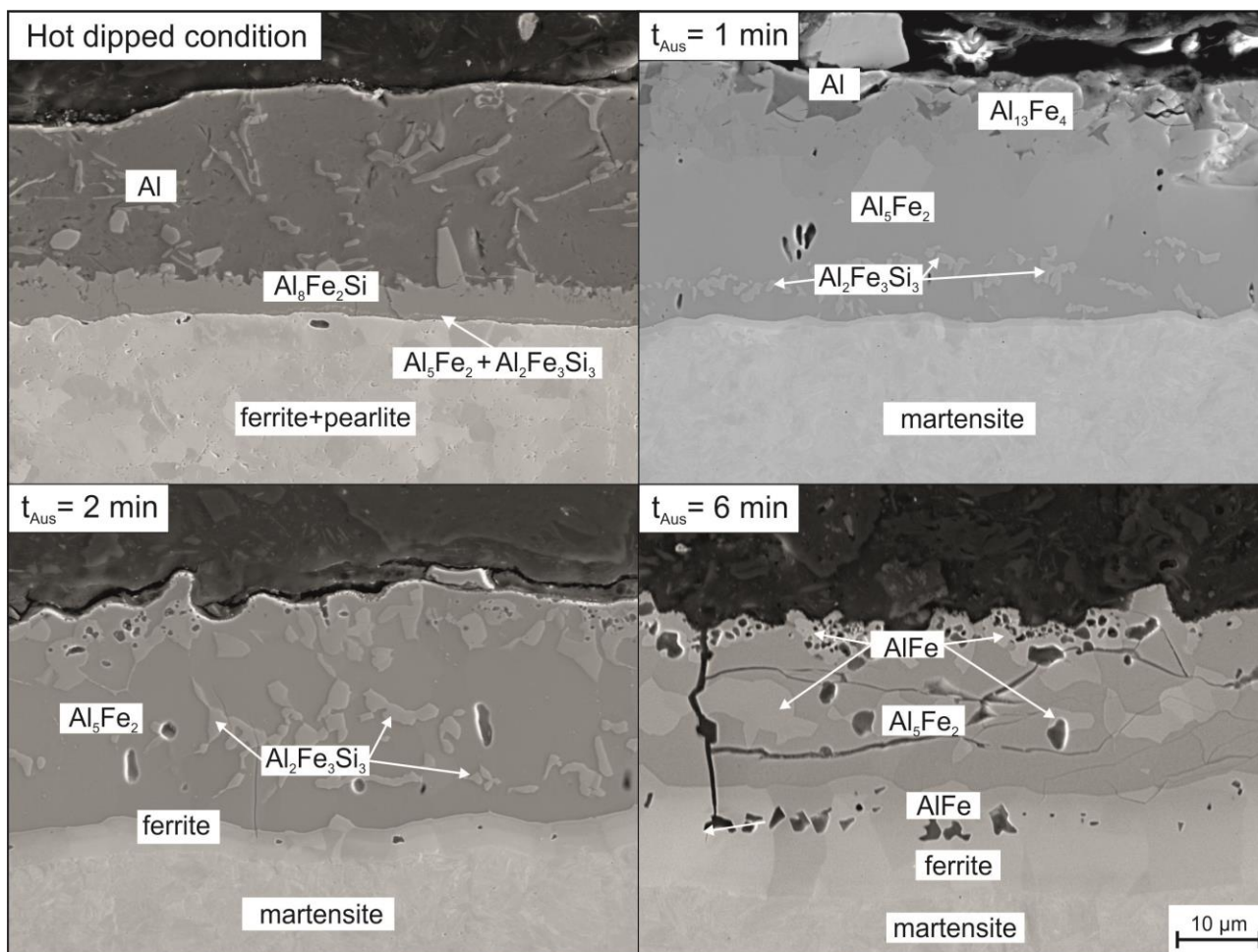
Fig. 1: SEM micrograph of the phase formation in the AlSi10Fe3 coating after hot dipping and austenitization for different dwell times at 920 °C.

The coated steel sheets are austenized at 920°C for a dwell time of 6 min in the conventional press-hardening process. During the first minute, strong diffusion of iron into the Al-base coating led to the growth of phases $Al_{13}Fe_4$ and Al_5Fe_2 in the direction of the coating. As indicated by **Fig. 1**, the growth of the Al_5Fe_2 phase was stronger compared to that of phase $Al_{13}Fe_4$. The faster formation of the phase Al_5Fe_2 can be explained by the high vacancy rate of 30% along the c axis in the orthorhombic Al_5Fe_2 lattice [9]. The high vacancy rate supports directional diffusion of iron towards the Al_5Fe_2 phase in the Al-base coating. The precipitations of type $Al_3Fe_2Si_2$ grew at the grain boundaries in the phase of type Al_5Fe_2. After two minutes, the Al-base coating was completely transformed into the intermetallic phases Al_5Fe_2 and $Al_2Fe_3Si_3$ (**Fig. 1**). The steel substrate was strongly enriched with aluminum near the steel/coating interface. Aluminum stabilizes the bcc lattice of iron. Thus, the austenitic microstructure transforms into α-Fe with increasing aluminum diffusion into the steel substrate during austenitization at 920°C. The formed α-Fe layer did not transform into martensite during the following quenching. Thus, a thin ferrite layer remained at the steel/coating interface after the press hardening process. The thickness of the formed α-Fe layer increased with increasing dwell time. Formation of $Al_xFe_ySi_z$ intermetallics in the steel substrate was not detected. The different diffusivity of Al and Fe in the intermetallic phases led to the formation and growth of Kirkendall pores at the steel/coating interface. The size of the Kirkendall pores was also increased with increasing dwell time, which can be traced back to the opposed diffusion of the elements Al and Fe at the steel-coating interface.

Between a dwell time of 2 and 6 min, the phases Al_5Fe_2 and $Al_2Fe_3Si_3$ transformed into the more Fe-rich phase AlFe. Silicon was solved in the phase AlFe (~12 at.-% [5]) and formed silicon-rich oxides on the coating surface. After a dwell time of $t_{Aus} = 6$ min, the coating consisted of a layered structure of the phases Al_5Fe_2 and AlFe. Furthermore, high crack density could be identified in the coating. After a dwell time of $t_{Aus} = 6$ min, the austenized steel sheets are conventionally

transported into the forming tool to be quenched and formed. During this process, the forming tools are in direct contact to the coating surface.

2.2 Wear mechanisms during press hardening

The hot-work tool steel X38CrMoV5-3 possesses a hardness of approx. 630 HV in quenched and tempered state. The hardness of phase Al_5Fe_2 was found to be much higher (1130 HV), while the hardness of phase AlFe (520 HV) was below the hardness of the hot-work tool steel at room temperature. Thus, especially phase Al_5Fe_2 should lead to strong abrasive wear of the tools during forming and quenching at lower temperatures. The low fracture toughness promotes the delamination of coating particles and further increases the abrasive wear of the tools.

Table 2:   Hardness and fracture toughness of the phases Al_5Fe_2 and AlFe [5,10]

	Hardness [HV0.1]	Fracture Toughness [MPa/m$^{1/2}$]
AlFe	520	26
Al_5Fe_2	1130	~1

However, the presented results were measured at room temperature. During the quenching and forming process, the coated steel sheets and thus the intermetallic phases undergo a temperature profile from approx. 800°C (after transport from the furnace into the tool) to room temperature. Consequently, the wear mechanisms of the hot-work tool steels during quenching and forming depend on the mechanical properties of the intermetallic phases at the respective forming temperatures. The hardness of the phases AlFe and Al_5Fe_2 at RT, 400°C and 800°C are presented in **Fig. 2**. In contrast, room temperature hardness of tool steel X38CrMoV5-3 is indicated as a dashed line.
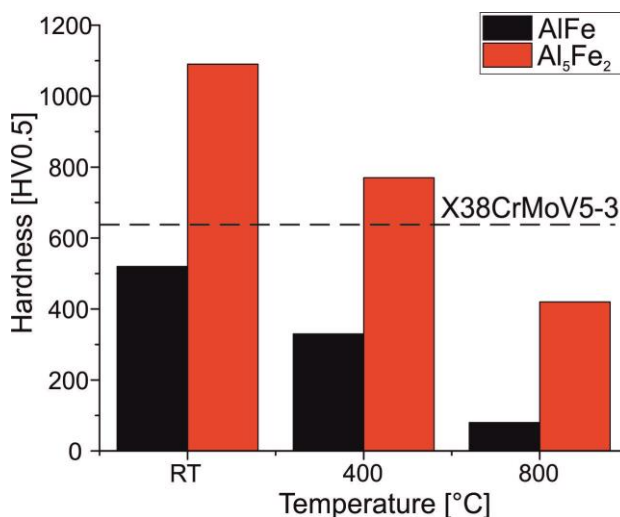
Fig. 2: Hardness of the intermetallic phases Al_5Fe_2 and AlFe at different temperatures

The hardness of both intermetallic phases decreased with increasing temperature. The hardness of phase AlFe was lower than the hardness of the hot-work tool steel at each temperature. A minimal hardness of 80 HV was measured at 800°C. The hardness of phase Al_5Fe_2 was lower than the hardness of the hot-work tool steel at 800°C, but increases above this hardness at lower temperature of 400°C and RT. Thus, the tool wear should be lower during cooling and forming from 800°C to 400°C than subsequently during cooling from 400°C to RT.

Wear experiments of the hot-work tool steel X38CrMoV5-3 against specimens of the phases Al_5Fe_2 and AlFe were performed to evaluate the temperature-dependent wear mechanisms. **Fig. 3** shows

the worn surface of the hot-work tool steel after wear experiments against AlFe and Al_5Fe_2 at 400°C and 800°C.
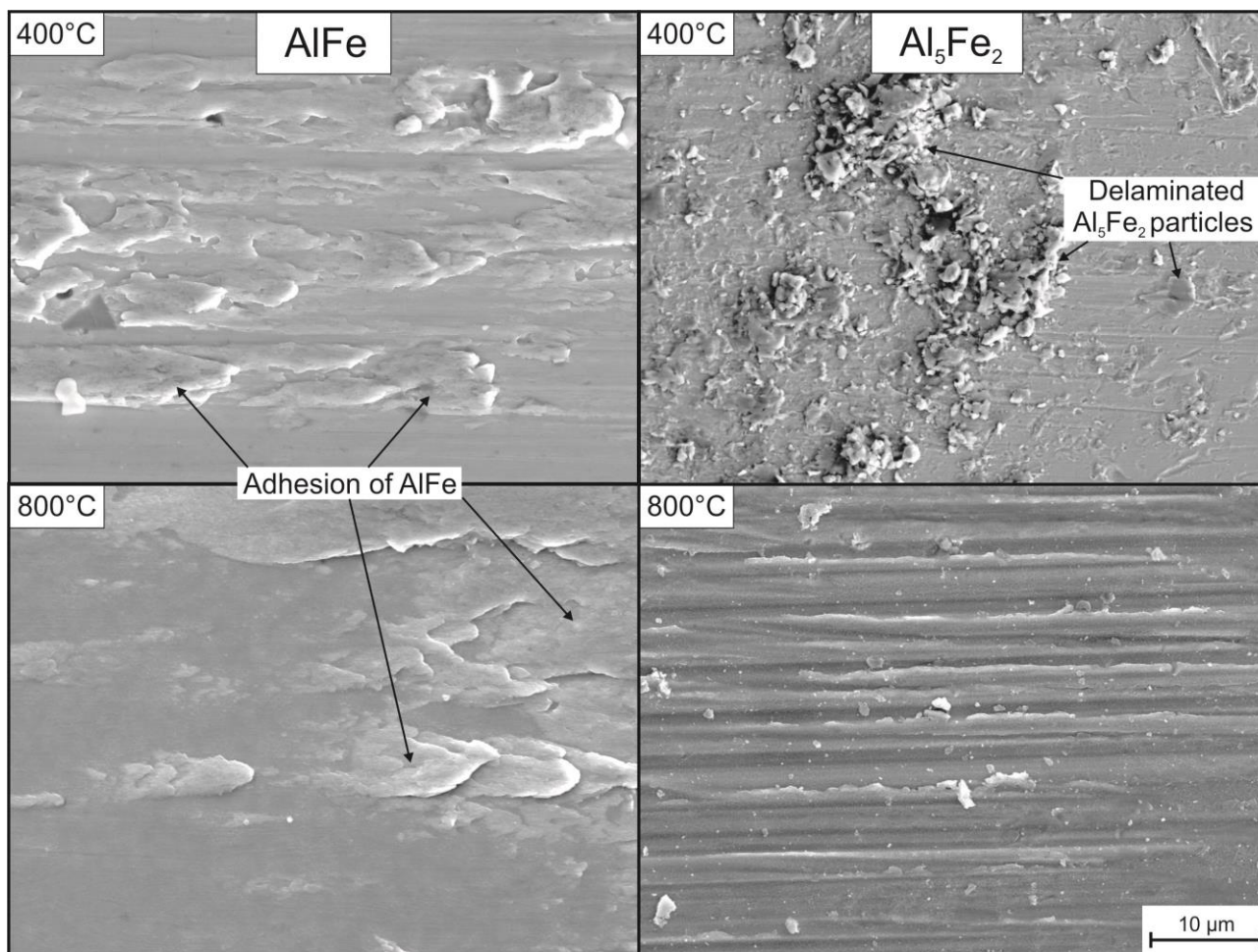

Fig. 3: SEM micrographs of the X38CrMoV5-3 hot-work tool steel worn surfaces after wear tests against AlFe and Al_5Fe_2 at 400°C and 800°C.

Fig. 3 shows that the phase AlFe mainly led to adhesive wear on the tool steel surface. Locally, welded particles of phase AlFe could be identified. The wear mechanism and intensity were almost similar for both investigated temperatures. Phase Al_5Fe_2 led to strong abrasive wear on the steel surface at 400°C, due to the delamination of brittle intermetallic particles. The delamination of intermetallic particles can be explained by the low fracture toughness of Al_5Fe_2. These particles remained on the tool steel surface and caused additional wear. Delamination of brittle intermetallic particles could only be locally identified on the steel surface after the wear experiment at 800°C. Thus, the fracture toughness of phase Al_5Fe_2 seemed to be strongly increased at this temperature. Investigations of the steel surface structure after the wear test at 800°C indicates that adhesive and abrasive wear occurred. Locally, melted aluminum as well as delaminated Al_5Fe_2 particles could be identified on the steel surface.

Summarized, wear mechanism on the hot-work tool steel surface can be described by the micro-mechanisms of adhesion and abrasion. Thereby, phase of type AlFe mainly led to adhesive wear. In contrast, phase Al_5Fe_2 promoted abrasive wear due its high hardness and the delamination of brittle intermetallic particles. While mainly adhesive wear occurred at 800°C, the amount of abrasive wear increased at lower temperatures.

3. Conclusions

The following key results were found within this work:
- During austenitization, diffusion of iron into the AlSi10Fe3 coating lead to the formation of $Al_xFe_ySi_z$ intermetallics in the coating.
- After two minutes, Al-base coating completely transforms into intermetallic $Al_xFe_ySi_z$ phases.
- The coating consists of a layered structure of phases Al_5Fe_2 and AlFe after $t_{Aus} = 6$ min (conventional press-hardening parameter). Furthermore, a high crack-density is formed due to the low fracture toughness of the intermetallic phases.
- The hardness of phases AlFe and Al_5Fe_2 decreases in the direction of higher temperatures. The hardness of phase AlFe is below the hardness of the hot-work tool steel X38CrMoV5-3 at all investigated temperatures. The phase Al_5Fe_2 possesses higher hardness than the hot-work tool steel from RT to 400°C. The hardness decreases below the hardness of the tool steel above 400°C.
- Phase Al_5Fe_2 mainly lead to abrasive wear on the tool steel surface, while phase AlFe promotes adhesive wear.

Acknowledgements

References

[1] T. Manzenreiter, M. Rosner, T. Kurz, G. Brugger, R. Kelsch, D. Hartmann, A. Sommer, BHM, 157 (2012), pp. 97-101

[2] D.W. Fan, B.C. De Cooman, Steel Research Int., 83 (2012), pp. 412-433

[3] A. Barcellona, D. Palmeri, Metall. Mater. Trans., A, 40 (2009), pp. 1160-1174

[4] H. Karbasian, A.E. Tekkaya, Journal of Materials Processing Technology 210 (2010), pp. 2103-2118

[5] M. Windmann, A. Röttger, W. Theisen, Surf. Coat. Technol. 226 (2013), pp. 130-139

[6] M. Windmann, A. Röttger, W. Theisen, Surf. Coat. Technol. 246 (2014), pp. 17-25

[7] U. Köster, W. Liu, H. Liebertz, M. Michel, Journal of Non-Crystalline Solids 153/154 (1993), pp. 446-452

[8] S. Kobayashi, T. Yakou, Mater. Sci. Eng., A, 338 (2002), pp. 44-53

[9] T. Heumann, S. Dittrich, Z. Met. 50 (1959), p. 617

[10] A. Kubošová, M. Karlík, P. Haušild, J. Prahl, Mater. Sci. Forum 567–568 (2008), pp. 349

A CONCEPT FOR DEEP CRYOGENIC TREATMENT OF TOOL STEELS

<u>V.G. Gavriljuk</u>[1], W. Theisen[2], A.I. Tyshchenko[1], V.A. Sirosh[1], A. Kortmann[3]

[1]G.V. Kurdyumov Institute for Metal Physics, 03680 Kiev, Ukraine, gavr@imp.kiev.ua
[2]Ruhr University Bochum, Chair of Materials Technology, 44780 Bochum, Germany, theisen@wtech.rub.de
[3]Ingpuls GmbH, 44894 Bochum, Germany, andre.kortmann@ingpuls.de

ABSTRACT. A short review of experimental data about the effect of deep cryogenic treatment, DCT, on the abrasive wear of tool steels is presented along with available hypotheses. Using Mössbauer spectroscopy, X-ray diffraction, mechanical spectroscopy and transmission electron microscopy, it is shown that the isothermal martensitic transformation proceeds in the course of DCT. Moreover, the softness of the virgin isothermal martensite initiates the plastic deformation during martensitic deformation, which results in the partial removal of carbon atoms from the solid solution by the gliding dislocations. This effect eliminates the precipitation of the $\varepsilon(\eta)$-carbide during subsequent tempering, shifts cementite precipitation towards higher temperatures and delays precipitation of special carbides at temperatures of secondary hardness. Thus, the precipitation potential of the γ solid solution is preserved and can be realized during the usage of tools increasing thereby the tools life. Based on the obtained results, a new concept of DCT is developed and the correction of its technology to the temperature range of the isothermal martensitic transformation is proposed.

KEYWORDS: Tool steel; Heat treatment; Deep cryogenic treatment; Martensitic transformation; Plastic deformation; Tempering; Wear; Mechanical properties.

INTRODUCTION

Cryogenic treatment of tool steels was proposed in the first half of the nineteenth century and more attentively studied since the fifties (see, e.g., [1, 2]]). In the nineties, first studies appeared concerning a mechanism responsible for its effect on the properties of tool steels. One distinguishes between the conventional, CCT, and deep, DCT, cryogenic treatments. The first one, also known as shallow cryogenic treatment, SCT, is used at temperatures between the room temperature, RT, and $-100\ °C$ and mainly aims a decrease in the fraction of the retained austenite. Its effect amounts to the increase of hardness accompanied by a decrease in toughness. The second one is performed usually at -196 $°C$ and leads to the increased wear resistance and toughness. It is remarkable that, in this case, hardness can be even decreased.

The last two decades were characterized by the increased interest of researchers to DCT and a number of obtained results are analyzed in the review articles [3-5]. At the same time, a definite gap exists between the scientific research and practical applications of this treatment. A reason for that is some scattering of experimental results and the absence of knowledge about phenomena taking place in the as-quenched steels cooled down to cryogenic temperatures. The aim of this paper is to discuss available results on the DCT in comparison with CCT and, based on the studies of a mechanism for DCT, propose some optimal technology of this treatment.

1 REVIEW OF EXPERIMENTAL RESULTS AND AVAILABLE HYPOTHESES

According to numerous studies, the increase in the wear resistance is the main effect of DCT, and, for brevity, we will pay due attention to this property. A pioneer work was published by Barron [6] who compared the effect of DCT at $-196\ °C$ and CCT at $-84\ °C$ on the abrasive wear of martensitic, stainless austenitic and plain carbon steels, as well as the cast iron. The wear resistance of martensitic tool steels was markedly improved due to DCT, whereas not significant effect, smaller than 10%, was observed in austenitic steels. No effect was found for the plain

carbon steels and the cast iron. Two essential preconditions for a positive effect of DCT were clearly demonstrated in this study, namely the thermodynamic instability of steels and the occurrence of carbon in the solid solution. In fact, they were ignored by the following researchers. The main feature of subsequent studies was a huge scattering of experimental data. E.g., for the same steel D2, Collins and O'Rourke [7] obtained the improvement in the wear resistance of about 10% in comparison with about 800 %, according to Barron [5].

The D2 type steels were the object for a number of studies on DCT effect. The decrease of the sliding wear rate up to 700 % due to DCT at −180 °C was reported by Meng et al [8]. A remarkable result of their measurements was that, at small sliding speeds of about 0.5 to 1.5 m/s, no difference occurred between the wear resistance subjected to DCT and standard quenching, whereas, with increasing sliding speed, the wear rate has not changed in the first case and significantly increased in the second one. Pellizzari and Molinari [9] studied two cold worked tool steels of D2 type, X155CrMoV12 1 and X110CrMoV8 2, after different heat treatments: (i) quenching at RT and DCT at -196 °C followed by double tempering at about 500 °C, (ii) applying DCT between two tempering stages and (iii) using one tempering stage after DCT. The decrease in the wear rate occurred if DCT was applied before double tempering, and even higher improvement of wear resistance has been achieved in case of single tempering. Oppenkowski [10] has also confirmed that DCT provides a possibility to use only single tempering. Das et al. [11] studied steel AISI D2 after austenitization at 1020 °C, DCT at −196 °C for 12 to 84 h and tempering at 210 °C. The highest decrease in the sliding wear rate was observed for the holding time of 36 h.

In the studies of high speed steels, the interesting finding was reported by Mohan Lal et al. [12] who have shown that the time of holding during DCT is more important than the decrease in its temperature, namely: the sliding wear resistance of steel M2 was higher in case of DCT at -110 °C for 24 h in comparison with DCT at -180 °C for 6 h. The same steel was tested by Mahmudi et al. [13] after austenitization at 1200 °C, DCT at −196 °C for 90 min and final tempering at 560 °C. The DCT-caused improvement of the resistance to sliding wear was better by 20 % in comparison with the conventional quenching at RT and by 15 % as compared to CCT at −80 °C. Even the higher effect on the abrasive wear of this steel, the improvement of about 43% in comparison with quenching at RT, was obtained by Googte et al. [14] due to DCT at -185 °C for 24 h. The high-speed steel T142 (1.27C, 4Cr, 9.5W, 3.2V, 10Co) was studied by Tated et al. [15] after austenitization at 1230 °C, DCT and triple tempering at 560 °C. As compared to the non cryo treated tools, the highest decrease in the flank wear, by 42%, is obtained in case of DCT at −185 °C for 8 h.

One of the first hypotheses for DCT is based on the enhanced precipitation of $\varepsilon'(\eta)$-carbide, as it was shown by Meng et al. [8]. These authors were the first to study the microstructure using transmission electron microscopy and ascribed the obtained DCT effect to fine disperse particles of η-carbide precipitated during tempering instead of the ε-carbide. It is relevant to note that η-carbide was observed earlier by Hirotsu and Nagacura [16] in the high carbon martensite subjected to low temperature tempering without any preliminary DCT or CCT. Later on, Taylor et al. [17] have shown that this "new carbide" is formed as a result of ordering in the carbon atoms distribution, which transforms the hcp ε lattice into the orthorhombic η one. They denoted it as ε'.

In a number of following studies, the precipitation of the $\eta(\varepsilon')$-carbide was also described as a reason for the improvement of wear resistance. As mentioned in [13, 18-21], these nano-carbide particles are precipitated during subsequent low temperature tempering or even in the course of DCT and the following heating to RT [19,21]. Such a concept was supported in a number of subsequent publications (e.g., [9, 22, 23]), although at least two experimental facts are not consistent with it. First, as mentioned above, the $\eta(\varepsilon')$-carbide was found to precipitate in the high carbon martensite without any DCT. Second, this intermediate carbide is dissolved at temperatures above 200 °C, whereas the positive effect of DCT occurs also in steels tempered at significantly higher temperatures, e.g. at 500 °C.

The hypothesis of "low temperature conditioning" (e.g., [7, 9, 14, 18, 24]) includes the precipitation of fine carbide particles and describes preconditions for this event in terms of time-dependent decomposition of primary martensite, i.e. some crystallographic and microstructural changes like martensite contraction, decrease of entropy etc. According to this concept, the long time soaking at cryogenic temperatures results in migration of carbon atoms towards the dislocations followed by formation of nanoclucters which, in turn, serve as nucleation sites for nano-carbides. This assumption is at variance with the absence of any detectable migration of carbon atoms in the Fe-C martensite at temperatures below −100 °C, as it follows, e.g., from Mössbauer spectra which are extremely sensitive to any small change in the atomic redistribution [25].

Any hypothesis of DCT should take into account a number of so far inexplicable experimental data about the increase in the fraction of small carbide particles with average diameter below 1 μm (e.g., [13, 14, 26, 27]) and even of 20 to 60 Å [18]. It can be only note in this relation that ultrafine precipitates of cementite of about 20 to 40 Å in size were detected in steels of D2 type, X220CrMoV 13 4 and X155CrMoV12, just after quenching at RT, as well as after subsequent DCT at −196 °C [25, 28]. These cementite particles were obviously precipitated due to the auto-tempering of martensite in the course of cooling down to RT. It is also important for further analysis that Gogte et al. [14] presented some impressive evidence of how DCT itself, without subsequent tempering, can cause the fracture of the coarse primary carbides and create the population of fine carbides resembling the "milky way" in the high speed steel T42.

2 MECHANISM FOR DEEP CRYOGENIC TREATMENT

2.1. Isothermal martensitic transformation.

Both above mentioned hypotheses deny any role of martensitic transformation in the effect of DCT on the properties of tool steels. This statement is based on the conviction that it is finished at temperatures above −100 °C. In other words, the martensitic transformation is identified with its athermal mode, whereas the isothermal one is ignored. As shown in Fig. 1, the dilatometric curve of cooling the steel X153CrMoV12 from 1080 °C down to −150 °C confirms that athermal marternsitic transformation is really completed at about −100 °C.
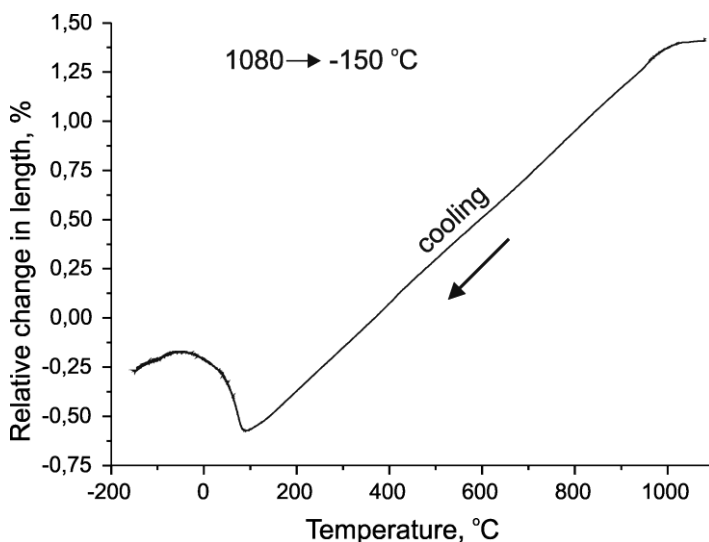
Fig. 1. Dilatometry of steel X153CrMoV12 during cooling from 1080 °C down to -150 °C with a cooling rate of 30 K/min from 1080 °C to 400 °C and under the flow of liquid nitrogen below 400 °C. $M_s = 130$ °C, $M_f \approx -100$ °C.

However, at lower temperatures, it continues with the isothermal kinetics. Some signs of martensitic transformation at a constant temperature were sporadically observed even in the beginning of nineteenth century (see, e.g., [29-31]). The first fundamental research was carried out in 1948 by Kurdyumov and Maximova [32] along with a Kurdyumov` concept of martensitic transformation in steels as a typical phase transformation with the nucleation and growth stages. Earlier, the martensitic transformation was described like the mechanical twinning.

The replacement of the burst athermal kinetics by the "soft" isothermal one is controlled by a balance between the driving force of transformation and the amplitude of thermal atomic vibrations. The increase in the driving force with decreasing temperature slows down in the cryogenic temperature range. It occurs, e.g., because of strengthening of the austenite and retards the burst

character of transformation which, in turn, reveals the nucleation stage if the energy of atomic vibrations remains sufficiently high to provide thermal fluctuations for the appearance of critical martensitic nuclei (see about details [33]). A further decrease in temperature retards the nucleation and, finally, the transformation ceases resulting in the transformation kinetics with a maximum at some intermediate temperatures.

The following experimental data give the evidence of martensitic transformation within the temperature range below −100 °C. Using mechanical spectroscopy, a phase transformation was revealed in steels of D2 type, X153CrMoV12 and X220CrMoV13-4, with a maximum at about −150 °C (Fig. 2)
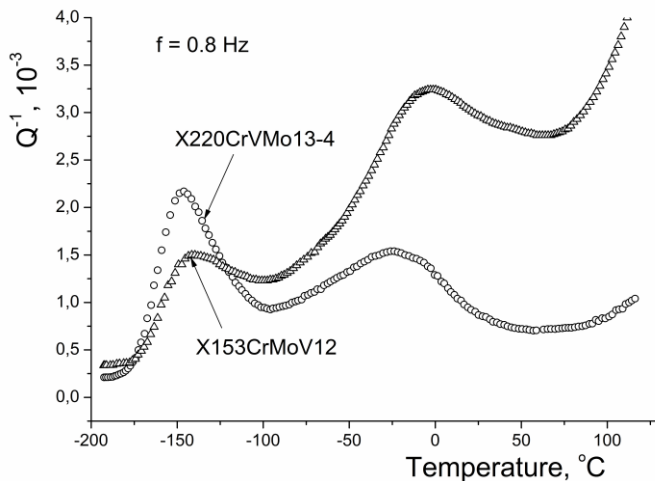
Fig. 2. Temperature dependence of internal friction for steels X153CrMoV12 and X220CrMoV13 4.

The temperature of both internal friction, IF, peaks did not change with the frequency, i.e. they do not belong to the relaxation processes. As shown in [28], a broad damping in between −50 °C and +50 °C is controlled by the vibrations of dislocations of which mobility increases with increasing temperature and, thereafter, decreases at approaching RT, where the carbon clusters formed during the ageing of martensite prevent dislocation movement. The low temperature peak belongs to martensitic transformation. Its intensity is proportional to the fraction of the transformed martensite. It follows from Fig. 2 that transformation proceeds with maximal intensity at −150 °C, which is consistent with the results in [32] obtained on the modeling steel X100Mn6. These data demonstrate that the isothermal martensitic transformation also occurs in the course of permanent cooling-heating, which suggests that the virgin isothermal martensite is present in the tool steels held for DCT in liquid nitrogen and subsequently heated to RT. The x-ray diffraction measurements confirm this conclusion (see Fig. 3).
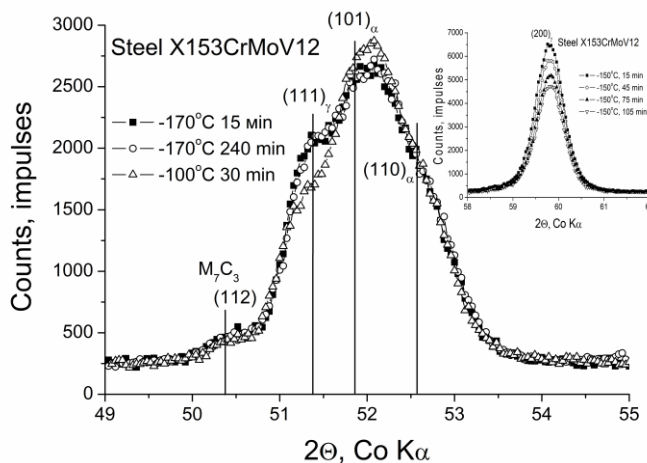

Fig. 3. Fragment of diffraction pattern of steel X153CrMoV12 quenched at RT, subsequently held at −170 °C for 15 and 240 min and thereafter heated up to −100 °C with holding for 30 min at this temperature. The evolution of the austenitic reflection $(200)_\gamma$ in the course of the isothermal martensitic transformation at −150 °C is shown in the upper right corner.
All the measurements were carried out at the temperatures of holding.

It is seen that the isothermal martensitic trysnformation is suppressed at −170 °C where the holding for 240 min does not change the intensity of martensitic reflections. The fraction of martensite has increased due to heating to −100 °C with holding at this temperature for 30 min. In consistency with the IF peak in Fig. 2, the holding at −150 °C assisted the intensive martensitic transformation, which can be estimated on the decrease in the fraction of the retained austenite.

The quantitative information about a scale of the isothermal martensitic transformation in the course of holding at cryogenic temperatures was obtained using Mössbauer spectroscopy which allows to estimate the fraction of the martensitic and austenitic phases with the accuracy of about 1.0 % (see in detail [25,28]). Mössbauer spectrum of steel X153CrMoV12 quenched at RT and cooled down to −196 °C with subsequent holding at this temperature for different time is presented in Fig. 4. Again, in accordance with the IF and x-ray results, see Figures 2 and 3, no transformation occurs during the holding in liquid nitrogen.
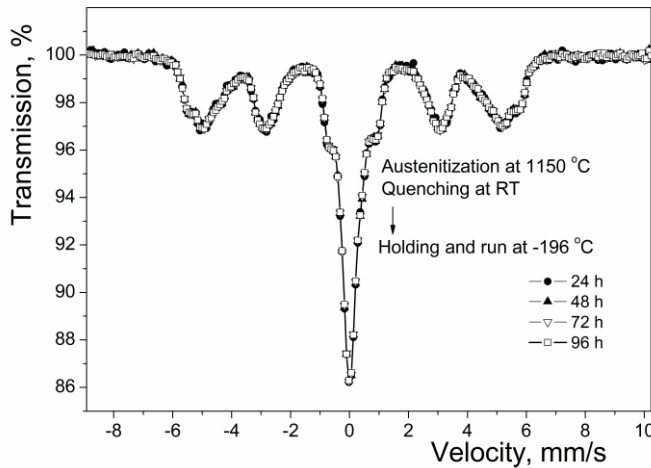
Fig. 4. Mössbauer spectrum of steel X153CrMoV12 after quenching from 1150 °C at RT and subsequent holding at -196 °C for 24, 48, 72, 96 hours.
All measurements are performed at -196 °C.

In another Mössbauer study, the sample was heated to −150 °C after preliminary cooling in liquid nitrogen, and, as expected, the isothermal martensitic transformation has being developed with holding time at this temperature. The data of Mössbauer measurements are presented in Table 1. About 8 % of the isothermal martensite was transformed during holding at −150 °C in addition to that obtained during the cooling from RT down to −196 °C.

Table 1. Areas (%, scatter ±1%) under components belonging to the martensite, retained austenite and carbides in Mössbauer spectra of steel X153CrMoV12 after quenching from 1150 °C at RT and subsequent holding at −196 or −150 °C. Measurements were performed at -196 °C, where martensitic transformation does not occur.

Temperature and time of holding	−196 °C, 96 h	−150 C, 24 h
Martensite	58.6	66.6
Austenite	32.6	24 .6
Carbides	8.9	8.3

Thus, it is established that the isothermal martensitic transformation occurs during deep cryogenic treatment of tool steels within the temperature range in between −100 °C and −170 °C with its highest intensity at −150 °C. This transformation also proceeds in the course of cooling/heating in between −100 °C and −196 °C and does not occur during holding in liquid nitrogen.

2.2. Plastic deformation of martenite during DCT and its effect on properties.

The virgin isothermal martensite is characterized by the following unique properties. Pietikainen [34] was the first to demonstrate that it is rather soft and acquires a low strength. Moreover [35], the microcracks are not formed in the course of the isothermal transformation and appear only during subsequent heating of the virgin martensite to temperatures of about − 50 °C when the ageing starts. Another feature of the low temperature martensite is its abnormally low tetragonality, which was first time observed by Lysak and Vovk [36]. Two main hypotheses were proposed for this phenomenon: (i) the intermediate fcc→hcp transformation occurs before the bcc martensite formation resulting in the partial location of carbon atoms in the tetrahedral interstitial sites which do not contribute to marensite tetragonality [37], (ii) the twinning on the {111} atomic planes transfers a part of carbon atoms from the **c** sublattice of the octahedral pores into the **a** and **b** ones, which decreases tetragonality [38]. The third feature of the isothermal martensitic

transformation and, correspondingly, of the isothermal martensite is that carbon atoms do not migrate at transformation temperatures [25,39].

Taking into account the properties of the low temperature isothermal martensite and based on the analysis of the mentioned above experimental data on DCT of tool steels, the following idea is proposed as a physical reason for the effect of DCT on the properties of tool steels: due to softness of the virgin martensite, the isothermal martensitic transformation is accompanied by plastic deformation.

The volume effect of transformation serves as a driving force of plastic deformation which, in turn, is expected to be accompanied by the following effects: (i) the previously formed RT martensite is expected to be included in the deformation process, e.g., like that occurs with cementite in pearlitic steels; (ii) the gliding dislocations should capture carbon atoms and transport them creating carbon dislocation atmospheres; (iii) the partial removal of carbon atoms from the solid solution is a reason for the abnormally low tetragonality of martensite; (iv) the carbon atoms at dislocations do not take part in the ageing of martensite and prevent formation of the low temperature carbide phases.

The data of transmission electron microscopy give the convincing proof of plastic deformation during DCT (see in detail [28,40]).
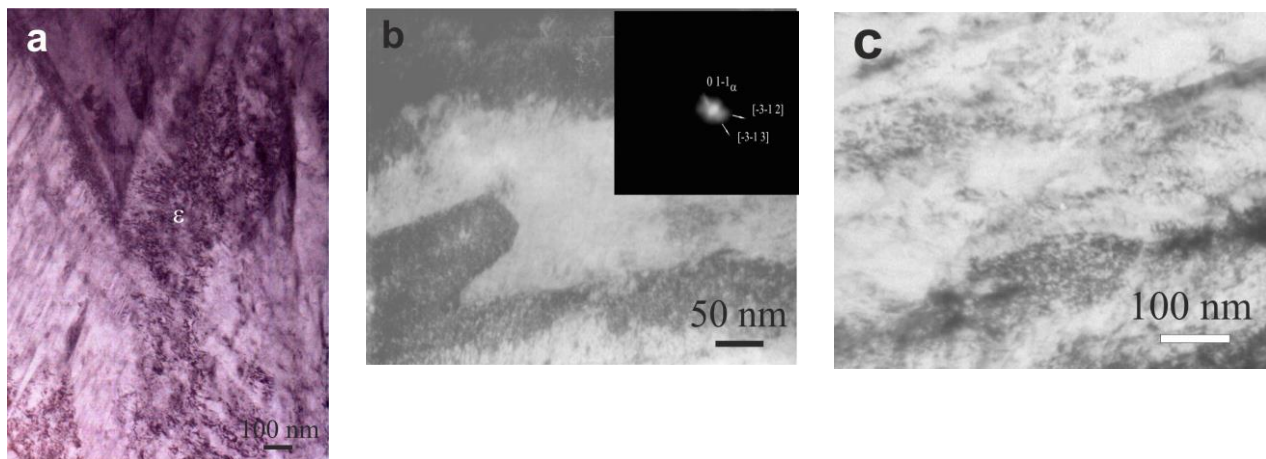

Fig. 5. Precipitation behaviour in steel X153CrMoV12 due to tempering for 2 hours: (**a**) ε-carbide after quenching at RT and tempering at 200 °C; (**b**) no η(ε')-carbide after DCT at −150 °C for 24 hours and tempering at 100 °C and (**c**) the same after DCT at −150 °C and tempering at 200 °C.

The ε-carbide is precipitated during the low temperature tempering of the martensite obtained at RT. The ε-carbide particles appear at about 100 °C and grow with increasing temperature (Fig. 5a). This intermediate carbide is transformed into cementite at about 300 °C. However, if the steel was subjected to DCT at −150 °C, no ε- or η(ε')-carbide precipitation occurs up to 200°C (Figures 5b,c). The analysis of TEM reflections shows how stressed is this martensite (see the insert in Fig. 5b). The obtained data are consistent with the observations carried out in the fifties by Wilson [41] who demonstrated that plastic deformation of Fe-C martensite quenched at RT eliminates precipitation of the ε-carbide during subsequent tempering. We can explain this effect based on the comparison of the carbon-dislocation binding enthalpy (~ 0.8 eV, [42]) and the solution heat of ε-carbide (~0.26 eV) and cementite (~0.4 eV) in the α-iron (see, e.g., [43]).

It is natural to suppose that plastic deformation in the course of DCT should also retard the ε→θ transformation and affect subsequent precipitation of special carbides. TEM data in Fig. 6 confirm this prediction. Special carbides M_7C_3 and M_2C are present in steel after quenching at RT and subsequent tempering at 500 °C (Fig. 6a). In contrast, the only coarse plates of θ-cementite and no special carbides are seen in the structure formed at this temperature after DCT at −150 °C and −196 °C (Figures 6b,c). This is why the secondary hardness does not become clearly apparent in case of DCT (see, e.g., [40]).
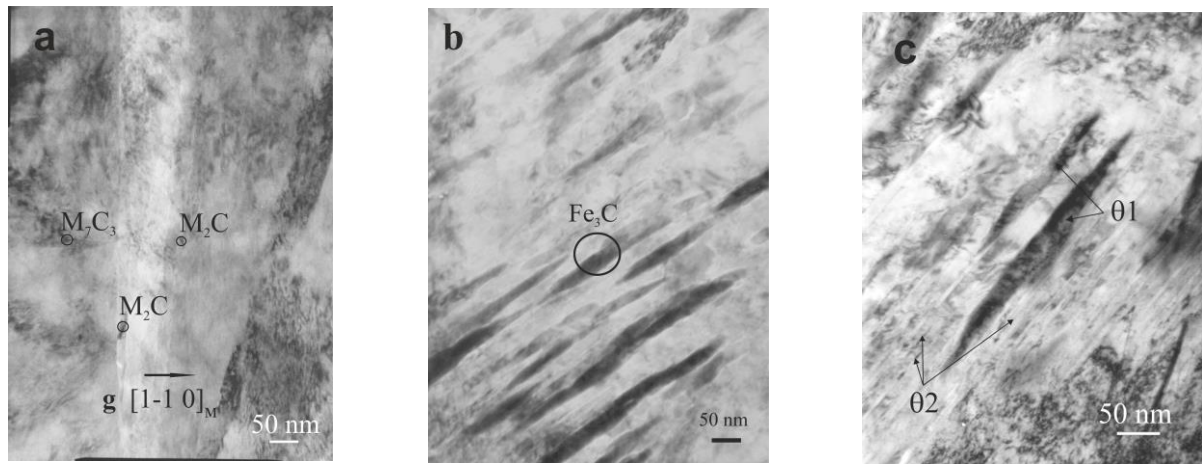
Fig. 6. Precipitation in steel X153CrMoV12 due to tempering at 500 °C for 2 hours after different preliminary treatments: (**a**) quenching at RT; (**b**) quenching at RT and DCT at −150 °C for 24 h; (**c**) quenching at RT and DCT at −196 °C for 24 h.

Using Mössbauer spectroscopy [40], it is shown that, after DCT and tempering at 500 °C, the α-solid solution contains clusters enriched in carbon and alloying elements (Cr, V) and, therefore, conserves a remarkable potential for precipitation, e.g., during subsequent tools service.
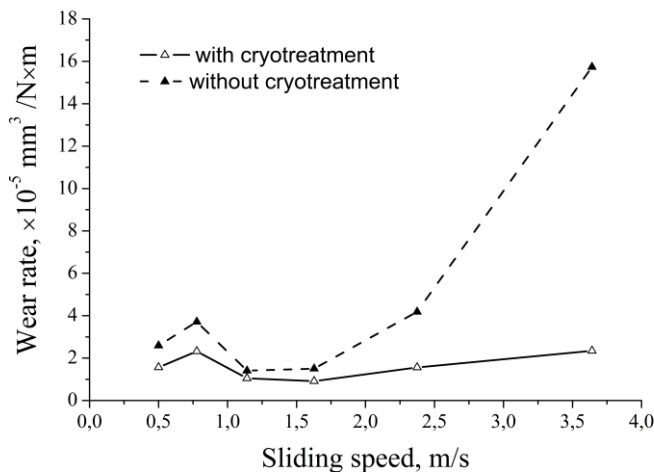
Fig. 7. Sliding were rate of D2 type steel as a function of sliding speed.

Taking this into account, one can interpret the above mentioned remarkable effect of sliding speed on the wear rate (Fig. 7), as firstly observed in [8]. DCT decreases the wear rate with increasing sliding speed, which increases temperature and assists the stress-induced precipitation of special carbides.

Therefore, plastic deformation occurs during the DCT and plays an important role in the carbide precipitation during tempering of tool steels. It is also worth noting that one can interpret the non-trivial fracture of primary M_7C_3 carbides and the "milky way" carbide picture caused by DCT in the high speed steel, as obtained by Googt et al. [14].

The occurrence of the isothermal martensitic transformation during DCT, the plastic deformation caused by this transformation and its effect on the subsequent carbide precipitation shed light on the phenomenon of DCT and makes possible to derive some recommendations concerning its optimal technology.

SUMMARY

The isothermal martensitic transformation constitutes a decisive structural phenomenon in tool steels subjected to deep cryogenic treatment. The isothermal martensitic transformation proceeds with the highest intensity in vicinity of −150 °C. In absence of ageing, the virgin low temperature martensite is rather soft, and plastic deformation of steel occurs due to the volume effect of transformation.

As a result of dislocation slip, the immobile at these temperatures carbon atoms are captured by dislocations and removed from the α solid solution. The binding between carbon atoms and

dislocations prevents precipitation of the low temperature ϵ-carbide during subsequent tempering and shifts precipitation of cementite and special carbides to higher temperatures.

The cementite is the only carbide formed at temperatures of about 500 °C after DCT, which explains the low effect of secondary hardness. Correspondingly, the α solid solution contains clusters of carbon and carbide forming elements, which creates a remarkable potential for further precipitation. Admittedly, the stress-induced precipitation of special carbides can occur during subsequent usage of tools, which increases the tools life.

 A change in technology of DCT can be recommended aiming the holding within the temperature range of −150 °C, which can cut the time of DCT and be the most effective for the increase in the wear resistance of tool steels.

REFERENCES

[1] Gulyaev, A.P., Grudov, P.P., Badayeva, A.B., 1949, Machines and Tools (in Russian), vol. 3-4, p. 3.
[2] Nordquist, W.N., 1953, Tooling and Production, vol. 7, p. 72.
[3] Collings, D.N., 1996, Heat Treatment of Metals, 2, p. 40.
[4] Baldissera, P., Delprete, C., 2008, The Open Mechanical Engineering Journal, vol. 2, p. 1.
[5] Singh Gyr, S., Singh, J., Singh, R., Singh, H, 2011, Int J Adv Manuf Technol, vol. 54, p. 59.
[6] Barron, R.F., 1982, Cryogenics, vol. 22(8), p. 409.
[7] Collins, D.N., O'Rourke, G., 1998, In: Heat Treating, Proceedings of the 18th Conference including the Liu Dai memorial symposium, 12-15 October 1998. Walton, H.W., Walls, R.A. (Eds), ASM International, p. 229.
[8] Meng, F., Tagashira, K., Azuma, R., Sohma, H., 1994, ISIJ International, vol. 34(2), p. 205.
[9] Pellizzari, M., Molinari, A., 2002, In: Proceedings of the 6th International Tooling Conference, Karstadt, Sweden, Sept.10-13, 2002. Bergström, J., Fredriksson, G., Johansson, M., Kotik, O., Thuvander, F. (Eds), Karstadt University, p. 657.
[10] Oppenkowsky, A., 2011, Cryobehandlung von Werkzeugstahl. Dissertation zur Erlangung des Doktor-Ingenieur. Ruhr-Universität Bochum; Bochum, Germany, 2011.
[11] Das, D., Dutta, A.K., Ray, K.K., 2009, Wear, vol. 266, p. 297.
[12] Mohan Lal, D., Renganarayanan, S., Kalanidhi, A., 2001, Cryogenics, vol. 41(3), p. 149.
[13] Mahmudi, R., Chasemi, H.M., Faradji, H.R., 2000, Heat Treatment of Metals, vol. 3, p. 69.
[14] Googte, C.L., Iyer, K.M., Paretkar, R.K., 2006, In: Proceedings of 7th International Tooling Conference, Torino, Italy, 2-5 May 2006. Rosso, M., Actis Grande, M., Ugues, D. (Eds), Politecnico di Torino, p. 151.
[15] Tated, R.G., Kajale, S.R., Iyer, K., 2006, In: Proceedings of 7th International Tooling Conference, Torino, Italy, 2-5 May 2006. Rosso, M., Actis Grande, M., Ugues, D. (Eds), Politecnico di Torino, p. 135.
[16] Hirotsu, Y., Nagakura, S., 1972, Acta Metall, vol 20(4), p. 645.
[17] Taylor, K.A., Olson, G.B., Cohen, M., Vander Sande, J.B., 1989, Metall Trans A, vol. 20(12), p. 2749.
[18] Yun, D., Xiaoping, L., Hongshen, X., 1998, Heat Treatment of Metals, vol. 3, p. 55.
[19] Yen, P.L., Kamody, D.J., 1997, Industrial Heating, vol. 64(1), p. 40.
[20] Huang, J.Y., Zhu, Y.T., Liao, X.Z., Beyerline, I.J., Bourke, M.A., Mitchell, T.E., 2003, Mat Sci & Eng A, vol. 339, p. 241.
[21] Stratton, P.F., 2007, Met Sci & Eng A, vol. 449-451, p. 809.
[22] Yugandhar, T., Krishnan, P.K., Bhaskar Rao, C.V., Kalidas, R., 2002, In: Proceedings of the 6th International Tooling Conference, Karstadt, Sweden, Sept.10-13, 2002. Bergström, J., Fredriksson, G., Johansson, M., Kotik, O., Thuvander, F. (Eds), Karstadt University, p. 559.
[23] Li, S., Min, N., Li, J., Wu, X., Li, C., Tang, L., 2013, Mat Sci & Eng A, vol. 575, p. 51.
[24] Collins, D.N., Dormer, J., 1997, Heat Treatment of Metals, vol. 3, p. 71.
[25] Tyshchenko, A.I., Theisen, W., Oppenkowski, A., Siebert, S., Razumov, O.N., Skoblik, A.P., Sirosh, V.A., Petrov, Y. N., Gavriljuk, V.G., 2010, Mat Sci & Eng A, vol. 527, p. 7027.
[26] Chasemi-Nanesa, H., Jahazi, M., 2014, Mat Sci & Eng A, vol. 598, p. 413.

[27] Vahdat, S.E., Nateh, S., Mirdamadi, S., 2013, Mat Sci & Eng A, vol. 585, p. 444.

[28] Gavriljuk, V.G., Theisen, W., Sirosh, V.V., Polshin, E.V., Kortmann, A., Mogilny, G.S., Petrov, Yu.N., Tarusin Ye.V., 2013, Acta Mater, vol. 61, p. 1705.

[29] Benedics, C., 1908, J. Iron and Steel Inst., vol. 77, p. 233.

[30] Hanemann , H., Scyrader, A., 1925, Trans ASST, vol. 9, p. 169.

[31] Bein, E.C., 1922, Chemical and Metallurgical Engineering, vol. 26, p. 543.

[32] Kurdyumov, G.V., Maksimova, O.P., 1948, Reports of Academy of Sciencies of USSR (in Russian), vol. 61, p. 83.

[33] Lobvodyuk, V.A., Estrin, E.I., 2005, Progress in physical sciences (in Russian), vol. 175(7), p. 745.

[34] Pietikainen, J., 1968, J Iron Steel Inst, vol. 206. p. 74.

[35] Pietikainen, J., 1985, Trans ISIJ, vol. 25, p. 340.

[36] Lysak, L.I., Vovk, Ya.N., 1965, Physics of Metals and Metallogr (in Russian), vol. 20, p. 540.

[37] Lysak, L.I., Nikolin, B.I., 1966, Physics of Metals and Metallogr (in Russian) vol. 22, p. 730.

[38] Roitburd, A.L., Khachaturyan, A.G., 1970, Physics of Metals and Metallogr(in Russian), vol. 30, p. 1189.

[39] Gavriljuk, V.G., Gridnev, V.N., Nemoshkalenko, V.V., Razumov, O.N., Polushkin, Yu.A., 1977, Physics of Metals and Metallogr (in Russian), vol. 43, p. 582.

[40] Gavriljuk, V.G., Sirosh, V.A., Petrov, Yu.N., Tyshchenko, A.I., Theisen, W., Kortmann, A.,2014, Metall Mater Trans A, DOI 10.1007/s11661-014-2202-8.

[41] D.V. Wilson, d.V., 1957, Acta Metall vol. 5, p. 302.

[42] Gavriljuk, V.G., Kushnareva, N.P., Prokopenko, V.G., 1976, Physics of Metals and Metallogr (in Russian), vol. 42, p. 1288.

[43] Gavriljuk, V,G., 2003, Mat Sci & Eng A, vol. 345, p. 81.

Keynote 2

Abrasion in Tunneling and Mining

A. Röttger[1] (roettger@wtech.rub.de, phone: +49(0)234-32-22366, fax: + 49(0)234-32-14104),

J. Küpferle[1], S. Brust[1], A. Mohr[1], W. Theisen[1]

[1]Lehrstuhl Werkstofftechnik, Ruhr-Universität Bochum, 44801 Bochum, Germany

Abstract. In future, tunneling and mining will play a major role due to the opening of new resources and living environment, as an irreversible consequence of the growing world population. To improve the efficiency of a tunneling or mining project, an increased durability of the used tools and the knowledge about the remaining service life constituent a key instrument in this context. It is the aim of this work to illustrate the different tribological systems which are present during a tunneling or mining process, depending on the soil or rather the material to be mined. In addition, different tool concepts, a description of the respectively tool-mineral interaction and common material concepts will be described, basically.

Introduction: Due to the increase in the world population from 7.28 mrd. people in 2015 to 9.6 mrd. people in 2050, more resources like energy, food, materials for consumer goods and more living space are required in the future [1]. To provide these demands, new technological solutions have to be developed, enabling a saving of limited resources by an improved efficiency of machines/plants or allowing the use of global available materials as substitution candidates. Independently of the respectively increase of the plants efficiency, there is no doubt that more resources are required, thus representing the continuing relevance of mining processes in the future. Beside more resources, more living space and the associated infrastructure is mandatory by an increase of the world population. Keeping in mind that megacities like Tokyo, Jakarta, Delhi or Shanghai are still overpopulated today, new living space and transport networks for example can only be developed by build upwards or into the ground. Especially, the height of skyscrapers is limited due to statically limitations, weather influences and geological conditions, thus underground urbanization becomes more attractive [2]. Although tunneling and mining are pursuing different objectives (tunneling= building of infrastructure; mining= extraction of resources), the used exploration techniques are almost the same. However, for the construction of a tunnel in heavily populated areas like cities, settlements of buildings and an associated damage as a result of a subsidence of the ground has to be avoided. For this purpose, more sensitive and saver techniques have to be used. In this context, tunneling machines, as shown in *Figure 1a* and **1b**, have gained an improved importance within the last decades. Tunneling machines are mobile factories, allowing the mining of rock and soil at the working face, the transport of the minded materials out of the tunnel and the buildup of the tunnel construction by tubbings, mortal and shotcrete at the same time. In the case of the extraction of resources, economic aspects and the accessibility to the deposit (depth) are mainly determining the mining conditions, thus blasting, drilling, rock milling and the use of excavators are commonly used. Beside the cost-intensive underground extraction of hard coal, soft coal is mainly extracted by opencast mining by a large-surface extraction using open cast mine excavators (see *Fig. 1c*), which can operate in a more economical way. This more economic mining process is the main reason for the still pronounced soft coal production in Europe. To ensure competitive lignite exploitation in comparison to low-wage countries, economic mining process as a result of minimized downtimes and increase extraction efficiency has to be ensured. The efficiency of a tunneling and mining process is mainly determined by the geological properties like hardness, bulk density as well as moisture content for example and the associated wear of the used tools [3]. However, strong wear is leading to a blunting of the tools which is counteracting a high extraction rate due to a deteriorated tool

performance [4]. In addition, if the wear limit of the respectively tools is reached, cost-expensive tool changes and repair measures are necessary. Especially in the case of a tunneling process, tool wear is a complex topic. If tunneling occurs by a closed shield technique, tool wear cannot be measured directly, thus there is no time resolved knowledge about the functionality and the remaining tool life. This means that an accurate prediction of the tool life time before a tunneling project must exist with regard to geological reports and experience which were gathered from previous projects. As a result of an insufficient knowledge about the geological conditions, an incorrect planning of tool change intervals may lead to additional maintenance intervals which causing a delay in construction and an increase of the overall project costs. This means that only a comprehensive understanding about the interaction between the tools and the geology allows the right selection of the mining and tunneling conditions (tool, mining method, machine parameters), ensuring an economic operation of a tunneling or mining process. This work focuses on the tribological system of surface mining and tunneling. It is the aim to describe the extraction mechanisms and the occurring interactions between the tool and the respectively ground, from a metallurgical point of view. Therefore, the used tool design and the wear resistant materials will be introduced, briefly.
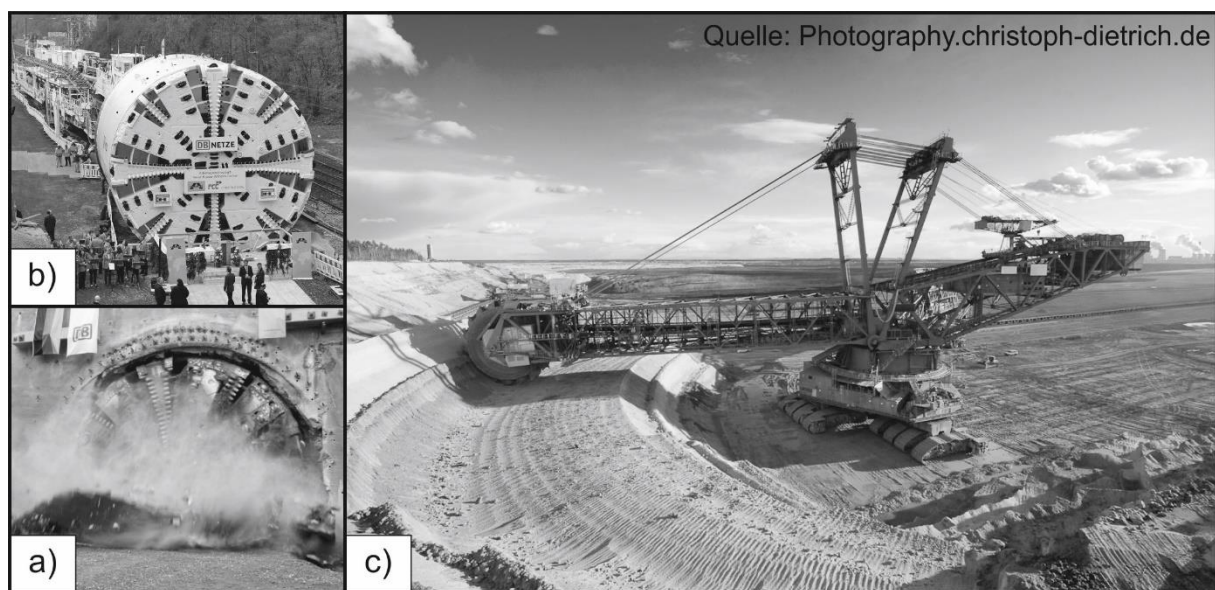

Figure 1:   a) Tunneling machine being ceremoniously started b) Tunnel breakthrough c) brown-coal excavator [g]

Materials for Mining and mineral processing: Soft coal is mainly extracted by open cast mining. Since 1930, wheel loaders are used for this application, allowing an economic mining of up to 240.000 t of coal per day [5, 6]. The coal mining takes place by a bucket-wheel, rotating in front of a cantilever arm, which is penetrating and parallel moved to the material to be mined. Due to the movement, the rotating buckets are collecting the coal and are feeding an adjacent conveyor belt. By a further bench conveyor, the coal or the overburden is transported with regard to the intended purpose to a power plant, a coal storage or to a stacker machine.

During mining, tribo-mechanical interactions between the extracted mineral and the bucket material occur, effecting strong wear by abrasion. Thereby, hard mineral particles (abrasives) are indenting and moved relative to the softer tool surface, effecting material removal, deformation or/and strain hardening. Counteracting these negative interactions, mining tools (teeth and shovel edges) are commonly protected by applying a wear resistant coating on a low alloyed steel substrate. Thereby, the function of the steel substrate can be found in the absorption and transmission of forces to adjacent component parts. In contrast, the deposited wear resistant coating is protecting the steel substrate against external influences. To achieve a high wear resistant and an associated high tool life, deposited materials have to counteract indentation and material removal by the

abrasives as well as catastrophic failure due to a brittle material behavior in the case of an impact load. To fulfill these requirements, wear resistant materials should feature a high hardness and a sufficient toughness, simultaneously. Due to the high hardness of the minerals 550 (apatite) – 1100 (quartz) HV0.05, pure metals do not possess a sufficient protection behavior and will be worn by the abrasives. In the case present, the microstructure of the wear resistant materials have to feature high volume fraction of particles like carbides, borides or nitrides having a higher hardness compared to the abrasives. Conventionally, the requested microstructure can be achieved by hard alloys, highly alloyed in carbon and/or boron, forming carbides, borides and carboborides with the hard phase forming elements like Cr, Ni, Fe, Mo, W, and V for example. For mining applications, Ni- and Fe-base hard alloys are of high importance. Their microstructure consists of a tough metallic matrix and primarily (blocky shape) and eutectically (network like shape) hard phases. In **table 1**, basically hard facing alloying concepts of the three main hard alloying systems for mining applications is tabled.

Table 1:   Overview of the essential alloying elements in Fe-, Ni- and Co-based hard alloys [7]

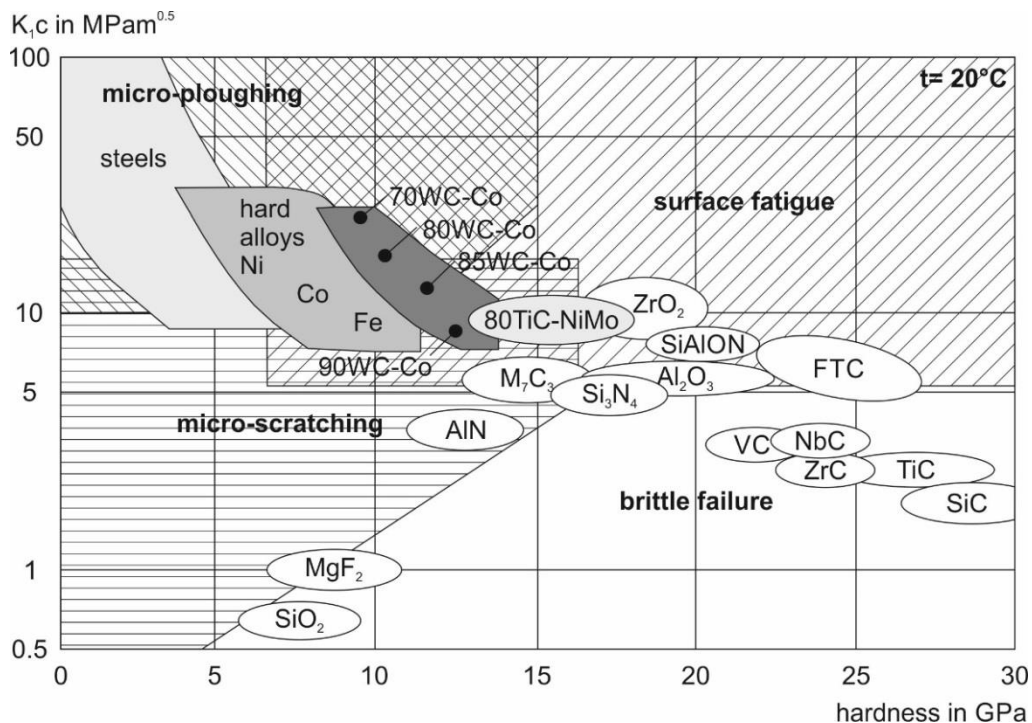| Matrix element	Alloying concept	Metalloid	Hard phase forming element	Type of hard phase
Fe	FeCrC FeCrVC FeCrXC	C, B, N	Cr, Mo, W, Ti, V,	$M_{23}C_6$, M_6C, M_7C_3, M_3C, M_2C, MC $M_{23}(C,B)_6$, M_2B, $M_3(C,B)$, M_3B_2
Ni	NiBSi NiCrBSi NiCrBSiX	C, B	Cr, Mo, W	M_3B, M_2B, MB_2, $M_{23}B_6$, $Ni_3(Al,Ti)$
Co	CoCrC CoCrWC CoCrMoC	C	Cr, W, Mo	M_7C_3, MC, M_2C, M_6C, $M_{23}C_6$ MB_2, MB, $Co_3(W,Mo)$

Figure 2:   Erosion wear mechanisms of wear resistant materials (toughness K_1c, hardness HV map), with regard to the work of [7-10]

As shown in **table 1**, the metalloids carbon and boron can form different hard phases with hard phase forming elements like Cr, M and V and with the matrix element Ni (Ni_3B) and Fe (Fe_2B, Fe_3C) itself. Thereby, the properties like hardness and fracture toughness of the respectively hard

phases depends on the bonding mechanisms which can be more metallic (soft) or strong covalent (hard) (see ***figure 2***). In the case of the mainly metallic-covalent bonded hard phases in ***table 1***, covalent bonding and the associated hardness increases with a decrease in the ratio of the metal/metalloid-ratio (M/X-ratio), whereby the metal are the refractory elements in the fourth (Ti, Zr, Hf), fifth (N, Nb, Ta) and sixth group (Cr, Mo, W) of the periodic table and the metalloids are carbon, boron and nitrogen. Basically, Cr-rich hard phase of type M_7C_3 and Ni-boride of type M_3B are of high interest for the here regarded hard alloys, characterizing the basic systems Fe-Cr-C and Ni-B-Si (Si improves weldability). Both hard phases possesses a higher hardness (M_7C_3~ 1500 to 2200 Hv0.05, Ni_3B~ 1100 to 1400 HV0.05) than the hardest mineral quartz (~1100 HV0.05) and thus effecting a sufficient resistance against abrasion. By changing the hard phase volume fraction (alloying concept, mainly amount of metalloids), the type (alloying concept, changing hard phase forming elements) as well as the morphology (processing route, solidification characteristic) of the hard phases, the respectively hard alloys can be adapted to the present tribological system. In ***figure 3***, the microstructure of conventionally used hard alloys for wear protection application is shown in deposition welded condition.
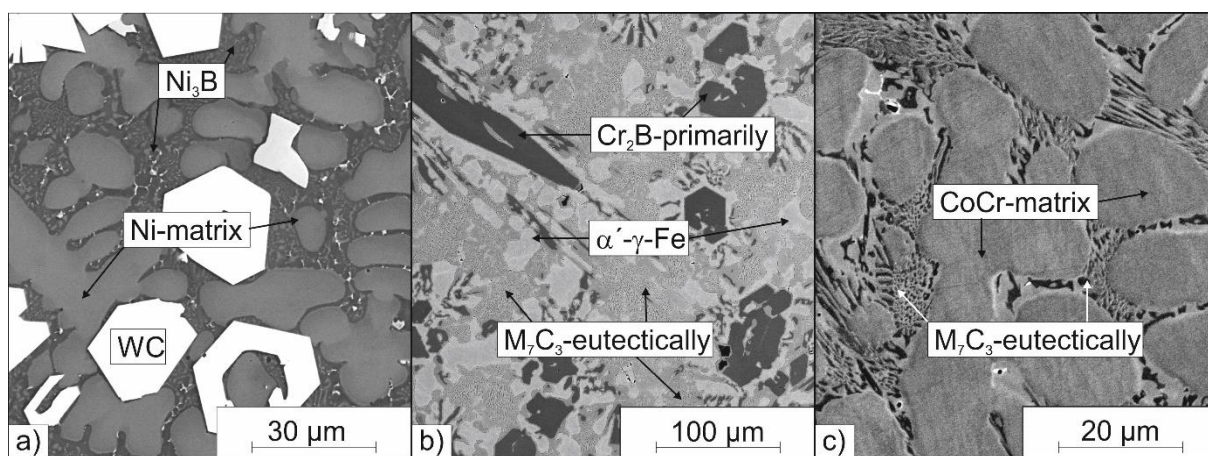

Figure 2: Microstructure of hard alloys: a) NiCrBSi+WC, b) FeCrCB, c) CoCrWC

In the case of the presence of coarse abrasives and a high load, small hard phases offer an insufficient protection against abrasion and will be worn out together with the soft metallic matrix. A high wear resistance is only obtainable, if the hard particles are adapted to the acting abrasives with respect to their volume fraction, size and hardness. However, thermodynamic restrictions with regard to the hard phase volume fraction and the solidification path counteracting these demands. In this context, Metal Matrix Composites (MMC), produced by sintering, thermal spraying or deposition welding, should be mentioned as a solution. The microstructure of MMC consists of a metallic matrix with additionally inserted ceramic particles, having a size of several μm to mm. In ***figure 4***, the characteristic microstructure of a Ni-based MMC, processed by build-up welding, is shown. Thereby, coarse carbides (brightly displayed) are distributed homogeneously in the darker displayed Ni-base metal matrix. Typical hard particles are spherical tungsten monocarbides, blocky fused tungsten carbide and Cr-carbide of type M_3C_2. Selection of hard particle depends on the present tribological system. In the case of sliding wear, tungsten monocarbides or cheaper Cr-rich M_3C_2 carbides are often used due to great costs to property ratio. A special position can be attributed to fused tungsten carbide (FTC). The microstructure of these hard particles consists of a eutectic network of WC and W_2C needles, possessing advantages if impact load is present. In the case of crack formation, further propagation occurs across the respectively needle interfaces, thus extend the crack length and the associated energy requirements for crack grow. This increased energy requirements results in a higher fracture toughness of about 6 to 7 $MPam^{0,5}$, which is extremely high for ceramic bonded materials (see also ***figure 2***). Beside the great material properties of tungsten carbides, the availability of raw materials and the metastable material behavior are disadvantages. Metastable behavior of fused tungsten carbide is shown in ***Fig 4b***. Thereby, strong reaction of the tungsten carbide with the Ni-base metal matrix is shown, promoting

the formation of more stable but also more brittle η- and κ-carbide-film at the carbide-matrix interface. The formation of this interlayer is promoting a metallurgical embedding of the carbides in to the metal matrix and is soften the abruptly change in properties at the carbide-metal interfaces. Due to the higher M/C-ratio of the η- ($M_6C=6$) and κ-carbides ($M_{12}C=12$) in contrast to fused tungsten carbides ($MC/M_2C \sim$ 1-2) or tungsten monocarbide (MC=1), overall volume fraction of the carbides is increased, leading to a strong embrittlement of the MMC. In addition, hardness of the new formed η- and κ-carbides is lower compared to the tungsten carbides. Opportunities to counteract η- and κ-carbides formation can be found in the processing the MMC at lower temperatures to avoid strong diffusion and to use a metal base, having a lower tendency to form these carbides, for examples.
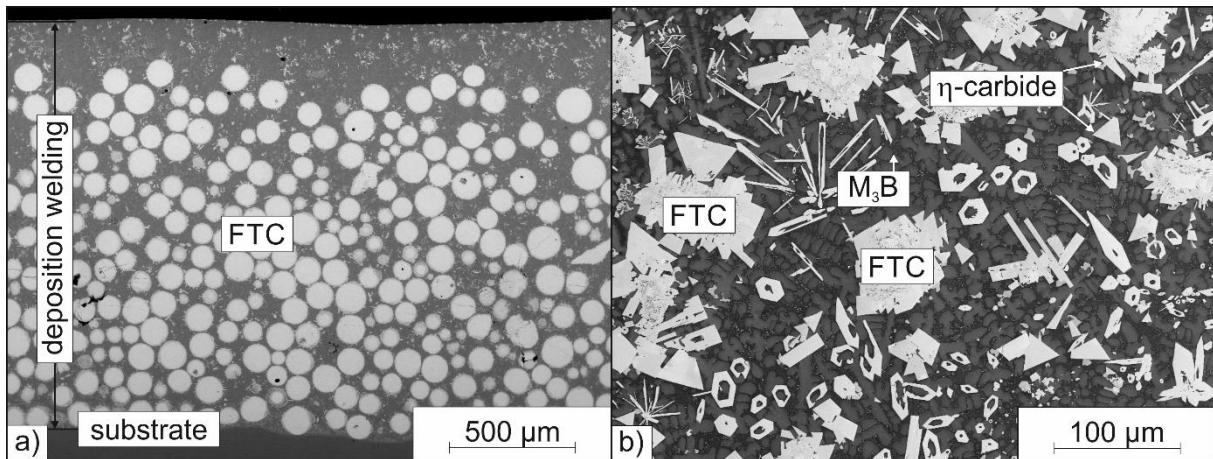
Figure 4: Microstructure of Metal Matrix Composites; a) NiCrBSi+30 mass% FTC processed by deposition welding, b) higher magnification of the FTC carbides in Ni-base matrix

In this context, Ni-base alloys of the systems NiBSi or NiCrBSi should be mentioned, which can be processed at lower temperatures in comparison to Fe-base materials. Due to the lower processing temperatures, less η-carbide formation takes place, thus materials having a high hardness and simultaneously high fracture toughness can be manufactured. Due to this less carbide dissolution, Ni-based MMC are preferably used for mining application, although Fe-base materials are cheaper and featuring the possibility of a martensitic hardening.
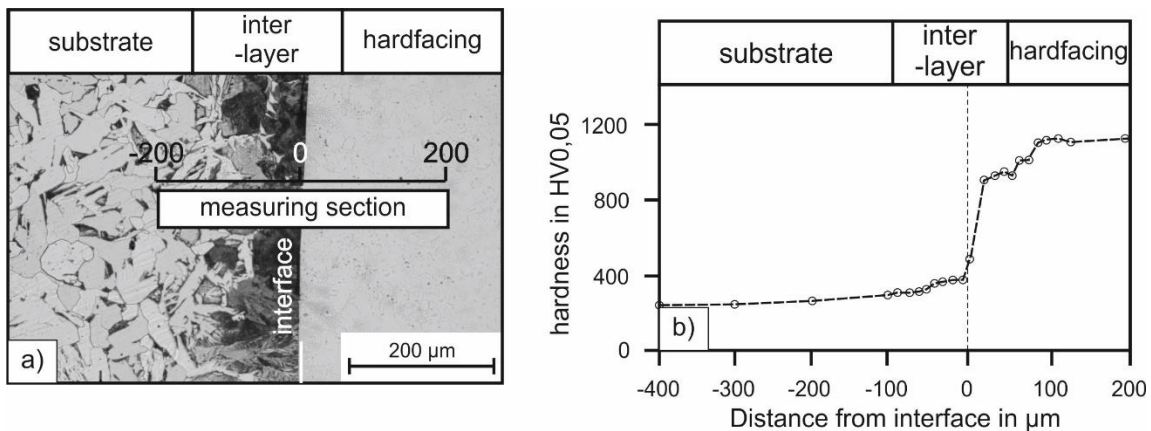

Figure 5: a) Interface of a hardfacing on a steel substrate; dilution as a result of an energy input during welding, b) hardness track across the substrate-weldment interface

Counteracting the aforementioned disadvantages, some works are dealing with the development of new hard particles [11-12]. In this context, oxide ceramics like alumina, zirconia or covalent bonded

ceramics like SiC, cBN and diamonds are of high interest, which can be attributed to their hardness, fracture toughness or both. On the one hand, oxides possess a worse wettability by liquid melts, thus only mechanical bonding is present. Otherwise, SiC and diamond for example will dissolute strongly in the Fe-base matrix for example, forming more stable phases like Fe-rich silicide and graphite [13]. Metallization of the particles surfaces by thin layer techniques (CVD, PVD) might be a solution and is surely a worthwhile focus of future research. In this context, these layers can promote the embedding of the carbides, while acting as interlayer for oxides or as a barrier coating in for metastable ceramics. As stated above, MMC materials are placed on steel substrate by deposition welding or thermal spraying to protect technical surfaces against abrasion, erosion or corrosion. Typical buildup welding techniques are gas welding, shielded gas welding and plasma powder buildup and laser welding which differ in the type of the heat source (flame, plasma, laser), the respectively filler materials (wire, rod, powder) and the deposition rate (1 to 25 kg) [14]. During build-up welding, heat input leads to a melting of the filler material as well as of the substrate material. As a consequence, the melt pools are blended which is well known as dilution (***Fig. 5a***). The dilution of the substrate material (mostly construction steel) and the highly alloyed hard facing alloy is forming an interlayer. Thereby, the chemical composition of this interlayer can be described as a gradient between the chemical compositions of the mixed materials, thus the change of the materials properties is softened at the interface. On this account, delamination of coating due to thermal stresses, formed at material transition, can be avoided. The change in the materials properties by the gradient transition from the substrate material to the hard facing alloy can be described by hardness profiles across the interfaces. In ***Fig. 5b***, hardness profile of a build-up weldment is shown. A hardness profile is characterized by an increase in hardness coming from the substrate material (left side) to the coating (right side). Thereby, rise in hardness can be explained by the heat affected zone, formed in the substrate material, and the dilution effect due to the mixing of the fully melted hard facing alloy and the partially melted substrate material.
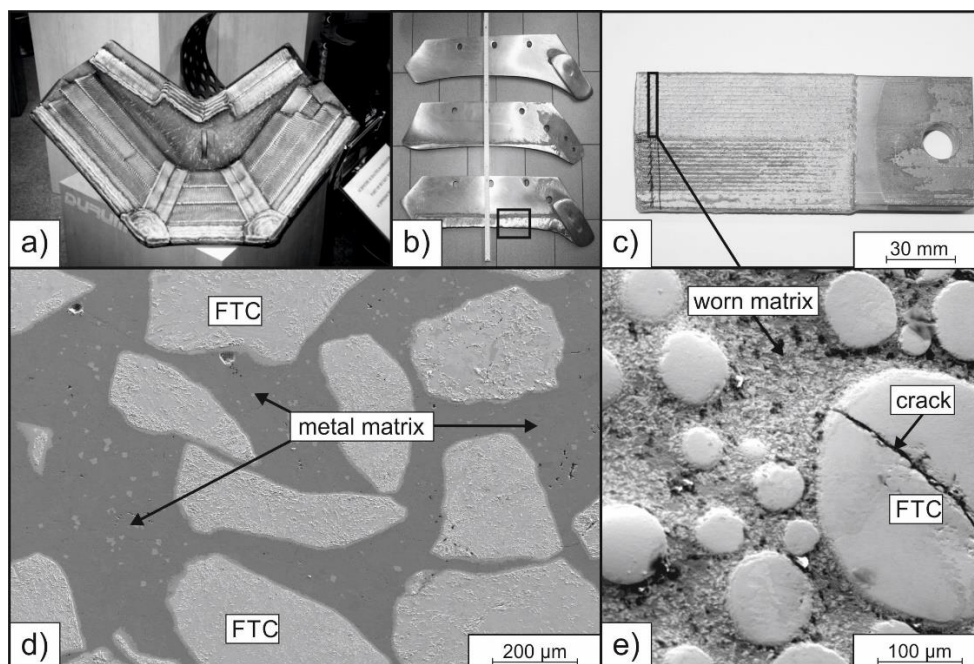

Figure 6:   Tools for mining and mineral processing locally protected by deposition welding, a) edge of an excavator bucket, protected by a hardfacing, b) cultivator c) mixer blade for minerals, d) microstructure of the a MMC applied on the cultivator (Fig 5b)) by InduClad, e) worn surface of MMC (Fe-base+sFTC) applied on the mixer blade in Fig 5c by laser welding [14, 15]

Abrasion in Tunneling

The basically selection of a tunneling method has to be determined with regard to geological (building ground and ground properties) as well as technical aspects (transportation and recycling of overburden, tunnel construction). Tunneling can be achieved by drilling and blasting, by tunneling machines and by sawing techniques using cutting blades for example. Subsequently, only drilling and tunneling by using tunneling machines will be described in the following, briefly.

Drilling: In the case of drilling, a hydraulic hammer drill is conventionally used. Thereby, a drill bit is placed in the front of a boring bar, which is penetrating the rock with a rotation speed up to 300 rounds/min, a stroke frequency of 40 to 60 hearts and a maximum torque of 500 to 600 Nm. The drill bit consist mainly of a of hot work steel substrate (X38CrMoV5-1, X40CrMoV5-1) which is reinforced by hard metal, cermets or polycrystalline diamond pins (see ***Fig. 7***) [16]. Studs made of cemented carbides are typically inserted by brazing or by mechanical clamping if lower loads are present during operation. In addition, channels for flushing purposes are present in the substrate material, supporting material removal. The interaction between the drill bit and the ground during drilling is mapped in ***Figure 8***. Thereby, the studs are frequently impacting on the ground which leads to crack formation and crack propagation. After several impacts, a close crack network is formed, promoting fragmentation of the material to be mined. Due to the additional rotating of the driller bit on the working face, the before produced fragments are scratched out and removed sideways by the flush. In the case of a softer and tougher rock the fragmentation is less efficient, thus mineral removal due to the rotating of the hard metal pins is more pronounced.
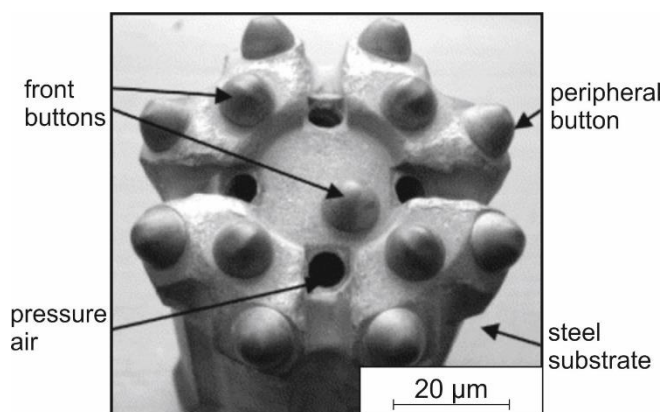

Figure 7: A rock drill bit equipped with 13 CC buttons [17]

The drilling tool has to be adapted to the geology and the machine parameters with respect to the amount of inserted studs, grade and shape of the used studs (round, sharp) and the geometry of the substrate body (flush pipes, cutting geometry, diameter). Especially, type of cemented carbide is dominating the efficiency of the drilling process. In ***Fig. 9***, different microstructures of conventionally used cemented carbide grades for mining applications are depicted. The microstructure consist of blocky tungsten carbide particles (bright displayed) having a size of 2 (fine grain grade) to >6 µm (coarse grain grade) µm, which are embedded into a darker Co-base binder matrix. Thereby, volume fraction of the tungsten carbide is in range of 75 to 90 vol.%. The property of cemented carbide is strongly influenced by the volume fraction of the Co-binder and the size of the tungsten carbide particles. In the case of fine to coarse grain cemented carbide grades, the hardness increase with increase in WC-content and in the direction of smaller WC-particles. At the same time, fracture toughness is decreased in the direction of smaller WC-particles. Especially, high hardness and high temperature stability for turning and drilling of metals is of high interest, thus fine grained and PVD/CVD-coated cemented carbides are commonly used. Counteracting grain growth and oxidation during the operation at elevated temperatures or to improve the chemical resistance, additionally hard particles like Mo_2C, TiC, TaC, Cr_3C_2, NbC and VC are regarded. In addition, novel developments in the field of cemented carbide are dealing with ultrafine grained WC. Contrary to the before mentioned relationship between WC-size and

properties, toughness as well as hardness increases at the same time in the case of ultrafine cemented carbide grades [18, 19].
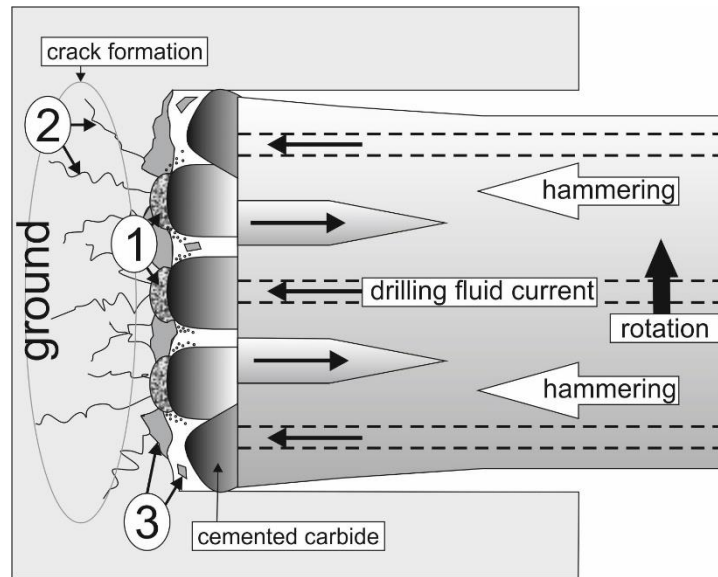

Figure 8:   Hard rock degradation process by drilling with regard to the work of Thuro [20]

During mining high impact load due to the rapid excavation process, changes in geology and boulders are present. In addition tribo-meachanical load is superposed by thermal fatigue and thermoshock due to high peak-temperatures during impact of about 1000°C, followed by an abrupt cooling. Therefore, cemented carbide for mining applications possesses a coarser WC-grain size and a binder-content of 5 to 30 vol.% compared to that grades used for metal processing, providing a high toughness and a sufficient hardness, simultaneously. For drilling application, cemented carbide grades have a medium to large WC-size (2-5 µm) and a Co-Content of about 5 mass%. Especially, bigger grains are useful for this application because of the better thermal conductivity and a lower thermal expansion in contrast to finer WC-sizes. For tunneling tools, like scraper knifes, chisels and reamers as discussed later, cemented carbides which are higher in Co-content of about 10 to 15 mass% are typically used. The properties vary in a hardness range from 500 to 1300 HV0.05 and a range in fracture toughness of 9 to 22 MPa$^{0.5,}$ depending on binder content and WC-size (typically 3-10 µm). Compared to cemented carbides for the metals processing, new development of hard metals for mining applications are dealing with an opposed motivation by increasing the WC-grain size and to strengthen the binder matrix by nano-grains for example [21].
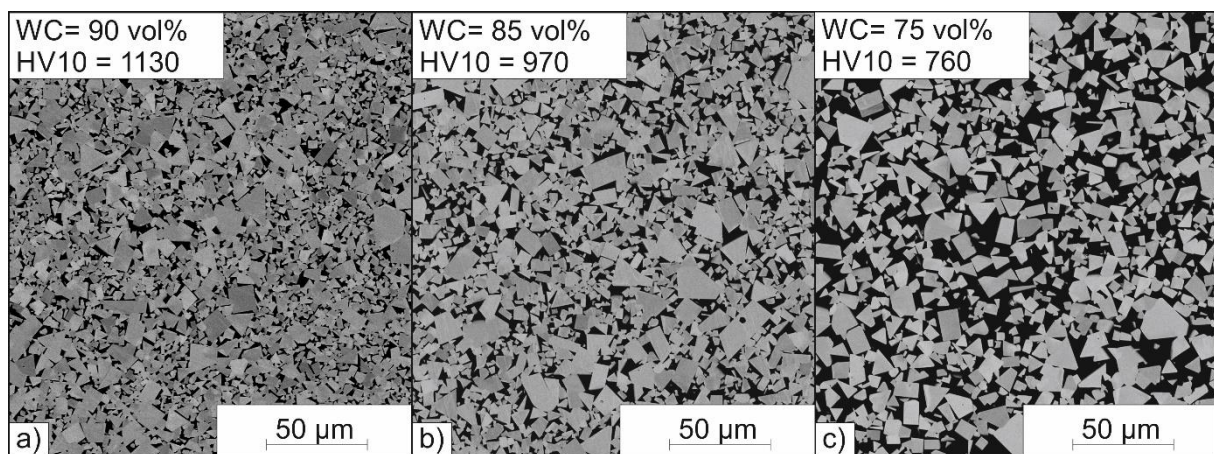

Figure 9:   Microstructure of different grades of cemented carbides used for mining applications; a) hard-grade: medium grain size and high WC-content, b) hard and tough grade: coarse grain size an medium WC-content and c) tough grade: biggest WC-grain size and lowest WC-content

With regard to the work of Betse et al., damage of hard metal during mining operation can be divided into five main mechanisms [17, 22]. 1) During drilling, high impact load can effect crack formation and propagation in WC-grains, leading to a fragmentation of the respectively grains. Thereby, fragments are losing their bonding to the Co-base binder matrix and will be worn out [***Fig. 10a***]. 2) Beside the material loss due to fragment formation, complete WC-grains can loss their bonding in the binder matrix and will be detached [***Fig 10b***]. 3) The third mechanism is characterized by an intensively removal by the binder matrix. Thereby, Co-binder matrix is removed by abrasives by scratching mechanisms. However, it is often supposed that the binder is strengthened during the drilling operation, thus the removal of fragments of the binder can be attributed to brittle behavior as described before for the WC-fragmentation mechanism. 4) Combining the before mentioned mechanisms, material removal by the break out of big fragments can occur, as shown in ***Fig. 10d***. 5) At least high temperatures can cause strong oxidation of the WC particles, forming W-rich oxides. If this oxidation process is overlapped by an additional mechanical load, the formed oxide layers can be removed easily due to their brittle behavior, leading to the so called tribochemical wear mechanism. Till now, damage mechanisms were mainly described by a negative change in the material behavior, leading to crack formation and propagation, the formation of oxides and finally to a material removal. However, based on micro scratch experiments using a diamond indenter, we found a more ductile behavior of the investigated hard metal grad (WC-Co5%). As shown in ***Fig. 11***, a plastic to brittle material behavior by scratching could be recognized. Thereby, small scratching loads lead to a more plastic deformation (micro-cutting) of the material, especially of the Co-base matrix. Whereby cracks are formed in the WC grains. If the load is increased, micro scratching and micro ploughing accompanied with a fragmentation of the WC grains is becoming more evident.
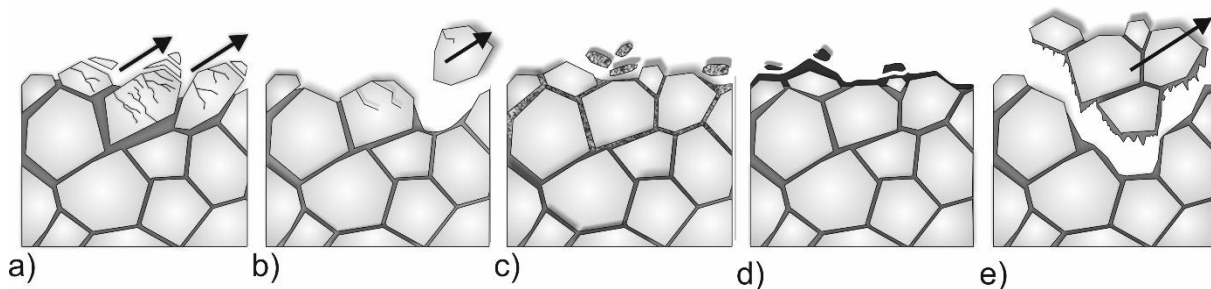

Figure 10:   Damage mechanisms of cemented carbide during drilling and mining with regard to [17], a) WC-removal by fragmentation, b) outtake of WC-grains, c) removal of the Co-matrix, d) surface oxidation, e) fragmentation of WC-Co-conglomerates

Till now, only the wear of the cemented carbide studs was discussed. However, if drilling occurs in softer rock or soil, steel substrate is worn out by abrasion. The reason for the more pronounced interaction between the abrasives and the steel substrate can be traced back to stronger penetration of the cemented carbide studs into the material to be mined. As a result, abrasives are transported between the respectively hard metal studs and are indenting and scratching the substrate material, promoting wear by erosion. Subsequently, the substrate material is erode continuously by the abrasives and the cemented carbide studs are lose their integration to the substrate material. If the erosion is in an advanced way, there is an insufficient embedding behavior of the cemented carbide studs into the steel substrate, thus a complete ripping out of the studs from the steel substrate can occur. This means a loss in functionality of the tool. For this reason, materials featuring a high resistance against indentation (high hardness) and scratching (sufficient hard phase content) by abrasives should be used.

Tunneling machines: Tunneling machines can be roughly divided into tunnel boring machines (TBM), single/double shield machines (TVM) and combinational shield machines. TBM are commonly used for hard rock where no stabilization of the face is necessary. Thereby, the material to be mined possesses a high strength, thus no risk of falls of rock is present. Enabling tunnel driving, TBM is pressed against the before build tunnel wall by a gripper system and the further

tunnel building can be achieved by tubbings (ring segments made of concrete) placed by an erector in a circular arrangement. At least, the space which is formed between the tubbings and the rock surface is filled by mortal. If some risk due to the falls of rocks may occur during operation, TBM can be also equipped by a shielding system. Tunneling in soft ground and below the groundwater level is a more complex process, because the working face has to be secured against collapsing and the penetration of the tunneling machine by water has to be avoided. For this purpose, shield machines are used which are equipped with a supporting system using compressed air, earth pressure or liquid substances (bentonite). With respect to the ground, different tools are used, which are placed on the shield, as illustrated in ***figure 12***. In the following, different tool concepts, the used materials and the wear mechanisms will be described for operating TBM in hard rock and soil.
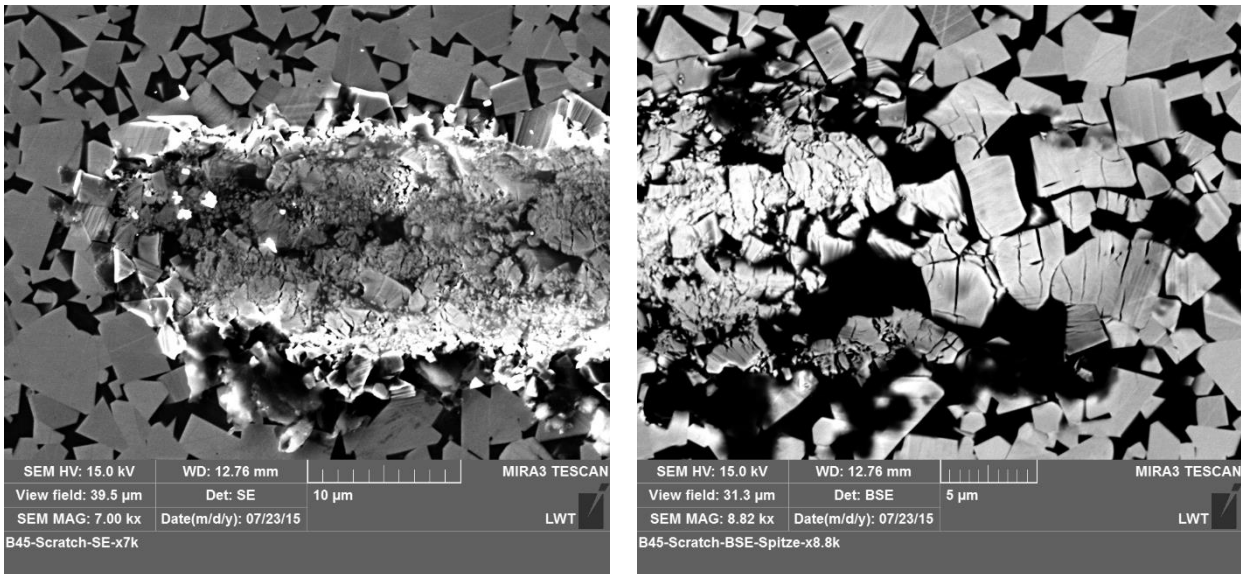
Figure 11: Microstructure of a cemented carbide, scratched by a diamond indenter; micro-cutting of the cemented carbide due to the ductile behavior of the Co-base binder matrix; micro-breaking inside of the respectively WC grains

Tools for hard rock: Independently of the type of the tunneling machine, similar tools are used with respect to the present geological conditions. Thereby, tunneling tools can separated into the three basically types of 1) cutting disk, 2) scraper and 3) removers. For hard rock or the penetrating of concrete walls, cutting disks as shown in ***Figure 13a*** are used. These tools are rotary mounted on the shield at different distances from the center of the cutting wheel. The circumferential layout of the cutting discs has to be attributed to the requirements of minimizing the eccentric forces, the eccentric moments of the cutter head and to reduce the overlapping areas among the cutter discs between two adjacent discs [21]. Due to the high penetration of the machine towards the mineral to be mined, the cutting disks are introducing high hertzian stresses into the ground. Thereby, maximum stresses are formed below the mineral which interacts with the cutting disk. Furthermore, high quasi-hydrostatic stresses are leading to crack formation below and parallel to the rock surface. The following crack propagation occurs between two adjacent cutting disks and finally a chip is extracted due to an elastic spring back of the mineral (see ***figure 14***). A detailed analysis of the stress distribution in cutting discs during tunneling can be gathered from the work of Rostami [22].

With regard to the work of Plinninger et al. six different damage mechanisms can be observed during hard rock tunneling by cutting disk, ranging from soft abrasion wear to a brittle fracture and mixed forms of both. From a material technology view on the wear of cutter disks, we distinguish between abrasion, wear due to a brittle material behavior and loses of tools functionality due to strong deformation of the cutter head (blunting of the cutting head). In the case of abrasion, the cutting disk made of martensitic hardenable steel is rotating over the material to be removed.

Thereby the abrasives can have a higher hardness than the steel of the cutting disk. In this case, abrasives are indenting into the steel matrix and promote an elastic-plastic deformation of the cutting disk steel, accompanied by strain hardening. In a next step, the abrasives are moved relative to the cutting disk steel surface, leading to abrasion wear by scratching and ploughing. Beside wear of the cutting tip in the case of hard rock, intensify wear at the flanks of the cutting disk may occur if soft rock, soil or clay-quartz like abrasion paste is present. This behavior can be attributed to a stronger penetration of the cutting disk into the softer materials, thus enhanced mineral removal at the flanks of the cutting disks takes place. Counteracting this located wear at the flanks of the cutting discs, CCS-cutter discs (constant cross section) were developed. By these type of cutting discs, the wear at the flanks leads to a self-sharpening effect, thus the cutting behavior is ensured during tunneling. Conventionally, so called V-shaped cutter discs varying in the disc diameter (330 to 508 mm) and disc edge angle are used [24]. Beside abrasion, primary wear of the cutting discs can cause catastrophic failure, if a brittle behavior of the material is present. Generally, this brittle material behavior can be traced back to high impact loads due to a bouncing of the cutting discs on the tunneling face as a result of a change in the geology or due to the presence of big boulders. To achieve a high life time of the tools, a high hardness, toughness and strength must be provided, simultaneously. Due to this account, hot work tool steels like X40CrVMo5-1 (1.2344) and X50CrVMo5-1 (1.2345) are commonly used. Hardness and toughness of both steels can be adjusted by a heat treatment, whereby quenching and tempering temperature has to be chosen with respect to the respectively alloying concept.
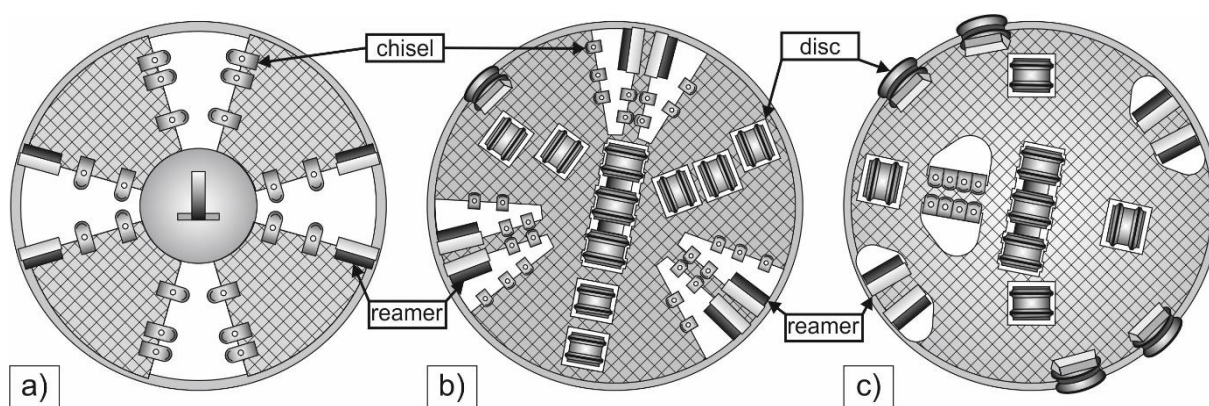

Fig. 12: Different types of tunneling machines; front view of the shield. Shield configuration is adapted to the machined ground; a) standard configuration, b) configuration for soil ground, c) configuration for hard rock.

Steel X40CrMoV5-1 possesses high hardness directly after quenching, as a result of a full martensitic microstructure. A further tempering in a range of 100 to 200°C is accompanied with a decrease in hardness and an increase in toughness. However, strong decrease in toughness is present, if the steels are tempered at temperatures of about 300 and 500°C. On the one hand it is proposed that this embrittlement effect at 300°C can be traced back to the formation of cementite (blue brittleness). On the other hand, embrittlement at tempering temperatures of about 500°C (temper embrittlement) may occur due to the segregation of the element phosphor, antimony, tin and arsenic at grain boundaries, thus promoting a brittle intergranular crack propagation [25]. In this context, tempering temperature has to be chosen with respect to these regions where blue brittleness or tempering embrittlement can be avoided. However, hardness increases at a tempering temperature of about 450°C and drops down again exceeding a hardness maximum of about 55 HRC for the steel X40CrMoV5-1 at a temperature of 530°C. This increase in hardness can be traced back to carbide formation, leading to a microstructure consisting of an annealed martensite metal matrix with finely distributed secondary carbides. Based the aforementioned relationships, highest hardness (strength) and a simultaneously high material toughness can be achieved by quenching and tempering at a temperatures of 500 to 550°C. It should be mentioned here that the heat treatment of steels is more complicated than represented here. Thereby,

secondary hardness peak and regions of embrittlement are strongly influenced by the alloying concept and the quenching temperature, for example. For further details on the heat treatment of steels see [25].
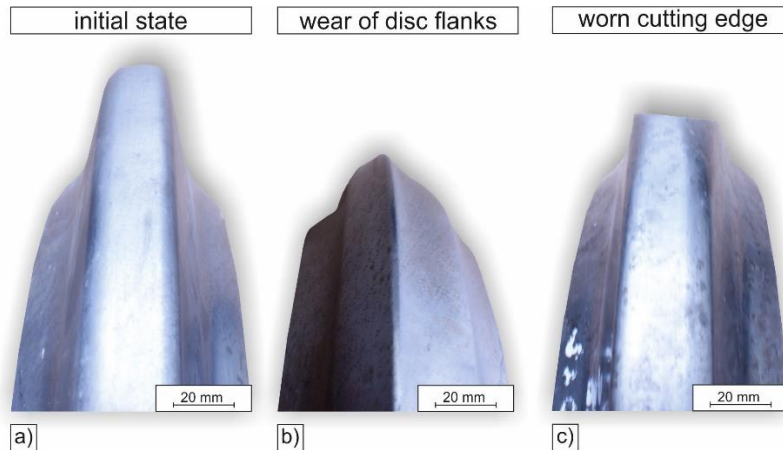

Figure 13: Tunneling tools used for the excavation of hard rock, a) new disc, b) constant worn disc, c) unilateral wear due to secondary wear (clamping of the bearing)

With regard to the work of Frenzel et al. wear of the cutting discs can be divided into primary and secondary wear. Thereby, primary wear is characterized by a direct influence of the counter body (rock, boulders, soil) to the cutting discs itself. In contrast, secondary wear means that wear takes place on other parts of the discs. Often, the bearing of the cutting discs is blocked by rotation due to damaged bearings or muck adhesion [26]. In this case, cutting discs are clamped mechanically in the bearing which is associated with a unilateral wear. By the conditioning of the muck with foams water for example, secondary wear can be reduced, efficiently. Beside the bearings, secondary wear can as well takes place at the housing of the cutting discs if an insufficient wear protection is given. In this case, seal retainers, hubs and wedges are subjected to an intensified secondary wear.
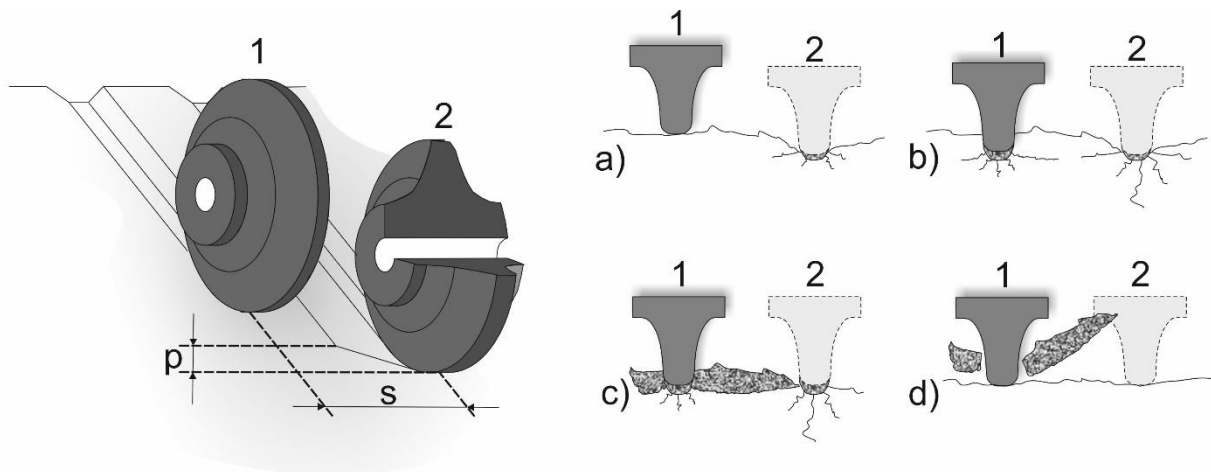

Figure 14: Scheme of the hard rock degradation process by using discs by with regard to the work of Thuro [20]

Tools for soil: Tunneling in soil is more complicated than tunneling in hard rock. This statement can be attributed to the complex tribological interaction between the ground and the tools. Therefore, the tools have to be chosen with regard to the ground. The standard tool configuration is shown in ***Fig. 12a*** and ***12b***. Thereby, the tunneling shield is equipped with cutting discs, chisels and reamers.

Excavation in soft ground is commonly performed by the use of chisels and reamers. These tools consist of a steel substrate which possesses a cutting edge made of cemented carbide. During

processing, this cutting edge is penetrated into the soil and cause a material removal at the working face by scratching mechanisms. During excavation, the removed ground passes across the tool surface, leading to material removal of the tool by abrasion. Therefore, surfaces of the chisel is protected against abrasion by studs made of cemented carbides and a hardfacing next to the cutting edge. The protection mechanism of the cutting edge and the studs made of cemented carbide can be described with the help of ***Fig. 15***. The cutting edge shows a wavelike material removal which can be explained by the staggered arrangement of the respectively chisels on the tunneling shield. With regard to our work, material removal of the cutting edge has to be discussed on the mechanisms micro-scratching and micro-braking of the cemented carbide, as discussed before (see ***figure 11***). Thereby, nanoscratch experiments show a plastic (binder matrix) to brittle (tungsten carbides) material behavior. In the case of low loads, micro-scratching and micro-ploughing could be observed. If the load was increased, micro-braking of the respectively tungsten carbide particles becomes more evident. But we believe that micro-braking represent the dominating wear mechanism in the case of tunneling tools. Thereby, cracks are formed in the cemented carbide as a result of the dynamic interaction between the tool and the ground. During the further tunneling process, cracks are propagating in the cemented carbide, forming a crack network and thus leading to a brittle material removal. Thereby, growth rate of the cracks is influenced by the load (circumferential speed of the tools, penetration rate, etc.) and the geology (density of soil, water content, particle size distribution, etc.).
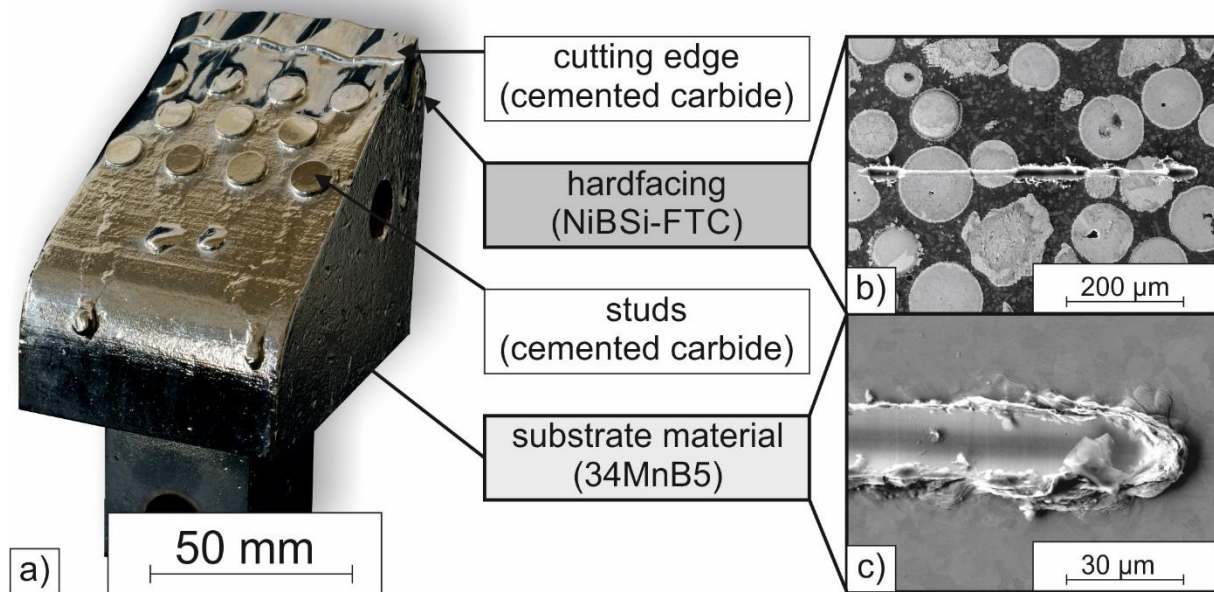

Figure 15:   Build-up of a chisel which is locally protected against abrasion by studs and a cutting edge made of cemented carbide and a hardfacing; Interaction of the respectively materials against scratching are shown for the hardfacing in ***figure 15b***, for the substrate material in ***figure 15c*** and for the cemented carbide in ***figure 11***.

In addition, strong wear of the substrate material can be observed directly behind the cutting edge. Thereby, material removal is pronounced sidewise of the studs, indicating a washing out of the substrate material by abrasion. In the further course of the substrate removal by wear, studs and the cutting edge are exposed, which might result into a break out of the cemented carbide components due to a loss of embedding. After a removal of the cemented carbide, strong wear of the substrate material will takes place, leading to total failure of the tool within a very short time. Due to the fact that the tunnel shield can rotate clockwise as well as counter clockwise, tools has to be protected against wear from both sides. Commonly, MMC-hardfacings (NiBSi/NiCrBSI-FTC) are applied on the substrate material by build-up welding techniques (see ***figure 15***). The microstructure and the wear mechanisms of these hardfacings were explained before, wherefore at

this point a repeated description shouldn´t take place. However, scratch across an MMC (NiBSi-FTC) hardfacing is shown in ***figure 15b***. Thereby, scratch width was decreased strongly if the indenter was coming from the metal matrix and strikes on a carbide.

In addition, failure of the chisels or reamers can also occur due to a strong plastic deformation of the respectively tools. These strong plastic deformations are the result of high impact load, which might occur if big boulders, metallic parts like T-beams or retaining walls are present. These massive structures in the ground cannot be crushed and therefore removed by the cutting tools. As a consequence, the tools are hitting periodically on the aforementioned structures which are remaining in front of the tunneling shield. To avoid undesirable interactions between the chisels and the reamers with boulders or retaining walls, tunneling shields are as well equipped with cutting discs. It is the tasks of the cutting discs to crush the boulders and therefore to counteract a damaging of the chisels and reamers by the boulders due to an impact load. In ***figure 16***, different tools which are used for tunneling in soil (chisels, reamers, discs) and hard rock (discs, reamers) are displayed in new and worn condition.
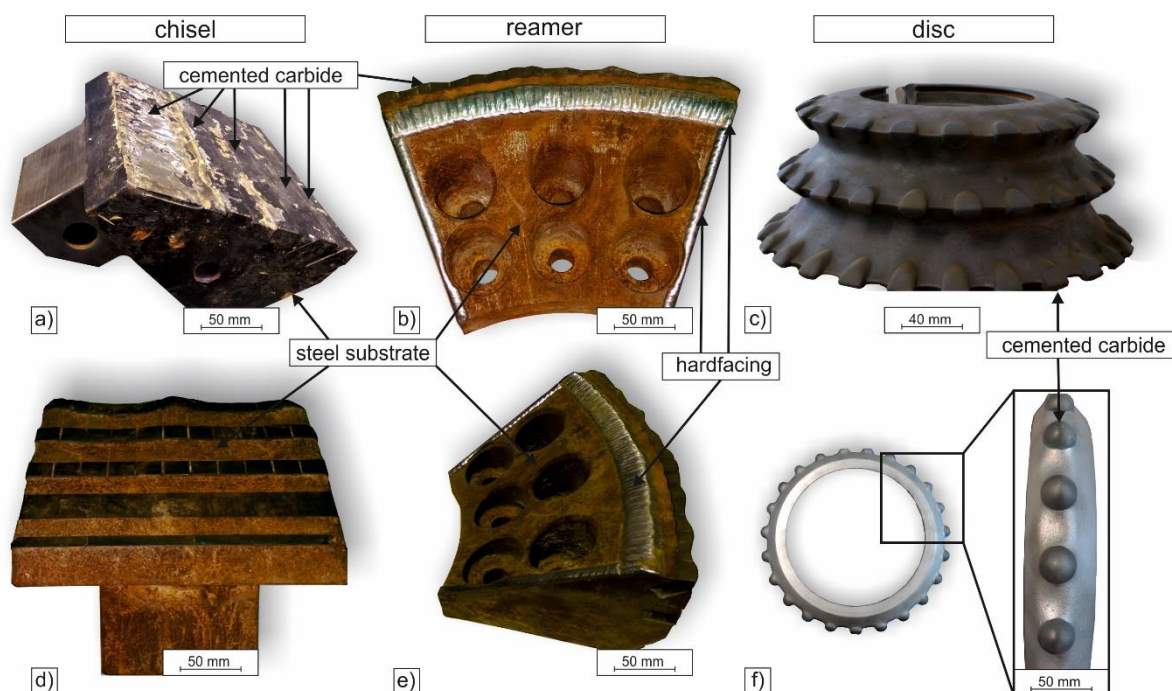

Figure 16: TVM-tools; a) chisel (initial state), b) worn reamer, placed on the exterior sections of a tunneling shield, c) cutting disc with cemented carbide studs, d) worn chisel, e) worn reamer, worn discs with cemented carbide studs

Conclusion and outlook of current research: In this paper the tribological systems of surface mining and tunneling processes were discussed with regard to the commonly used tool concepts, the different materials and the acting wear mechanisms. Thereby, hardfacing alloys, cemented carbides and metal matrix composites were introduced in this context. Based on the microstructural scale, the interaction between the tool microstructure and the present geology and the resulting wear mechanism was introduced, briefly.

Commonly, tools for mining and tunneling applications are made of a weldable construction steel substrate which is locally protected against abrasion by hardfacings or inserted cemented carbide studs or cutting plates. In both cases, high amount of the critical element tungsten is required for the materials production. Counteracting a further shortage of suitable wear resistant materials, new materials as a substitution candidate have to be found. In this context, hard particles for the production of MMC materials and hard particles for the production of new cemented carbides or cermet are required.

The inaccessibility of the tunneling tools counteracts a mapping of the wear condition during operation. On this account, the remaining service life cannot be determined. As a result, maintenance times for a tool change are designed in such a way that a complete breakdown of the tunneling tools will not take place. If the geology is changed unpredictable, wear limit can be achieved earlier or later. In both cases, an efficient use of the tool is not reached. Therefore, high technological as well as scientific interests exist to evaluate the tool life based on a realistic wear prediction before a tunneling project. Nowadays, wear prediction of the tunneling tools base on experiences gathered from previous tunneling projects or were evaluated in laboratory scale by determining the abrasivity of the present ground. However, all laboratory tests (LCPC, Cerchar) do not map the real tribological system and the existing experiences are just giving a rough idea about the wear behavior. Summing up, to counteract the aforementioned disadvantages, new realistic wear test and data logging systems which allow evaluating the remaining service life have to be developed.

Literature

[1] Population division of the Department of Economics and Social Affairs of the United Nations Secretariat: *World Population Prospects: The 2010 Revision. World Population change per year (thousands) Medium variant 1950-2050*, **2020**

[2] H. W. Parker*: Tunneling, urbanization and sustainable developments: The infrastructure connection*, Tunneling and Underground Space Technology, 11(2); (**1996**), pp. 143-150

[3] M. Thewes, Ch. Budach, M. Galli: *Laboratory tests with various conditioned soils for tunneling with pressure balance shield machines*, 4th BASF TBM Conference in London/GB, released in Tunnel 06/**2010**

[4] J. Rostami, E. A. Gharahbagh, A. M. Palomino, M. Mosleh: *Development of soil abrasivity testing for soft ground tunneling using shield machines*, Tunneling and Underground Space technology, 28 (**2012**), pp. 245-256

[5] B. A. Kennedy, *Surface Mining*, 2nd Edition, **1990**, Society for Mining and Metal

[6] Walter Durst, Werner Vogt: *Schaufelradbagger*. Trans Tech Publications, Clausthal-Zellerfeld **1986**, ISBN 0-87849-057-4

[7] A. Packeisen, W. Theisen: Metal Cutting of Hard Alloys – Turning and Grinding, Part 1: Structure and Properties of Hard Alloys, Mat.-wiss. U. Werkstofftwech. 30, (1999), 151-158

[8] I. Preis: Fatique, performance and mechanical reliability of cemented carbides, Ph. D. Thesis, TUT, 2004

[9] P. Kulu, R. Veinthal, M. Saarne, R. Tarbe: Surface fatigue processes at impact wear of powder materials, Wear 263 (2007), 463-471

[10] H. Berns; Hartlegierungen und Hartverbundwerkstoffe, Gefüge, Eigenschaften, Bearbeitung, Anwendung; Springer 1998

[11] T. Ishida, H. Moriguchi, A. Ikegaya: *Development of cemented carbide tool of reduced rare metal usage*, SEI Technical Review, 73, 2011, pp. 52-56

[12] L. Tercero Espinoza, T. Hummen, A. Brunot, et al.: *CRM_innonet-Substitution of Critical Raw materials-Critical Raw Materials Substitution Profiles*, **2013**

[13] A. Röttger: *Entwicklung neuer Schichtverbunde auf Fe-Basis gegen Abrasion*, PhD-thesis Ruhr-Universität Bochum, **2011**

[14] F. Schreiber: *Verschleißschutz durch Auftragschweißen: Werkstoffauswahl und Anwendungstechnik*, Fachartikel der Fa. Durum Verschleißschutz GmbH, http://www.durum.de/_de/fachartikel.htm (**28.09.2015**)

[15] R. Winkelmann, A. Röttger, C. Krause: *Inductively supported coating*, Elektrowärme International, 4, **2012**, pp. 51-56

[16] M. Reyes, A. Neville: Degradation mechanisms of Co-based alloy and WC metal-matrix composites for drilling tools offshore, Wear 255 (2003), 1143-1156

[17] U. Beste, T. Hartzell, H. Engqvist, N. Axén: Surface damage on cemented carbide rock-drill buttons, Wear 249 (2001), 324-329

[18] X. Ren, H. Miao, Z. Peng: *A review of cemented carbides for rock drilling: An old but still tough challenge in geo-engineering*, Int. Journal of Refractory Metals and Hard Metals, 39 (**2013**), pp. 61-77

[19] J. Xiong, Z. Guo, M. Yang, et al.: *Tool life and wear of WC-TiC-Co ultrafine cemented carbide during dry cutting of AISI H13 steel*, Ceramics International 39 (**2013**), pp. 337-346

[20] K. Thuro: *Geologisch-felsmechanische Grundlagen der Gebirgslösung im Tunnelbau*, Habilitationsschrift, Münchener Geol. Hefte Reihe B: Heft 18, Technische Universität München **2002**

[21] I. Konyashin, F. Schäfer, R. Cooper, B. Ries, J. Mayer, T. Weirich: *Novel ultra coarse cemented carbide grades with reinforced binder for mining and construction*, International Journal of Refractory Metals and Hard Metals, Vol 23, 4-6 (**2005**), pp. 225-232

[22] J. Rostami: International Journal of Rock Mechanics & Mining Sciences 57 (**2013**) 172–186

[23] M. Hongsu, Y. Lijun, G. Qiuming, W. Ju: *TBM tunneling in mixed-face ground: Problems and solutions*, International Journal of Mining Science and Technology, 25 (**2015**), 641-647

[24] C. Balci, D. Tumac: Tunnelling and Underground Space Technology 30 (**2012**) 183–193

[25] W. Theisen, H. Berns: *Eisenwerkstoffe-Stahl und Gusseisen*, Springer Verlag Berlin, **2008**

[26] C. Frenzel, H. Käsling, K.- Thuro: *Factors Influencing DISC Cutter Wear*, Geomechanik und Tunnelbau 1 (**2008**), Heft 1, DOI: 10.1002/geot.200800006, Seiten 55-60

ABRASIVITY OF ROCK AND SOIL

J. Küpferle[1], A. Röttger[1], W. Theisen[1], M. Alber[2]

[1] Chair of Materials Technology, Faculty of Mechanical Engineering, Ruhr-University Bochum, Universitaetsstraße 150, 44801 Bochum
[2] Chair of Engineering Geology, Faculty of Geology, Ruhr-University Bochum, Universitaetsstraße 150, 44801 Bochum

KEYWORDS

ABSTRACT

The abrasivity of rock and soil is a commonly determined property, which is used for the estimation of the wear of excavation tools. Therefore, different laboratory test have been developed over the last decades. Within this work, the often used LCPC- and Cerchar-test are presented. The influence of the steel sample material on the determined abrasivity is analyzed in terms of the tribological system, which describes the components and interactions influencing the wear of the tunneling tools. The problems and inaccuracies in terms of the test methods are discussed and described from the view of materials technology. To determine a sufficient wear-prediction model for excavation tools, laboratory tests like LCPC and Cerchar are useful, but they have to be considered in the tribological context. This means that it is necessary to map as much characteristics as possible from the associated tribological system. The different system components and their interactions have to be taken into account to determine a precise and sufficient wear-prediction model. The mandatory influence of the steel sample material on the results of the presented test methods and thus on the abrasivity of rock and soil has been pointed out.

INTRODUCTION

In recent years, mechanized tunneling and especially tunneling with a TBM has gained in importance. The constantly increasing need for infrastructure and construction sites aroused the intensified interest for underground expansions. The mechanized tunneling with a TBM has become very popular because of some significant advantages. Due to the simultaneously excavation and removal of the ground next to the subsequent tunnel lining, the efficiency of the process is higher compared to other tunneling methods (e.g. blasting or dredging). This increase leads for example to higher advance rates and thus to lower costs caused by shorter project duration. To exploit these advantages, the planning and budgeting of those tunneling projects plays a significant role. Calculations related to the estimated tunneling progress and thus to the overall costs are depending on multiple parameters and influencing factors. One of those parameters can be found in the wear of the tunneling tools, which are mounted on the cutter head. When tunneling tools are subject to excessive wear, penetration and thus the advance rate decreases. The tools have to be replaced during a maintenance interval, which leads to very high costs due to unplanned downtimes. With the help of wear-prediction models, the wear of the tools in dependency of the met geology is investigated. Therefore, actual approaches are based on the abrasivity of the geology and some soil mechanic properties (e.g. equivalent quartz content (EQu) or shear strength). From the view of materials technology, wear has to be considered in the predominant tribological system. This means that it is necessary to take all components, which

have a major influence on the wear of the tools into account (e.g. the tool material, the geology and the interactions in between). This work focusses on these interactions in terms of the tribological system to assess actual used wear-predictions. Thus leading to a better understanding of the wear processes, which in turn is the key to more sufficient wear-prediction models for TBM tools. To illustrate the influence of the tribological system and its components, commonly used testing methods to determine the abrasivity of hard-rock and soil have been performed (LCPC- and Cerchar-Abrasivity-Test). The results are analyzed related to the influence of the used steel sample material to clarify the importance of the TBM tool material on the tribological system and thus on the wear of the tools.

1 EXPERIMENTAL

In the course of the investigations, specimens for the different test methods were made of various materials in accordance with the requirements of the different standards. The materials used, their classification, heat treatment and hardness in Vickers are listed in Table 1. These grades are also used in mining and tunneling for welded steelworks (construction steel), chain links (quenched and tempered steel) or excavation tools (tool steel, cemented carbide). The intention is to investigate the influence of these material groups on the test results in order to derive realistic wear predictions for the wear pairs that occur in real applications. The use of heat-treated steels, tool steels with high carbide content and cemented carbide is intended to widen the scope of application and thus the validity of its statements.

Table 1. Categorization of material groups with regard to the different properties and features, which are picked up in the following chapters. The numbering refers to the diagrams in chapter 2.

Material	Material group	No.	Heat-teatment	Hardness [HV]	Microstructure
C45 (1.0503)	unalloyed quenched and tempered steel	1	soft-annealed	130 ± 15	ferritic/pearlitic
		2	normalized	180 ± 15	ferritic/pearlitic
		3	tempered	320 ± 15	tempered martensite
		4	quenched	440 ± 15	martensitic
S275 (1.0044)	construction steel	5	soft-annealed	120 ± 15	ferritic/pearlitic
		6	normalized	130 ± 15	ferritic/pearlitic
		7	tempered	190 ± 15	ferritic/pearlitic
		8	quenched	250 ± 15	ferritic/pearlitic
34CrNiMo6 (1.6582)	quenched and tempered steel	9	soft-annealed	250 ± 15	ferritic/pearlitic
		10	normalized	320 ± 15	pearlitic/martensitic
		11	quenched and tempered	460 ± 15	tempered martensite
		12	quenched	590 ± 15	martensitic
42CrMo4 (1.7225)	quenched and tempered steel	13	soft-annealed	220 ± 15	ferritic/pearlitic
		14	normalized	310 ± 15	ferritic/pearlitic
		15	quenched and tempered	450 ± 15	tempered martensite
		16	quenched	600 ± 15	martensitic
X40CrMoV5-1 (1.2344)	hot-work tool steel	17	soft-annealed	150 ± 15	ferritic/pearlitic
		18	tempered (SHM)	450 ± 15	tempered martensite
		19	quenched	440 ± 15	martensitic
X210Cr12 (1.2080)	cold-work tool steel	20	soft-annealed	470 ± 15	carbide-rich
		21	quenched	860 ± 15	carbide-rich
		22	tempered at low temp.	780 ± 15	carbide-rich

		23	tempered at high temp.	680 ± 15	carbide-rich
X155CrVMo12-1 (1.2379)	cold-work tool steel	24	soft-annealed	390 ± 15	carbide-rich
		25	quenched	750 ± 15	carbide-rich
		26	tempered at low temp.	870 ± 15	carbide-rich
		27	tempered (SHM)	690 ± 15	carbide-rich
HS6-5-2 (1.3343)	high-speed tool steel	28	soft-annealed	400 ± 15	carbide-rich
		29	quenched	860 ± 15	carbide-rich
		30	tempered (SHM)	890 ± 15	carbide-rich
K40	cemented carbide (medium grain)	31	-	1800 ± 15	90% carbide, 10% matrix

1.1 Heat treatment

In order to create the desired microstructure and the correlating mechanical properties, materials are heat treated according to the manufacturers' instructions (Tab. 1). To keep the article concise, the heat treatment parameters are not listed.

1.2 Hardness measurement

The Vickers (HV 10 and HV 0.05) hardness of the samples was determined according to DIN EN ISO 6507-1 (hardness tester KB-30s; test load 98.7 N). In order to maintain reproducibility, five values were measured for each sample and averaged

1.3 LCPC tests

The LCPC test was performed in accordance with the standard AFNOR P18-579 [1] with sand-blasted impellers of dimensions 50 × 25 × 5 [mm] and air-dried soil samples (500g ± 2g) of grain size 4 to 6.3 mm. The test duration was 5 min. and the rotational speed of the impeller was set to 4,500 rpm. The steel impeller rotates in the soil sample thus leading to wear of the impeller (Fig. 1). LCPC abrasiveness coefficient (LAC) was determined from the mass difference of the impellers according to equation (1), in which m_0 is the mass of the impeller before and m is the mass after the test; M is the mass of abrasive used. Three measurements were performed for each material and averaged. As abrasive, crushed quartz gravel and fused corundum were used, crushed to the required grain size. The used abrasives for all performed tests are listed in table 2.

$$LAC = (m_0 - m)/M \text{ [g/t]} \tag{1}$$
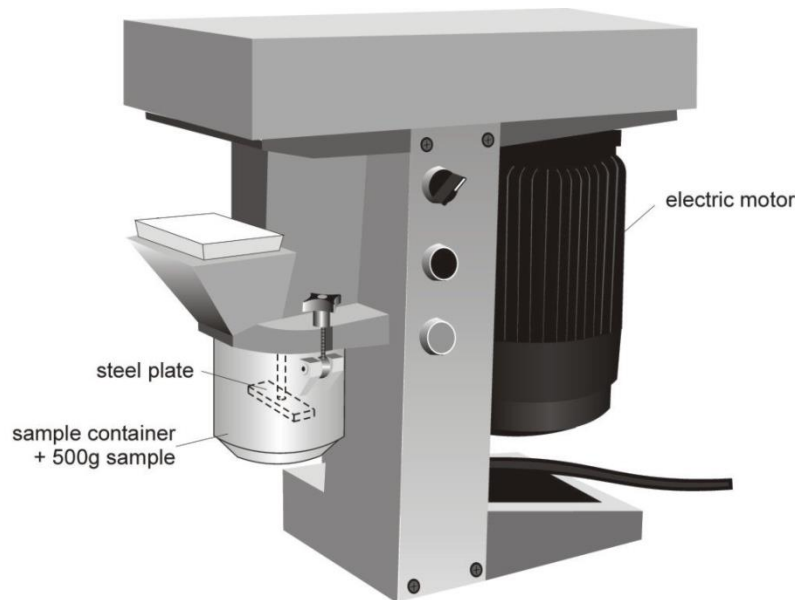
Figure 1. Schematic experimental set-up of the LCPC-test [2].The abrasive is filled in the sample container, which contains the steel impeller/plate. The impeller is driven by an electric motor.

Table 2. Outline of the used abrasives for the investigated test methods. Only for the Cerchar-Tests, the Equivalent-Quartz-Content (EQu), the Uniaxial-Compressive-Strength (UCS) and the Rock-Abrasivity-Index (RAI) were determined [3].

Test-method	Abrasiv	Mohs-hardness	EQu [%]	UCS [MPa]	RAI [-]
LCPC	quartz gravel	6 - 7			
"	fused corundum	9			
Cerchar	Bebertal-sandstone	6 - 7	65	72	46,9
"	Keuper-sandstone	6 - 7	90-95	26	23,4 - 24,7

1.4 Cerchar-Test

The Cerchar-Abrasivity-Test was developed in 1973 by the "Laboratoire du Centre d'Etudes et Recherchers des Charbonnages de France" (CERCHAR), which published the first test specification in 1986 [4]. A steel sample is scratched across a rock surface under an applied static load. The wear of the tip represents the abrasivity of the hard-rock, which is classified with the Cerchar-Abrasivity-Index (CAI). The first test setup was optimized in 1989 [5] (Fig. 2) and additionally characterized in the french specification "NF P 94-430-01" in 2000 [6]. The 90° conical tip of the test body, which is mounted in a socket, is scratched across a predefined freshly broken or sawn rock surface over a distance of 10mm. A static load of 70N is applied on the test body. In terms of the used test body material, only the hardness is defined in the actual specifications. The first specification recommends test bodies with a hardness of 54-56 HRC [3]. WEST (1989) recommends a hardness of 40 HRC for his modified apparatus [5]. The wear of the tip is used to determine the CAI with an optical microscope. Therefore, the diameter of the worn tip d [mm] is multiplied with a factor of 10 (Equ. 2).

$$CAI = d_V \cdot 10 \ [-] \qquad (2)$$

The Cerchar-tests were performed with test bodies made of different steels and heat-treatments as mentioned in table 1. For every material, at least five values were measured and averaged. Two sandstones with freshly broken and sawn surfaces were used as abrasives (Bebertal and Keuper).
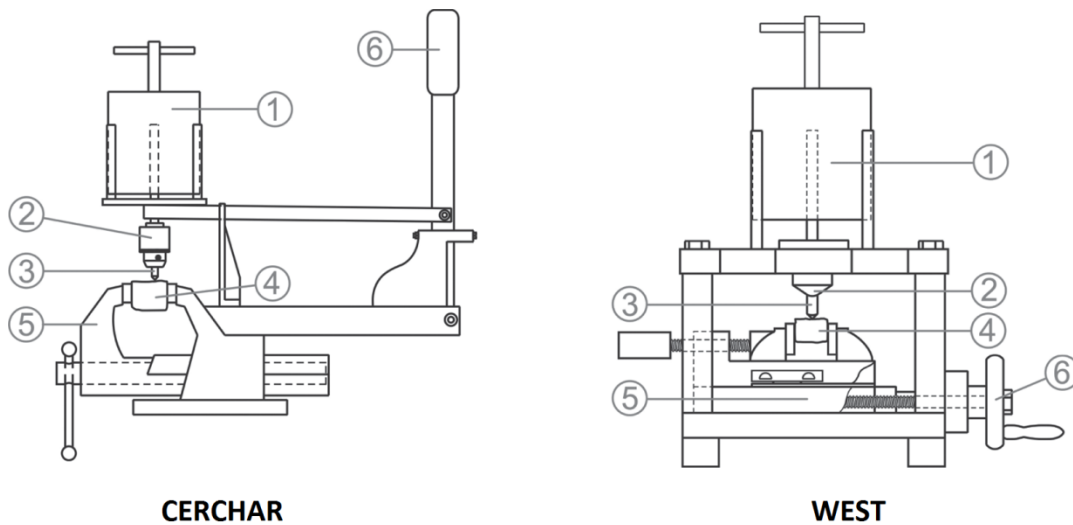
Figure 2. a) Setup after CERCHAR [4]. b) modified setup after WEST [5]. 1-load; 2-sampleholder; 3-test body; 4-rock sample; 5-mounting; 6-crank-handle [7].

2 RESULTS

2.1 LCPC-tests

The results of the performed LCPC-test with the various impeller materials are shown in figure 4 (LAC values for the crushed quartz gravel and the fused corundum against hardness of the impeller in Vickers). The LAC and thus the abrasivity of the abrasive decreases with increasing hardness of the sample. The various specimen materials are categorized in different groups referring to their present microstructure (ferrite/pearlite, bainite/martensite, carbide-rich and cemented carbide). Related to the higher Mohs-hardness of the fused corundum (Tab. 2), the LAC values are higher as for the quartz gravel over the whole hardness range. The LAC seems to decrease linearly with increasing steel impeller hardness. Only for the carbide-rich materials (marked with 21 till 30) the progression of the LAC is not distinct. The LAC increases slightly with increasing hardness. The impeller made of cemented carbide leads to the lowest LAC values for both abrasives.
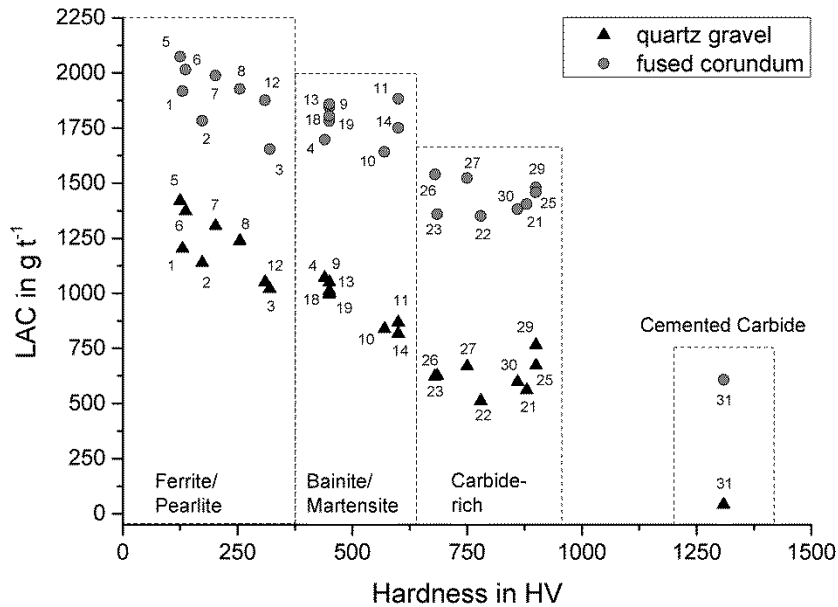
Figure 4. LAC value against hardness of the impeller for the abrasives crushed quartz gravel and fused corundum. The used materials are grouped referring to their microstructure. The numbering denotes the relevant impeller material and heat treatment state (Tab. 1).

2.2 Cerchar-tests

The experiments presented were done with the abrasives Keuper- and Bebertal sandstone in two different surface conditions (sawn and freshly broken). As for the LCPC-test, the sample materials were varied. The results of these tests are shown in figure 5 and 6.

In figure 5a the CAI value for the Keuper-Sandstone with a sawn surface is plotted against the hardness of the used specimen material. The results for the different materials show a high deviation. Furthermore the scattering of the CAI over the entire hardness range is significant high. CAI values from 1 till 7 can be seen for the same abrasive. Figure 5b illustrates the differences in the CAI in dependency of the hard-rock sample surface condition. The determined values on the freshly broken surface (Fig. 5b) are lower over the whole hardness range of the used test body in comparison to the CAI values for the same abrasive on a sawn surface (Fig. 5a).
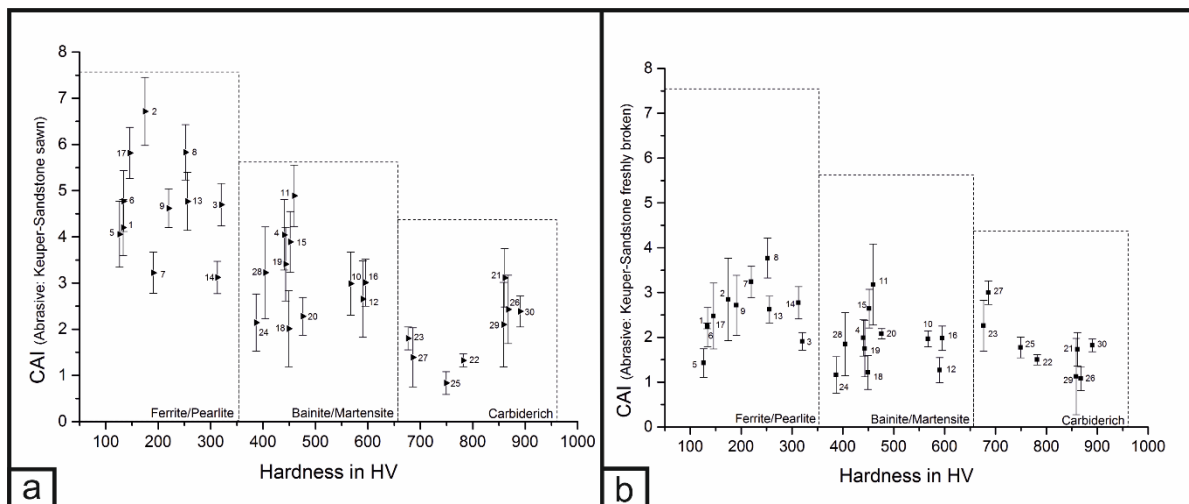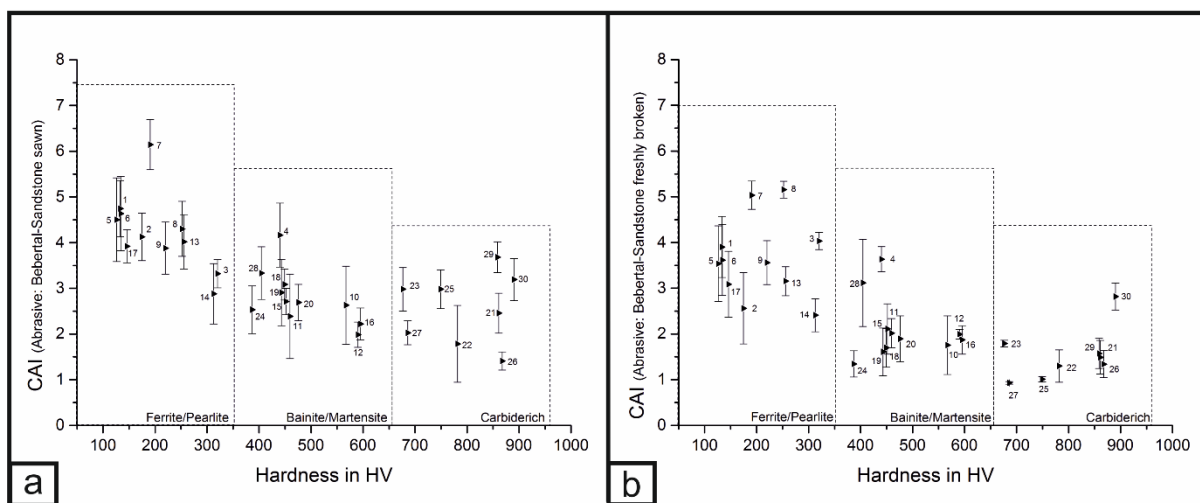
Figure 5. CAI value against hardness of the test body for the abrasive Keuper-sandstone with a) sawn and b) freshly broken surface. The used materials are grouped referring to their microstructure. The numbering denotes the relevant test body material and heat treatment state (Tab. 1).

Figure 6 shows the CAI values for the abrasive Bebertal-sandstone with a sawn (Fig. 6a) and a freshly broken surface (Fig. 6b). As indicated in figure 5, a high deviation in the values over the whole hardness range can be seen. Especially for the carbide-rich sample materials no direct correlation between hardness and resulting CAI-value can be found. This discontinuity can be transferred to all samples, due to the high scattering and irregular progression of the determined CAI values, leading to no distinct correlation between hardness of the sample and CAI of the abrasive. The influence of the surface condition of the abrasive can be seen in both figures (Fig. 5 and 6. For most sample materials, the CAI on a freshly broken surface is lower compared to a sawn surface.

Figure 6. CAI value against hardness of the specimen for the abrasive Bebertal-sandstone with a) sawn and b) freshly broken surface. The used materials are grouped referring to their microstructure. The numbering denotes the relevant test body material and heat treatment state (Tab. 1).

3 DISCUSSION

The presented results of the LCPC- and Cerchar-tests will be discussed in terms of the tribological system. Therefore, tribological system related to a TBM tool is presented and analyzed at first. The tribological system summarizes all components, interactions and influences that have an impact on the stress and thus on the wear of the investigated object [8]. A tribological system always consists of four main system components: base unit, counter body, load spectrum and ambient/intermediate medium [8]. Schematically, figure 7 shows the tribological system "TBM-tool", which is composed of the tunneling tool (base unit), the working face/geology (counter body) and the load spectrum (contact pressure, advance rate, etc.). The ambient/intermediate medium (e.g. groundwater or bentonite) is not considered in this work.
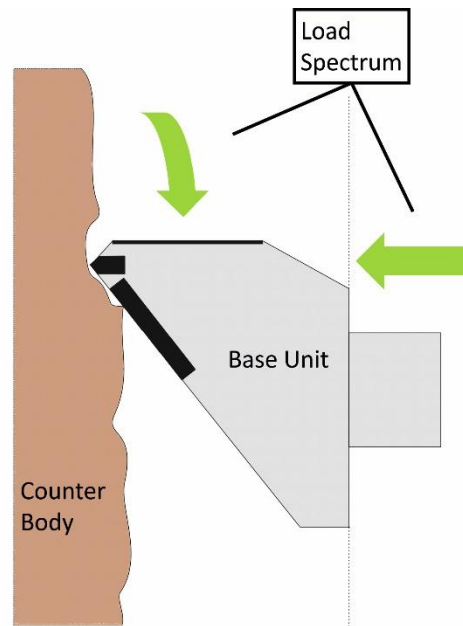
Figure 7. Tribological system for a TBM tool in soil. The tool (base unit) scratches over the tunnel face/geology (counter body) and excavates the soil. This degradation process and the correlated wear of the tool are strongly dependent on the load spectrum of the tunneling process (e.g. advance rate, penetration, rotational speed).

The wear of the TBM tool is dependent on the interactions between these system components. It becomes obvious that if one component is varied, the system is changed thus leading to different wear-mechanisms and wear-rates of the tool. If we transfer this knowledge to the presented laboratory test methods, first problems and inaccuracies occur. In a laboratory scale test set-up, the tribological system cannot be reproduced exactly. The load spectrum of a tunneling process cannot be simulated in wear test in a laboratory scale, thus leading to the first deviations in the investigated tribological system. In the same line, the used base unit and counter body have a mandatory influence on the achieved results. Thus leading to the key question of this work: The influence of the sample material on the investigated test methods to determine the abrasivity of soil and rock.

The results for the LCPC-test presented in figure 4 reveal that the microstructure of the used steel impeller has a significant influence on the LAC. The LAC decreases with increasing macro-hardness of the microstructure from ferrite/pearlite, bainite/martensite, carbide-rich to cemented carbide (Fig.4). The first impression that the regression curve of the LAC values over the hardness of the sample material decreases linearly has to be regarded with suspicion. If the carbide-rich samples (marked with 21-30) are only considered, the LAC slightly increases with increasing hardness. The explanation for this behavior is based on the composition of the microstructure (grain size, hard particle size and distribution, etc.). These correlations are investigated and discussed in [9] and will not be remarked in this work, additionally. The severe influence of the steel impeller material on the abrasivity of the investigated soil becomes obvious. If the focus lies on real tunneling application, a wide range of different steel grades is used in a TBM. For example frameworks or the shield made of ferritic/pearlitic steels, parts of the conveying system made of bainitic/martensitic steel grades and tools made of carbide-rich materials or cemented carbide. Another example would be a composite tool, which consists of a ferritic/pearlitic or bainitic/martensitic substrate, carbide-rich build-up weldments and cemented carbide inlets. These examples in correlation with the results of the LCPC-tests (Fig. 4) illustrate the mandatory influence of the sample material on the tribological system and thus on the wear of the tools.

The results of the Cerchar-tests show an analogous behavior (Fig. 5 and 6). The influence of the different system components in a tribological system on the wear or respectively abrasivity can be demonstrated. Figure 5a illustrates the influence of the sample material on the CAI. As for the LAC, the CAI decreases with increasing hardness although the deviation and scattering of the measurements are high. The previous mentioned discrepancy for the carbide-rich sample materials can be seen in the CAI values too. The abrasivity increases with increasing hardness for the steel grades marked with 21 till 30 (Fig. 5a). By taking figure 5b into account, the influence of the surface condition (counter body in the tribological system) can be seen. The CAI values for the Keuper-sandstone with a freshly broken surface (Fig. 5b) are significantly lower compared to the values on a sawn surface (Fig. 5a). The change in the surface condition leads to a change in the rock mechanical properties (e.g. cohesive forces between grains and particles). The influence of the counter body in the tribological system can be proved additionally with figure 6. The differences in the CAI for the Bebertal-sandstone in dependency of the surface condition can be seen by comparing figure 6a and 6b. The CAI values determined on a freshly broken surface are lower compared to the sawn surface whereby the progression of the values over the sample hardness (Fig. 6b) differentiate from the progression of the CAI of the Keuper-sandstone with a freshly broken surface (Fig. 5b). Although the Keuper- and Bebertal-sandstone have the same Mohs-hardness of 6-7 (Tab. 2), the CAI values and thus the classification of the abrasivity differ. Again the rock mechanical properties of the abrasive reveal a significant influence on the abrasivity and thus on the tribological system (load spectrum of the system is changed). The uniaxial compressive strength (UCS) and the equivalent quartz content (EQu) of the investigated abrasives differ (Tab. 2). Although the EQu of the Bebertal-sandstone (65%) is much lower than the EQu of the Keuper-sandstone (90-95%), the CAI of the Bebertal-sandstone is approximately equal (Fig. 5a and 6a) or even higher (Fig. 5b and 6b). If the UCS of the abrasives is taken into account, the differences in the CAI become more comprehensible. The UCS of the Bebertal-sandstone is more than three times higher than the UCS of the Keuper-sandstone (72 and 26 MPa). PLINNINGER et al. [3] and ROSTAMI et al. [10] have already mentioned that several rock mechanical properties have to be taken into account, if the abrasivity of hard-rock should be determined sufficiently. An example would be the Rock-Abrasivity-Index (RAI) [3], which is determined by the multiplication of the UCS and the EQu. This leads to a RAI for the Bebertal-sandstone of 46, 9 and for the Keuper-sandstone of 23,4 – 24,7 (Tab. 2). The RAI seems to be a more precise approximation for the classification of the abrasivity. In the context of the previous explained tribological system, it becomes obvious that the accuracy of such index values increases with the number of considered rock mechanical properties and influencing factors. So the central statement of these observations is again the mandatory influence of every system component and their interactions in the tribological system.

By transferring these correlations to the need of sufficient wear-prediction models for TBM-tools, the major concerns in terms of the validity become obvious. Models which are based on the abrasivity of the geology determined with the LCPC- or Cerchar-test cannot be precise due to the insufficient mapped tribological system. Improved wear-prediction models have to take the different system components into account. Base unit, counter body, load spectrum and ambient/intermediate medium have to be regarded. Their interactions and thus their influence on the wear have to be described by meaningful parameters, which are directly linked with the associated tunneling project.

4 CONCLUSION

This work deals with the determination of the abrasivity of hard-rock and soil, which is used to generate wear-prediction models for TBM tools. Two test methods were performed with different steel sample materials. The results of the LCPC- and Cerchar-tests illustrate the impact of the

used sample material on the classification of the abrasivity of an investigated abrasive. Wear-prediction models, which are based on such laboratory scale index values are very imprecise and show a large scattering. To determine sufficient models, the application-oriented tribological system with all components and interactions has to be taken into account. First approaches in terms of the counter body were done in literature [3, 10], but not for the other system components. This work illustrates the influence of the base unit on the abrasivity of the ground and thus on the tribological system. The abrasivity is strongly dependent on the used sample material. The mentioned correlations lead to the comprehension that it is necessary to map the tribological system with all components to determine precise wear-prediction models.

5 ACKNOWLEDGEMENT

6 REFERENCES

[1] AFNOR, 1990, Norme Experimentale P18-579: Granulats – Essai d'abrasivité et de broyabilité, AFNOR Association française de normalization, Paris, 6 S.

[2] Düllmann, J, Alber, M, Plinninger, R, 2014, Determining soil abrasiveness by use of index tests versus using intrinsic soil parameters, Geomechanics and Tunnelling 7, No. 1.

[3] Plinninger, R, 2002, Klassifizierung und Prognose von Werkzeugverschleiß bei konventionellen Gebirgslösungsverfahren im Festgestein, Muenchener geologische Hefte, B17: 1 - 146.

[4] Centre d'Etudes et Recherches de Charbonnages de France (Cerchar), 1986, The CERCHAR abrasiveness index, Verneuil 12S.

[5] West, G, 1989, Rock abrasiveness testing for tunneling, International Journal of Rock Mechanics and Mining Sciences & Geomechanics Abstracts, Vol. 26, No. 2, pp. 151-160.

[6] AFNOR, 2000, Norme experimentale NF P 94-430-1: Roches Determination du pouvoir abrasive d'uneroche Partie 1: Essai de rayure avec une pointe, Paris.

[7] Plinninger, R, Kaesling, H, Thuro, K, & Spaun, G, 2003, Testing conditions and geomechanical properties influencing the CERCHAR abrasiveness index (CAI) value, International journal of rock mechanics and mining sciences, Vol. 40(2), pp. 259-263.

[8] Czichos, H, Habig, K, 2010, Tribologie-Handbuch: Tribometrie, Tribomaterialien, Tribotechnik, ISBN 978-3-8348-0017-6, Vieweg+ Teubner Verlag, GWV Fachverlag GmbH, Wiesbaden.

[9] Kuepferle, J, Roettger, A, Alber, M, Theisen, W, 2015, Assessment of the LCPC abrasiveness test from the view of material science, Geomechanics and Tunneling, Vol. 8, Issue 3, pp. 211-220.

[10] Rostami, J, Ghasemi, A, Gharahbagh, E, Dogruoz, C, & Dahl, F, 2014, Study of dominant factors affecting Cerchar abrasivity index, Rock Mechanics and Rock Engineering, 47(5), 1905-1919.

NEW WEAR-RESISTANT MATERIALS FOR MINING APPLICATIONS

S. Brust, A. Röttger, W. Theisen

Lehrstuhl Werkstofftechnik, Ruhr-Universität Bochum, 44801 Bochum, Germany

brust@wtech.rub.de

Abstract

Economic and political driving forces are leading to an ambitious search for substitutes for fused tungsten carbide (FTC) in ultra-high wear-resistant metal matrix composites (MMC), which are used for mining applications. In the presented paper, possible substitutes such as alumina (Al_2O_3), zirconia (ZrO_2) and silicon carbide (SiC) are discussed. To enhance the wettability of oxides (e. g. Al_2O_3, ZrO_2) by Fe-base melts or to counteract strong dissolution of metastable covalent bonded hard-particles (e.g. SiC) it is proposed to coat the particles with a thin titanium nitride (TiN) layer by means of chemical vapor deposition (CVD). For this reason a CVD-apparatus for particle coating was constructed and is shown in this paper. In addition, it is demonstrated that such a TiN coating on the oxide particles can increase the wettability and therefore improve the embedding behavior of the particles into a Fe-base matrix. In addition, it is shown that TiN coatings on covalent bonded hard-particle SiC can be used as a diffusion barrier coating, thus counteracting a dissolution of the hard-particles during processing by sintering techniques. However, due to the difference in linear thermal expansion coefficients the coating tends to delaminate, partially.

Keywords: Metal Matrix Composites, Wear-Resistance, Chemical Vapor Deposition, Surface Metallization, Diffusion Barrier Coating, Particle Coating

Introduction

To protect mining tools against abrasive wear the state of the art material for protective coatings can be found in metal matrix composite (MMC) consisting of a Ni-base metal matrix which is reinforced with additions of fused tungsten carbide (FTC). The use of FTC can be traced back to its superior tribo-mechanical properties which are characterized by a high hardness of 2000 – 3500 HV0.05 and a simoultaneously sufficient fracture toughness of 5-7 $MPam^{0.5}$ [1].

However, due to several studies [2, 3] the European Union (EU) classified the element tungsten as critical, leading to an ambitious search for substitution candidates. The criticality of elements is defined by its supply risk and their economic importance (Figure 1). The supply risk is characterized by the substitutability and recycle rate of the element and the country concentration and governance of the supplying county. Since China is supplying 85% of tungsten for the European Union it is controlling its availability [2]. More than 60% of the annual tungsten output is used for the production of tungsten carbide which is mainly processed to wear protection products like cemented carbide or particles to produce wear resistant build-up weldings [4]. But in contrast to cemented carbide, recycling of worn tungsten carbide in wear resistant build-up weldings is not possible, making the substitution of FTC in protective coatings an essential part for the decoupling of international material policies.

In addition to the political driving force for the search of substitutions, there is an economic driving force due to high price of tungsten combined with a high price volatility. Within the last decade, the price for tungsten ore (WO_3) has risen over 200%, accompanied by a price volatility of up to 50 % in one year [5]. For most production routes nickel-based alloys are used for MMCs containing FTC, since FTC tends to dissolute in iron-based alloys as a result of the higher processing temperatures. Thus, substitution of FTC by other hard-particles does also give the chance to replace the Ni-based matrices by cheaper iron based matrices.
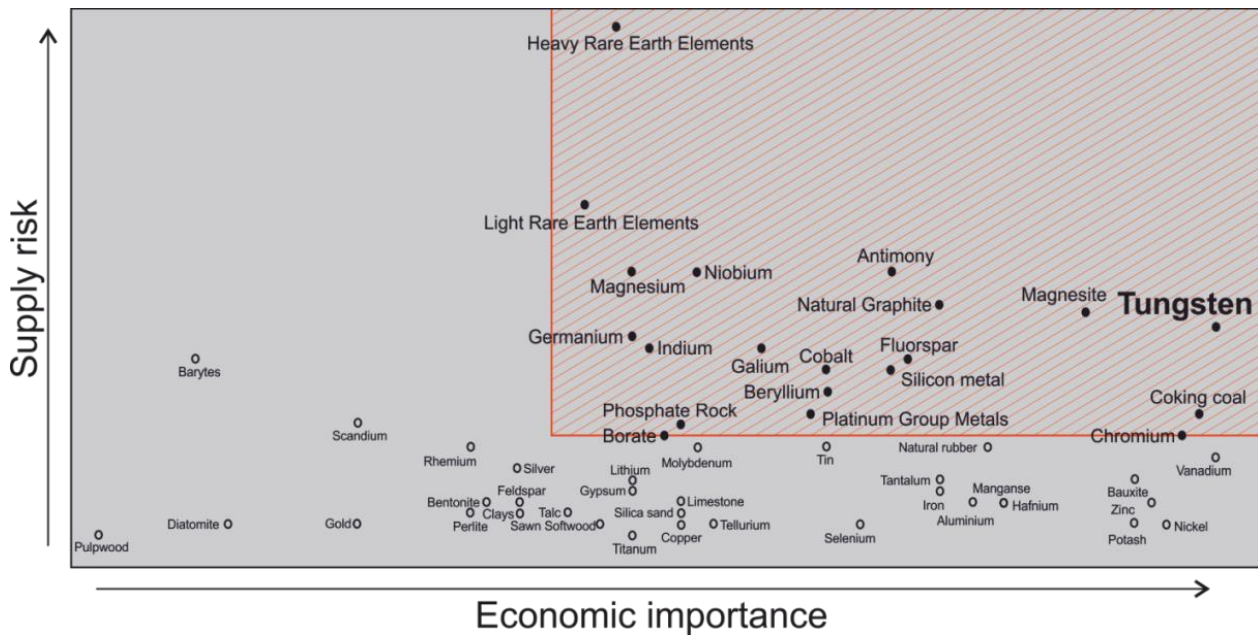
Figure 1: Critical raw elements for the EU, withdrawn from [2]

1. Material concepts

Potential substitutes for FTC need to possess higher hardness than the hardest mineral quartz (~1100 HV 0.05) for sufficient wear protection. Mainly ceramic materials feature such a high hardness. Röttger [6] classified hard materials according to their chemical bonding in a van Arkel-Ketelaar triangle (Figure 2).

All of the mentioned hard materials are ceramics with mainly covalent and ionic bonds, whereat diamond is completely covalent and other compounds made of B, C, N and Si with each other are almost completely covalent. The group of ionic hard materials consists mainly of metal oxides. Some ceramic materials exhibit some rather metallic properties like high thermal and electrical conductivity, indicating existence of dislocated electrons within these materials. These metallic hard materials consist of compounds of transition metals with B, C and N [7, 8].

The groups of hard materials differ in their interaction behavior with iron-base melts, leading to different challenges which have to be mastered to use them as reinforcements in MMCs. Oxide ceramics show very little chemical interaction with iron-base melts (Figure 3 a)) leading to weak bonding between hard-particle and matrix which results in poor tribo-mechanical properties. Three main reasons can be found for this behavior: 1) oxide ceramics are thermodynamically very stable [9]. Thus, dissolution of these compounds is very unlikely since the reaction products have to be more stable than the starting materials. 2) the solubility of oxygen in iron melts is low [10]. This make the dissolution of metal oxides in Fe-base melts even more unlikely, since if oxygen cannot be dissolved in iron, it needs to nucleate and form gas. For this nucleation energy is required. 3) the interfaces between oxides and iron are incoherent which leads to high interfacial energy [1, 11]. In addition, steel melts wet oxide ceramics badly leading to porous materials. This can be attributed to the predominantly ionic and covalent natures of these materials which results in bad electron exchange with the respective melt.
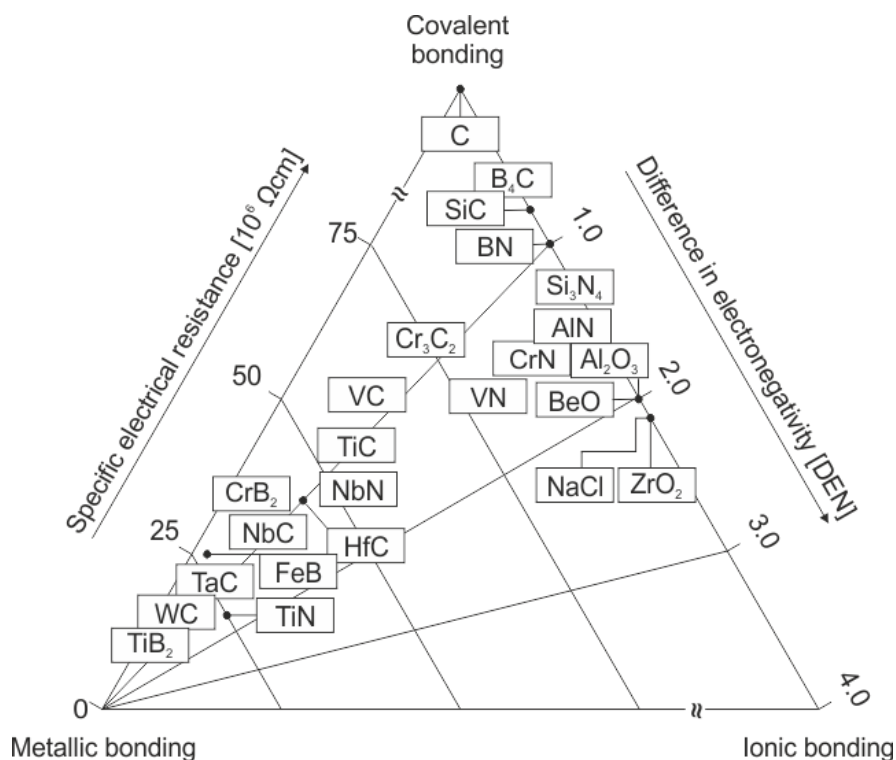
Figure 2: Classification of hard materials according to their specific electrical resistance and their difference in electronegativity, withdrawn from [6]

However, due to the good mechanical properties of these hard-materials they constitute interesting substitution candidates for FTC. Alumina and zirconia feature high hardness of up to 2100 HV0.05 and especially the alumina-zirconia mixture (AlZrO) possesses also a high fracture toughness, exceeding those of FTC [7]. To achieve substance-to-substance bonding between these oxides and the iron-base matrix, it is necessary to modify the hard-particles' surface. Metallization of ceramic surfaces with titanium is known from brazing technology. These thin titanium layers can be deposited mechanically or by physical vapor deposition (PVD) or chemical vapor deposition (CVD). This applied layer reacts with the ceramic during the joining process forming interfacial products which are rich in titanium and in turn are wetted well resulting in improved bonding [12–14].

These kinds of interlayers have also been used for surface metallization of oxide particles to increase wettability and bonding strength between hard-particles and Fe-base matrices. Winkelmann et al. [15] demonstrated that such kind of interlayer on AlZrO-particles consisting of titanium leads to metallurgical bonding between hard-particles and steel matrix. In [16] it was shown by Jouanny-Trésy et al. that titanium nitride (TiN) can also be used as interlayer for the production of alumina reinforced M3/2 high-speed steels with Cu_3P addition. These additions leads to the formation of low melting phosphide phase which wets the coated ceramic and thus leading to a lower porosity at the interface and improved particle-matrix bonding resulting in an improved wear-resistance.

The group of covalent hard materials exhibit the highest hardness of all known materials. This arouses the attention of researches to utilize them as particle reinforcement in composite materials. The group involves among others super-hard materials such as diamond (up to 10,000 HV), cBN (up to 4600 HV) and C_3N_4 (up to 4000 HV) [7]. However, substitutes for FTC must be readily available in large amounts and exhibit a reasonable cost-performance ratio. This is true for silicon carbide (up to 3500 HV), which is used as structural material as well as cutting tool. For abrasive machining it used in large amounts in particle shape. Disadvantageously, this group of materials tends to dissolute when in contact with most metals at elevated temperatures (Figure 3 b)) which is due to the fact that they are metastable and their constituent elements have high solubility in most metals [6, 17, 18]. Silicon carbide reacts with iron forming more stable iron silizides (FeSi and Fe_3Si) and graphite according to equation (1) [6, 18]:

$$2\ SiC + 4\ Fe \rightarrow Fe_3Si + FeSi + 2\ C_{Graphite} \quad (1)$$
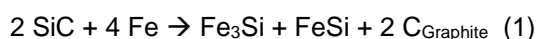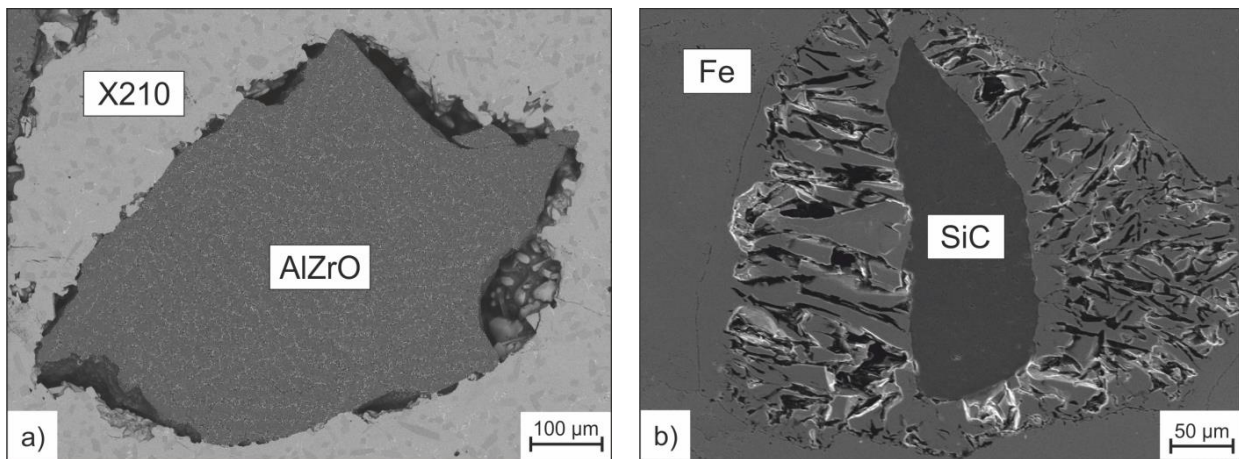
Figure 3: a) AlZrO-particle in Fe-base matrix b) SiC-Particle in Fe-base matrix

Terry et al. [18] tried to prevent the dissolution of SiC in steel by using titanium as alloying element. The assumption that the dissolution can be stopped by an in-situ formed protective layer consisting of TiC could not be verified since the TiC layer was not closed enough. The same is true for an in-situ formed Al_2O_3 layer. However, coating of SiC particle by Ni and Ni-Cu prevented dissolution of the particles when sintered into Fe-base alloy. Röttger [6] used successfully a protective interlayer consisting of titanium (deposite by PVD) to embed SiC in an Fe-base alloy. However, partial dissolution of the SiC-particles was still observed. Diffusion barrier coating for SiC can also consist of TiC or TiN [19, 20]. This mainly stops silicon diffusion, but carbon diffusion cannot be stopped completely. Also some metals, such as molybdenum, can penetrate these TiN-layers.

Some of the metallic hard materials can also dissolute in metal matrices (like tungsten carbides as mentioned above), but this can be controlled in technical processes. These compounds belong to the family of interstitial compounds consisting of a simple cubic face-centered metallic structure with interstitial carbon or nitrogen [7]. Thus, in the majority of cases the interface between metallic hard-particle and metal matrix is coherent or semicoherent and corresponding hard-particles are wetted well by the metal matrix phase [1, 11]. Detrimentally, those metallic hard phases such as TiC are only available in small grid sizes which can be too small for high abrasive wear as for example in mining or stone machining application.

In this paper the production route of novel particle reinforced Fe-base MMCs is shown. AlZrO and SiC were selected exemplarily for covalent and ionic particles. These particles were coated with TiN by the means of chemical vapor deposition (CVD) and subsequently mixed with steel powder and densified via supersolidus liquid-phase sintering (SLPS). The additional production step of particle coating is justified economical by a huge difference in price for the hard-particles. FTC costs between 50 – 60 €/kg whereas AlZrO- and SiC-particles cost between 5 – 7 €/kg. In addition, due to the much lower density of AlZrO (4.7 g/cm³) and SiC (3.2 g/cm³) compared to FTC (16 – 17 g/cm³) the price difference per volume of the materials is even bigger. Based on this assumption these substitutes are by a factor of 24 to 63 cheaper than FTC. Furthermore, the replacement of Ni-base matrix by Fe-base matrix is not considered in this calculation.

2. Coating of particles

Modification of particle surfaces by coating techniques is used in a wide range of industrial applications. Properties such as wetting, adhesion, biocompatibility, catalytic activity or protection against wear, corrosion or oxidation are improved for applications in composites, catalysis, energy production and micro- and optoelectronics. These coatings can either be applied wet by sol-gel or impregnation techniques or deposited due to gas phase reactions by pyrolysis or physical or chemical vapor deposition (PVD and CVD) [21].

To coat ceramic particles for the production of particle reinforced Fe-based MMCs the deposition of a thin, wear and thermal resistant coating is necessary, which in addition is wetted well by iron-base alloys and exhibit coherent to semi-coherent interfaces to the respective metal. This is the case for transition metal carbides and nitrides which can be deposited by PVD or CVD technique. Since the filling aspect ratio of CVD coatings is higher than for PVD coatings, it is more appropriate for the coating of particle beds. In addition, due to the higher processing temperature, diffusion between substrate and coating is stronger in CVD processes leading to better adhesions of the coating to the hard-particle substrates [22].

Chemical vapor deposition of TiN thin films is a well investigated and controllable process for industrial applications and suitable precursors are readily available in large scale amounts. For instance it can be deposited by reaction of titanium tetrachloride ($TiCl_4$) and ammonia (NH_3), which can be expressed in simple terms by equation (2) [23]:

$$6\ TiCl_4 + 8\ NH_3 \rightarrow 6\ TiN + N_2 + 24\ HCl \quad (2)$$
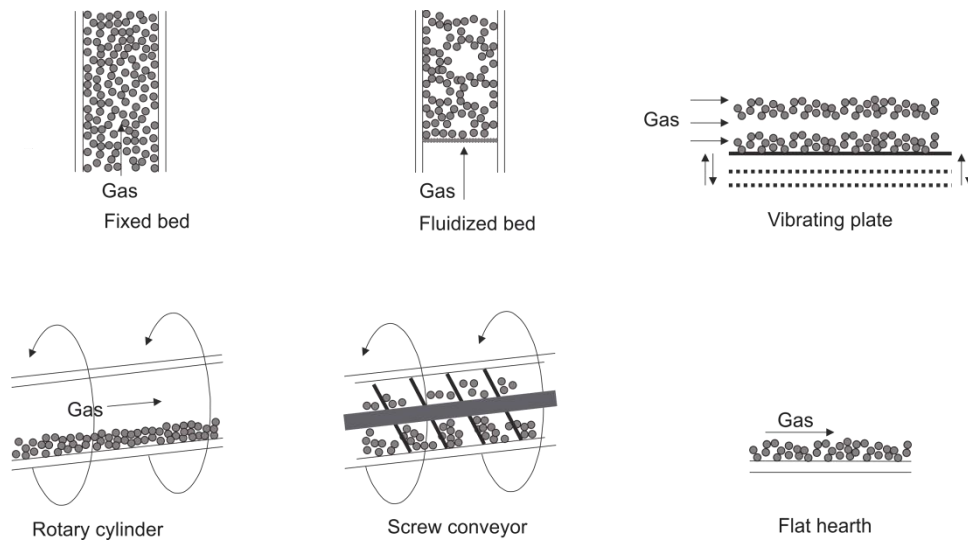
Figure 4: Possible set-ups for particle coating by CVD, adapted from [21, 24]

During the coating process a redistribution of the particles is necessary to achieve homogenous coatings on all particle surfaces. This due to two main reasons: 1) temperature gradients inside of the particle bed; 2) consumption of the precursor and generation of byproducts during the flow through the particle bed. In addition, in a fixed particle bed particle/particle and particle/wall contact points can result in uncoated surface areas. Besides that, particles can agglomerate due to the thin film growth [21]. Movement of particles can either be achieved mechanically by vibration or rotation or via gas flow and subsequent fluidization of the particle bed (Figure 4) [24]. Due to the risk of blocking by deposition products and damage by aggressive byproducts (like HCl, see equation (2)), mechanical parts should be avoided in CVD systems. Furthermore, since the gas supply is installed anyway, particle redistribution by fluidization is obvious in CVD-systems.

3. CVD device for particle coating

To achieve the aforementioned deposition of titanium nitride on hard-particles, a low pressure chemical vapor deposition (LPCVD) device was developed and set-up. LPCVD is superior for coating particle beds since diffusivity in the gas phase is enhanced which improves the exchange of precursors and byproducts within the bed. $TiCl_4$ and NH_3 were selected as precursors and nitrogen (N_2) is used as carrier gas for $TiCl_4$. Furthermore nitrogen is used as fluidization gas to achieve particle redistribution. To avoid clogging of the frit, the gas inlets of NH_3 and $TiCl_4$ are separated and the gases are not mixed bevor entering the reaction chamber (Figure 5).
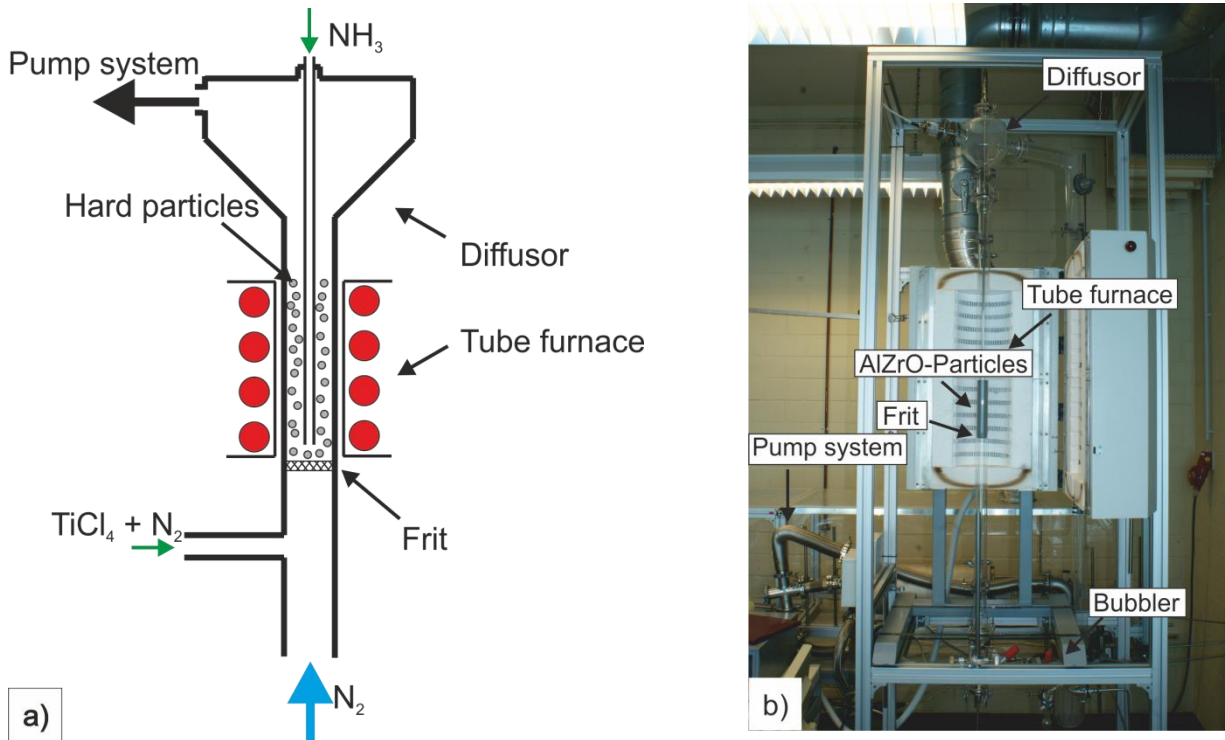
Figure 5: LPCVD device for particle coating; a) schematic diagram; b) photo

4. Results and Discussion

Figure 6 shows SEM images of uncoated AlZrO-particles. The particles are unregularly shaped (a) and at high magnifications the eutectic structure of alumina and zirconia can be seen (b). The surface appearance changes after the coating process in the aforementioned CVD-device (Figure 6 c)). The eutectic structure is covered by a cauliflower-like TiN structure (d). Cracks or flaking offs can just rarely be found, which can be explained by similar linear thermal expansion coefficient α_{th} of TiN ($\alpha_{th}=9.35 \cdot 10^{-6} K^{-1}$), Al_2O_3 ($\alpha_{th}=8\text{-}9 \cdot 10^{-6} K^{-1}$) and ZrO_2 ($\alpha_{th}=7.5\text{-}10.5 \cdot 10^{-6} K^{-1}$) at room temperature as well as at elevated temperatures [7].
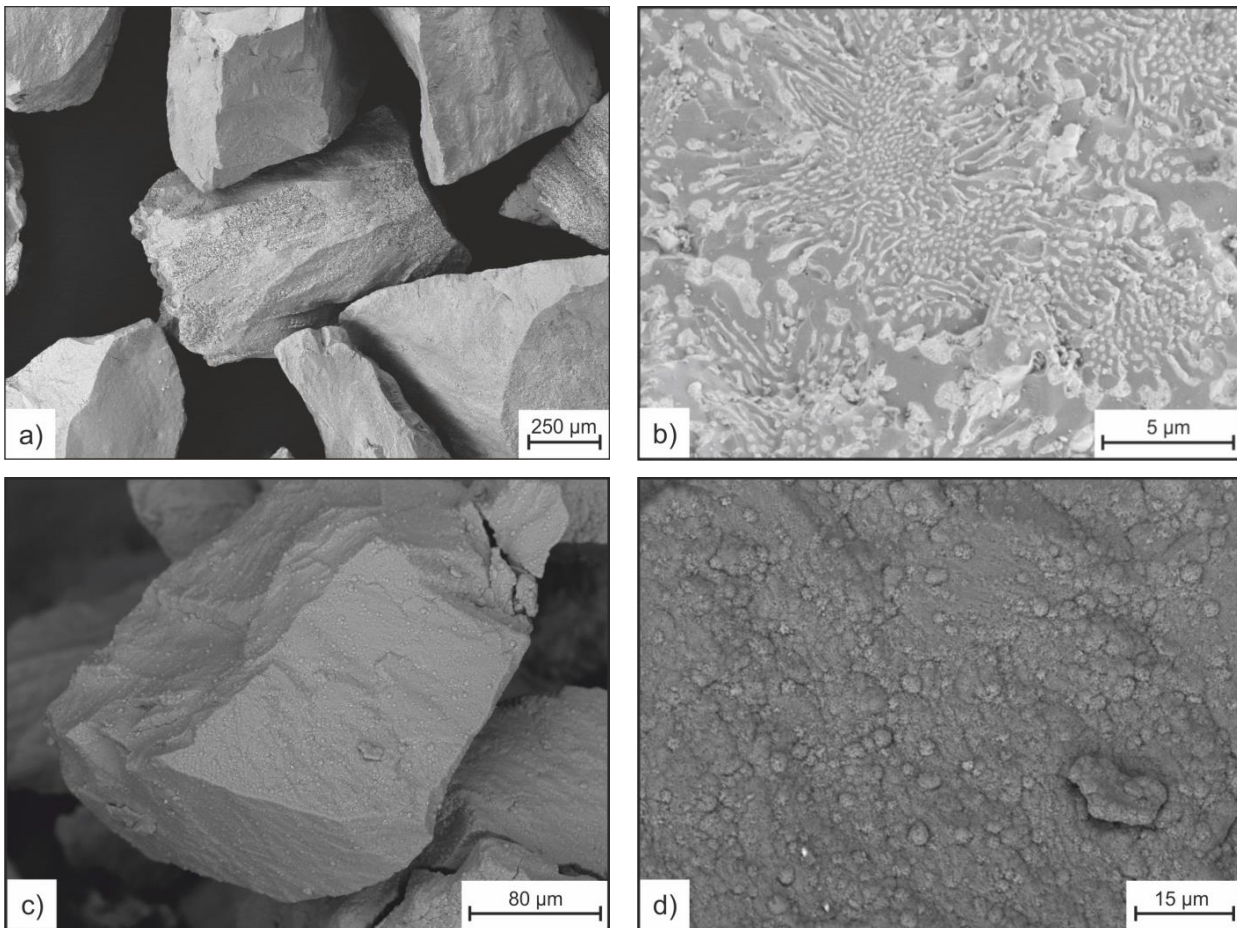
Figure 6: SEM images of a) + b) uncoated AlZrO and c) + d) TiN coated AlZrO

In Figure 7 a TiN coated AlZrO-particle embedded in a Fe-base hardfacing alloy X210CrNiBMo10-4-2-2 (X210) matrix is shown. The MMC was produce by supersolidus liquid-phase sintering (SLPS) at 1190 °C for 5 min in vacuum. Due to the coating the porosity at the interface particle/matrix is drastically decreased (compare to Figure 3 a); densified with the same matrix material under the same conditions). This demonstrates the improved wetting behavior of the X210 melt on TiN compared to alumina and zirconia.

However, thermally induced strain is a bigger issue for coating of SiC particles since the linear thermal expansion coefficient of SiC is

Figure 7: SEM image of TiN coated AlZrO-particle in Fe-base alloys

smaller (α_{th}=4.4 – 5.7·10^{-6}K^{-1}). This causes flaking offs during the processing (coating and sintering) of the coating on the SiC-particles. At free surface area the Fe-base melt reacts with the SiC-particle according to equation (1) leading to dissolution of SiC and infiltration of the particle by the melt (Figure 8 a)). Nevertheless, if the coating remains stable, the SiC-particles can be embedded into the X270CrVMoB13-7-3-2 (X270) matrix by consolidation via SLPS (Figure 8 b)).

No reaction between SiC and TiN could be observed after consolidation. However, when processed at higher temperatures a reaction forming silicon nitrides (Si_3N_4), titanium carbide (TiC) and titanium silizides Ti_xSi_y cannot be ruled out [6]. This would destroy the diffusion barrier coating. A preferred formation of vanadium carbides (VC) was observed at the interface TiN/X270 steel matrix. This can be explained by the mutual and complete solubility of TiN and VC [7]. Hence, the TiN coating can act as a nucleation point for VC solidification during sintering. For further developments of coated SiC in Fe-base MMCs the authors suggest either multilayer coatings or

adapted coating materials exhibiting similar linear expansion coefficient to SiC to prevent delamination of the diffusion barrier coating.
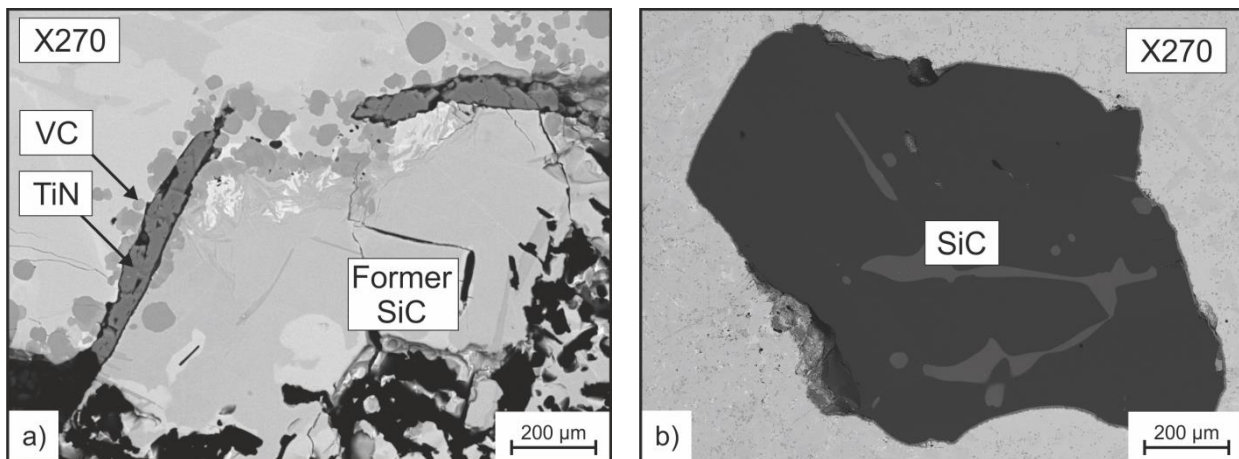

Figure 8: TiN coated SiC in X270 martix; a) dissolution of SiC due to flakings; b) stable SiC

5. Conclusions

In this work the need of substitutes for fused tungsten carbide in particle reinforced high-wear resistant MMCs was shown due to political and economic reasons. Possible substitutes can be found among the nonmetal-like hard materials (e.g. Al_2O_3, ZrO_2 and SiC). However, since the wetting behavior of iron alloys on oxides is poor and SiC dissolutes when in contact to iron at elevated temperatures, these hard-particles need to be coated by a transfer layer, which was performed within this work by the means of CVD. This transfer layer can consist of TiN which increases the wettability of the oxide-particle and acts as a diffusion barrier on SiC, preventing its dissolution in Fe-base alloys. It could be demonstrated that this concept is very successful for oxide particles but it is not sufficient for the protection of SiC. It does prevent the dissolution of SiC but due to the difference of the linear thermal expansion coefficient of TiN and SiC the coating tends to flakings.

6. Outlook

Future research by the authors will focus on three main topics: 1) TiN coating properties and interaction between hard materials and TiN; 2) interfacial reactions and wetting of steel alloys on TiN; 3) mechanical properties of the developed MMCs. The gained knowledge will be used to improve the bonding and wetting behavior of the hard-particles by the Fe-base melt, respectively reduce delamination of the coating on the SiC-particles.

7. Acknowledgement

References

[1]   Berns H. Hartlegierungen und Hartverbundwerkstoffe. Berlin Heidelberg: Springer-Verlag;
      1998.

[2]   European Commission. Report on critical raw materials for the EU. Report of the Ad-hoc
      Working Group on defining critical raw materials 2014.

[3]   Wittenberg A. Report on "Trans-Atlantic Workshop on Rare Earth Elements and Other Critical
      Materials for a Clean Energy Future". Belgium: Hosted by the MIT Energy Initiative
      Massachusetts Institute of Technology; 2010.

[4]   International Tungsten Industry Association. Primary uses of tungsten. [October 07, 2015];
      Available from: http://www.itia.info/tungsten-primary-uses.html.

[5]   Börsennews.de. [October 07, 2015]; Available from:
      http://www.boersennews.de/markt/rohstoffe.

[6]   Röttger A. Entwicklung neuer Schichtverbunde auf Fe-Basis gegen Abrasion. Dissertation.
      Bochum; 2011.

[7]   Riedel R. Handbook of ceramic hard materials. Weinheim, Germany: Wiley-VCH; 2000.

[8]   Schatt W, Wieters K, Kieback B. Pulvermetallurgie: Technologien und Werkstoffe. 2nd ed.:
      Springer Berlin Heidelberg; 2007.

[9]   Barin I. Thermochemical data of pure substances. 2nd ed. Weinheim, Basel: VCH
      Verlagsgesellschaft; 1993.

[10] Kitchener JA, Bockris JO, Gleiser M, Evans JW. Note on the solubility of oxygen in gamma
      iron. Transactions of the Faraday Society 1952(48):995.

[11] Pagounis E, Talvitie M, Lindroos VK. Influence of the metal/ceramic interface on the
      microstructure and mechanical properties of HIPed iron-based composites. Composites
      Science and Technology 1996;56(11):1329–37.

[12] Nascimento RM, Martinelli AE, Buschinelli A. Review Artivle: Recent advances in metal-
      ceramic brazing. Cerámica 2003;49:178–98.

[13] Lugscheider E, Tillmann W. Methods for brazing ceramic and metal-ceramic joints. Materials
      and Manufacturing Processes 1993;8(2):219–38.

[14] Walker CA, Hodges VC. Comparing Metal-Ceramic Brazing Methods: The adcanteges and
      disadvantages of the various methods for joining metals to ceramis are outlined. Welding
      Journal 2008:43–50.

[15] Winkelmann R, Röttger A, Krause C. Inductive supported coating. Heat Processing 2013(01).

[16] Jouanny-Tresy C, Vardavoulias M, Jeandin M. C.V.D. Coating of Alumina Reinforcing
      Particles to Improve the Wear Resistance of H.S.S. Based Composites. Materials and
      Manufacturing Processes 1994;9(5):901–20.

[17] Chou TC, Joshi A, Wadsworth J. Solid state reactions of SiC with Co, Ni, and Pt. Journal of
      Materials Research 1991;6(4):796–809.

[18] Terry BS, Chinyamakobvu OS. Assessment of the reaction of SiC powders with iron-based
      alloys. Journal of Materials Science 1993;28:6779–84.

[19] Roger J, Audubert F, Le Petitcorps Y. Reactivity of M/TiN/SiC systems (M = W and Mo) at
      high temperature. Journal of Materials Science 2010;45(11):3073–9.

[20] Roger J, Audubert F, Le Petitcorps Y. Thermal Stability of W- x Re/TiC/SiC Systems = 0, 5
      and 25 at % Re) at High Temperature. Adv. Eng. Mater. 2009;11(5):399–407.

[21] Vahlas C, Caussat B, Serp P, Angelopoulos GN. Principles and applications of CVD powder
      technology. Materials Science and Engineering: R: Reports 2006;53(1-2):1–72.

[22] Pierson HO. Handbook of chemical vapor deposition: Principles, Technology, and
      Applications. 2nd ed. New Jersey, USA: Noyes Publications.

[23] Kafizas A, Carmalt CJ, Parkin IP. CVD and precursor chemistry of transition metal nitrides.
      Coordination Chemistry Reviews 2013;257(13-14):2073–119.

[24] Kunii D, Levenspiel O. Fluidization Engineering. Newton: Butterworth-Heinemann; 1991.

Wear Resistant Materials Containing Recycled TiC

A. Mohr[1] (mohr@wtech.rub.de),

A. Röttger[1] (roettger@wtech.rub.de),

W. Theisen[1] (theisen@wtech.rub.de)

[1]Lehrstuhl Werkstofftechnik, Ruhr-Universität Bochum, 44801 Bochum, Germany

Abstract

High mechanical loads, corrosion and abrasion decreases the life time of many tooling materials used in the modern economy. One way to increase the wear resistance of tooling materials can be found in the addition of hard particles for example titanium carbide.
Titanium carbide (TiC) has a high hardness, good corrosion resistance and a low density.
Because of the aforementioned characteristics, TiC is used in Metal Matrix Composites (MMCs) to increase the wear resistance of the material. However, TiC is a cost-intensive material, thereby providing a strong incentive for recycling of TiC from worn parts or machining chips. Due to a new recycling process it is possible to recycle TiC from worn parts or machining chips.
In this study, the recycled TiC (RecyTiC) is investigated with regard to the morphology, particle size, chemical composition and phase analyses. In addition, the results were compared to industrial produced TiC. In the next step, the RecyTiC was reused for the production of MMCs. The MMCs reinforced with RecyTiC was also characterized with respect to the microstructure and wear behavior.

Keywords: MMC, TiC, Recycling, Wear,

Introduction

Many applications require resistance to corrosion and wear at the same time. Such demands can be met by using hard alloys or MMC materials, highly alloyed in chromium, molybdenum or nitrogen. Hard alloys consist of a metal matrix (Fe-, Co or Ni-Basis) and fine precipitations of hard particles like carbides, borides or nitrides which increase the wear resistance [1]. The hard particles ensure a sufficient wear resistance if they are harder than the acting abrasive particles and possess a sufficient size. Otherwise, attacking abrasives will rip and wear out the hard phases together with the metal matrix [2,3]. In applications areas with coarse abrasives, fine hard particles do not provide the required wear resistance. In these cases Metal Matrix Composites are one opportunity to achieve a high wear resistance and a high life time of the components. Therefore, the microstructure of MMC can be optimized with respect to the required mechanical, physical and tribological properties in consideration to the existing tribological system [4,5]. MMCs are produced by mixing a metal based powder with coarse hard particles (WC/WSC,TiC) and a following compaction of the mixture by sintering techniques or deposition welding for example.
An industrially produced MMC can be found in the material Ferro-Titanit®, which is produced by Deutsche Edelstahlwerke GmbH. The material Ferro-Titanit® consists of an iron or nickel based metal matrix with TiC addition of about 33 mass%. Compared to other wear resistant materials, like cemented carbide, the material FerroTitanit® is suitable for conventional machining technologies like drilling, milling and turning [6]. The resulting chip material, which includes expensive materials like

TiC, chromium and molybdenum are regarded as scarp. Therefore, the basically aim of the present study is to recycle TiC from the received chips and also from worn parts.

Because of the chemical resistance of the TiC, a dissolution of the metallic matrix and the associated extraction of TiC by the use of an acid is feasible. Therefore, a new TiC-recycling process with regard to the material FerroTitanit® was developed and patented by the VDEh-Betriebsforschungsinstitut GmbH (BFI) in cooperation with Deutsche Edelstahlwerke GmbH [7]. In this recycling process hydrochloric acid and an oxidant, for example hydrogen peroxide, is used for the dissolving of the metal matrix.

However, for a re-use of the recycled TiC (RecyTiC) a characterization of the change in chemical composition, particle size and morphology with respect to the initial state (industrial produced TiC) is of high interest. Therefore, the aim of the present study is to characterize the RecyTiC and to compare the extracted material with the properties and the morphology of industrial produced TiC, which represent the initial state. The hard phases RecyTiC and TiC are characterized by Scanning Electron Microscope (SEM), Energy dispersive X-ray (EDX), Laser Diffraction and Synchrotron Radiation. After the characterization, the RecyTiC as well as the industrial produced TiC are re-used for the densification of MMC materials by hot pressing. The produced MMC containing RecyTiC (MMC-R2) and the reference material including industrial TiC (MMC-2) are investigated by SEM observations. In addition, wear tests of the densified MMC against the abrasive corundum, varying in size, were performed with respect to the norm ASTM G105.

1. Experimental

1.1 Materials and processing

The raw material for the recycling process was provided by the Special Materials Division of Deutsche Edelstahlwerke GmbH (Krefeld, Germany). Two Ferro-Titanit® MMCs varying in the chemical composition of the metal matrix and in TiC content (approx. 30 mass %) was used for the recycling process. Sample MMC-1 consists of a soft martensitic microstructure and finely distributed TiC (30 mass %), as shown in **Figure 1a)**. Contrary, sample MMC-2 possess a carbon martensitic metal matrix and a TiC amount of 33 mass %. Also chromium-rich carbides, finely distributed in the microstructure of sample MMC2, can be detected. Both MMCs were powder metallurgical produced by hot isostatic pressing. After densification MMC-1 was solution annealed at 850°C for 2-4 hours to achieve for a homogenous microstructure and to achieve a good machinability.
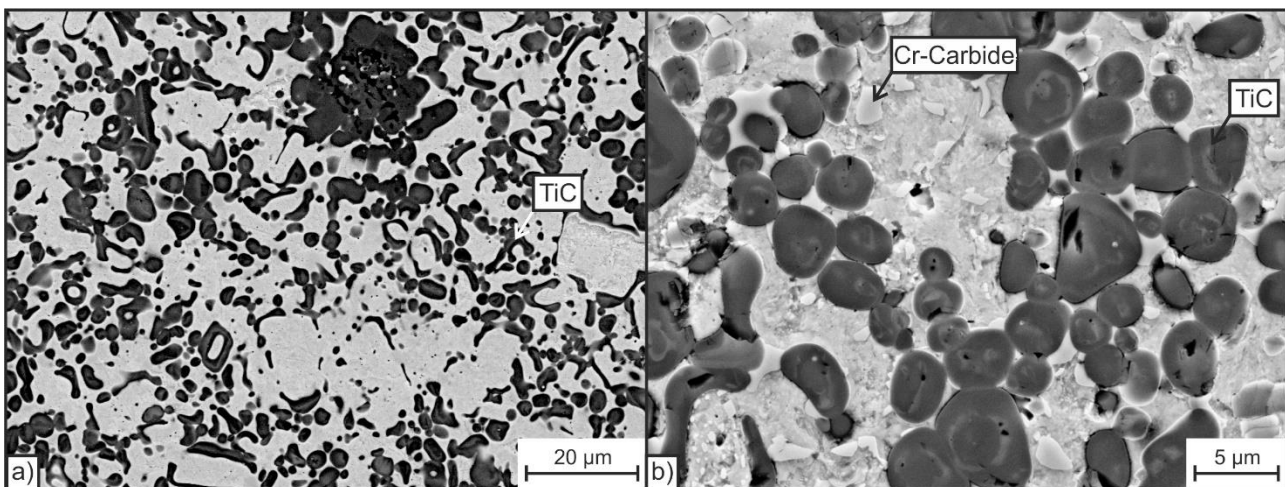
Figure 1: *Microstructure of the sample MMC-1 (a)) in solution annealed state and sample MMC-2 (b)) in soft-annealed state.*

Allowing a machinability of MMC-2, samples were soft-annealed at 750°C for 10 hours. After the heat treatment, samples were machined and the received chips were supplied for the recycling process. The recycling of the TiC was done by VDEh-Betriebsforschungsinstitut GmbH (BFI) in cooperation with Deutsche Edelstahlwerke GmbH in laboratory scale. For the recycling process, hydrochloric acid and hydrogen peroxide were used [7]. Beside chip material also compacted material with the scale 2cmx2cmx2cm were recycled. Furthermore the RecyTiC were cleaned with water and dried in a vacuum mixer.

Table 1:   Chemical composition of the materials used [mass-%] [8]

	TiC	C	Cr	Mo	Ni	Fe
MMC-1	30	-	13.5	5	4	Bal.
MMC-2	33	0.75	13.5	3	-	bal.

In addition, TiC recycling was performed additionally in a demonstrator, allowing the extraction of 500 kg of chip material in one batch. These RecyTiC was used for the industrial production of the sample MMC-R2 by DEW, whereby R in the samples designation indicates the use of recycled TiC for the samples production. Therefore, the RecyTiC was milled with the metal matrix and compacted by hot isostatic pressing. After HIP, samples were cut by electro discharge machining and heat treated for 1 h at a temperature of 1080°C and quenched in oil. Finally, the material was tempered at 460°C for 2 h, thus achieving the required tribological and mechanical properties. The produced components were used for the wear tests and microstructure analyses. Also MMC-2 with industrial produced TiC was investigated as reference material.

1.2 Microstructure

Microstructural examinations of the recycled TiC and the samples microstructure were performed via scanning electron microscopy (SEM) using a secondary electron detector, an acceleration voltage of 15 kV and a working distance of 8.5 mm. Chemical analyses were performed by energy dispersive X-ray (EDX) using an acceleration voltage of 15 kV and a working distance of 8.5 mm. All EDX measurements were corrected with ZAF (Z: atomic number, A: Absorption, F: fluorescence). To analyze the chemical composition of the RecyTiC, EDX signal was calibrated using SiC as a reference. Determination of the different phases of the RecyTiC was performed by diffraction method with synchrotron radiation. The measurements took place at the Delta electron storage ring in Dortmund (Germany) using a wavelength of $\lambda = 0.45919$ Å under reflection mode. To reduce the influence of the texture of several phases, Debye-Scherrer circle segments (140-155°) were integrated and conditioned with the program Fit2D (ESRF). Integrated diffractograms were further imported into X-Pert analyzing software and phase analysis was performed using the ICDD-JCDPS database PDF-4.

For further microstructural investigations of the samples MMC-2 and MMC-R2 the compacted material was cut by electro discharge machining and embedded in a conductive polymer resin. Afterwards, samples were ground with SiC abrasive paper and then polished with 6, 3, and 1 µm diamond suspension. Final polishing was carried out using SiO_2 suspension with a particle size of 0.25 µm. To determine the volume fraction and morphology of TiC, SEM micrographs of the samples were analyzed by quantitative image analysis with the software ImageJ.

1.3 Wear tests

Abrasive wear testing was performed by pin-on-paper test according to ASTM G105. A rotating (47*8 rev min^{-1}) cylindrical specimen with a diameter of 5 mm was moved across an abrasive paper (corundum, hardness~ 2100 HV0,05,), with a vertically applied load of 37 N. As a result of the

samples mass loss (Δm) of its surface (A), density (ρ) and the length of the wear path (l),wear rate was calculated with regard to equation 1.

$$Wab = \frac{\Delta m}{\rho AL} \qquad \text{equation 1}$$

The wear resistance is defined as the inverse of the wear rate. For each specimen, the average wear rate of three measurements was calculated with a maximum allowed deviation of 2.5 %. Each specimen was tested on corundum as abrasive paper, having an average particle size of 60 μm (Mesh220) and 180 μm (Mesh80).

2. Results and Discussion

2.1 Characterization of the RecyTiC

As it can be seen in **Table 2**, EDX measurements indicate a change in the chemical composition of the RecyTiC compared to industrially produced TiC. The initial TiC consists of the elements Ti and C in a substoichiometric composition which is in accordance with the data sheet of the manufacturer. The measurement of the RecyTiC-MMC-1 offers, besides Ti and C, a significant amount of molybdenum. The diffusion of molybdenum into TiC is mentioned in literature by Le Flem et al. [8]. Also investigations by Hill et al. show an enrichment of the TiC by the elements molybdenum and vanadium during the production of TiC reinforced MMC by hot pressing, if the element molybdenum is present in the metal matrix [10]. Thereby, the element Mo is substituting the element Ti in the RecyTiC (see **Tab. 2**).

Table 2:   Chemical composition of the TiC and RecyTiC in mass% measured by EDX.

	C	Ti	Mo	Cr
TiC	17.1±0.1	82.9±0.1	-	-
RecyTiC-MMC-1	16.4±1.7	76.6±1.8	6.2±1.23	-
RecyTiC-MMC-2	17.2±0.4	70.2±0.1	5.4±0.1	5.3±0.4

Compared to the RecyTiC extracted from sample MMC-1, RecyTiC extracted from sample MMC-2 possesses lower molybdenum content. This behavior can be traced back to the higher molybdenum content in the metal matrix of sample MMC-1 compared to sample MMC-2 (cf. **Table 1**). Also the measurements of RecyTiC-MMC-2 offer chromium besides the elements Ti, Mo and C. In addition to the EDX measurements a phase analysis by synchrotron radiation was performed. The results of the phase analysis are given in **Figure 2**. Measurement of RecyTiC extracted from sample MMC-1 has revealed that only TiC can be detected (**Figure 1a)**).
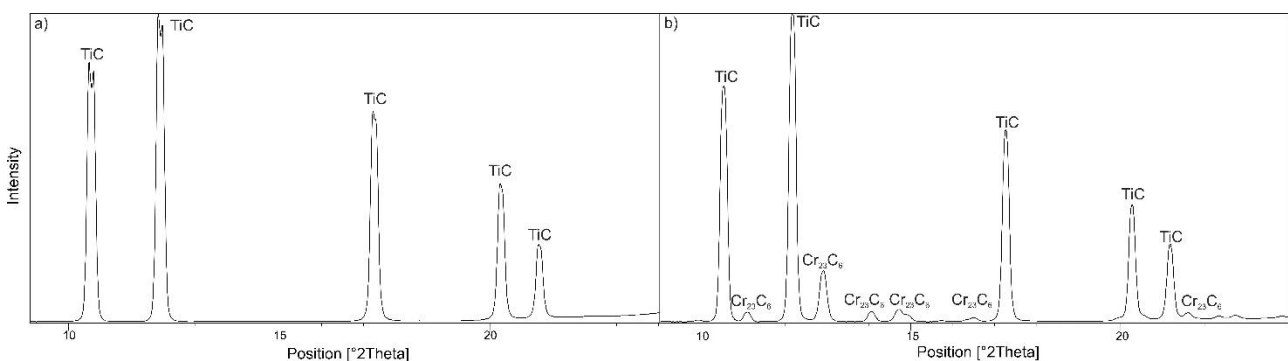
Figure 2: *Phase analysis of RecyTiC-MMC-1 (a) and RecyTiC-MMC-2 (b).*

In contrast, phase $Cr_{23}C_6$ besides TiC can be identified (**Figure 2 b)**) in the phase analyses of the RecyTiC extracted from sample MMC-2. Both investigated MMCs possess the same chromium content of 13.5 mass% (**Table 1**), however no Cr-rich carbides were found in RecyTiC extracted from sample MMC-1. The reason for this behavior can be found in the carbon content of the metal matrix of both samples. Sample MMC-1 is based on a carbon-free soft martensitic metal matrix. In contrast, sample MMC-2 feature a carbon martensitic metal matrix with a carbon content of 0.75 mass%, thus leading to the formation of Cr-rich carbide during soft annealing process, performed at 750°C for 10h. Due to the high chemical stability of the chromium-rich carbides, phase $Cr_{23}C_6$ can be detect in the diffractograms beside the phase TiC. As a consequence, the purity and the chemical composition of the recycled TiC depend on the chemical composition and the heat treatment condition of the starting material.

Beside a change in the chemical composition, the conditioning (heat treatment, densification, machining) of the starting material influences the particle size of the later gained RecyTiC. Therefore, particle size of the TiC in the three different conditions a) initial state, b) recycled from chips, c) recycled from bulk materials was investigated by laser diffraction technique (**Figure 3**).
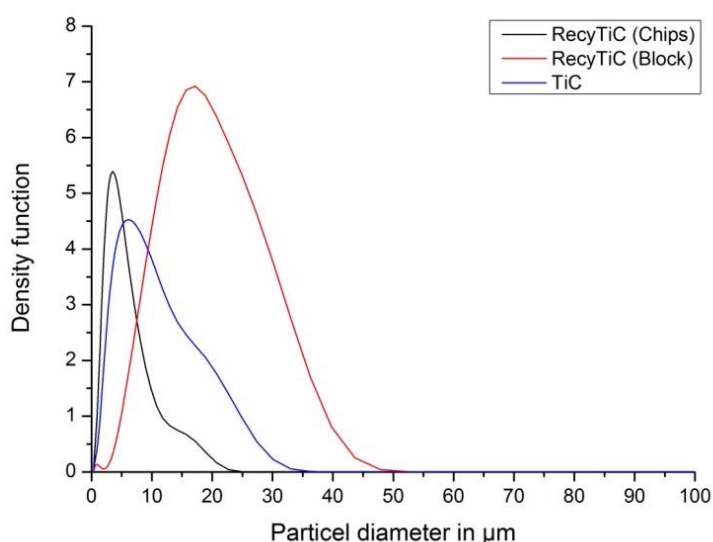
Figure 3:   *Particle size of the RecyTiC respectively TiC depending of the machining grade.*

The average particle size of the initial TiC powder was measured to $d_{50}=10$ µm. In contrast the RecyTiC dissolved from machining chips have a smaller particle size of $d_{50}=3$ µm. The change in the particle size can be explained by the brittle behavior of the TiC and the associated strong TiC-fragmentation during the machining process. An analysis of the chip material indicates that spiral chips are created during the machining process (**Figure 4**). This leads to a high mechanical stress in the material, thus promoting fracturing of the TiC during machining due to the low fracture toughness in a range of 1.5-3.6 MPa m$^{-1/2}$ of TiC [10]
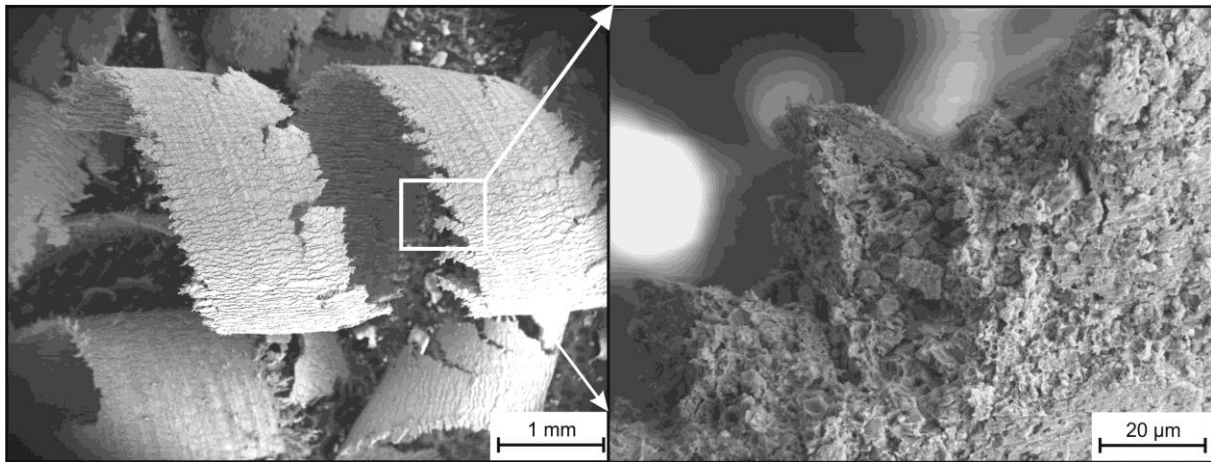
Figure 4:   *SEM Picture of the chip material used for the recycling process.*

Also RecyTiC from bulk material without an additional machining process was investigated. Compared to the particle size of the initial TiC, the particle size of the RecyTiC increases. The increase of the particle size can be traced back to diffusion reaction during the densification of the material, thus sintered agglomerates of TiC are present. SEM investigations of the RecyTiC confirm the change in the particle size (**Figure 5**). Also a change in the morphology of the RecyTiC can be detected. Thereby, the initial TiC (**Fig. 5c**) features a blocky shape. In contrast, the RecyTiC from chip material (**Fig. 5a**) have a round shape and the RecyTiC dissolved out from bulk parts having (**Fig. 5b**) a sponge like shapes.
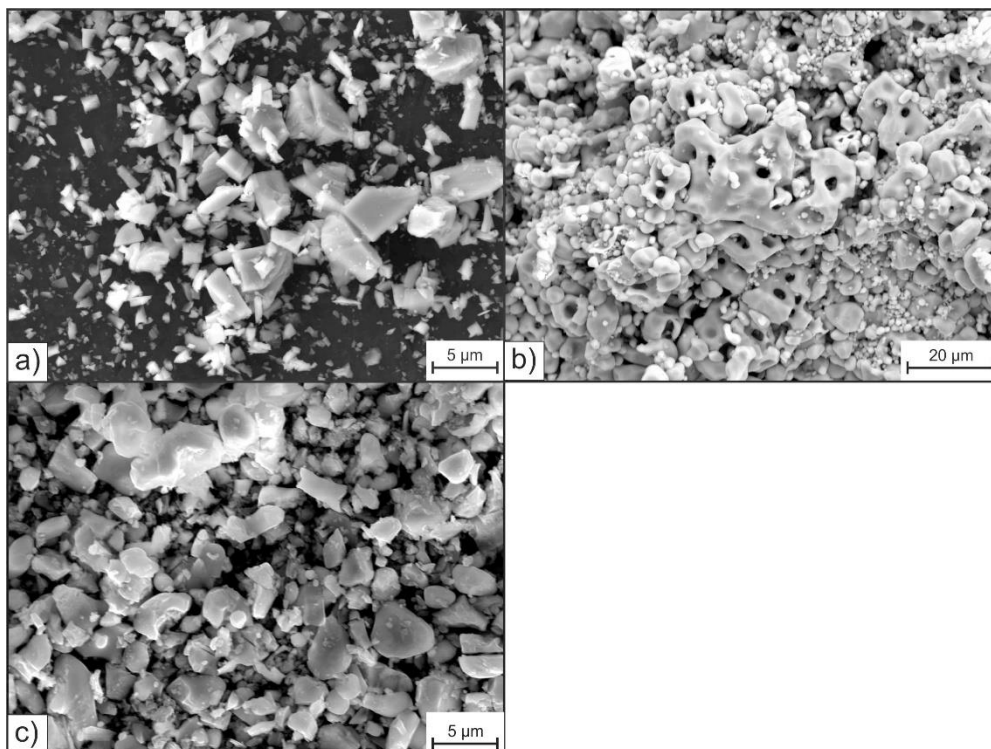
Figure 5:   *Morphology of the investigated TiC in a) initial state, b) recycled from bulk materials, c) recycled from chips*

2.2   Characterization of the MMCs containing RecyTiC

As mentioned in chapter 1.1 TiC was also recycled in an industrial scale demonstrator and was lead back into the carbon martensitic metal matrix of the material MMC-2. Therefore the RecyTiC was milled with the metal matrix powder of the material MMC-2 (see **Table 1**) and densified by HIP. After

the densification a quenching and tempering consist of an austenitization at 1080°C/1h and tempering at 460°C/2h was performed. The microstructure of the reference material MMC-2 and the sample MMC-R2 containing RecyTiC in heat treated condition is shown in *Fig. 6*. The microstructure of the sample MMC-2 is characterized by TiC particles, which are homogenously distributed in the metal matrix. Most TiC particles have a round shape and are sintered together, thus forming agglomerates. With the help of optical image analysis (cf. *Tab. 2*), volume fraction and average size of the TiC was determined. Sample MMC-2 possess a TiC volume fraction 45±2.9 vol-%. Thereby, average size of the TiC was measured to 8.3±1.3 µm². The microstructure of sample MMC-R2 containing RecyTiC is shown in *Figure 6 b)*. Thereby, RecyTiC is homogeneously distributed in the metal matrix. The morphology of the RecyTiC can be described as a blocky shape and differs to the morphology of the TiC in the reference material (MMC-2). In addition, formation of RecyTiC-agglomerates could not be found in the densified material. Compared to the reference sample MMC-2 the volume fraction of RecyTiC is decreases to 40.1±1.7 vol.-% and the average particle size was measured to 2.9±0.6 µm². The decrease of the particle size can be explained the strong TiC-fragmentation during machining of the starting material, forming the chips for the recycling process. As mentions in chapter 2.1, the machining grade of material which is used in the recycling process has an influence on the size of the RecyTiC. For the densifications of the material MMC-R2 only RecyTiC from chip material was used (cf. *Fig. 3*). This leads to small RecyTiC size in the milled powder mixture which also leads to a smaller TiC size in the compacted material
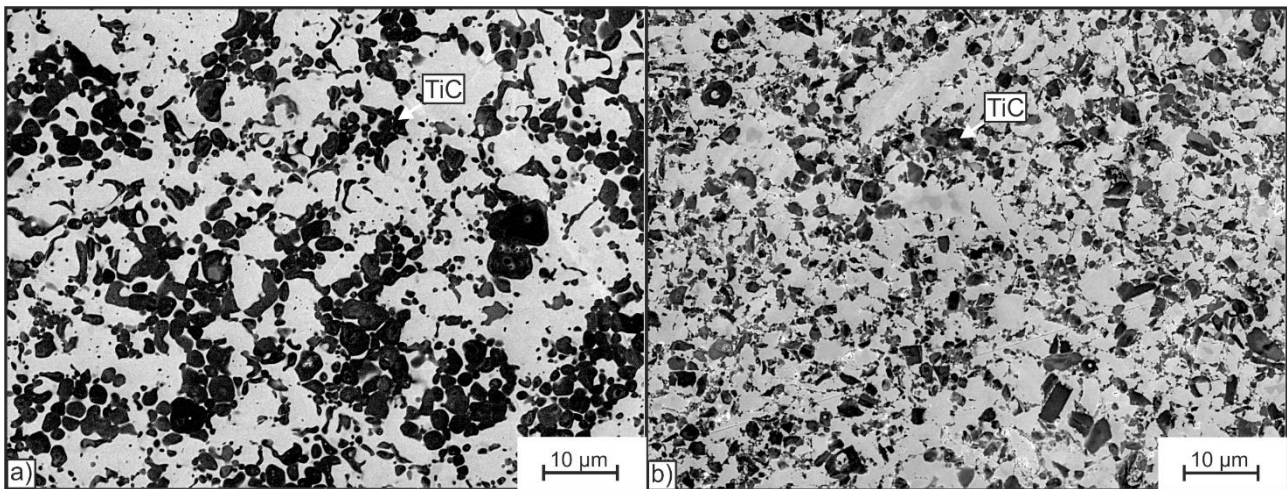
Figure 6:   *Microstructure of the material MMC-2 (a)) and MMC-R2 (b)) in heat treated state.*

The change in size, morphology and volume content of the TiC respectively RecyTiC between MMC-2 and MMC-R2 influences the mechanical, tribological and chemical properties of the material. As mentioned before, tribological properties were tested by pin-on-paper test according to ASTM G105. The results of the wear test are given in *Fig. 7* showing the abrasive wear resistance of sample MMC-2 and MMC-R2 against the abrasive corundum, having a particle size of Mesh80 and Mesh220.

Table 3:   *Particle sizes and volume content of the TiC in MMC-2 respectively RecyTiC in MMC-R2 measured by optical image analyses.*

Sample	Average Size [µm²]	Diameter [µm]	Vol.-%
MMC-2	8.3±1.3	3.2±0.2	45.1±2.9
MMC-R2	2.9±0.6	1.9±0.8	40.1±1.7

The reference sample MMC-2 possesses a wear resistant of 4.59±0.03 (Wab^{-1}*10^4) against the coarse (Mesh 80) and 15.2±0.02 against the fine abrasive (Mesh 220). The wear behavior of sample

MMC-R2 is similar to those of sample MMC-2. However, the wear resistance against fine abrasive is lower compared to sample MMC-2. This behavior can be explained by the difference in the samples microstructure with respect to the size of the TiC/RecyTiC. The worn surfaces in *Fig. 8a* and *Fig. 8b* reveals that the titanium carbides act as obstacles for the grooving abrasives and reduce the mass loss.
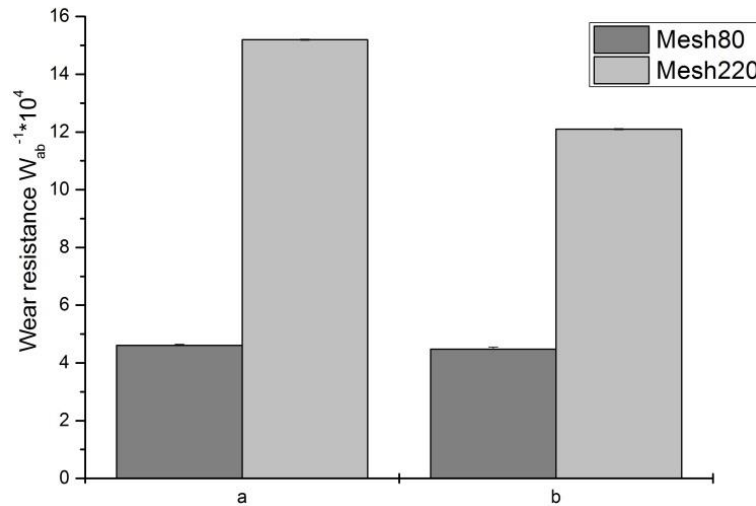

Figure 7:   *Wear resistance of MMC-2 (a) and MMC-R2 (b) in heat treated state.*

Against coarse abrasive the particle size of the TiC and RecyTiC is too small for an effective wear resistance which leads to a grooving out of the TiC/RecyTiC. In case of the fine abrasive the bigger particle size of TiC in sample MMC-2 (cf. *Tab.3*) provide a more effective protection of the matrix against abrasives. This protection is not given by the smaller RecyTiC in sample MMC-R2. However, it is also in evidence that some of the hard-particles break out by microcracking. This circumstance reduces the wear resistance twofold: the mass loss is increased and the broken carbides act as additional abrasive particles. The microcracking can be explained by the low fracture toughness of TiC, which is in a range of 1.5-3.6 MPa $m^{-1/2}$, depending on the chemical composition [11]. Microcracking can be detected in both investigated materials. Concluding, the wear resistance is mainly influenced by the particle size of TiC and RecyTiC.
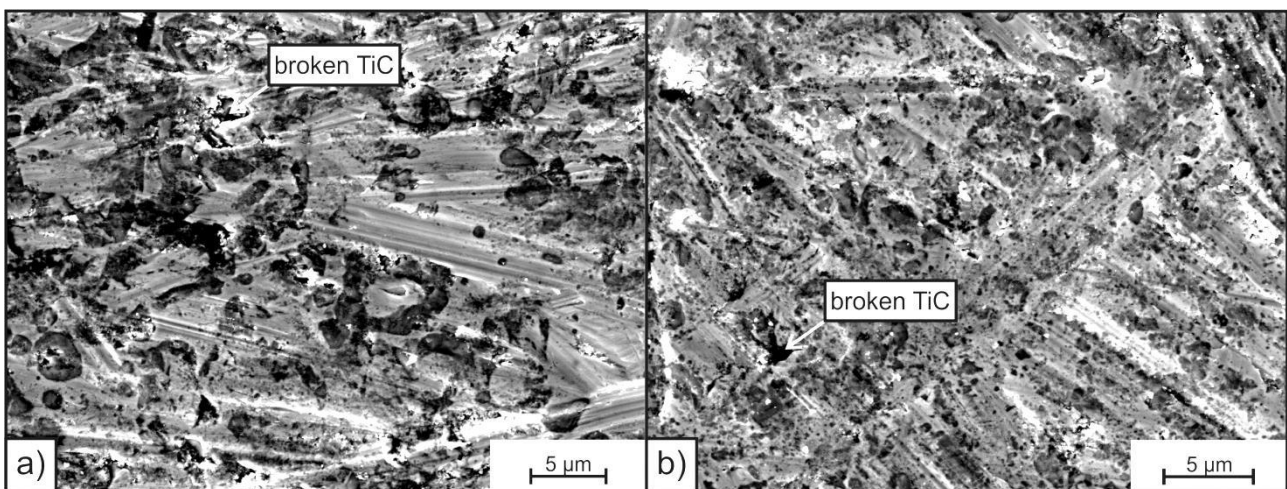
Figure 8:   Worn surface of the material MMC-2 (a)) and MMC-R2 (b)) in heat treated state.

Conclusion

In this study, the properties of recycled TiC, so called RecyTiC, from two TiC reinforced Fe-based materials (sample MMC-1 and MMC-2) was described. It was shown that the chemical composition of the recycled TiC changes due to diffusion of molybdenum into the TiC during processing of the MMC by HIP densification. The measured molybdenum content in the RecyTiC depends on the molybdenum content of the starting material.

The influence of the machining process on the raw material, forming the chips, and the associated size and morphology of the TiC was investigated. Thereby, machining leads to a small particle size of RecyTiC due to the brittle fracture of TiC leading to a fragmentation of the hard particles during the machining process. However, if the RecyTiC was extracted from worn parts (bulk material) bigger size of the gathered RecyTiC could be achieved. This behavior can be attributed to the absence of a machining process (no fragmentation of the TiC particles) and the densification of the starting material MMC-1 and MMC-2, thus TiC agglomerates are formed.

In addition, it was shown that the RecyTiC could be reused for the production of new MMC. Due to the change in morphology and especially in the size of the RecyTiC, microstructure and the associated tribological and mechanical properties of sample MMC-R2 differ from sample MMC-2.

Acknowledgment:

References

[1] H. Berns (Ed.), Hartlegierungen und –verbunde: Gefüge, Eigenschaften, Bearbeitung, Anwendung, Springer Verlag and Springer, Berlin, 1998

[2] K.-H. Zum Gahr, Microstructure and wear of materials, Tribology series, vol. 10, Elsevier, Amsterdam, 1987.

[3] W. Theisen, Herstellung verschleißbeständiger Metallmatrix-Verbunde auf Fe-Basis, Materialwissenschaft und Werkstofftechnik 36 (8) (2005) 360-364-

[4] H. Berns, Comparison of wear resistant MMC and white cast iron, Wear 254 (1-2) (2003), 47-54

[5] S. Weber, J.R. Li, W. Theisen, Microstructure and wear properties of novel sintered cold work steel and realted particle reinforced composite materials, Materials Science and Technology (2009).

[6] F. Frehn, Neue korrosions- und verschleißfeste, bearbeitbare Harstoffe: Ferro-Titanit für die chemische Technik, Werkstoffe Korros, 1979,30, 870-872

[7] Patent DE 10 2011 000 955 A9: Verfahren zur Rückgewinnung von Hartstoffpartikeln.

[8] Deutsche Edelstahlwerke GmbH: Ferro-Titanit®: Pulvermetallurgische Hartstoffe, hrsg. von DEW, Krefeld

[9] M. Le Flem, A. Allemand, S. Urovy, et al. Microstructure and thermal conductivity of Mo-TiC cermets processed by hot isostactic pressing, Journal for Nuclear Materials

[10] H. Hill, S. Weber, S. Huth, P. Niederhofer, W. Theisen, The impact of processing on microstructure, single phase properties and wear resistance of MMCs, Wear 271, 2011, 1895-1902.

[11] C. Maerky, M. O. Guillou, J.L. Henshall, R.M. Hooper, Indentation hardness and fracture toughness in single crystal TiC0.96, Materials Science and Engineering A 209 (1996), 329-336.

Keynote 3

INDENTATION AND SCRATCH TESTING – EXPERIMENT AND SIMULATION

F. Pöhl[1], S, Schwarz[2], P. Junker[2], K. Hackl[2], W. Theisen[1]
[1]Lehrstuhl Werkstofftechnik, Ruhr-Universität Bochum, 44801 Bochum, Germany
poehl@wtech.rub.de

[2]Lehrstuhl Materialtheorie, Ruhr-Universität Bochum, 44801 Bochum, Germany

ABSTRACT

Most modern wear resistant materials feature a multiphase microstructure and the macroscopic wear behavior is controlled by the local mechanical properties of the single phases. Indentation testing and in particular nanoindentation allows for the local mechanical characterization of materials and their phases. This paper addresses the determination of important mechanical parameters such as hardness, Young's modulus and indentation energy parameters of single phases in multiphase wear resistant materials. Important influencing factors such as matrix influence on the indentation results of an embedded hard phase, the indentation-size-effect (ISE), the effect of crystallographic orientation, and the fracturing behavior of hard phases are addressed. In addition, the results of scratch tests on the cold work tool steel X210Cr12 and a WC-Co hard metal are presented in order to investigate aspects of the mechanical behavior under abrasion. The deformation behavior under indentation and scratch loading was analyzed by scanning electron microscopy (SEM) and atomic force microscopy (AFM). Besides the experiments supplementary numerical simulations of indentation and scratching testing with the use of the Finite-Element-Method (FEM) are presented.

KEYWORDS

Indentation, scratch testing, deformation behavior, FEM, hard phase

INTRODUCTION

Most abrasion resistant metallic materials are multiphase materials with hard phases embedded in a softer matrix. Due to the small size of the hard phases (e.g. carbides) and their relatively low fracture toughness the mechanical characterization is a complex task and standard characterization methods such as tensile test would fail. Nanoindentation is a suitable method for the local mechanical characterization and has been successfully used for the determination of mechanical parameters of wear resistant materials and their phases [1]. Important mechanical parameters that can directly be calculated from the indentation results are hardness, Young's modulus as well as elastic and plastic indentation energy. Though, several aspects such as matrix influence on the indentation results of an embedded hard phase, the indentation-size-effect (ISE), the effect of crystallographic orientation, or the fracturing behavior of hard phases need to be considered for an accurate measurement and interpretation of the results [2-4]. In this context test related numerical simulations of the indentation process can contribute to the understanding of these aspects and can be used for material development and optimization. Examples of such FEM simulations of nanoindentation are given in [5-8].

With respect to abrasion-resistant metallic materials the local mechanical properties as well as the local deformation behavior of multiphase materials are crucial information for the understanding of the abrasive wear behavior on micro and macro length scale. In addition to nanoindentation tests the abrasive wear behavior can experimentally analyzed by controlled single scratch tests. The tests and their evaluation allow for the quantification of the resistance to scratching and for the determination of the dominating micro-mechanisms of abrasion according to ZUM GAHR [9]. With focus on multiphase materials the influence of phase type, morphology, distribution, and size can be analyzed. In addition to the local mechanical characterization by means of nanoindentation as well as single scratch tests numerical simulations provide supplementary insights into the abrasive

wear behavior. In this context quantities such as phase type, morphology, distribution, and size can systematically be varied and their effect on scratch resistance and resulting stresses and strains can be analyzed. Approaches of numerical simulation of scratch testing can be found in [10-12]. Recent progress in the development of damage models is highly promising in numerically capturing crack initiation and propagation in multiphase materials under mechanical load [13, 14].

This paper addresses the mechanical behavior under indentation and scratch loading considering wear resistant multiphase materials. Firstly, results on important aspects of nanoindentation such as matrix influence on the indentation results of an embedded hard phase, the indentation-size-effect (ISE), the effect of crystallographic orientation, and the fracturing behavior of carbides are presented and discussed. Supplementary FEM simulations are shown in order to give insights into the complex deformation processes. In this context measured mechanical properties of hard phases (carbides) as reinforcement in wear resistant materials are presented.

Secondly, the abrasive wear behavior is studied by the results of scratch tests on multiphase materials. Scratch experiments were performed on the cold work tool steel X210Cr12 as well as a WC-Co hard metal and evaluated in order to reveal the influence of carbides on the scratch behavior and to quantify the dominating micro mechanisms. Results of FEM simulations are presented to give deeper insights into the mechanical behavior of multiphase materials. As an example the crack propagation behavior in a microstructure consisting of hard phases and ductile matrix was numerically investigated and qualitatively compared to the crack propagation in a WC-Co hard metal.

1. MATERIALS AND METHODS

The examined phases and materials including an overview of the conducted experiments are summarized in **Tab. 1**. The sample preparation for nanoindentation and microstructure analysis consisted of grounding with SiC paper followed by successive polishing with diamond suspension with average grain sizes of 6, 3, and 1 µm. Final polishing was performed with oxide polishing suspension with an average grain size of 0.25 µm.

Tab. 1: Summary of investigated materials including the conducted experiments

phase/material	nanoindentation	scratch test	SEM	AFM
VC	✓	-	-	-
TiC	✓	-	-	-
NbC	✓	-	✓	✓
X210Cr12 (M_7C_3)	✓	✓	✓	✓
X210Cr12 (matrix)	✓	✓	✓	✓
WC-Co (12 wt% Co)	-	✓	✓	-
Al_5Fe_2	✓	-	✓	-
X51CrMnN(0.64)20-18	✓	-	✓	-
X2CrNi18-9	✓	-	-	-

Nanoindentation tests were conducted with a CSM indenter (type NHT) equipped with a Berkovich diamond tip. The indentation parameters were an indentation depth of 400 nm with a loading/unloading rate of 50 mN/min as well as a dwell time of ten seconds at maximum load. The hardness and Young's modulus were calculated with the traditional Oliver and Pharr method [15]. In addition, the ratio of elastic to total indentation energy was determined. As apparent in **Fig. 1** the indentation energy is given by the area under the loading and unloading curve. The total indentation energy (W_{pl}) contains the two contributions; the plastic (W_{pl}) and elastic indentation energy (W_{el}). A scratch tester of the company CSM (type NST) was used for scratch tests with a spherical diamond indenter (radius r = 2 µm). A normal load of 20 mN and 60 mN with a scratch speed of 50 µm/min was applied in the case of the X210Cr12 and a progressive scratch with increasing normal load from 3 mN to 800 mN with a loading rate of 200 mN/min in the case of the WC-Co hard metal.
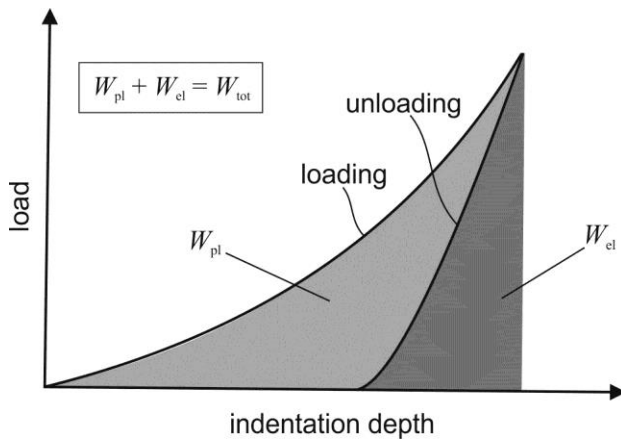
The box in the figure reads: $W_{pl} + W_{el} = W_{tot}$

Fig. 1: Schematic illustration of a typical load-displacement curve (P-h curve) with grey-marked elastic and plastic indentation energy

The topography and deformation of residual indentation imprints and scratch grooves were analyzed by atomic force microscopy (AFM) with an AFM in the contact mode (Bruker, type nanos). The scanning speed was varied between 10 and 40 µm/s. The software Image Plus 2.9 was used for data evaluation and three-dimensional visualization.

Scanning electron microscopy (Tescan, type Mira3) was used to analyze the microstructure, phase morphology, residual imprints, and scratch grooves. Addionally, in-situ indentation experiments were conducted with an SEM indentation module of the company Nanomechanics (type NanoFlip). FEM simulations were performed using the FEM software ABAQUS (version 6.11). Indentation testing was simulated with a conical rigid tip with an included half-apex angle θ of 70.3° indenting an elasto-plastic material or phase, respectively. A conical indenter with a half-apex angle of 70.3° leads to the same area-to-depth function as that of a Berkovich indenter. Numerous studies have shown that this approach sufficiently captures the response of a full-3D model [16]. Details concerning the FEM modeling are given in [2, 17].

Scratch testing was simulated with a 3d model and an irregular rigid abrasive grain scratching an elasto-plastic material including damage. Analogous models are described in [18]. The material model used for the simulations presented in **Figs.** 20 a) and b) can be found in [13, 14]. It is based on two scalar quantities: firstly, the HELMHOLTZ free energy which depends on the elastic strain and a damage parameter has to be specified and furthermore an approach for the dissipation which depends on the rates of microstructural change has to be formulated. Here, the rates of the damage parameter and the plastic strains enter the dissipation. For the well-known problem of mesh dependent finite element results the material model makes use of a rather simple but extremely effective strategy for regularization which can also be found in more detail in [13, 14].

2. RESULTS AND DISCUSSION

Local mechanical characterization of multiphase materials be means of nanoindentation

The macroscopic mechanical behavior of multiphase materials is controlled by the mechanical properties of the single phases and, thus, there is a great interest in measuring their local mechanical properties. Though, the mechanical characterization of single phases in the order of microns or nm is a complex task and standard characterization methods such as tensile test would fail. This is in particular the case when macroscopic brittle phases (e.g. carbides) are to be examined. A proven method for local mechanical characterization of single phases is Nanoindentation. **Fig. 2** shows the local indentation process with the indenter being in contact with the surface, with a maximum load of 50 mN applied to the indenter, and after unloading. Through the measurement of the load-displacement curve (P-h curve) and its analysis (Oliver and Pharr method) important mechanical parameters such as hardness and Young's modulus can directly be determined. Though, several aspects need to be considered for an accurate measurement and interpretation of the results. Firstly, this chapter presents general aspects and phenomenon that

often occur during nanoindentation of small phases and single grains of polycrystalline materials, respectively. Secondly, and with respect to wear resistant metallic materials (abrasion), results of nanoindentation experiments on carbides are shown.
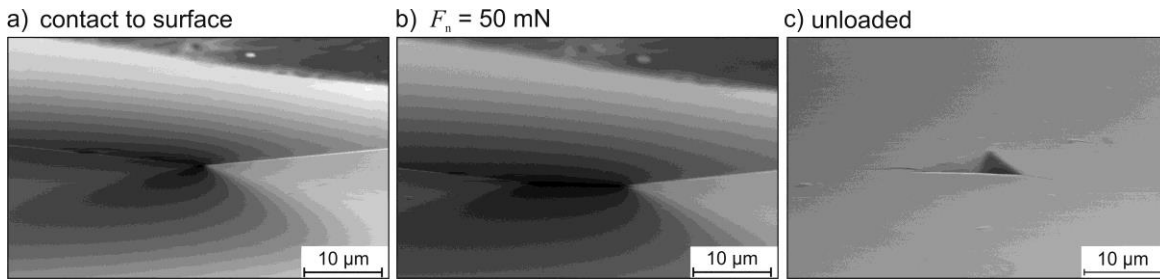

Fig. 2: Illustration of the in-situ indentation process of the phase Al_5Fe_2

Specific aspects of the indentation of single phases and grains of polycrystalline materials which are exemplarily addressed are:

- Influence of the matrix on the indentation results of an embedded hard phase
- Indentation-size-effect (ISE) in metallic and ceramic materials
- Influence of crystallographic orientation on the indentation results
- Fracturing behavior of brittle phases

Fig. 3 shows a residual imprint in NbC carbide embedded in a softer tool steel matrix. FEM simulations of this configuration give an insight into the deformation behavior of the compound and reveal that both carbide and surrounding matrix are plastically deformed. Since the matrix has lower strength the measurement represented by the P-h curve is significantly affected. In this example, the maximum force of the P-h- curve is underestimated by 28 %. As a result, hardness and Young's modulus of the hard phase (both are lower for the steel matrix) are also underestimated. In addition to hard phase size, morphology, and indentation depth the mechanical properties of hard phase and matrix are also critical influencing factors [2]. With the use of test-related FEM simulations the matrix influence can be characterized for given configurations and may reveal affected test data. The slope of the loading curve also gives indications of possible matrix influences since it can be significantly reduced by the matrix.
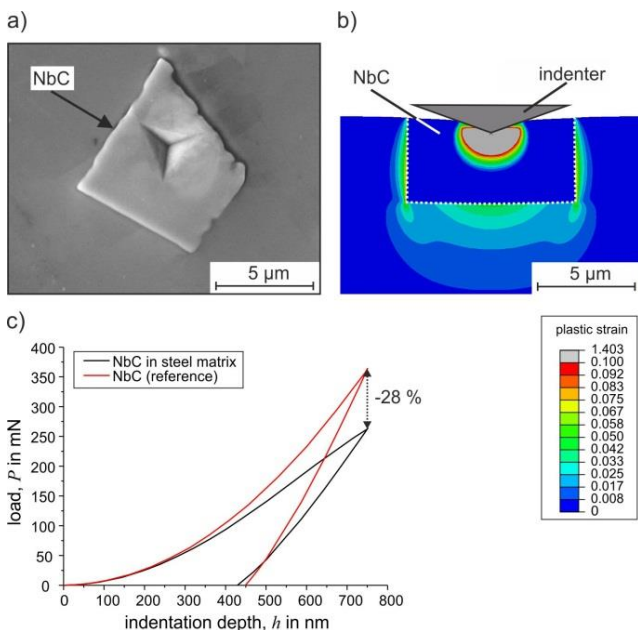
Fig. 3: a) Residual indentation imprint in an NbC embedded in a softer steel matrix b) numerically calculated plastic strain distribution in the NbC and the matrix caused by indentation c) matrix influence on the numerically calculated P-h curves

Another important phenomenon that can significantly affect the indentation results is the indentation-size-effect (ISE). In the case of self-similar indenters (e.g. Berkovich indenter) the ISE is expressed by an increase in measured hardness (strength) with decreasing indentation depth and in the case of spherical indenters by an increase in measured hardness with decreasing indenter diameter. The ISE is accounted for the local density of geometrical necessary dislocations (GNDs) induced in the material during indentation. According to the NIX and GAO model the density of GNDs is significantly increasing with decreasing indentation depth of a self-similar indenter (e.g. Berkovich indenter) or with decreasing diameter of a spherical indenter [19]. In addition to the density of the statistical stored dislocations (SSDs) the distinct increase in the density of the GNDs leads to an increase in strength and, thus, an increase in measured hardness. **Fig. 4** a) illustrates the significant increase in hardness with decreasing indentation depth of the highly affected austenitic steel X2CrNi18-9 measured with a Berkovich indenter. FEM results given in Fig. 4 b) proof that the increase in hardness can be explained by an increase in strength. With graded mechanical properties the experimental P-h curve in **Fig. 4** c) can be reproduced in good agreement. The cause of the local higher strength depending on indentation depth is found in the increase in GND density according to NIX and GAO.
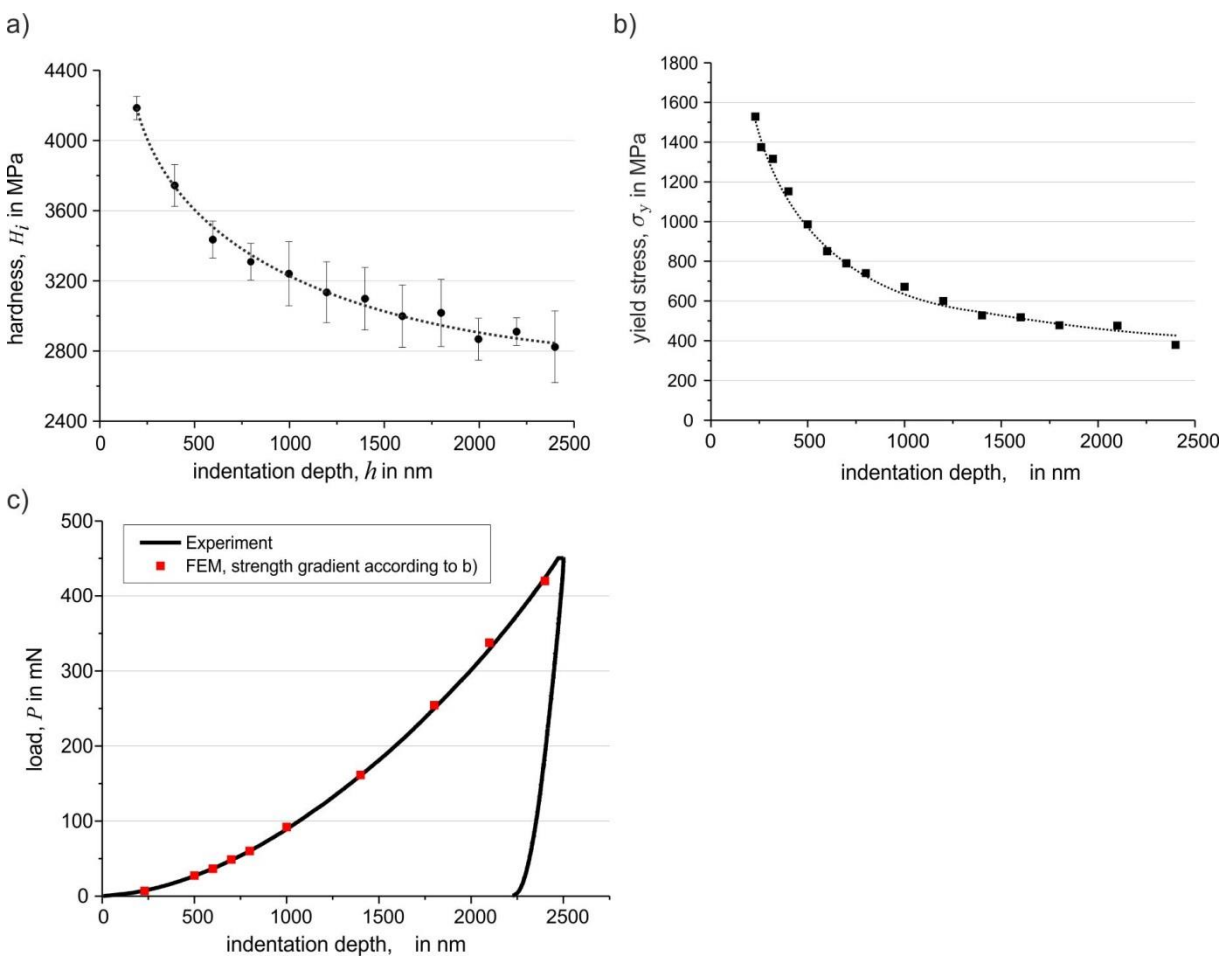
Fig. 4: a) Indentation size effect for the austenitic steel X2CrNi18-9 measured with a Berkovich indenter b) determined depth-dependent flow stress of X2CrNi18-9 c) comparison between the experimental P-h curve of X2CrNi18-9 and the numerically calculated loading curve with the depth-dependent flow stress given in b)

Not only metals, but also ceramic materials can show an ISE [20-23]. **Fig. 5** reveals that monocarbides such as TiC can exhibit an ISE. Compared to e.g. austenitic steels the ISE is less pronounced, even though it is distinctly visible at shallow indentation depths of the Berkovich indenter. Since it is caused by GNDs the results indicate that dislocation movement is a dominant deformation mechanism during indentation of monocarbides. SHINDE et al. and BREVAL also revealed with transmission electron microscopy (TEM) severe dislocation slip caused by

indentation in (TiW)C and TiC carbide at ambient temperature, respectively [24, 25]. In conclusion, caution should be exercised by comparing the hardness of different materials measured at different indentation depths and with different indenter geometries. This applies to metallic materials as well as to hard phases and ceramics such as carbides.
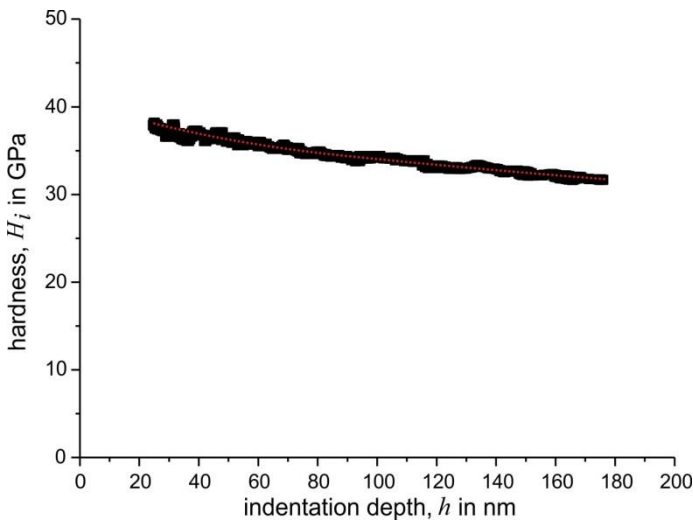
Fig. 5: Indentation-size-effect (ISE) for TiC (Berkovich indenter)

Since crystalline materials are mechanically anisotropic locally derived properties such as hardness are depend on the crystal orientation that is being indented. An example of the anisotropic mechanical behavior is given in **Fig. 6**. The figure shows the grain orientation image of an austenitic stainless steel derived by electron back scatter diffraction (EBSD) technique. A matrix with 256 single indents was established in order to quantify the hardness of the individual grains. From **Fig. 6** it is evident that the hardness is higher for green near (101)-oriented grains in comparison to the blue near (111)-oriented grains. Due to the imposed stress field and the orientation-dependent activation of dislocation gliding plastic deformation is more easily achieved in the (111)-oriented grains. Thus, plastic deformation is facilitated leading to lower hardness values. Mechanically anisotropic behavior is an important influencing factor on the indentation results not only for polycrystalline metals, it is also important for e.g. carbides. HANNINK et al. found significant hardness anisotropy in cubic carbides (TiC, VC, and NbC) which are dependent on the active slip system in the crystal [26].
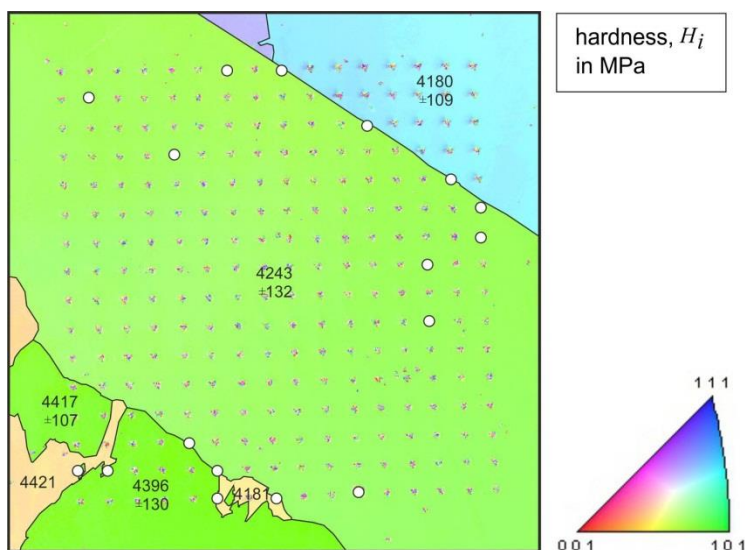
Fig. 6: Crystallographic anisotropic mechanical behavior of X51CrMnN(0.64)20-18 revealed by electron back scatter diffraction (EBSD) and nanoindentation. The average hardness is labelled in the single grains.

The last aspect being shortly addressed is the deformation and fracturing behavior of macroscopic brittle phases under indentation load. The macroscopic behavior of hard phases under ambient temperature and uniaxial loading or bending is usually brittle with no plastic deformation. In contrast, however, the deformation behavior under indentation load especially in small scale testing is relatively ductile. The ductile behavior finds expression in indentation imprints with little or no fracture in the nm regime as apparent in **Fig. 7** a). This is due to the highly hydrostatic stress conditions induced by the indenter. The high hydrostatic component of the stress tensor can mainly inhibit brittle fracture at low loads and leads to the activation of dislocation glide. Though, the limited dislocation movement and interaction between slip bands in hard phases such as carbides in combination with higher indentation loads can result in the formation of cracks [24]. These cracks can be used to estimate the fracture toughness of the phases with empirical equations [4]. **Fig. 7** shows indentation imprints in NbC and the very brittle intermetallic phase Al_5Fe_2. While for the NbC no crack formation is observed the imprint in Al_5Fe_2 has large cracks at the corners. **Fig. 8** illustrates the formed cracks in Al_5Fe_2 under maximum applied load of 50 mN.

a)   b)
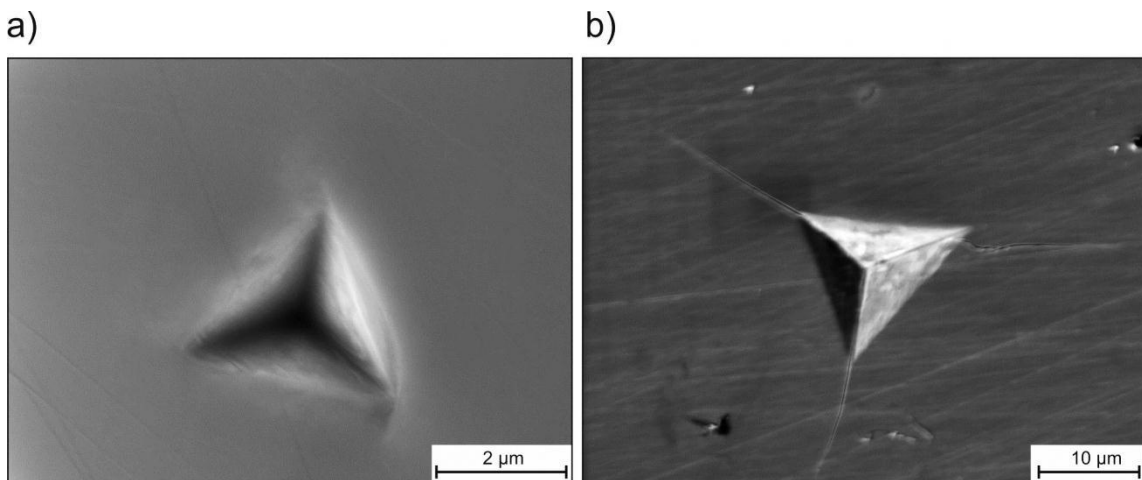
Fig. 7: a) SEM image of an indentation imprint in NbC b) SEM image of an indentation imprint in AL_5Fe_2 with formed cracks at the corners
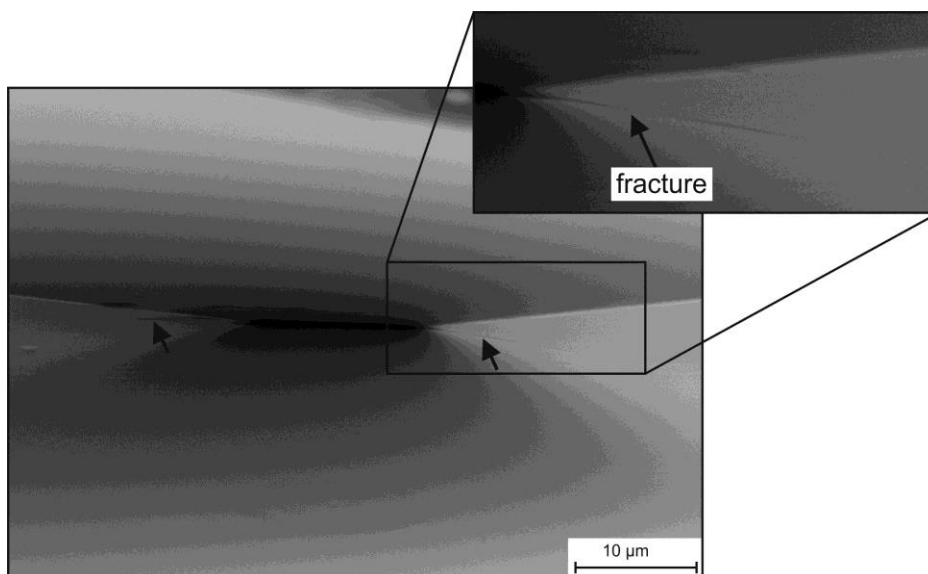
Fig. 8: SEM image of in-situ indentation and crack propagation in Al_5Fe_2

As can be seen in **Fig. 9** higher loads (h_{max} = 750 nm) also lead to crack formation in NbC. The SEM image in a) illustrates the inhomogeneous deformation by deformation bands and crack formation. **Fig. 9** b) shows a 3d image of the crack at the corner of the imprint. Among the analysis of deformation behavior and estimation of fracture toughness the induced cracks can significantly

influence the P-h curve and, thus, measured hardness and Young's modulus by the appearance of pop-in events. Comparison of the two P-h curves in **Fig. 10** reveals that the pop-in event significantly influences the progression of the curve. The forces are shifted to lower forces leading to lower hardness, Young's modulus, and W_{el}/W_{tot} values.
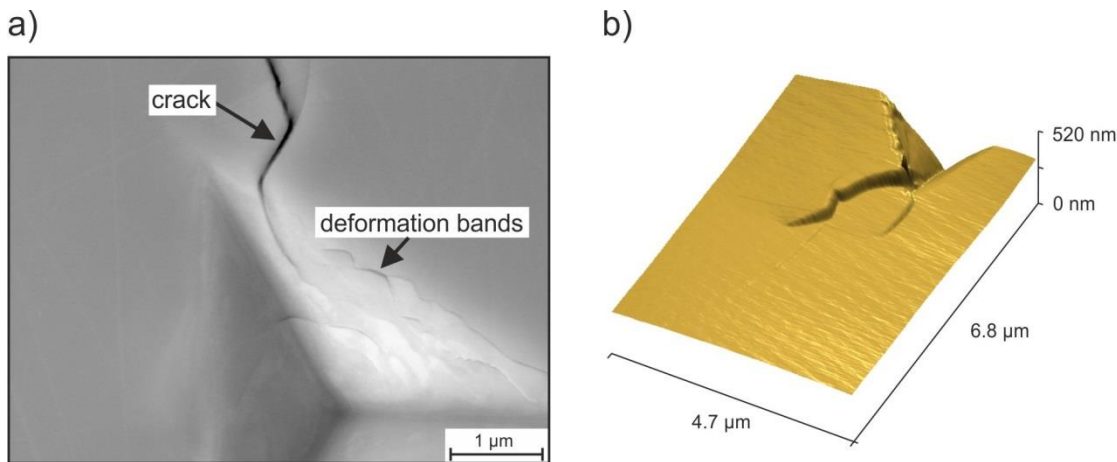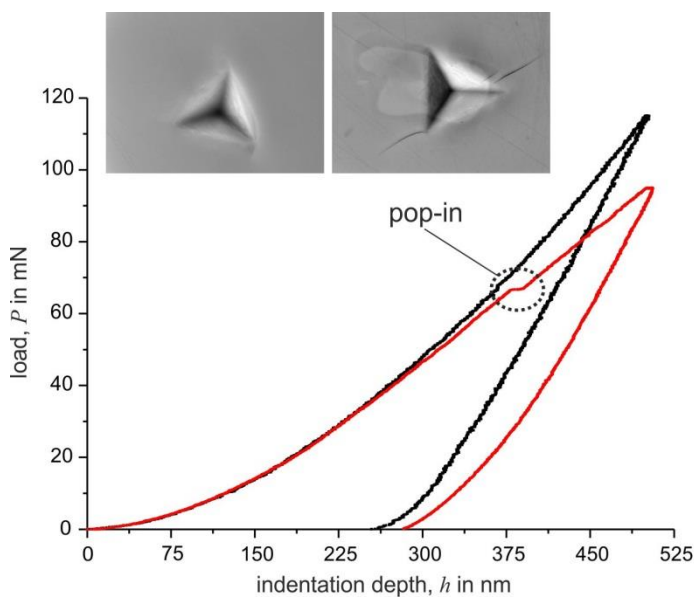

Fig. 9: a) SEM image of indentation imprint in NbC (h_{max} = 750 nm) showing deformation bands and a formed crack b) 3d topography image of a formed crack at the edge of the imprint in NbC

	H_i in GPa	HV	E in GPa	W_{el}/W_{tot} in %
NbC	33.3	3087	357	56
NbC (with pop-in)	23.4	2169	321	43

Fig. 10: Measured P-h curves and parameters for NbC showing the effect of crack formation which finds expression in a pop-in event

With respect to abrasion-resistant metallic materials the mechanical properties as well as the local deformation behavior of hard phases and martensitic steel matrix are considered more closely. Wear resistant steels and in particular tool steels often feature a microstructure consisting of hard phases embedded in martensitic matrix. Carbides such as VC, TiC, NbC or M_7C_3 are frequently used in a high amount as reinforcement particles in abrasion-resistant metallic materials. Due to their high hardness they can effectively act as barriers to attacking abrasive particles. **Tab. 2** summarizes the mechanical parameters of typical hard phases (carbides) and the martensitic steel matrix of the cold work tool steel X210Cr12. Due to the dominant covalent bond the monocarbides VC, TiC, and NbC show the highest hardness with values between 2763 HV and 2964 HV (indentation depth of 400 nm). In comparison the M_7C_3 carbides have a distinct lower hardness of

1773 HV at equal indentation depth. The lowest hardness is observed for the martensitic steel matrix (784 HV). The determined W_{el}/W_{tot} ratios of the phases show the same ranking compared to the hardness with monocarbides having the highest, M_7C_3 a slightly lower, and martensitic matrix the lowest ratio. This also holds true for the ranking of the Young's modulus. **Fig. 11** illustrates typical indentation imprints in the martensitic matrix and M_7C_3 carbide.
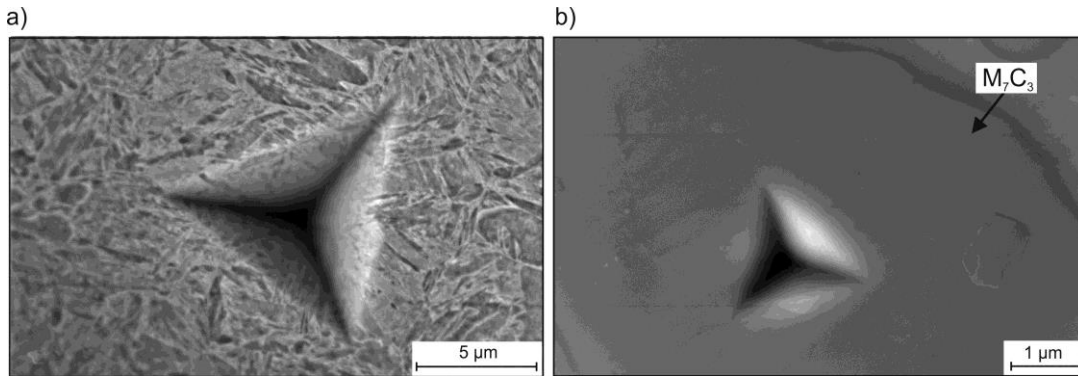
Fig. 11: a) SEM image of an imprint in the martensitic matrix (etched) b) SEM image of an imprint in an M_7C_3 carbide

The measured parameters together with the fracture behavior as exemplarily showed before give insight into the deformation behavior of the single phases. On the one hand this also improves the understanding of the mechanical behavior of multiphase materials and on the other hand the knowledge can be used for the development and optimization of multiphase microstructures for given applications. With this regard numerical simulations are useful tools. An example is given in **Fig. 12**. It shows the results of FEM simulations revealing the influence of volume fraction of spherical monocarbides with 80 HRC embedded in a matrix with 69 HRC on the compound macro Rockwell hardness.

Tab. 3: Mechanical properties of typically used carbides in tool steels and martensitic steel matrix

Phase	Indentation hardness H_i in GPa	Converted Vickers hardness	Young's modulus in GPa	W_{el}/W_{tot} ratio in %
VC [23]	30.7 ± 2.0	2845 ± 182	423 ± 20	50 ± 3
TiC [23]	29.7 ± 2.5	2763 ± 227	392 ± 26	57 ± 5
NbC [23]	32.0 ± 3.8	2964 ± 352	431 ± 36	54 ± 4
M_7C_3	18.9 ± 3.6	1773 ± 332	268 ± 21	44 ± 6
Martensite (q) (X210Cr12)	8.2 ± 0.2	784 ± 14	193 ± 10	30 ± 1
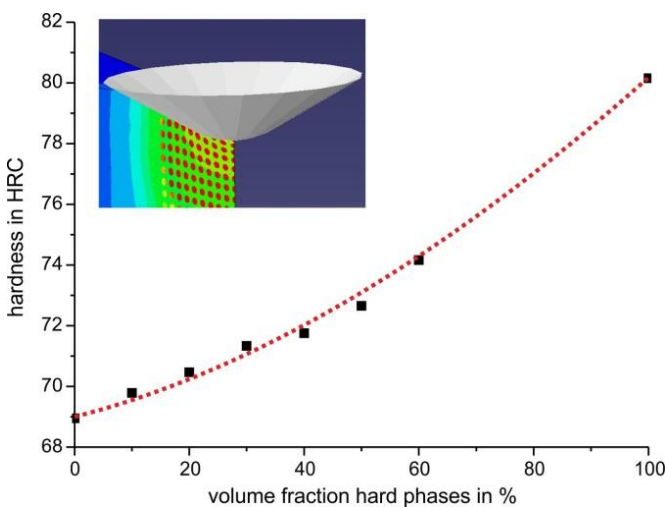
Fig. 12: Numerically calculated relationship between Rockwell hardness and volume fraction of spherical hard phases with hardness 80 HRC embedded in a matrix with 69 HRC

Scratch behavior of multiphase materials

The deformation behavior under abrasion with focus on the acting micro-mechanisms can be characterized with scratch tests under controlled laboratory conditions. Most modern abrasion resistant steels are multiphase materials consisting of higher hard phase amounts embedded in a softer matrix. **Fig. 13** shows the microstructure of the wear resistant cold work tool steel X210Cr12. It consists of chromium-rich M_7C_3 carbides embedded in a martensitic steel matrix. The macroscopic abrasive wear behavior is controlled by the local mechanical properties of the single phases.
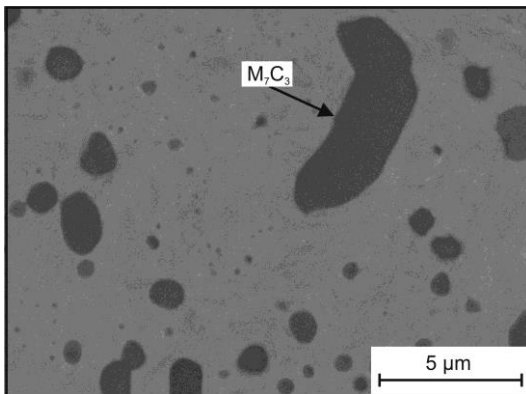
Fig. 13: Microstructure of the cold work tool steel X210Cr12 consisting of martensitic matrix and embedded M_7C_3 carbides

The mechanical properties measured by nanoindentation are given in **Tab. 3**. The high hardness of the carbides strongly improves the abrasive wear resistance. The carbides effectively act as a barrier to attacking abrasive particles. Though, the wear resistance is dependent on morphology, size, and distribution of the carbides and is also dependent on abradant hardness, size, and morphology [27]. The hard carbides are embedded in a martensitic steel matrix with lower hardness which ensures an adequate fracture toughness of the compound system.

Fig. 14 illustrates the deformation behavior of the multiphase material under scratch testing. The constant normal load of the indenter leads to the penetration and scratching of the matrix. The matrix is either flowing to the edges of the scratch (microploughing) or is removed by microcutting. Due to the relatively high toughness of the matrix no microcracking is observed. AFM measurements reveal that microploughing and in particular microcutting are the dominating micro mechanisms (see **Fig. 15**). The f_{ab}-parameter was calculated for four different positions along the scratch in the matrix and calculated to 0.81 ± 0.04.
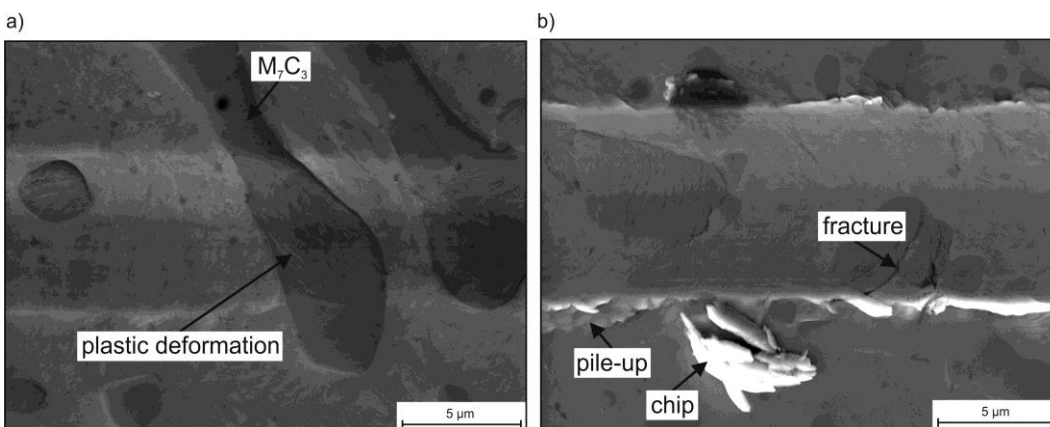
Fig. 14: a) SEM image of a scratch ($F_n = 20$ mN) in X210Cr12 with microploughing and plastic deformation of M_7C_3 b) SEM image of a scratch ($F_n = 60$ mN) in X210Cr12 with microploughing, microcutting, and fractured M_7C_3
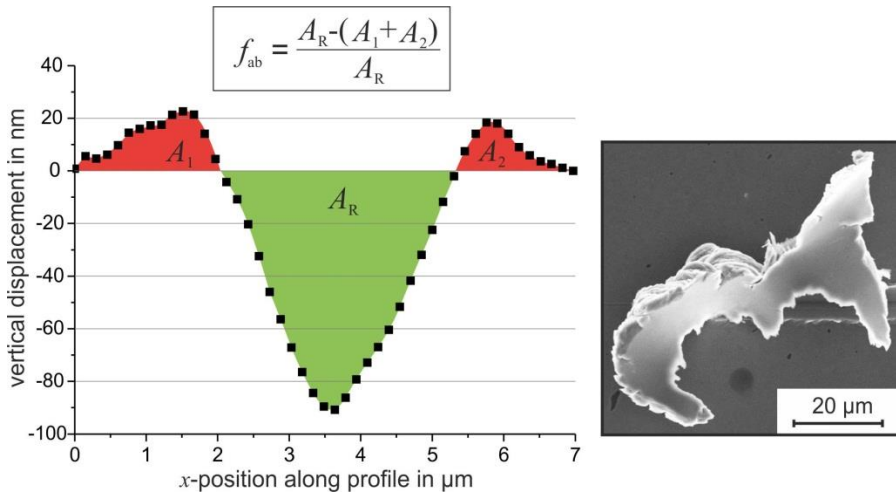
Fig. 15: a) Surface height profile of the scratched martensitic matrix (F_n = 20 mN) and marked areas for the calculation of the f_{ab}-parameter b) Large formed chip by scratching the martensitic matrix

Obtained from **Figs. 16** a) and c) as the indenter enters into contact with large M_7C_3 the penetration depth significantly decreases. At the same time **Figs. 16** b) and d) reveal that the scratch width is also reduced which leads to an overall reduction in material loss and, thus, to an increase in wear resistance. This holds true for carbide sizes larger than the scratch width.
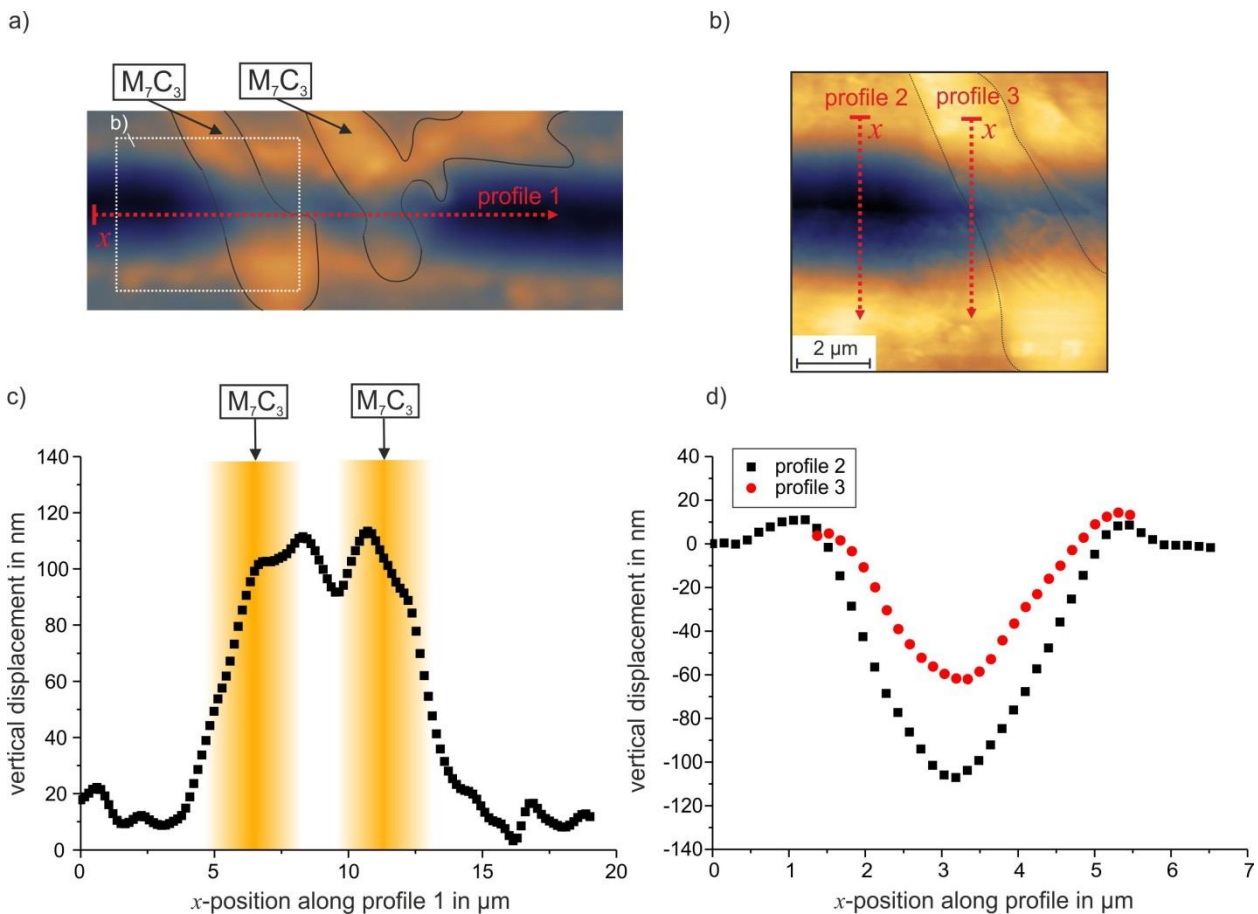
Fig. 16: AFM images and surface profiles of a scratch (F_n = 20 mN) in X210Cr12 (the scratch direction is always from left to right) a) AFM topography image of the scratch b) detail of a) showing the scratch at the transition between matrix and M_7C_3 carbide c) Surface height profile along profile 1 showing the reduction in scratch depth caused M_7C_3 d) Surface height profile along profile 2 and 3 showing the reduction of scratch depth and width caused by M_7C_3

Fig. 17 illustrates the scratch behavior in the case of carbides smaller than the scratch width. It can be seen that the carbide size is too small to be effective. The carbides are pushed into the matrix, ploughed to the sides or chipped out. The local deformation behavior of the carbides is plastic deformation and isolated fracturing (see **Fig. 14**).
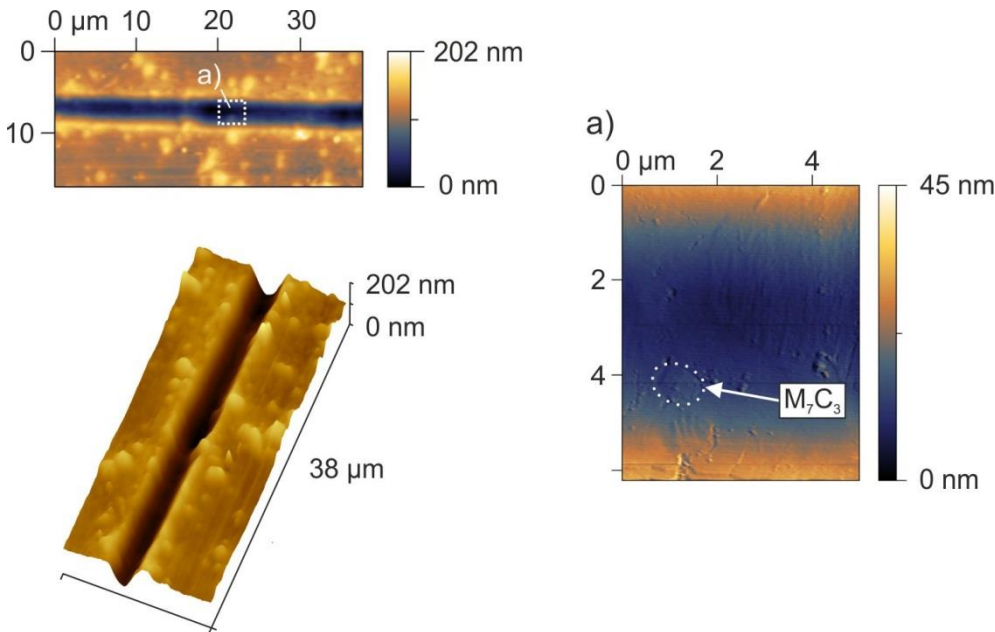
Fig. 17: AFM topography images of a scratch in X210Cr (F_n = 20 mN) with M_7C_3 carbides being smaller than the scratch width

The influence of carbides with different sizes can be analyzed with FEN simulations. As apparent in **Fig. 18** a) small carbides (smaller than the scratch width) are not effective and do not highly increase the wear resistance. They are pushed away or chipped out by the abrasive particle. In contrast, as can be seen in **Fig.18** b) single carbides larger than the scratch width can effectively hinder the abrasive particle from scratching the material. The hard phase cannot be pushed away or chipped out. For a constant load scratch depth and width are both reduced. Such numerical investigations can be established to analyze the influence of hard phase morphology, distribution, or amount on the scratch behavior and, thus, on the abrasive wear behavior. With the use of material parameter determination of hard phases and matrices by nanoindentation different hard phase types and matrices can also be considered. This allows the systematic variation of hard phase type, morphology, distribution, and matrix in order to assist the developing process of materials and microstructures with superior abrasive wear behavior.
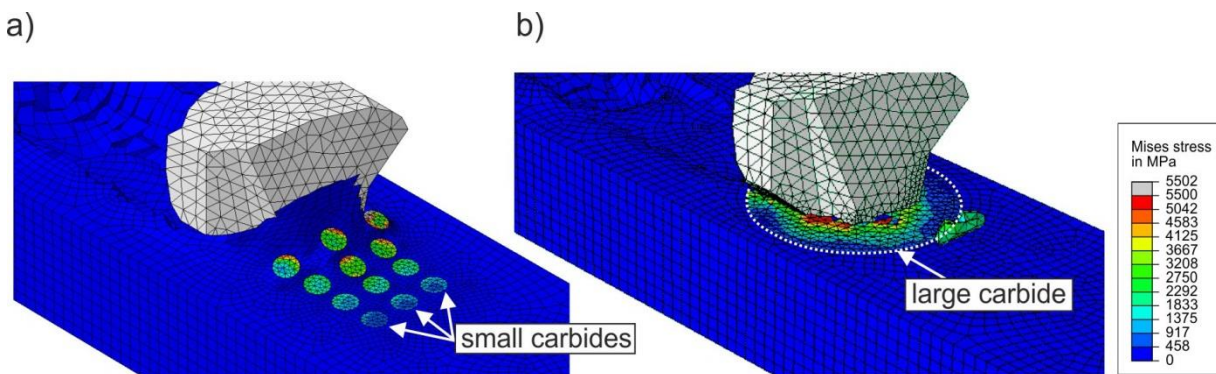
Fig. 18: FEM simulations showing a) the influence of small carbides on the scratch behavior with the abrasive grain being larger than the carbides and b) the influence of carbides being larger than the abrasive grain

Fig. 19 shows the microstructure of a Co-based hard metal with WC. Typical applications are cutting tools used for metal cutting application. In order to achieve a high wear resistance the material consists of a large amount of hard WC. This leads to a very high hardness and compared to tool steels relatively low fracture toughness of the compound. Due to the lower fracture toughness the fracturing and crack propagation behavior is of great relevance. Within the fracture process the Co binder phase plays an important role and has a dominant contribution to the fracture resistance [26].
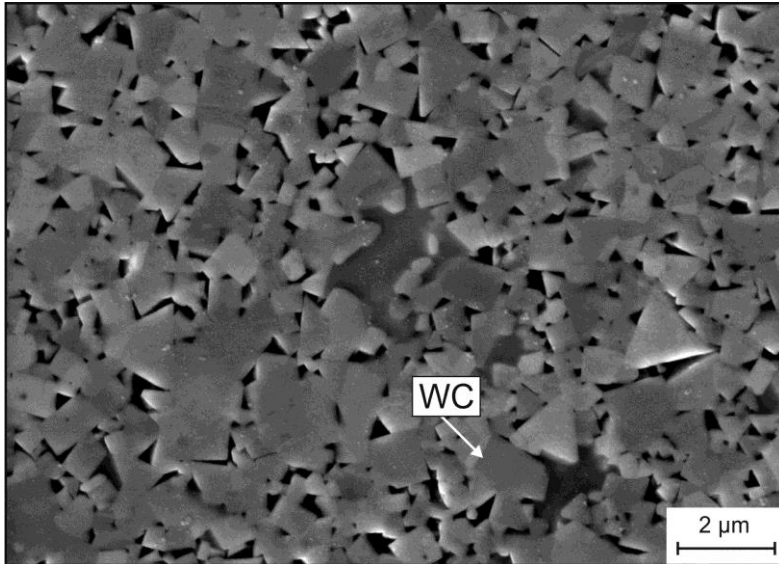
Fig. 19: SEM image of the microstructure of WC-Co hard metal

An induced crack (by Vickers indentation, HV10) is illustrated in **Fig. 20**. The crack propagates mainly along the Co-matrix very closed to the WC-Co interface with isolated WC cleavage. The dominant Co-matrix influence on the fracture behavior indicates that the plastic deformation of the Co-matrix contributes the major portion of the dissipative work during fracture of the compound [26]. Numerical simulations can qualitatively capture the complex fracturing behavior of multiphase materials with carbide phase. **Figs. 20** b) and c) show the numerical simulation of crack propagation in a multiphase material consisting of ductile matrix and embedded blocky hard phases. Analogous to the experiment the effect of secondary hard phase becomes visible. The crack propagates mainly along the ductile matrix. Though, the propagation path is influenced by the hard phases and under unfavorable geometric aspects the hard phase also fractures. From **Fig. 20** it can also be seen that a considerable amount of plastic deformation is occurring in the matrix. Numerical simulations can be established in order to reveal the influence of hard phase morphology, size, or amount on fracture behavior and crack propagation. Furthermore, it can be used for alloy development and microstructure design. The simulations also help to investigate and to better understand the deformation behavior under scratch testing and abrasion load, respectively. As can be seen in **Fig. 21** the deformation during scratching (spherical indenter) changes from elastic to elastic-plastic and elastic-plastic behavior with fracture depending on the applied load. The details in **Figs. 21** a) and b) show fractured particles next to the edges of the scratch. The particles consist of mostly undamaged and partly fractured WC and heavily deformed Co-matrix. Massive cracking is not observed.
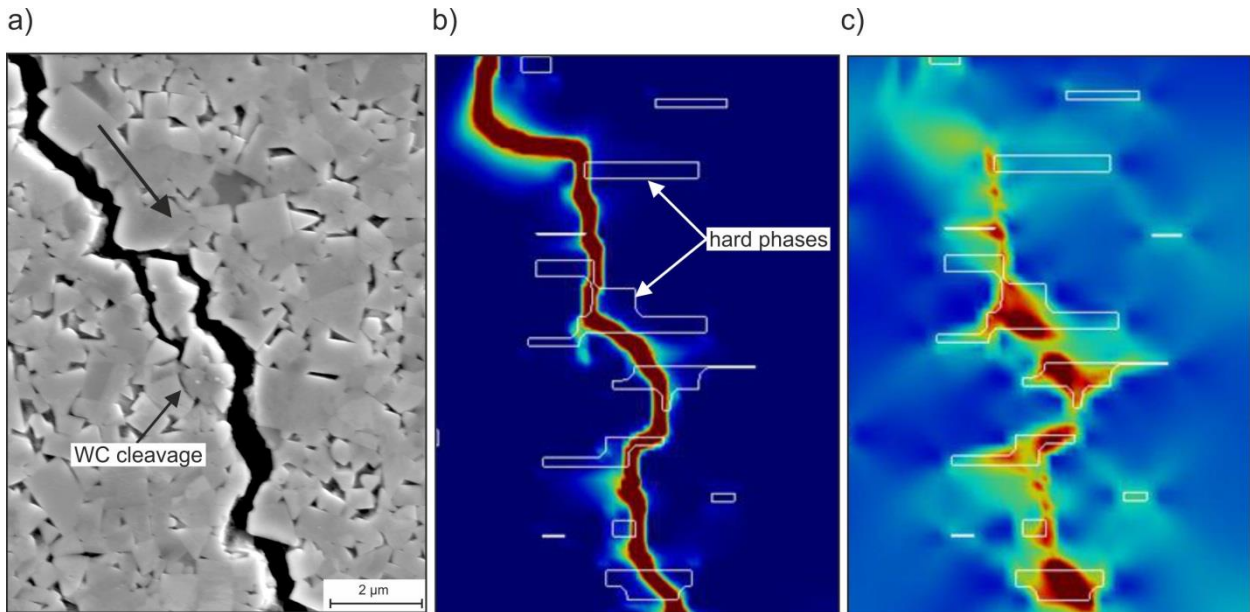
Fig. 20: a) SEM image of formed crack in WC-Co hard metal (the large arrow indicates the propagation direction) b) numerical simulation of crack propagation in multiphase material consisting of matrix and hard phases showing the damage (red color) c) numerical simulation of crack propagation showing the plastic deformation
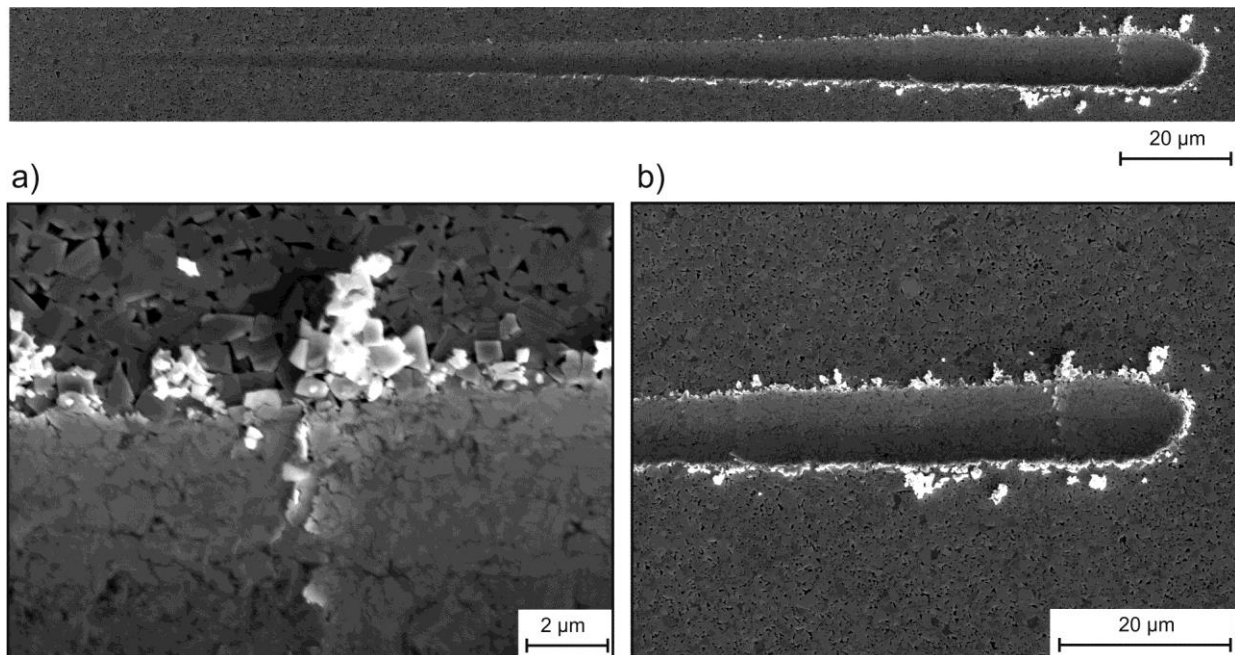

Fig. 21: SEM images of a progressive scratch showing different stages of deformation (F_n progressively increased from 3 mN to 800 mN)

3. CONCLUSIONS

The main conclusions to be drawn are:

- Experimental data and numerical simulations show that the matrix can significantly influence the indentation results of an embedded hard phase. With the use of test-related FEM simulations the matrix influence can be characterized for given configurations and may reveal affected test data.
- In the case of self-similar indenters (e.g. Berkovich indenter) the indentation-size-effect (ISE) is expressed by an increase in measured hardness (strength) with

decreasing indentation depth caused by the local increase in the density of geometrical necessary dislocations. The results show an ISE for the austenitic steel X2CrNi18-9 and also for TiC. Compared to e.g. austenitic steels the ISE is less pronounced, even though it is distinctly visible at shallow indentation depths of the Berkovich indenter.

- Mechanically anisotropic behavior caused by crystallographic grain orientation was revealed by nanoindentation in combination with electron back scatter diffraction (EBSD) technique for the austenitic steel X51CrMnN(0.64)20-18.
- Nanoindentation technique can also be used for the analysis of the fracture behavior of hard phases. The deformation behavior is expressed in discontinuous deformation bands and formed cracks. Cracking may cause pop-in events which leads to an underestimation of hardness and Young's modulus.
- In combination, single phase mechanical properties and numerical simulations are useful for revealing the influence of the microstructure on the macroscopic mechanical behavior. As an example it was shown the results of FEM simulations revealing the influence of volume fraction of spherical monocarbides with 80 HRC embedded in a matrix with 69 HRC on the compound macro Rockwell hardness.
- The scratch behavior of X210Cr12 shows that the matrix is either flowing to the edges of the scratch (microploughing) or is removed by microcutting. Due to the relatively high toughness of the matrix no microcracking is observed. AFM measurements reveal that microploughing and in particular microcutting are the dominating micro mechanisms. As the indenter enters into contact with large M_7C_3 the penetration depth significantly decreases (constant load). At the same time the scratch width is also reduced which leads to an overall reduction in material loss and, thus, to an increase in wear resistance. This holds true for carbide sizes larger than the scratch width.
- Numerical simulations of scratch testing allow the systematic variation of hard phase type, morphology, distribution, and matrix in order to assist the developing process of materials and microstructures with superior abrasive wear behavior.
- Numerical simulations were conducted in order to better understand the fracture behavior of WC-Co hard metal. Analogous to the experiment the effect of secondary hard phase becomes visible. The crack propagates mainly along the ductile matrix. Though, the propagation path is influenced by the hard phases and under unfavorable geometric aspects the hard phase also fractures. It could be seen that a considerable amount of plastic deformation is occurring in the matrix. Numerical simulations can be established in order to reveal the influence of hard phase morphology, size, or amount on fracture behavior and crack propagation. Furthermore, it can be used for alloy development and microstructure design. The simulations also help to investigate and to better understand the deformation behavior under scratch testing and abrasion load, respectively.

REFERENCES

[1] Hill, H, Weber, S, Huth, S, Niederhofer, P., Theisen, W, 2011, The impact of processing on microstructure, single-phase properties and wear resistance of MMCs, Wear, 271, 9-10, pp. 1895-1902

[2] Pöhl, F, Huth, S, Theisen, W, 2014, Finite element method-assisted acquisition of the matrix influence on the indentation results of an embedded hard phase, Materials Science and Engineering: A, 559, 2013, pp. 822-828

[3] Wang, Y, Raabe, D, Klüber, C, Roters, F, 2004, Orientation dependence of nanoindentation pile-up patterns and of nanoindentation microtextures in copper single crystals, Acta Materilia

[4] Feng, Y, Zhang, T, 2014, Determination of fracture toughness of brittle materials by indentation, Acta Mechanica Solida Sinica, 28, 3, pp. 221-234

[5] Dao, M, Chollacoop, N, van Fliet, KJ, Venkatesh, TA, Suresh, S, 2001, Computational modeling of the forward and reverse problems in instrumented sharp indentation, Acta Materialia, 49, pp. 3899-3918

[6] Sun, Y, Bell, T, Zheng, S, 1995, Finite element analysis of the critical ratio of coating thickness to indentation depth for coating property measurements by nanoindentation, Thin Solid Films, 258, pp. 198-204

[7] Taljat, B, Pharr, GM, 2004, Development of pile-up during spherical indentation of elastic-plastic solids, International Journal of Solids and Structures, 41, 14, pp. 3891-3904

[8] Rosenberger, MR, Forlerer, E, Schvezov, CE, 2007, Modeling the micro-indentation of metal matrix composites, Materials Science and Engineering A, 463, pp. 275-283

[9] Zum Gahr, KH, 1983, Furchungsverschleiß in: Reibung und Verschleiß Mechanismen – Prüftechnik – Werkstoffeigenschaften, Ed. Zum Gahr, KH, DGM, Oberursel, pp. 135-156

[10] Holmberg, K, Laukkanen, A, Ronkainen, H, Wallin, K, Varjus, S, Koskinen, J, 2006, Tribological contact analysis of a rigid ball sliding on a hard coated surface Part I: Modeling stresses and strains, Surface & Coatings Technology, 200, pp. 3793-3809

[11] Prasad, A, Dao, M, Suresh, S, 2009, Steady-state frictional sliding contact on surfaces of plastically graded materials, Acta Materialia, 57, pp. 511-524

[12] Wredenberg, F, Larsson, PL, 2010, On the stress distribution at scratching of thin film structures, Coatings Technology and Research, 7, 5, pp. 623-635

[13] Junker, P, Schwarz, S, Makowski, J, Hackl, K, 2015, A gradient-based regularization approach without field functions, Continuum Mechanics and Thermodynamics, under review.

[14] Schwarz, S, Junker, P, Hackl, K, 2015, A regularization approach for damage models based on a displacement gradient, Proc. Appl. Math. Mech. 15, 151 – 152

[15] Oliver, WC, Pharr, GM, 1992, An improved technique for determining hardness and elastic modulus using load and displacement sensing indentation experiments, Materials Research, 7, 6, pp. 1564-1583

[16] Cai, X, 1992, Finite-element method for simulation of elasto-plastic indentations by various indentors, Materials Science Letters, 11, pp. 1527-1531

[17] Pöhl, F, Huth, S, Theisen, W, 2014, Indentation of self-similar indenters: An FEM-assisted energy-based analysis, Journal of the Mechanics and Physics of Solids, 66, pp. 32-41

[18] Wielage, B, Lampke, T, Müller, L, Weber, D, 2008, Verifizierung numerischer Verfahren zur Modellierung abrasiver Verschleißprozesse durch die Berechnung von Scratchtests, Materialwissenschaft und Werkstofftechnik, 39, 12, pp. 963-966

[19] Nix, WD, Gao, H, 1998, Indentation size effects in crystalline materials: A law for strain gradient plasticity, Journal of the Mechanics and Physics of Solids, 46, 3, pp. 411-425

[20] Nino, A, Tanaka, A, Sugiyama, S, Taimatsu, H, 2010, Indentation size effect for the hardness of refractory carbides, Materials Transactions, 51, 9, pp. 1621-1626

[21] Gong, J, Wu, J, Guan, Z, 1999, Analysis of the indentation size effect on the apparent hardness for ceramics, Materials Letters, 38, pp. 197-201

[22] Peng, Z, Gong, J, Miao, H, 2004, On the description of indentation size effect in hardness testing for ceramics: Analysis of the nanoindentation data, Journal of the European Ceramic Society, 24, pp. 2193-2201

[23] Pöhl, F, Weddeling, A, Theisen, W, 2015, Mechanical characterization of hard phases by means of nanoindentation, Proceedings of 3rd Symposium on Nb-Mo alloying in steel and iron

[24] Shinde, SL, Jayaram, V, Sinclair, R, 1983, Microstructural characterization of deformation and precipitation in (W,Ti)C, in: Science of hard materials, Ed. Visvanadham, RK, Rowcliff, DJ, Gurland, J, Plenum Press, New York, pp. 137-154

[25] Breval, E, 1981, Microplasticity at room temperature of single-crystal titanium carbide with different stoichiometry, Journal of Materials Science, 16, pp. 2781-2788

[26] Hanning, HJ, Kohlstedt, DL, Murray, MJ, 1972, Slip system determination in cubic carbides by hardness anisotropy, Proceedings of the Royal Society London A, 326, pp. 409-420

[27] Ed. Berns, H, 1998, Hartlegierungen und Hartverbundwerkstoffe, Gefüge, Eigenschaften, Bearbeitung, Anwendung, Springer, Berlin Heidelberg

[28] Hong, J, Gurland, J, 1983, A study of the fracture process of WC-Co alloys, in: Science of hard materials, Ed. Visvanadham, RK, Rowcliff, DJ, Gurland, J, Plenum Press, New York, pp. 649-666

ALLOY DESIGN IN THE SYSTEM FE-C-B

M.Sc. Jonathan Lentz, Dr.-Ing. Arne Röttger, Prof. Dr.-Ing. W. Theisen

Lehrstuhl Werkstofftechnik, Ruhr-Universität Bochum, 44801 Bochum, Germany

Lentz@wtech.rub.de, phone: +49(0)234-32-25967, fax: + 49(0)234-32-14104

ABSTRACT

In this study, the Fe-C-B system is used as a basis for alloy development of tool steels. Thereby, boron is used as hard phase forming element. The effect of chromium on the phase stability, microstructure and hard phase properties of Fe-C-B-Cr alloys is investigated. In this manner, thermodynamic equilibrium calculations are performed and experimentally validated. Laboratory alloys were casted and investigated using scanning electron microscopy (SEM), energy dispersive spectroscopy (EDS) and electron backscatter diffraction (EBSD). Nanoindentation was performed to investigate the effect of Cr on the micromechanical properties of the particular hard phases (elastic modulus and indentation hardness). It is shown, that Cr stabilizes the orthorhombic, Cr-rich M_2B type boride with a hardness of 22.8 GPa. In addition Cr stabilizes the Cr-rich $M_{23}(C,B)_6$ carboboride, which possess a lower hardness (14 GPa). In a next step, the findings are implemented in an alloy development and alloying additions of chromium, silicon and manganese are used to specifically stabilize the M_2B type boride with high Cr content to adjust a high hardness of the M_2B phase. Subsequently, a scratch test is performed to investigate the governing wear mechanisms in the developed alloy.

KEYWORDS

Steel development, tool steel, boron, hard phase properties, nanoindentation, CALPHAD

INTRODUCTION

A cost effective material, developed to withstand high wear attack, is tool steel. This group of steel is used for highly stressed parts for example in the field of mining or metal processing. Nevertheless, the durability of tool steels is still limited due to wear. Thereby, the major wear mechanism is grooving wear by hard counter bodies (abrasion). Consequently, the continuous development of tool steels with enhanced wear resistance is of high macroeconomic interest.

A metallurgical approach to maintain a high resistance against abrasion is realized through a sufficient amount of hard phases (5~15 vol.-%) which are embedded inside a tough metallic matrix. To optimize wear resistance, volume content, morphology and distribution of the hard phases should be individually adapted to the tribological system and to the interaction with the abrasive objects. Besides, an important parameter influencing the performance for wear protection applications are the hard phases' micromechanical properties. In this context, a comparison of different types of hard phases namely carbides, nitrides and borides shows that borides generally are favorable in terms of hardness. Hence, it seems likely to utilize Boron (B) as hard phase forming element in tool steels [1,2]. In this approach carbides, which are commonly used as hard phases and require high amounts of expensive or short resources such as vanadium or tungsten, are substituted by borides. These borides are formed with cheaper and widely available elements like iron (Fe), manganese (Mn) or chromium (Cr). The element carbon (C) is then primarily used to maintain the hardenability of the iron matrix and is uncoupled from formation of hard phases. Concluding, the utilization of B is promising to enhance application properties and at the same time to reduce the cost.

In this study, the systematic alloy design based on the Fe-C-B system is presented. Thermodynamic equilibrium calculations are used to design laboratory alloys. In this manner, the alloying elements Cr, Si and Mn are used to systematically adjust the phase content and the chemical composition of particular phases. Furthermore, the mechanical properties of the hard

phases are optimized with an adapted chemical composition of the hard phases. The calculations are experimentally validated using laboratory alloys. The microstructures of these alloys are investigated using scanning electron microscopy (SEM), energy dispersive X-ray spectroscopy (EDS) and electron backscatter diffraction (EBSD). Furthermore, the hardness and elastic modulus of the particular phases is measured using the nanoindentation technique. Finally, a scratch test is performed to investigate the governing micromechanical effects, concerning the wear-protection by the embedded hard phases.

1. EXPERIMENTAL PROCEDURE

Thermodynamic equilibrium calculations based on the CALPHAD method were used to design the phase content and chemical composition of the particular phases present in the alloy using the software ThermoCalc version S. Thermodynamic data were taken from the database TCFe6.2. The phases, LIQUID, FCC_A1, BCC_A2, CEMENTITE, M2B_tetr, M23C6, and Cr2B_orth, were regarded in the calculation. Furthermore, a pressure of 10^3 mbar and an amount of quantity of 1 mol were taken into account.

Laboratory melts are manufactured to validate the equilibrium calculations and to investigate the microstructure and micromechanical properties of the alloys. In order to allow comparability of the thermodynamic equilibrium calculations and the laboratory melts, specimens were cut from the casting and heat-treated with regard to a hardening temperature of 900 or 1000 °C for 200 h in an inert gas furnace with argon atmosphere present and subsequently quenched in water.

Table 1: Chemical composition of the laboratory melts measured by optical emission spectrometry in mass% and hardening temperature T in °C

Alloy	T in °C	C	B	Cr	Si	Mn	Fe
0.6C-0.6B		0.71	0.76	0.01	0.11	0.02	Bal.
0.6C-1.8B		0.69	1.92	0.03	0.16	0.02	Bal.
0.6C-0.6B-2.5Cr	1000	0.58	0.66	2.25	0.11	0.01	Bal.
0.6C-0.6B-7.5Cr		0.59	0.57	6.75	0.14	0.02	Bal.
0.6C-0.6B-12.5Cr		0.59	0.57	11.86	0.16	0.02	Bal.
0Cr	900	0.75	1.98	0.04	2.27	3.81	Bal.
10Cr		0.65	1.97	10.00	2.41	3.77	Bal.

Prior to the microstructural examinations, the specimens were sectioned, ground on abrasive paper, and polished stepwise with 6 µm, 3 µm, and 1 µm diamond suspensions and etched with 3% alcoholic HNO_3. The microstructure of the specimens was investigated using the SEM Tescan MIRA3 in backscatter electron contrast (BSE) at a working distance of 7 mm and an acceleration voltage of 20 kV. The Cr content of the respective phases was measured using EDS system OXFORD X-Max 50 at a working distance of 15 mm and an electron-beam current of 5 nA. EBSD measurements were performed using the EBSD detector Nordlysnano by Oxford instruments.

Hardness and elastic modulus of the respective phases were measured using the in-situ indentation module NanoFlip (Nanomechanics, inc.), using a diamond, cube corner indenter and a load of 50 mN at a constant strain rate of 0.2%/s and dynamic indentation method. Hardness and elastic modulus were evaluated as an average value for an indentation depth between 600-850 nm applying the method of Oliver and Pharr. For the estimation of elastic modulus, the Poisson ratio of the M_2B was assumed to be a constant value of 0.25, for $M_3(C,B)$ and $M_{23}(C,B)_6$ phases a value of 0.36 was taken into account [3–6]. The indentation hardness was converted to Vickers hardness scale for reasons of comparability, knowing that the minimal indentation depth of 6 µm with regard to DIN EN ISO 14577 was not achieved [7]. Scratch testing was performed using the scratch module NST by CSM instruments, a conical diamond indenter with a tip radius of 2 µm and a constant load of 100 mN for a scratch length of 600 µm (speed 150 µm/min).

2. RESULTS & DISCUSSION

Fig. 1 a) is showing the quasi-binary phase diagram of the Fe-C-B system for a constant C content of 0.6 mass%, calculated with ThermoCalc, whereby the C content of 0.6 mass% is regarded to maintain the martensitic hardenability of the iron matrix. The Fe-0.6C-B system shows borides/carboborides of Fe_2B, $Fe_3(C,B)$ and $Fe_{23}(C,B)_6$ type, which are present besides the α-Fe and γ-Fe iron phases. The hypoeutectic region is located at B contents smaller than 3.4 mass% B and characterized by the primary solidification of γ-Fe cells. Higher B contents are stabilizing the primary solidification of the Fe_2B phase. The low melting phase of the system is $Fe_3(C,B)$. At temperatures between 800 and 600 °C the $Fe_3(C,B)$ phase becomes thermodynamically unstable and the $Fe_{23}(C,B)_6$ phase (τ-phase) is formed due to this miscibility gab. The B solubility of the $Fe_3(C,B)$ phase is decreasing with lower temperatures and thus the Fe_2B phase is stabilized through the release of B at temperatures smaller than 600 °C.
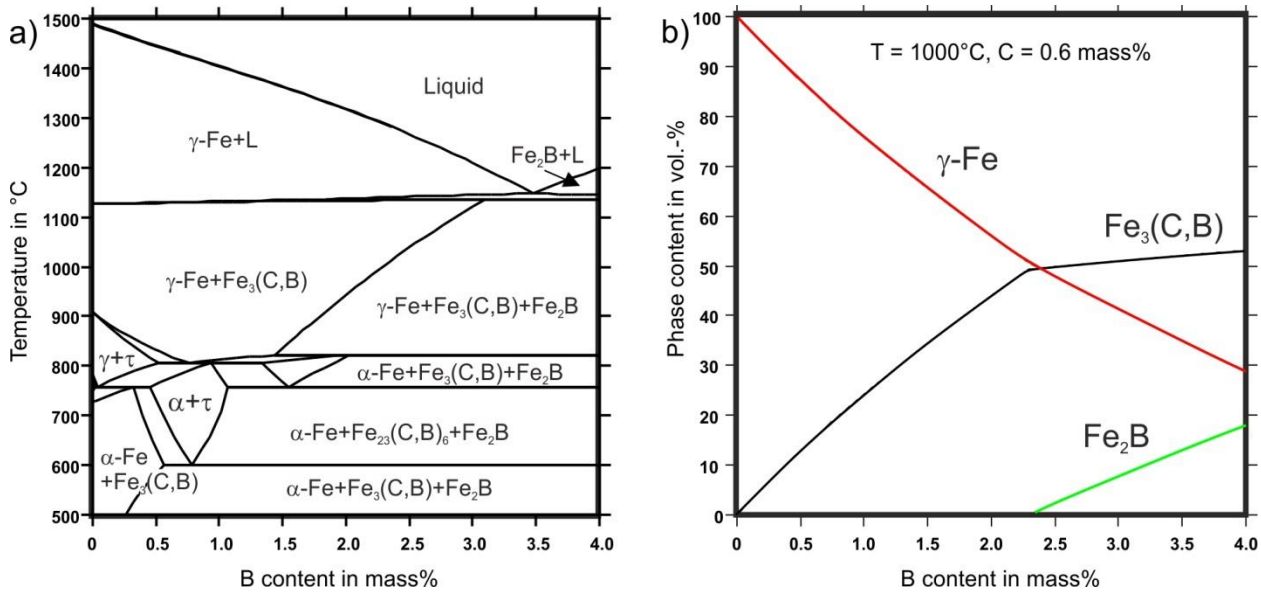
Fig. 1: a) Quasi-binary cross-section of the Fe-C-B system (constant C content of 0.6 mass%) b) Phase content in Fe-0.6C-B alloys at 1000 °C calculated with TC

The interdependence of the B content and the volume content of the particular phases that are present in Fe-0.6C-B alloy at a temperature of 1000 °C is depicted in Fig. 1 b). At low B contents, the volume content of the $Fe_3(C,B)$ phase is increasing almost linear with a slope of 22 vol.-% per mass% B until the Fe_2B phase is stabilized at a content of 2.3 mass% B. Furthermore, the volume content of the Fe_2B phase is increasing with 9 vol.-%, and the $Fe_3(C,B)$ phase with 2.5 vol.-% per mass% B. Following, B contents greater than 2.3 mass% are required to stabilize the Fe_2B phase in the Fe-C-B system, which is connected to a high volume content (> 50 vol.-%) of the $Fe_3(C,B)$ hard phase.

In Fig. 2 the microstructures of the 0.6C-0.6B (Fig. 2 a) and 0.6C-1.8B (Fig. 2b) are shown. A coarsened eutectic structure consisting of 14.8 vol.-% $Fe_3(C,B)$ phase in case of alloy 0.6C-0.6B and 40.5 vol.-% Fe_2B + $Fe_3(C,B)$ phases in case of alloy 0.6C-1.8B is present besides a martensitic iron matrix. In contrast to the thermodynamic calculations shown in Fig. 1, the Fe_2B phase is present at a B content below 2.3 mass%. This can be attributed to the technical non-equilibrium solidification process, whereby B is segregating in the remaining melt and the Fe_2B phase is stabilized [8].
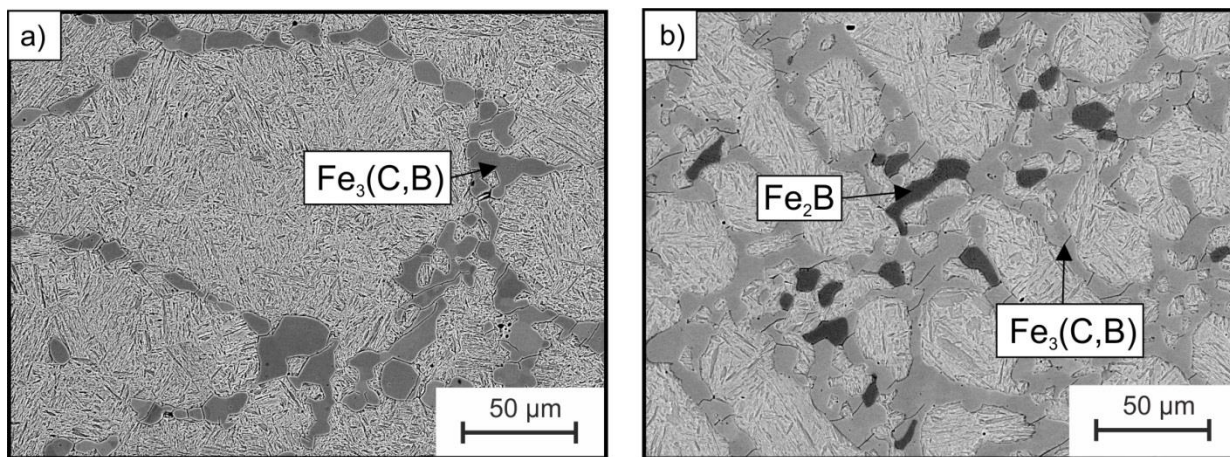
Fig. 2: SEM image of a) alloy 0.6C-0.6B and b) 0.6C-1.8B in BSE contrast

Against the background of alloy design, the most important parameters concerning the hard phases are mechanical properties like high hardness, elastic modulus and fracture toughness. In addition, a low C solubility of the hard phases is required following the alloying approach to use B as hard phase forming element and preserve C for matrix hardening. In this context, a low metal to metalloid ratio is beneficial to reduce the chemical-binding of expensive alloying elements. In addition, the Fe_2B phase has the highest hardness of the Fe-C-B system's hard phases (~1600 HV), shows only marginal C solubility and also a low metal to metalloid ration (M/(B+C)=2) [9,10]. In contrast, the $Fe_{23}(C,B)_6$ phase has a lower hardness (1100 HV), high metal to metalloid ratio (M/(C+B)=3.83) and a high solubility for C. The $Fe_3(C,B)$ phase shows high solubility for both C and B, whereby the chemical composition and the micromechanical properties are dependent on the temperature region of formation. I.e. eutectic $Fe_3(C,B)$ shows B contents up to 22 atom% and a hardness around 1300-1400 HV [11]. Concluding, the Fe_2B phase is beneficial in terms of micromechanical properties. Although, the Fe_2B phase is stabilized by the more pronounced B segregation occurring during technical solidification processes through, a stabilization of Fe_2B in the ternary Fe-C-B system requires high B contents, which is connected to hard phase contents greater than 45-50 vol.-%. Regarding the alloy development of steels, sufficient fracture toughness and forming capacity cannot be achieved with a volume content >15-20 vol.-%.

In this context, the element Cr can be used to further stabilize the orthorhombic M_2B type boride, which exceeds the mechanical properties of the hard phase M_7C_3 (~ 1400-1600 HV, $6.3 MPa\sqrt{m}$) [12–14]. The effect of Cr addition on the phase stability and composition of the particular phases at a temperature of 1000 °C is shown in Fig. 3, whereby the B and C content of alloy 0.6C-0.6B is taken into account. Fig. 3 a) is showing the influence of the overall Cr content on the phase quantity of the particular phases (in vol.-%) that are present in alloy 0.6C-0.6B-xCr. At a Cr content of 0 mass%, 16 vol.-% $M_3(C,B)$ phase is present. Furthermore, it becomes evident, that the $M_3(C,B)$ phase is vanishing in favor of 10 vol.-% of $M_{23}(C,B)_6$ and 5 vol.-% of M_2B phase at a Cr-content of ~1 mass%. Moreover, the M_2B phase is transforming from a tetragonal into an orthorhombic crystal structure above a Cr content of 4.5 mass%. At the same time, the volume content of the M_2B phase is slightly increasing from 5 vol.-% at 4.5 mass% Cr to 8 vol.-% at 10 mass% Cr.

Furthermore, the Cr content of the particular phases is increasing with the overall Cr content of the alloy, as shown in Fig 3. b). The Cr content of the $M_{23}(C,B)_6$ and iron matrix is showing a proportional dependence on the overall Cr content, whereby values of 35 atom% inside the $M_{23}(C,B)_6$ and 10 atom% Cr inside the iron phase are reached at 15 mass% overall Cr content. The Cr content of the tetragonal M_2B phase is increasing constantly from 3 up to 12.5 atom% at an overall Cr content of 4.5 mass%. A further increase of the Cr content above 4.5 mass% is stabilizing the orthorhombic M_2B structure with a Cr content of 20 to 42 atom% at 15 mass% overall Cr content. The $M_3(C,B)$ phase shows only marginal solubility for Cr.
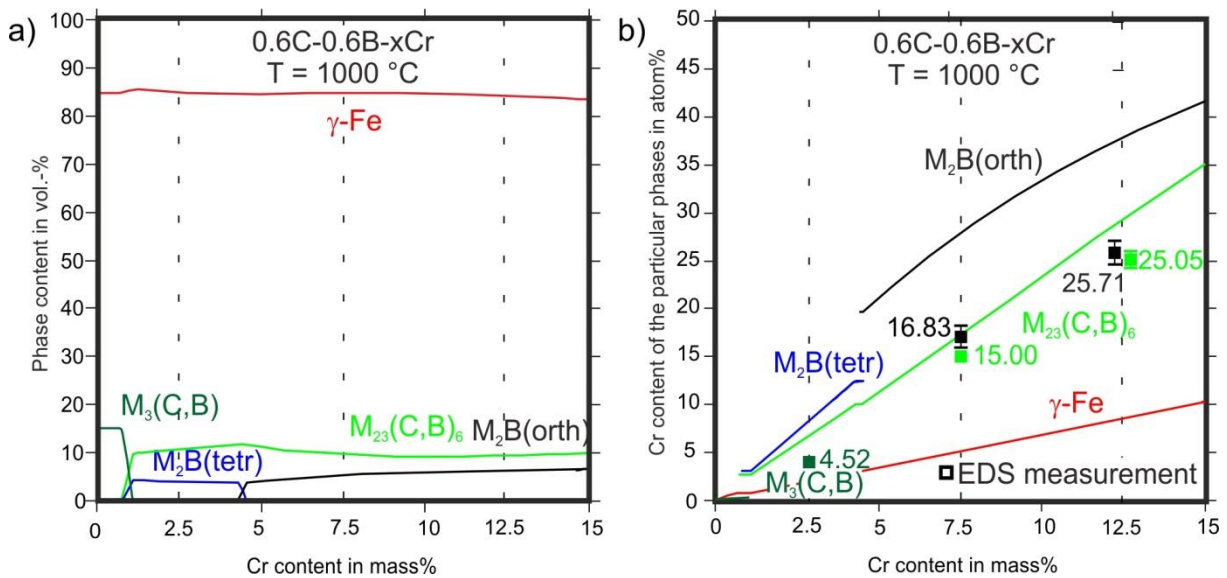
Fig. 3: Thermodynamic calculation of the influence of overall Cr content on a) volume fraction of the phases and b) Cr content of the particular phases for alloy 0.6C-0.6B-xCr at 1000 °C. Experimental EDS measurements at the particular phases are depicted through squares in b)
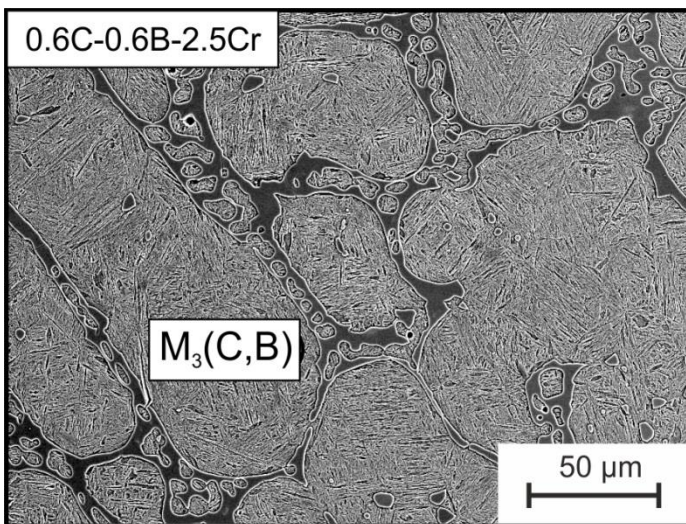

Fig. 4 SEM image of alloy 0.6C-0.6B-2.5Cr in BSE contrast

In contrast to the calculation, the microstructure of alloy 0.6C-0.6B-2.5Cr is showing the coarsened, single-phase eutectic network, which was identified as $M_3(C,B)$ by EBSD point measurement (Fig.4). This is in disagreement with the calculation (see Fig.3), which is indicating the stability of the tetragonal M_2B and $M_{23}(C,B)_6$ phase instead. Differences of calculation and microstructure may be attributed to inaccuracy of the thermodynamically database and also to differences of the technical condition of the alloy and the calculated thermodynamic equilibrium.

Nevertheless, the microstructures of alloy 0.6C-0.6B-7.5Cr (see Fig. 5 a) and 0.6C-0.6B-12.5Cr (Fig. 5 b) are in agreement with the calculations. The eutectic structure is consisting of orthorhombic M_2B and $M_{23}(C,B)_6$ phases. Furthermore, disperse distributed and small precipitates of 1-5 µm in diameter, which appear to be formed in solid state, are present in alloy 0.6C-0.6B-12.5Cr and 0.6C-0.6B-7.5Cr (see Fig. 5 right-side). These precipitates are identified as $M_{23}(C,B)_6$ phase using a EBSD mapping (see Fig.6).
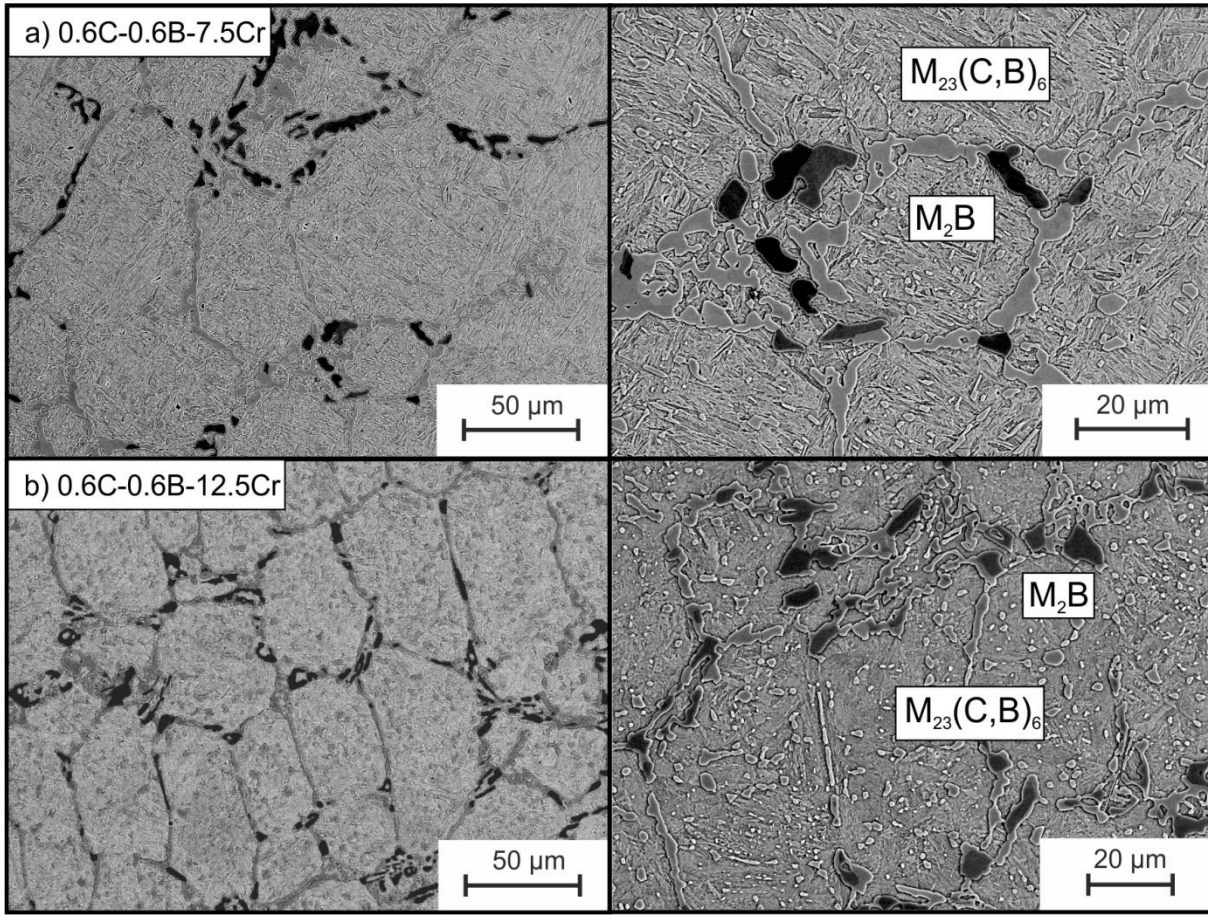
Fig. 5: SEM image of alloy 0.6C-0.6B-7.5Cr and 0.6C-0.6B-12.5Cr in BSE contrast (right: higher magnification)
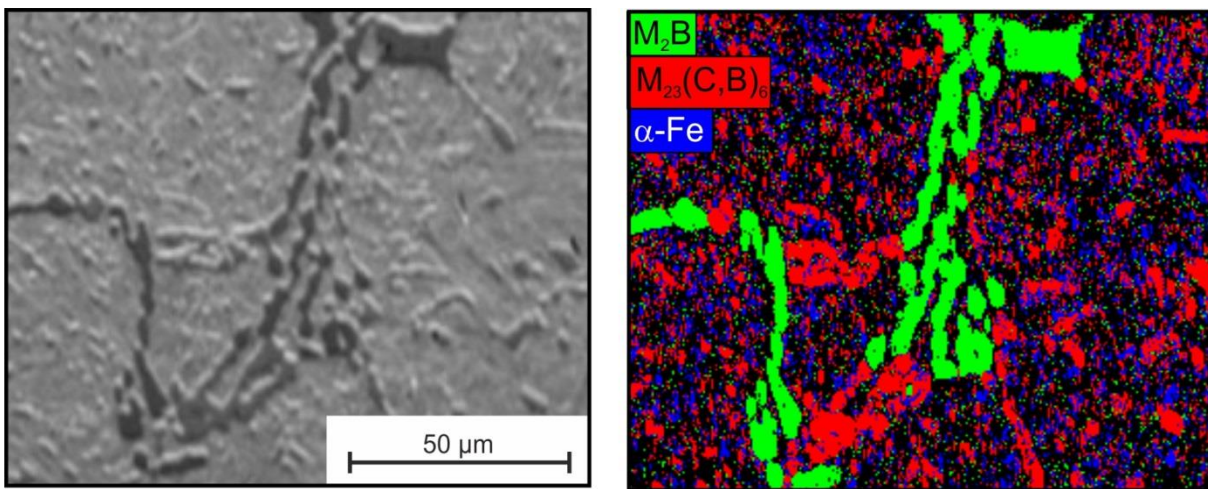
Fig. 6: SEM image in BSE contrast (left) and EBSD-mapping (right) of alloy 0.6C-0.6B-7.5Cr
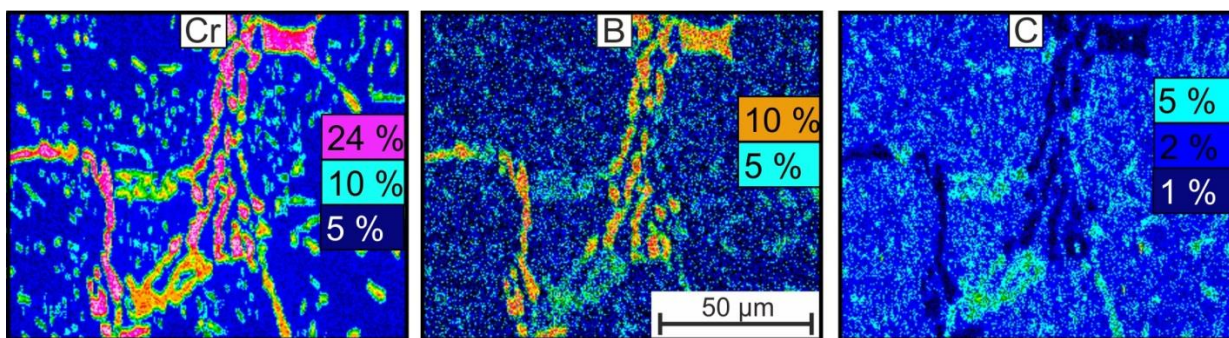
Fig. 7: Quantitative EDS mapping of alloy 0.6C-0.6B-7.5Cr (contents in mass%)

Fig. 7 illustrates the elemental distribution of Cr, B and C in alloy 0.6C-0.6B-7.5Cr for the same area shown in Fig. 6. It is shown that the elements Cr and B are enriched inside the M_2B phase. Though, C is enriched inside the $M_{23}(C,B)_6$ phase, which is also showing an intermediate Cr and B content. In addition, the results of EDS point measurements are depicted in Fig. 3 b). Thereby, it becomes evident that the Cr content present in the M_2B phases is approximately 10 atom% lower than estimated by the calculation. The deviation of the measurement and calculation is smaller in case of the $M_{23}(C,B)_6$ phase, which is overestimated about around 3 atom% by the calculation.
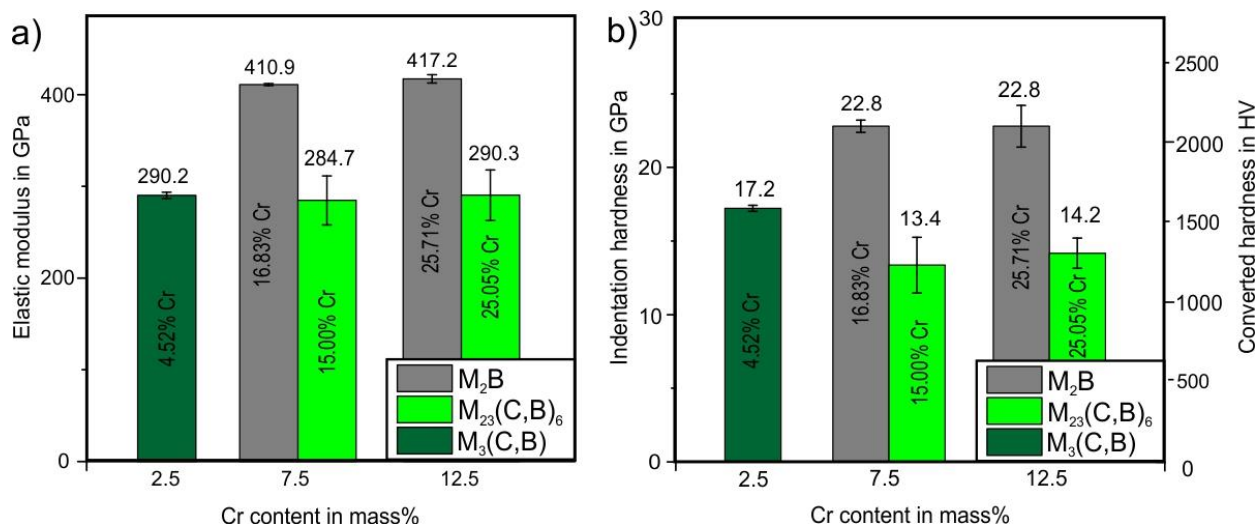
Fig. 8: Elastic modulus and hardness of the particular phases present in alloy 0.6C-0.6B-2.5Cr, 0.6C-0.6B-7.5Cr and 0.6C-0.6B-12.5Cr and EDS results for Cr content of the particular phases in atom%

The elastic modulus of the M_2B, $M_3(C,B)$ and $M_{23}(C,B)_6$ phases is shown in Fig. 8 a). The elastic modulus of $M_3(C,B)$ and $M_{23}(C,B)_6$ phases is almost equal with a value around 290 GPa, while the M_2B phase has a higher modulus with a value between 411 and 417 GPa. Fig 9 b) is showing the indentation hardness of the particular phases. The hardness is increasing from $M_{23}(C,B)_6$ phase with 14 GPa (~1300 HV), to 17.2 GPa (~1600 HV) in case of the $M_3(C,B)$ phase up to 22.8 GPa (2100 HV) for the M_2B phase. A dependency of the elastic modulus or indentation hardness of the M_2B and the $M_{23}(C,B)_6$ phase on Cr contents of the phases is not determined. An investigation of the indentation size effect showed that the indentation hardness of the Fe_2B phase is strongly decreasing up to a depth of 600 nm [15,16]. At higher indentation depth the hardness-curve levels out. However, a constant value is not reached up to an indentation depth of 1200 nm. In this study, the indentation size effect cannot be neglected, because the hardness was evaluated for indentation depths between 600-850 nm. However, the effect is small since an indentation depth of >600 nm is reached. In addition the results are consistent, because the sequence of averaging was kept constant in all measurements. Comparing the hardness of the Cr-rich, orthorhombic M_2B phase with a value for Fe_2B obtained at same indentation depth (~17.5 GPa – 1600 HV) shows, that the Cr-rich, orthorhombic M_2B phase (22.8 GPa - 2100 HV) is considerable harder [16]. This is in accordance with values between 1850-2100 HV0.1 [12,17] and a modulus of 399.4 GPa [5] found in the literature. Thereby it was shown, that the covalent bonds present in the crystal structures were strengthened by the presence of Cr.
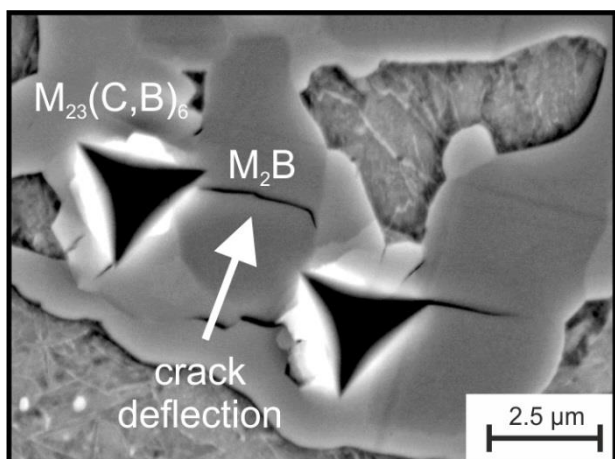
Fig. 9: Crack deflection at the interface M₂B /M₂₃(C,B)₆

Moreover, a deflection of cracks at the interfaces of separate hard phase types was observed in case of cracks were induced during the nanoindentation test, as shown in Fig. 9 for the M_2B /$M_{23}(C,B)_6$ interface. In context of wear resistance, a multi-component hard phase structure is beneficial as compared to a single-phased structure to impede crack propagation. This may attribute to the increase of fracture toughness of such hard phase networks.

Concluding, the element Cr is effective to stabilize the M_2B phase with a high hardness of 22.8 GPa, but is also accompanied by the stabilization of the $M_{23}(C,B)_6$ phase, which features a lower hardness (~14 GPa). Thus, further steps of alloy design are aiming on stabilizing the M_2B type boride, instead of the $M_3(C,B)$, $M_{23}(C,B)_6$ phases and simultaneously maintaining a sufficient C content for martensitic hardening.

In this manner, the effect of the elements Si and Mn is investigated in the following, whereby a C content of 0.75 mass% and a B content of 2 mass% are regarded. The volume content of the particular phases was calculated as a function of the Si content in Fig. 10 a) at a temperature of 700 °C, which corresponds to the stability region of the $M_{23}(C,B)_6$ phase in the pure Fe-C-B system (see Fig. 1 a). It becomes evident that Si is effectively destabilizing the $M_{23}(C,B)_6$ phase and stabilizing $M_3(C,B)$ and M_2B phase. Furthermore, the influence of the alloying element Mn at a temperature of 900 °C and an alloying content of 0.75 mass% C, 2 mass% B and 2.5 mass% Si is shown in Fig. 10 b). It is shown, that the volume content of the M_2B phase is increasing with the Mn content and at the same time the volume content of the $M_3(C,B)$ phase is decreasing.
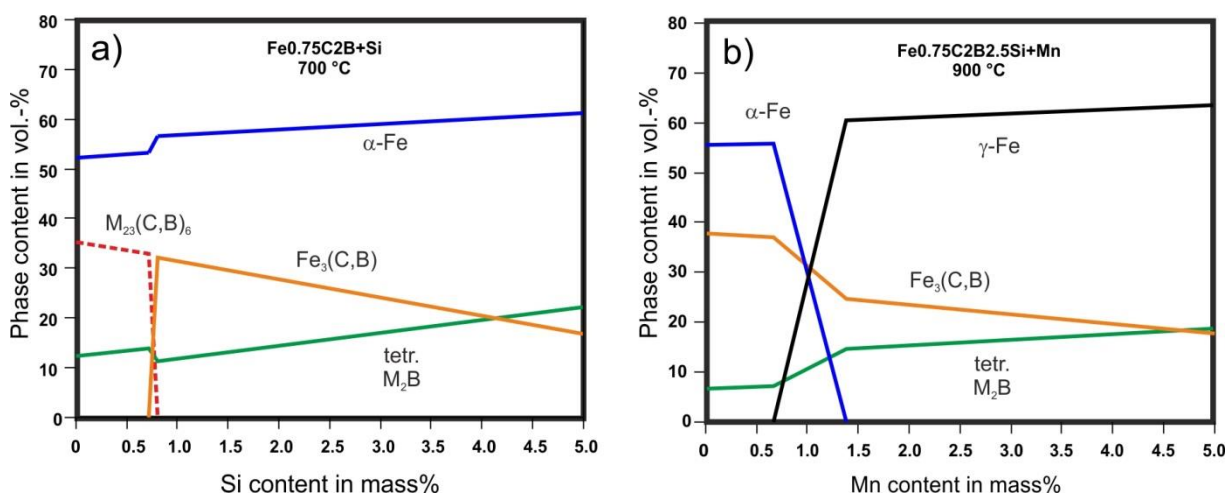

Fig. 10: Phase-quantity graphs of alloy a) Fe0.75C2B-XSi at 700 °C b) Fe0.75C2B2.5Si-XMn at 900 °C

In the following, a content of 2.5 mass% Si and 3.8 mass% Mn is used to stabilize ~20 vol.-% M_2B phase and the effect of Cr on the stability of the particular phases in this more technical alloying system is investigated using thermodynamic calculation in Fig. 11 a). In accordance with the effects observed in the quaternary system Fe-C-B-Cr (see Fig. 3), Cr is stabilizing the M_2B and $M_{23}(C,B)_6$ phase in alloy Fe0.75C2B2.5Si3.8Mn-XCr. However, the volume content of the M_2B phase is increased to 22 vol.-% (for Cr contents >2.2 mass%). Furthermore, the stability range of the tetragonal M_2B phase was extended and the overall Cr content necessary to induce the transformation into the orthorhombic M_2B phase is shifted to 6.8 mass% (instead of 4.5 mass%). A detailed characterization of this alloying system is given in a different study [18]. However, the

most important finding is depicted in Fig. 11 b, whereby hardness and Cr content of the particular phases present in tempered laboratory melts was experimentally measured. It was found that the transformation of the tetragonal into the orthorhombic M_2B phase is occurring at an overall Cr content between 4-6 mass%, which corresponds to a Cr content of 17.5 mass% inside the M_2B phase. The increase of Cr content and transformation of tetragonal into orthorhombic M_2B is accompanied by an increase in hardness of the M_2B phase (17 GPa to 21 GPa). An interdependence of hardness and Cr content was not found in case of the $M_{23}(C,B)_6$ phase.
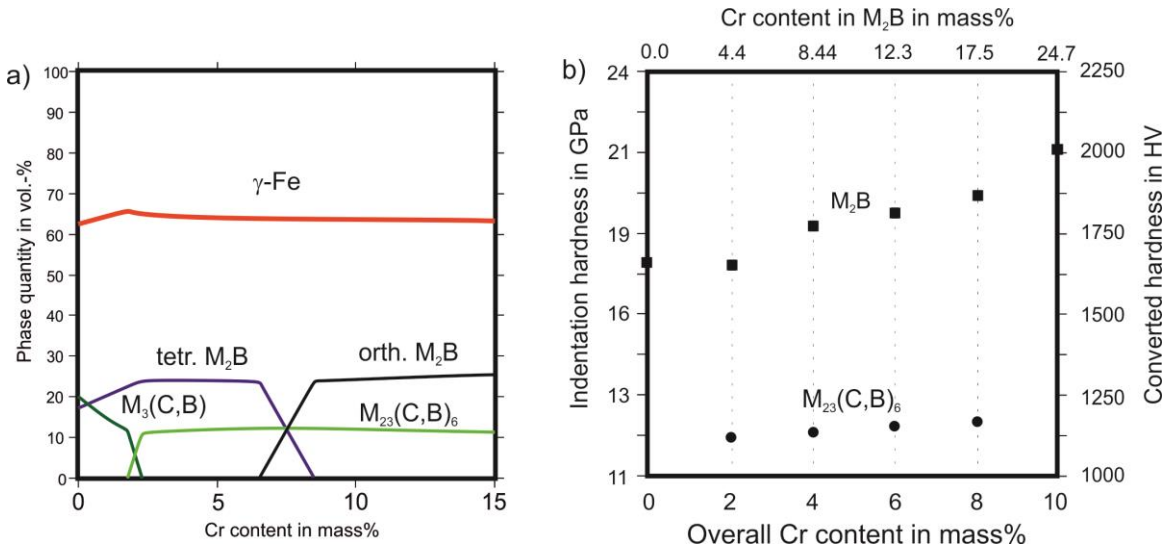
Fig. 11: a) Phase-quantity graph of alloy Fe0.75C2B2.5Si3.8Mn-XCr at 900 °C b) hardness and of M_2B and $M_{23}(C,B)_6$ phase in dependence of the Cr content [18]

The microstructure of the Fe0.75C2B2.5Si3.8Mn-XCr with 0 and 10 mass% Cr (see Fig 12) is showing eutectic hard phase structures consisting of the $M_3(C,B)$ and tetragonal M_2B phase (alloy 0Cr) and respectively $M_{23}(C,B)_6$ and orthorhombic M_2B phase (alloy 10Cr) besides a martensitic matrix. Concluding, Cr additions are connected to the stabilization of the Cr-rich orthorhombic M_2B phase but also to the stabilization of $M_{23}(C,B)_6$ phase and destabilization of the $M_3(C,B)$ phase. In addition, a finer distribution of the particular hard phases was achieved inside the microstructure.
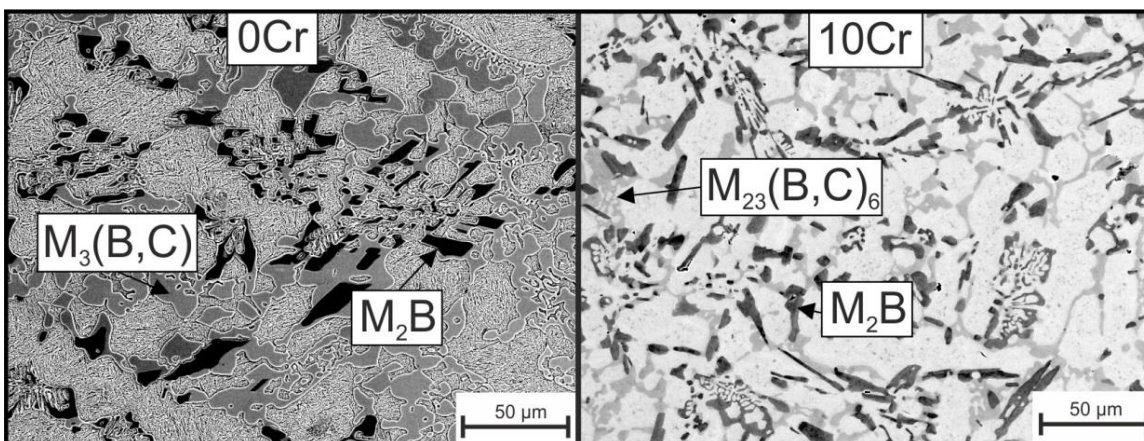

Fig. 12: SEM image in BSE contrast of alloy Fe0.75C2B2.5Si3.8Mn-XCr with 0 (0Cr–left) and 10 mass% Cr (10Cr-right)

The wear mark of a scratch test, performed for the alloy Fe0.75C2B2.5Si3.8Mn-10Cr, is shown in Fig 13 a). The governing micro-mechanism is micro-ploughing, in case of the iron matrix. In case of the hard phases pile ups, chips or cracks are not visible, that would indicate the micro mechanisms micro-ploughing, micro-fracturing or micro-cutting. It can be discussed, that the hard phases are plastically deformed and at the same time pushed inside the iron matrix, which is then also plastically deformed. Fig 13 b) is showing the scratch depth of the wear track. A reduction of the scratch depth up to 200 nm is observed, when the scratch passes a hard phase. Thereby, the M_2B

phase is more effective than the $M_{23}(C,B)_6$ phase. This is illustrating the effectiveness of the M_2B type hard phases in wear protection application and also indicating that the M_2B phase is preferable as compared to $M_{23}(C,B)_6$ phase.
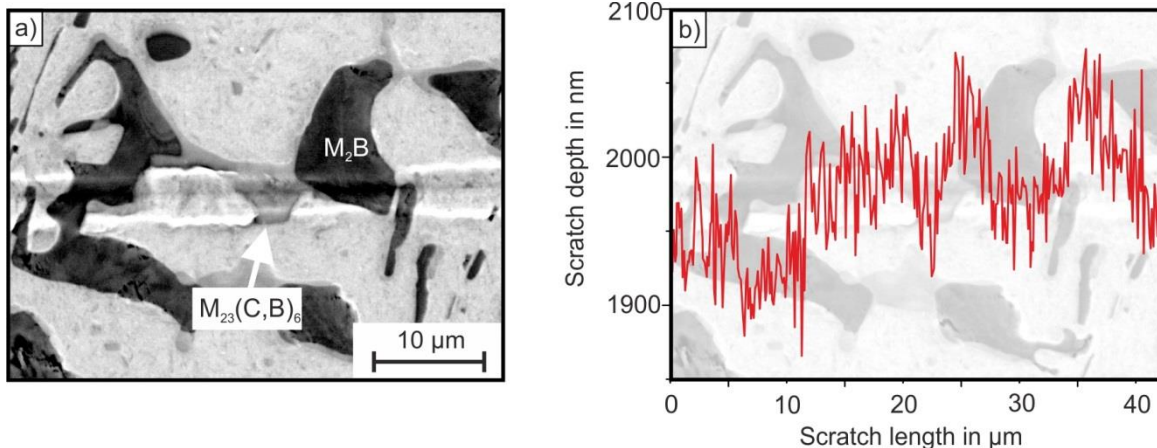

Fig. 13: a) SEM image in BSE contrast of the wear mark of a scratch test for alloy 10Cr (load 100 mN) b) graph of the scratch depth

3. SUMMARY

This contribution is focusing on alloy design based in the Fe-C-B system. The effect of Cr in the quaternary Fe-C-B-Cr was investigated with respect to phase stability and micromechanical properties of particular phases. Furthermore, the elements Cr, Si and Mn were used to stabilize the orthorhombic M_2B phase and to adjust a high Cr content as well as high hardness of the M_2B phase

- The Fe-C-B system was investigated with respect to phase stability and phase properties.
- The M_2B type hard phase was identified as preferable hard phase, because of its high hardness (~1500-1700 HV0.01 – 17.5 GPa), low carbon solubility and low metal to metalloid ratio.
- In the Fe-C-B system, the M_2B phase cannot be stabilized by B or C additions without exceeding a hard phase content of 45-50 vol.-%, which is accompanied by a loss of fracture toughness and forming capacity of the alloy.
- It was shown that Cr can be used to stabilize the orthorhombic M_2B phase.
- A hardness of 22.8 GPa (2100 HV) and elastic modulus of 415 GPa was measured for the orthorhombic Cr-rich M_2B phase which corresponds to an increase of ~400-600 HV as compared to tetragonal Fe_2B.
- Cr addition is also accompanied by the stabilization of the $M_{23}(C,B)_6$ phase, which features a lower hardness (~14 GPa) and lower elastic modulus (~290 GPa).
- In the Fe-C-B-Cr system, an interdependency of Cr content of the M_2B and the $M_{23}(C,B)_6$ phases and the micromechanical properties was not determined
- Cr, Si and Mn are used to further stabilize the M_2B phase, whereby a transition of the tetragonal M_2B into the orthorhombic M_2B is occurring at Cr contents between 4 and 6 mass%. This phase transition is connected to an increase of hardness of the M_2B type phases (17 GPa to 21 GPa).

ACKNOWLEDGEMENTS

References

[1] Berns H. Hartlegierungen und Hartverbundwerkstoffe: Gefüge, Eigenschaften, Bearbeitung, Anwendung. Berlin: Springer; 1998.

[2] Theisen W, Berns H. Ferrous Materials. Berlin, Heidelberg: Springer Berlin Heidelberg; 2008.

[3] XIE J, SHEN J, CHEN N, Seetharaman S. Acta Materialia 2006;54:4653–8.

[4] Jiang C, Srinivasan SG, Caro A, Maloy SA. J. Appl. Phys. 2008;103:043502.

[5] Xiao B, Feng J, Zhou CT, Xing JD, Xie XJ, Cheng YH, Zhou R. Physica B: Condensed Matter 2010;405:1274–8.

[6] Wang B, Wang DY, Cheng Z, Wang X, Wang YX. Chemphyschem a European journal of chemical physics and physical chemistry 2013;14:1245–55.

[7] DIN Deutsches Institut für Normung e. V. Metallische Werkstoffe - Instrumentierte Eindringprüfung zur Bestimmung der Härte und anderer Werkstoffparameter(14577). Berlin: Beuth Verlag; 2012. [October 23, 2015].

[8] Lentz J, Röttger A, Theisen W. Acta Materialia 2015;99:119–29.

[9] Berns H, Saltykova A, Röttger A, Heger D. Steel Res Int. 2011;82:786–94.

[10] C. Friedrich, G. Berg, E. Broszeit, C. Berger, Friedrich C, Berg G, Broszeit E, Berger C. Mat.-wiss. u. Werkstofftech 1997;28:59–76.

[11] Lentz J, Röttger A, Theisen W. Gefügeausbildung und mikromechanische Eigenschaften einzelner Phasen von untereutektischen Fe-C-B Legierungen, in: Mayer S, Panzenböck M, Clemens H (Eds.). Fortschritte in der Metallographie. Bonn: INVENTUM GmbH; 2014. p. 283–288.

[12] Ma S, Xing J, Liu G, Yi D, Fu H, Zhang J, Li Y. Materials Science and Engineering: A 2010;527:6800–8.

[13] Feng J, Xiao B, Zhou R, Jiang YH, Cen QH. Procedia Engineering 2012;31:676–81.

[14] Goldfarb I, Kaplan WD, Ariely S, Bamberger M. Philosophical Magazine A 1995;72:963–79.

[15] Campos-Silva I, Hernández-Sánchez E, Rodríguez-Castro G, Rodríguez-Pulido A, López-García C, Ortiz-Domínguez M. Surface and Coatings Technology 2011;206:1816–23.

[16] Rodríguez-Castro G, Campos-Silva I, Chávez-Gutiérrez E, Martínez-Trinidad J, Hernández-Sánchez E, Torres-Hernández A. Surface and Coatings Technology 2013;215:291–9.

[17] Suwattananont N, Petrova R. Solid State Sciences 2012;14:1669–72.

[18] Röttger A, Lentz J, Theisen W. Materials & Design 2015;88:420–9.

WEAR AT ELEVATED TEMPERATURES - MICROSTRUCTURAL INVESTIGATIONS OF TOOL MATERIALS AFTER HIGH TEMPERATURE SLIDING WEAR

M. Walter[1] (walter@wtech.rub.de, phone: +49(0)234-32-25962, fax: + 49(0)234-32-14104),

G. Egels[1], A. Röttger[1], W. Theisen[1]

[1]Lehrstuhl Werkstofftechnik, Ruhr-Universität Bochum, 44801 Bochum, Germany

Abstract

The presented study investigates the hardness and sliding wear behavior of cemented carbides and high-speed tool steels at elevated temperatures. Therefore, experimental analysis focus on the behavior and the microstructural changes of the aforementioned materials during sliding wear at room temperature, 400°C, and 600°C. Investigations are performed with respect to materials mechanical properties, which are represented by high temperature hardness measurements. As a result a main output of this study is an overview about the interdependencies of the microstructure and the high temperature hardness of tool materials (cemented carbides, high-speed steels). Results show that the absolute value of the room temperature and the high temperature hardness of cemented carbides are connected to the WC-carbide volume fraction. In contrast, the development of the hardness with increasing temperature is mainly influenced by the volume fraction and the characteristics of the binder matrix. In addition to the investigation of cemented carbides, the hardness of HS 6-5-3 steel grade at elevated temperatures was investigated. The value of the high temperature hardness of HS 6-5-3 high-speed steel is comparable to the hardness of cemented carbide materials, having higher binder content of 30 vol.-%.The absolute value and the temperature dependent course of the high temperature hardness of the high-speed steel are further influenced by the applied heat-treatment. Moreover, detailed wear experiments and microscopic analyses of the worn surfaces of selected materials are presented. These investigations show the main differences between room temperature sliding wear and high temperature sliding wear. In the systems studied, an increase in testing temperature leads to a rapid decrease of friction and wear rate. Microscopic investigations reveal that, the reason for this effect is the formation of a tribochemical wear layer at the surface of the wear bodies. This layer suppresses direct metallic contact and changes the characteristics of the tribological system. Discussed issues of high temperature sliding wear are the formation and stability of tribochemical wear layers, their connection to and support by the bulk material as well as the fracturing and damage of the layer-bulk-material compound.

Keywords: High temperature sliding wear, high temperature hardness, cemented carbides, high-speed steel, tribochemical wear layer

Introduction

Hot rolling is a key process of the industrial manufacturing chain of steel products. This forming process utilizes the low yield strength and increased formability of steels at elevated temperatures to enable lower rolling forces and higher degrees of reduction at the same time. Nevertheless, the contact of the roll surface and the hot product leads to a high temperature stress of the roll material. Roll materials have to endure the combination of high rolling forces and thermal stresses at the same time [1]. The relative motion between the roll surface and the product further promotes high temperature sliding wear. Therefore, materials used for hot rolling need to combine high strength and wear resistance at elevated temperatures [2]. Mechanical features like high temperature hardness consequently decide if and at which point of the hot rolling production line a

material can be used. Conventionally used materials of the intermediate and finishing stands of hot rolling lines are cemented carbides and high-speed steels. These materials combine a high hardness and a high wear resistance at elevated temperatures [1]. Nevertheless, the microstructural behavior of these materials under high temperature sliding wear has been investigated and compared insufficiently. Therefore, this study focuses on the sliding wear behavior of cemented carbide and high-speed steel materials at elevated temperatures with respect to mechanical properties, microstructural changes and the formation of tribochemical wear layers.

1. Experimental

Materials and heat treatment

The chemical compositions of the investigated materials and their hardness at room temperature are given in *Table 1*.

Table 1: Chemical composition (mass-%) and properties of the investigated materials in initial state

Notation	Co	Ni	Cr	W	V	Si	C	Fe	Hardness in HV10
WC- 10 mass-% Co	10.0	-	-	-	-	-	-	-	1736
WC- 30 mass-% Co	30.0	-	-	-	-	-	-	-	632
WC- 30.5 mass-% Co, Ni, Cr	14.0	15.0	1.5	-	-	-	-	-	589
C60	-	0.4	0.4	-	-	0.4	0.57	Bal.	216
HS 6-5-3 (QT)	-	-	4.0	6.4	2.8	0.5	0.90	Bal.	643

For experiments squared specimens (10 x 10 x 4 mm) of the cemented carbides, the high-speed steel (HSS) and the C60 steel were prepared. Steel grade C60 was further used as the counter-body in the wear experiments. Therefore, hemispheres (r = 5 mm, h = 10 mm) were produced from this material and heat-treated in accordance to the industrial manufacturing route (austenitized at 1000°C followed by a slow furnace cooling within 2h down to room temperature) to achieve a ferritic-pearlitic microstructure.

Cemented carbides were used in initial state, produced by liquid phase sintering. In contrast, HS 6-5-3 high-speed steel was used in as-cast quality and in heat-treated condition, further indicated as QT. The steel HS 6-5-3 was soft annealed at 650°C/ 6 h, air-quenched from 1150°C/ 15 min. and tempered three times at 500 – 620°C/ 2 h. [3]. After the heat-treatment, the surface of the specimens was ground with 18 µm abrasive paper and polished with a 3 µm and 1 µm diamond paste and ¼ µm SiO_2 polishing suspension. Experiments were done in this microstructural surface condition to enable comparable experimental conditions.

Microstructural examinations were performed by means of scanning electron microscopy (SEM) using a MIRA3 TESCAN SEM. Figures were taken at a working distance of 15 mm and an acceleration voltage of 20 keV in secondary electron (SE1) mode.

Hardness measurements and wear experiments

Wear and hardness experiments were performed with an Optimol SRV4 measuring device. Hardness testing was done by a specific modification of the measuring device. The measurements were carried out in accordance to DIN EN ISO 6507-1 with an applied load of 98.07 N (HV10) in a temperature range from room temperature (25°C) to 800°C. To avoid a strong oxidation of the surface of the specimen during testing, forming gas was used. High temperature hardness measurements were done using all aforementioned materials in heat-treated conditions. High temperature wear experiments were only done using the combinations C60 steel (pin) versus WC-30.5 mass-% Co, Ni, Cr (disc) and C60 steel (pin) versus HS 6-5-3 (disc). During the wear experiments polished C60 pins were tested against the polished surface of WC- 30.5 mass-% Co, Ni, Cr and HS 6-5-3 discs with a frequency of 30 Hz over a stroke distance of 1.5 mm applying a

normal force of 30 N (t = 1.5 h) in a sliding wear test. In accordance to the actual industrial process wear experiments were performed in air. Measured quantities of the sliding wear experiments are the volume loss of the C60 steel pin, the time dependent friction coefficient and the time dependent integral wear path of the tribological system.

The integral wear path is a measured quantity which contains information about the total wear occurring in the regarded system. It displays the height-loss of the pin and the disc sample in combination. Therefore, this value is a parameter of the entire system and not of a single constituent. Due to the measurement of the height of the pin and disc combination, thermal expansion during testing at elevated temperatures influences the value of the integral wear path strongly. This thermal influence needs to be regarded to avoid a systematic error. In this study the influence of the thermal expansion on the results of the wear tests was considered by a number of pre-tests. Pre-testing consisted of an exact determination of the temperature at the contact point of pin and disc, as well as several neutral temperature and thermal expansion tests with no motion between the parts. Using these neutral tests it was possible to determine the testing temperatures of pin and disc very precisely. Further it was possible to determine the critical point of thermal stability of the testing system. After this point thermal expansion reaches a constant level and wear tests can be performed under constant conditions.

2. Results and Discussion

In the first section, the results of the high temperature experiments using cemented carbides are presented. On the one hand, the investigations focus on the measured results of the hardness and wear experiments. On the other hand the microstructural changes of the cemented carbide materials during sliding wear at different temperatures are investigated. The second section deals with the corresponding results of the high temperature experiments using HS 6-5-3 steel.

2.1 High temperature properties and sliding wear behavior of cemented carbides

The microstructure of cemented carbides consists of a binder matrix (Co, Ni etc.) and a high volume fraction of tungsten carbide as a hard phase. The mechanical properties of cemented carbide materials are determined by the fractions and characteristics of these two components [4]. The materials WC- 10 mass-% Co and WC- 30 mass-% Co are a combination of a Co-matrix and a varying amount (90 or 70 mass-%) of WC-carbides. Besides the different Co-binder weight fractions the used materials possess different WC-carbide grain sizes (*Fig. 1*). While the grain size of WC- 10 mass-% Co is fine (< 1 µm) the grain size of WC- 30 mass-% Co is rather coarse (1-5 µm). These facts lead to a large difference of the room temperatures hardness of the materials [4]. The hardness of sample WC-10 mass-% Co is nearly 1100 HV10 higher than the hardness of sample WC- 30 mass-% Co. The difference of the room temperature hardness of the materials WC- 30 mass-% Co and WC- 30.5 mass-% Co, Ni, Cr (*Fig. 2*) is less pronounced. Although containing different binder compositions these cemented carbides have a similar hardness. In this case the nearly equal size and the amount of WC-carbides lead to comparable properties. The WC-carbide amount has a dominant influence on the mechanical properties, especially on the hardness and the bending strength [5]. An increase of the WC-carbide volume fraction increases the hardness strongly, while a change of the binder composition has only a minor influence.
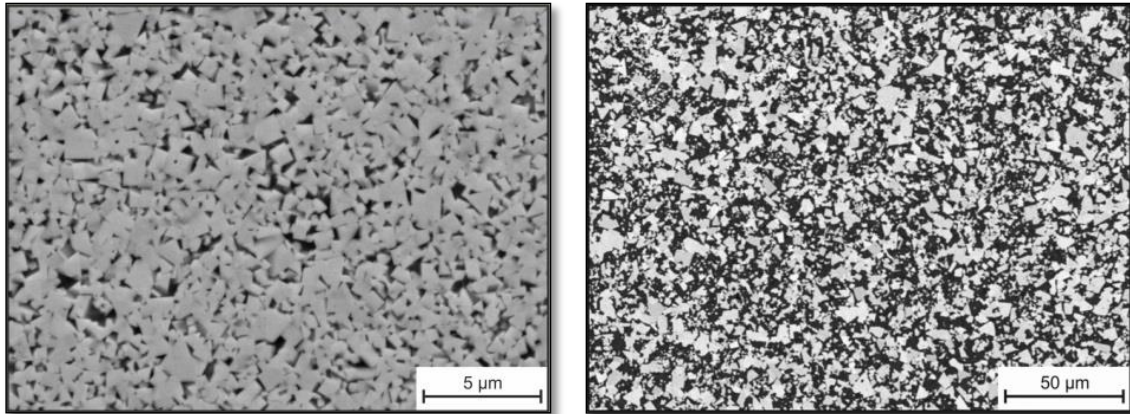
Fig. 1: SEM micrographs of the initial microstructure of the cemented carbide WC- 10 mass-% Co (left) and WC- 30 mass-% Co (right)
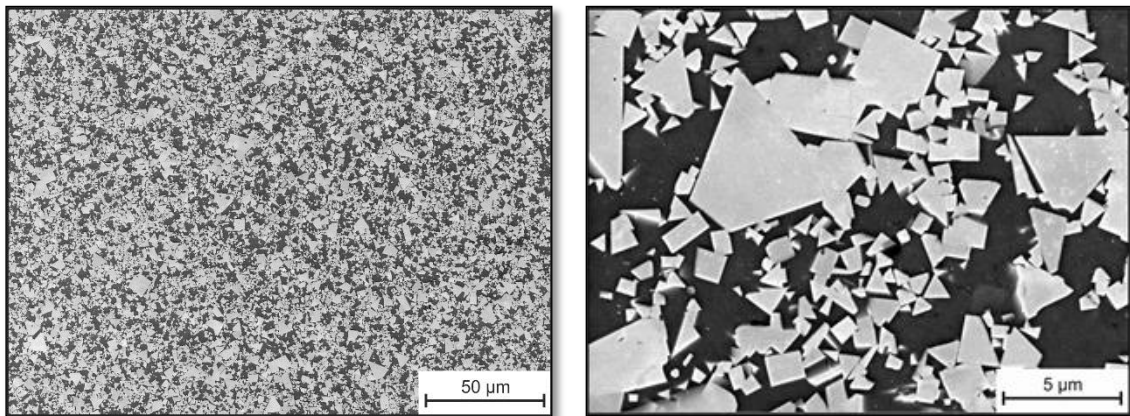

Fig. 2: SEM micrographs of the initial microstructure of the cemented carbide WC- 30.5 mass-% Co, Ni, Cr (left), close-up of the WC-carbide distribution (right)

Fig 3. a) shows that the room temperature results and correlations of the hardness of cemented carbides can be transferred to elevated temperatures. The depiction of the hardness depending on temperature of the cemented carbides shows the same hardness ratio between the materials at room temperature as well as at high temperature. Furthermore it can be seen that, the hardness of WC- 30 mass-% Co and WC- 30.5 mass-% Co, Ni, Cr decreases constantly with increasing temperature. In opposite the high room temperature hardness of WC- 10 mass-% Co decreases steeply with increasing testing temperatures. Reaching a temperature of 600°C the hardness of WC- 10 mass-% Co is about 25 % lower than the room temperature value. An even more pronounced hardness decrease occurs exceeding a temperature of 600°C. In a temperature range from 600 to 800°C hardness of sample WC-10 mass-% Co decreases to a value of about 600 HV10. These results show that the mechanical properties of WC- 10 mass-% Co are much more sensitive to a temperature increase than the properties of cemented carbide materials which contain a larger binder amount. Cemented carbides with a lower WC-content show much more stable high temperature hardness than WC- 10 mass-% Co. This behavior of WC- 10 mass-% Co can be traced back to its high overall hardness. Due to the much higher absolute value of hardness the hardness degradation at elevated temperatures is more pronounced. An additional explanation focusses on the fact that cemented carbides, which contain large fractions of WC-carbides, behave similar to polycrystalline WC. Cemented carbides with lower binder content are significantly harder than binder rich grades and show equal mechanical properties than single crystal WC-carbide. Furthermore, their hardness decreases very rapidly with increasing temperature, behaving again similar to single crystal WC-carbide [6]. Indentation can take place more easily at elevated temperatures, because of the rapid hardness loss. This lowers the wear resistance of cemented

carbides with high binder fractions at elevated temperatures, because of unstable high temperature properties. Cemented carbides containing a higher binder fraction show more stable properties at elevated temperatures. The higher binder fraction provides a better support of the WC-carbides. The binder phase excellently integrates the hard phases at elevated temperatures, because of more stable mechanical properties. This leads to a better performance of binder rich cemented carbides at elevated temperatures [7]. Consequently, hard phases are able to increase the wear resistance of these materials effectively. Therefore, WC- 30 mass-% Co and WC- 30.5 mass-% Co, Ni, Cr are suitable materials for applications stressed by high temperature sliding wear. According to this conclusion and to the fact that the high temperature hardness and microstructures of WC- 30 mass-% Co and WC- 30.5 mass-% Co, Ni, Cr do not differ significantly, only WC- 30.5 mass-% Co, Ni, Cr was regarded in sliding wear experiments. High temperature wear tests were done with the intention of finding general and specific aspects of the high temperature sliding wear behavior of cemented carbides. Experiments were done using a WC- 30.5 mass-% Co, Ni, Cr basic body (disc) and C60 steel as the counter body (pin). Therefore, ***Fig. 3 a)*** shows the hardness as a function of temperature of C60 steel. The comparison of the hardness of WC- 30.5 mass-% Co, Ni, Cr and C60 steel shows that independent of the testing temperature the hardness of C60 steel is lower than the hardness of WC- 30.5 mass-% Co, Ni, Cr. C60 steel will be the primary worn element of the regarded tribological system. The further analyses of wear mechanisms of the WC- 30.5 mass-% Co, Ni, Cr basic body need to consider this fact. ***Fig. 3 b)*** to ***d)*** present the results of the wear experiments (pin: C60/ disc: WC- 30.5 wt.% Co, Ni, Cr) at 25°C, 400°C and 600°C. The diagram of the volume loss of the C60 steel pin (***Fig.3 b***) shows a strong decrease of the volume loss of the pin by increasing the testing temperature from 25°C to 400°C [8]. The worn volume of C60 steel pin decreases in this temperature range to less than 10 % of the room temperature value. With a further increase of the testing temperature the volume loss of C60 steel pin shows no further decrease and rather shows a slightly growing volume loss. In addition to this ***Fig. 3 c)*** and ***d)*** show the time dependent integral wear path and friction coefficient during wear experiments. The course of the integral wear path depending on time is shown in ***Fig. 3 c)***. The graph of the experiment performed at 25°C shows a non-linear increase of the integral wear path during the first period of the test. The integral wear path increases strongly during this period. After this period the increase changes and becomes linear. It can be concluded that at the beginning of the presented room temperature sliding wear tests a bedding-in period occurs. After this period the system shows a constant wear behavior. The courses of the integral wear paths of the experiments at elevated temperature differ from the room temperature experiment. Firstly, the courses of the integral wear paths at elevated temperatures don't show a sharp increase at the beginning of the wear experiment. Secondly, the wear-rates at elevated temperatures are approximately independent on time. The increase of the integral wear path is continuous during the entire experiment. Furthermore, some discontinuities occur during the experiment. These discontinuities couldn't be prevented even after several repetitions of the tests. The ratio of the integral wear paths of the test at 400°C and 600°C are in accordance with the results of the measured volume loss of the C60 steel pin. The integral wear paths of the test performed at 600°C as well as the volume loss of the pin exceed the values measured during the test at 400°C. The results from the time dependent measurement of the friction coefficient complete the presented study. The friction coefficients of the wear tests at room temperature and elevated temperatures differ from each other strongly. The high temperature experiments show high friction coefficients, which scatter continuously and largely around a mean value. In addition, the friction coefficients scatter discontinuous with large deflections [8]. The room temperature wear test in opposite shows two periods of the development of the friction coefficient and less scattering. The friction coefficient decreases steadily during the first period of the experiment. After this it reaches a constant value and levels around this value with only minor scattering. The course of the friction coefficient shows no large deflections.
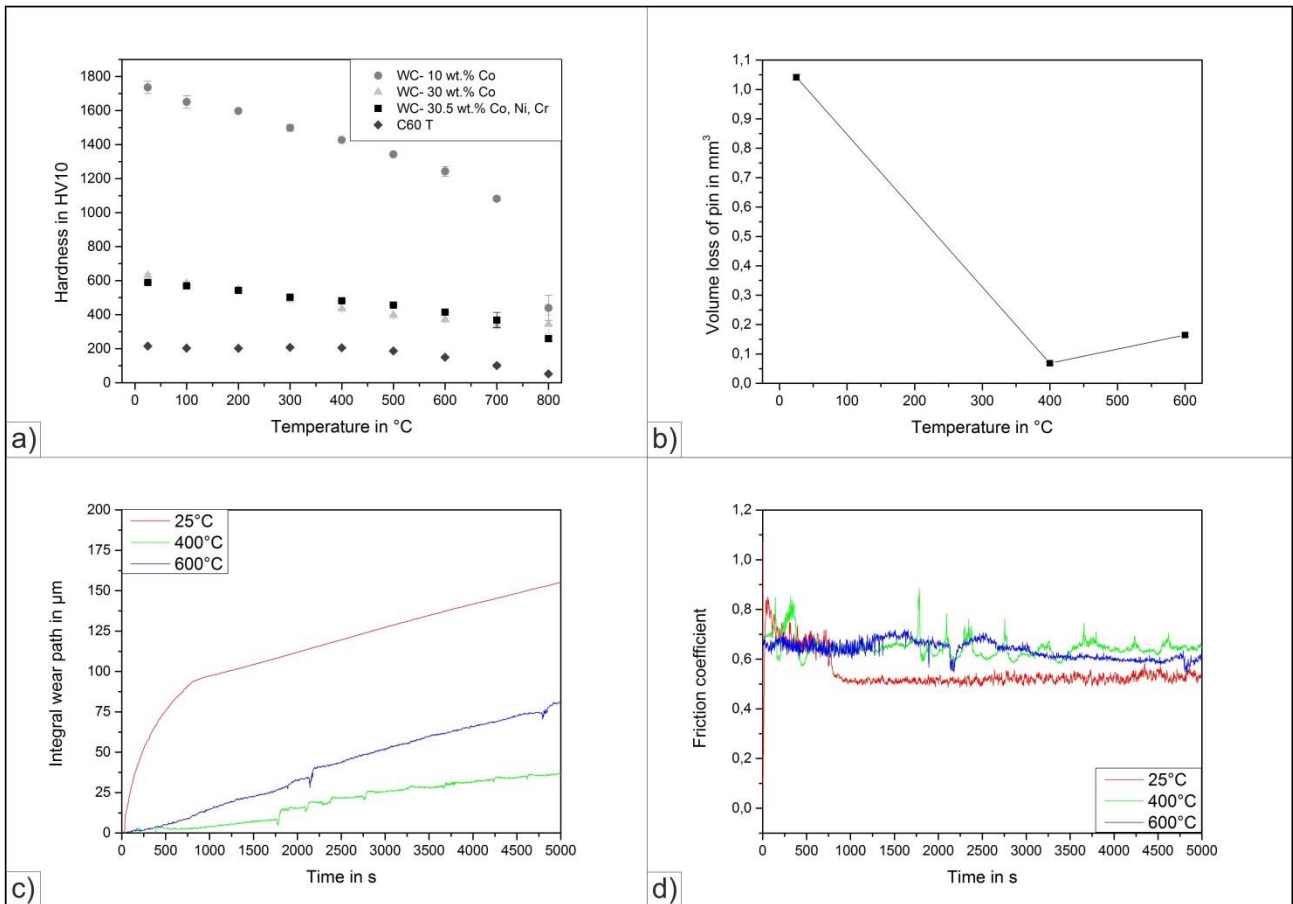
Fig. 3: a) Hardness depending on temperature of the cemented carbides and C60 steel, b) Volume loss of C60 steel pin during wear tests at 25°C, 400°C and 600°C, c) Integral wear path depending on time, d) Friction coefficient depending on time during wear tests at 25°C, 400°C and 600°C (pin: C60/ disc: WC- 30.5 mass-% Co, Ni, Cr)

To explain the ratios and developments of the wear rates and friction coefficients at different temperatures, it is necessary to investigate the microstructures of the cemented carbide material after sliding wear. Therefore, *Fig. 4* to *6* show SEM micrographs of the wear scar microstructures of the cemented carbide, tested at different temperatures.
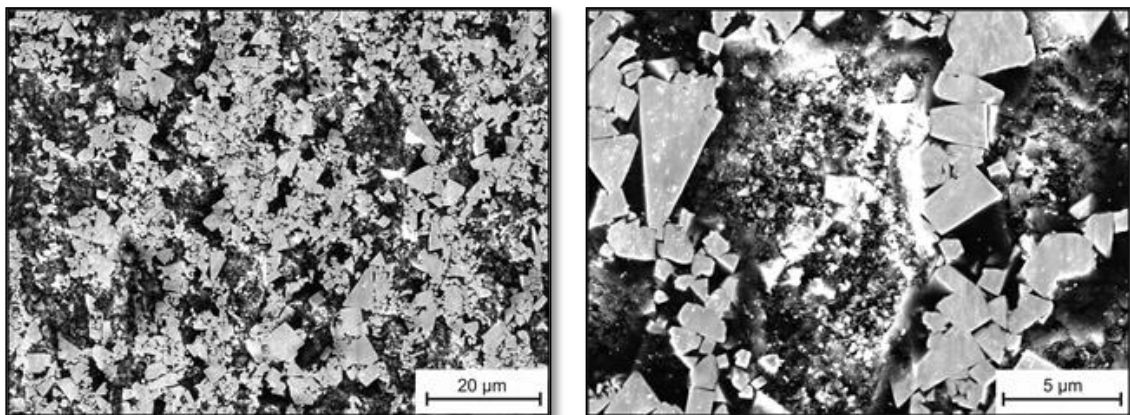
Fig. 4: SEM micrographs of the wear scar microstructure of the cemented carbide WC- 30.5 mass-% Co, Ni, Cr after 25°C wear test (pin: C60/ disc: WC- 30.5 mass-% Co, Ni, Cr)
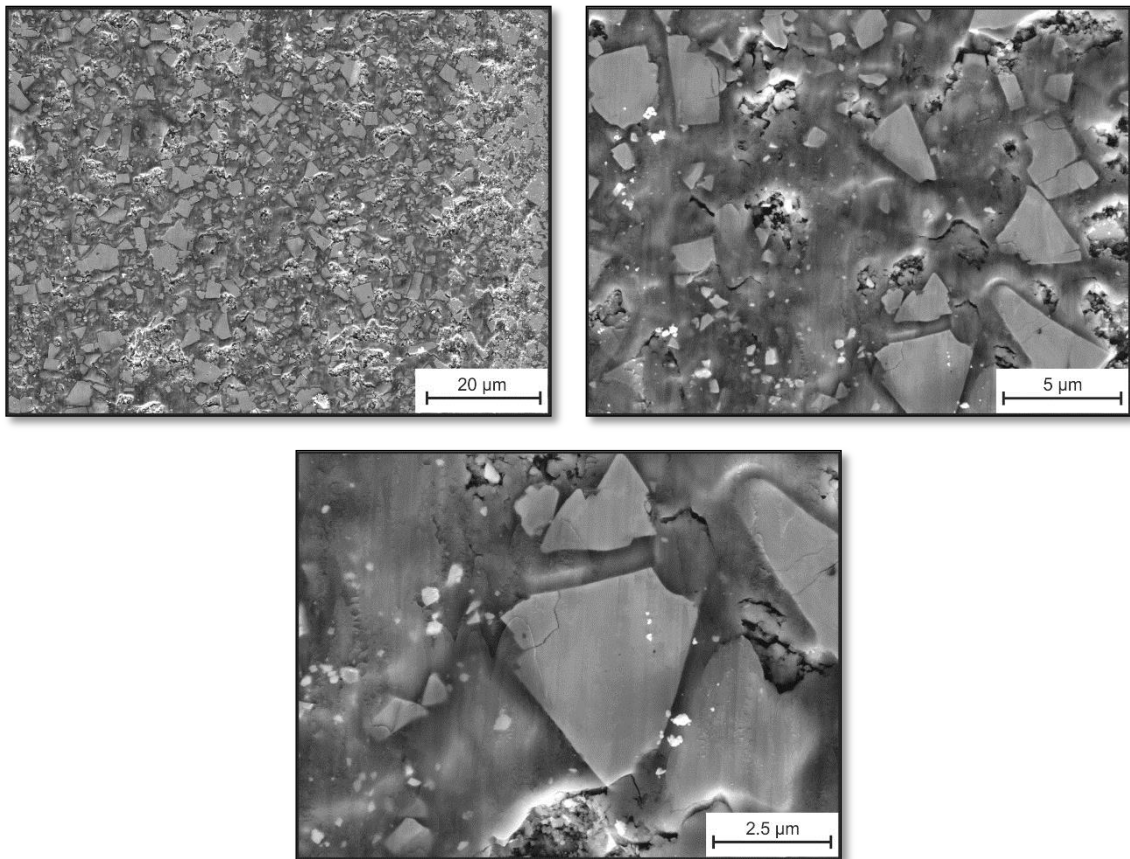
Fig. 5: SEM micrographs of the wear scar microstructure of the cemented carbide WC- 30.5 mass-% Co, Ni, Cr after 400°C wear test (pin: C60/ disc: WC- 30.5 mass-% Co, Ni, Cr)

The microstructure of the cemented carbide (**Fig. 4**) after the wear experiment performed at room temperature consists of a dominant amount of exposed WC-carbides. WC-carbides show no large impact of sliding wear. In comparison to the initial state, the shape and the distribution of the WC-carbides in the microstructure of the cemented carbide are unaffected. In contrast, the binder-matrix is affected strongly [9]. The matrix appears rough and cleft. Furthermore, a lot of wear particles are localized in the matrix areas. These observations indicate that the impact of a sliding wear exposure of cemented carbide at room temperature is mainly influenced by the binder-matrix. The tungsten carbides are only minor affected. Furthermore, it can be concluded that, the major amount of wear in the investigated tribological system is located at the much softer C60 steel pin. A comparison of the components of the tribological system shows that, the hardness and the content of hard phases of the cemented carbide are much higher. C60 steel possesses a lower wear resistance in contrast to cemented carbide, resulting in a higher mass loss of the C60 pin during testing. Nevertheless, the binder-matrix of the cemented carbide material shows signs of wear impact as well [9]. Thus, the properties of the binder-matrix are key factors which determine the wear behavior of cemented carbide materials and need to be considered during microstructural investigations in detail. The influence of an increased testing temperature on the wear behavior of cemented carbide materials can be seen in **Fig. 5** and **6**. The microstructures of the worn samples after high temperature testing differ significantly from the microstructures tested at room temperature. The main difference can be found in the formation of a tribochemical wear layer during high temperature wear. During wear the gathering of wear products (oxides, carbides and other wear particles) in the matrix areas leads to the formation of a well densified surface layer consisting of hard phases and wear products. This layer covers the whole wear scar. At 400°C the surface of the wear scar appears dense and well integrated. The WC-carbides are embedded into a compact layer. The matrix between the hard phases is compact and no large gaps between the carbides are visible. Nevertheless, cracks and small fractures occur in the layer.
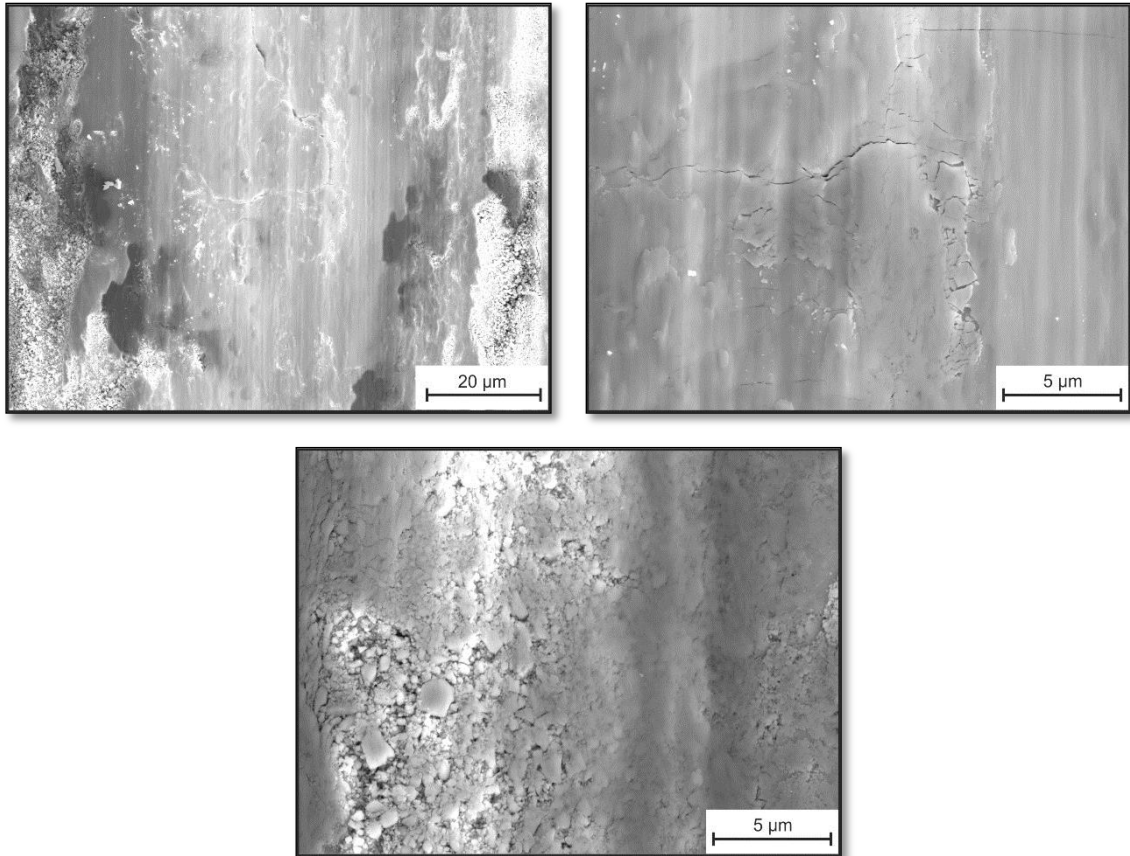
Fig. 6: SEM micrographs of the wear scar microstructure of the cemented carbide WC- 30.5 mass-% Co, Ni, Cr after 600°C wear test (pin: C60/ disc: WC- 30.5 mass-% Co, Ni, Cr)

Furthermore, the WC-carbides which are embedded into this layer show damages. Cracks occur through the hard phases and especially at their sharp edges. This damage of the hard phases did not occur during room temperature testing [10]. Reasons for this damage are assumed to be connected with the formation of the tribochemical wear layer and the embedding of the hard phases into this layer. It can be assumed, that the differences of the Co-base binder matrix and the wear layer properties (tensile strength and deformability) lead to this effect. The support of the hard phases by the binder matrix decreases during high temperature sliding wear. Thermal softening and the lower strength of the wear layer matrix, thereby promote brittle failure of the WC-carbides. Therefore, the formation of the tribochemical wear layer dominates the wear behavior of the cemented carbides at elevated temperatures. A self-protection of the components of the tribological system occurs, because the wear layer separates the components. This leads to lower wear of the cemented carbide disc and the C60 steel pin, because of no direct contact of the metallic materials. Nonetheless, a tribochemical wear layer formed by compacted particles suffers from low mechanical stability. Cracks and fractures, especially along the matrix-hard-phase-interface, exist in large number. These imperfections of the layer lead to the failure of the self-protection layer at a certain point respectively layer thickness. Damage occurs, parts of the layer and hard phases fracture and wear as well as friction increase. This effect leads to jumps in the curves of the integral wear path and the friction coefficient. Therefore, it can be concluded that the benefit of a self-protection layer is bordered by its stability. A thick and weakly compacted layer will fracture easily under mechanical load, leading to an increase in wear and friction. This effect is assumed to take place during the wear experiments at 600°C. The wear layer grows at this temperatures much more pronounced, leading very quickly to a critical thickness. A mechanical stressing of this instable surface leads to the failure of the tribochemical wear layer (**Fig. 6**).

2.2 High temperature properties of and wear behavior of HS 6-5-3 steel

The microstructure of the high-speed tool steel HS 6-5-3 is displayed in **Fig. 7**. In quenched and tempered state this steel possesses a hardness of approx. 640 HV10. The microstructure consists of annealed martensite and carbides of types MC, M_2C and M_6C [11, 12].
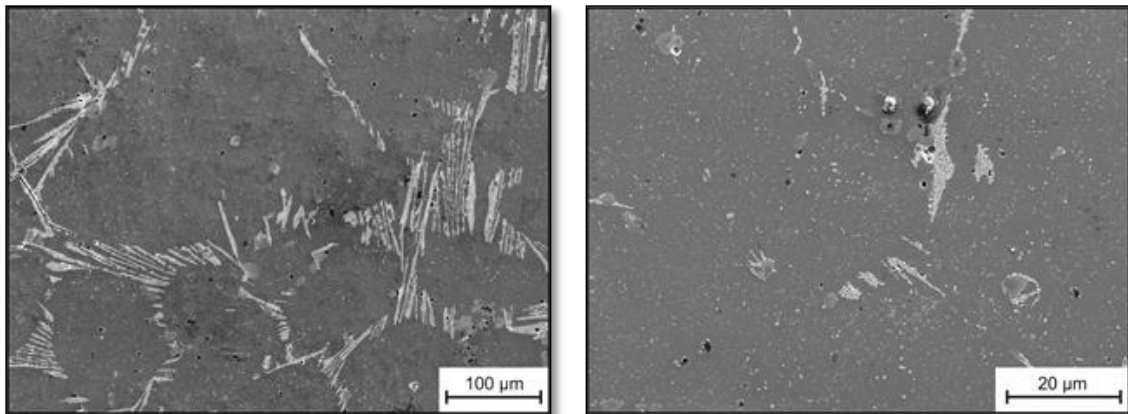

Fig. 7: SEM micrographs of the microstructure of the high-speed steel HS 6-5-3 in quenched and tempered state

Similar to the experiments performed in **section 2.1** the HSS was investigated due to its high temperature hardness and its performance during high temperature sliding wear (**Fig. 8**). **Fig. 8 a)** shows the development of the hardness of this steel as a function of temperature. Till 500°C the hardness decreases only slightly and in a constant way. Exceeding a temperature of 500°C the decrease in hardness is more pronounced, as a result a low hardness of less than 250 HV10 can be found at a temperature of 800°C. The strong decline in hardness falls exactly beyond the temperature range of the maximum tempering temperatures (500–600°C). Above this temperature the well-defined and stabilized microstructure during heat-treatment is affected by thermal softening mechanisms again pronouncedly. This results in a strong decrease in hardness. Therefore, the use of high-speed tool steels at elevated temperatures is affected and limited by the applied heat-treatment strongly [11]. The tempering stabilizes the mechanical properties of a HSS till a certain temperature. Above this temperature microstructural changes reoccur, leading to an unpredictable behavior of the material and the structural component. Regarding this fact the maximum tempering temperature of the studied HSS needs to be chosen above the maximum testing temperature. The performance of the HSS during sliding wear tests is shown in **Fig. 8 b)** to **d)**. Similar to the results of the wear experiments using the cemented carbide basic body, the wear rates (**Fig. b** and **c**) of these tests decrease with increasing temperature. Furthermore, the wear rates at any temperatures are lower than in the experiments presented in **section 2.1**. In contrast, the development of the time dependent friction coefficients depending on temperature differs from the previous presented courses. The courses of the friction coefficient between HSS and C60 steel during sliding wear show a contrarily development. At room temperature the friction coefficient is very high and is characterized by a large scattering [13]. At elevated temperatures the friction coefficient decreases and scatters only little.
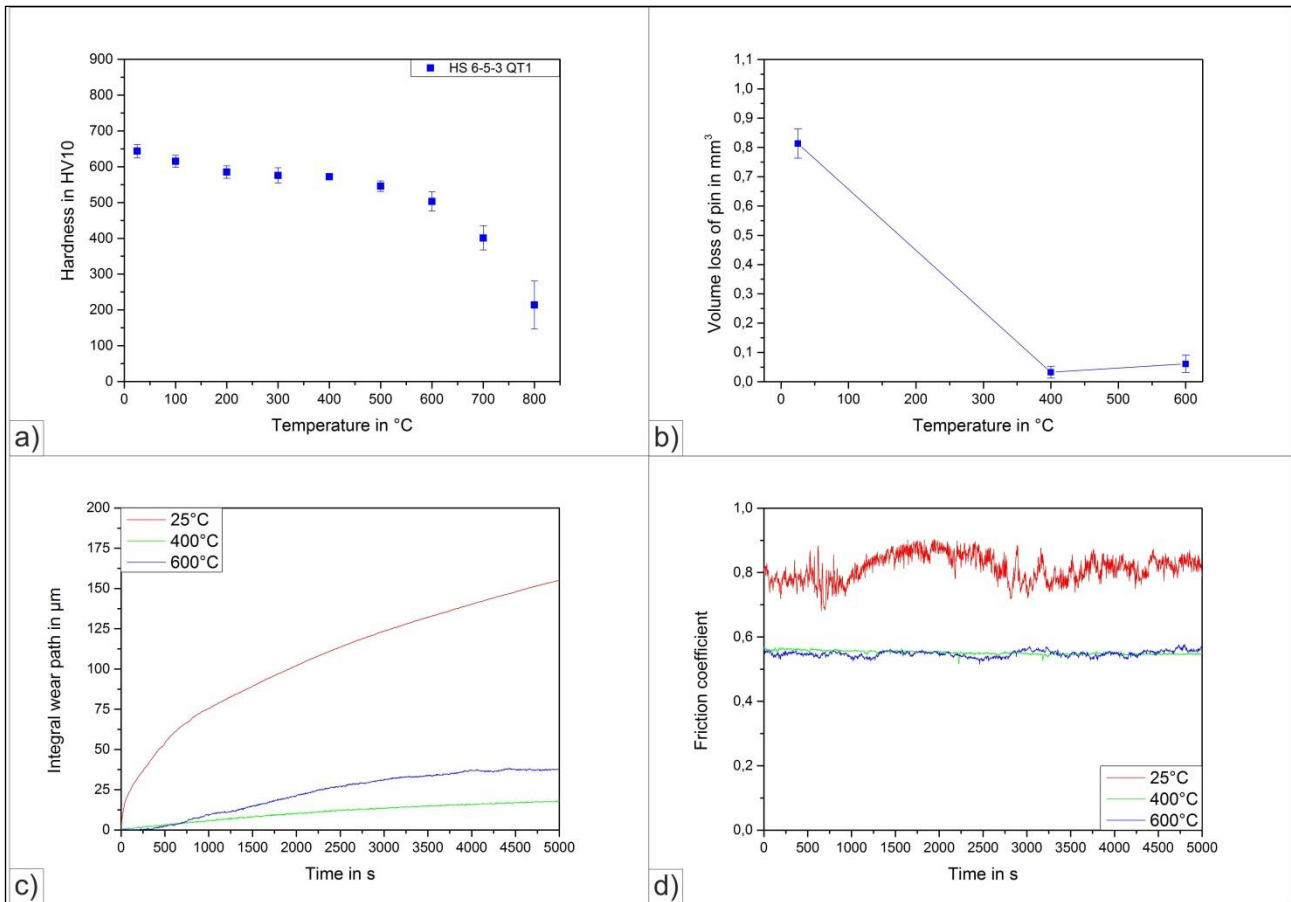
Fig. 8: a) Hardness depending on temperature of the steel HS 6-5-3 in quenched and tempered condition, b) Volume loss of C60 steel pin during wear tests at 25°C, 400°C and 600°C, c) Integral wear path depending on time, d) Friction coefficient depending on time during wear tests at 25°C, 400°C and 600°C (pin: C60/ disc: HS 6-5-3 in quenched and tempered condition)

With respect to the aforementioned results **Figs. 9** to **11** show the corresponding wear scars of the HSS basic bodies after sliding wear tests. Similar to the results obtained by the tests of **section 2.1** a change of the wear scar microstructure depending on testing temperature can be observed. The worn surfaces produced by experiments at elevated temperatures are covered by a tribochemical wear layer. The room temperature wear scars in opposite still indicate the initial high-speed steel microstructure after wear testing for 1.5 h (**Fig. 9**). More detailed analyses of these wear scars show grooves in the metal-matrix and small, loose wear particles. The carbides in the high-speed steel microstructure are less influenced by wear. Carbides are not scratched or ploughed and are well embedded in the steel matrix. Furthermore, wear products are agglomerated at the different types of carbides [14, 15].
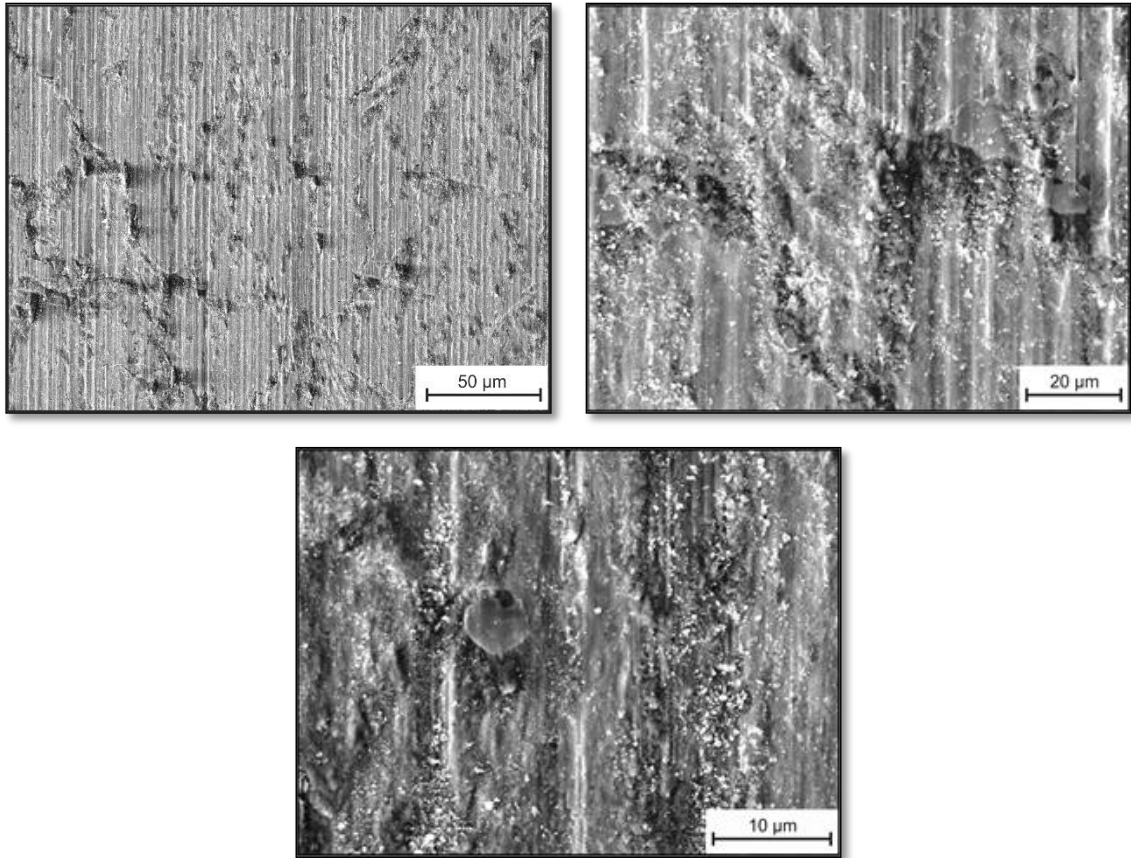
Fig. 9: SEM micrographs of the worn microstructure of the steel HS 6-5-3, after 25°C wear test (pin: C60/ disc: HS 6-5-3 QT1)

The wear scars resulting from experiments at elevated temperatures are entirely covered by a tribochemical wear layer. No indications of the initial microstructure can be detected from a top view of the worn samples at a temperature of 400°C. Further the tribochemical wear layer produced by testing at 400°C and 600°C are not similar and indicate different structures. The wear scar resulting from 400°C sliding wear test is covered entirely with a partly dense and partly fractured layer (**Fig. 10**). This tribochemical layer appears mainly oxidic. The SEM analyses show that the layer consist of compacted wear products. These products form an oxide-rich intermediate phase between the high-speed steel and C60 steel, which lowers wear at elevated temperature by preventing direct metallic contact. Unfortunately a lot of areas of this layer show large cracks and fractures. The high brittleness of the oxide layer leads to a quick crack initiation resulting in pronounced failure under mechanical load [16].
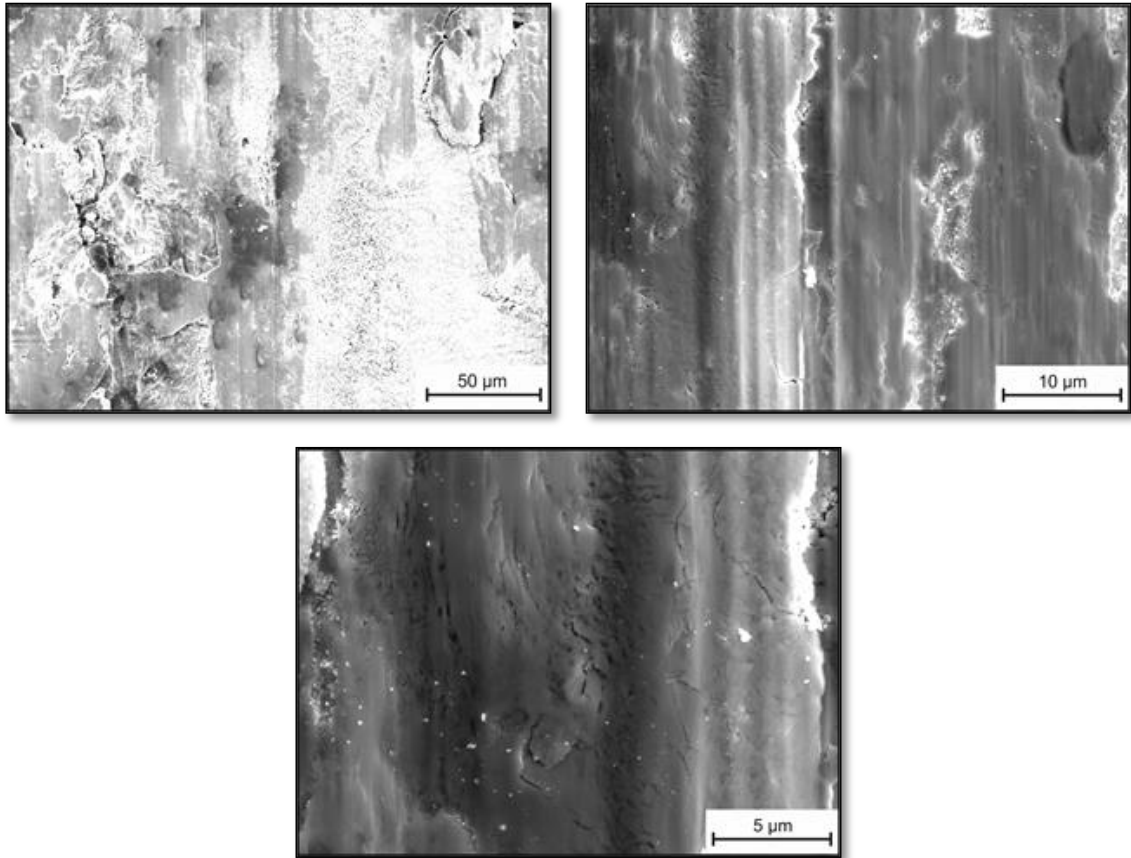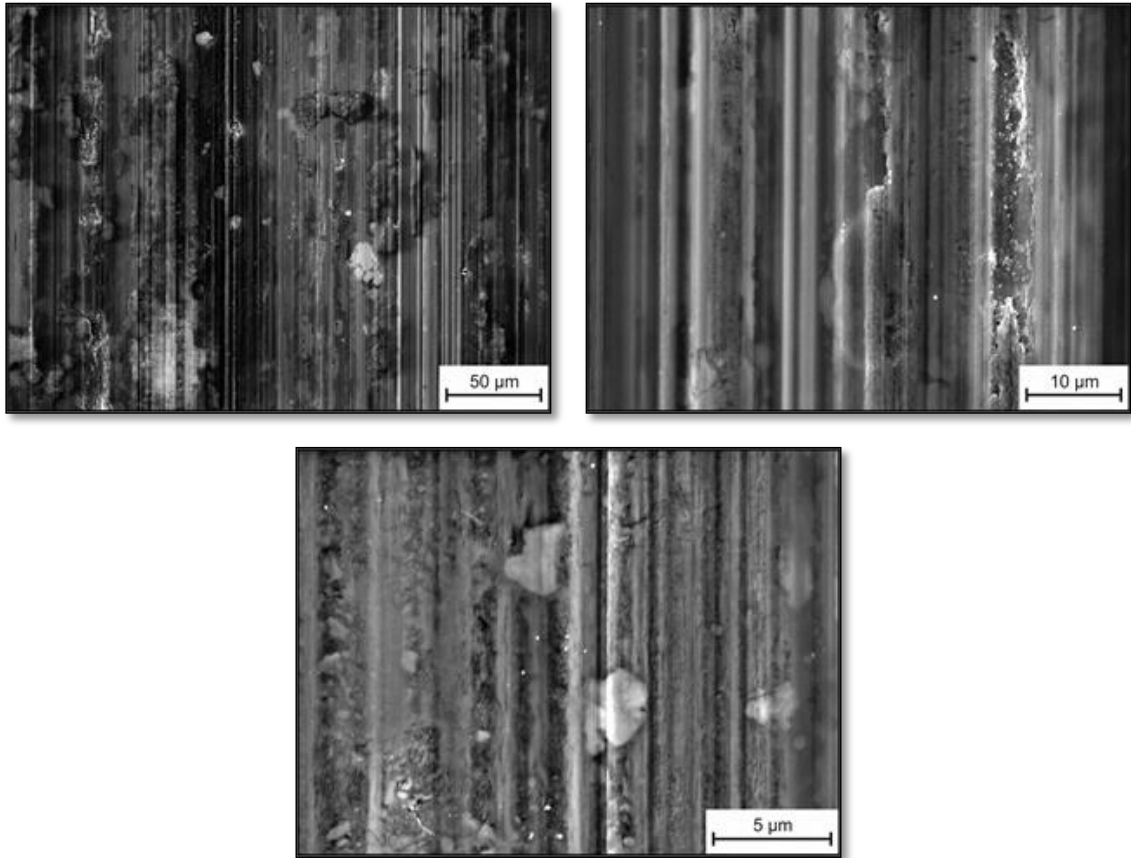
Fig. 10: SEM micrographs of the wear scar microstructure of HS 6-5-3, after 400°C wear test (pin: C60/ disc: HS 6-5-3)

The tribochemical wear layer of the wear test at 600°C in opposite does not show largely fractured areas. The layer appears more dense and compact. In addition wear grooves are visible which are comparable to the wear grooves appearing at room temperature (***Fig. 11***). Furthermore, the wear layer is not homogeneous. It consists of small and large particles compacted to a dense layer. Small cracks inside the layer are visible. These cracks are localized at the grooved and fractured areas. Summing up, the presented results show that the microstructural state of the wear scars of the high-speed steel depending on temperature is strongly dependent on the formation of a tribochemical wear layer during testing. The formation and influence of this wear layer is much more pronounced at elevated temperatures than at room temperature. Inside a tribological system a wear layer changes the surface characteristics of the components and thereby changes the mechanisms of friction and sliding wear. This influence is more pronounced at elevated temperatures, because thermal activated processes, like oxidation, are accelerated at elevated temperatures [16].

Fig. 11: SEM micrographs of the wear scar microstructure of HS 6-5-3, after 600°C wear test (pin: C60/ disc: HS 6-5-3)

Concluding, the high temperature wear behavior of tool materials depends on several key factors. Firstly, the microstructural constitution and the mechanical properties of the tool material at elevated temperatures are important influencing factors which decide about the performance of a material [17]. On the one hand, the material needs to bare the applied loads without fracturing. On the other hand the bulk material needs to support the formed tribochemical wear layer, to benefit from its properties. Therefore, high hardness and tensile strength at elevated temperatures improve the resistance against the impact of high temperature wear. The microstructural constitution in addition decides about the formation and stability of the formed wear layer. Hard phases can act as punctual microstructural barriers during sliding wear and are initial points of the layer formation. Thus, their distribution, size, shape, type and chemistry need to be considered. The formation of the wear layer, its stability and connection to the bulk material need to be considered as well. At elevated temperatures the characteristics of the wear layer itself are of great relevance. An increased oxidation tendency of metallic materials at elevated temperatures promotes the formation of a tribochemical layer. Therefore, the development and growth of a characteristic surface zone is much more pronounced. A formed wear layer influences sliding wear more significantly. Including a wear layer, surfaces covered by a tribochemical layer of oxides, wear particles (carbides and metal-matrix fragments) and third bodies from the ambient medium transfer the relative motion. This suppression of direct metallic contact essentially changes the characteristics of the tribological system. It is possible to decrease wear and friction and consequently improve the performance of a tool material. Nevertheless, it is also possible to damage the basic tool material by an unstable layer. A thick and brittle layer will fracture pronouncedly during application. Large areas of damaged surfaces can form and influence the process. Fractured areas act as initial points of further damages which can propagate from the surface into the bulk material leading to materials failure. Therefore, the structure and stability of the wear layer itself is a further key factor of high temperature wear. The differences of the wear layer characteristics of cemented carbides and high speed steels are depicted well by the results of

this study. Both materials respond to sliding wear at elevated temperatures with the formation of a wear layer. The structure of the wear layers nevertheless differs significantly. The temperature dependence of the layer structure varies with the basic tool material tested. At 400°C the cemented carbide material forms a tribochemical wear layer, which is well densified. Hard phases and wear products form a connected surface zone. This interaction and reciprocal support of hard phases and compacted wear products forms a self-protection of the materials and decreases wear. At a temperature of 600°C the structure of the wear layer changes significantly. The layer is more homogeneous and shows no embedded carbides. It can be assumed that the high oxidation tendency of the cemented carbide material and the C60 steel lead to a rapid growth of the tribochemical wear layer at 600°C. Overstepping a critical thickness the layer forms cracks and fractures under mechanical load. This decreases the positive influence of a high temperature wear layer. The high-speed steel moreover forms a wear layer with a dense and well compacted structure at 600°C testing temperature. In opposite to the cemented carbide material the surface zone of the high-speed steel is well densified and integrated at temperatures above 400°C. Nevertheless, the characteristics of the observed surface structures are very complex and need to consider various parameters like the oxidation tendencies and the high temperature stability of the used tool materials and its components, as well as the chemical and microstructural composition of the layer itself [18]. Therefore, further studies need to focus on the characteristics of the wear layer and its interaction with the bulk material.

3. Conclusions

The following key results were found within this work:
- The absolute value of the high temperature hardness of cemented carbide materials is directly dependent on the WC-carbide volume fraction, the development of the hardness with increasing temperature in opposite rather depends on the volume fraction characteristics of the matrix.
- The absolute value of high temperature hardness of high-speed steels is comparable to cemented carbide materials with larger matrix fractions. The absolute value and the temperature dependent course of the high temperature hardness of HSS are directly related to the applied heat-treatment. Therefore, they can be influenced and increased by an optimization of the heat-treatment.
- High temperature hardness and the performance of a material under high temperature sliding wear are directly correlated. A high hardness and tensile strength at elevated temperatures increase the resistance of a material against the mechanisms of wear at elevated temperatures, because of the increased support and integration of the wear affected surface zone.
- During sliding wear the cemented carbide and high-speed steel tool materials show the same temperature dependency. In the studied systems an increase in testing temperature leads to a rapid decrease of friction and wear rate.
- The reason for decreasing wear and friction is the formation of tribochemical wear layers. These layers suppress direct metallic contact and change the characteristics of the tribological system. A protection of the bulk material by the tribochemical layer occurs.
- Key issues of the topic of tribochemical wear layers are the formation and stability of these layers, their connection to and support by the bulk material, as well as the fracturing and damage of the layer-bulk-material compound.

Acknowledgements

References

[1]   M. Nilsson, M.Olsson, Wear, 307 (2013), pp. 209-217

[2]   M. Pellizzari, D. Cescato, M.G. De Flora, Wear, 267 (2009), pp. 467-475

[3]   R. Bhattacharya, G. Jha, S. Kundu, R. Shankar, N. Gope, Surface & Coatings Technology, 201 (2006), pp. 526-532

[4]   W.H. Rackoff, E.L. Klaphake, Publication of Iron and Steel Society, (1990), pp. 281-306

[5]   X. Wang, K. S. Hwang, M. Koopman, Z. Fang, L. Zhang, Int. Journal of Refractory Metals and Hard Materials, 36 (2013), pp. 46-51

[6]   M. Lee, Metallurgical Transactions A, 14 A (1983), pp. 1625-1629

[7]   A. Fischer, Habilitation, Ruhr-Universität Bochum (1994)

[8]   J. Pirso, S. Letunovitš, M. Viljus, Wear, 257 (2004), pp. 257-268

[9]   K. Bonnya, P. De Baetsa, Y. Pereza, J. Vleugelsb, B. Lauwersc, Wear, 268 (2010), pp. 1504-1517

[10]   S. Balamurugan, G. Mathan, A. Dey, G. Mukherjee, M. Sahu, J.C. Pandey, Engineering Failure Analysis, 26 (2012), pp. 182-191

[11]   J. Wook Park, H. Choon Lee, S. Lee, Metallurgical and Materials Transactions A, 30A (1999), pp. 399-409

[12]   H. Qua, B. Liao, L. Liu, D. Li, J. Guoa, X. Renc, Q. Yanga, CALPHAD: Computer Coupling of Phase Diagrams and Thermochemistry, 36 (2012), pp. 144-150

[13]   C. Rodenburg, W.M. Rainforth, Acta Materialia, 55 (2007), pp. 2443-2454

[14]   H. Zhu, Q. Zhu, A. Tieu, B. Kosasih, C. Kong, Wear, 302 (2013), pp. 1301-1318

[15]   N.F. Garza-Montes-de-Oca,W.M. Rainforth, Wear, 267 (2009), pp. 441-448

[16]   Q. Zhu, H.T. Zhu, A.K. Tieu, M. Reid, L.C. Zhang, Corrosion Science, 52 (2010), pp. 2707-2715

[17]   A.J. Gant, M.G. Gee, Wear, 251 (2001), pp. 908-915

[18]   C. Rynio, Dissertation, Ruhr-Universität Bochum (2014)

Author Index